BEHAVIOUR OF LIGHTWEIGHT CONCRETE BEAMS STRENGTHENED WITH CARBON FIBRE REINFORCED POLYMER IN SHEAR

Mustafa Hameed Farhan Al-Allaf

School of Computing, Science and Engineering

College of science and Technology

University of Salford, Salford, UK

Submitted in Partial Fulfilment of the Requirements for the Degree

Doctor of Philosophy, February 2017

Behaviour of Lightweight Concrete Beams Strengthened with Carbon Fibre Reinforced Polymer in Shear

Mustafa Hameed Farhan Al-Allaf
School of Computing Science and Engineering, University of Salford, United Kingdom
2017

ABSTRACT

Epoxy bonded fibre reinforced polymer (FRP) composites are widely used for the retrofit of ailing reinforced concrete structures, for both shear and flexure. This technology provides unique features compared with conventional retrofitting systems. Among these FRP has good corrosion resistance, lightweight and excellent mechanical properties. Furthermore, the manual lay-up system allows using the FRP reinforcements to any member's shape.

A significant amount of research has been carried out to understand the shear behaviour of normal weight concrete (NWC) members strengthened with FRP composite. Increasing interfacial (shear) and normal stresses with increasing plastic deformation lead to FRP debonding and/or FRP rupture failures. The response of strengthened concrete members subject to load is governed by the bond strength and the material characteristics of the epoxy bonded FRP reinforcement and the concrete. However, lightweight concrete (LWC) beams, which use Pulverised Fuel Ash (Lytag) instead of normal aggregates, retrofitted to increase shear capacity with epoxy bonded FRP have not been studied comprehensively to understand the characteristics of FRP/ lightweight concrete joining and the shear resisting mechanism.

This study comprises of experimental, numerical and analytical investigations of the interface behaviour between carbon fibre reinforced polymer (CFRP) reinforcement and lightweight and normal weight concrete. In addition, the shear behaviour and failure modes of LWAC and NWAC beams is studied. The influence of various variables on the response of the CFRP/lightweight concrete joint and the shear response of reinforced concrete beams are examined by testing large numbers of the experimental series.

Three-dimensional non-linear finite element and mathematical models are employed to study the response of the CFRP-to-lightweight concrete interface and the FRP contribution to the shear resistance of lightweight concrete beams have been proposed in this study. Proposed finite element models and relationships were compared with experimental results. The results

of the finite element and analytical models demonstrated the capability of these models in predicting the interface behaviour of lightweight concrete/FRP joints and the shear strength gained due to CFRP reinforcement used to retrofit lightweight concrete beams in shear.

ACKNOWLEDGMENTS

This thesis would not have been possible without the help and support of many people. I would like to gratefully acknowledge the contributions of those named below and those whom I may have unfortunately forgotten.

Above all, I would like to thank my supervisor, ***Dr. Laurence Weekes***, for the kind support, patient guidance, and valuable suggestions that helped to produce this thesis in its present form. Thank you to ***Dr. Levingshan Augusthus-Nelson*** for his guidance with analytical modelling.

I am indebted to the financial support by the Iraqi government. And I would like to acknowledge the staff of Cultural department in Iraq embassy in the United Kingdom. Sincere thanks are expressed to School of Computing Science and Engineering of the university of Salford for providing the experimental facilities and technical support to undertake this research.

I would like to thank all my family members, especially my mother and my wife ***Noor Al-Hadeethi*** for supporting and encouraging me to pursue this degree. Without my wife's encouragement, I would not have finished the ***PhD degree***.

LIST OF PUBLICATIONS

- Al-Allaf, M.H., Weekes, L., Augusthus-Nelson, L. and Leach, P., (2016). An experimental investigation into the bond-slip behaviour between CFRP composite and lightweight concrete. Construction and Building Materials Journal, 113, 5–27.

- Al-Allaf, M.H., Weekes and L., Augusthus-Nelson, (2015). Experimental study on bond-slip behaviour between CFRP sheets and lightweight concrete. In proceedings of the 8th Biennial Conference on Advanced Composites in Construction (ACIC 2015), Cabmbridge, UK.

- Al-Allaf, M.H., Weekes and L., Augusthus-Nelson, (2016). Experimental study on bond-slip behaviour between CFRP sheets and lightweight concrete. In proceedings of the 2nd International Conference on Mechanics of Composites (MECHCOMP2 2016), Porto, Portugal.

Papers submitted

- Al-Allaf, M.H., Weekes, L. and Augusthus-Nelson, (2016). Shear behaviour of lightweight concrete beams strengthened with CFRP composite. Paper submitted for publication in Composite Structures Journal (submitted on 30 Nov 2016) (Under review).

- Al-Allaf, M.H., Weekes, L., Augusthus-Nelson, L. and Yu Wang (2016). Analytical Modelling of the Load-Slip Behaviour between CFRP Composite and Lightweight Concrete. Paper submitted for publication in Journal of Magazine of Concrete research (submitted on 18 Dec 2016) (Under review).

- Al-Allaf, M.H., Weekes, L. and Augusthus-Nelson. Simplified bond-slip model for interfaces between FRP reinforcement and lightweight concrete. Paper submitted in the proceedings of the SMAR2017 Conference, Zurich, Switzerland (submitted on 14 Jan 2017).

LIST OF CONTENT

LIST OF TABLES

CHAPTER ONE

CHAPTER TWO

CHAPTER THREE

CHAPTER FOUR

CHAPTER FIVE

CHAPTER SIX

LIST OF FIGURES

CHAPTER ONE

CHAPTER TWO

CHAPTER THREE

CHAPTER FOUR

CHAPTER FIVE

CHAPTER SIX

NOMENCLATURE

Unless otherwise noted in this thesis, all units are metric: dimensions are in millimetres, stresses are in MPa, moduli are in MPa or GPa and forces are in N or kN.

A_c	Gross- section area of concrete prism
A_f	FRP reinforcement area
E_c	Modulus of elasticity of concrete
E_f	Modulus of elasticity of FRP reinforcement
F_{Exp}	Experimental force corresponding to primary slip mm slip
$F_{P,max}$	Maximum primary force
$F_{P,max}$	Maximum degradation primary force
F_P	Primary force
F_d	Degradation force
F_{max}	Maximum debonding force
$F_{p,CEB}$	Primary force corresponding to maximum primary slip
G_a	Elastic shear modulus of the adhesive
G_c	Elastic shear modulus of concrete
G_f	Interfacial fracture energy
L_f, L	Bonded length of FRP reinforcement
L_e	Effective length of FRP reinforcement
P_c	Load applied to the concrete prism
P_{max}	Maximum applied load
P_d	Maximum debonding force
$P_{fd,max}$	Maximum design debonding load
P_u	Ultimate bond strength
S_f	Centre-to-centre spacing of the FRP reinforcement
V_{exp}	Experimental FRP shear contribution
$V_{lRD,c}$	Shear resistance of the RC members
V_{pre}	Predicated FRP shear contribution
V_t	Total shear resistance
b_c	Width of concrete sample
b_f, w_f	Width of FRP reinforcement

b_w	Beam web width
d_f	Effective depth of FRP reinforcement
f_c'	Concrete cylinder compressive strength
f_{ck}	Characteristic compressive strength of concrete
f_{ctk}	The characteristic tensile strength of concrete
f_{ctm}	Mean tensile strength of concrete (EC2)
f_{cu}	Cube compressive strength (BS8110)
$f_{frp,e}$	Effective stress of the FRP
$f_{r,LWAC}$	Modulus of rupture of lightweight concrete
$f_{r,NWAC}$	Modulus of rupture of normal weight concrete
f_t, f_{ct}	Concrete tensile strength
f	Concrete compressive stress at any strain ε
f_y	Steel yield stress
k_1	Modification factors that account for the concrete strength
k_2	Modification factors that account for the wrap scheme
k_b	Geometry factor
k_c	Factor accounting for the state of compaction of concrete
l_1	Maximum Primary length of FRP reinforcement
l_d	Degradation length of FRP reinforcement
l_e	Effective length of FRP reinforcement
l_p	Primary length of FRP reinforcement
n_f	Number of FRP layers
s_1	Maximum Primary slip (Maximum slip)
s_2	Maximum debonding slip
s_3	Maximum degradation slip (Ultimate slip)
s_{lp}	Slip in primary zone
s_{max}, S_{Fy}, S_0, S_{peak}	Maximum slip between FRP reinforcement and the concrete substrate
s_u	Ultimate slip between FRP reinforcement and the concrete substrate
t_a	Thickness of adhesive layer
t_a	Distance from the top free ends of FRP reinforcement
t_c	Thickness of half concrete prism

t_f	Thickness of FRP reinforcement
u_c	Displacement of the concrete prism
u_{frp}	Displacement of the FRP reinforcement
w_{fe}	Effective FRP reinforcement width
β_f	Angle of the FRP principal tensile fibres
β_r	The ratio between the average bond stress and the maximum bond stress
β_t	Shear transfer coefficient
β_w	FRP width factor
γ_c	Partial factor of concrete
ε_0	Ultimate concrete strain at the maximum compressive stress f_c'
ε_1 and ε_2	principal strains in FRP reinforcement
ε_c	Concrete strain
$\varepsilon_{fd,max}$	Maximum FRP strain in the degradation zone
ε_{fd}	FRP strain in the degradation zone
$\varepsilon_{fp,max}$	Maximum FRP strain in the primary zone
ε_{fp}	FRP strain in the primary zone
$\varepsilon_{frp,e}$, ε_{fe}	Effective FRP strain
ε_{frp}, ε_f	Strain in FRP reinforcement
$\varepsilon_{max,d}$	Maximum design debonding strain
ε_{max}	Maximum strain in FRP reinforcement
ε_u, ε_{fu}	Ultimate FRP strain
ε_x	Axial strain in FRP reinforcement
ε_{xy}	Shear strain in FRP reinforcement
ρ_c	Concrete density
ρ_f	Ratio of the FRP reinforcement
σ_c	Axial stress in concrete
σ_f	Axial stress in FRP reinforcement
τ_{av}, τ_u	Average bond shear stress
τ_{max}, $\tau_{b,max}$, τ_{bFy}	Maximum bond shear stress
τ_s	Constant bond stress

φ_{frp}	Strain distribution factor
Δb	Working width of concrete
E_s	Modulus of elasticity of steel
E_x, E_y, and E_z	The elastic modulus of the FRP composite in three directions
G_{xy}, G_{yz}, and G_{xz}	Shear modulus of the FRP composite for three planes
h	Beam high
V_c	Shear resistance attributed to concrete
V_f	Shear resistance attributed to FRP reinforcement
V_s	Shear resistance attributed to shear reinforcement
α	Parameters (M.CEB model)
v_{xy}, v_{yz} and v_{xz}	Major Poisson's ratio of the FRP composite for three planes
F	debonding force
R	Reduction factor to lightweight concrete
c	Density class of concrete
d	Effective depth of the beam
l	length of the crack plane
r	Radius of Moher's circle strain state
s	slip between FRP reinforcement and the concrete substrate
α	Reduction factor
η	Constant
θ	Principal compressive stress inclination
τ, τ_f, τ_b	Bond shear stress/Interfacial shear stress
$\boldsymbol{\upsilon}$	Poisson's ratio
$\boldsymbol{x_i}$	Strain gauges' position
$P_a, P_{a,max}$	The normalised and maximum load ration
φ_{frp}	Strain distribution factor

ABBREVIATIONS

NWAC	Normal weight aggregate concrete
LWAC	Lightweight aggregate concrete
NWC	Normal weight concrete
LWC	Lightweight concrete
NWRC	Normal weight reinforced concrete
LWRC	Lightweight reinforced concrete
EBR	Externally bonded reinforcement
CFRP	Carbon fibre reinforcement polymer
GFRP	Glass fibre reinforcement polymer
AFRP	Aramid fibre reinforcement polymer
SLS	Single lab shear test
DLS	Double lab shear test
MDLS	Modified double lab shear test
LVDTs	Linear Voltage Displacement Transducers
CF	Concrete prism failure
DC	Debonding in concrete
AD	Adhesive debonding
FR	CFRP rupture
SEM	Scanning electron microscope
EDX	Energy dispersive X-ray
S. D	Standard deviation
C.V	Coefficient of variation
LWA	Lightweight aggregate
PFA	Pulverised-fuel ash
FEA	Finite Element Analysis

CHAPTER ONE

INTRODUCTION

1.1. Research Background

Many modern civil engineering constructions are sophisticated and constructed for long-time behaviour. Since, there are many old RC members which are now not fulfilling the design requirements, for example, reinforced concrete member has been under-designed or wrongly constructed. Occasionally, to avoid their deterioration and to meet recent increases in service loads such as bridge subject to increased vehicle loads, it is important to increase the strength of these structures to meet the new loading requirements (Sas, 2009). In some cases, it may not be economically feasible to replace old structure with a new one. Therefore, the maintenance of serviceability and upgrade of members during its life can be one of the biggest issues facing the civil engineer (Al-Juboori, 2011).

Various strengthening or repairing system have been successfully used to upgrade the strength of the old RC structures. Previous retrofitting systems concerned on applying steel plate to the surface of concrete (Täljsten, 1991), so that the materials act compositely. For the time being, the steel plates have been substituted by externally attached fibre reinforced polymers (FRP composites) (Sas, 2009). FRP reinforcement represents a potential solution to upgrade and strengthens existing RC members either in shear or flexural reinforcement (Al-Rousan and Issa, 2011; Lu et al., 2009; Täljsten, 2003 and Khalifa and Nanni, 2000).

FRP plates or sheets have used as a popular method for shear and flexure strengthening of reinforced concrete (RC) elements. This technology provides unique advantages compared with conventional retrofitting systems such as steel jacketing or externally attached steel plates and external post-tensioning. Among these FRP has good corrosion resistance, lightweight and excellent mechanical properties. Furthermore, the hand lay-up allows adaption of FRP reinforcements to the shape of any structural members. (Abdalla, 2002 and Matta et al., 2009, Al-Rousan and Issa, 2011)

A significant amount of research has been carried out last two decades with an objective of providing the best methods of using FRP reinforcement to retrofit RC members. From these

research, meaningful conclusions were reported in different design codes and guidelines (fib Bulletin 14, 2001; CNR-DT-200, 2004 and ACI 440.2R08, 2008).

Various methods and objectives have been employed using FRP composite for repairing or retrofitting reinforced concrete elements in different places around the world. Such field applications have been adopted in Great Britain, Japan, China, Germany, France, Italy, Greece, Switzerland, Poland, Sweden, Canada, and the United States on structures and structural elements such as RC beams, columns, walls, arches, decks/slabs, and tunnels (Bonacci and Maalej, 2000). Figure (1.1) illustrates the reported objective of using the FRP reinforcement in a different field.

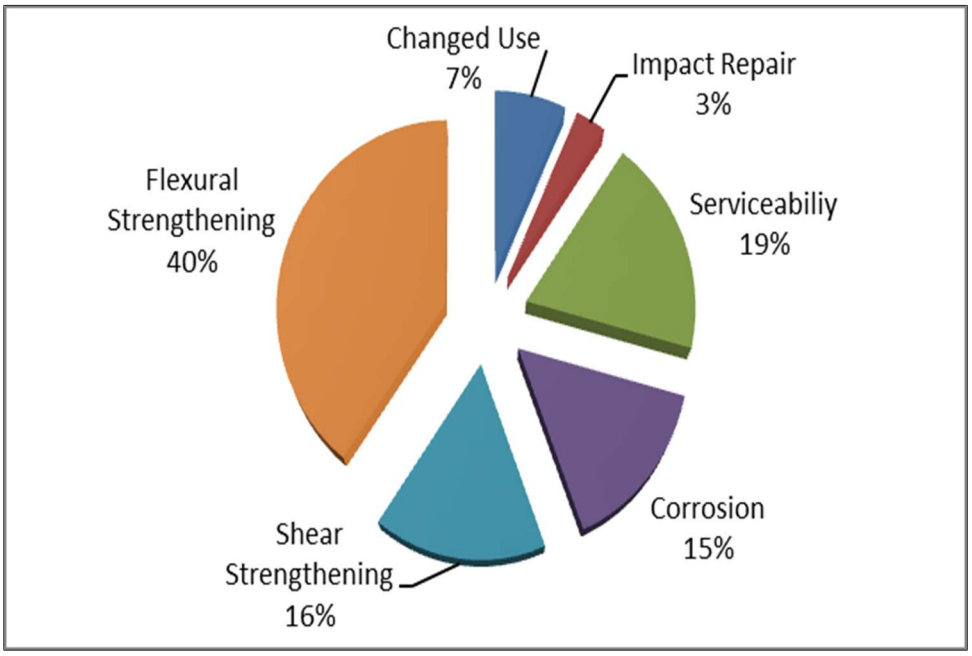

Figure (1.1): Objectives of using FRP External Reinforcement (Bonacci and Maalej, 2000).

There is a wide range of recent, current, and the possible applications of using FRP reinforcements to strength the new and existing structures. Some of the widely used FRP applications in civil engineering structures are shown in Figure (1.2).

(a): Application of FRP fabrics on concrete columns for seismic retrofitting.

(b): Strengthening of a concrete deck of a building using FRP strips on the top and underside of the deck.

(c): FRP sheets and strips that are bonded to existing reinforced deficient concrete bridge structural members.

Figure (1.2): Application of FRP used for repairing and strengthening RC structure (Al-Juboori, 2011).

Flexural and shear failures are the main critical failure patterns of the RC members. Flexural failure of under-reinforced sections is ductile and develops progressively with significant cracking and displacements, which show a warning of failure. On the contrary, shear failure is extremely brittle and does not allow significant redistribution of shear forces; therefore, shear failure develops without warning and is usually disastrous. Shear-deficient beam failed in shear prior to achieving the full flexural capacity. Thus, RC structures should have sufficiently more margin with regards shear capacity when compared with flexural capacity. Therefore, retrofitting and repairing of the reinforced concrete members could be required to improve the shear capacity of the reinforced concrete structures. Structures that are deficient in shear can be strengthened or repaired by using FRP composites (Bellamkonda, 2013).

Many experimental and theoretical studies have been conducted regarding the shear strengthening of normal weight reinforced concrete (NWRC) structures retrofitted externally with FRP. Limited studies were found in the literature review for FRP strengthening of lightweight reinforced concrete (LWRC) structures tested for shear failure, in spite of the shear capacity of lightweight concrete (LWC) being lower than normal weight concrete (NWC).

LWC has become established as an important and versatile material in modern construction. The reasons for development taking place in this field are technical and economic. The use of lightweight concrete has shown that it has many advantages. It's lower density means that the dead weight of the structure can be reduced with a consequent reduction in the size of foundations. Alternatively, the dimensions of elements can be considerably enlarged without having to alter erection systems, or the geometric shape of an element can be greatly simplified without increasing its overall weight (Lytag UK, 2011).

The surface dry density of LWC ranges between 60-85% of that of NWC. The density of LWC is about 55% lower than that of NWC when immersed in water (Concrete Society, 1978 and Madandoust, 1990). This increased the ability to float in water which is a clear feature for use in marine structures, for example, offshore production platforms and floating docks. LWC has excellent fire resistance and insulating properties, the required thickness of the walls cast with LWC is roughly 20% lower compared with NWC. Heat transfers through LWC walls are reduced by about 20% compared with NWC walls and can be reached up to 50%, depend on the density of the LWC (Zunz, 1968).

Conversly, LWA are not strong as conventional aggregates. When the cracks star to develop; theses cracks will pass through th aggregate particles without any resistance. The failure is developed by the tensile stresses initiated within the aggregate particles as well as by the failure developed in the concrete paste surrounding the aggregate particles. The crack width and intensity are higher in LWC compared with NWC. Briefly, LWC is weak compared with NWC. Furthermore, the cracking strength or the tensile strength of LWC is significantly lower than the NWC of the same grade of concrete. This issue also influnce the shear capacity of LWC, bond between steel and concrete as well as the anchorage strength, etc. (Clarke, 2002). LWC has been used increasingly over the past decades (Aljaafreh, 2016). Table (1.1) summarises the most important LWC buildings constructed in the last 70 years. In the coming decades, it is therefore expected that structures constructed using LWC will occupy a significant proportion of the concrete infrastructures. When deteriorated, these structures may be retrofitted using efficient systems such as FRP reinforcement.

Table (1.1): Applications of lightweight concrete in tall buildings, bridges and recent applications (Zareef, 2010).

Project	Year	Concrete grade (MPa)	Density Kg/m^3
Tall Buildings:			
Towers of Marina City, USA	1962	25	1680
Building of Australia Square, Australia	1967	30	1870
Tower of Lake Point, USA	1968	25	1730
Building of the Standard Bank, South Africa	1968	35	1950
Building of the BMW administrative, Germany	1973	30	1850
Extension of the post office I, Germany	1992	20	1500
Bridges:			
Woodrow Wilson Bridge, USA	1961	35	1840
Martinez Benicia Bridge, USA	1962	28	1840
Silver Creek Overpass Bridge, Utah	1968	29	1600
The Friarton Bridge, UK	1988	30	1700
Cooper River Bridge, USA			

Recent Applications:			
Auditorium Maximum, Germany	1994	25	1600
House of Youth Center, Berlin, Germany	2001	15	1200
German Technical Museum, Berlin, Germany	2001	25	1400
Gartmann Family House, , Switzerland	2004	8	1100
Amts- and Landgericht, Frankfurt/Oder, Germany	2006	15	1200
MPU Heavy Offshore Lifter, Rotterdam, Netherland	2009	35	1250

This study will focus on the interface response of the carbon fibre reinforced polymers (CFRP)/LWAC joints and the shear retrofitting of lightweight reinforced concrete beam (LWRC) externally strengthened using CFRP. Designer knowledge concerning the response of RC members strengthened in shear with FRP reinforcement is still an area where the conventional design concepts are concisely addressed (Al-Juboori, 2011), particularly for lightweight concrete structures. Not only strengthening and repairing of these members constructed from NWC but also, in the future, strengthening and repairing of LWC members will be a serious challenge for engineers due to the deterioration of structural elements cast from LWC (Al-Rousan et.al. 2011).

1.2. Research Motivation

Shear strengthening of reinforced concrete structures with FRP is widely recognised as an economic and efficient technique of retrofitting. The shear strengthening of LWRC structures with FRP has not received any attention even though the shear capacity of LWRC structures is less than the shear capacity of NWRC members. Therefore, the concrete contribution to design shear resistance is reduced for LWRC elements.

Previous experimental studies showed that there is a considerable variance in shear response between lightweight and normal weight concrete members especially after the occurrence of diagonal shear cracks. NWC elements were able to sustain much shear forces till the flexural failure, whereas the LWC was unable to achieve enough shear strength and suddenly failed in extremely brittle failure modes (Juan, 2011). Shear failure of LWC members has been one of the critical problems that may cause structural collapse (Tang et al., 2009). The major challenge facing the construction industry nowadays is how to provide higher-strengths concrete and lighter in weight appropriate for various engineering applications such as

offshore and marine structures, slabs and joists in tall buildings and bridge structures (Al-Rousan et.al. 2011).

Unfortunately, there is limited data available in the literature reviews which addresses LWRC members retrofitted with FRP and this highlights the issues concerning the validity of current FRP design codes and guidelines for different types of concrete, especially for LWAC. Thus, better assessment of the current FRP design codes and guidelines to establishing the use of FRP reinforcement as an efficient shear strengthening system. The current design codes and guidelines used to examine the FRP behaviour are empirically derived based on data from testing normal weight concrete, a new study to examine the FRP performance with LWRC beams deserves investigation.

Studying the interface response of FRP/ LWAC joints and the shear response of reinforced lightweight concrete beams is very important to understand the effectiveness of using CFRP composites to strength LWAC. Previous studies showed that the tensile strength of concrete and aggregate interlock have a significant effect on the FRP- normal weight concrete interface (Pan and Leung, 2007). The fundamental difference between NWRC and LWRC members having the same compressive strength in shear behaviour is due to lower concrete tensile strength and aggregate interlock which may influence the effectiveness of strengthening reinforced concrete members with FRP composites.

Lower stiffness of lightweight aggregate particles (LWA) and higher cement ratio result in large plastic deformation. In addition to larger crack widths in LWAC, compared with those members constructed from NWAC, they are likely to increase the stresses in FRP reinforcements and at the concrete-FRP interface. In general, increasing in shear and normal stresses leads to CFRP debonding and unexpected CFRP rupture failures while contributing to the overall load carrying capacity, thus the effectiveness of using FRP reinforcement for shear retrofitting LWRC structures may be influenced by this issue.

This study investigates experimentally, numerically and theoretically, the bond behaviour of LWAC samples reinforced with CFRP composites and the shear strength of LWRC beams, considering the main variables identified to evaluate the full behaviour of CFRP with LWRC. The direction of this research will contribute to knowledge by providing new test data regarding the shear strength of (LWAC) structures retrofitted with CFRP sheets.

1.3. Scope of Research

This study aims to provide new data concerning the behaviour of shear strengthened LWRC beams using CFRP reinforcement. It is necessary to study the bond characteristics and the performance of using CFRP to retrofit LWRC beams compared with companion NWRC beams.

The objective of this study is to provide a comprehensive investigation of the response of the FRP-to-concrete interface for samples cast with LWAC. In addition, the study will investigate the shear behaviour and failure modes of LWRC beams strengthened with CFRP composites experimentally, numerically and theoretically, with the aim of improving the current understanding, the objective of this study can be summarised by the following points:

1. To provide a full literature review regarding the response of the FPR/concrete joints and the shear behaviour of RC beams strengthened with CFRP composites.
2. A new strategy of the double lap shear tests was adopted in this study to get an accurate behaviour of the FRP/lightweight concrete joints.
3. To investigate the influence of different variables on the behaviour of the FRP-to-lightweight concrete interface and to includes their effects on the current design codes and guidelines.
4. To evaluate the performance of CFRP used to improve shear strength of LWRC beams and to examine the validity of the existing theoretical models and design equations to predict the shear resistance of FRP.
5. To propose new mathematical models to estimate the interface relationships, taking into consideration the effect of the LWC properties on the interface behaviour and the contribution of CFRP reinforcement to shear resistance of the RC beams depending on the experimental results through an extensive program of work.
6. To simulate the interface behaviour in finite element software and the shear capacity of LWRC beams to predict the maximum bond strength of the CFRP/LWC joints and the serviceability and shear strength and failure modes of LWRC beams. The outcomes of the experimental and theoretical investigation were compared together and general conclusions concerning the response and the prediction of the FRP-to-concrete interface as well as the behaviour of the LWRC strengthened with FRP reinforcement in shear will be presented.

1.4. Layout of this Thesis

This thesis is divided into seven chapters as follows:

- **Chapter 1**

Presents the general background regarding this study and aims and the objective of this thesis.

- **Chapter 2**

Provides a full review of the available studies related to this research, the characteristics of the FRP/concrete joint are presented and discussed in details. In addition, to the experimental, theoretical and finite element analysis investigations using FRP materials in strengthening reinforced concrete beams for shear are presented and discussed.

- **Chapter 3**

Describes the CFRP-concrete bond test Programme. The effect of various variables on the behaviour of CFRP/concrete joint is presented here. Results analysis and discussion are presented in this chapter.

- **Chapter 4**

Details related to the lightweight and normal weight reinforced concrete beams, their design and fabrication, the test setup, and the instrumentation used in the experimental program are presented in details. The test results and the findings from those results are analysed and discussed in this chapter.

- **Chapter 5**

The FE models proposed for the analysis of the experimental bond-slip tests and the beam shear test are examined in details. The comparison between the experimental and theoretical results is also presented in this chapter.

- **Chapter 6**

Develops new theoretical models to predicate the interface behaviour between the FRP and lightweight/normal weight concrete substrates. Two different models are proposed in this study. The first method (simplified model) and the second proposed model (modified CEB-FIP 1990 Bond-Slip models). A new design proposal to predicate the shear contribution of the FRP reinforcement was developed in this chapter.

- **Chapter 7**

Presents a summary of the main outcomes of this study and recommendation for future work. The structure of the thesis is illustrated schematically in Figure (1.3).

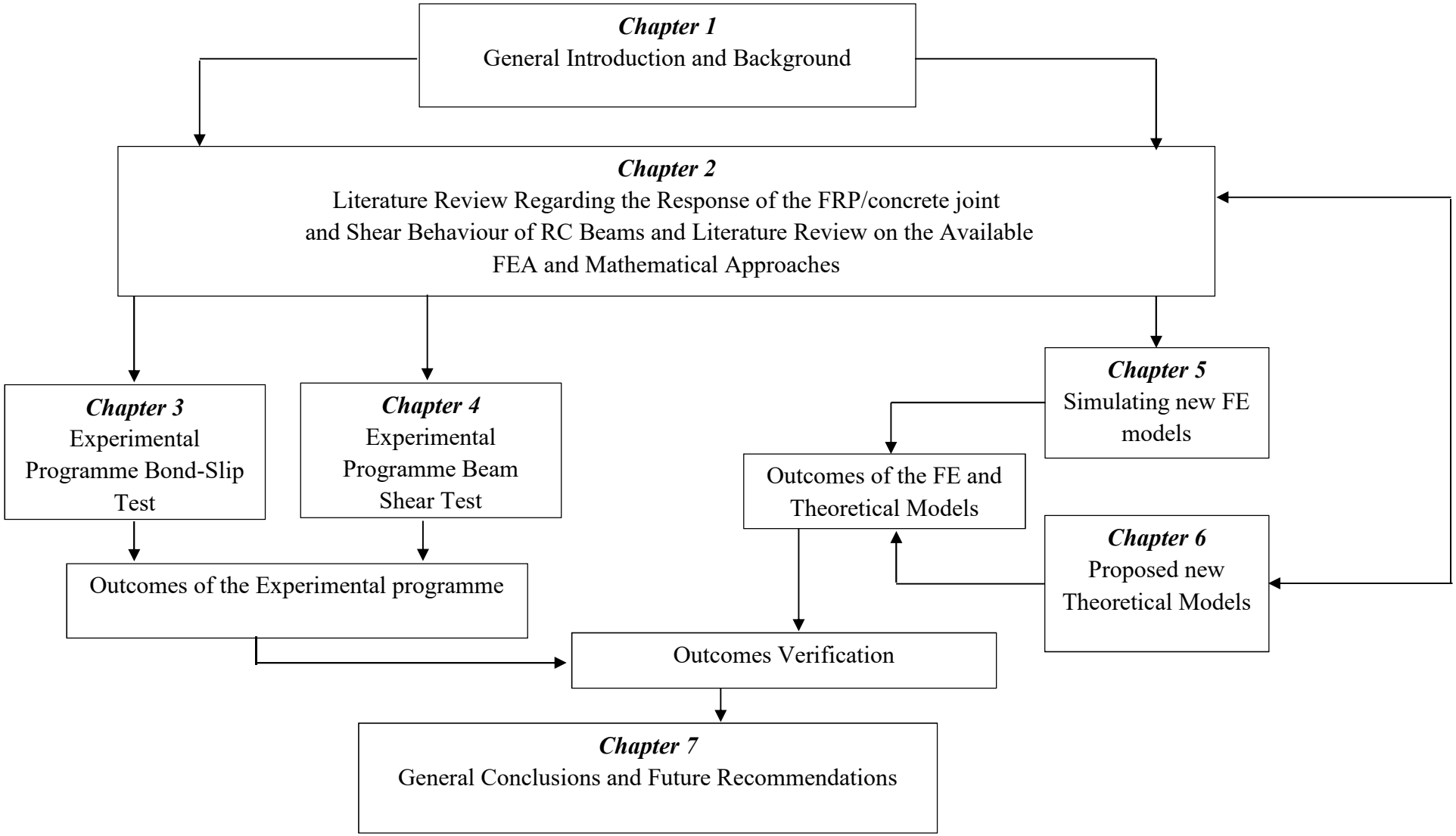

Figure (1.3): Outline of the thesis.

CHAPTER TWO

LITERATURE REVIEW

2.1. Introduction

Externally bonded carbon fibre-reinforced polymer (CFRP) systems present a potential solution to upgrade different types of reinforced concrete members. This thesis focuses on the interfacial behaviour between the CFRP and the substrate of LWAC. In addition, the shear strengthening of LWRC beams will also be studied. This chapter is concerned with issues found in the literature related to existing knowledge of FRP and lightweight aggregate concrete (LWAC) structures. Also studied are previous research on the interfacial characteristics of FRP/concrete joints, the shear behaviour of NWC beams retrofitted in shear with FRP reinforcement and the shear behaviour of beams made from LWC.

2.2. FRP Composites

The composition of the FRP sheet is a fibres reinforcement and epoxy primer material. Figure (2.1) shows the typical composition of an FRP system. A wet lay-up method is the widely used FRP strengthening system. In this method, the FRP sheet is soaked with epoxy primer and attached to the surface of the concrete with an extra amount of epoxy primer or epoxy adhesive. Another two methods such as pre-cured and Pre-preg methods which also utilised to install FRP sheets to the concrete surface. In the latter two methods, the FRP sheets have been previously soaked with epoxy primer and require an extra amount of epoxy primer or epoxy adhesive to attach the FRP reinforcement to the surface of concrete (Colalillo, 2012).

A multi-directional or uni-directional FRP composite are the main two type of reinforcement, FRP reinforcement available in three different types which are carbon sheet/plate (CFRP), glass sheet/plate (GFRP), or aramid sheet/plate (AFRP). The modulus of elasticity and the tensile strength of the CFRP reinforcement are significantly higher than the GFRP and AFRP reinforcement. Choosing the best type of the FRP reinforcement for shear and flexural strengthening depends on the material's cost and the environmental behaviour. For instance, GFRP reinforcement is now cheaper and more chemical resistance compared with CFRP reinforcement, (Colalillo, 2012). The ISIS Design Manual 4 (2008) and CNR-DT-200 (2004) both present a full discussion of the features and specifications of various types of FRP

systems. Figure (2.2) shows the properties of different FRP reinforcement and typical steel reinforcement.

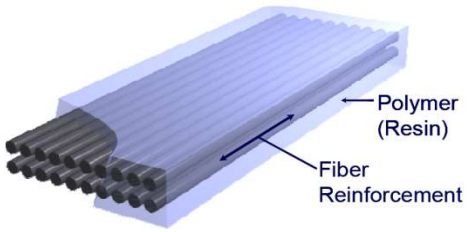

Figure (2.1): Representation of FRP material (Al-Juboori, 2011).

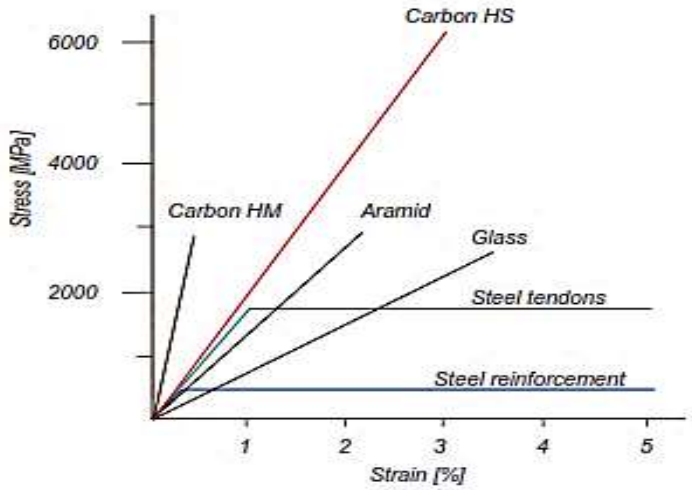

Figure (2.2): Properties of various FRP reinforcement compared with steel reinforcement (Sas, 2011).

2.3. Externally bonded reinforcement (EBR) system

The main FRP retrofitting system is a wet lay-up method which is widely used to attach the FRP reinforcement to the surface of concrete. For adhesively bonded system, the following procedures are adopted: Firstly, a grinding is applied to remove the weak cement paste (the beam's corners should be rounded in case of shear retrofitting); Secondly, the dust, grease or mud should be removed by a vacuum or washing by water; Thirdly, a thin layer of epoxy primer is applied to improve the bond capacity of the surface of the concrete; and Finally, an extra amount epoxy resin material is used to attach the FRP strips or sheet to the surface of the beam. An alternative procedure for installing FRP strips which is similar to this used for EBR sheets are adopted, but adhesive epoxy can be used to cover the FRP reinforcement in both side in addition to epoxy resin to achieve full bond capacity between the FRP

reinforcement and the concrete surface (Barros et al., 2007), as shown in Figure (2.2). The Wet Lay-Up system will be used for shear retrofitting in this present study.

Figure (2.3): Strengthening with EBR reinforcement technique (Barros et al., 2007).

2.4. Strengthening Schemes

FRP reinforcement can be attached in different retrofitting systems with various direction, free ends anchorage, and the bonded area. The external reinforcement can be installed as strips with a suitable distance from center-to-center of the FRP strips and FRP width or as a full sheet along the shear span of the beam. The shear strength provided by fully bonded FRP sheet are significantly higher than those samples strengthened with wider FRP strips. FRP reinforcement should be oriented to get the required shear strength improvement. For instance, FRP reinforcement attached in a perpendicular direction to the longitudinal axis of the beam showed a good shear resistance. However, FRP inclined in a perpendicular direction to the compressive strut inclination showed a better shear retrofitting compared with transverse FRP reinforcement. (Colalillo, 2012). A multi-directional FRP reinforcement gives the required shear retrofitting in each orientations with respect to the longitudinal axis of the beam, this type of reindoecment is useful for seismic retrofitting when the shear stresses and crack orientations may alter (Chen et al., 2003).

The common types of FRP shear configuration systems can be classified in three main strengthening techniques: (i) Closed-shaped system, (ii) U-shaped system and (iii) Side-bond system. Wrapping the FRP reinforcement around all the faces of the beam (Closed-shaped) system shows the most practical retrofitting system. An overlap length of 150 mm was recommended by ISIS Design Manual, 4 (2008) to secure a full connection between the FRP reinforcement (Colalillo, 2012). Rounded edges are required for shear retrofitting to prevent FRP rupture due to high-stress concentrations developed in the FRP reinforcement close the

beam corners. The minimum recommended corner radius was 35 mm (CSA S6-06) and 20 mm as suggested by other design codes such as (CSA S806-02) and (CNR-DT-200).

It is not possible to attach closed-shaped strengthening system for T- section beam and U-shaped system may be applied as an alternative strengthening configuration. The shear performance provided by U-shaped techniques are significantly lower than closed-wrapped configurations leading to one free edge on each side of the beam, which reduces the required length to achieve the full bond strength between the FRP reinforcement and concrete. The lowest shear strength is provided by side-bond retrofitting, the FRP reinforcement attached to the sides face of the beam, leading to two (top and bottom) free end on both sides of the beam which increase the possibility of the FRP debonding from concrete surface (Colalillo, 2012). Figure (2.4) illustrates the different retrofitting schemes which are used to strength reinforced concrete beams.

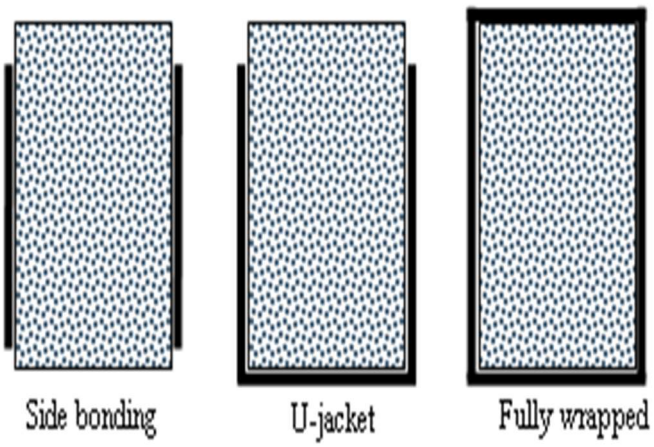

Figure (2.4): FRP shear strengthening configurations (Al-Juboori, 2011).

Free end anchorage is one of the possible solutions to prevent or delay the global debonding of the FRP reinforcement from the surface of the concrete. This can be applied at the free edges of the FRP reinforcement to enhance the bond strength between FRP reinforcement and concrete.

There are several types of the free ends anchorage techniques, for example, (i) adding of horizontal FRP sheet applied over the free ends of the FRP reinforcement were developed to minimise the possibility of FRP debonding, (ii) using mechanical anchorage/sandwich panel anchored to the surface of concrete at the free end of the FRP reinforcement and (iii) inserting the FRP anchors through the beam web to fasten the free ends of the FRP reinforcement (ISIS

Design Manual 4, 2008). Using fully wrapped configurations system for seismic retrofitting or developing an appropriate free ends anchorage with U-shaped configurations are very important to get the required shear strength and to eliminate the bond failures (Colalillo, 2012). Averting the use of side-bond configuration system for the seismic application was recommended by Monti and Liotta, (2007) in order to achieve the full confinement effects and to prevent precocious debonding failures.

2.5. Lightweight Aggregates (LWA)

There is a wide range of different lightweight aggregates. These differ in raw material, chemical and mineral composition, specific gravity, water absorption, strength, physical and chemical properties and pore structure as well as the process of manufacturing. In spite of this fact, their properties can be estimated with simple formulae These, in general, depend on the particle densities.

Lytag aggregate is used as the coarse aggregate to produce Lightweight concrete in this study. The choice of this type of aggregate was made because it can provide the engineer with better strength/density ratios. Previous studies have shown that it had good response in different structural uses (Madandoust, 1990). Lytag is produced in the UK from pulverised-fuel ash (PFA). Large quantities of suitable PFA are produced in the UK as a powdered by-product of pulverised-fuel (bituminous coal) operated furnaces of power stations. The waste material is produced from the power station in the UK which is usually unburnt carbon in the form of coke. Fine coal and a suitable amount of water (generally about 12-15%) are added to the PFA in a mixer and this mixture is then fed at a controlled rate to the specially manufactured dish pelletising pans. A small amount of water is added as a fine spray through the process of pelletisation to form rounded green pellets. The size and the degree of compaction of the green pellet depend on the feeding rate, amount of water, the rotation speed and the angle of inclination of the pan. The green pellets are then fed onto a sinter strand and heated to a temperature ranging between 1000°C and 1250°C. The final product is took the shape of a block of hard brick-like rounded nodules, lightly linked by fusion at their points of contact (Clarke, 2002).

2.6. Lightweight Aggregates Concrete (LWAC)

Structural lightweight concrete defines as a concrete with a density range of approximately 1100 – 2000 kg/m^3 with 28 days concrete compressive strength of 17 MPa. The compressive strengths of LWC are usually correlated with the density of the material and is of importance

for structural use (ACI 213R, 2003). LWC can be cast from the lightweight fine aggregates and coarse lightweight aggregates or lightweight coarse aggregates with conventional fine aggregate (Clarke, 2002).

2.6.1. Density

The density of the LWC is significantly lower than the NWC which is 15-40% lower but with crushing strength equal to that achieved by NWC. The response of LWC is closely related to its density which is affected by the various parameters such as the relative density of the lightweight aggregates, aggregate moisture content, entrained air, the cement content, and the environmental conditions such as drying or wetting conditions (Chandra and Berntsson, 2002). Figure (2.5) illustrates the influence of the concrete oven-dry density on the cube crushing strength of lightweight concrete cast with various types of aggregates.

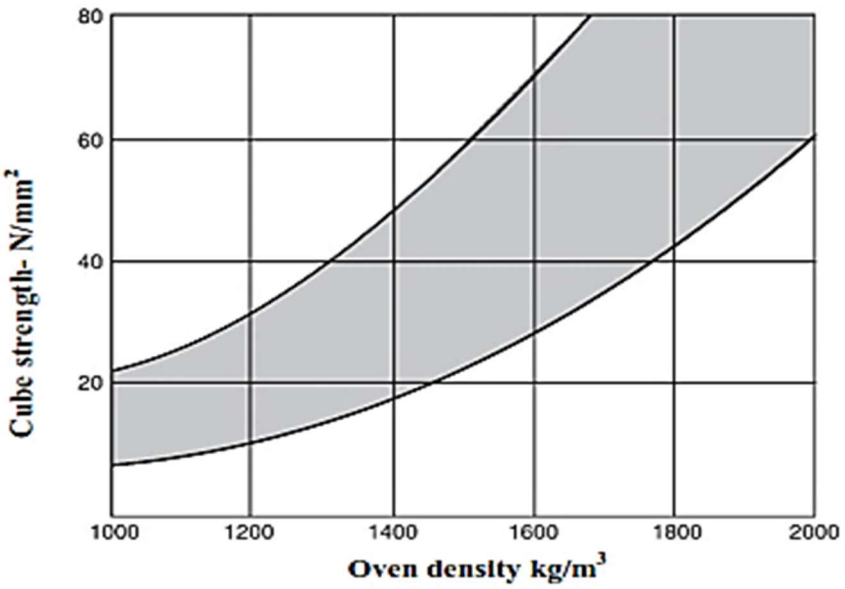

Figure (2.5): Cube strength versus oven-dry density (Clarke, 2002).

2.6.2. Compressive Strength

The crushing strength of LWC depends on several variables including type of LWA, the cement quantity, water/cement ratio, and concrete age (Clarke, 2002). Overall, the strength of the LWC correlates with the lightweight aggregate density. Due to the higher water absorption of LWA, the water/cement ratio in LWC mixes is not directly comparable to NWC. But, the influence of free content water in the mix is identical to that in NWC. In short, higher water content reduces the concrete strength.

Overall, as cement content increases the concrete compressive strength increases. A greater cement contents are needed for LWC compared with NWC. For example, A 10% higher cement content will increase the concrete strength by about 5% (Clarke, 2002). AS for NWC, the uniaxial concrete compressive strength of LWC increases with time. However, the increase is less influenced by poor moisture curing or dry environment. The reserve of water within the internal pores of the LWA provide the internal curing (Chandra and Berntsson, 2002).

2.6.3. Tensile Strength

Conventionally, the tensile strength of concrete is defined as a function of compressive strength. The rigidity of the lightweight aggregates particles, the concrete's moisture content and aggregates distribution are the main variable effect the lightweight concrete tensile strength (ACI 213R-03). The shear resistance, diagonal tension cracks strength, bond between the steel and concrete and anchorage strength capacity of the reinforced and prestressed concrete are considerably influenced by the tensile strength of concrete. The tensile/compressive strength ratio for LWAC with compressive strength over 20 N/mm^2 ranges from 5-15% (EuroLightCon, 1988).

2.6.4. Modulus of Elasticity

The stiffness of the concrete is generally related to the stiffness of the coarse aggregates and the concrete mix proportions. The modulus of elasticity of the concrete will decrease with (a) a decrease in the stiffness of the mortar which is lower than the NWC due to higher cement ratio and (b) a decrease in the stiffness of the coarse aggregate, since the modulus of elasticity of LWA is generally lower than those of NWC. It also follows that concretes made with fine and coarse lightweight aggregate will have a lower modulus of elasticity compared with LWC made from lightweight coarse aggregate and normal sand (Clarke, 2002).

Generally, the modulus of elasticity for LWC is ranged between 0.5 to 0.75 of that of NWC. Strength variations in LWA grading usually have a marginal effect on the static modulus of elasticity if the mix volumes of concrete keep constant (ACI 213R, 2003).

2.6.5. Bond and Anchorage

The bond strength of LWC is like that of NWC but, as for normal weight concrete, higher water contents should be eliminated. Anchorage strength in LWC is significantly lower than that in NWC due to the lower bearing capacity developed by the relative weakness of LWA particles which needs special detailing (BS8110-2, 1985). The bond strength required to calculate the design anchorage and lap lengths for LWC are assumed as 80% of those for the same grade of NWC (BS8110-2, 1985).

2.7. The Bond between FRP and the Concrete

External bonding of FRP reinforcement is widely used for the retrofit of ailing reinforced concrete structures. In this system, the behaviour of retrofitted concrete structures is governed by the bond strength and the material characteristics of the epoxy bonded FRP and the concrete which provide an effective stress transfer.

Several failure modes in FRP-retrofitted reinforced concrete structures are directly caused by FRP debonding in a thin layer of concrete adjacent to FRP composite. Therefore, for the economic and safe design of externally bonded FRP systems, the behaviour of the FRP-to-concrete joint requires full understanding.

The bond of FRP composite to the concrete is a vital issue influencing the effectiveness of the technique of strengthening and repairing existing structures.

2.8. Failure Patterns in FRP Retrofitted Members

Failure in the bond between the FRP reinforcement and concrete surface develops in different modes, for example, concrete surface failure, FRP debonding, a bond failure between concrete and adhesive material or debonding in the adhesive material (Hadigheh, 2014) as shown in Figure (2.6).

Debonding can lead to a precocious failure as well as cause a significant decreasing in the maximum bond strength between FRP and concrete (Wu et al., 2006). The joint failure relies on the quality of bond between FRP reinforcement and the concrete surface which is affected by many variables (Gunes et al., 2013).

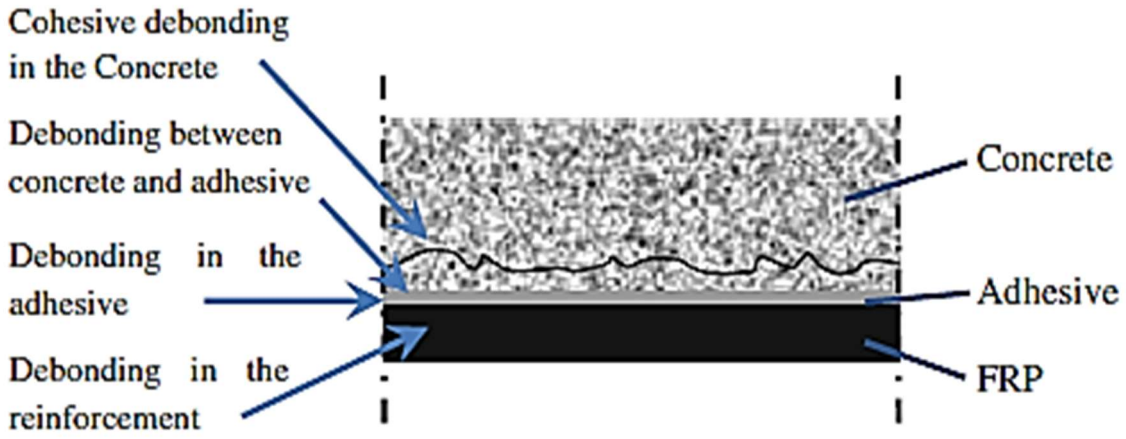

Figure (2.6): Debonding mechanisms between FRP and concrete (Pellegrino and Cruz, 2015).

The highest normal and shear stress occurring in the loaded RC members lead to FRP debonding which is one of the prevalent modes of failure in EBR strengthened members (Hadigheh, 2014). Debonding failure for laminates or sheets used for flexural and shear retrofitting may be classified into the following four categories:

1. Free end debonding.
2. Concrete cover separation.
3. Intermediate crack debonding.
4. Diagonal crack debonding.

Longitudinal steel reinforcement yielding and crushing of concrete are the typical failure modes of the reinforced concrete beams. However, for the beam strengthened with FRP reinforcement, the failure is extremely brittle, FRP fibre rupture develops immediately after crushing of concrete (Hadigheh, 2014).

2.8.1. Free End Debonding

Due to the curvature of the beam, and where, because the FRP reinforcement is simply trying to stay straight, debonding occurs at the end of the FRP reinforcement and extends gradually through the FRP/concrete joint till the global debonding of the FRP reinforcement from the surface of concrete (Oehlers, 2006). This failure is extremely brittle and named as *free end debonding*. The stresses developed in the FRP/concrete joint are shown in Figure (2.7).

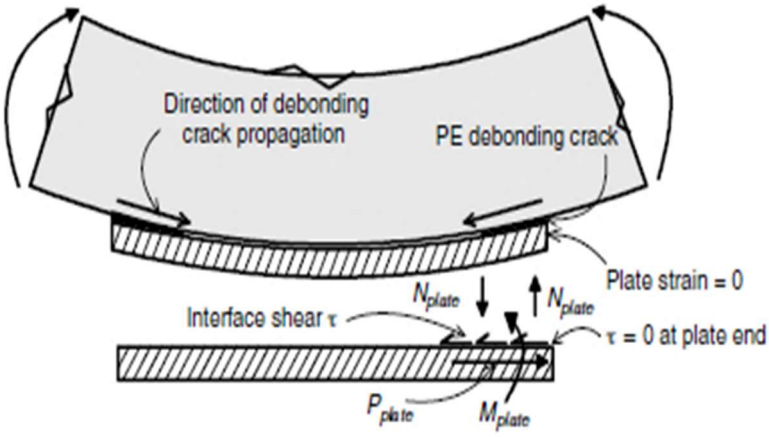

Figure (2.7): Free end debonding in RC beam retrofitted with FRP reinforcement (Oehlers, 2006).

2.8.2. Concrete Cover Separation

Once a crack develops in the concrete close to the end of the FRP reinforcement, the crack extends to the level of the longitudinal tension steel reinforcement and then gradually progresses in a horizontal direction along the level of the reinforcement, leading to the failure in a thin layer of concrete adjacent to the longitudinal steel reinforcement (Smith and Teng, 2002a) as shown in Figure (2.8).

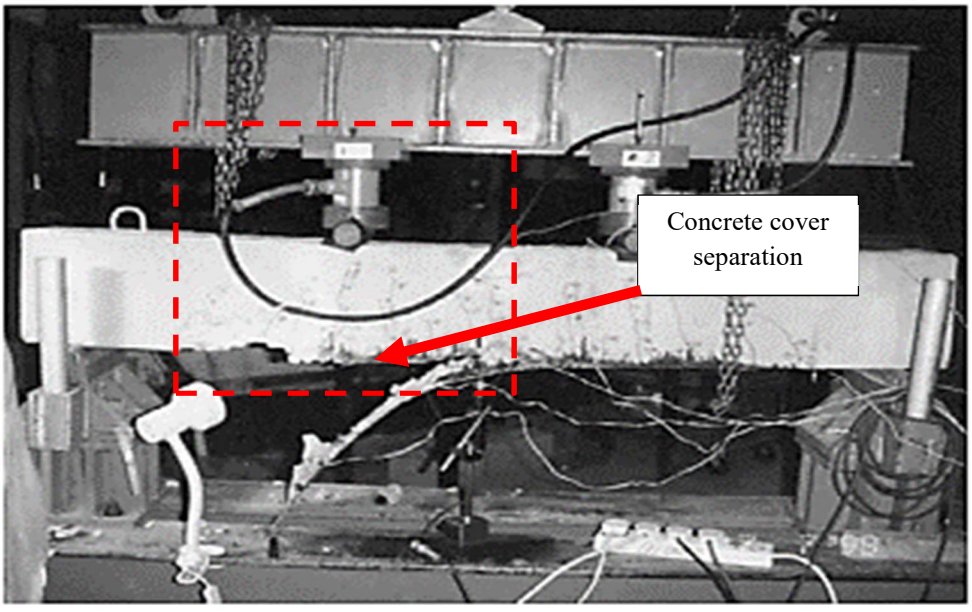

Figure (2.8): Concrete cover separation with FRP debonding (Smith and Teng, 2002b).

2.8.3. Intermediate Crack Debonding

When FRP reinforcement bridges a flexural or shear crack developed in the surface concrete, stress concentration initiates in the FRP reinforcement around the location of the crack. These stresses cause FRP debonding along the bond agent. Flexural crack debonding is the typical failure mode when the FRP reinforcement intersects flexural cracks developed in the concrete surface, or intermediate debonding when the FRP reinforcement bridges shear-flexural cracks (Hadigheh, 2014).

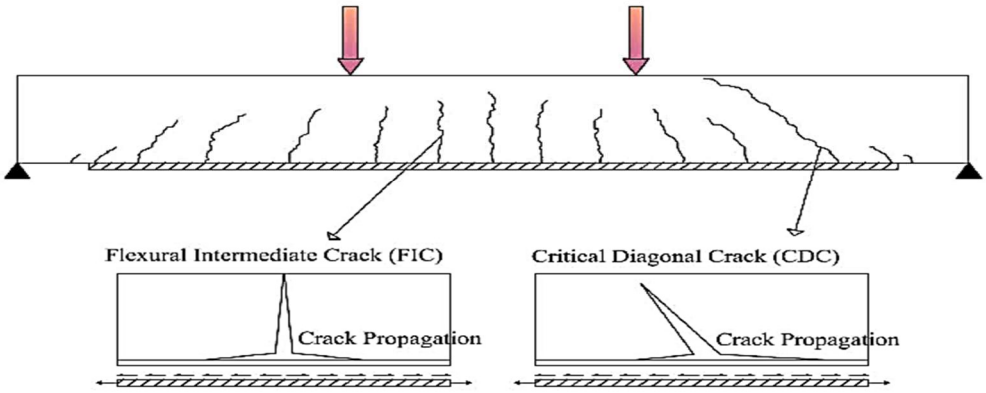

Figure (2.9): Intermediate cracks debonding (Hadigheh, 2014).

2.8.4. Diagonal-Crack-Debonding

Loss of friction and aggregate interlock at the interface of the diagonal shear cracks causes this debonding failure. This debonding failure develops at the location of the diagonal shear cracks and progressively extends towards the far end of the FRP reinforcement (Oehlers et al., 2003) (Figure 2.10). In this failure mode, FRP reinforcement prevents the initiation of the diagonal shear crack debonding compared with non-strengthened members.

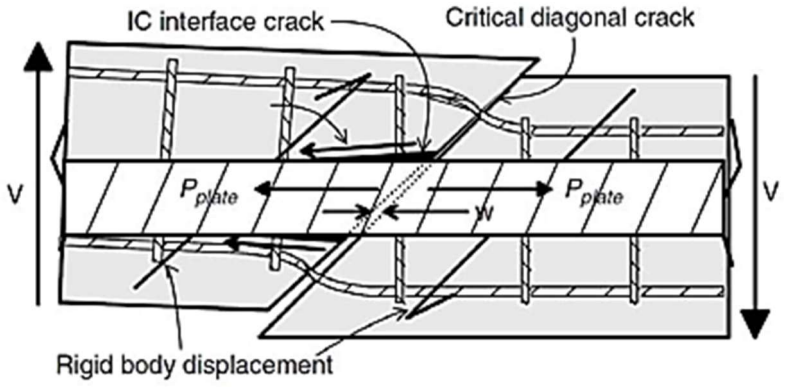

Figure (2.10): Critical diagonal shear crack propagation (Oehlers, 2006).

2.9. Bond- Slip Test

For FRP- retrofitted members, FRP debonding usually causes the potential failure patterns. The failure in bond between FRP and concrete could influence the safety of the member assuming that the required ductility enhancement and the maximum bond strength cannot be reached (Hadigheh, 2014). The potential failure mode for retrofitted structures is a sophisticated mechanism due to the complexity of the in FRP-concrete joints behaviour (Wu et al., 2002).

A significant amount of experimental tests (Chajes et al., 1996; Täljsten, 1997; Ueda et al., 1999; Bizindavyi and Neale, 1999; De Lorenzis et al., 2001; Nakaba et al., 2001; Seracino, 2001; Nehdi et al., 2003; Perera et al., 2004; Xiao et al. 2004; Guo et al., 2005; Dai et al., 2005; Xia and Teng, 2005; Foster and Khomwan, 2005; Yao et al., 2005; Cao et al., 2007; Pan and Leung, 2007; Subramaniam et al., 2007, Camli and Binici, 2007; Iwashita et al., 2007; Yang et al., 2007; Zhao et al., 2007; Cao et al., 2007, Mazzotti et al., 2008; Bilotta et al., 2009; Woo and Lee, 2010; Grande et al., 2011; López-González et al., 2012; Serbescu et al., 2013; Hosseini and Mostofinejad, 2014, Hadigheh et al., 2015 Daud et al., 2015; Mertoglu et al., 2016 and Barbieri et al., 2016) and numerical studies (Brosens and Van Gemert, 1998; Dai et al., 2006 and Ferracuti et al., 2007) have been accomplished by researchers to examine the response of the FRP-concrete joints, but standard behaviour has not been agreed.

Once the failure of the FRP-to-concrete interface develops, small interfacial cracks start widening, and bond failure is developed between FRP reinforcement and the surface of concrete, the debonding failure is followed by a relative slip between the concrete and the FRP reinforcement (Hadigheh, 2014). The response of the FRP-concrete joint can be described by the shear stress-slip trends or from load-slip curves, although both methods have drawbacks in predicting actual local stress-slip behaviour (Lu et al., 2005).

Various experimental test models had been proposed to investigate the response of the FRP-concrete joint. A small-scale sample had been used to investigate the response of FRP/concrete joint due to the difficulty of testing of large-scale samples (Hadigheh, 2014). The widely-adopted models available in the literature can be classified as; double-lap shear single-lap shear test, and beam tests.

2.10. Previous Experimental Studies on Bond-Slip Behaviour

FRP reinforcement represents one of the possible solutions to increase the load capacity of the externally retrofitted reinforced concrete members. The normal and interfacial shear stresses will be created in the FRP reinforcement due to interfacial cracks developed and transferred by bond action from the concrete surface. A good bond between FRP and the concrete surface is needed to obtain the required bond stress transference through the FRP/concrete joints. The bond strength of the adhesively bonded joint is affected by different variables for example, the concrete cracking and concrete crushing strength, concrete surface treatment, the axial rigidity of the FRP reinforcement, the bonded length and width of the FRP reinforcement. the influences of these variables might be investigated through the retrofitting systems (Hadigheh, 2014).

2.10.1. Concrete Strength

The concrete strength is one of the most important parameters that influence the maximum bond strength of the FRP-concrete joints. (Chajes et al., 1996) concluded that the peak shear stress is correlated linearly with concrete crushing strength. Dai et al., (2005) examined the effect of concrete strengths on the response of the FRP/concrete joint. It was concluded that the fracture energy required to cause the local debonding of the FRP-to-concrete joint is significantly influenced by the crushing and tensile strength of concrete (Dai et al., 2005).

Conversely, no noticeable relation was obtained between the concrete crushing strength and the maximum bond strength of the joint as concluded by Pan and Leung, (2007). They noted that the concrete surface tensile strength had significant effect on the maximum bond strength of the FRP-concrete joint whilst the concrete crushing strength or the cracking strength of concrete had marginal effect on the maximum load capacity of the tested samples cast with different crushing strengths of concrete ranging between 35 to 60 MPa

Several samples manufactured with a various thickness of the adhesive layer and concrete compressive strength was examined by LópezGonzález, (2012) to investigate the influence of compressive strength of concrete on the maximum bond strength. LópezGonzález, (2012) noticed that the maximum bond strength was significantly enhanced for samples cast with high strength concrete. LópezGonzález, (2012) observed that the samples cast with low crushing strength, the fracture of concrete develops in a thick layer of concrete while for the samples cast with high crushing strength, the fracture of concrete develops in a thin layer or

just in the interface between the concrete and the adhesive layer (LópezGonzález et al., 2012).

2.10.2. Concrete Surface Treatment

Surface preparation of concrete is also an important parameter influencing bond strength. Even before research had developed on the use of FRP, surface roughness has been considered as a crucial factor in the FRP-to-concrete joint. A significant reduction in bond strength of the FRP-concrete interface due to the existence of the dust or other harmful materials developed in the surface of the concrete. Thus, before attaching the FRP reinforcement, the surface of concrete should be grinded and a thin layer of concrete paste should be removed to enhance the surface preparation of the concrete and to get the required bond stress transference between FRP and concrete in bond-slip tests (De Lorenzis et al., 2001). Concrete fracture basically develops in a very thin layer of the concrete adjacent the FRP composite (Dai et al., 2006).

Chajes et al., (1996) investigate the influence of two preparations: (smooth finish) and mechanical abrasion (aggregate slightly exposed). Grinding with a stone wheel gave the best bond shear stresses (10% better than without preparation). (Yoshizawa et al., 1996) investigate two concrete surface preparations: water jet and ordinary sander. They concluded that the water jet on the concrete surface showed higher bond strength (about 37% higher than the sander). A similar study was carried out by Toutanji, (2001) in which they had used an ordinary sander and water-jet for surface preparation. The water-jet method revealed higher bond strength compared with the sanding method.

2.10.3. FRP Bonded Length

The previous studies have shown that there exists a critical bonded length after which there is no significant increase in the maximum load carrying capacity of the FRP-concrete joints. Researchers have described this length as the effective bond length (Taljsten 1997; Yao et al., 2005 and Cao et al., 2007). Tensile stresses in concrete are transferred to FRP reinforcement mainly through shear stresses in the adhesive layer in a short length close to the loaded end of the FRP reinforcement. As the load increases, small interface cracks start to develop and extend from the loaded end toward the far end of the FRP. The active bond zone moves to a new area further away from the loaded end, indicating that only part of the bond is effective. This part is defined as the effective bond length.

The concept of the effective bond length is also described from the strain distribution along the length of the FRP reinforcement for which the effective bond length is defined as the distance from the maximum strain point to the point of zero strain. The anchorage or effective bond length of the FRP reinforcement carries the total bond strength at which the local debonding of the FRP reinforcement debonded locally at the loaded end, causing the effective bond length to move to another active bonding zone. This shifting continues till the FRP is totally deboned from the concrete surface, this develops when the FRP reinforcement length is greater than the effective bond length (Parth Athawale, 2012) and (Ouezdou, 2008).

In cases where the length of the FRP is less than the required bond length, the failure develops before achieving the maximum bond strength. Thus, it was recommended to use enough length of the FRP reinforcement in the bond-slip test in order to achieve the required stress transferring through the FRP/concrete joint. It is well known that the using of the larger length of FRP may increase the debonding process before the global failure. In other word, the ductility of the FRP/concrete joint will significantly increase with application of the longer bond length of the FRP system (Chen and Teng, 2001 and Woo and Lee, 2010). The influence of the FRP bond length had been extremely investigated in lap-shear test (Taljsten, 1997; De Lorenzis et al., 2001; Nakaba et al., 2001; Seracino, 2001; Xiao et al. 2004; Yao et al., 2005; Yang et al., 2007; Camli and Binici, 2007; Cao et al., 2007; Mazzotti et al. 2008 and Woo and Lee, 2010).

2.10.4. Bonded Width of the FRP Reinforcement

Many studies had been carried out to investigate the influence of using wider FRP reinforcement on the response of the FRP/concrete joint. Studying the influence of FRP bonded width is crucial as it gives an idea about the suitable width of the FRP reinforcement required in the flexural retrofitting system and the required distance between the FRP strips in retrofitted shear elements (Subramaniam et al., 2007). Subramaniam et al., (2007) observed that the overall behaviour of the load-displacement trend for samples attached with various FRP bonded width is identical in shape with significant difference in maximum load capacity of the joint (see Figure (2.11)).

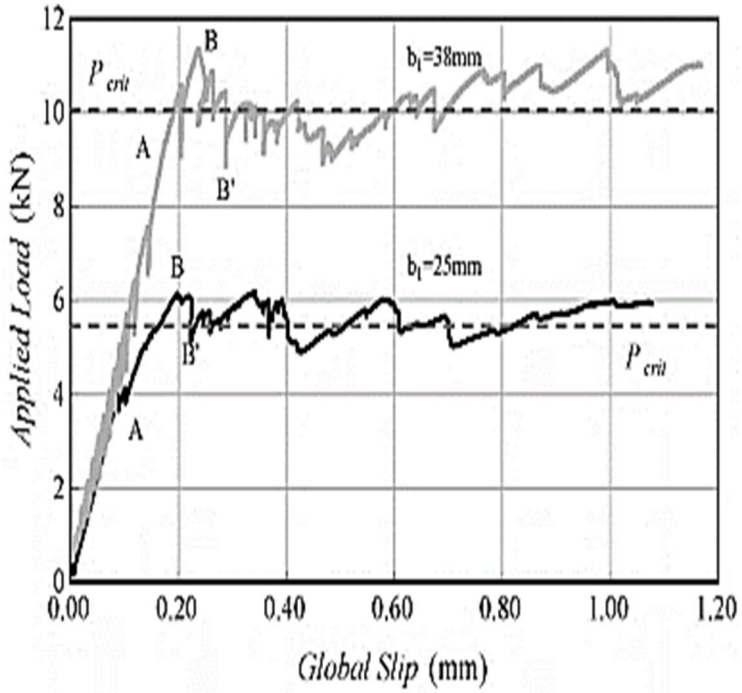

Figure (2.11): Influence of the FRP bonded width on the maximum load capacity of FRP/concrete joint (Subramaniam et al., 2007).

2.10.5. FRP Stiffness

De Lorenzis et al., (2001) concluded that the axial stiffness of the FRP reinforcement had a significant effect on the response of the FRP/concrete joint. The area of the bond versus local slip trend is kept constant with the application of different thicknesses of the FRP reinforcement. But, the ductility of the joint decreases for higher axial rigidity of the FRP reinforcement.

Pull off tests were carried out by Barnes and Mays, (2001) on concrete samples strengthened with steel reinforcement. Barnes concluded that the bond capacity of the steel-concrete joint increases with thicker steel reinforcement or thicker adhesive material used to bond the steel plate to the concrete surface. Hadigheh, (2014) concluded that the maximum applied a load of the FRP-concrete joint increases by application of higher thickness of the FRP reinforcement. after a certain thickness, the bond strength of the FRP/concrete joint did not increase significantly for samples with thicker FRP reinforcement (Hadigheh, 2014).

2.10.6. Adhesive Properties

The existing data in the literature regarding the effect of the adhesive material properties in the maximum bond strength is limited. It was concluded that the shear modulus of the

adhesive material has a significant effect of the behaviour of the FRP/concrete joints (Dai et al. 2005). A rubber modified resin was used by Gao et al., (2004). Results showed that a 20 % rubber (including 26 % acrylonitrile and 32 % carboxyl) mixed with resin improved the bond strength by 12 %. However, the failure pattern did not change.

2.11. Theoretical Bond–Slip Models

The assumptions adopted for local bond stress-slip relations are important to understand the bond behaviour of the FRP-concrete joint. In the last decade, different mathematical models had been proposed to obtain the local shear stress–slip interfacial behaviour of the bonded joints. These models are derived based on the results of pull tests. Bond-slip models which have been established by (1) (Nakaba et al., 2001; (2) Sato and Vecchio, 2003; (3) Lu et a., 2005 and (4) Pellegrino and Modena, 2008) are presented in this section.

(1) Nakaba et al., (2001)

An interfacial shear stress-slip model derived from the results of the double-lap shear test was developed by Nakaba et al., (2001) which was assumed to take the form of a Popovic's trend. Two identical blokes of concrete mortar pre-attached by FRP reinforcement on both sides of the sample were tested and examined by Nakaba et al., (2001) to investigate the behaviour of the FRP/concrete joint using double-lap shear model. Concrete compressive strength and FRP axial rigidity are the main variables considered in this test. The local shear stress-slip relationship can be expressed as follows (Equation (2.1) and (2.2)):

$$\frac{\tau_b}{\tau_{b,max}} = \frac{S}{S_{max}} \cdot \frac{n}{(n-1)\left(\frac{s}{s_{max}}\right)^n} \tag{2.1}$$

$$\tau_{b,max} = 3.5\, {f_c'}^{0.19} \tag{2.2}$$

Where, τ_b is the interfacial stress in (MPa) at the slip S in (mm) and $\tau_{b,max}$ is the peak interfacial shear stress at the peak slip S_{max} which was assumed as 0.065 mm. n is a coefficient assumed as 3.0, which obtained from statistical analysis using the least squares method.

(2) Sato and Vecchio, (2003)

Sato and Vecchio, (2003) derived a new interfacial shear stress-slip models based on the crack tension stiffening effect and the crack width principles. They assumed a bilinear

interfacial shear stress-slip form. The maximum interfacial shear stress and the maximum slip can be obtained by the following equation (Equation (2.3) and (2.4)):

$$\tau_{bFy} = 6.6\sqrt{G_f} \quad (2.3)$$

$$S_{Fy} = 0.057\sqrt{G_f} \quad (2.4)$$

Where, τ_{bFy} is the maximum shear stress in (MPa) at the maximum slip S_{Fy} in (mm) and G_f is the interfacial fracture energy needed for local deboning of the FRP reinforcement from the surface of concrete. They noted that shear stress relationships may differ for samples cast with similar concrete strength and have the same strengthening configuration due to heterogeneity nature of concrete.

(3) Lu et al., (2005)

Three different shear stress-slip models with a various level of sophistication were proposed by (Lu et al., 2005). The bond stress-slip relationships are given by the following models:

(a) Precise model

Lu et al., (2005) used the meso-scale finite element model to predict an accurate bond-slip model of the FRP-to-concrete bonded joints. The bond stress-slip relationships are given by the following equations (Equation (2.5) and (2.6)):

$$\tau = \tau_{max}\left(\sqrt{\frac{s}{s_0 A} + B^2} - B\right) \qquad if\ s \le s_0 \quad (2.5)$$

$$\tau = \tau_{max}\, e^{-\alpha\left(\frac{s}{s_o}-1\right)} \qquad if\ s > s_0 \quad (2.6)$$

Where,

$$A = (s_0 - s)\,/s_0 \quad (2.7)$$

$$B = s_e/[2(s_0 - s_e)] \quad (2.8)$$

$$\tau_{max} = 1.5\beta_w f_t \quad (2.9)$$

$$s_0 = 0.0195\beta_w f_t + s_e \quad (2.10)$$

$$\beta_w = \sqrt{(2.25 - w_f/b_c)/(1.25 + w_f/b_c)} \quad (2.11)$$

$$s_e = \tau_{max}/K_0 \quad (2.12)$$

Where, f_t is the concrete tensile strength in (MPa), τ_{max} is maximum bond stress in (MPa) which occurs at maximum slip S_0 in (mm), β_w is the width ratio factor, w_f is the width of FRP strips in (mm) and b_c is the width of concrete element in (mm), S_e is the elastic component of S_0. The terms K_0, K_a and K_c are defined as (Equation (2.13), (2.14) and (2.15)):

$$K_0 = K_a K_c/(K_a + K_c) \quad (2.13)$$

$$K_a = G_a/t_a \quad (2.14)$$

$$K_c = G_c/t_c \quad (2.15)$$

Where, G_c is the elastic shear modulus of concrete in (GPa), t_c is the effective thickness of the concrete in (mm), G_a(GPa) is the elastic shear modulus of the adhesive, and t_a is the adhesive layer thickness in (mm).

(b) Simplified model

A new simplified model was derived by Lu et al., (2005) to predict the bond-slip response of the FRP-to-concrete bonded joint. This model defines the local shear stress (or the bond stress) at any location along the length of the FRP reinforcement in terms of the relative slip at that point as (Equation (2.16) and (2.17)):

$$\tau = \tau_{max}\sqrt{\frac{s}{s_0}} \qquad if\ s \le s_0 \quad (2.16)$$

$$\tau = \tau_{max}\, e^{-\alpha\left(\frac{s}{s_o}-1\right)} \quad if\ s > s_0 \quad (2.17)$$

Where:

$$s_0 = 0.0195\,\beta_w f_t + s_e \quad (2.18)$$

$$G_f = 0.308\beta_w^2\sqrt{f_t} \quad (2.19)$$

$$\alpha = \frac{1}{\frac{G_f}{\tau_{max}s_0}} - \frac{2}{3} \quad (2.20)$$

In which τ_{max} and β_w can be calculated with Equations (2.9) and (2.11) respectively. G_f is the interfacial fracture energy in (MPa mm), equal to the area underneath the bond–slip curve.

(c) Bilinear model

To propose a simple design model, a new bilinear bond–slip curve was developed by employing further simplifications to the simplified model. The man variable in this model such as the maximum bond stress and total interfacial fracture energy are similar to those proposed in the simplified model. This bilinear model is described by equations (2.21), (2.22) and (2.23):

$$\tau = \tau_{max}\frac{s}{s_0} \qquad if\ \ s \leq s_0 \tag{2.21}$$

$$\tau = \tau_{max}\frac{s_f - s}{s_f - s_0} \qquad if\ \ s_0 < s \leq s_f \tag{2.22}$$

$$\tau = 0 \qquad if\ \ s > s_f \tag{2.23}$$

Where:

$$s_f = 2G_f/\tau_{max} \tag{2.24}$$

τ_{max}, β_w and G_f can be calculated by using Equation (2.9), Equation (2.11) and Equation (2.19) respectively. Figure (2.12) shows the difference between the three bond-slip models which were proposed by Lu et al., (2005). It can be noticed that there is little difference between the precise and simplified models, the prediction of the bilinear model is also shown in this Figure.

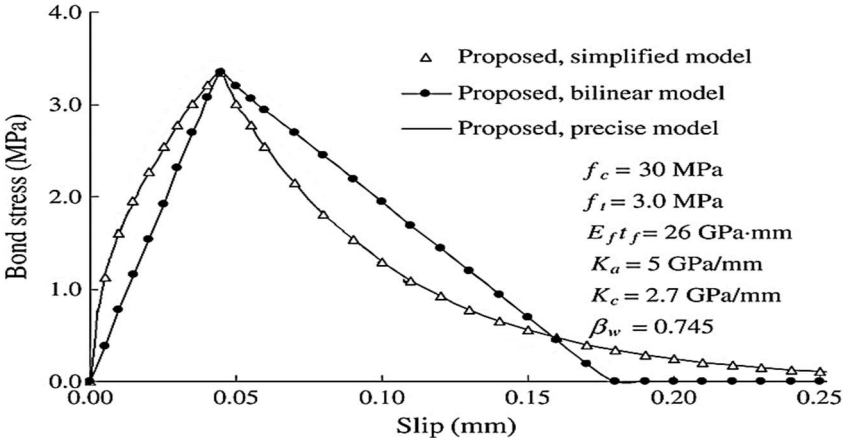

Figure (2.12): Bond–slip models adapted from (Lu et al., 2005).

(4) Pellegrino and Modena (2008)

Based on the outcomes of the pull off shear and beam tests, a non-linear empirical local shear stress-slip model was proposed by Pellegrino and Modena, (2008). Pellegrino and Modena, (2008) noted that the FRP axial rigidity (the multiplication of the thickness and the modulus of elasticity of the FRP reinforcement) can affect the joint response and the maximum load capacity of the FRP/concrete interface. The ascending and the descending trend of the bond-slip model is characterised by equations (2.25) and (2.27):

$$S = \tau_{max}(S/S_{peak})^{0.575} \qquad for \quad S \leq S_{peak} \tag{2.25}$$

$$S = \tau_{max}(S^{\propto} - S_{ult}^{\propto})/(S_{peak}^{\propto} - S_{ult}^{\propto}) \qquad for \quad S > S_{peak} \tag{2.26}$$

Where,

$$\propto = -1.3162/(n_f t_f E_f)^{0.187} \tag{2.27}$$

Where τ_{max}, is the maximum shear stress at the maximum relative slip, S_{peak} and the ultimate achieved relative slip, S_{ult}. S is defined as the slip at any point along the bond length.

Where,

$$\tau_{max} = 3.1(n_f t_f E_f)^{0.32} \tag{2.28}$$

$$S_{peak} = 0.075/(n_f t_f E_f)^{0.2} \tag{2.29}$$

$$S_{ult} = 10.5/(n_f t_f E_f)^{0.6} \tag{2.30}$$

Where, n_f is the layer's number of FRP reinforcement, t_f is the thickness of each layer in (mm), and E_f is the FRP modulus of elasticity.

2.12. Proposed Bond strength models

Many theoretical models have been proposed to predict the bond strengths of FRP-Concrete bonded joints. The summary of some available bond strength models namely (i) Yang et al., (2001), (ii) Izumo et al., (1999), (iii) Sato et al., (2003) and (iv) Iso et al., (2003) is presented in this section were the following units are used: Newtons for bond strength, MPa for stresses and elastic modulus, and mm for lengths and widths.

(i) Yang et al., (2001)

The bond strength model proposed by Yang et al., (2001) is given by (Equation 2.31):

$$P_u = \left(0.5 + 0.08\sqrt{\frac{E_f\, t_f}{100 f_t}}\right)\tau_u\, w_f\, L_e \qquad (2.31)$$

Where, $\tau_u = 0.5\, f_t$, $L_e = 100$ mm

In which, P_u is the bond strength, τ_u is average bond stress, L_e is the effective bond length, w_f is the width of FRP sheet, E_f is the elastic modulus of FRP, t_f is the thickness of FRP sheet, f_t is the tensile strength of concrete and b_c is the width of the concrete prism,

(ii) Izumo et al., (2003)

JCI (2003) published two equations of bond strength model depending on FRP type proposed Izumo et al., (1999). These equations are given as (Equation (2.32) and (2.33)):

For carbon-fibre reinforcement sheets:

$$P_u = \left(3.8\, f_c'^{2/3} + 15.2\right) L\, E_f\, w_f\, t_f\ \times 10^{-3} \qquad (2.32)$$

For Aramid-fibre reinforcement sheets:

$$P_u = \left(3.4\, f_c'^{2/3} + 69\right) L\, E_f\, w_f\, t_f\ \times 10^{-3} \qquad (2.33)$$

Where L is bond length and f_c' (MPa) is the compressive strength of concrete.

(iii) Sato et al., (2003)

The bond strength model given by Sato et al., (1997); Sato et al., (2001) and JCI, (2003) is described by the following equation (Equations (2.34) to (2.37)):

$$\tau_u = 2.68\, f_c'^{0.2} E_f\, t_f\ \times 10^{-5} \qquad (2.34)$$

$$L_e = 1.89\left(E_f\, t_f\right)^{0.4} \qquad (2.35)$$

If $L_e > L$, then $L_e = L$ (2.36)

$$P_u = \left(w_f + 2\Delta b\right) L_e\, \tau_u \qquad (2.37)$$

Where Δb is the working width of concrete and it is equal to 3.7 mm, L_e is the effective bond length, τ_u average bond stress.

(iv) Iso (2003)

The bond strength model proposed by (Iso, 2003) and published in (JCI, 2003) is given by (Equations (2.38) to (2.40)):

$$\tau_u = 0.93\, f_c'^{0.44} \quad (2.38)$$

$$L_e = 0.125\, \left(E_f\, t_f\right)^{0.57} \quad (2.39)$$

$$P_u = \tau_u\, w_f\ L_e \quad (2.40)$$

2.13. Finite Element Simulation of FRP-concrete Joints

Many techniques had been used to simulate the interface response between the FRP and the concrete; (Arduini et al., 1997; Barnes and Mays, 2001; Wong and Vecchio, 2003; Lu et al., 2005b; Chen et al., 2007; Coronado and Lopez, 2006; Chen et al., 2011; O'Mahoney et al. 2013 and Xu and Wei, 2013). Chen et al. (2011) used a band crack model to model the behaviour of the concrete element in conjunction with interface elements to model the interface between FRP and concrete.

Lu et al. (2009) used COMBIN39 (a nonlinear spring element) in ANSYS (ANSYS, 2009) software to simulate the interface between the FRP elements and the supports. The study of Lu et al. (2006) provides a numerical study of the FRP stress distribution at debonding failure in U-jacketed or side-bonded beams using a rigorous FRP-to-concrete bond–slip model and assuming different crack width distributions.

2.14. Shear Failure Mechanism in Reinforced Concrete Beams

Shear failure of shear reinforced concrete beams is caused by the initiation of diagonal tension cracks within the web of the beam which can become unstable and fail. In order to resist the shear stresses produced by the applied loads, the beam web develops several shear transfer mechanisms that include:

a) Shear strength provided by compression zone of concrete (V_{cc});
b) Aggregate interlocking at the crack faces (V_{ca});
c) Shear strength or the dowel action provided by longitudinal reinforcement (V_d), the resistance provided by the dowel action is dependent on the amount of flexural reinforcement (ρ); and

d) The shear reinforcement resistance (V_s) from shear links for beam with shear reinforcement.

Figure (2.13) shows the shear force transfer through a reinforced concrete section (MacGregor and Wright, 2005). The mechanism of shear failure in reinforced concrete beams is affected by many factors such as the ratio of shear steel reinforcement, the longitudinal tension steel reinforcement ratio, concrete strength, shear span ratio, type and size of the aggregates and the geometry of the beam cross section (Sas, 2011). The total shear capacity of reinforced concrete section can be calculated from the following equation:

$$V = V_{cc} + V_{ca} + V_d + V_s \tag{2.41}$$

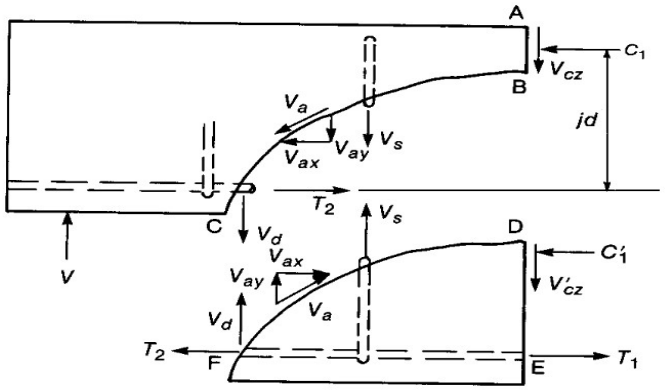

Figure (2.13): Mechanism of shear force transfer (MacGregor and Wright, 2005).

A truss model was developed by Swiss engineer Ritter and The German engineer Mörsch in 1899 and 1902, respectively, this model provides a good concept to describe the forces developed in a cracked concrete beam. Therefore, this model became the basis of the current design codes and guidelines such as the ACI code, British Standards and the Eurocode. The truss model, also named as the strut-and-tie model postulates that after cracking of the concrete, the response of an RC beam becomes analogous to that of a truss with a top longitudinal compression cord, a bottom longitudinal tension cord, vertical steel ties and diagonal concrete struts as shown in Figure (2.14) (Al-Juboori, 2011). The figure shows the possible failures partners of the RC and the typical truss model.

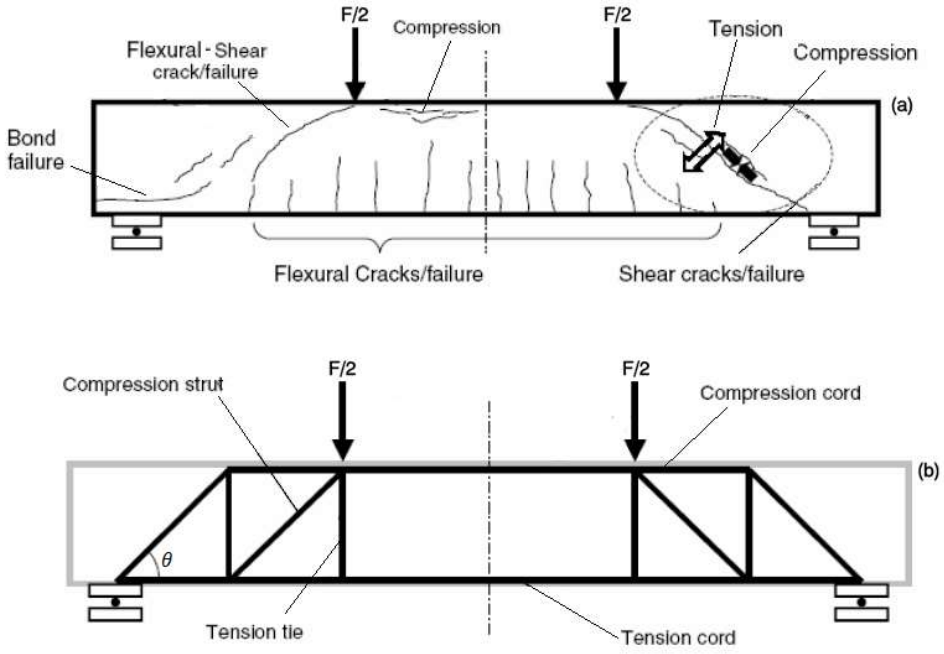

Figure (2.14): (a) Some of the potential failures for reinforced concrete beams **(b)** The truss model with struts and ties (Al-Juboori, 2011).

2.15. Shear Failure Mechanism in Reinforced Lightweight Concrete Beams

Much research has been carried out on reinforced LWC members and they have been shown to have a similar response as for members cast with normal aggregates with some differences to an extent in performance. Especially from the shear and diagonal tension resistance, these properties are sufficiently different to require design modification. The current design codes and guidelines treat this problem by introducing reduction factors to NWC equations. This is because LWC has lower cracking strength compared with NWC of similar grade concrete (Hanson, 1961 and Juan, 2011).

The shear failure mechanism of the LWC beams is similar to those beams cast with a conventional type of the aggregates until the development of diagonal cracking. After that, the NWC beams are unable to resist shear cracks and attained the required shear strength to develop flexural modes of failure. The crack development and propagation in LWAC are quite different from that in NWAC. In LWC under tension force, the failure is developed by tensile stresses in the LWA as well as by failure in the concrete matrix surrounding the aggregates. Generally, the tensile strength of LWA is significantly lower than the concrete matrix. In the case of NWC, the failure usually develops by breaking the bond at the boundary between the concrete matrix and the surface of the aggregate. Diagonal shear

cracks of LWC is random and its position cannot be precisely expected. The shear mechanism of LWC is significantly complex and indeterminate causing to the usefulness of empirical formulas in predicating the shear strength of the lightweight concrete members (Juan, 2011).

2.16. Current Code Treatment for Lightweight Concrete Beams Shear Strength

The concrete contribution of the LWC beams is treated by the current codes and gridlines as a function of normal weight concrete contribution which has a similar concrete grade (compressive strengths). The easiest way to calculate the shear strength of the LWC by introducing a constant reduction factor for the equivalent grade of NWC shear strength including the wide range of normal and manufactured lightweight aggregates and aggregate properties available (Juan, 2011). The ACI 318-08 and Eurocode 2 treatment are addressed in this section, as too are the superseded code BS8110.

2.16.1. ACI 318-08 Treatment for Lightweight Concrete Beams Shear Strength

The American Concrete Institute's Building Code (ACI-318, 2008) addresses the shear design of lightweight aggregate concrete beams by reducing the concrete contribution component in the shear strength equation by using two approaches. In first approach, $\sqrt{f_c'}$ was replaced by $(f_{ct}/6.7)$. The coefficient 6.7 was derived from tests by Hanson, (1961).

An alternative approach when estimating the design shear capacity of a LWC section may be used if an engineer is unable or hesitant to determine the cylinder splitting strength. Reduction factors are available that determine the shear capacity of LWC beam as a fixed percentage of NWC shear strength. Two reduction factors, A 0.85 for concrete cast with sand and coarse lightweight aggregates and 0.75 for concrete cast with lightweight coarse and fine aggregates is provided because research on tensile strength of lightweight concrete obtained from splitting test shows an enhancement in tensile strength when conventional sand is used instead of lightweight fine aggregates (ACI-318, 2008).

2.16.2. BS 8110 Treatment for Lightweight Concrete Beams Shear Strength

The British Standard (BS8110, 1985) assumes that the total shear resistance of a beam is the sum of the shear capacity of the concrete cross-section and that of the shear reinforcement. The LWC cross section shear strength is assumed as 0.8 of the value for the NWC

compressive strength. This reduction factor is also used to the maximum limit of shear stress that can be carried by the concrete section, either $0.63\sqrt{f_{cu}}$ or 4 MPa whichever is lower, even when shear reinforcement is provided. It also limits the maximum allowable compressive strength to 40 MPa.

Ahamad et al., (1994) noted that allowing the concrete compressive strength to exceed 40 MPa in calculating the maximum shear strength provided by LWC section. they noted that this value provides an adequate margin of safety and the coefficient of reduction can be increased to 0.85 simultaneously.

2.16.3. Eurocode 2 Treatment for Lightweight Concrete Beams Shear Strength

The Eurocode 1992 (Eurocode 2, 2014) treatment of LWC is also based on the same principal for NWC. The first term in the concrete shear capacity equation is multiplied by a reduction factor due to the lower tensile strength of LWC with no change in the second term which accounts for axial compression in the member. The partial factor of concrete $C_{Rd,c}$ is also reduced for lightweight concrete from $0.18/\gamma_c$ for normal weight concrete to $C_{lRd,c} = 0.15/\gamma_c$ for lightweight concrete.

Eurocode 2 addressed two variables to treat the lower shear strength of the LWC. In the first variables, a constant reduction is assumed in the $C_{lRd,c}$ term while the second reduction variable , η_1 classify the lightweight aggregates into different density as shown in Equation (2.42) (Juan, 2011):

$$\eta_1 = 0.40 + 0.6c/2200 \quad (2.42)$$

The shear capacity formula for the LWC addressed by Eurocode 2 for beams without shear reinforcement and not subject to axial loads is shown in Equation (2.43) below with recommended values and lightweight concrete adjustments.

$$V_{lRD,c} = \left[0.15/\gamma_c k(0.40 + 0.06c/2200)\ (100\rho f_{ck})^{1/3}\right] b_w d \quad (2.43)$$

Where, γ_c is partial factor of concrete and c is the density class, giving factors listed in Table (2.1).

Table (2.1): Tensile strength reduction factors in the draft European code (Eurocode 2, 2014).

Density class	Maximum oven-dry density (Kg/m^3)	Factors
2.0	1801-2000	0.9
1.8	1601-1800	0.85
1.6	1401-1600	0.8
1.4	1201-1400	0.75

2.17. Shear Behaviour of RC beams Strengthened with FRP

In retrofitted members, the complexity of shear mechanism is significantly increased by adding FRP reinforcement. Many variables affect the response of the RC beams retrofitted with FRP shear reinforcement. The effect of these variables was assessed by examining data from various experimental studies and new design models were proposed by other researchers to estimate the shear strength gained due to FRP reinforcement based on this experimental data. FRP debonding and FRP rupture are the main failure patterns of the RC beams strengthened with FRP reinforcement. Debonding failure is developed by the properties of the weakest materials in the FRP/concrete joint, that is, the concrete, between the concrete and adhesive or in the adhesive layer. Rupture failure develops when the normal stresses in the FRP reinforcement increase further than the maximum tensile strength of the fibre. Rupture failure can be distinguished by a sudden extending of failure until the occurrence the global debonding of the FRP from the surface of concrete (Sas, 2011).

2.18. Previous Studies on Shear Strengthening of (RC) Beams with (CFRP)

A considerable amount of experimental and numerical studies were reported in the literature over twenty years ago to investigate the shear behaviour of reinforced concrete beams retrofitted with externally attached FRP reinforcement. Most of them focused on the shear response of FRP-strengthened or repaired NWRC beams with different geometry, shear reinforcement ratio and FRP retrofitting techniques.

2.19. Existing Experimental Studies and Parameters Studied

An extensive literature survey containing the details of tests were carried out on NWRC beam specimens repaired or retrofitted with FRP reinforcement. Details of the most available studies classified according to the parameters investigated are described in this section.

2.19.1. Strengthening Techniques

In RC beams (with or without shear reinforcement) failed by FRP debonding, U-wrapped provided significantly better shear performance over side-bonds. While for RC beams failed by FRP rupture, closed-wrapped provided significantly better shear performance over U-wraps due to the anchorage provided around the beam corners. The studies by Triantafillou, (1998) and Adhikary et al., (2004) provide direct insight regarding the effect of strengthening configuration on shear behaviour of RC beams.

A series of tests was carried out by Triantafillou, (1998) to increase the experimental database for the shear strengthening of RC beams using FRP. Eleven shear critical concrete beams were loaded, nine of them strengthened externally with side bond shear CFRP reinforcement, the other two samples were employed as control samples without CFRP reinforcement. Triantafillou, (1998) noted that the shear strengthening of reinforced concrete beams using CFRP reinforcement reveals a highly effective retrofitting system. Within the limit of the conventional design code of practise, based on ultimate limit states, the design of the RC members retrofitted with FRP reinforcement can be addressed in analogy with the conventional design method used for shear reinforcement links, provided then an effective FRP strain is used in the formulation.

Adhikary et al., (2004) tested eight RC beams strengthened with continuous sheets of CFRP reinforcements. Many variables such as strengthening configuration, direction or depth of CFRP, the number of layers and the effect of using two perpendicular sheets were examined to assess their effects on the shear strength of the RC beams. It was observed that the diagonal shear crack in beams strengthened with side bond occurred at a higher load than for the control beams. Beams retrofitted with double horizontal and vertical layers of CFRP sheets showed slightly higher diagonal shear crack resistance than those beams with a single layer. Adhikary et al., (2004) also observed that the beams with full sheet depths failed by splitting and crushing of the concrete layer behind the CFRP sheets which caused debonding failure in some beams, while in beams strengthened with double-layers of sheets, ruptures in the parallel direction were observed. Adhikary et al., (2004) concluded that the depth of sheet layers across the beam significantly increase the shear strength of RC beams**.** The highest shear strength gains in RC beams retrofitted with vertical full U-wrapping were observed with up to 119%. increase in shear capacity as compared to the control beam without shear

retrofitting. The test results showed that the shear strength of beams did not increase with additional sheet layers.

2.19.2. Fibre Inclination and FRP Width

Results from previous studies listed below revealed that the width of the FRP reinforcement attached to the concrete surface has a significant effect on the maximum shear strength of the reinforced concrete beam. The FRP should be oriented to get the desired strength, thus, the fabric used in FRP strengthening systems generally has the highest tensile strength in the direction of the principal fibres. Studies by Monti and Liotta, (2007) and Sundarraja and Rajamohan, (2009) are described herein to represent those found from the literature review which focused on the effect of orientation and width of FRP on the effectiveness of this strengthening techniques.

Monti and Liotta, (2007) tested twenty-four beams under-reinforced in shear, strengthened with side-shaped and U-shaped strengthening system with different width of FRP reinforcement and CFRP orientation as shown in Figure (2.15). Monti and Liotta (2007) concluded that the oriented FRP reinforcement showed a good shear behaviour compared with samples retrofitted with vertical strips. Monti and Liotta (2007) noted that the FRP reinforcement oriented perpendicularly to the compressive strut inclination show the best way to cross the diagonal shear crack as well as the higher shear contribution to the total shear strength of the tested beams. They also noted that reducing the distance between the FRP strips or using wider FRP reinforcement revealed a significant improvement in shear strength provided by FRP.

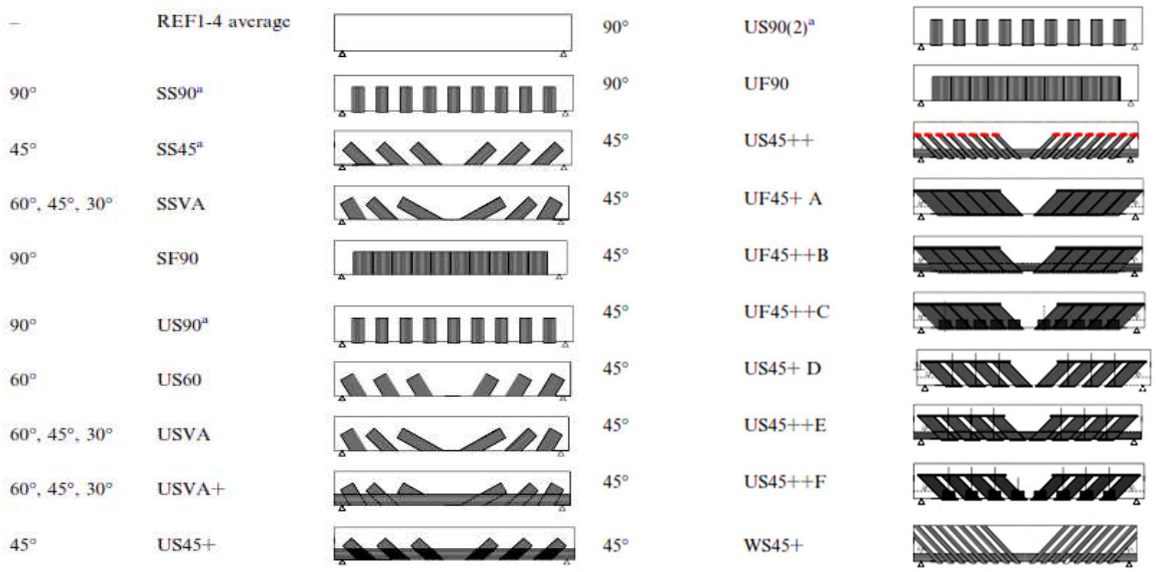

Figure (2.15): Specimens strengthening scheme details (Monti et al 2007).

Sundarraja and Rajamohan, (2009) used vertical and inclined GFRP strips in the form of side-bonds and U-wraps to retrofit reinforced concrete beams in shear. The main objective of this study was to increase the experimental data regarding the response of RC beams strengthened with FRP. In addition, to evaluate the effect of inclined GFRP strips bonded externally to concrete beam webs to retrofit RC beams failing in shear. The parameters investigated in this test were the spacing and width of GFRP and the spacing of internal steel strips. Sundarraja and Rajamohan, (2009) observed a slight variance in the behaviour between samples retrofitted with side-bonds and U-wrapped. They also concluded that the shear strength is significantly increased by using wider FRP reinforcement. A significant enhancement in the shear strength of the strengthened tested samples by altering the FRP reinforcement direction from 90° to 45°.

2.19.3. Shear Reinforcement ratio

The behaviour of the strengthened beams with FRP reinforcement is affected by the shear reinforcement ratio. The previous study showed that the shear strength gained due to CFRP reinforcement decreases as the shear steel reinforcement increased for both modes of failure (debonding and rupture of the FRP reinforcement). The study by Pellegrino and Modena, (2002) is described herein to represent those found in the literature review which focused on the interaction between the transverse shear reinforcement and the FRP composite.

Pellegrino and Modena, (2002) provided new insight into the complex failure mechanisms that investigate the shear capacity of RC elements with shear steel and FRP reinforcement. Eleven rectangular beams designed with a different ratio of the shear reinforcement and FRP were tested. The experimental test samples were divided into two groups: the first group composed of four samples without shear reinforcement, and the second group composed of seven samples reinforced with the same ratio of shear reinforcement. Various thickness of side-bonded FRP reinforcement was applied along the length of the tested samples.

Shear failure due to loss aggregate interlock or shear failure due to CFRP debonding were the failure modes of the control sample without shear reinforcement and the strengthened samples respectively. It was observed that the samples with shear reinforcement developed many diagonal shear cracks compared with the control sample. In this study, the crack distributions did not considerably alter for samples retrofitted with FRP reinforcement and the all the strengthened samples developed many shear cracks similar to those observed in

samples with shear links. Pellegrino and Modena, (2002) noted that the FRP had the same effect on beam crack distributions as for internal shear reinforcement and the shear strength provided by FRP reinforcement decreased with an increase of the shear steel ratio.

2.19.4. Shear Span to Depth Ratio

The shear span to effective depth ratio *(a/d)* has a significant effect on the shear behaviour of the reinforced concrete beams retrofitted with FRP reinforcement. The efficiency of the FRP system increases with the (a/d) ratio up to span to depth ratio equal to 4; after this ratio, the shear strength gains become steadily smaller. Two studies by Khalifa and Nanni, (2002) and Lee et al., (2011) are now described in this section.

Twelve full-scale RC beams retrofitted with CFRP were tested by Khalifa and Nanni, (2002) as simply supported rectangular RC beams failing in shear by four–point bending to study the shear behaviour of RC beams designed with shear deficiencies. The transverse steel ratio, the shear span to depth ratio and CFRP distribution were the main factors investigated in this study. The test specimens were divided into two groups according to the presence of shear stirrups in the half span, the first series consisted of four beams reinforced with 10 mm steel stirrups, while eight beams without steel stirrups in the half span were tested in the second series. Both test series were further subdivided based on the shear to span ratio which was selected as a/d=3 and 4, also different CFRP strengthening configurations (U-warp and two sides bond), the number of layers and CFRP direction. The results obtained by Khalifa and Nanni, (2002) showed that the gain in the shear capacity of RC beams strengthened externally with CFRP increases by between 40-138% dependent upon the variables investigated. They also concluded that the CFRP contribution is effected by the shear span to depth ratio and the presence of steel stirrups.

Lee et al., (2011) tested fourteen reinforced concrete (RC) T-section deep beams shear retrofitted with a CFRP composite. Lee et al., (2011) concluded that the CFRP sheets strengthening length have a noticeable effect on the shear behaviour of retrofitted deep beams. Hence, the shear strength gains from externally attached CFRP reinforcement increases as the retrofitting development length increases. Also, they observed that the CFRP sheets orientation have a considerable effect on the shear response of the loaded deep beams in ultimate carrying capacity and ductility. As compared to the ($90^o/90^o$), ($90^o/0^o$) and ($45^0/135^o$) fibre direction combinations, the two horizontal layers of CFRP sheets may

provide a greater contribution to the shear strength of the inclined compression strut by arch action. Using anchorage techniques for U-wrapped configuration of CFRP composite was shown to be very effective in increasing the maximum shear strength, initial stiffness, and ductility, due to an anchorage effect.

2.19.5. Effect of Beam Size

Leung et al., (2007) carried out an extensive experimental program in which fifteen rectangular beams were tested under the four-point bending scheme to evaluate the effect of size on the failure of geometrically similar concrete beams retrofitted with FRP reinforcement. The objectives of this study were to provide data on beams of large size to examine the validity of design equations for practical size beams and to investigate if the strengthening effectiveness for different depth beams was similar. Leung et al., (2007) noted that the maximum load capacity provided by U-wrapped reinforcement significantly decreased as beam size increased. While samples with closed-wrapped reinforcement did not considerable influence by this issue, the increase in load capacity attributed to the U-wraps was up to 60% for the small size specimens, while this was between only 3% and 7% for the medium size and large size samples, respectively.

2.19.6. Effect of Concrete Type

Al-Rousan et.al. (2011) investigated the shear behaviour of pre-cracked reinforced concrete beams cast with expanding slate used as a coarse aggregate. Expanding slate is a lightweight aggregate manufactured by the rotary kiln processes. The experimental programme was conducted in two stages. In the first stage, a reinforced concrete beam was cast with conventional aggregates retrofitted with CFRP reinforcement in shear. The beams had a cross section of 150 x 225 mm width and depth respectively, and a length of 1500 mm. The shear strength of CFRP reinforcement was examined in this test. In the second stage, the experimental test was carried out to study the shear behaviour of RC beams cast with expanding slate. The effect of shear span to depth ratio (a/d) and the effect of concrete compressive strength was investigated in this programme. The RC beams had a cross section of 200 x 250 mm width and depth respectively and a length of 3600 mm. The RC beams in the second stage of this test were tested to failure to study the shear contribution. The beams that failed at one end due to shear failure were repaired with CFRP reinforcement and tested again for shear to study the shear contribution of CFRP. Al-Rousan et.al. (2011) concluded that the modes of failure for RC beams repaired with CFRP changed from shear to flexure

after being strengthened with CFRP reinforcement. The Shear strength of RC beams cast with expanding slate increases with the decrease in *a/d* ratio. However, this study didn't provide a comparison between RC beams cast with expanding slate and samples cast with conventional aggregates. The main focus of this study was to study the response of the repaired samples with different variables.

2.19.7. Loading Type

Most of the available studies were tested under monotonic loads. Only three studies by Anil, (2006); Anil, (2008) and Colalillo and Sheikh, (2014a) were found to loaded under reversed cyclic loads and the study by Carolin and Täljsten, (2005) used fatigue loads.

2.19.7.1. Previous Studies with Monotonic Loads

Two identical shear deficient rectangular beam samples were loaded by Sheikh et al., (2002. These samples were designed similar to those located in a tall building which required retrofitting. The shear reinforcement ratio was increased in one half the beam as shown in Figure (2.16). The samples were loaded in three-point loading condition; the monotonic loads were applied at the mid-span of the beam. The control sample was tested up the maximum applied load of 1750 kN. The control sample failed in shear due to diagonal shear cracks. Another sample was loaded up to shear cracking load of 1100 kN which was identical to that recorded in the control sample.

The applied load was sustained for three days and during this time the FRP reinforcement was applied along the shear span using closed-shaped strengthening techniques. After that then the sample was loaded again until sample flexural failure at a maximum applied load of 2500 kN. FRP rupture was developed at the corner close the centre of the beam due to high normal and shear stresses occurred close to this region. Sheikh et al., (2002) noted that the strengthening was effective in enhancing the maximum load carrying capacity of the strengthened samples by an approximately by more than one and half times over the control sample. Flexure failure was the failure pattern of the strengthened samples compared with control samples which were failed in shear.

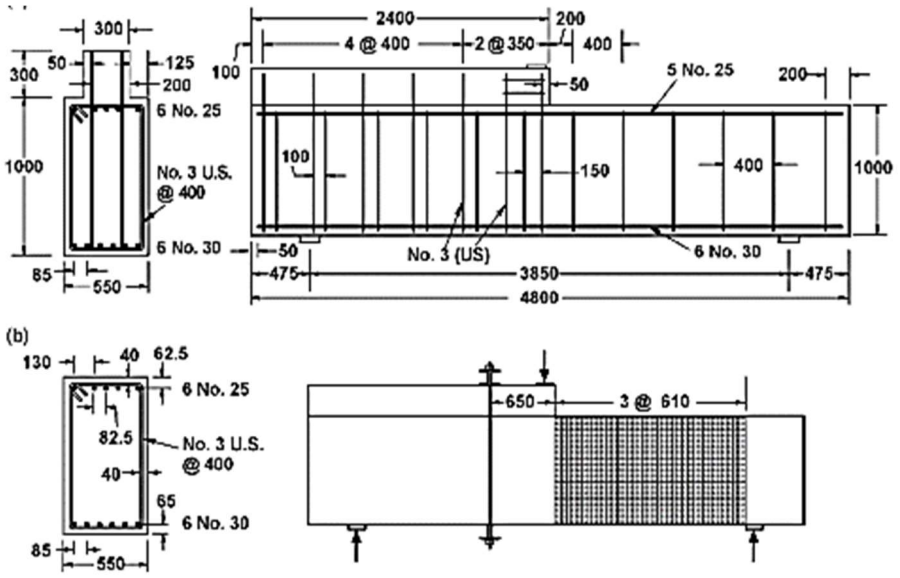

Figure (2.16): Beam and reinforcement details (Sheikh et al 2002).

2.19.7.2. Previous Studies with Reversed Cyclic Loads

There are few experimental studies with FRP retrofitted beams tested under reversed cyclic loading conditions. The studies by Anil, (2006) and (2008) are described in this section to represent those studies found in the literature review which focus on the performance of RC beams retrofitted with CFRP subject to reversed cyclic loading.

Anil, (2006) examined the effect of cyclic load on the shear response of T-beams strengthened externally with CFRP reinforcement, the effect of the free ends anchorage was studied in this study. Anil, (2006) tested two control samples and four samples strengthened with various types of free end anchorages and FRP strengthening techniques were tested in shear. Anil, (2006) concluded that the shear capacity of samples with end anchorage were significantly higher than samples without this technique. The typical test setups are shown in Figure (2.17).

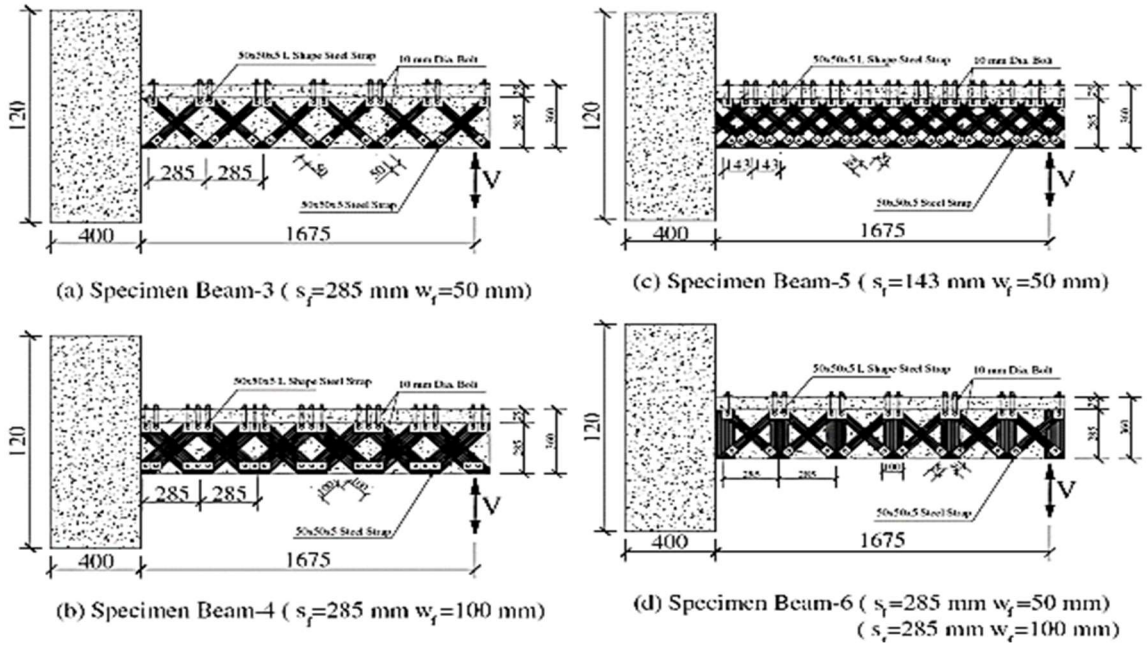

Figure (2.17): Arrangement of FRP strips on strengthened specimens (Anil 2006).

Another six T-beams samples were tested by Anil, (2008). The sample's geometry and the test setups were similar to that tested in the earlier study by Anil, (2006). The tested samples were cast with low concrete crushing strengths. In the earlier study by Anil (2006), the FRP reinforcements were attached in complicated strengthening configurations, while in this study the FRP reinforcement was installed perpendicularly to the longitudinal axis of beam. Anil, (2008) noted that the samples cast with low crushing strength of concrete strength failed in lower load compared with anchoraged samples.

2.19.7.3. Previous Studies with Fatigue Loads

Carolin and Täljsten (2005) tested a number of rectangular concrete beams 3.5 m to 4.5 m long. Different parameters, such as fatigue and free end anchorage were studied. In this study, different failure modes had been identified, for example, CFRP rupture, anchorage failure, and combinations thereof. It was concluded that samples tested under fatigue loads showed a higher shear capacity compared with a control sample. The higher crack intensity for fatigue tested samples are likely to induce more stresses in the FRP reinforcement which increase the shear contribution provide by CFRP reinforcement.

2.19.8. Anchorage System

Many studies have revealed that structures strengthened with CFRP reinforcement experienced premature failure due to FRP debonding. As a result, a number of studies were conducted to provide some sort of anchorage for the CFRP reinforcement to prevent or delay debonding failure and to improve the structural performance of the strengthened structures. Various anchorage systems were investigated in the literature, most commonly: adding horizontal CFRP strips, using CFRP anchors, using near surface mounted (NSM) strips, and various types of mechanical anchorage systems that use steel bolts and plates.

Hutchinson and Rizkalla, (1999) investigated the use of horizontal strips on top of diagonal CFRP strips to provide anchorage for the main strengthening FRP reinforcement There was an increase of 16% in shear strength due to the addition of the horizontal strips. This was compared to a 10% increase in shear strength for samples without FRP anchorage was provided.

Belarbi et al., (2012) investigate the efficiency of using various mechanical anchorage systems. Tests were carried out on full-scale T-beams strengthened with CFRP reinforcement that was anchored with 1) horizontal strip, 2) mechanical anchorage, or 3) sandwich panel mechanical anchorage. All three systems showed anchorage that resulted in improving the total shear capacity. However, samples with anchored sandwich panel mechanical anchorage system showed the best shear performance compared with other systems. Figure (2.18) show the typical arrangement of the mechanical anchorage system developed by Belarbi et al., (2012).

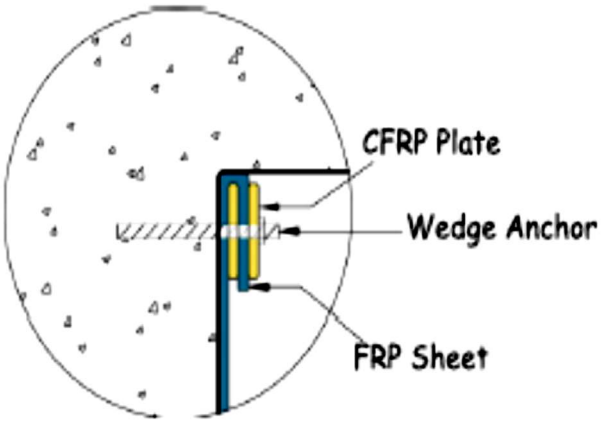

Figure (2.18): The typical arrangement of the sandwich panel mechanical anchorage system (Belarbi et al., 2012)

2.20. FRP Design Proposals

Several design models were proposed many years ago to predicate the shear contribution provided by FRP reinforcement which used to strength RC members, some of these models are proposed by different authors using a simple approach, and some of them are addressed in current design standards and guidelines (Colalillo, 2012). The details of the effective variables for the different design models for FRP shear retrofitting are shown in Table (2.2).

The debonding or the rupture models are the main design proposals considered in the current design code and guidelines or the models proposed by authors as specified in Table (2.2). The effect of the bonded length of the FRP reinforcement (effective bond length), the axial rigidity of the FRP, and the dimensions or the shape of the FRP reinforcement are also addressed in most of the available debonding failure models. Finally, the influence of the shear steel reinforcement and the compressive strut inclination are included in the last two parameters for both debonding or rupture models There are a limit number of models developing an equation for estimating the shear contribution provided by the FRP reinforcement for fully wrapped samples. Debonding models for side-shaped and U-shaped has received much attention in the current design code and guidelines, the anchorage length which is a function of the FRP axial rigidity and the concrete tensile or compressive strength is the main variable in the current debonding models (Colalillo, 2012).

Table (2.2): Summary of design models effective parameters (Colalillo, 2012).

Design models	Effective parameters						
	Debonding failure model	Rupture failure model	Debonding model			Shear crack angle	Influence of steel reinforcement
			Effective length	FRP axial rigidity	FRP width and spacing		
Concrete Society TR-55 (2000)	Y	Y	Y	Y			
fib Bulletin 14 (2001)	Y	Y		Y		Y	
JSCE-CES-41 (2001)		Y					
CNR-DT-200 (2004)	Y	Y	Y	Y	Y	Y	
CSA S6-06	Y		Y	Y		Y	

ACI 440.2R-08	Y		Y	Y			
Chen and Teng (2003a, b)	Y	Y	Y	Y	Y	Y	
Deniaud and Cheng (2004)	Y		Y	Y			Y
Cao et al. (2005)	Y		Y	Y	Y		
Monti and Liotta (2005)	Y	Y	Y	Y	Y		
Kim et al. (2008)	Y					Y	Y
Pellegrino and Modena (2008)	Y		Y	Y			Y
Mofidi and Chaallal (2011)	Y		Y	Y	Y	Y	Y

2.20. Current Design Guideline Provisions for FRP Shear Contribution

The objective of this section is to review the design provisions of the major design guidelines related to the shear retrofitting of RC beams with FRP. Various FRP design methods including international design are used to predict FRP shear contribution, standards, such as (1) fib Bulletin 14, 2001; (2) TR-55, 2000; (3) ACI 440.2R-08 and (4) CSA S6-06, 2006. These are now considered in order.

(1) Fib Bulletin 14 (2001)

A technical report for externally attached FRP reinforcement was published by the International Federation of Structural Concrete (*fib*). The FRP shear strength provided by the FRP reinforcement can be calculated from the following equation (Equation (2.44)):

$$V_f = 0.9\rho_f E_f \varepsilon_{fde} bd\left(\cot\theta + \cot\beta_f\right)\sin\beta_f \tag{2.44}$$

Where, ε_{fde} is design effective strain which is obtained by dividing the effective strain ε_{fe} by a safety factor of 0.8. The effective strain is governed by the FRP retrofitting configuration and the FRP material type. The guidelines state that the effective strain is a function of the axial rigidity of FRP ($\rho_f E_f$) and the compressive strength of concrete as follows:

For full carbon-FRP (CFRP) wraps (Equation (2.45)):

$$\varepsilon_{fe} = 0.17\left(\frac{f_{cm}^{2/3}}{E_f\rho_f}\right)^{0.3}\varepsilon_{fu} \tag{2.45}$$

For side-bonded or U-shaped CFRP reinforcement (Equation (2.46)):

$$\varepsilon_{fe} = \min\left[0.65\left(\frac{f_{cm}^{2/3}}{E_f\rho_f}\right)^{0.56} x\ 10^{-3}; 0.17\left(\frac{f_{cm}^{2/3}}{E_f\rho_f}\right)^{0.3} \varepsilon_{fu}\right] \quad (2.46)$$

For Full aramid-FRP wraps (Equation (2.47)):

$$\varepsilon_{fe} = 0.048\left(\frac{f_{cm}^{2/3}}{E_f\rho_f}\right)^{0.47} \varepsilon_{fu} \quad (2.47)$$

Where, E_f is in GPa, ε_{fu} is the ultimate FRP tensile strain and f_{cm} is the cylindrical compressive strength of concrete in MPa.

(2) <u>ACI 440.2R (2008)</u>

In the ACI code (ACI 2008), the FRP contribution is given by (Equation (2.48)):

$$V_f = \frac{A_f f_{fe}\left(\sin\beta_f + \cos\beta_f\right) d_f}{s_f} \quad (2.48)$$

For fully-wrapped FRP systems, the limit of the maximum effective-strain is depending on limiting the shear crack widening to ensure sufficient aggregate interlocking at the crack faces, while the effective strain for the U-shaped and side-bonded FRP systems is computed based on FRP configuration system as follows:

For Full FRP-Wrapped reinforcement (Equation (2.49)):

$$\varepsilon_{fe} = 0.004 \leq 0.75\varepsilon_{fu} \quad (2.49)$$

And for side-bonded or U-shaped FRP reinforcement (Equation (2.50)):

$$\varepsilon_{fe} = k_v\varepsilon_{fu} \leq 0.004 \quad (2.50)$$

Where,

$$k_v = \frac{k_1 k_{2\, l_e}}{11{,}900\ \varepsilon_{fu}} \leq 0.75;\ l_e = \frac{23{,}300}{\left(n_f t_f E_f\right)^{0.58}} \quad (2.51)$$

And,

$$k_1 = \left(\frac{f_{cm}}{27}\right)^{2/3} \quad (2.52)$$

$$k_2 = \begin{cases} \frac{d_f - l_e}{d_f} & for\ U-jacketing \\ \frac{d_f - 2l_e}{d_f} & for\ side\ bonding \end{cases} \quad (2.53)$$

Where l_e is the effective length of the FRP reinforcement, k_v is the bond-reduction factors and the terms k_1, k_2 are modification coefficient that includes the effect concrete strength and the strengthening configurations system, respectively. The effective depth of FRP reinforcement is taken as the distance from the center of the bottom flexural reinforcement to the top free end of the FRP reinforcement. f_{fe}, is the effective stress of the FRP reinforcement.

(3) CSA S06-06 (2006)

The CSA S6-06 assumes a full model to estimate the total shear capacity of the reinforced concrete section retrofitted with FRP reinforcement. Equation (2.54) is addressed in this code to evaluate the shear contribution of the FRP reinforcement.

$$V_f = f_{fe}\rho_f b_w d_f \left(\cot\theta + \cot\beta_f\right)\sin\beta_f \quad (2.54)$$

The Effective strain limits are similar to that reported in ACI, 2008. The maximum limit of the effective FRP strain is assumed as 4000 μm/m for Close-shaped samples to avoid the loss of friction at the diagonal shear crack faces, as expressed by Equation (2.48). The same limit was assumed for U-shaped and the k_2 was only derived for the samples retrofitted with U-wrapped. In this equation, the effective depth of the FRP reinforcement, d_f is assumed as the higher value between 0.9d and 0.72h.

(4) Concrete Society TR-55 (2000)

The Concrete Society TR-55 (2000) published a technical report for the externally strengthened RC concrete members. The effective length (l_e) is a function of the FRP modulus of elasticity (E_f) (GPa) and the thickness of the FRP (t_f) (mm). The formula is expressed as (Equation (2.55)):

$$L_e = \frac{461.3}{(t_f E_f)^{0.58}} \tag{2.55}$$

According to the CSA S6-06 and ACI 440.2R-08 design guidance, the maximum effective strain was assumed as 4000 μm/m. For the fully-wrapped beam, the effective FRP strain can be expressed as follows (Equation (2.56)):

$$\varepsilon_{fe} = \varepsilon_{fu}\left(0.5622\left(\rho_f E_f\right)^2 - 1.2188\left(\rho_f E_f\right) + 0.778\right) \tag{2.56}$$

Where, ε_{fu} is the ultimate rupture strain of FRP, E_f is the Young modulus and ρ_f is the reinforcement ratio. However, the multiplication of these two parameters should not exceed 1.1 MPa. For the U-wraps and sides only, the effective strain formula is different compared to the full wraps of the beam. This formula is expressed as (Equation (2.57)):

$$\varepsilon_{fe} = 0.0042\ \frac{(0.835 f_{cu})^{\frac{2}{3}} w_{fe}}{(E_f t_f)^{058} d_f} \tag{2.57}$$

Where, f_{cu} is a cube compressive strength (MPa), w_{fe}, is the effective FRP width. The effective width is calculated based on the FRP retrofitting system and the compressive strut inclination. Assuming θ = 45°, the effective FRP width is equal to $(d_f - l_e)$ for U-wrapped reinforcement and $(d_f - 2l_e)$ for FRP reinforcement attached externally on both side of the beam. The shear contribution of the FRP depends on six parameters which are the effective FRP strain, the modulus of elasticity of the FRP, the gross-sectional area of FRP, the spacing from the centre-to-centre of FRP strip and effective FRP depth. This can be calculated by using the formula below (Equation (2.58)):

$$V_f = \varepsilon_{fe} E_f \left(\frac{A_f}{S_f}\right) d_f \left(1 + \cos\beta_f\right) \sin\beta_f \tag{2.58}$$

2.22 Existing Finite Element Studies

The Finite Element method is a numerical method which can approximate and solve complex structural problems to within acceptable boundaries. Finite element analysis was first developed by the aircraft industry to predict the behaviour of metals forming for wings. The ANSYS (2009) finite element program has been comprehensively developed to the extent

that it has applications across the whole engineering spectrum (Lawrence, 2003). Civil engineers are frequently interested in modelling materials such as steel and concrete, the latter requiring complex methodology in its representation. As concrete is an orthotropic material that exhibits nonlinear behaviour during loading, this behaviour is numerically implemented in ANSYS (Barbosa and Ribeiro, 2004). A number of previous researchers have used the finite element method to provide insight into the behaviour of the CFRP strengthened RC beams.

Al-Mahaidi et al., (2001) used nonlinear finite element modelling and analysis with DIANA (DIANA, 2000) to investigate the response of three shear deficient T-beams retrofitted using web-bonded CFRP plate by assuming perfect bond between the CFRP reinforcement and the concrete surface. Finite element analysis was shown to be capable of predicting the ultimate shear strength, the stiffness of the beams and strain levels in CFRP plates with acceptable accuracy. The cracking patterns and crack inclinations produced by the finite element model were also comparable to the patterns observed from testing. The experimental results have shown that repairing beams with CFRP plate improves their shear strength. The increase in strength ranged between 68% and 87%.

A numerical study was presented by Santhakumar et al., (2004) to simulate the behaviour of RC beams retrofitted with CFRP laminates using ANSYS software. The effect of retrofitting on un-cracked and pre-cracked reinforced concrete beams was investigated, and there was good agreement between the results obtained from the numerical study with the experimental data. In this study, it was noticed that there was no considerable difference in response between the un-cracked and pre-cracked strengthened beams using the FE models.

Abbas, (2010) used nonlinear analysis of reinforced concrete beams strengthened with plate steel or Carbon Fibre Reinforcements Plastic Plates. Abbas, (2010) modelled six beams three of them tested experimentally by Zarnic, (1999) and he used them as a case study (one) and the other three overhanging beams were presented as case study two. One beam from each case study was considered as a control beam and the other two beams in each case study were strengthened externally with CFRP and steel plates. There was good agreement between the finite element results in this study compared with experimental results obtained from previous studies and the other available numerical results.

Fathelbab et al., (2011) investigated the flexure, shear and combination flexure and shear behaviour of simply supported beams retrofitted externally with FRP using ANSYS

(ANSYS, 2009) software. Different configurations of FRP sheets in flexure, shear and flexure/shear were used as the main parameters of this study. The results were compared with a control beam model of a simply supported RC beam without strengthening. It was noticed that all the retrofitted RC beams have a greater shear strength, ductility, and delay the failure and deboning failure as compared to the control beam.

Mahmoud (2012) proposed finite element models to analyse reinforced concrete beams with and without and CFRP reinforcement using ANSYS version 9 (ANSYS, 2009). Three-dimensional concrete elements (Solid65) and (Solid46) element for representing CFRP laminate were used to simulate the RC beams. The numerical results had been compared with previous experimental studies and FE model results which were obtained using ANSYS version 5. The obtained FE results showed a success for the proposed model to analyse the ultimate strain values for concrete and steel at failure loads, for different opening sizes with the experimental data from other researchers which proved the efficiency of the proposed models.

Jayajothi et al., (2013) used non-linear finite element analysis (FEA) to simulate the failure modes of RC beams retrofitted with CFRP laminates in flexure and shear. ANSYS (ANSYS, 2009) was used to model four beams, two beams used as control beam without and the other two beams strengthened with CFRP. The experimental results were compared with the results of load deflection relationships and crack patterns were obtained by analysis and they found good agreement between experimental and numerical results. Also, they found a difference in behaviour between the models of RC concrete beams without CFRP and with beams strengthened with CFRP.

Obaidat et al., (2010) used non-linear finite element analysis to simulate the response of the reinforced concrete beam strengthened with CFRP reinforcement using ABAQUS software (ABAQUS, 2007). Elastic orthotropic and isotropic material properties were assumed to represent the CFRP reinforcement; also a cohesive model was used to simulate the behaviour of the FRP-concrete interface. Obaidat et al., (2010) concluded that the change in length of CFRP reinforcement may result in various responses of strengthened samples. The beam with higher CFRP bonded length showed a high stiffness and high shear load compared with samples retrofitted with CFRP strip did not cover the full depth of the beam. Obaidat et al., (2010) recommended using a CFRP reinforcement covering the whole beam depth when strengthening for shear.

2.23. Previous Studies on Shear Behaviour of Lightweight Aggregate Concrete

Shear failure of lightweight concrete elements has been a serious issue that may lead to structural collapse; the characteristic parameters for this complex issue have been suggested over the last 50 years. In general, these variables include the LWA type, the compressive and tensile strength of concrete, flexural steel ratio, slenderness ratio, etc. which have been studied by many authors. Based on the results of much research, the (ACI Committee 213R-03) concluded that LWC structures, subject to shear and diagonal tension, show basically the same response as NWC elements. A significant reduction in maximum shear capacities or tensile due to lower tensile strength and the aggregates interlocks at the diagonal shear cracks interfaces. In other words, LWCs would generally have a lower shear strength than NWC of the same compressive strength (Tang et al., 2009).

The shear capacity of LWA concrete cross sections is assumed as 0.7 of the value for the similar grade of NWC according to the Japanese Society of Civil Engineers (JSCE, 2007). This value for reduction was developed based on the experimental test results carried out on NWC and LWC beams (Tang et al., 2009). Information about how the ACI-318-08, (2008); BS 8810, (1985) and Eurocode 2, (2004) codes deal with lightweight concrete which is addressed in section (2.9), a summary of previous studies which were carried out on shear behaviour of LWC beams is described in this section.

Hanson (1958 & 1961) tested fifty-seven RC beams cast with lightweight coarse aggregates using expanded clay, expanded slate, expanded shale, expanded blast furnace slag and carbonaceous shale from coal processing for coarse aggregate. For design purposes, Hanson (1958 & 1961) suggested that the diagonal tension cracking load be considered as the unfactored shear strength. Compared to concrete beams cast with conventional aggregates, the diagonal cracks resistance of NWC varied from 60% to 100% of the shear resistance for a given compressive strength, with the variation based on the type of lightweight aggregate. Hanson (1958 & 1961) developed a new method to calculate the shear resistance of the LWC gross section. This method was identical in shape to that for NWC. However, the effect of lower diagonal crack strength was included by introducing a constant reduction factor due to lower splitting tensile strength.

Evans and Dongre (1963) studied the response of reinforced concrete lightweight concrete beam using Aglite coarse aggregates. The aim of this study was to assess the structural

behaviour of reinforced concrete beams cast with Aglite, in addition, to investigate the mechanical properties of Aglite concrete. Evans and Dongre (1963) noted that the LWC had a splitting tensile strength of about 75% of that of NWC. Furthermore, Evans and Dongre (1963) suggested that the maximum shear stress carried by concrete cross sections was 0.4 MPa with for concrete samples cast with concrete cube strengths of approximately 20 MPa. This limits the maximum shear stress to 2 MPa for concrete reinforced with shear links.

Swamy and Bandyopadhyay (1979) tested twenty-four lightweight T-beams made from Lytag and expanded slate and compared them with control samples cast with conventional aggregates. Swamy and Bandyopadhyay (1979) concluded that the shear mechanism in compression zone of concrete was similar for all LWC beam and compared with identical control beams. The initiation and propagation of diagonal shear cracks were the same in LWC samples as for NWC specimens, the LWRC generally had higher crack widths compared with their corresponding control normal weight. In this study, the samples cast with Lytag aggregates revealed lower cracking load compared with control NWRC beams. While the samples cast with expanded slate aggregate cracked at the same load as those recoded in NWRC beams. Swamy and Bandyopadhyay (1979) concluded that the maximum shear capacity of the LWRC beam cast with expanded slate was about 75% to 95% of those samples cast with NWRC and was about of 83 to 95% for samples cast with Lytag.

Juan, (2011) tested sixty-four lightweight and normal weight concrete beams without transverse reinforcement and sixteen reinforced concrete beams cast with NWC used as control samples. All the beams were loaded under monotonically increasing third point loading until ultimate shear failure. The aim of this study was to investigate the shear behaviour and crack patterns of lightweight concrete beams. The results were analysed and compared with available design codes and guidelines as well as the empirical formulas for LWC. In this study, diagonal shear cracking developed at lower loads compared with control normal weight concrete and lightweight aggregate concrete due to the lower splitting tensile strength of the LWC beams compared with NWC had the same grade of compressive strength of concrete. Nevertheless, after the diagonal shear cracking occurrence in foamed concrete and lightweight aggregate-foamed concrete could keep resisting a significant amount of shear before ultimate shear failure. The may be attributed due to the irregular and angular cracking path at the visible level compared to the smooth crack texture at the micro level.

2.24. Critical Discussion

Different variables have been addressed to investigate their effect on the interfacial response of FRP-normal weight concrete joints. The main variables, which are addressed in the literature, are a concrete strength, FRP bonded length, FRP stiffness, FRP bonded width and the properties of the adhesive material. However, the bond between the lightweight concrete and FRP has not received much attention. Hence, this study presents the pull-off experimental results obtained from lightweight concrete prisms with epoxy bonded Carbon FRP (CFRP) materials. The bonded length, width, thickness and the orientation of CFRP sheets were varied, in order to examine the characteristics of the CFRP-to-concrete interface and the efficiency of using CFRP reinforcement to retrofit the LWAC structures. A modified double-lap shear test arrangement is used to investigate the fracture failure of the FRP-concrete interface to minimise errors and provide more reliable results.

Issues concerning the study of the shear behaviour of reinforced beams strengthened with carbon fibre reinforced polymer (CFRP) sheets/strips contained in various codes of practice have been critically discussed. It was observed that the material properties of CFRP influenced the provisions contained in equations of the codes and guidelines.

A significant amount of research has been carried out to study the shear behaviour of RC concrete beams retrofitted with FRP composites, the influence of the strengthening configurations, the bonded length of the FRP reinforcement, the orientation of the FRP reinforcement, shear reinforcement ratio, the dimension and shape of the beam, shear span to depth ratio and the type of loading also investigated in some of them. The outcomes of these studies showed that the increasing of the FRP axial rigidity had a marginal effect on FRP debonding failure, but it can enhance the rupture failures resistance (Triantafillou, 1998; Pellegrino and Modena, 2002). Increasing the ratio of FRP reinforcement by increasing the bonded area of the FRP reinforcement provides more shear capacity and significantly enhanced the bond strength between FRP reinforcement and concrete.

Oriented FRP reinforcement showed better shear performance compared with those installed in a perpendicular direction to the longitudinal axis of the beam. The studies by Monti and Liotta, (2007) revealed that the FRP reinforcement perpendicular to the compressive strut inclination had a significant influence on crack patterns and the total shear resistance of the reinforced concrete beam. A summary of the most important studies available in the literature summarised in Table (2.3) (Belarbi et al., 2012).

The shear capacity of the strengthened sample was subtracted from the shear capacity of a control sample to quantify the shear strength enhancement due to FRP reinforcement. This analysis has been adopted by other researchers to calculate the shear contribution provided by FRP reinforcement. This method of calculation does not explicate changes in the reinforced concrete shear resistance when FRP is included (Colalillo, 2012). The alternative analysis should be used depend on the FRP strain to account the exact shear strength provided by FRP reinforcement.

Limited studies available in the database investigated the interaction between the longitudinal tensile and the FRP reinforcement in retrofitted beams with or without shear stirrups to provide information about the effect of dowel action of the longitudinal reinforcement on the FRP performance.

Testing large-size samples have not studied compressively to investigate the influence of this variable on the shear response. About 80% of the previous studies tested small-scale samples. In the literature reviews, there are two studies by (Leung et al., 2007) and (Belarbi et al., (2012), testing samples with 720 mm 900 mm depth respectively. A considerable difference in specimens strengthened with U-shaped systems was noticed compared with small-scale samples. Further study is important to investigate the response of CFRP used to retrofit practical sizes of beams.

Studying the influence of the concrete compressive strength as one of the most important variables affect the behaviour of the RC beams strengthened with FRP reinforcement has not received any attention. It is necessary to evaluate the applicability of design guidelines and codes for shear deficient RC beams with low strength concrete retrofitted with CFRP.

The majority of reviewed experimental, numerical and theoretical studies consisted of samples subject to monotonic loading. Those studies primarily examined the static response of the FRP strengthened beams under monotonically increased loading. There were very limited studies which examined the shear behaviour of RC beams retrofitted with FRP under cyclic loading, especially under repeated cyclic loading although many structures such as bridges and marine structures are subjected to cyclic loads rather than static ones. This is often overlooked in the analysis and design of RC beams strengthened with FRP sheets.

The effect of shear crack inclination on the contribution of CFRP should be considered and further experimental study should be carried out by incorporating original shear plan such as

steel plate at an angle of inclination between 21.8° and 60° in RC beams strengthened with CFRP to examine the effect of shear crack inclination on the CFRP shear contribution to the ultimate strength of reinforced concrete beams.

Limited studies investigated the shear retrofitting of lightweight aggregate concrete by using FRP reinforcements instead of normal aggregate concrete in spite of the shear capacity of LWRC beams being less than the shear capacity of NWRC. The absence of data for LWRC beams retrofitted in shear with CFRP increases the issue concerning the applicability of current FRP design guidelines and codes for the different type of concrete and especially for LWRC. The validity of current design guidelines and codes procedures to predict the shear strength of CFRP used to retrofit LWAC should be considered and the shear behaviour and failure modes of LWAC should be investigated to inform the industry regarding this type of concrete. This study examines experimentally, numerically and theoretically, the interfacial FRP–LWAC joint, and the shear behaviour of LWRC beams reinforced with CFRP sheets/strips, to assess the full behaviour of CFRP with LWRC structures.

Table (2.3): Test variables of the available studies.

First Author and year	Number of the sample	Beam shape and dimensions						**Test variables and FRP properties**							Test details			
		Rectangular section	T-beam section	different shear span	different depth	Slender span beam	Deep span beam	concrete compressive strength	Flexural steel ratio	shear steel ratio	FRP reinforcement type	FRP orientations	FRP ratio	Strengthening system	Static loads	Fatigue loads	Cyclic loads	Free end anchorages
Al-Sulaimani (1994)	3	Y				Y						Y	Y	Y				
Chajes (1995)	8		Y			Y						Y	Y	Y	Y			
Chaallal (1998)	2	Y				Y						Y			Y			
Triantafillou (1998)	9	Y				Y						Y			Y			
Grace (1999)	9	Y				Y					Y	Y	Y	Y	Y			
Khallifa (1999)	2	Y				Y							Y		Y			
Khallifa (2000)	5	Y				Y							Y	Y	Y			
Deniaud (2001)	10		Y	Y	Y	Y				Y	Y	Y	Y		Y			Y
Chaallal (2002)	10		Y				Y			Y			Y		Y			
Khallifa (2002)	8	Y		Y		Y				Y		Y			Y			
Pellegrino (2002)	8	Y				Y				Y			Y		Y			
Sheikh (2002)	1	Y					Y								Y			
Diagana (2003)	4	Y					Y					Y	Y		Y			
Wong (2003)	3	Y		Y		Y						Y			Y			
Adhikary (2004)	7	Y				Y								Y	Y			Y
Adhikary (2004)	8	Y				Y					Y			Y	Y			Y
Carolin (2005)	18	Y				Y				Y		Y	Y	Y	Y	Y		
Zhang (2005)	6	Y		Y		Y						Y	Y		Y			
Anil (2006)	4		Y									Y	Y				Y	
Bousselham (2006a)	16		Y	Y		Y	Y			Y			Y		Y			
Bousselham (2006b)	8		Y	Y		Y	Y			Y			Y		Y			
Pellegrino (2006)	8	Y				Y				Y			Y		Y			

First Author and year	Number of the sample	Beam shape and dimensions						**Test variables and FRP properties**							Test details			
		Rectangular section	T-beam section	different shear span	different depth	Slender span beam	Deep span beam	concrete compressive strength	Flexural steel ratio	shear steel ratio	FRP reinforcement type	FRP orientations	FRP ratio	Strengthening system	Static loads	Fatigue loads	Cyclic loads	Free end anchorages
Leung (2007)	12				Y	Y							Y		Y			
Monti (2007)	19	Y				Y						Y	Y		Y			Y
Mosallam (2007)	6	Y					Y				Y		Y		Y			
Anil (2008)	5		Y			Y						Y	Y	Y			Y	Y
Grande (2008)	7	Y		Y		Y							Y		Y			
Kim (2008)	9	Y		Y			Y					Y	Y		Y			
Pellegrino (2008)	4	Y				Y				Y			Y		Y			
Sundarraja (2008)	8	Y					Y			Y				Y	Y			
Grande (2009)	7	Y				Y				Y			Y	Y	Y			
Sundarraja (2009)	8	Y				Y						Y	Y	Y	Y			
Lee (2011)	14		Y	Y			Y					Y		Y	Y			
Mofidi (2011)	14		Y							Y			Y	Y	Y			
Lee (2012)	10	Y				Y						Y		Y	Y			
Belarbi (2012)	6		Y			Y						Y			Y			Y
Panda (2013)	18		Y			Y				Y				Y	Y			Y
Bousselham (2013)	12		Y		Y							Y	Y		Y			
Alsayed (2013)	6	Y				Y						Y	Y		Y			
Colalillo (2012, 2014a)	15	Y				Y				Y			Y				Y	
Mofidi (2014)	10		Y							Y			Y		Y			
Ozden (2014)	10		Y								Y				Y			Y
Mostofinejad (2016)	7	Y										Y	Y	Y	Y			Y
Robert Foster (2016)	15		Y		Y	Y							Y		Y			Y

CHAPTER THREE

EXPERIMENTAL PROGRAM

BOND-SLIP TEST

3.1. Introduction

This chapter presents the experimental test programme which was employed to investigate the response of the CFRP-to-lightweight concrete interface compared with companion samples cast with normal weight aggregate concrete. The experimental programme consists of testing the material mechanical properties and fifty concrete prism tests using a new strategy of double-lap shear tests at the University of Salford's Structures Laboratory. The details of the experimental tests program carried out in this study were presented in this chapter including samples design and manufacturing, fabrication, test setups, instrumentation, loading conditions, and the experimental results and discussion on the double-lap shear test outcomes. In addition, the parametric study of the bond characteristics is mentioned in this chapter.

3.2. Bond-Slip Test

The bond behaviour between CFRP composite and concrete is vital in shear and flexural retrofitting for transfer of bond stress between the FRP reinforcement and concrete surface. In this research, the experimental set-up represents double-face shear debonding tests on CFRP reinforcement bonded to the surface concrete prisms cast with LWAC and NWAC. The CFRP bonded lengths, width, thickness and fibre orientation of CFRP sheet were varied in order to understand the fracture behaviour and the effectiveness of CFRP on lightweight concrete. It is envisaged that these tests will present reliable relationships for the interfacial bond between LWAC and CFRP composite. The specific aims of this test are:

1. To determine the maximum bond and effective bond length at debonding by testing a large number of concrete prisms cast with LWAC and NWAC strengthened with CFRP composite.

2. The experimental results were used to check the validity of the proposed theoretical model which is developed in this study and the available theoretical models which have been established by other Authors.

3.3. Test Programme

The entire experimental program comprises 55 concrete prisms divided into four phases, each phase examines a different number of samples cast with LWAC and NWAC bonded with CFRP sheets in eight different CFRP configuration techniques (each technique was repeated in three to four LWAC samples and two NWAC samples). All specimens of NWAC and LWAC were cast as the same grade of concrete (i.e. the same compressive strength) to minimise any uncertainties between these two types of concrete. The details of each series are described as follows:

1. Series (BN/L1) contained twenty-one concrete prisms: twelve specimens were cast with LWC and nine specimens were cast with NWC. The specimens were bonded with CFRP sheets of 100 mm width and varying lengths of 100, 150 and 200 mm. The main purpose of this series of tests was to determine the bond strength properties, bond-slip behaviour and effective bond length.
2. Series (BN/L2) contained twelve concrete prisms: eight prisms were cast with LWAC and four specimens were cast with NWAC. This series was designed to study the behaviour of CFRP bonded sheets when a pull-out force was inclined to the direction of FRP fibre. The angle between the FRP fibre and the loading direction was varied at orientation angles of 0^o, 45^o and 90^o.
3. Series (BN/L3) contained ten concrete prisms in which six prisms were bonded with LWAC and four prisms were cast with NWAC. This series examined the effect of using double parallel and perpendicular layers of CFRP sheets.
4. Series (BN/L4) contained twelve concrete prisms: eight prisms were cast with LWAC and four prisms were cast with NWAC. The width of the CFRP sheet (50, 100 and 150 mm) was varied in this series. The main purpose of these tests was to study the effects of the CFRP-to-concrete width ratio. The detail of strengthening techniques is shown in Table (3.1).

Table (3.1): Detail and strengthening techniques of the tested samples.

Specimen	Strengthening Detail	Strengthening Configurations
BN/L1-1	CFRP sheet (100x100) mm with 0^0 orientation	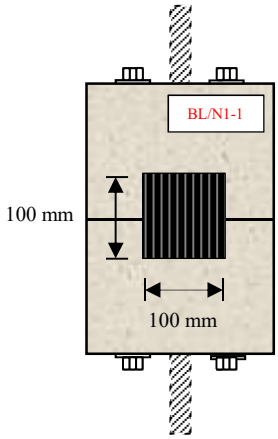
BN/L1-2	CFRP sheet (100x150) mm with 0^0 orientation	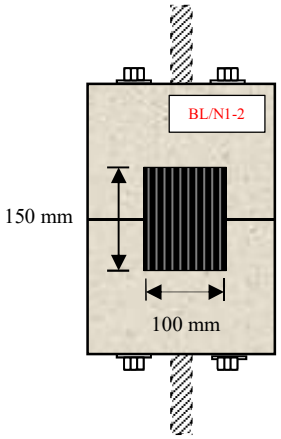
BN/L1-3	CFRP sheet (100x200) mm with 0^0 orientation	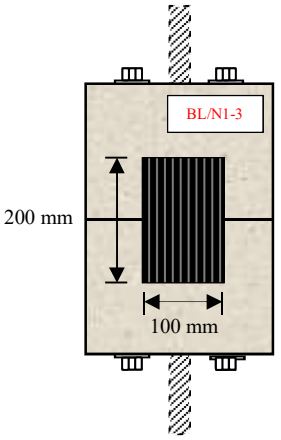

BN/L2-1	CFRP sheet (100x100) mm with 90^0orientation	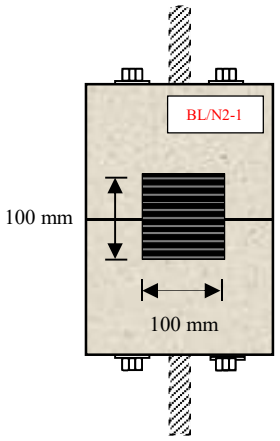
BN/L2-2	CFRP sheet (100x100) mm with 45^0orientation	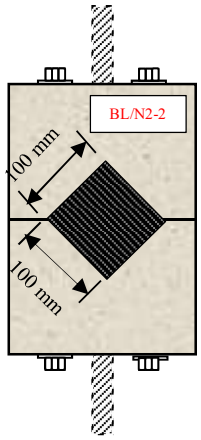
BN/L3-1	Double CFRP sheet (100x100) mm with $0^0/0^0$ orientation	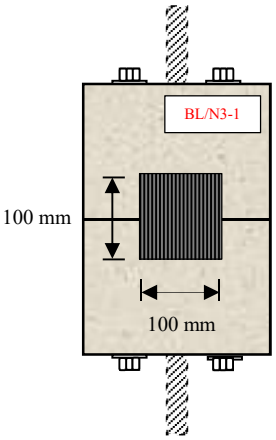

BN/L3-2	Double CFRP sheet (100x100) mm with $0^0/90^0$ orientation	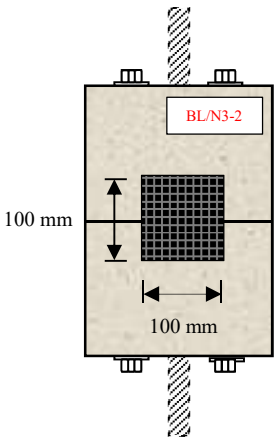
BN/L4-1	CFRP sheet (50x150) mm with 0^0 orientation	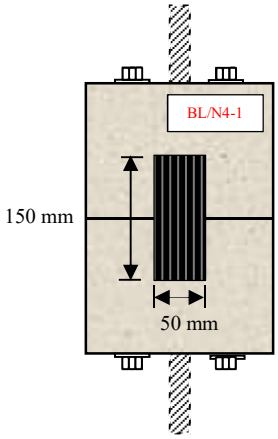
BN/L4-2	CFRP sheet (150x150) mm with 0^0 orientation	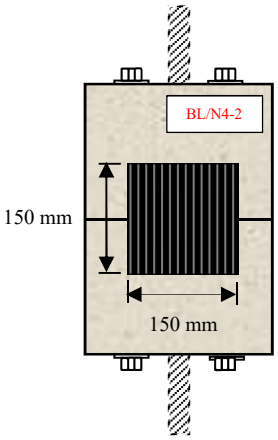

Note: the letters ‘’BL’’ refer to LWAC samples and ‘’BN’’ refer to NWAC.

3.4. A New Strategy of Double-Lap Shear Test (DLS)

Different test arrangements have been employed to investigate the bond-slip response of FRP/concrete joints. For instance: single-lap shear tests, double-lap shear tests, and beam tests. The outcomes of these tests revealed that the bond-slip responses vary from one experiment to another. Thus, it is not readily to understand the real response of the FRP/concrete joint, especially in double-lap shear tests. The expected reason for this variance in results may be attributed to the moment developed by the eccentricity between the top and bottom bar ends when the samples were positioned on the test machine to apply a tensile force which played an important role in the local bond strength (Nakaba et al. 2001).

Modifications are used in this study to minimise the required time to prepare the samples for testing and reduce the issues developed with samples manufacturing and handling as well as securing the alignment between the top and bottom bars when the samples are positioned in the testing machine. The same strategy and model dimensions were carried out by Al-Juboori, (2011) to investigate the bond response between CFRP and normal weight concrete prior this study.

In this study, the CFRP–concrete bonding was examined by testing a number of specimens with CFRP reinforcement bonded to concrete prisms. The nominal dimensions of the prismatic concrete prisms were as follows: length, L = 280 mm; width, b = 200 mm; and height, h = 90 mm. The CFRP reinforcement was attached in the centre on both sides of the concrete blocks. The concrete blocks were sawn into two separate parts as shown in Figure (3.1), and then re-jointed by two 6 mm threaded rods.

In a typical test, the tensile load is applied to the steel bar ends, which had been cast in the concrete block (the steel bar diameter was 18 mm). Figures (3.1) and (3.2) show the steel bars inside the timber moulds, which have also been cut into two parts with the concrete block. To avoid any moment caused by the eccentricity between the top and bottom grips when the specimens are set on the loading machine, there are two longitudinal holes of 8 mm diameter (two aluminium tubes), provided to facilitate clamping of the sample ‟ halves‟ before testing whilst loading into the tensile test machine. The threaded rods were released before testing, as shown in Figure (3.3 (c)). Also, a plastic sheet was placed between the two parts of the concrete

block to avoid any undesirable bond between the concrete blocks from the adhesive entering this interface.

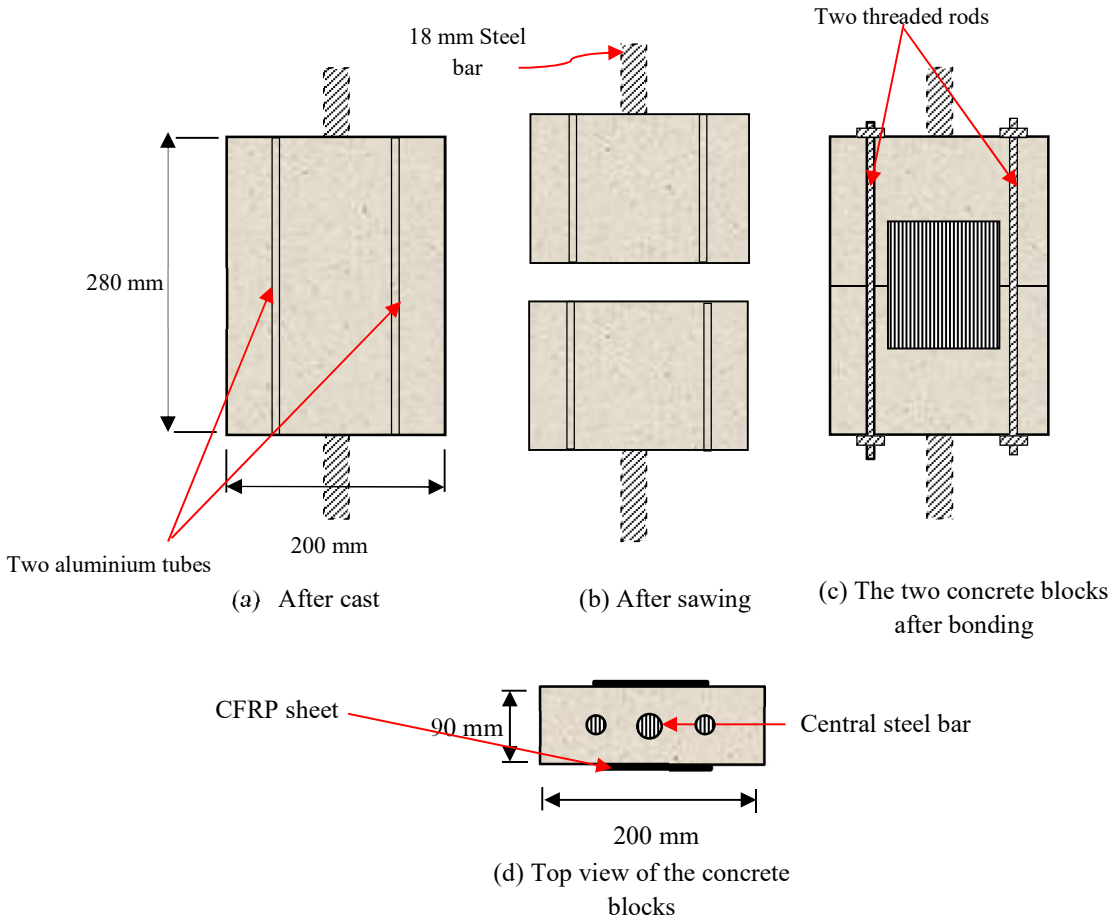

Figure (3.1): Process of preparing the two concrete blocks for bond testing.

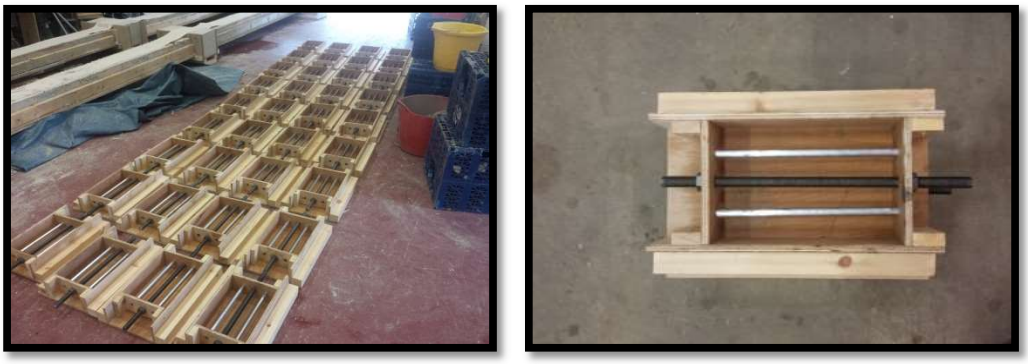

Figure (3.2): Timber moulds used to cast the specimens.

3.5. Test set-up

In this study, the samples were tested in a 50 kN capacity Instron tensile test machine. To negate the effects of any eccentricity causing moment on the sample during testing, a 'ball- and- socket' connection was employed as shown in Figure (3.3b). In most of the cases, the ultimate slip was less than 1.5 mm. The displacement of 0.24 mm/min was kept during the test program in order to eliminate the inertial effect of applied load and to measure enough data over a small period of time (the experiment was expected to last about 1 to 3 mins with the loading rate of 0.24 mm/min). The global slip was measured using two linear variable displacement transformers (LVDTs), which were set up on both sides of the concrete block as shown in Figure (3.3a).

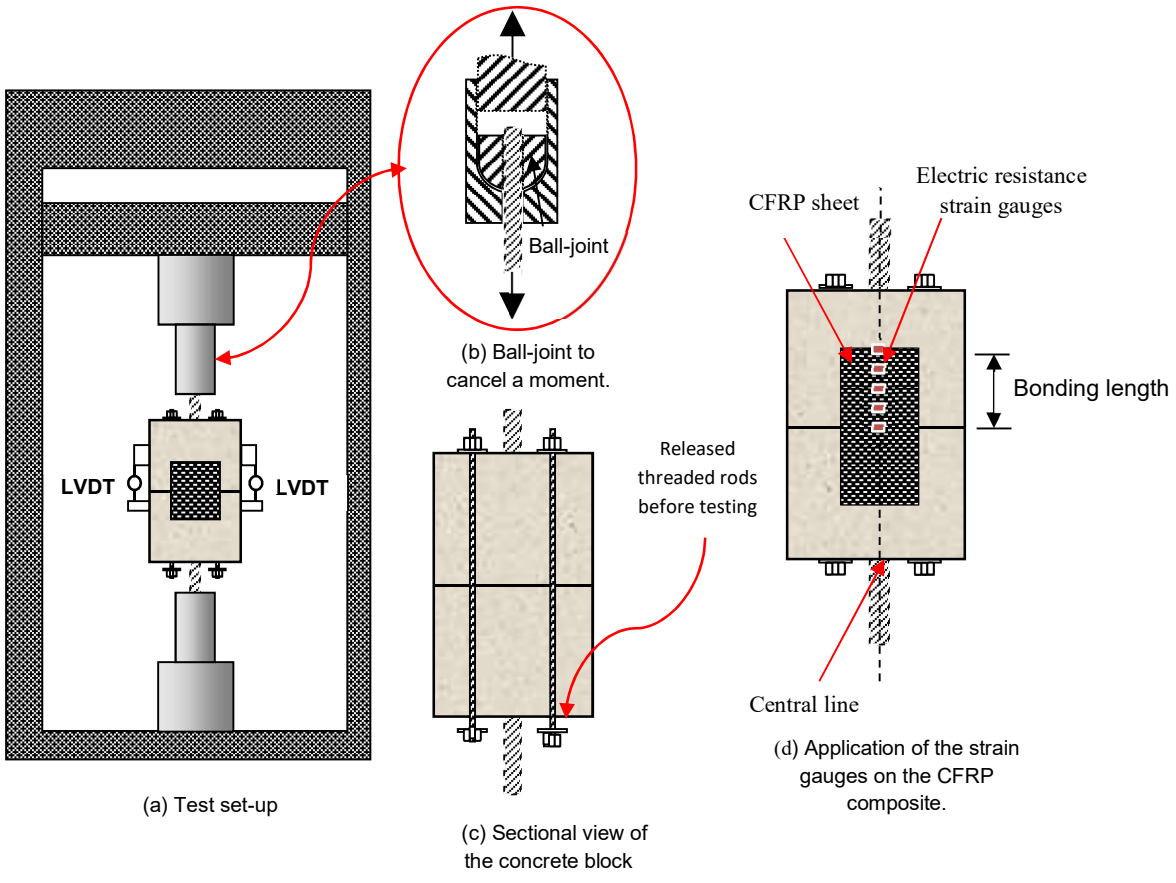

Figure (3.3): Detail of bond-slip test.

To investigate the strain distribution along the length of the CFRP sheet, a series of 3 mm-long Tokyo Sokki Kenkyuio co., Ltd strain gauges were attached to the top surface of the CFRP sheets on two samples of BL/N1-1, BL/N1-2 and BL/N1-3 as shown in Figure (3.3d). The gauge factor, gauge resistance and temperature compensation for the strain gauges was 2.12±1 %, 120±0.5 Ω and 11.9x10^{-6}/°C, respectively.

In all samples, the strain gauges were attached along the centre line of the bonded width. Strain gauges were attached at close distances along the length of CFRP sheet in one part of the sample. The first strain gauge was installed at the centre of the concrete samples and the others were installed along the bond length of the CFRP reinforcement. The location of the strain gauges are reported in Table (3.2).

Table (3.2): Position of the strain gauges along the bonded length.

	Distance of the strain gauge from the Center of specimen (mm)								
Bonded Length of CFRP sheet (mm)	SG-1	SG-2	SG-3	SG-4	SG-5	SG-6	SG-7	SG-8	SG-9
50	0	10	25	40	50				
75	0	10	25	40	50	60	75		
100	0	10	25	40	60	70	80	90	100

3.5. Material Properties

3.5.1. Concrete Mixture

Type I ordinary cement that conformed to the requirements of (BS EN 197, 2000) was used in the preparation of NWAC and LWAC mixtures. Coarse granite and sand aggregates were used in the preparation of NWAC mixtures, whereas Pulverized Fuel Ash (Lytag) and sand aggregates were used in the preparation of lightweight aggregate concrete (LWAC) mixture; the typical shape of Lytag aggregates are shown in Figure (3.4). The oven dry loose bulk density of Lytag aggregates is typically in the range of 700 to 800 kg/m^3. Normal weight aggregates have typical loose bulk densities of 1550 kg/m^3 (Lytag UK, 2011). Thus, the weight of Lytag aggregate is approximately 50% of normal weight aggregate. Lytag aggregate absorbs approximately 15% of its own weight when immersed under water (Lytag UK, 2009).

This must be allowed for in the mix design and batching to secure that the correct volume of water is added. In Tables (3.3) and (3.4), the physical and chemical analysis of Lytag aggregate are summarised based on manufacturing information and the results obtained by the State Company of Geological Survey and Mining (SCGSM) in Iraq (SCGSM, 1983).

Figure (3.4): Typical Lytag shape.

Table (3.3): Physical properties of Lytag aggregates (Lytag UK, 2011).

Moisture Content as delivered	15%
Long term Moisture Content	30%
Particle Density	1300-2650 kg/m^3
Permeability	1.3x10^{-1} m/s

In this work, the nominal size of natural gravel ranges between 14 to 20 mm while, Lytag aggregates having a maximum aggregate size of 14 mm comply with the gradation recommended by BS 882, (1992) and BS 3797, (1990) for structural concrete as shown in Table (3.5) for natural weight aggregates and Table (3.6) for Lytag aggregates. Graded and normal weight natural sand with a maximum particle size of 5 mm was used as fine aggregate throughout, the grading of the sand conformed to the requirement of BS 882, (1992) as shown in Table (3.7).

Table (3.4): Chemical analysis of Lytag aggregates (SCGSM).

Oxides	% by weight
SiO_2	48.86
Al_2O_3	23.97
Fe_2O_3	5.42
CaO	4.8
MgO	2.8
SO_3	< 0.07
Na_2O	0.9
K_2O	2.7

Table (3.5): Grading of natural aggregates.

No.	Sieve size (mm)	% Passing	% passing of the overall limit of BS 882
1	20	100	90-100
2	14	57.2	40-80
3	10	32	30-60
4	5	3.2	0-10

Table (3.6): Grading of Lytag aggregates.

No.	Sieve size (mm)	% Passing	% passing of the overall limit of BS 3797
1	20	100	100
2	14	97	95-100
3	10	75.3	50-95
4	5	8.8	0-15

Table (3.7): Grading of natural sand aggregates.

No.	Sieve size	% Passing	% passing of the overall limit of BS 882
1	5 mm	98	89-100
2	2.36 mm	88	60-100
3	1.18 mm	82	30-100
4	600 µmm	68.5	15-100
5	300 µmm	14.3	5-70
6	150 µmm	1.6	0-15

3.5.2. Mix Design

For the purpose of comparison, one grade of NWAC and LWAC mixtures were designed in this research. The mix designs for NWAC concrete were carried out according to British standard procedures based on *The Design of Normal Concrete Mixes* by Teychenne et al (1988), whereas the mix designs for lightweight concrete were largely based on information provided by the aggregate manufacturers and previous research (Lytag UK, 2006; Al-Shamaa, 2010 and BS EN 13055, 2016).

The objective of the concrete mix design was to have a slump of 75 mm, and a 28-day cube compressive strength of 40 N/mm^2. Various trial mixes were used to achieve the required strength; the mix details of normal and lightweight concrete are given in Table (3.8).

Table (3.8): The mix properties of concrete.

No.	Concrete Type	Water kg/m^3	Cement kg/m^3	Sand kg/m^3	Coarse Agg kg/m^3	Design strength N/mm^2
1	NWAC	192	400	667	1184	40
2	LWAC	216	480	485	715	40

3.5.3. Mixing, Casting and Curing

NWAC and LWAC block samples were cast in a specially designed 90 mm thick wood formers of net internal dimensions of (200 x 280 mm) and externally vibrated. A tilting drum mixer was used for mixing the concrete. All the LWAC and NWAC were cast in a single batch each. In addition, six concrete cubes (100 x 100 x 100 mm), four concrete cylinders (150 dia. x 300 mm) and six prisms (100 x 100 x 400 mm) were cast from each batch to determine the uniaxial compressive strength, the Young's modulus of elasticity and the modulus of rupture of lightweight and normal weight concrete (see Table (3.9)). Initially, the materials used to produce LWAC were batched by weight. The water absorption of the Lytag particles should be considered when calculating the final batch weight (Lytag UK, 2009).

The process of producing LWAC was adopted based on information provided by the aggregate manufacturers as summarised below:

1. Mixing of Lytag batch for 30 seconds.
2. Adding half of the total water and mixing for 1 minute.
3. The mixer left standing for 15 minutes to allow aggregate water absorption. During that period, the mixer was kept covered to minimise evaporation.
4. Adding the total amount of sand and further mixing for 1 minute.
5. Adding the cement and mixing for 1 minute.
6. Adding the remaining half of the water.
7. Further mixing for two minutes.

The mixing procedure of normal weight concrete was adopted as specified in BS 1881-125 (2013). Constituent materials were mixed as outlined below:

1- Mixing the batch of coarse and fine aggregate for 30 seconds.
2- Adding half of the total water and further mixing for 1 minute.
3- The mixer left standing for 8 minutes to allow aggregate to absorb water.
4- Adding the cement and further mixing for 30 seconds.
5- Adding the remaining half of the water and further mixing for two minutes. Figure (3.5) shows the casting specimens.

Figure (3.5): Casting the bond-slip samples.

3.5.4. Concrete Mechanical properties

The mechanical properties for the LWAC and NWAC used in the study were evaluated according to British codes, which are detailed with each test below. The mechanical properties such as compressive strength, modulus of elasticity, flexural strength and concrete dry density will be presented in the following sections.

3.5.4.1. Concrete Cube Compressive Strength

Six (100 x 100 x 100) mm cubes each of the LWAC and NWAC mixture were prepared and tested for compression strength according to BS1881-116 (1983). All of the LWC cubes that were tested in this series failed with the failure plane passing through the aggregate, indicating that the LWAC was affected by the tensile strength of the aggregate as shown in Figure (3.6).

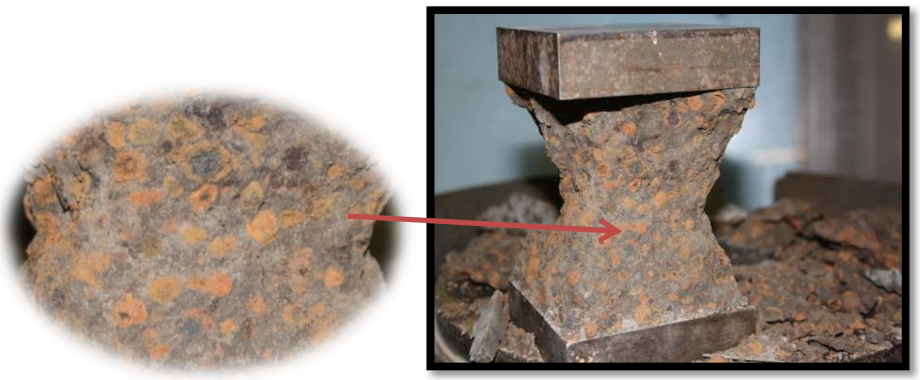

Figure (3.6): Typical failure plane of LWAC cube.

3.5.4.2. Modulus of Elasticity

The modulus of elasticity of LWAC and NWAC specimens was established according to the method described in BS1881-121 (1983). The test involved step loading of cylinders (150 x 300 mm) from the lightweight and normal weight concrete mix used in the bond-slip test up to 30% of the maximum crushing load. The average modulus of elasticity for LWAC was (22900 N/mm^2). The equipment and specimen setup during testing are shown in Figure (3.7). The average modulus of elasticity for the LWAC is approximately 77% to those of the NWAC of similar strength.

Figure (3.7): Modulus of elasticity test.

3.5.4.3. Flexural tensile strength

In this work, flexural tensile strength tests were carried out on NWAC and LWAC concrete mixtures in accordance with BS1881-118 (1983). As explained in the previous section, six prisms (100 x100 x500 mm) of each mixture were cast and tested to obtain the concrete tensile strength. Figure (3.8) shows the relationship between the tensile strength and the square root of cube compressive strength of the LWAC and NWAC mixtures. Based on the theses results, a linear empirical equation is suggested for the flexural tensile strength as shown in Equation (3.1) and (3.2).

$$f_{ct\,(LWAC)} = 0.458\sqrt{f_{cu}} \quad (3.1)$$

$$f_{ct\,(NWAC} = 0.532\sqrt{f_{cu}} \quad (3.2)$$

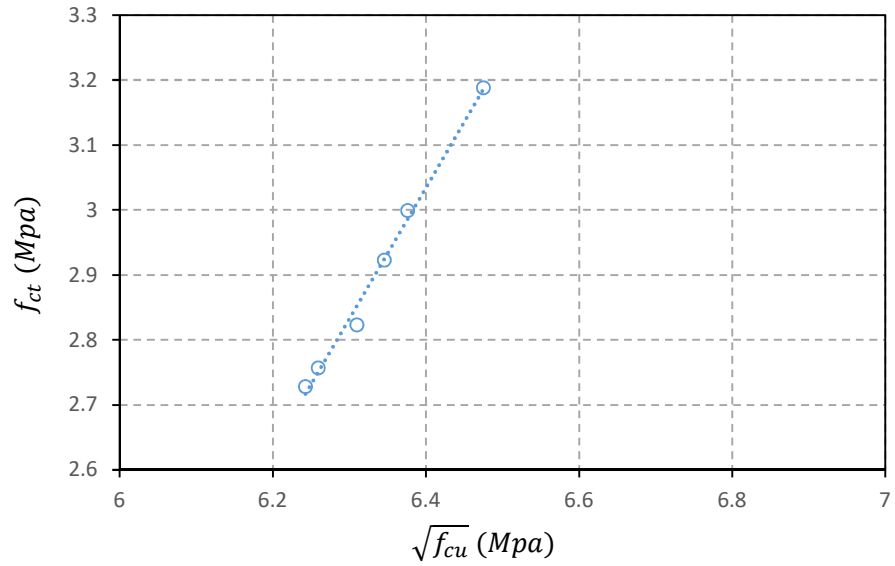

(a) LWAC Mixture.

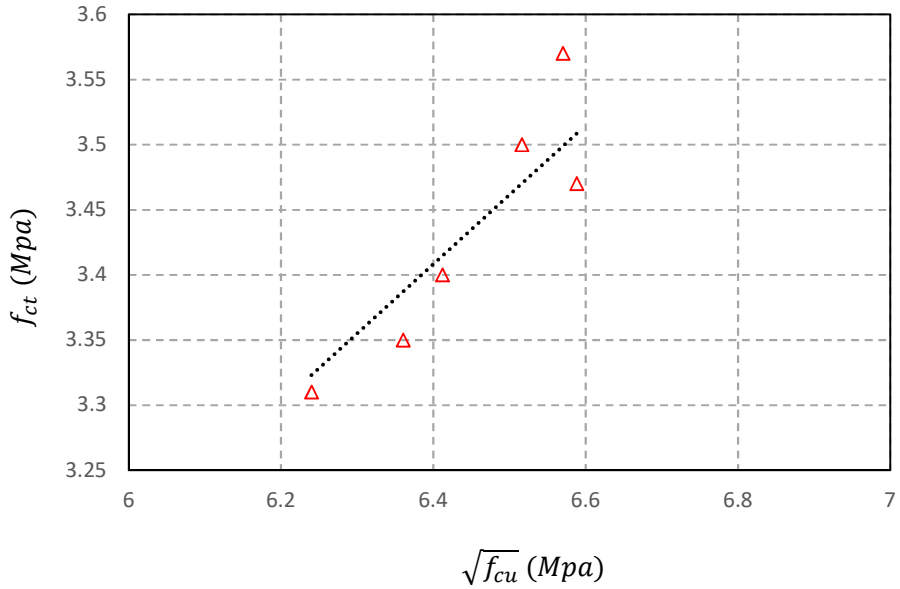

(b) NWAC Mixture.

Figure (3.8): Relationship between tensile strength and cube compressive strength of the LWAC and NWAC mixture.

3.5.4.4. Hardened Density

The average of six concrete cubes (100 x100 x 100) mm for each mix design was used to obtain the oven-dried density according to the BS1881-114 (1983). Table (3.9) presents a summary of these mechanical properties.

Table (3.9): Concrete mechanical properties.

Concrete Type	Average cube concrete strength f_{cu} (MPa)	Average flexural tensile strength f_{ct} (MPa)	Average modulus of elasticity E_c (MPa)	Average concrete density ρ_c (kg/m^3)
NWAC	41.6	3.4	29670	2345
LWAC	40.1	2.9	22900	1760

3.5.5. CFRP sheet

A unidirectional CFRP sheets (C Sheet 240) supplied by Weber UK, (2008) were attached to the concrete blocks. The sheets physical and mechanical properties are summarised in Table (3.10) based on information provided by Weber UK, (2008).

Table (3.10): Physical and mechanical properties of the CFRP sheet.

Physical properties	
Fibre density	1.7 kg/cm^3
Sheet weight	200 g/cm^2
Thickness	0.1178 mm
Mechanical properties	
Modulus of elasticity	240 GPa
Tensile strength	4000 MPa
strain at failure	1.6%

3.5.6. Adhesives Layers

Epoxy plus primer (EN-Force primer) and epoxy plus adhesive (EN-Force bonding adhesive) were used to bond CFRP composite to the concrete substrate, respectively. Both primer and adhesive are two-component epoxy based adhesives. Part A of the epoxy is the base component

while Part B is the hardener which should be made of approximately 2/3 base and 1/3 hardener according to the manufacturer recommendations. The physical and mechanical properties of the primer resin and the physical properties of adhesive bonding are summarised in Table (3.11) and (3.12) based on information provided by (Weber UK, 2013).

Table (3.11): Physical and Mechanical properties of the Primer resin.

Physical properties	
Colour	Translucent
Density	1.12 kg/litre
Thickness of application	100µm
Mechanical properties	
Compressive strength	100 N/mm^2
Tensile strength	19 N/mm^2
Flexural strength	30 N/mm^2
Bond to concrete	> 5.3 N/mm^2
Young's modulus	5 kN/mm^2

Table (3.12): Physical properties of the bonding adhesive.

Colour	White, semi transparent
Density	1.3 kg/litre
Thickness of application	300µm

3.6. Bonding of CFRP to concrete Surface

The surface of the concrete is needed to be prepared using suitable techniques to get the required bond stresses transference as well as to improve the bond strength between the CFRP sheet and concrete substrate. The thin layer of concrete mortar adjacent to the CFRP reinforcement should be removed to secure that the FRP reinforcement is attached directly to the surface of the concrete sample. This allows the FRP/concrete joint to transfer more shear and normal stresses as well as to increase the bond strength between CFRP reinforcement and concrete surface.

In this study, the surfaces of the concrete blocks, where the CFRP sheet would be glued, were ground to a fine finish with a stone wheel to remove the top layer of mortar, just until the aggregate was visible (approximately 2-3 mm). Due to the very small dimension of the marble powder glued to the wheel, the concrete surface was very smooth as shown in Figure (3.9). Then, the concrete surface was covered with a thin layer of primer. After that, the CFRP sheets were applied to both sides of the concrete prisms with two-component epoxy adhesive with a relatively uniform thickness of 1–1.2 mm. The same procedure was adopted by Al-Juboori, (2011). The steps of the preparation of the samples are summarised in Figure (3.10).

Figure (3.9): Surface preparation of the samples.

(a) Preparing the sample moulds. (b) Casting the samples. (c) Striking the samples and grinding.

(d) Cutting the samples. (e) Re-joining the samples. (f) Planning the samples.

(h) Cutting CFRP sheet. (i) Bonding CFRP to the concrete surface. (g) Testing samples.

Figure (3.10): Sample manufacturing and testing.

3.7. Results Analysis

The experimental results of the pull-off double shear-lap tests between the CFRP sheets and the lightweight/normal weight concrete prisms are now presented and discussed in order to understand the bond characteristics, fracture behaviour and the effectiveness of CFRP to retrofit LWAC compared to NWAC

3.7.1. Failure Condition Summary

Failure conditions noticed from the experimental program are provided here to discuss the observed failure modes based on these test observations. This includes photos taken during and after testing, which show typical failure modes in the tested LWAC and NWAC specimens.

In general, the failure conditions of the LWAC samples were due to crack propagation within the concrete. This led to a brittle failure of the concrete and sometimes resulted in concrete debonding. In contrast, the most common failure observed in the NWAC samples was concrete debonding and sometimes adhesive debonding. The crack intensity was more prevalent in LWAC specimens compared to NWAC specimens, it can be noticed that crushing of the concrete underneath of CFRP composite for samples cast with LWAC was evident.

Figure (3.11a and b) compares the concrete failure between two samples having the same strengthening techniques of CFRP composite, one made from LWAC and the other one from NWAC used as an example in this study. The higher peeling width and thickness in the LWAC samples compared to similar strength NWAC may be due to the lower shear strength for Lytag aggregates compared to that of normal aggregates.

As bond failure developed in the specimens BL1-1, BL3-1, BL3-2 and BL4-1, small diagonal cracks developed at the centre of the specimen. These cracks never extended significantly outwards from the centre of the samples. The angle of the cracks suggests an edge effect, affecting the crack propagation, the same failure observed by McSweeney and Lopez. (2005) and Yao et. al (2005) prior to this study. As more load was applied, these samples developed additional small cracks near the centre of the concrete prism. Once the crack appeared, they propagated rapidly towards the upper surface of the tested concrete sample, which led to the sudden brittle failure of the concrete prism by the formation of a diagonal fracture plane as

shown in Figure (3.12a and b). The same failure mode was observed for the NWAC samples of the BN3-1 and BN3-2 series as shown in as shown in Figure (3.12c and d).

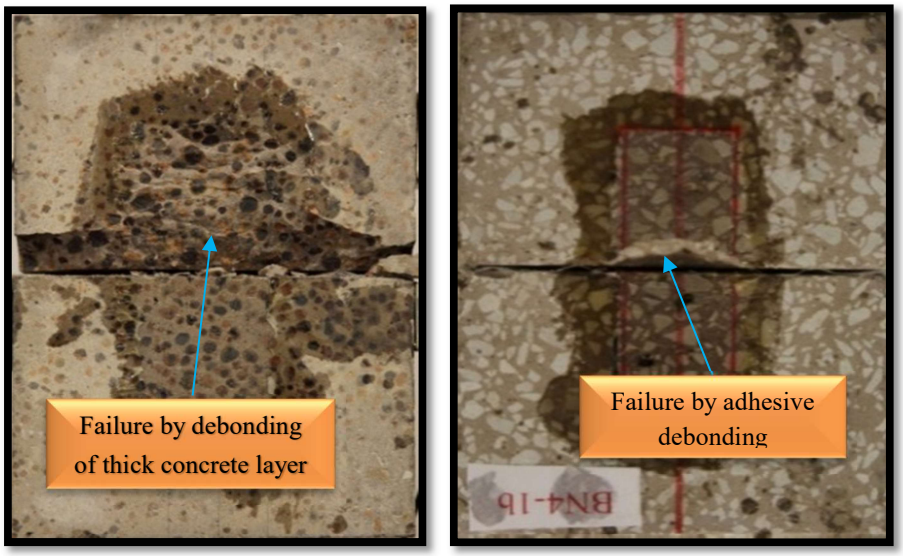

(a) LWAC samples (b) NWAC samples

Figure (3.11): Comparison of failure modes between LWAC and NWAC samples.

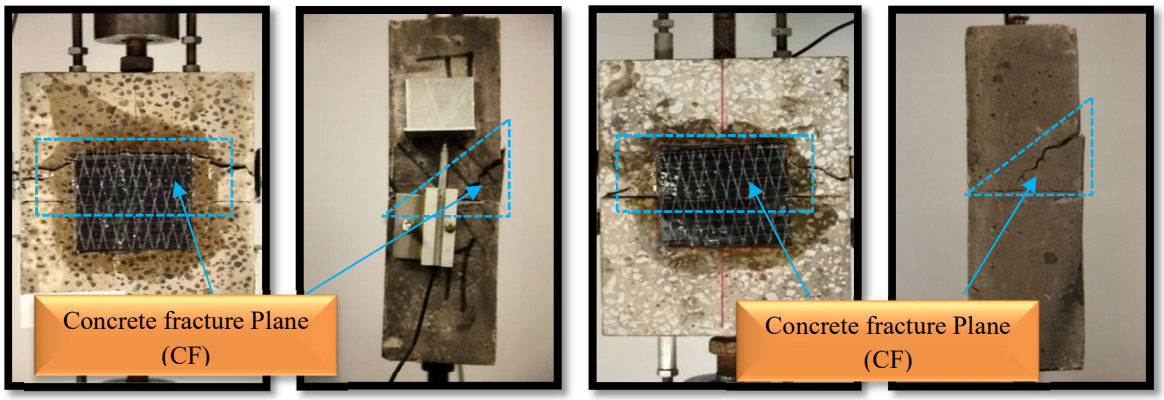

(a) (b) (c) (d)

Figure (3.12). Typical failure in the concrete prism (CF) in LWAC and NWAC specimens (a) Front view of LWAC specimen, (b) Side view of LWAC specimen, (c) Front view of NWAC specimen, (d) Side view of NWAC specimen.

All the samples of BL1-2, BL1-3 and BL4-2 and BN4-2 series failed due to concrete debonding adjacent to the adhesive-concrete interface, where concrete layers of different thickness were broken and attached to the CFRP sheet. The debonding failure between the CFRP sheet and the

concrete was extremely brittle and the duration of the debonding process was mainly influenced by the bond area.

The failure process started with small concrete cracking evident near the specimen centre. As the load increased, the small cracking in the concrete initiated CFRP debonding from the concrete surface near the sample centre and then propagated towards the upper far end of the FRP sheet. This eventually led to full detachment of CFRP strips from the concrete surface as shown in Figure (3.13).

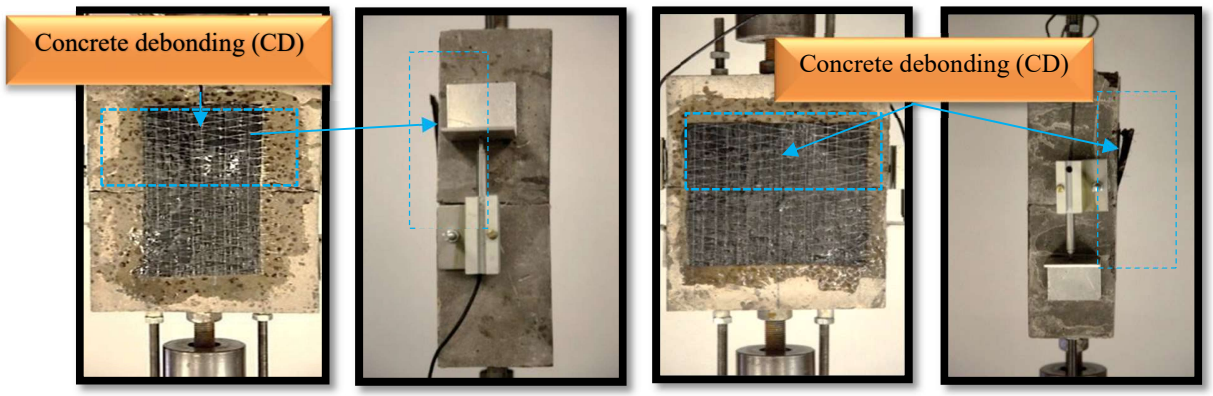

(a) (b) (c) (d)

Figure (3.13): Typical failure concrete debonding of LWAC specimens (a) Front view of BL1-3 specimen, (b) Side view of BL1-3 specimen, (c) Front view of BL4-2 specimen, (d) Front view of BL4-2 specimen without CFRP sheet.

The samples of BN1-1, BN1-2, BN1-3, and BN4-1 series showed combined failure modes. All these samples failed by debonding of small pieces of concrete near the sample centre followed by debonding of a thin layer of concrete just under the CFRP sheet in samples BN1-1, BN1-2 and BN1-3 or adhesive debonding in BN4-1. This may be due to the higher stiffness of normal weight particles and the surrounding cementitious matrix which resists the crack propagation from the centre of the concrete sample toward the free end leading to stress concentration. This concentration causes debonding of the concrete near the centre of the sample. Figure (3.14) shows the typical failure mode of these specimens.

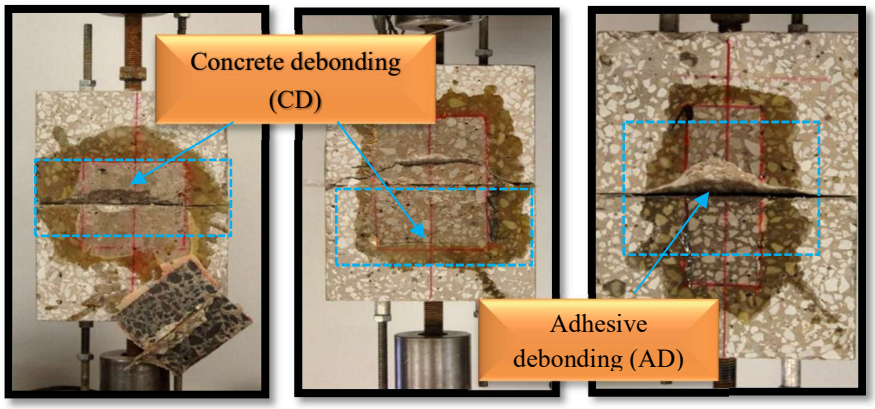

Figure (3.14): Typical combined failure concrete debonding of NWAC specimens (a) Failure of specimen BN1-1, (b) Failure of specimen BL1-2, (c) Failure of specimen BL4-2.

The three specimens of each BL2-2 series which have CFRP sheet orientated at 45^0 with respect to the direction of applied load, failed by concrete failure near the centre of the sample as shown in Figure (3.15a). In contrast, the BN2-2 samples series failed by adhesive debonding near the centre of the samples as shown in Figure (3.15b). The remaining specimens of BL2-1 and BN2-1 series which have CFRP sheet orientated at 90^0 with respect to the direction of applied load failed by CFRP sheet rupture as shown in Figure (3.16). This is expected due to the fact that the fabric used in CFRP systems generally has the highest tensile strength in the direction of the principal fibres.

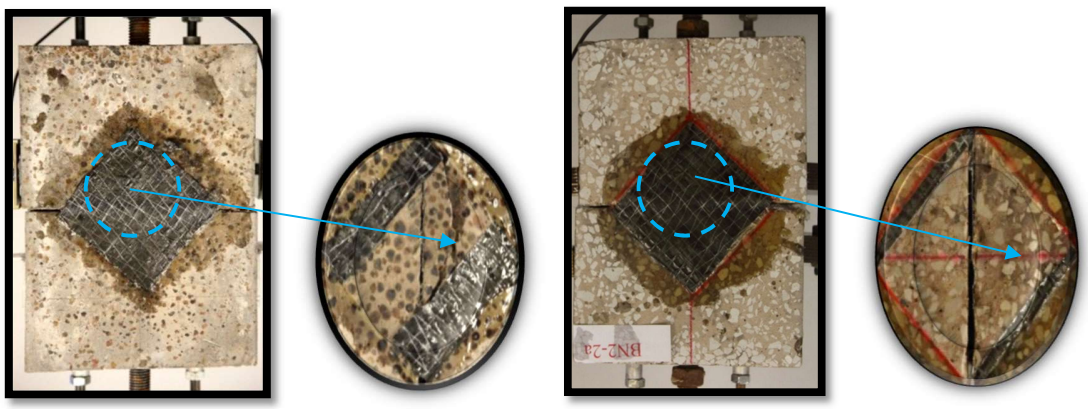

Figure (3.15): Typical failure mode of concrete sample with 45^0 fibre orientation (a) Failure of specimen BL2-2, (b) Failure of specimen BN2-2.

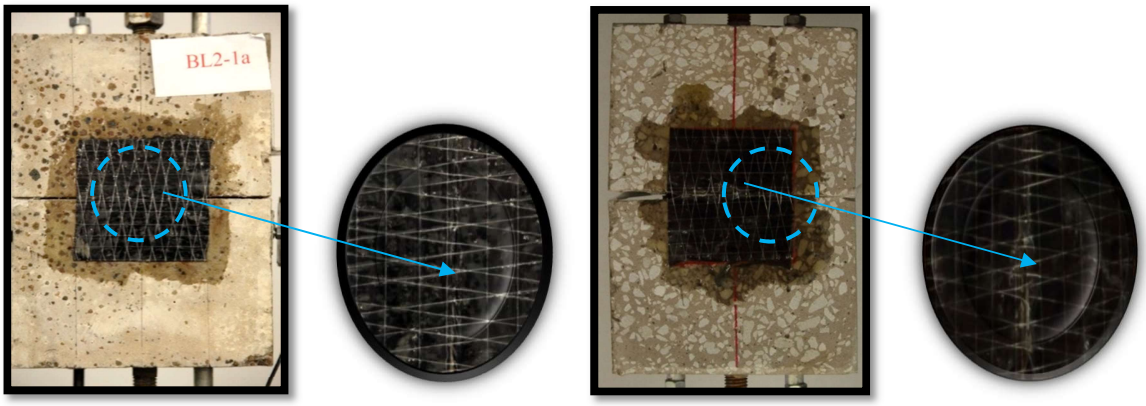

(a) (b)

Figure (3.16): Typical FRP rupture failure of concrete sample with 90^0 fibre orientation (a) Failure of specimen BL2-1, (b) Failure of specimen BN2-1.

3.7.2. Load–Slip Relationships

The global load-slip curves are presented in this section to show the applied load at the bar end versus the average slip measurements collected from the two LVDTs gauges that were attached on both sides of the concrete block close the centre of the sample. Figures (3.17) to (3.24) show the experimental bond-slip results of the tested samples. The load-slip response of the most tested can be categorised into two major zones. The first stage is defined as 'primary zone' and the second stage is defined as 'degradation zone'.

During the primary zone, the displacement increases linearly with the load. The slopes of curves which have the same strengthening technique are similar. Rapid increases in the global slip indicate the initiation of small interfacial cracks at the interface between concrete and the CFRP reinforcement, then the slopes of the curves were decreased which is indicated the occurrence of the degradation zone until the development of the large interfacial cracks. Eventually, when the large cracks reach a specific length, debonding develops at the interface. The main differences between the curves were observed for the later stage of loading as the degradation zone was realised. Some of the reasons for this variance are attributable to:

- The eccentricity between the top and bottom grips which results in higher bending stresses after the initiation of local debonding (regardless of the new strategy used in this test).
- The variance in concrete strength which influences the bond-slip for the CFRP/concrete joint.

In this Study, both specimens cast with LWAC and NWAC showed the same load-slip response. However, the difference in maximum debonding load and the slope of the load-slip curves can be easily highlighted in Figures (3.17) to (3.24). It can be seen that the NWAC samples showed higher bond strength and higher slope of the load-slip curves than those samples cast with LWAC, especially in the degradation zone. This is attributed to the higher shear strength and stiffness of NWAC compared with LWAC. Figures (3.17) to (3.19) which show the load-global slip relationships of the LWAC and NWAC specimens with different bond lengths. It can be seen that the load-slip curve tends to form a plateau response for samples with longer lengths of the CFRP sheet and the length of the plateauing trend increases with the length of the CFRP composite followed by a considerable increase of global slip with marginal increases in bond strength till the total debonding of the CFRP sheet from concrete surface.

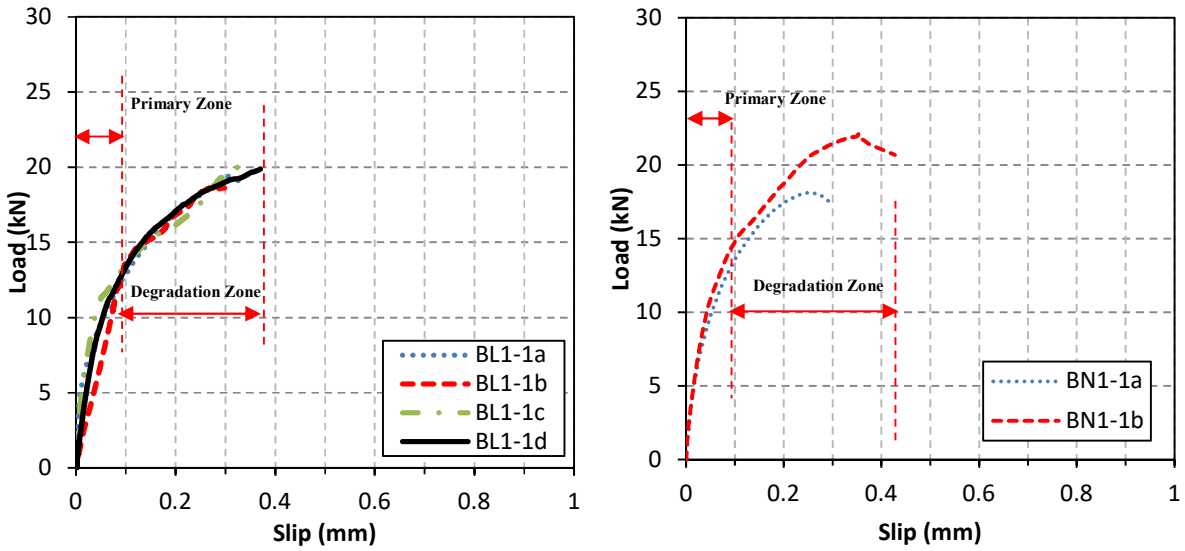

(a) LWAC Specimen (b) NWAC Specimen

Figure (3.17): Load versus total slip, experimental bond-slip results of BL/N1-1 specimens.

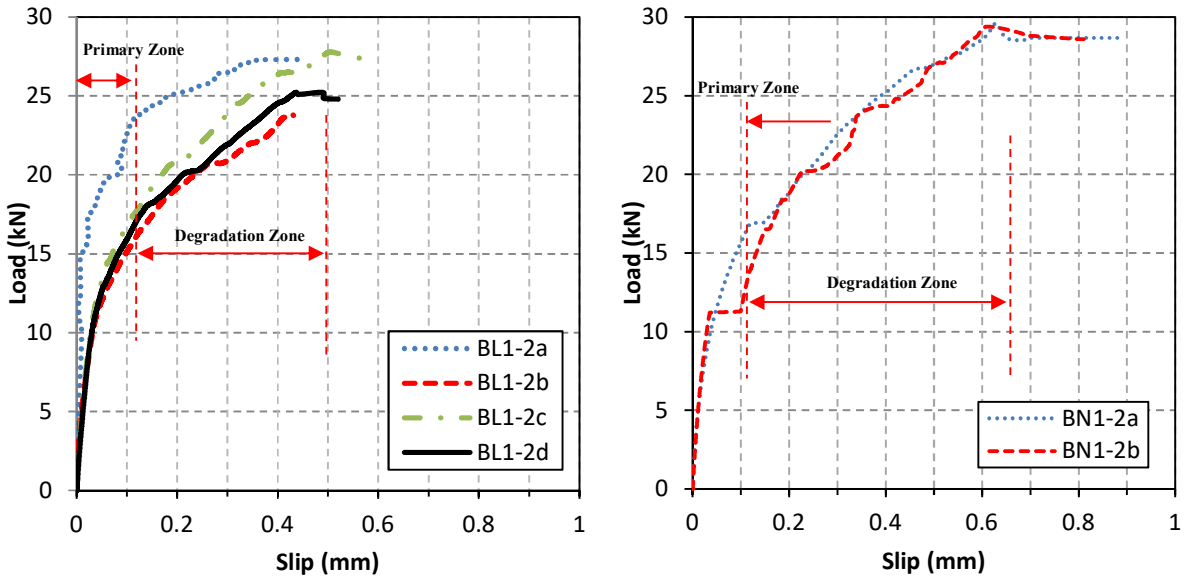

(a) LWAC Specimen (b) NWAC Specimen

Figure (3.18): Load versus total slip, experimental bond-slip results of BL/N1-2 specimens.

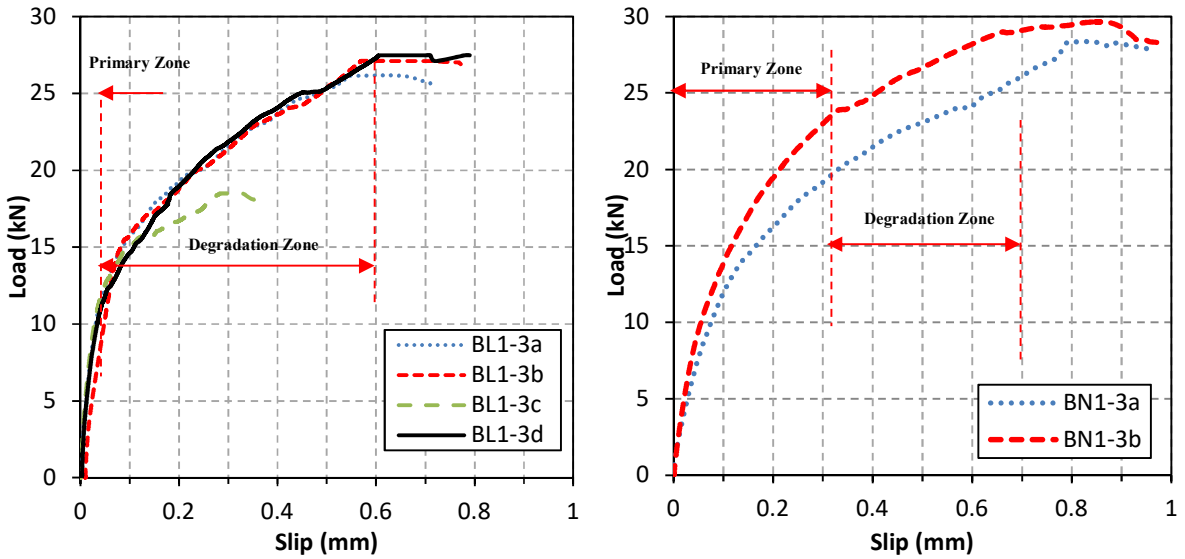

(a) LWAC Specimen (b) NWAC Specimen

Figure (3.19): Load versus total slip, experimental bond-slip results of BL/N1-3 specimens.

For those LWAC and NWAC specimens with varied CFRP thickness and width of CFRP sheets, the slope of the load-slip curve in the in primary zone increases as the CFRP stiffness and bonded width increase. This indicates that an increase in bonded width or FRP thickness can

strongly increase the stiffness of the CFRP-concrete interface. as shown in Figures (3.20) to (3.23).

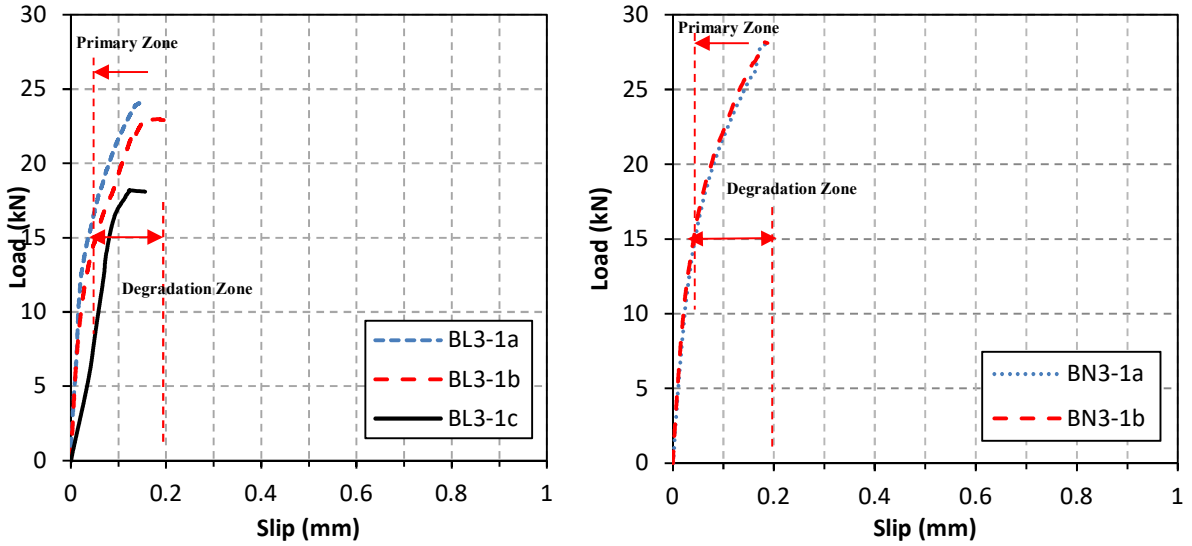

(a) LWAC Specimen (b) NWAC Specimen

Figure (3.20): Load versus total slip, experimental bond-slip results of BL/N3-1 specimens.

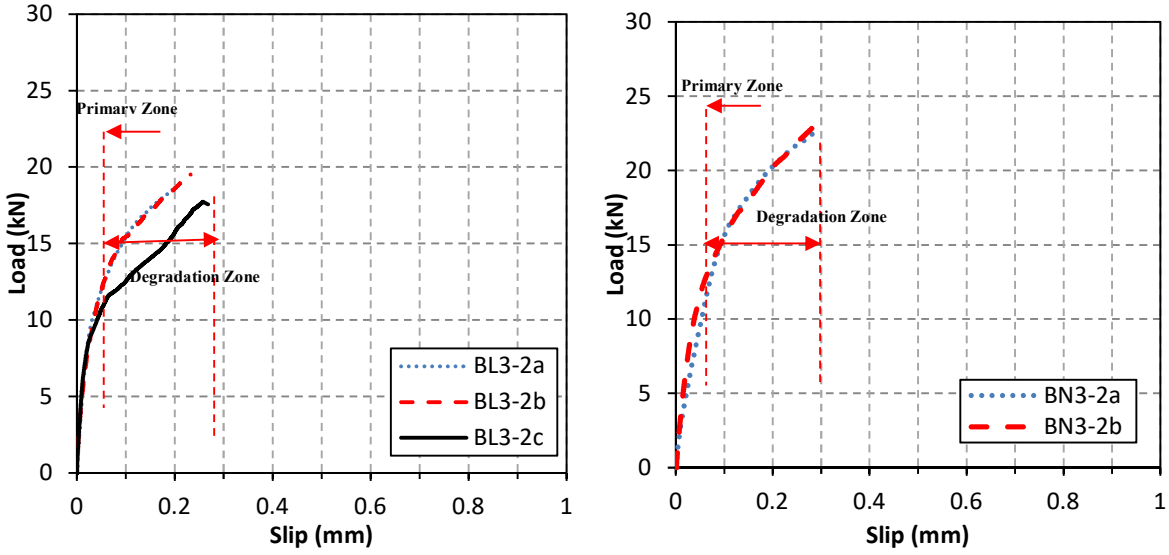

(a) LWAC Specimen (b) NWAC Specimen

Figure (3.21): Load versus total slip, experimental bond-slip results of BL/N3-2 specimens.

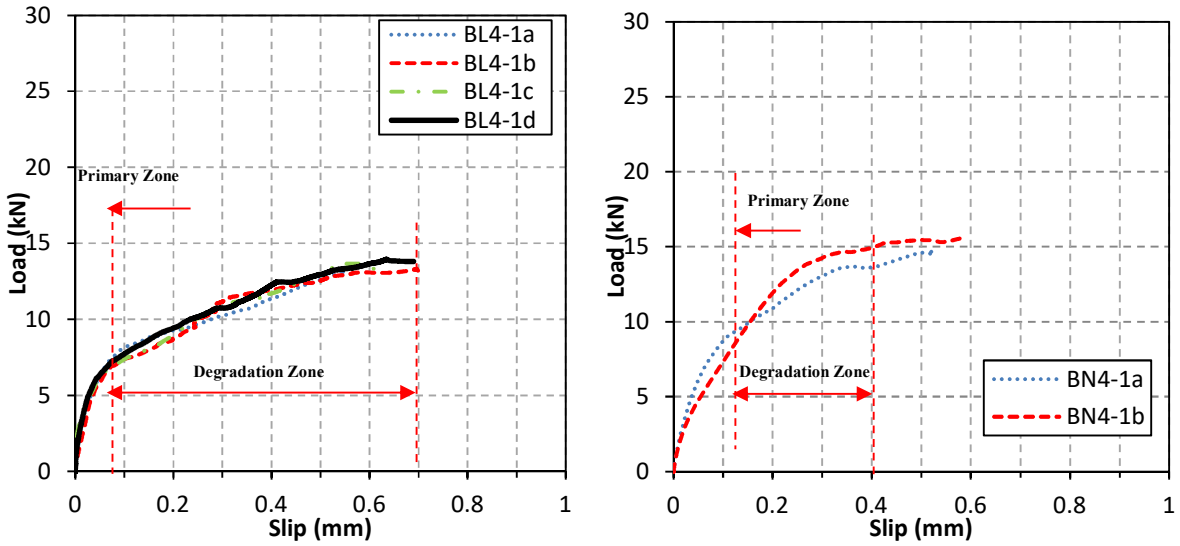

(a) LWAC Specimen (b) NWAC Specimen

Figure (3.22): Load versus total slip, experimental bond-slip results of BL/N4-1 specimens.

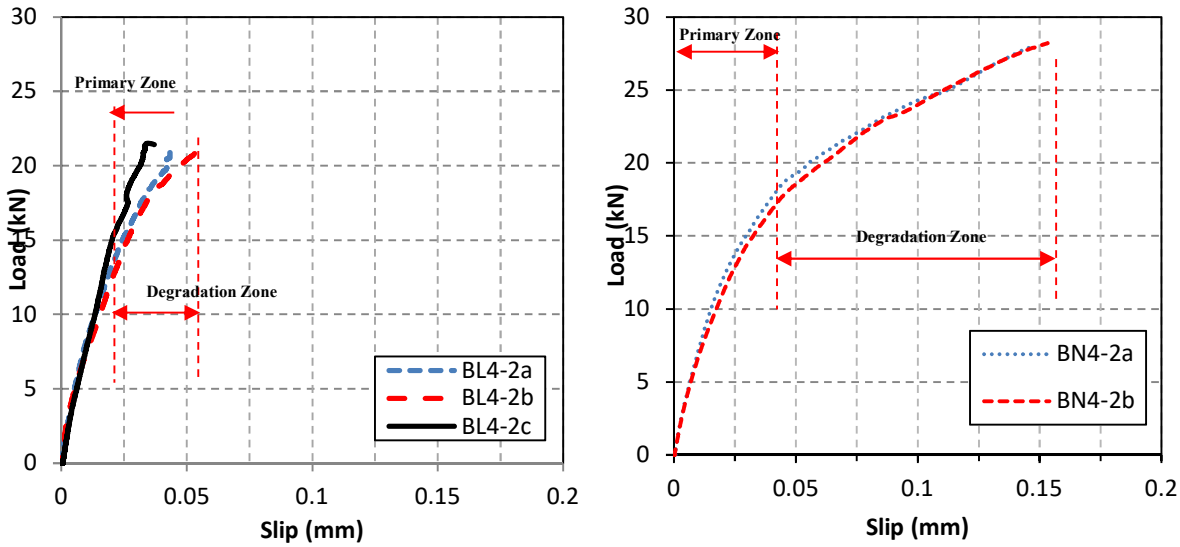

(a) LWAC Specimen (b) NWAC Specimen

Figure (3.23): Load versus total slip, experimental bond-slip results of BL/N4-2 specimens.

The load-slip relationships for all the LWAC and NWAC specimens with 45° fibre orientation of CFRP sheet are identical in shape. The applied tensile load increases linearly with an increase in a global slip in the primary zone and after a specific stage, a non-linear load-slip response observes which indicates the initiation of the interfacial cracks within the joint. For further loading, the load-slip response tends to form a plateau trend until the final failure developed as the CFRP reinforcement detached from the surface of concrete, as shown in Figure (3.24).

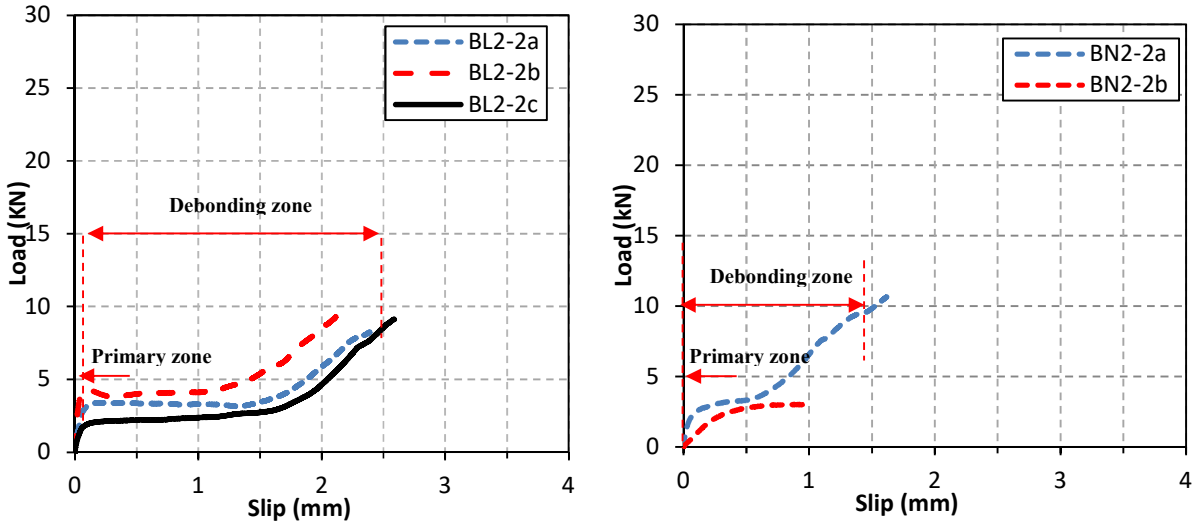

Figure (3.24): Load versus total slip, experimental bond-slip results of BL/N2-2 specimens.

3.7.3. CFRP Strain Distributions

Data is collected from strain gauges mounted on the upper surface of the CFRP sheet on one side of the two specimens in each BL1-1, BL1-2 and BL1-3 series and two specimens of each BN1-1, BN1-2 and BN1-3 series. These data are used as an example to understand the process of debonding and to show the typical strain distribution profile along the length of the CFRP sheet. Figures (3.25) to (3.36) show the distributions of strain at different levels of maximum load (20%, 40%, 60%, 80%, 90% and 100% of the maximum load) for LWAC and NWAC samples with different bonded lengths.

Each curve plotted corresponds to the strain distribution along the CFRP sheets at a particular load. When the applied load (P) is smaller than about 60% of the maximum load (P_{max}), the CFRP strains decrease quickly with distance from the centre of the concrete prism. This

descending trend is attributed to the low axial stiffness of the bonded CFRP composite sheet with respect to that of the concrete substrate, it can be also noted that the LWAC and NWAC showed similar trends at very low level of loading, approximately less than 40% of the maximum load.

Increasing the load before primary debonding leads to upward shifting of the curve, but the strain trend does not change. However, when the load value goes beyond 60% of the maximum load, cracks start to develop, and this cracking leads to a clear change of the strain distribution in the CFRP sheet. The profiles tended to attain a linear shape and the slope of the strain curve near the specimen centre tended to decrease in some tested samples. Since the slope of the curve reflects the rate of change in strain in the CFRP Sheet (which is proportional to the local shear stress), the decrease of the slope shows shear softening along the CFRP-concrete interface.

At a certain load level before local debonding, the strain profile at the beginning of the bonded length almost remains constant up to the failure of the joint. This means that the concrete prism begins failure at the loaded end. It also follows that the portion of the CFRP sheet near the loaded end of the specimen cannot transfer load. The strain gauges far from the centre measure strain which indicates the load transfer zone shifted away from the loaded end of the specimens towards the centre of the sample. The same conclusion was obtained by Yao et al. (2005).

In the study, the ‘Active transfer strain zone’ is defined as the distance between the points of the maximum strain at the centre of the sample to the point of the minimum strain. The strain distributions of the two LWAC samples having 50 mm bonded length (BL1-1a and BL1-1b) have been plotted in Figures (3.25) and (3.26). The patterns of strain distribution of these samples were similar to those obtained for NWAC samples (BN1-1a and BN1-1b) as shown Figure (3.27) and (3.28). The active transfer strain length was approximately 50 mm up to the maximum load level. The maximum recorded strain reading in the case of LWAC samples was approximately 4600 μm/m and 3600 μm/m for NWAC samples.

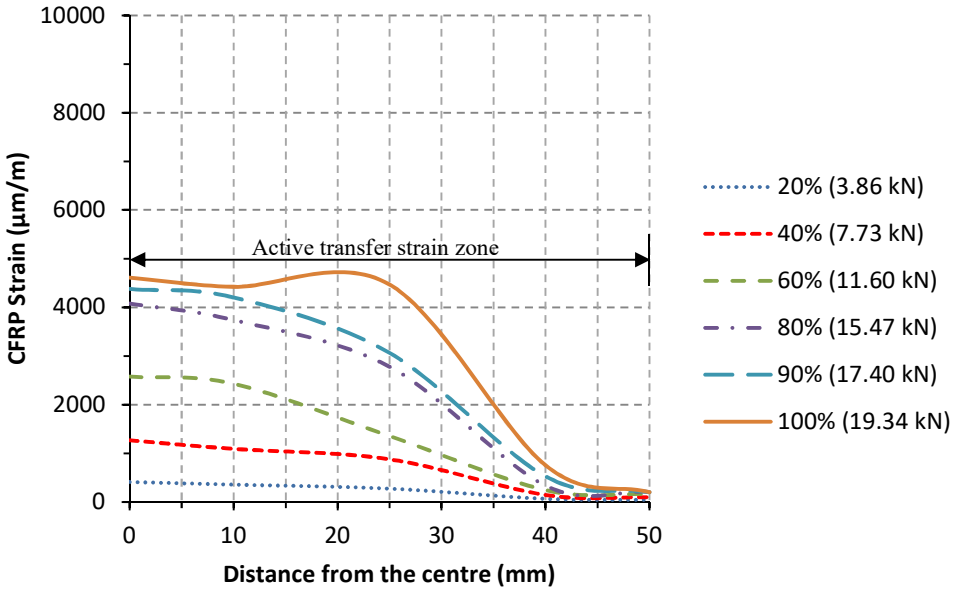

Figure (3.25): Strain versus distance from the centre of the specimen BL1-1a.

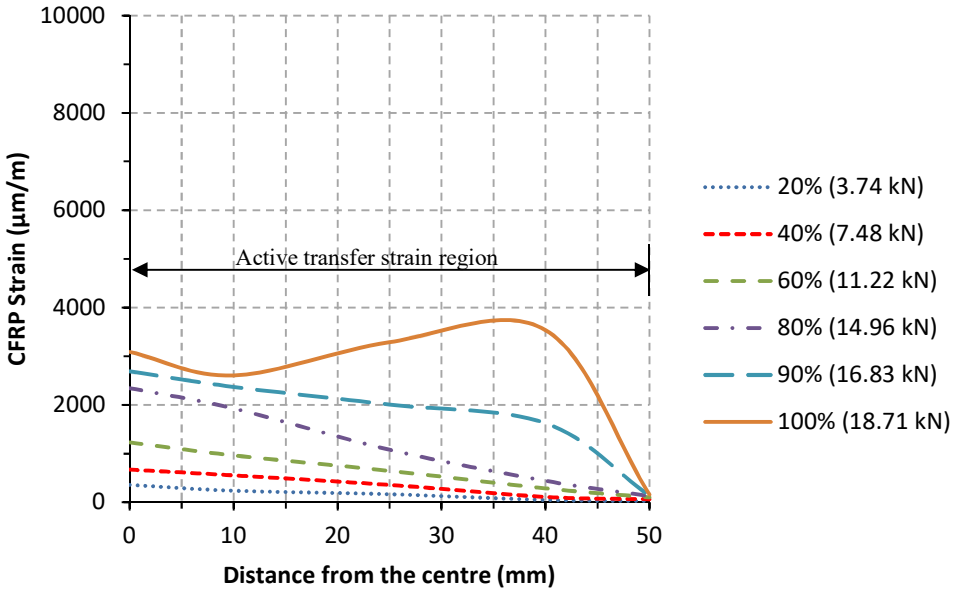

Figure (3.26): Strain versus distance from the centre of the specimen BL1-1b.

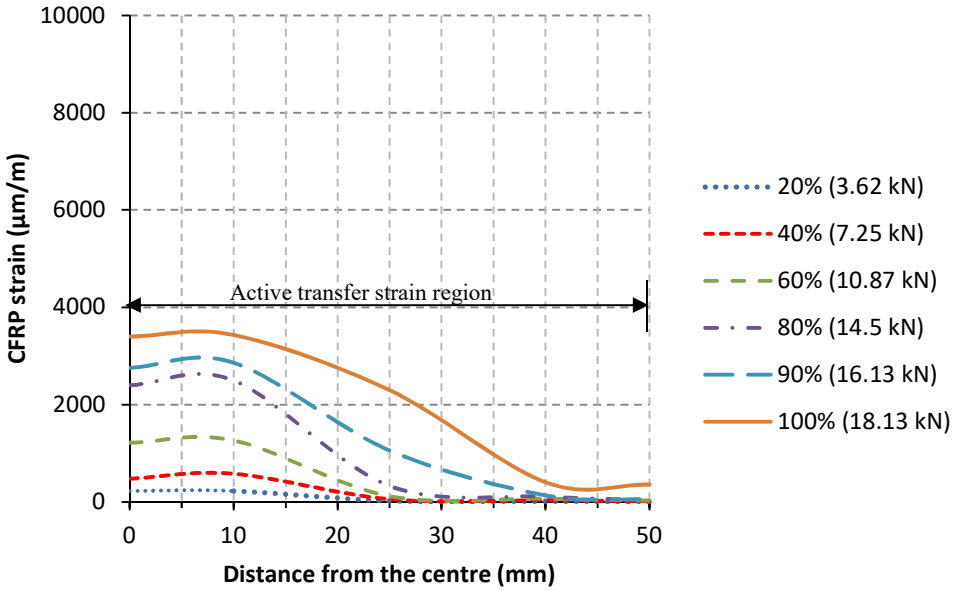

Figure (3.27): Strain versus distance from the centre of the specimen BN1-1a.

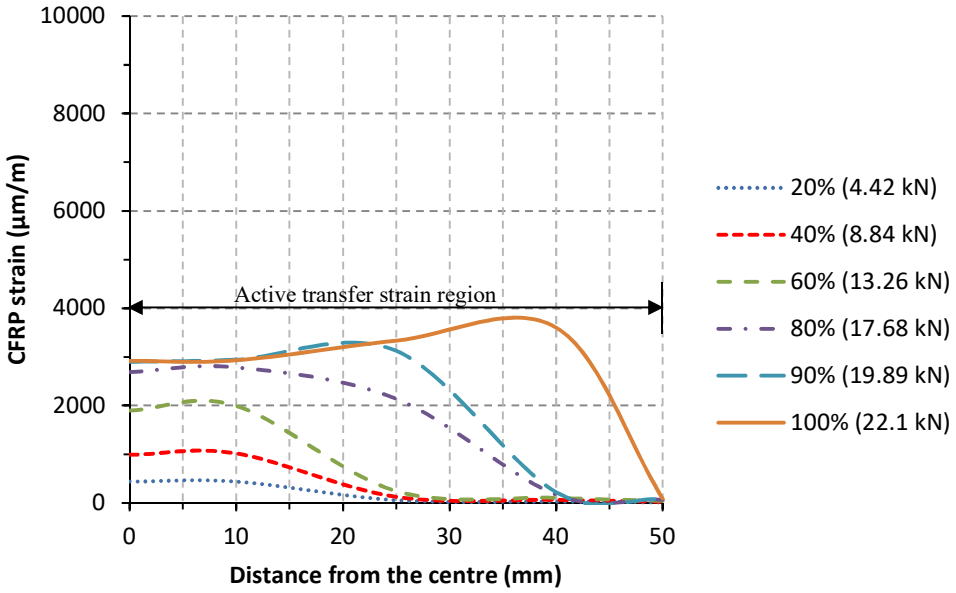

Figure (3.28): Strain versus distance from the centre of the specimen BN1-1b.

Figures (3.29) and (3.30) show the strain distribution of LWAC samples having 75 mm bonded length (BL1-2a and BL1-2c). It can be noted that the active transfer strain zone moved to 75mm at the maximum load level. The same behaviour was observed for samples cast with NWAC

having 75 mm bonded length. The maximum recorded strain reading was approximately 6800 µm/m for LWAC and NWAC samples.

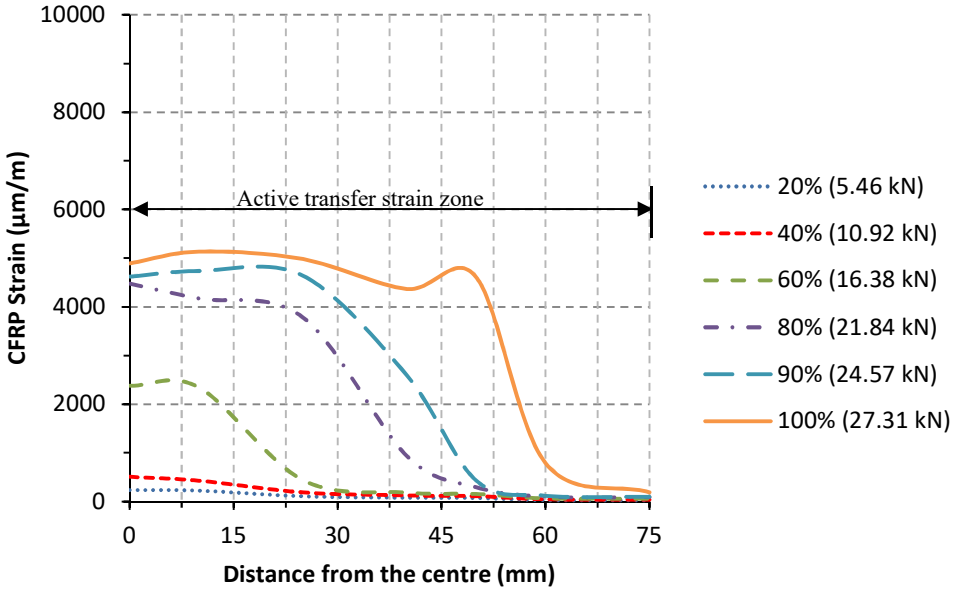

Figure (3.29): Strain versus distance from the centre of the specimen BL1-2a.

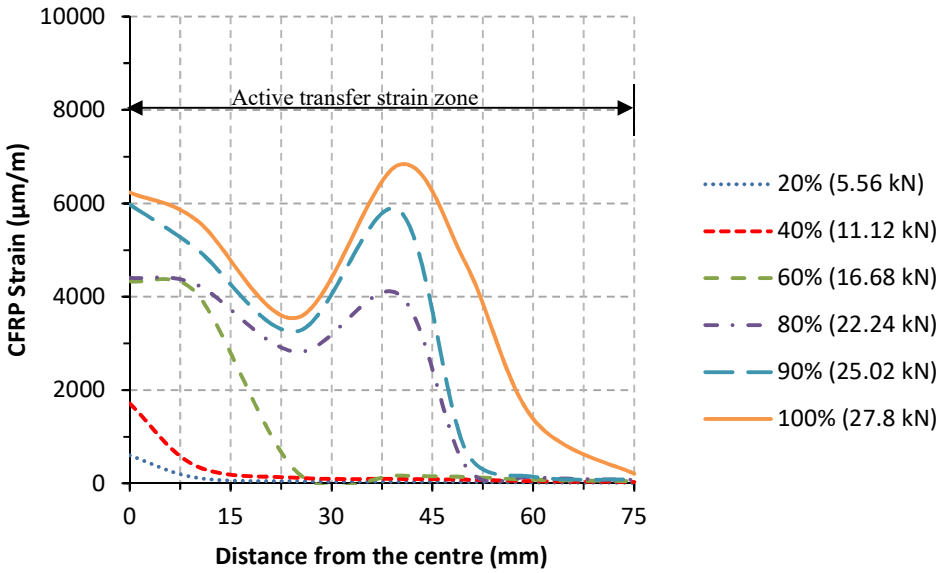

Figure (3.30): Strain versus distance from the centre of the specimen BL1-2c.

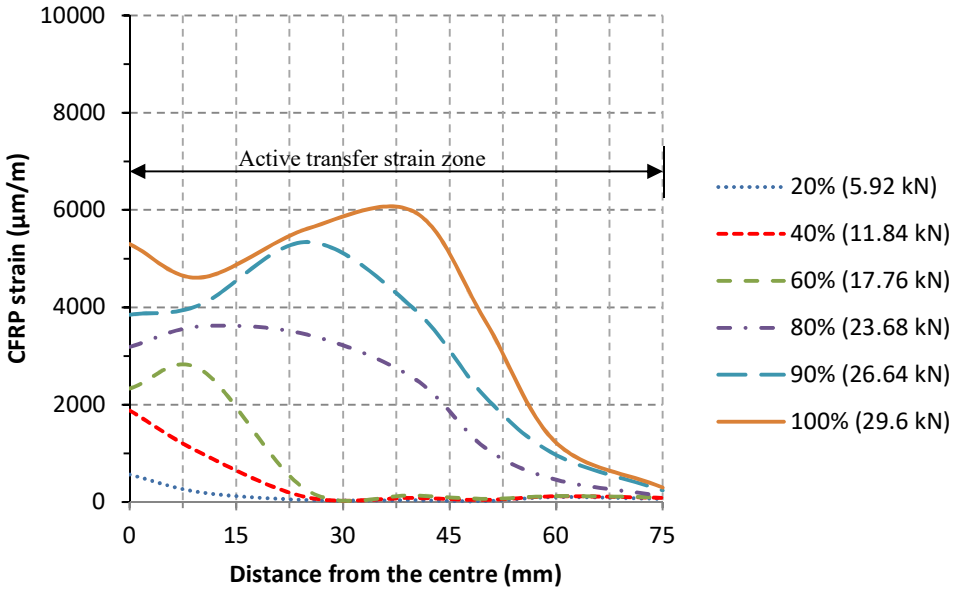

Figure (3.31): Strain versus distance from the centre of the specimen BN1-2a.

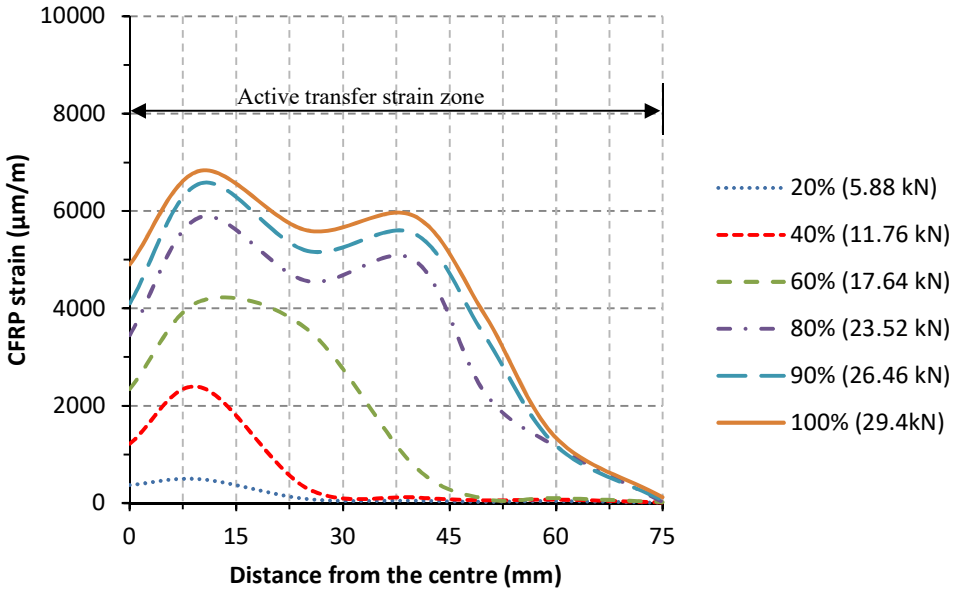

Figure (3.32): Strain versus distance from the centre of the specimen BN1-2b.

Figures (3.33) to (3.36) show the strain distribution of LWAC samples having 100 mm bonded length (BL1-3b and BL1-3c) and the NWAC samples (BN1-3a and BN1-3b). No more movement of the active transfer zone was observed for these samples, the active transfer zone

approximately ranges between 70-75 mm. The same behaviour was observed for samples cast with NWAC having 75 mm bonded length. The maximum recorded strain reading was approximately 8300 µm/m in the case of LWAC specimens and 4800 µm/m for NWAC samples.

Comparison between LWAC and NWAC samples showed that there is no significant difference in strain distribution at the low level of the applied load (up to 40% of the maximum load), the difference can be noticed after 60% of maximum load (cracking stage). The changes in strain distribution between lightweight and normal weight concrete depend on the crack intensity and crack propagation which is more prevalent in LWC samples compared with normal weight samples. It can also be observed that the normal weight concrete samples showed a flatter distribution while lightweight samples showed non-uniform strain distribution in most cases particularly, at the end of CFRP sheet due to local debonding of concrete.

The noticeable difference between LWAC samples and those of NWAC in terms of strain distribution are that the strain gauges attached near the far end of the CFRP sheet in the case of LWAC samples read higher strain compared with samples cast with NWAC. This is strongly related to the higher crack intensity due to the lower tensile strength of Lytag aggregates which allow propagation of the cracks over a large area of the concrete substrate, contrasting with that of natural weight aggregates.

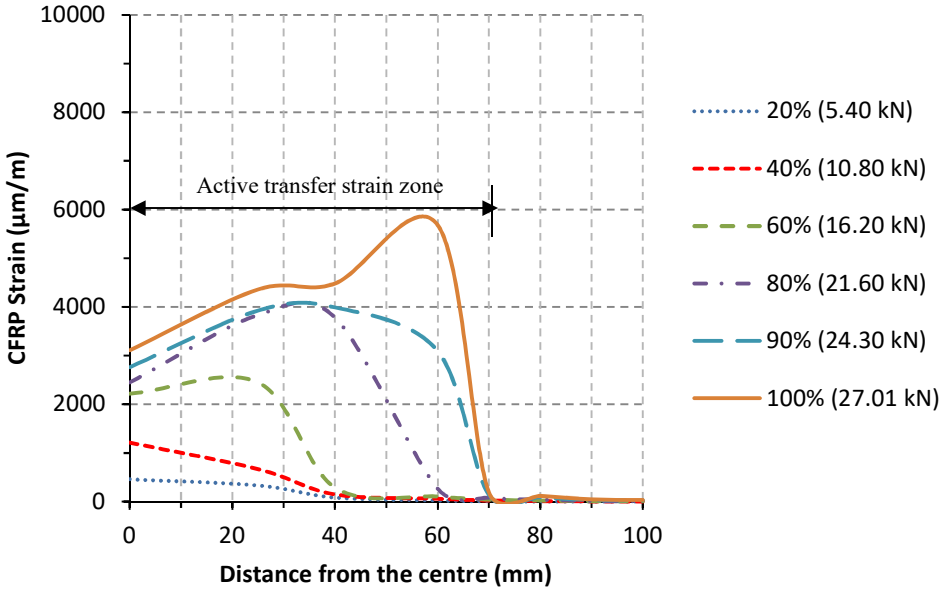

Figure (3.33): Strain versus distance from the centre of the specimen BL1-3b.

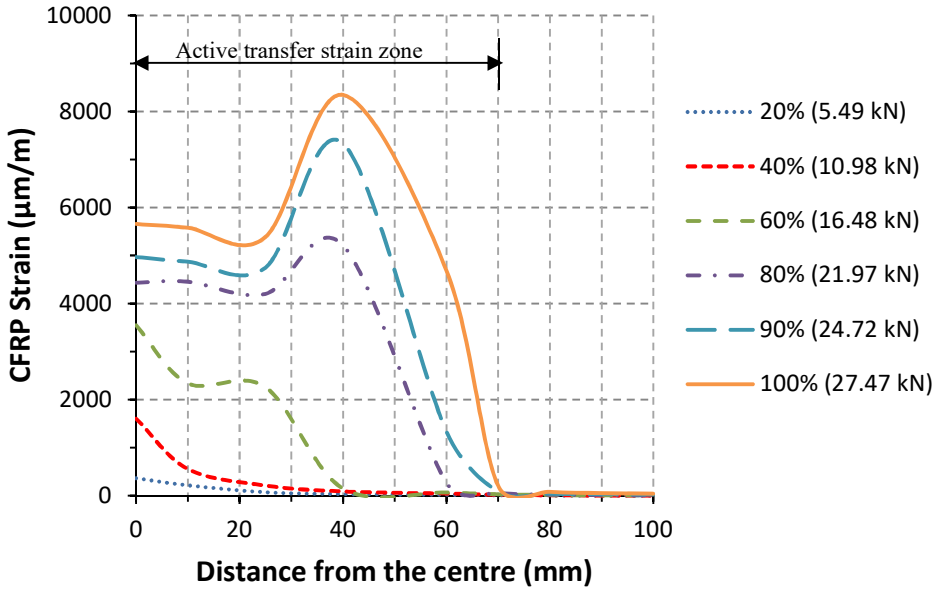

Figure (3.34): Strain versus distance from the centre of the specimen BL1-3c.

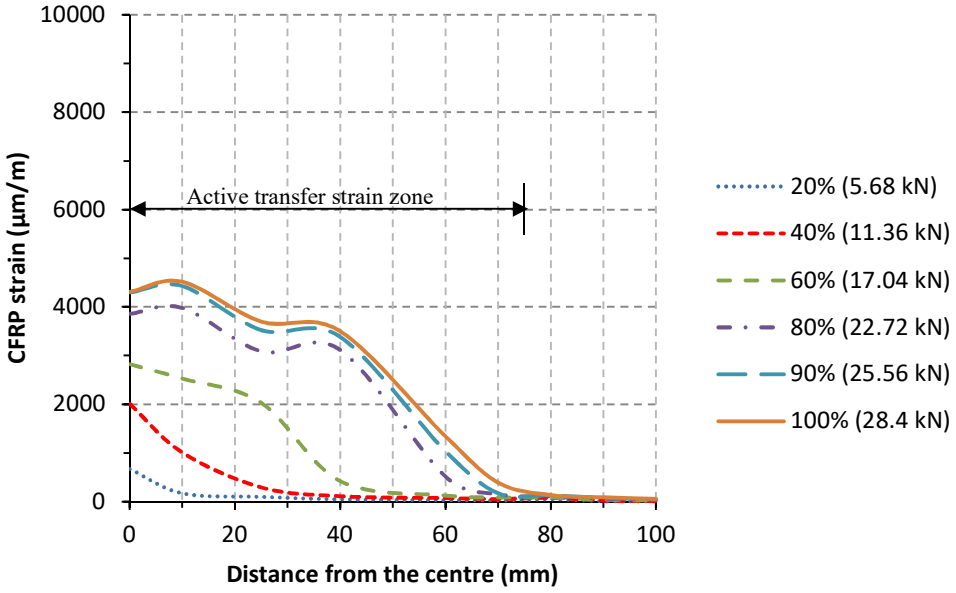

Figure (3.35): Strain versus distance from the centre of the specimen BN1-3a.

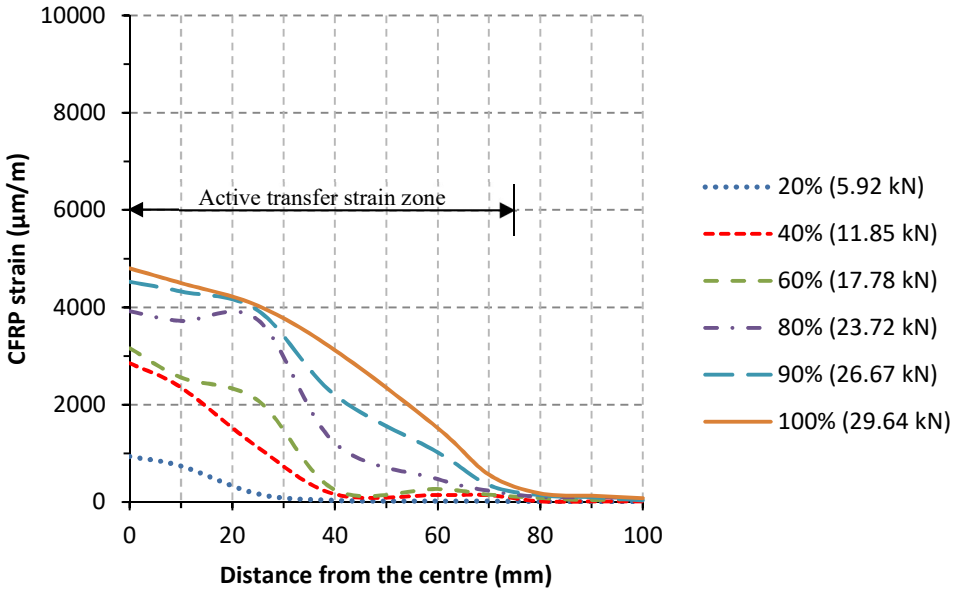

Figure (3.36): Strain versus distance from the centre of the specimen BN1-3b.

3.7.4. Local Shear Stress Distribution

Figures (3.37) to (3.48) show the typical distributions of the average local shear stress along the length of CFRP composite at different levels of maximum load for the samples of BL/N1-1, BL/N1-2 and BL/N1-3 series. The readings of strains along the length of CFRP sheet have been used to find the average local shear stress. In this analysis. A linear elastic behaviour was assumed for the CFRP reinforcement, the mean value of shear stress between two subsequent strain gauges attached along the length of the FRP composite was employed to plot the local shear stresses using the following equation (Equation (3.3)) (Mazzotti et al, 2004 and 2008):

$$\bar{\tau}_{(i+1)/2} = \frac{E_f\, t_f (\varepsilon_i - \varepsilon_{i-1})}{\Delta x} \tag{3.3}$$

Where, E_f and t_f are the modulus of elasticity and the thickness of CFRP sheet. x_i is the strain gauge position and ε_i is the measured strain. Δx is the difference between two subsequent strain gauges. The mean shear stress obtained from Equation (3.3) is lower than those recorded in the actual tested specimen.

Generally, at low levels of applied load, the local bond stress increases gradually close the centre of the samples. For further loading, the bond stress increased away from the centre of the sample. At this stage, the linear response of the load-slip trend ends and the large interfacial cracks start to develop. The FRP/concrete joint starts its degradation or softening stage, during that the bond stress close the sample's centre decreases gradually. Local debonding of the CFRP composite from the surface of concrete develops close the centre and then extends progressively towards the far end of the CFRP sheet. The maximum interfacial bond stress is achieved close the far end of the CFRP at 100% of the maximum load before global debonding if the length of the CFRP sheet higher than the effective length (for the sample with 100 mm bonded length of the CFRP reinforcement. These stages of the debonding process are the same as those described for the FRP/concrete joint by Yuan et al. (2004).

It can be seen that the average local shear stress fluctuates along the length of CFRP reinforcement in LWAC and NWAC samples. It is noticeable that the maximum bond stress can be achieved near the far end of CFRP composite at 100% of maximum load; this may be due to the effect of local concrete crushing near the far end of the CFRP sheet. The lowest bond stresses were noticed close the centre of concrete specimens is due mainly to the larger strain gauge measurements between two subsequent stain gauges close to this region.

For further comparison, the maximum average local shear stress for those specimens cast with LWAC is recorded as 9.5 MPa for the BL1-1 specimen's series and 14.5 MPa and 11.6 MPa for the BL1-2 and BL1-3 specimens, respectively. While for NWAC samples the shear stress is recorded as 6.6 MPa for the BN1-1 specimen's series, 8.4 MPa for the BN1-2 samples and 14.46 for the BN1-3 specimens.

For some samples, negative values of the bond shear stress were obtained along the bonded length of the CFRP reinforcement at 60%, 80%, 90 % and 100% of the maximum load levels. This is assigned to the differences in the CFRP strain measurements as results of higher cracks intensity close the far end of the of the sheet or by the influence of the bending stresses developed after the occurrence of the local debonding near the far end of CFRP sheet. The same behaviour was observed by Serbescu, (2013)

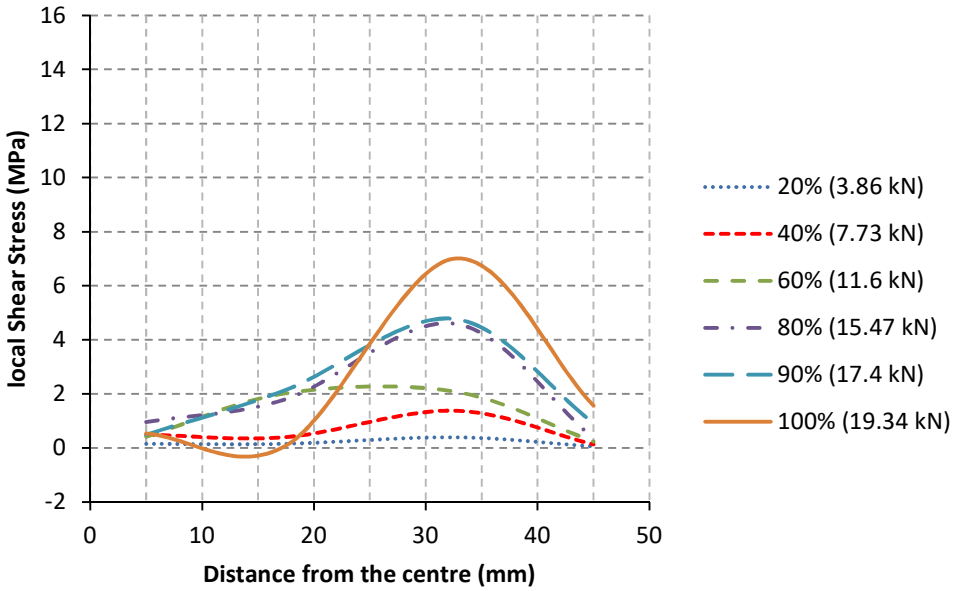

Figure (3.37): Shear stress versus distance from the centre of the specimen BL1-1a.

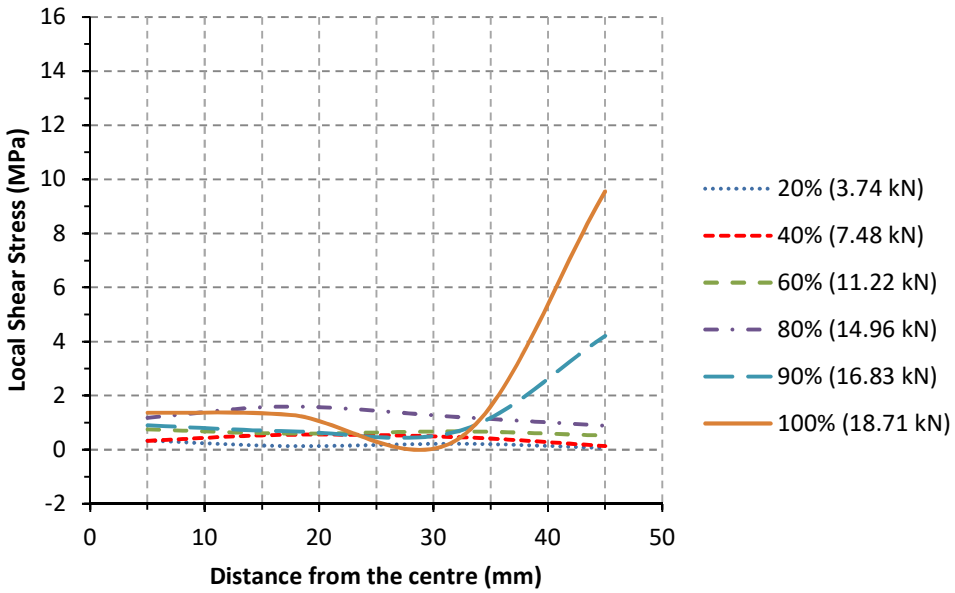

Figure (3.38): Shear stress versus distance from the centre of the specimen BL1-1b.

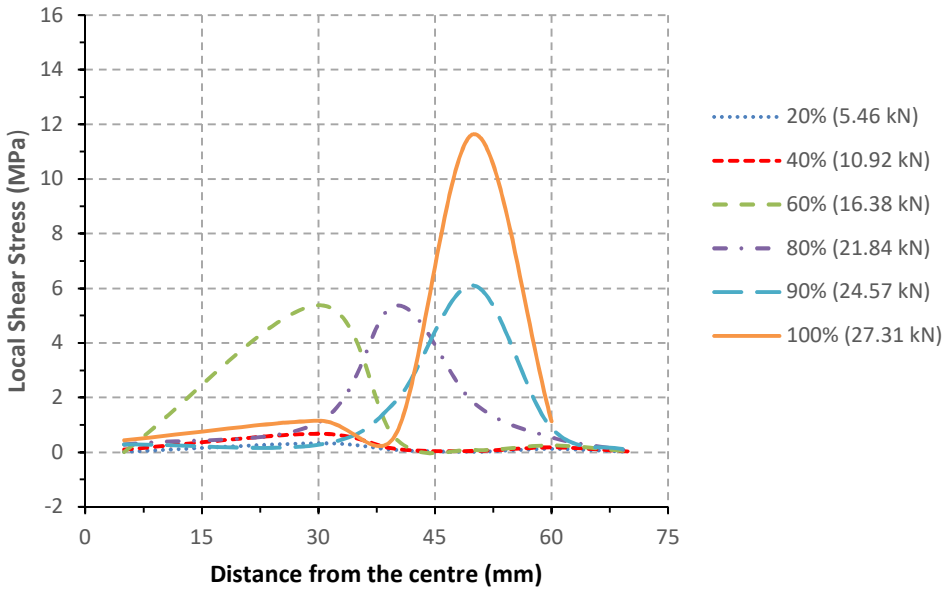

Figure (3.39): Shear stress versus distance from the centre of the specimen BL1-2a.

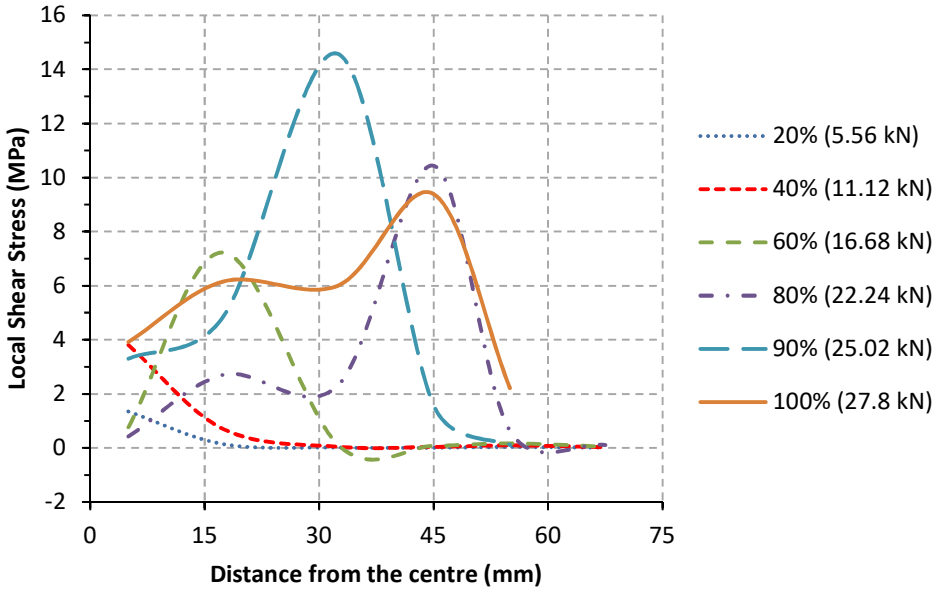

Figure (3.40): Shear stress versus distance from the centre of the specimen BL1-2c.

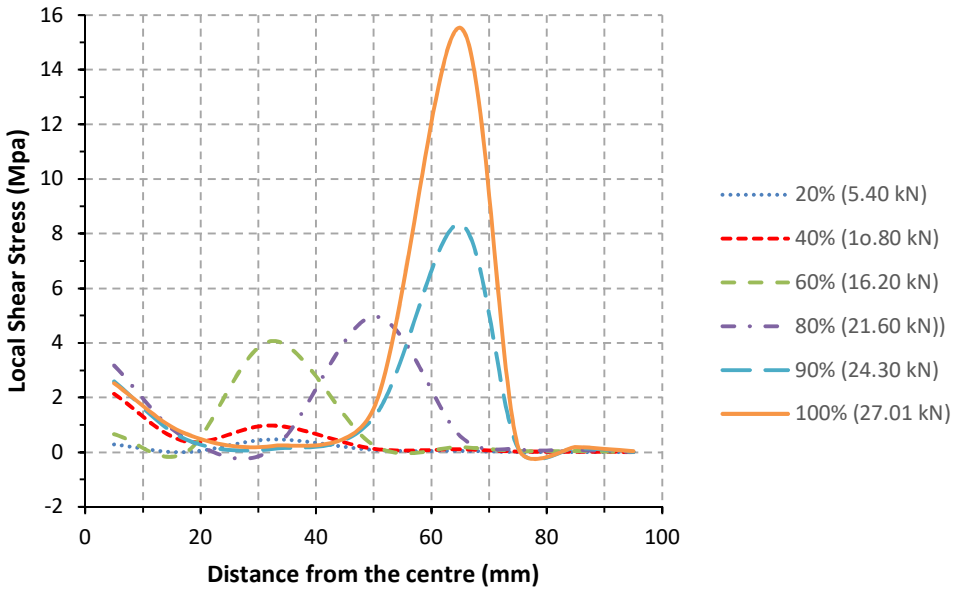

Figure (3.41): Shear stress versus distance from the centre of the specimen BL1-3b.

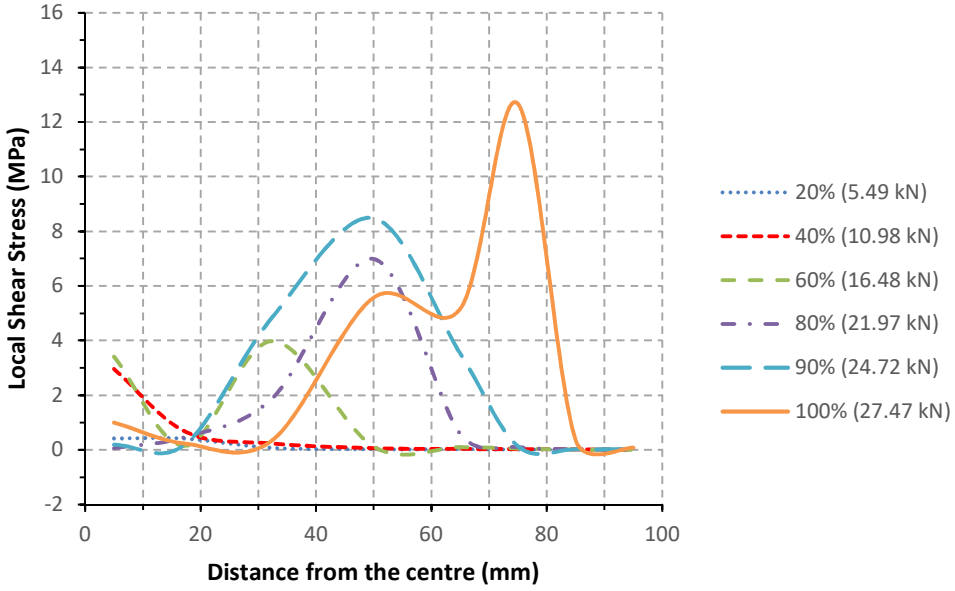

Figure (3.42): Shear stress versus distance from the centre of the specimen BL1-3c.

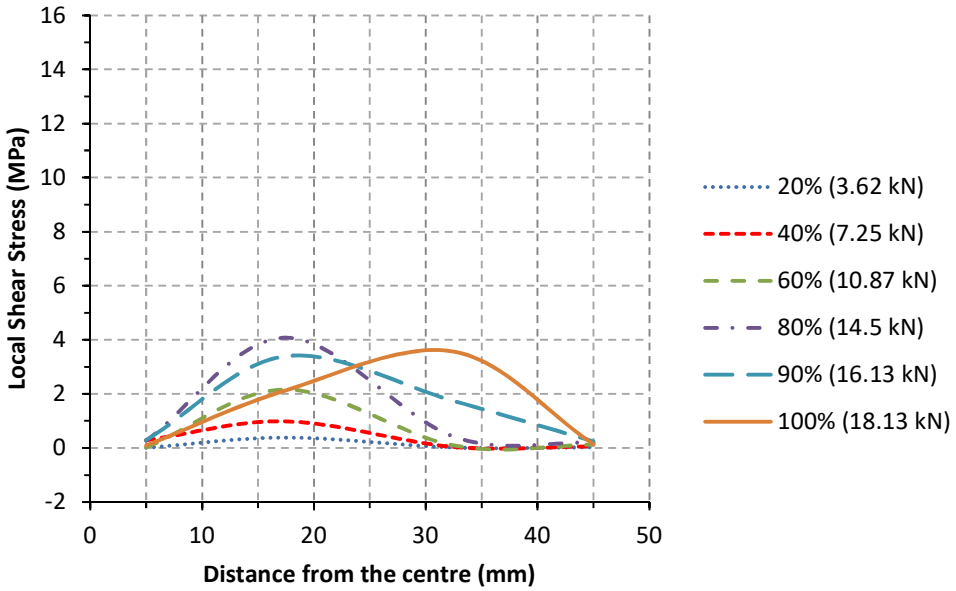

Figure (3.43): Shear stress versus distance from the centre of the specimen BN1-1a.

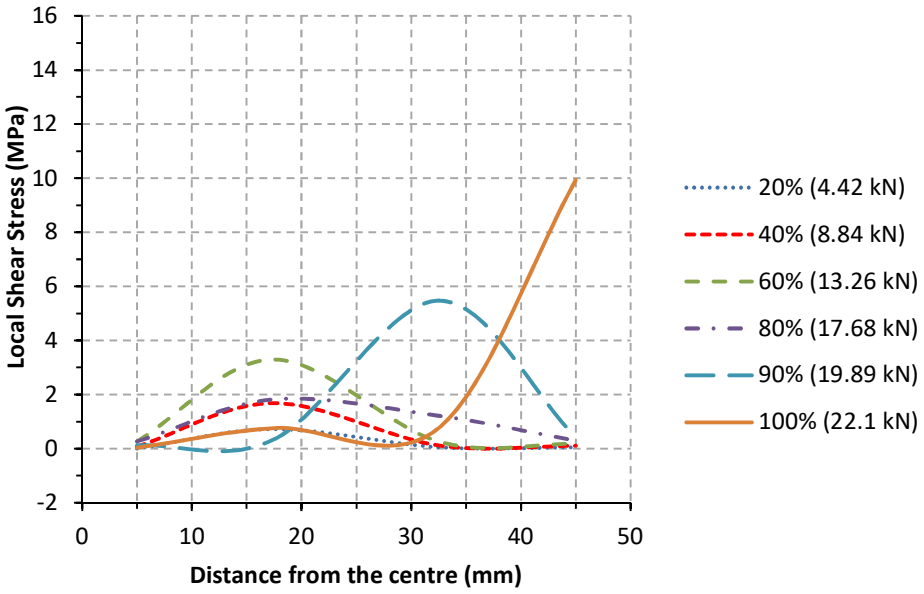

Figure (3.44): Shear stress versus distance from the centre of the specimen BN1-1b.

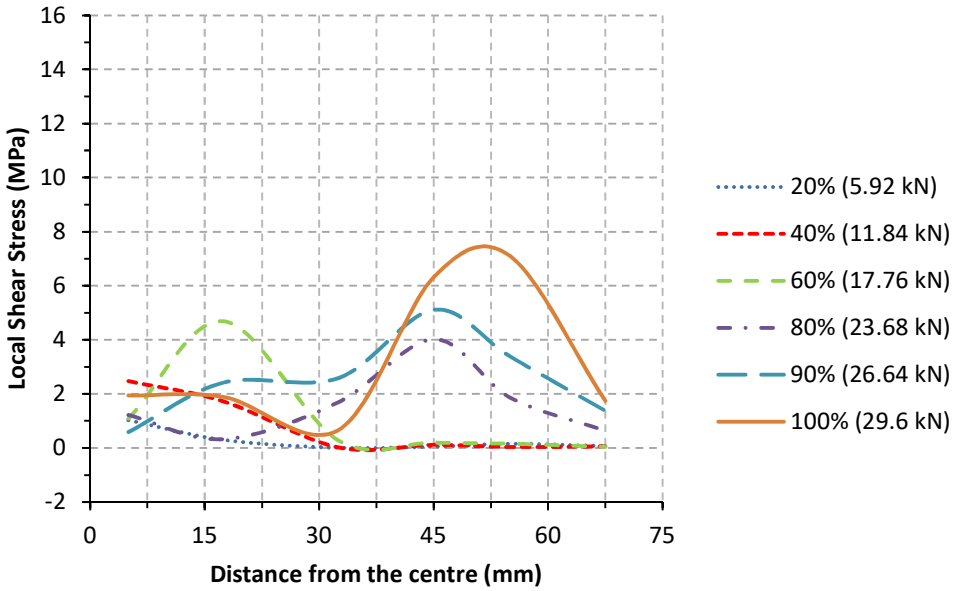

Figure (3.45): Shear stress versus distance from the centre of the specimen BN1-2a.

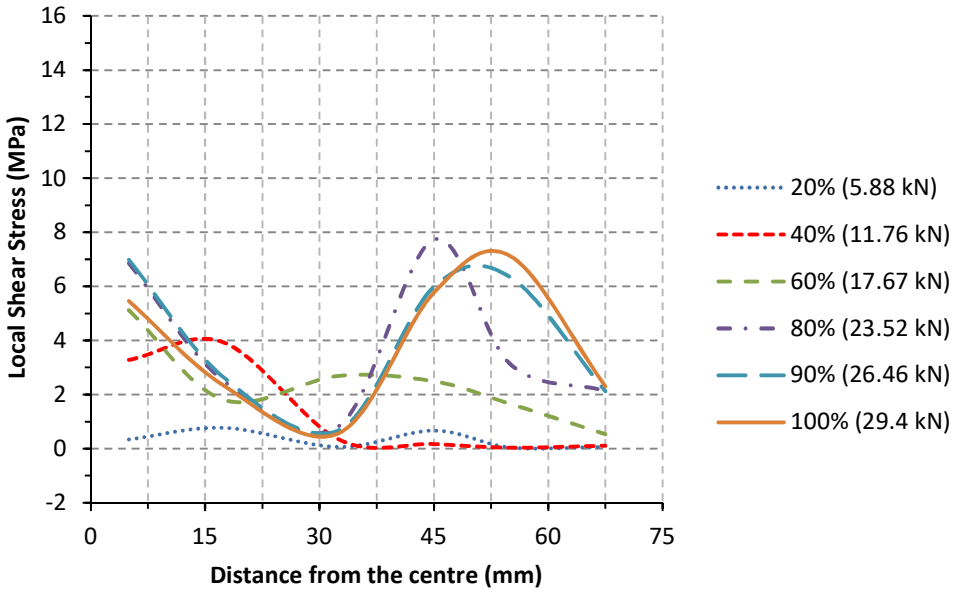

Figure (3.46): Shear stress versus distance from the centre of the specimen BN1-2b.

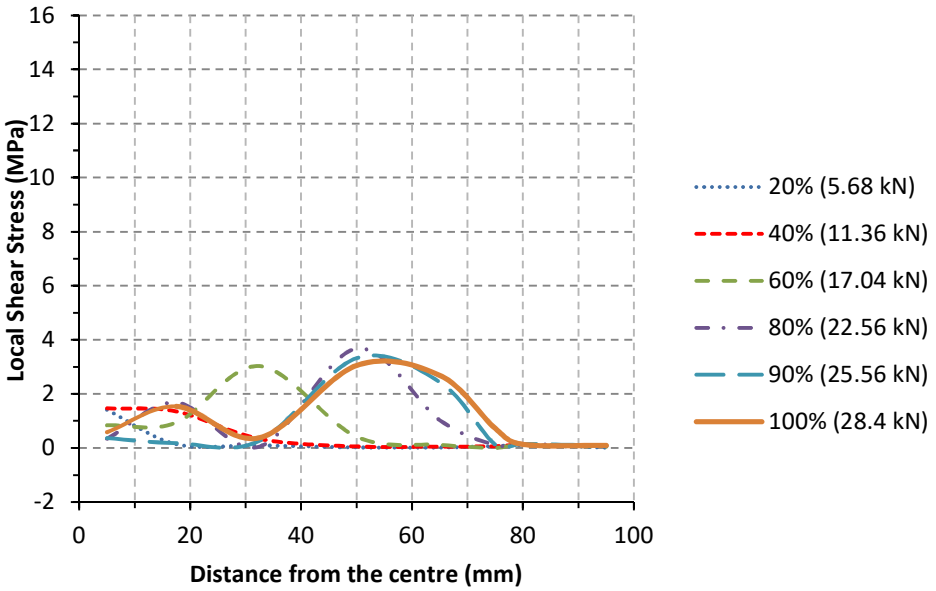

Figure (3.47): Shear stress versus distance from the centre of the specimen BN1-3a.

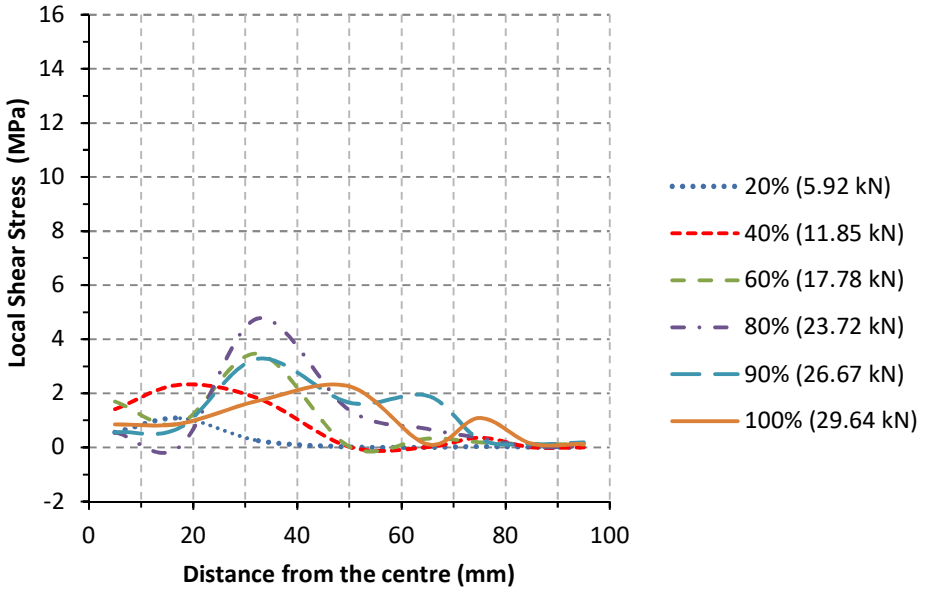

Figure (3.48): Shear stress versus distance from the centre of the specimen BN1-3b.

Figure (3.49) describes the shear stress versus global slip curves of a point located at 17.5 mm from the centre of the BL/N1-2 samples which are used as an example to show the typical shear stress-slip response of LWAC and NWAC samples. Local shear stress is derived based on Equation (3.3). The shear stress-global slip response shows a non-uniform ascending and descending trend and the curves response varied for samples with identical strengthening configurations and concrete strength. This is attributed to the effect of crack intensity and the location of stain gauges above the cracks which significantly affect the strain reading as well as the stress-slip curve along the length of the CFRP reinforcement.

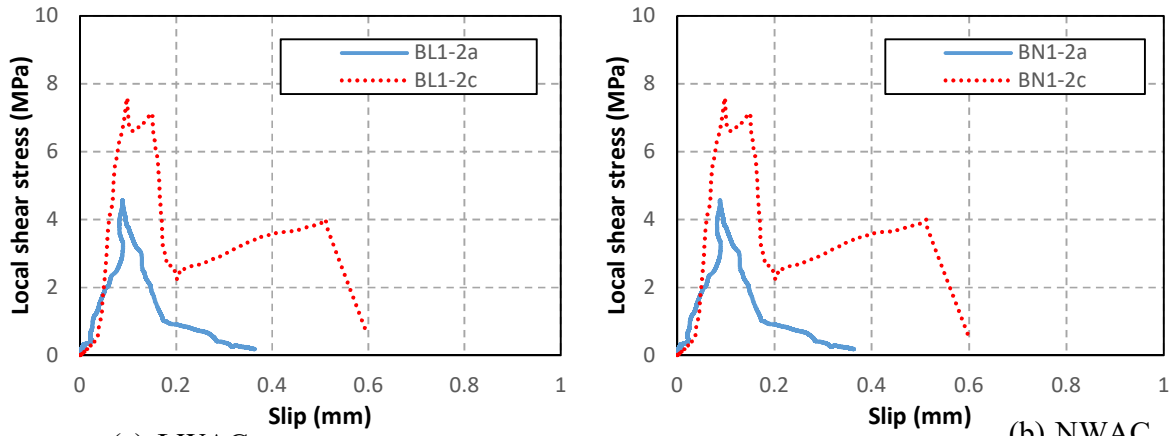

(a) LWAC (b) NWAC

Figure (3.49): Shear stress slip of the BL/N1-2 samples.

3.7.5. Load-Strain Curves

Load versus strain values of the CFRP to the concrete interface of both the LWAC and NWAC samples at a different location from the specimen's centre are presented in Figures (3.50) to (3.52). It can be seen that the load-strain plot for each tested sample consists of three main stages: linear (uncracked stage), non-linear (cracked stage) and plateau stages (local debonding stage).

The load increases pointedly with a marginal increase in strain measurements up to ($0.6P_u$) for all of the tested samples. After the linear stage, small cracks start to initiate in the FRP/concrete joint and the response of the joint becomes non-linear. After the development of larger cracks, the load-strain plot tends to form a plateau trend with a marginal increase in strain reading while the load increases significantly until global debonding failure occurs. It can be noticed that the strains considerably increase before local debonding of the CFRP reinforcement. This trend in

behaviour of the load-strain curves shows no noticeable difference between LWAC or NWAC samples.

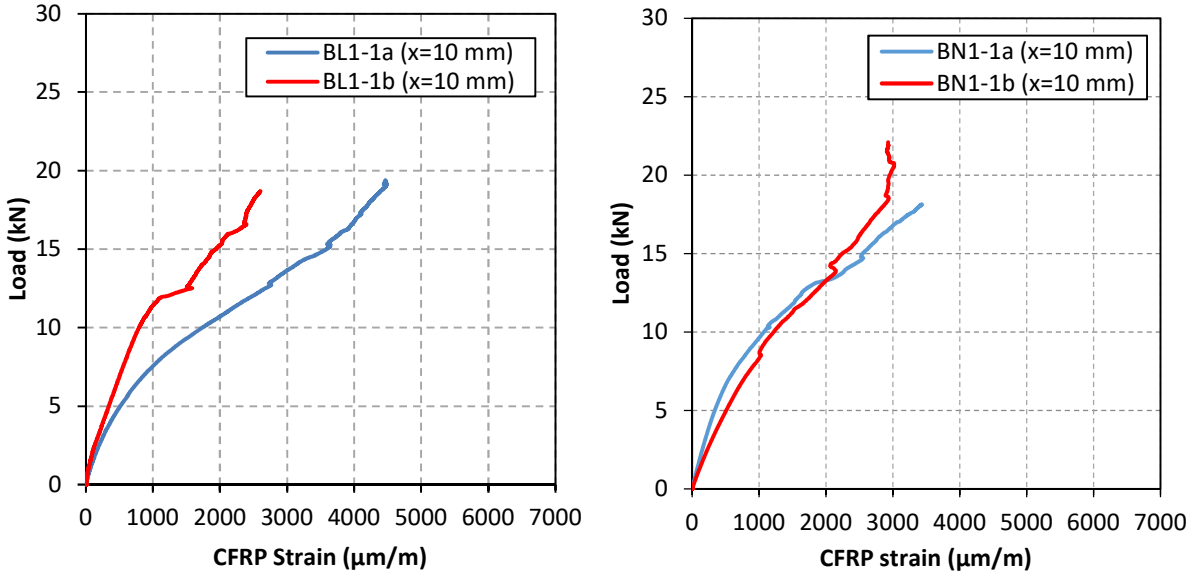

(a) LWAC (b) NWAC

Figure (3.50): Load versus CFRP strain of the specimen BL/N1-1.

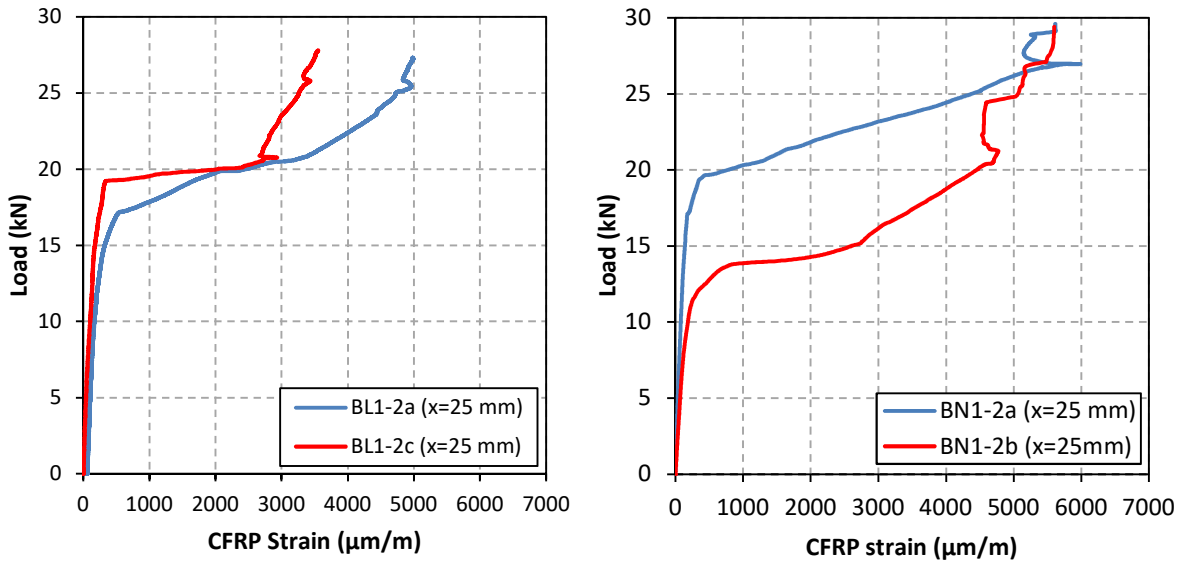

(a) LWAC (b) NWAC

Figure (3.51): Load versus CFRP strain of the specimen BL/N1-2.

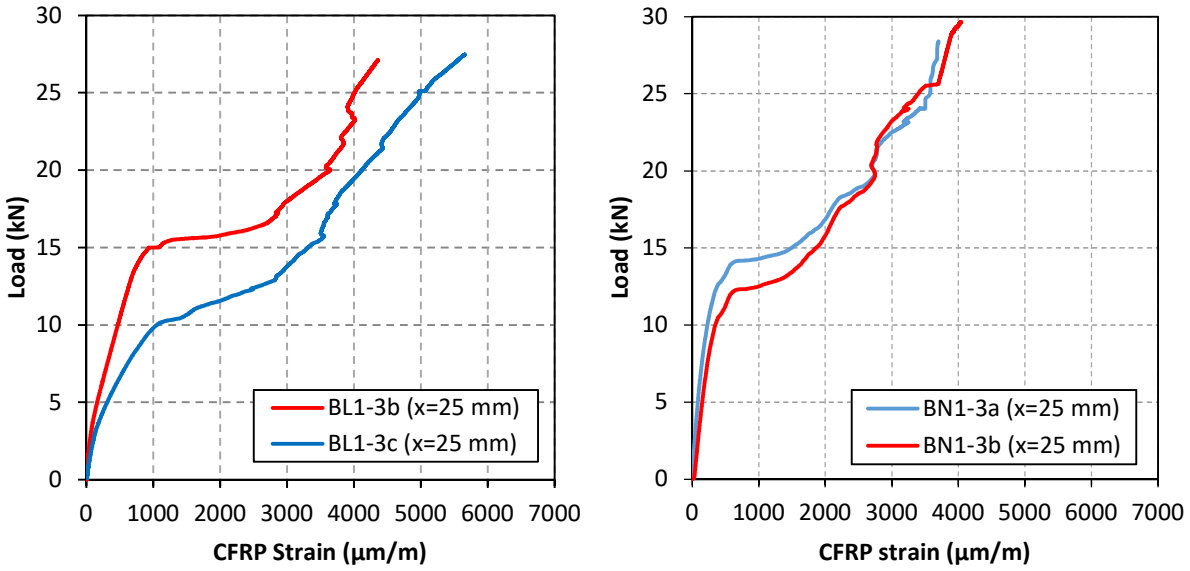

(a) LWAC (b) NWAC

Figure (3.52): Load versus CFRP strain of the specimen BL1-3.

3.7.6. Effect of Concrete Type on Interfacial Bond Behaviour

The effect of concrete type on bond strength and slip at failure is discussed in this section. In general, the LWAC bond test specimens showed significantly lower bond strength and slightly lower slip at failure than those of NWAC of similar strength grade and identical CFRP strengthening system. The average bond strength of LWAC samples is lowered between 76% - 97% of those NWAC of similar strength grade as shown in Table (3.13).

Considering the average bond strength of each series, a new empirical formula is derived in this study based on the linear regression analysis carried out on the results of the tested NWAC and LWAC samples as shown in Figure (3.53). It can be noted that the LWAC bond strength is approximately 0.85 of the NWAC samples having the same strengthening techniques and based on this analysis, a new reduction factor (R) is assumed as 0.85 in this analysis as explained in Equation (3.4).

$$P_{LWAC} = R.P_{NWAC} \quad (3.4)$$

Table (3.13): The average bond strength ratio of LWAC to NWAC samples.

Series ID	LWAC Average bond strength	NWAC average bond strength	$\left(\frac{P_{LWAC}}{P_{NWAC}}\right) X100$
BL/N1-1	19.47	20.11	97%
BL/N1-2	26.03	29.50	88%
BL/N1-3	24.81	29.02	85%
BL/N3-1	21.78	28.10	78%
BL/N3-2	18.62	22.76	81%
BL/N4-1	13.46	15.10	89%
BL/N4-2	21.41	28.15	76%

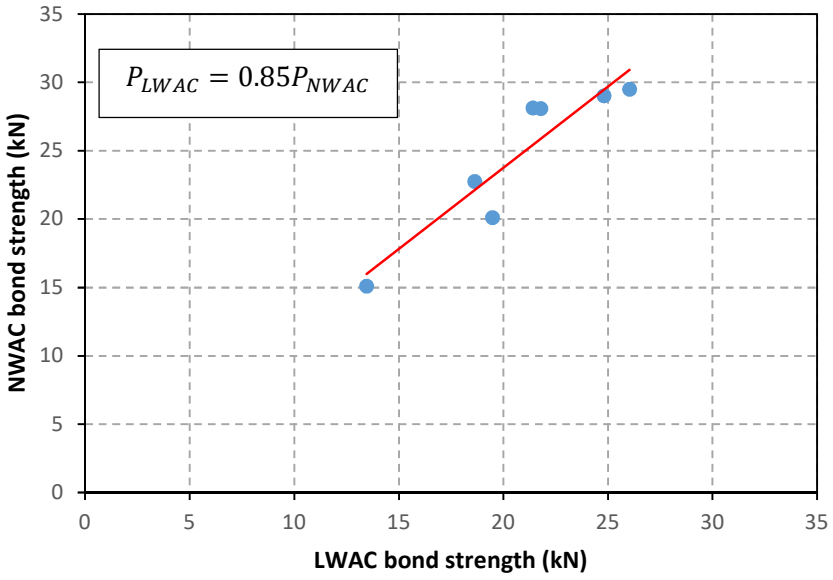

Figure (3.53): Relationship between the bond strength of LWAC and NWAC samples.

Debonding of the specimens in bond shear tests primarily develops inside the concrete. Furthermore, interlocking along the debonding area may influence the bond response in samples

cast with LWAC. The bond strength is dependent on the residual friction along the bond agent of the CFRP reinforcement. Thus, the composition of the lightweight and normal weight concrete required to be examined in the study of the interfacial behaviour of the FRP/concrete joints to investigate the effect aggregate interlocks and the residual friction on the maximum bond capacity between FRP reinforcement and concrete substrate. The effect of LWAC should be considered in the current design guidelines by introducing a safety reduction factor due to the lower surface tensile strength. The lower strength accelerates substrate failure compared with NWAC samples which show higher debonding loads.

The basic difference in shear behaviour between the normal and lightweight aggregate concrete is due to the lower tensile strength of concrete and aggregate interlock which may affect the efficiency of retrofitting RC structures with FRP reinforcement. The shear capacity of the RC members is proportional to the aggregate interlocking effect (Martian and Pantazopoulou, 2001). It was concluded that the aggregate interlock influences significantly the shear carrying capacity according to the *Modified Compression Field Theory* (Vecchio and Collins, 1986). At the ultimate limit state, the aggregates in the concrete prevent sliding along the plane in which the crack forms. This effect is hard to control in experimental tests because it depends on the type, size and the distribution of these aggregates in the debonding plane. In lightweight concrete retrofitted with epoxy bonded CFRP for shear deficiencies, the failure path is in the substrate of concrete due to lower tensile stresses of the aggregate particles as well as by fracture of the matrix.

The Lytag aggregates are not strong enough to resist the formation of a crack, as it will extend which leads to concrete failure and FRP debonding along the bonding agent. Figure (3.54) is used as an example to show the difference in behaviour between LWAC and NWAC samples. It can be noticed that the cracks developed in LWAC samples at lower load compared with NWAC samples. The second stiffness zone of the LWAC sample was reduced at the beginning of cracking stage which causes sample failure at lower debonding load compared with NWAC sample. It can be concluded that the lower stiffness's of lightweight aggregate particles and higher crack intensity in LWAC compared with companion samples cast with NWRC are likely to increase the shear and normal stresses in FRP reinforcements and at the concrete-FRP interface. The increasing in shear and normal stresses may be lead to premature FRP debonding,

thus the efficiency of using FRP for shear retrofitting is not fully exploited in lightweight concrete.

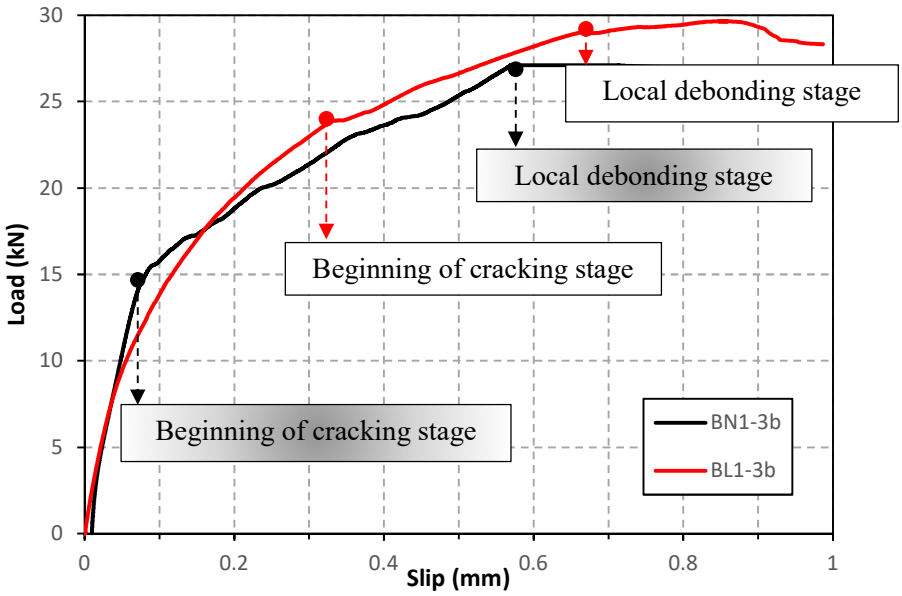

Figure (3.54): Load-slip curve of BN/L1-3 samples.

3.7.7. Effect of CFRP Sheet Bonded Length

When the FRP/concrete joint is under pure shear force, at higher loading level, a crack develops in the FRP/concrete joint at the loaded end of the FRP reinforcement and gradually extends until reaching the far end of the FRP reinforcement. The FRP/concrete joint cannot sustain more force and the interfacial bond between FRP reinforcement and concrete surface suddenly drops once the interface crack reaches a specific length. The anchorage length or the effective bond length is one of the most important properties of the FRP/concrete joint and does not increase with longer length of the FRP reinforcement (Hadigheh, 2014).

For the three cases of the BL/N1-1, BL/N1-2, and BL/N1-3 series have the same width and thickness (w_f = 100 mm and t_f =0.1178 mm) and have different bonded length of CFRP sheet (50, 75, and 100 mm), the bonded length measured from the centre of specimens to the far end of CFRP sheet on one side of the concrete sample as shown in Figure (3.55). Test results indicate that the increase of CFRP sheet length beyond 75 mm does not lead to higher load capacity in both LWAC and NWAC samples. However, a larger bond length leads to a longer deformation process as debonding propagates along the interface. Based on the mechanism mentioned above,

the effective bond length was assumed to be approximately 75 mm for LWAC and NWAC samples which showed similar behaviour. Hence it can be concluded that the effective bond length is not influenced by concrete type. The test results of these samples are reported in Table (3.14). The maximum applied load is plotted versus the CFRP bonded length in Figure (3.56). Based on this plot, the load remains constant after L_f = 75 mm in both LWAC and NWAC samples.

Table (3.14): Results of BL/N1-1, BL/N1-2, and BL/N1-3 series.

Specimen ID	Maximum Load (P_{max}) (kN)	Maximum Slip Corresponding to Maximum Load (s_{max}) (mm)	Failure modes
BL1-1a	19.34	0.30	CF
BL1-1b	18.71	0.27	CF
BL1-1c	19.99	0.32	CF
BL1-1d	19.86	0.37	CF
BL1-2a	27.31	0.36	DC
BL1-2b	23.80	0.43	DC
BL1-2c	27.80	0.50	DC
BL1-2d	25.22	0.46	DC
BL1-3a	26.15	0.54	DC
BL1-3b	27.11	0.56	DC
BL1-3c	18.50	0.28	DC
BL1-3d	27.48	0.60	DC
BN1-1a	18.13	0.25	CF+DC
BN1-1b	22.10	0.35	CF+DC
BN1-2a	29.60	0.69	CF+DC
BN1-2b	29.40	0.61	CF+DC
BN1-3a	28.40	0.79	CF+DC
BN1-3b	29.64	0.85	CF+DC

Note: (a) CF, Concrete prism failure (b) DC, debonding in concrete (c) t_f, is the one side thickness of CFRP sheet.

For further comparison, Figure (3.57) shows the changes in the normalised load ratio (P_a / $P_{a,max}$). The $P_{a,max}$ value used in this study for comparison is the average of the maximum load for BL1-2 and BN1-2 specimen's series from both LWAC and NWAC, while the P_a value is the average of the maximum achievable load for specimens with 50 mm, 75 mm and 100 mm bonded length. When the bonded length changes from 50 mm to 75 mm in LWAC samples, the normalised load ratio increased by about 34%; beyond 75 mm bonded length, the maximum load did not increase significantly and in fact decreased by about 5%. For the NWAC samples, changing the bonded length from 50 mm to 75 mm leads to an increase in the normalised load ratio by 47 %. Beyond 75 mm bonded length, the maximum debonding load did not increase significantly and in fact decreased by about 1.6%

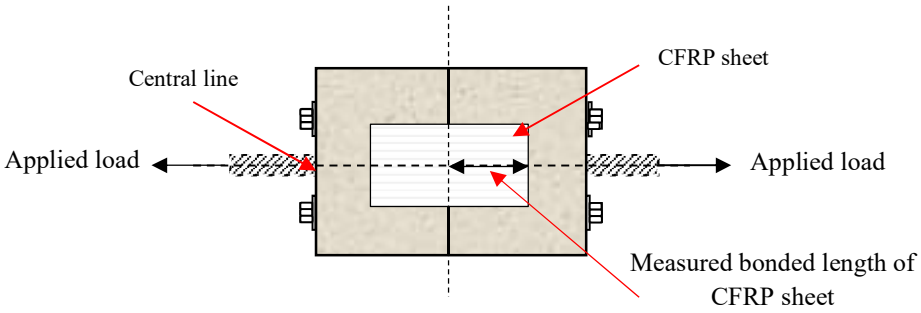

Figure (3.55): Measured bonded Length of FRP composite.

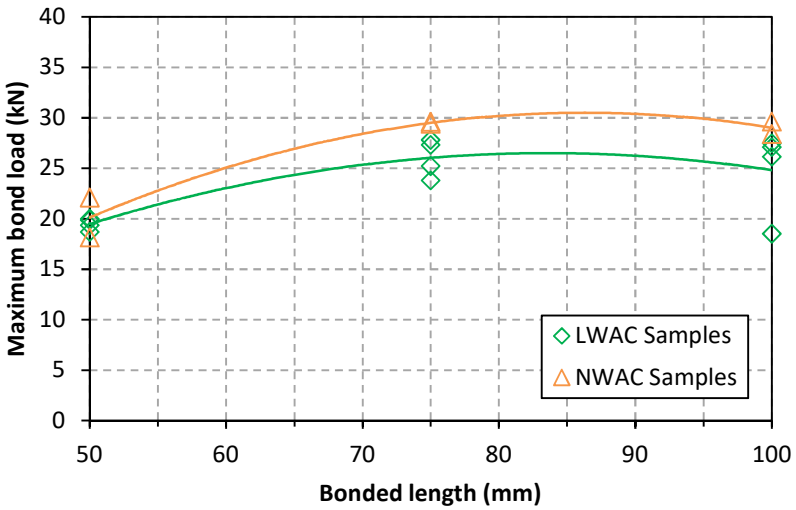

Figure (3.56): Interpolation between the maximum load and the bonded Length of CFRP.

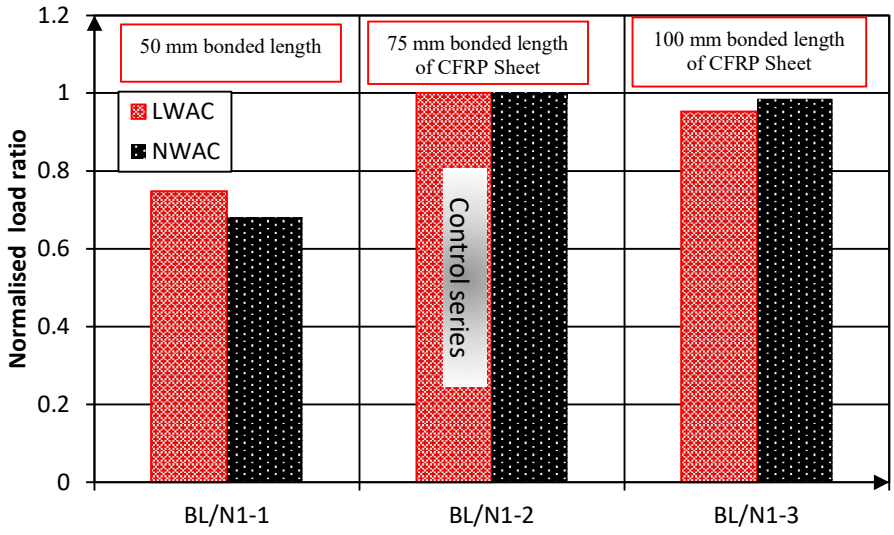

Figure (3.57): Effect of CFRP bond length on the normalised Load ratio.

Figures (3.58a and b) demonstrate the effect of increasing the bond length of CFRP sheet on the maximum load. The load-slip relationship for one sample has been selected from each testing series with various CFRP bond lengths as these are all similar in shape. The load increases linearly with an increase in slip and after a certain stage shows nonlinear up to failure.

It can be seen that the load-slip curve appears to be a plateau for LWAC and NWAC samples with 75 mm and 100 mm bonded length where the load continues to increase with small change of load values till the global debonding of the CFRP sheet from the concrete substrate which confirms that the effect length of the CFRP sheet was at least 75 mm. The same behaviour was observed by McSweeney and Lopez, (2005).

An alternative method to determine the effective bond length based on "Active transfer strain zone region" is proposed. The effective bond length is defined as the distance between the points of the maximum strain at the centre of the sample and the point of zero strain near the far end of CFRP sheet (Hadigheh, 2014). The maximum active strain zone ranges between 70-75 mm. Therefore, the bonded length of the CFRP sheets in the LWAC and NWAC series of tests is considered about 75mm. It can be also noticed that there is no significant difference in behaviour for specimens having different bonded lengths. However, the increase in CFRP bonded length

leads to concrete debonding for LWAC samples or concrete failure followed by concrete debonding in the case of NWAC samples as observed in these tests.

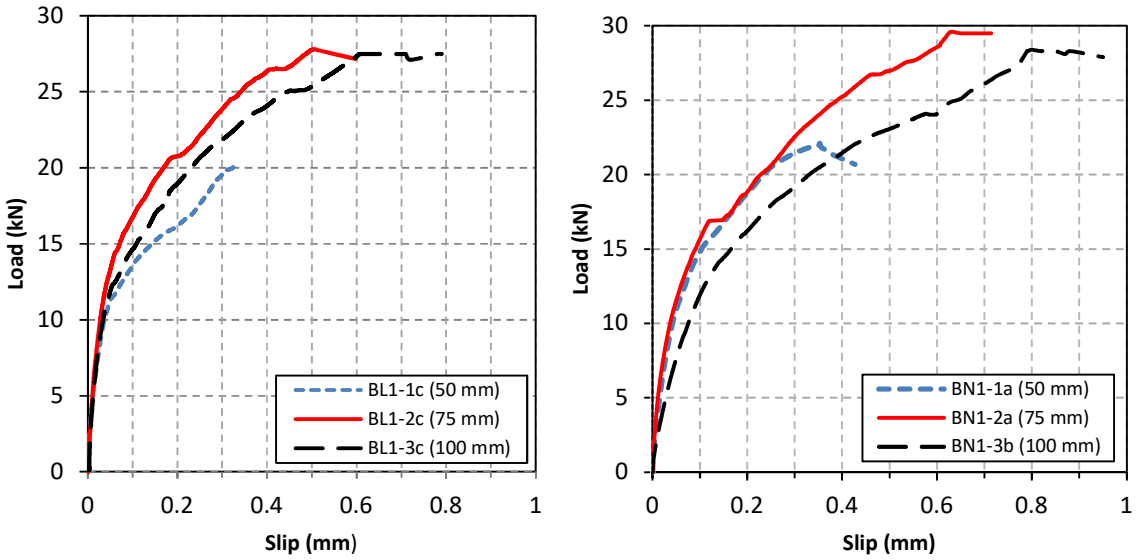

(a) LWAC specimens. (b) NWAC specimens.

Figure (3.58): Influence of CFRP bond length on the maximum load of the tested samples.

3.7.8. Effect of Orientation of the CFRP Sheet on Bond Behaviour

The fibre orientation of CFRP sheet is one of the parameters that most influences the interfacial behaviour between concrete and FRP composite. The test results of BL/N2-1 and BL/N2-2 are shown in Table (3.15). All the specimens were subjected to a pure tensile load, thus if there is an angle between the load and the fibre direction, this tends toward a lesser contribution of the CFRP sheet with the strength. It is seen that the specimens of BL/N2-1 series did not fail at any noticeable load. Failure of BL/N2-1 specimens was occurred suddenly at a small load, as the two concrete prisms separated at the centre of the specimens without any resistance. The same behaviour was observed by Al-Juboori, (2011).

Figure (3.59) shows the variation of the normalised maximum load ratio versus the fibre orientation of CFRP composite for both LWAC and NWAC samples. It can be concluded that the increase of the fibres angle with respect to load direction from 0^0 to 45^0 decreases the normalised load ratio by 51% compared with companion samples BL1-1 in the case of specimens cast with LWAC and 66% in the case of NWAC specimens. With further increase in the angle to 90^0, the load ratio decreases by 97 % for LWAC samples and 89% for NWAC

samples. This can be attributed to the nature of CFRP composite properties which are classified as orthotropic, the maximum strength being parallel to the fibres direction.

Table (3.15): Results of BL/N2-1 and BL/N2-2 series.

Specimen ID	Maximum Load (P_{max}) (kN)	Maximum Slip Corresponding to Maximum Load (s_{max}) (mm)	Failure modes
BL2-1a	0.81	2.31	FR
BL2-1b	0.57	3.62	FR
BL2-1c	0.47	0.37	FR
BL2-1d	0.99	1.49	FR
BL2-2a	8.24	2.33	DC
BL2-2b	11.14	2.42	DC
BL2-2c	9.12	2.50	DC
BN2-1a	5.13	2.22	FR
BN2-1b	0.93	2.51	FR
BN2-2a	10.64	1.61	AD
BN2-2b	3.01	0.95	AD

Note: (a) DC, de-bonding in concrete (b) FR, CFRP rupture (c) AD, adhesive debonding (d) t_f, is the one side thickness of CFRP sheet.

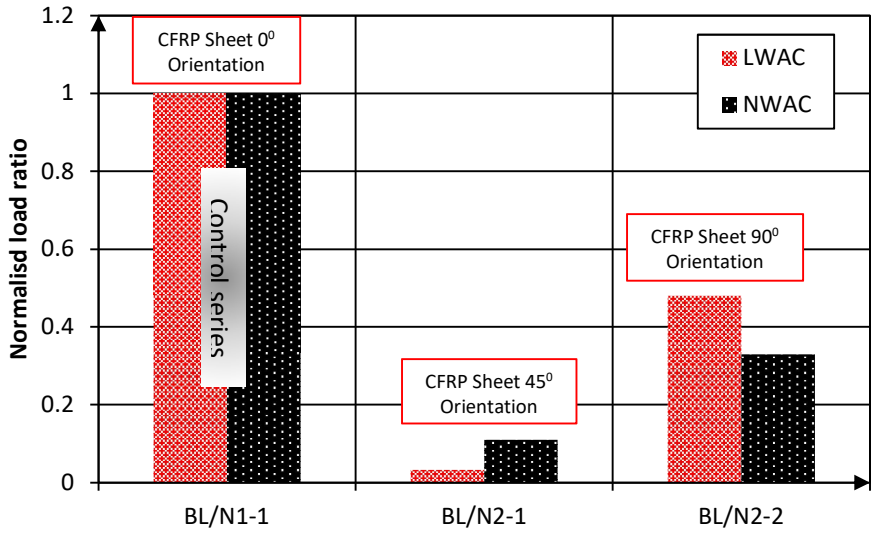

Figure (3.59): Effect of the fibre orientation on the normalised load ratio.

Figures (3.60a and b) show the initial stiffness for the load-slip plot decreases as the fibre angle increases with respect to the load direction. The noticeable thing about this figure is that the LWAC samples strengthened with 45^0 fibres orientation of the CFRP sheet forms more cracks near the specimen's centre which propagate in a stable manner through the CFRP-concrete interface until failure occurs. This crack propagation is accompanied by a drop-in rigidity easily highlighted by the nonlinearity of the load-displacement plots for these samples.

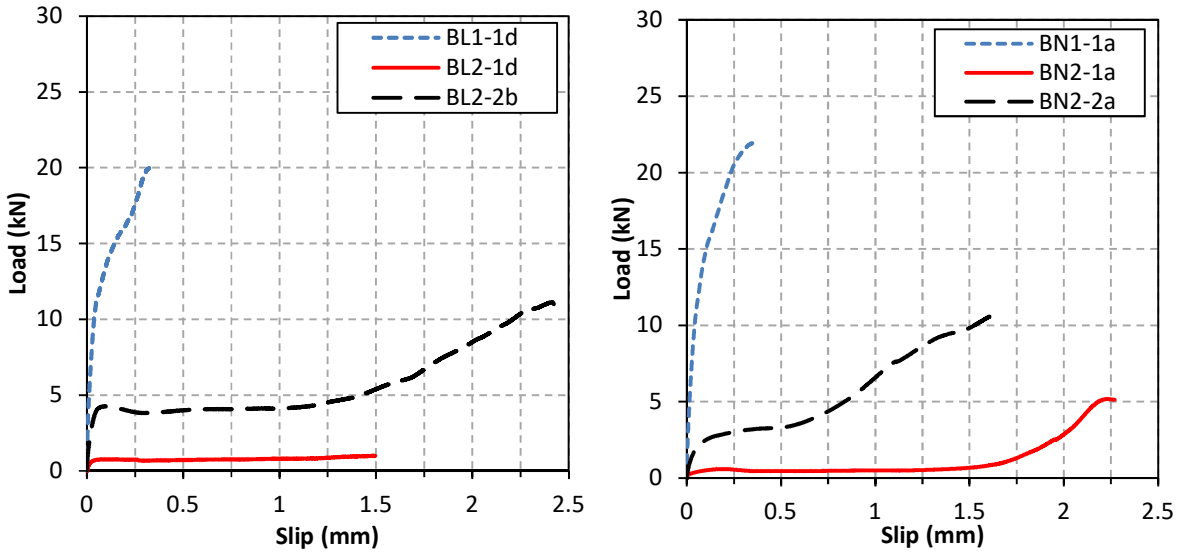

(a) LWAC specimens. (b) NWAC specimens.

Figure (3.60): Influence of CFRP fibre orientation of tested samples.

3.7.9. Effect of CFRP Sheet Thickness on Bond Behaviour

The impact of the CFRP sheet thickness on the interface behaviour of the samples cast with LWAC and NWAC is discussed in this section. It can be noticed that the failure of all the specimens is categorised as a concrete failure (CF) which is described in section (3.7.1). The experimental results of the three cases of BL/N1-1, BL/N3-1, and BL/N3-2 series having the same dimensions and different bonded thickness and orientation of CFRP sheet are used to examine the influence of using two parallel and perpendicular layers of CFRP composite. The test results reported in Table (3.16).

For LWAC samples, the increase in the normalised load ratio from one to two parallel layers $0^0/0^0$ was approximately 12%, while the change of strengthening technique from one to two perpendicular layers $0^0/90^0$ does not provide any contribution as shown in Figure (3.61). This means that increasing the thickness provides limited benefit for strengthening. In contrast, the difference between the normalised load ratios of BN3-1 (same direction) and BN1-1 is approximately 39%. Besides this, the difference in average load ratio of BN3-2 (two perpendicular layers) of CFRP sheet compared with BN1-1 is approximately 12%. It can be concluded that the load capacity for double-parallel-layered specimens is higher than the load capacity for double-perpendicular-layered specimens. This means that if the load direction is parallel to two layers, this scenario is better than having double-perpendicular layers. It can be noted that the maximum debonding load does not increase significantly for specimens with thicker CFRP sheets. This is due to stress concentrations at the centre of samples as a result of higher axial rigidity provided by thicker CFRP sheets which accelerate joints failure.

Table (3.16): Results of BL/N3-1 and BL/N3-2 series.

Specimen ID	Maximum Load (P_{max}) (kN)	Maximum Slip Corresponding to Maximum Load (s_{max}) (mm)	Failure modes
BL3-1a	24.16	0.14	CF
BL3-1b	22.99	0.16	CF
BL3-1c	18.19	0.16	CF

BL3-2a	18.69	0.20	CF
BL3-2b	19.54	0.23	CF
BL3-2c	17.72	0.22	CF
BN3-1a	28.01	0.18	CF
BN3-1b	28.19	0.18	CF
BN3-2a	22.44	0.28	CF
BN3-2b	23.09	0.28	CF

Note: (a) CF, Concrete prism (b) tf, is the one side thickness of CFRP sheet.

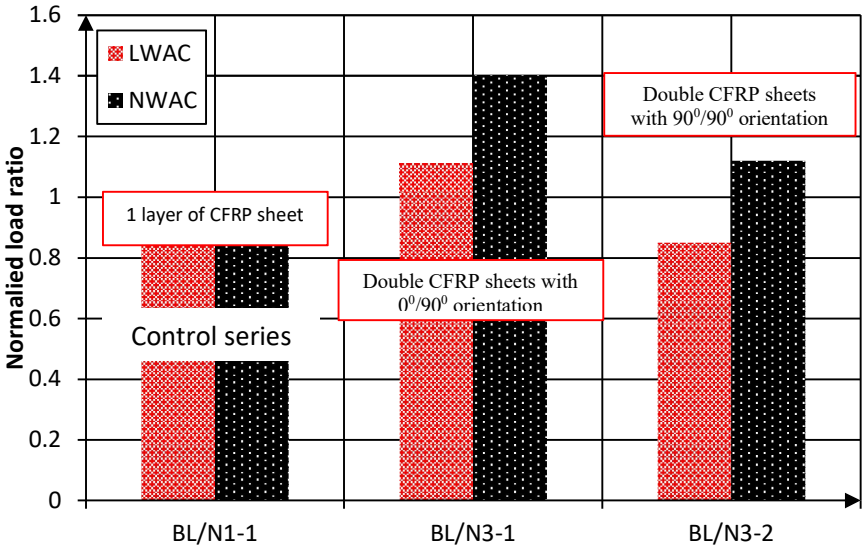

Figure (3.61): Effect of CFRP thickness on the normalised load ratio.

For further observations, Figures (3.62a and b) show the comparison of the load-slip response of the three cases. As shown in these figures, the initial stiffness of the CFRP-concrete joints with the $0^0/0^0$ sheet is higher than that of the $0^0/90^0$ sheet and for the sample with one layer 0^0 sheet. This high stiffness appears to promote a higher failure load and lower slip compared with other cases. Despite the increase of the maximum debonding load with an increase in CFRP sheet layers, the global slip decreases with use of more CFRP layers.

A similar response was observed for both LWAC and NWAC samples. Therefore, it can be concluded that when the strength criteria govern the design of RC elements, an increase in the CFRP axial rigidity may lead to a higher bond strength. However, in the case of ductility, the higher stiffness leads to extremely brittle failure of the CFRP-concrete joints, particularly for LWAC which shows more brittle behaviour compared with NWAC.

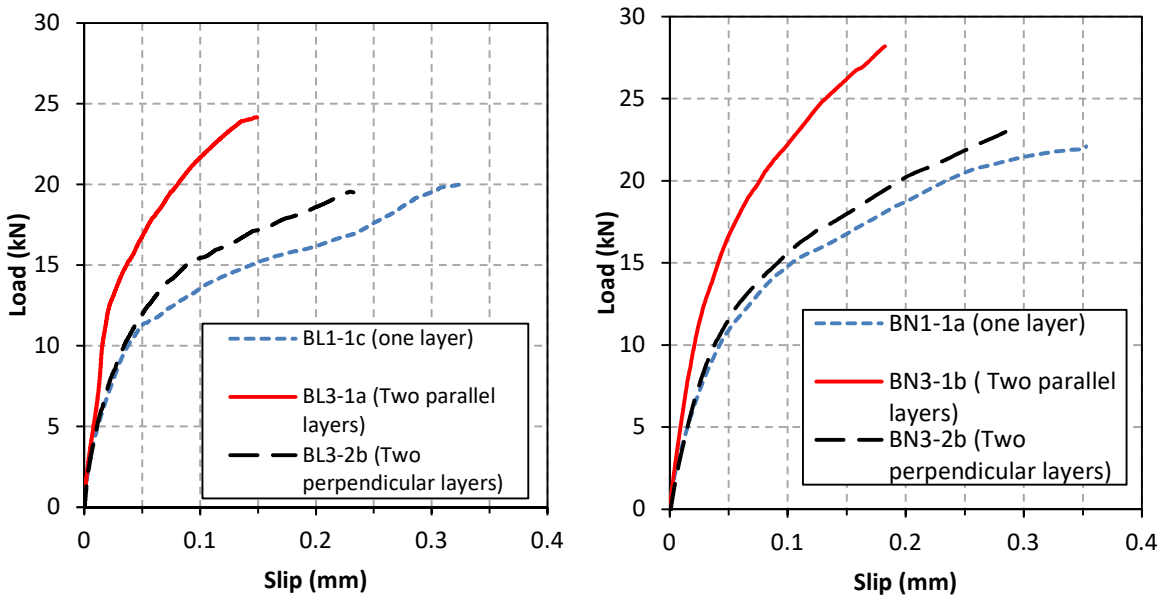

(a) LWAC specimens. (b) NWAC specimens.

Figure (3.62): Influence of CFRP bond thickness of LWAC and NWAC samples**.**

3.7.10. Effect of CFRP-to-Concrete Width Ratio on Bond Behaviour

The effect of CFRP to concrete width ratio ($w_r = b_f/b_c$) on the interface behaviour is examined in the samples BL/N4-1, BL/N1-2, and BL/N4-2. The results of the double-lap shear tests are reported in Table (3.17). All these samples have the same thickness (t=0.1178 mm), bonded length of CFRP composite (L_{frp}=75 mm) and various width of CFRP sheet (50, 100, and 150 mm). The CFRP-to-concrete width ratios are 0.25, 0.5 and 0.75 respectively.

It may be noted that with increase in width, the maximum load increases when the width ratio is changed from 0.25 (for 50 mm CFRP width to 200 mm concrete width) to 0.5 (for 100 mm CFRP width to 200 concrete widths) for both LWAC and NWAC samples. This trend may be attributed to the distribution of shear stresses over a larger bonded area. However, increasing the width ratio to 0.75 (for 150 mm CFRP width to 200 concrete widths) leads to premature sample failure at load lower than the failure of samples with 0.5 width ratio in the case of LWAC samples or approximately the same load for samples with 0.5 width ratio in case of NWAC samples.

Hence, when the width of the concrete samples is kept the same, samples, the bond strength with small width ratio increases as the width of the CFRP reinforcement increases (Changing the width ratio from 0.25 to 0.5). However, for samples with 0.75 width ratio, the bond strength decreases with CFRP reinforcement width. In this case (samples with 0.75 width ratio), the width of concrete samples was not sufficient to achieve the required level of stress transference from the surface of the concrete to the CFRP reinforcement. Thus, the confinement effect provided by CFRP reinforcement decreases which accelerate the failure of the interfacial bonded joint at lower loads. Therefore, the bond strength may not enhance using wider CFRP reinforcement. The same behaviour was observed in the previous works (De Lorenzis et al. 2001; Xia and Teng 2005).

Table (3.17): Results of BL/N4-1 and BL/N4-2 series.

Specimen ID	Maximum Load (P_{max}) (kN)	Maximum Slip Corresponding to Maximum Load (s_{max}) (mm)	Failure modes
BL4-1a	13.20	0.54	CF+DC
BL4-1b	13.10	0.58	CF+DC
BL4-1c	13.60	0.54	CF+DC
BL4-1d	13.95	0.63	CF+DC
BL4-2a	21.04	0.043	DC
BL4-2b	21.69	0.058	DC
BL4-2c	21.51	0.037	DC
BN4-1a	14.80	0.53	CF+AD
BN4-1b	15.55	0.57	CF+AD
BN4-2a	28.10	0.14	DC
BN4-2b	28.21	0.15	DC

Note: (a) CF, Concrete prism failure (b) DC, debonding in concrete (c) AD, Adhesive (c) t_f, is the one side thickness of CFRP sheet.

It can be concluded that increasing the CFRP sheet widths leads to concrete debonding for both LWAC and NWAC samples. The impact of CFRP-to-concrete width ratio on the maximum load and slip is shown in Figure (3.63a). The slip corresponding to width ratio at the maximum load decreases by a higher value of width to the concrete ratio as shown in Figure (3.63b). This indicates that ductility of the CFRP–concrete interface decreases for wider CFRP sheet.

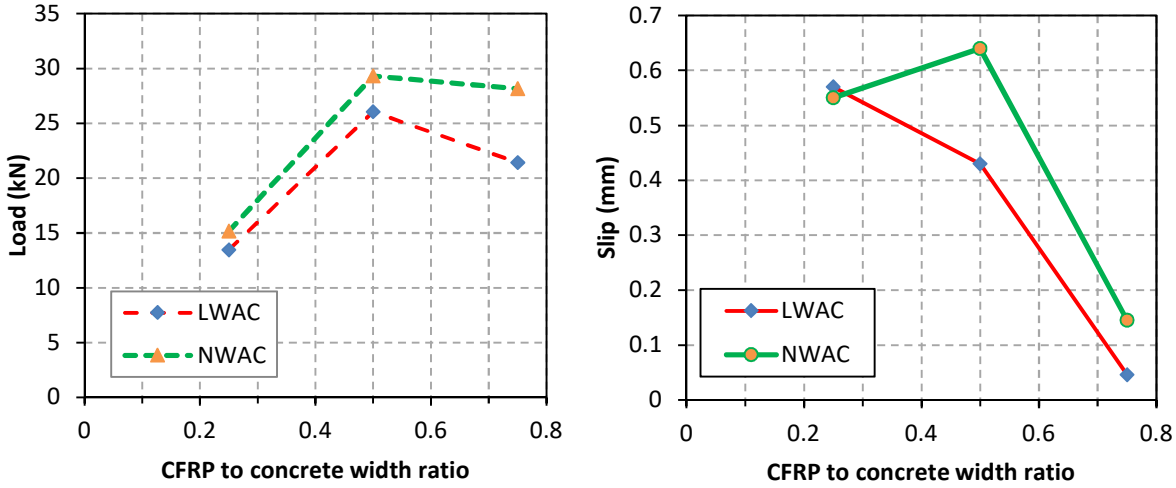

(a) (b)

Figure (3.63): Correlation between FRP-to-concrete width ratio and: (a) the maximum load (b) slip.

Referring to Figure (3.64), the specimens reveals higher initial stiffness for the load-slip plot, when the CFRP width increases versus the concrete prism width. Small interface cracks have enough space to extend in samples with wider bonded area of CFRP composite and when the large crack develops, the probability to intersect small cracks on its path is higher. These small cracks help to link these large cracks through the loading process. Thus, the bond strength between larger CFRP sheet width and concrete surface is higher in contrast with the specimens with lower CFRP to concrete width ratio.

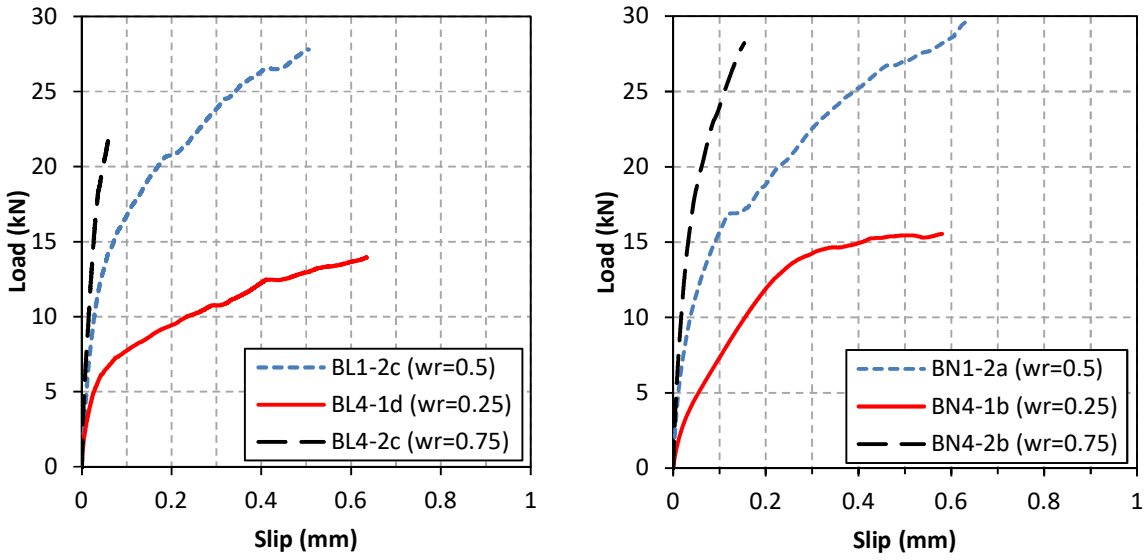

(a) LWAC (b) NWAC

Figure (3.64): Influence of CFRP width on the tested samples.

3.8. Summary

The influence of various variables on the response of the FRP-to-concrete joint was examined and discussed in this chapter. Variables investigated are the CFRP bonded length, fibre orientation, the thickness of CFRP sheet and CFRP-to-concrete width ratio. The influence of these parameters on the response of the samples cast with LWAC and NWAC are investigated in details through extensive programme of work.

According to the experimental results, it was shown that the crack propagation in LWAC specimens occurred within the concrete, which leads to premature failure of concrete or CFRP debonded with a thick concrete layer near the far end of CFRP sheet rather than adhesive debonding or CFRP debonded by thin concrete layer substrate just below the CFRP sheet in case of NWAC samples. The crack intensity was the highest in LWAC specimens and the lowest in NWAC specimens, it was also noticed that there was crushing of concrete underneath of CFRP composite for samples cast with LWAC.

The LWAC specimens showed significantly lower bond strength and slightly lower slip at failure than those of NWAC of a similar strength grade. This is attributed to lower tensile strength of concrete substrate and aggregate interlocks along the bonded surface for LWAC which may influence the performance of CFRP used to retrofit reinforced concrete elements.

An Experimental assessment has been done to study the effect of CFRP bonded length on the behaviour of the CFRP/concrete joints for specimens cast with LWAC and NWAC. The results showed that the effective bond length of CFRP sheet is not effected by concrete type.

The effect of fibre orientation of CFRP sheets was also considered in these tests. All the specimens were subjected to pure tensile force, therefore if there is an angle between the load and fibre direction this tends toward a lesser contribution of the CFRP sheet to the strength. A slight difference in failure modes was observed between LWAC and NWAC samples with 45^0 fibre orientation.

One major parameter in the interface behaviour of the FRP to concrete bonded joints is the CFRP sheet thickness. In this research, the effects of the CFRP sheet thickness is studied for samples cast with LWAC and NWAC specimens. Results indicate that increasing the number of layers of CFRP gives limited benefit. This benefit is not in line with the cost and the effort increases associated with its application. The CFRP sheet thickness has the same influence on the interfacial behaviour of the LWAC and NWAC samples. However, LWAC recorded lower debonding loads compared with NWAC samples.

The effect of the CFRP-to-width ratio is investigated in this study. The maximum debonding load increases for the samples with wider CFRP reinforcement. However, for large values of width ratio, the load carrying capacity decreases with wider CFRP. No significant difference was noticed in behaviour between LWAC and NWAC samples and the same failure of modes was observed for LWAC and NWAC samples with a different width of the CFRP sheet.

The behaviour of the FRP/lightweight concrete joint was examined in this study including the influence of various variables on the bond response, failure patterns, load-slip curves, load-strain, strain distributions, local shear stress distributions. The outcomes of these tests showed that the CFRP reinforcement can effectively be used in the retrofitting of lightweight concrete members. However, the lightweight samples showed lower bond strength compared to normal weight concrete specimens. Thus, more research is needed to understand of the behaviour of the FRP/concrete joints cast with LWAC.

CHAPTER FOUR

EXPERIMENTAL PROGRAM

BEAM SHEAR TEST

4.1. Introduction

The objective of the experimental program was to investigate the enhancement in shear strength of reinforced (LWC) beams compared with companion reinforced (NWC) beams due to different strengthening system of the CFRP reinforcement. Six reinforced LWAC and NWAC beams without shear reinforcement were loaded at the University of Salford's Structural Laboratory. The details of the experimental tests program carried out in this study are presented in this chapter including samples design and manufacturing, fabrication, test setups, instrumentation, and the results analysis and discussion of the beams shear test outcomes.

4.2. Shear Tests for LWRC and NWRC Beams

Physical tests on rectangular LWRC and companion NWRC beams strengthened with different configurations of CFRP were conducted. The main objectives of this study were:

1. To provide a better understanding of the shear behaviour and failure modes of LWRC beams strengthened with CFRP strips under monotonic loads.
2. To evaluate the performance and shear strengthening gained from using the CFRP to retrofit LWRC beams compared with companion NWRC beams.
3. To study the variation of CFRP strain through the length of the beam, for this purpose strain gauges were used in various regions along the length and through the depth of the RC beams to provide strain readings under monotonic loads conditions.

The effect of various parameters on the effectiveness of the shear strengthening provided by CFRP used to retrofit LWRC beams is studied, these parameters are:

a. Concrete type (lightweight and normal weight concrete).
b. Type of strengthening techniques (U-wrapped and Closed-wrapped).

4.3. Sample Referencing Name

The test samples vary due to a different type of concrete and CFRP strengthening techniques used in this study. Referencing names were used depend on the type of concrete and the CFRP strengthening configurations. These referencing names were employed during this study and is clarified in Figure (4.1).

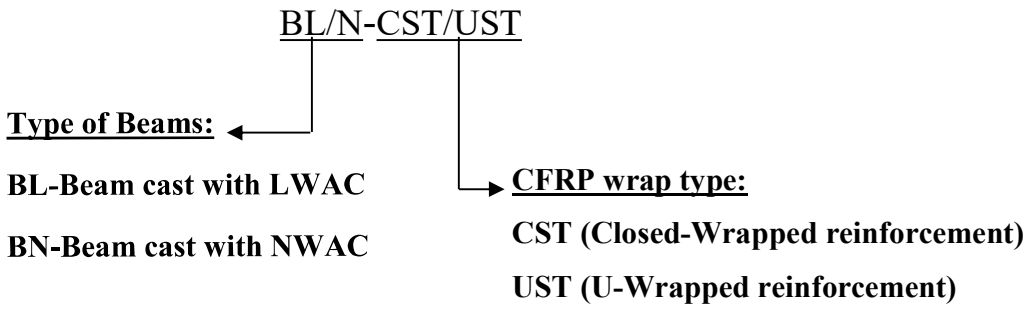

Figure (4.1): Samples referencing name.

4.4. Test Programme

The entire experimental program comprised six beam specimens cast with lightweight and normal weight concrete. Both the NWRC and LWRC beams were geometrically similar and cast using the same grade of concrete (i.e. the same compressive strength). The details of each series are described as follows:

- Series **(BL-UST/CST)** comprised three beams cast with LWAC without shear reinforcement except two shear links adjacent to the supports; one of the beams was without external CFRP reinforcement and the remaining two beams were each strengthened with U-shaped (UST) and close (CST) epoxy bonded external CFRP strips. The purpose of this series of tests was to provide insight regarding the shear behaviour of LWRC beams without shear reinforcement strengthened with CFRP under monotonic loading.
- Series **(BN-UST/CST)** comprised three companion beams cast with NWAC without shear reinforcement except two shear links adjacent to supports either side; one beam was used as a control beam without CFRP reinforcement and two beams were strengthened with CFRP similar to the lightweight concrete beams. The purpose of this series of tests was to provide insight regarding the shear behaviour of companion normal weight concrete under monotonic loading and the test results were used to compare with LWAC specimens strengthened with CFRP composites.

4.5. Test Set-up

All the reinforced LWRC and NWRC beams were designed to have the same dimensions of 200 mm wide by 300 mm deep and 2000 mm long. The simply supported beams were loaded under four-point conditions, the supports of the beam were located at a distance of 150 mm from the both ends of the sample. Displacement controlled monotonic loading conditions were employed. The shear span to effective depth ratio was taken as a/d=2.27 to secure shear failure which satisfies the definition of a shear beam (Mosallam & Banerjee, 2007). All the beams were reinforced for flexure with three bottom and two top 16 mm diameter longitudinal deformed steel reinforcements (H16 steel bar). The longitudinal steel ratio for both top and bottom reinforcement ρ_s for all beams was 1.67%. The reinforcement was detailed according to ACI-2008 (ACI, 2008) to achieve the required flexural strength and to secure shear failure of the samples strengthened with CFRP. Figure (4.2) shows the steel reinforcement details. The effective depth of the beam and the clear cover distance was 264 mm and 28 mm respectively.

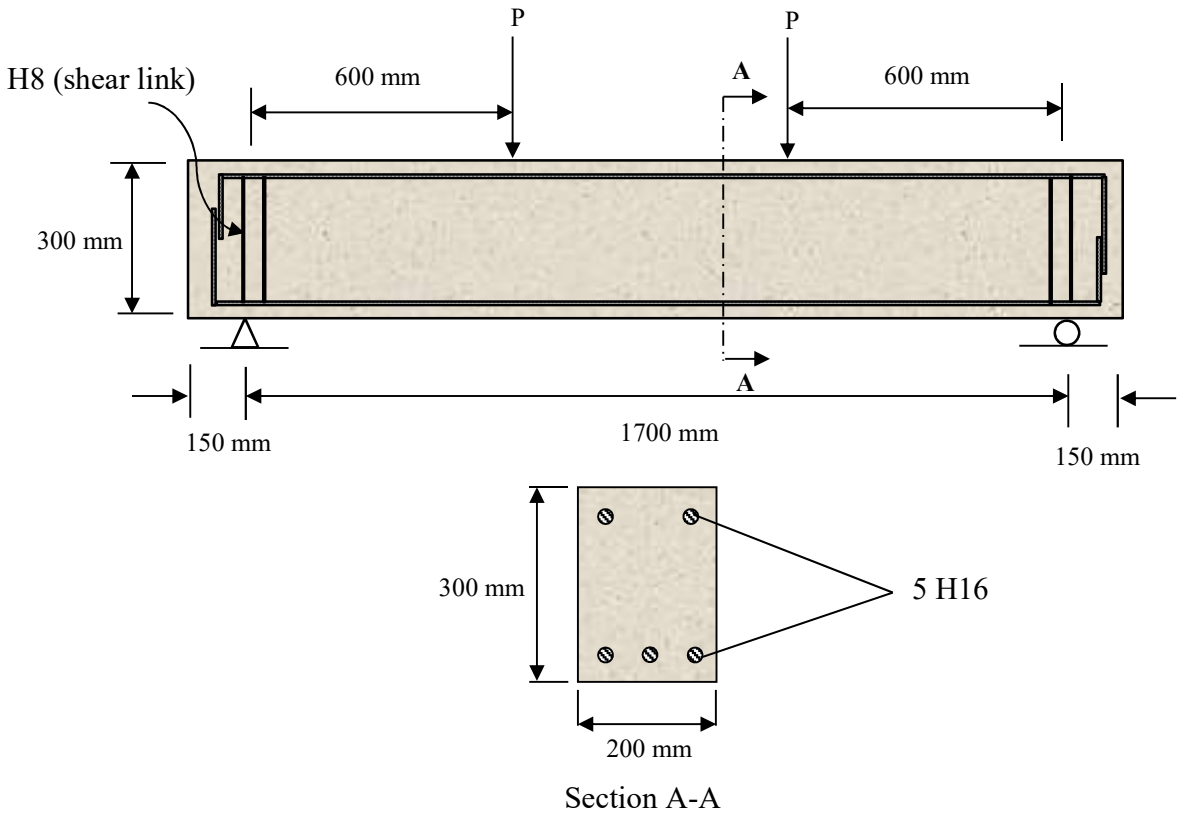

Figure (4.2): Beams Reinforcement details.

Four-point loading is traditionally provided by the arrangement shown in Figure (4.3). Two circular steel columns (100 mm dia.) were erected and bolted to the laboratory strong floor through a large steel abutment using high strength bolts. A large steel I-section (reaction frame) was bolted to the top of the two circular steel columns. This large I-section carried a hydraulic jack with a 500 kN capacity. The steel frame was designed to carry the total applied loads without significant displacement due to its high stiffness. The test data and results were collected and measured at the same time at a rate of 5 Hz using an MTS data acquisition system.

A load cell attached to a hydraulic jack with a 500 kN capacity was used to record the applied load during the test. The monotonic loads were applied to a spreader beam. This spreader beam was seated on 25 mm diameter steel rollers welded to the steel plates (length=200 mm and width=100 mm) bedded on the top surface of the sample to avoid local crushing of concrete at the load point. The sample is placed over the two support points, each support point comprising of a 200 x 400 mm trapezoidal steel block, with a 25 mm diameter steel roller seated on the top surface of a 100 mm steel plate. One of the steel rollers was welded to the steel plate, and a (length=200 mm and width=100 mm) steel plate was provided on top of the roller to avoid local crushing of concrete at the support as shown in Figure (4.3).

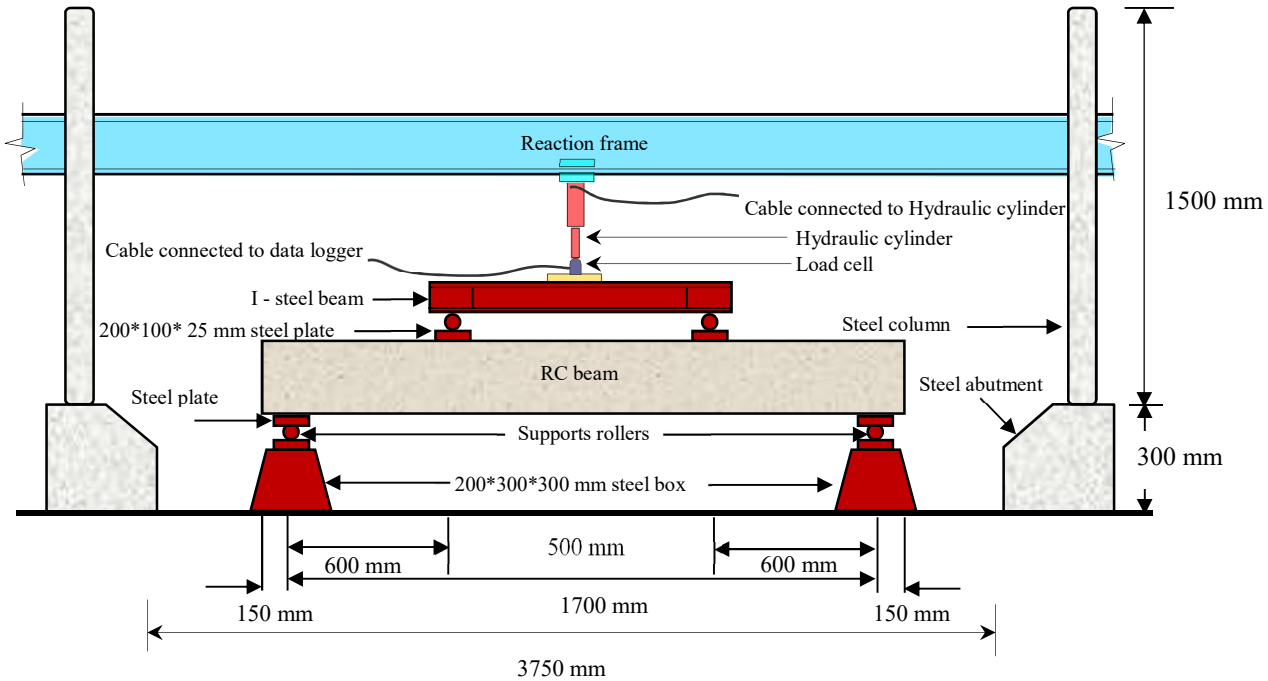

Figure (4.3): Details of test Set-up.

4.6. CFRP Reinforcement

CFRP reinforcement was used in this test with various shear strengthening system. Closed-shaped CFRP reinforcements were attached as strips on all the faces of the beam. These strips were orientated at 90^0 with respect to the longitudinal axis of the beam.

Also, U-shaped systems were attached on tension and the two side faces of the beam as strips. The U-shaped CFRP reinforcements were orientated at 90^0 with respect to the longitudinal axis of the beam as for Closed-shaped systems. The width of CFRP reinforcement was 100 mm and the distance from centre-to-centre of the attached CFRP strips was 150 mm. These CFRP reinforcements were attached along the shear span of the lightweight and normal weight samples, from the support point up to the point of load application on both sides of the beam. The CFRP ratio was taken in this test $\rho_f = 0.0785\%$, the summary of test variables is shown in Table (4.1). The details of specimen strengthening systems are shown in Figure (4.4).

Table (4.1): Summary of test parameters.

Sample	CFRP ratio $\rho_f(\%)$	CFRP strengthening Type	CFRP Orientation
BL	0	-	-
BL- UST	0.0785	U-Shaped	90^0
BL- CST	0.0785	Closed-shaped	90^0
BN	0	-	-
BN- UST	0.0785	U-shaped	90^0
BN- CST	0.0785	Closed-shaped	90^0

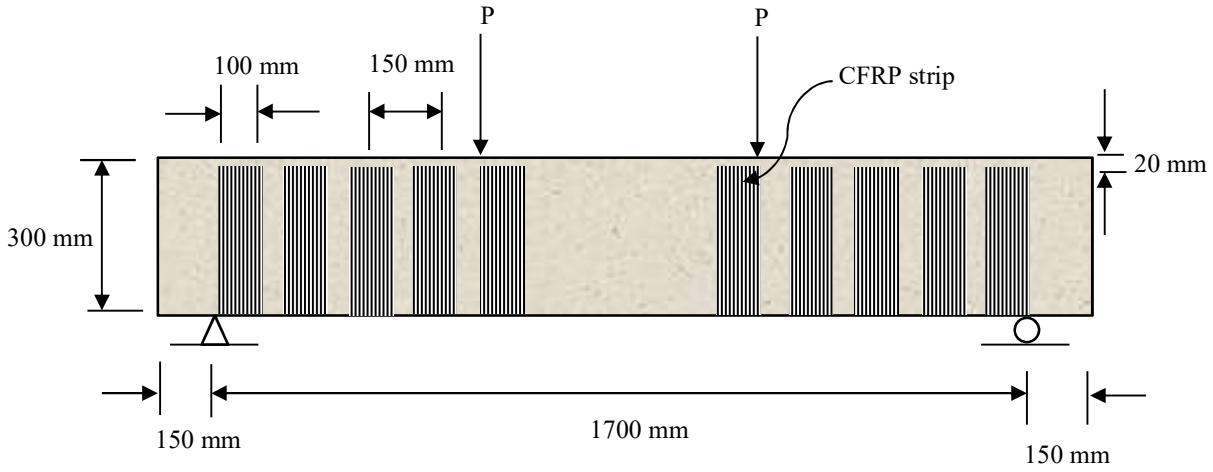

BL/N-UST samples.

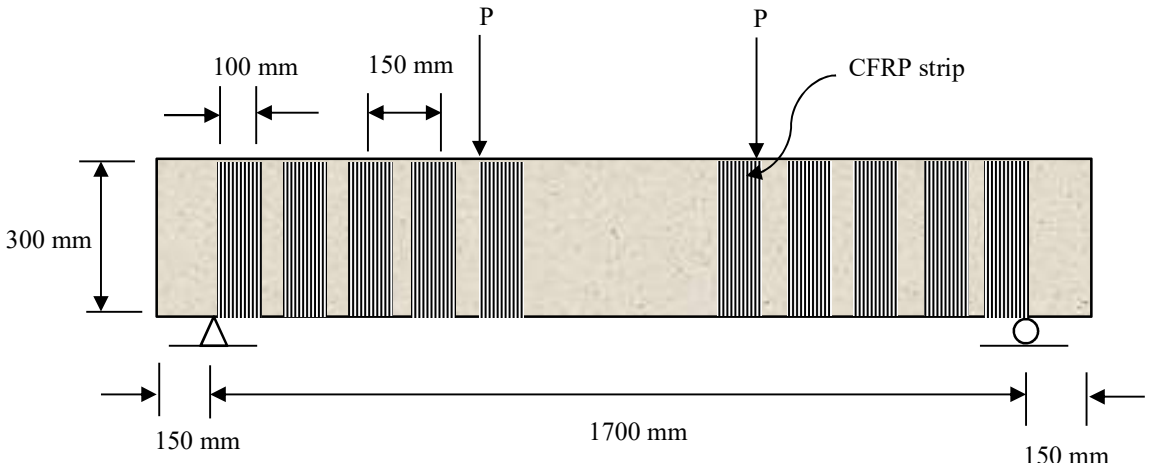

BL/N-CST samples.

Figure (4.4): Strengthening Details.

4.7. Samples Fabrication

This section presents the details of samples fabrication and the instrumentation of the LWAC and NWAC concrete samples.

4.7.1. Formwork Fabrication

The formwork was fabricated to cast three LWRC or three NWRC samples at the same time. All forms were assembled to produce the desired specimen dimensions. A strong plywood sheet base

was manufactured to carry the total weight of the reinforced concrete samples. The base was built by placing a large plywood sheet of 25 mm thick over four long pieces of rectangular section timber, one on each side to support and carry the base plywood sheet. Six pieces of 25 mm thick plywood sheets with a 300 mm depth and 2000 mm length were constructed and attached to the sides of the beams and two 25 mm thick plywood sheets were used to surround the erected moulds from the exterior side to support them. These plywood sheets were screwed to ease the process of disassembling and reassembling as shown in Figure (4.6). Two horizontal clamps were employed to keep the beam moulds strong and stable during the casting.

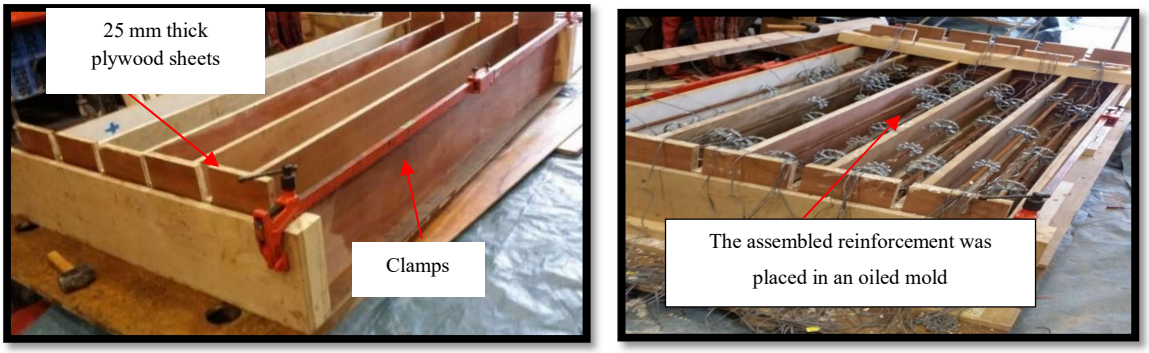

Figure (4.5): Construction of formwork.

4.7.2 Instrumentation

This section details all measurement instrumentation used to record data during the experimental tests. The instruments include longitudinal steel reinforcement strain gauges, CFRP strain gauges, and Linear Variable Differential Transformation (LVDTs).

4.7.2.1. Steel Strain Gauges

Ten FLA-6-11 strain gauges provided by Tokyo Sokki Company were used to record the strain measurements at different positions along the length of the central bottom steel bar in each of the normal and lightweight samples. The gauge factor, gauge resistance and the gauge length 2.12±1 %, 120±0.5 Ω, 11.9x10^{-6}/°C and 6 mm respectively. Strain gauges were positioned externally at 250 mm, 400 mm, 550 mm, 700 mm, and 850 mm on both sides of each beam, as shown in Figure (4.6). The gauges were denoted as “LS” combined with a number starting from 1 to 10 to identify their position from the left beam end.

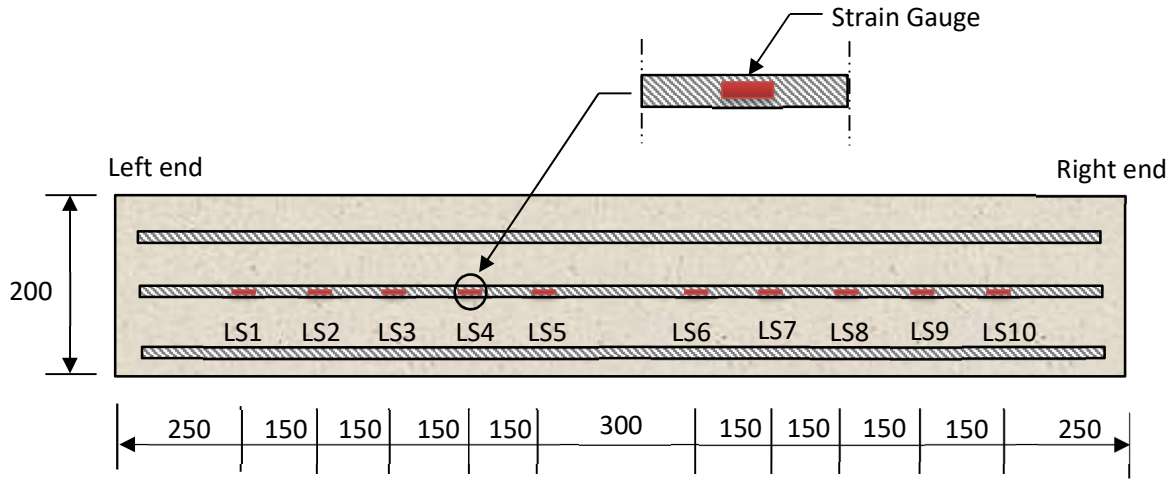

Figure (4.6): Position of Strain gauges attached to the central bottom steel bar (all dimensions in mm).

The process of installing the strain gauges on the steel bar is summarised in Figure (4.7). Firstly, the strain gauges locations along the length of the longitudinal steel bar were slightly grinded by grinder machine. An accurate grinding is vital to prevent the reduction in the longitudinal steel reinforcement area as shown in Figure (4.7a). Before installation of the strain gauges, the sample was cleaned of rust, grease or mud to secure sufficient bond between the strain gauge and the surface of the steel bar. Two-component of adhesive material was used to attach the strain gauges to the surface of the longitudinal steel bar. A tiny amount of the two-component of the adhesive material was required to allow the strain gauges to measure more precise elongations through the test (Alotaibi, 2014).

Figure (4.7b) shows a strain gauge attached to the bar surface. After glueing the strain gauges, some Acrylic coating liquid was used to keep the strain gauges and protect them safe from being ruptured or dislocating (see Figure (4.7c)). The steel bars were left for a couple of hours to increase the strength of the adhesive material. Finally, plastic cable ties were used to tie together the strain gauge wires with steel bars and to eliminate the probabilities of the strain gauges being ruptured. Insulation tape (Butyl tape) was also wrapped around the strain gauges to provide more insulation and to prevent any contact between the strain gauge's wire and the reinforcing steel bar (see Figure (4.7d)).

(a) Grinding steel bars by sander.

(b) Installing of the strain gauges.

(c) Covered the strain gauge.

(d) Butyl tapes & Plastic cable.

Figure (4.7): The process of installing the steel strain gauges.

4.7.2.2. CFRP Strain Gauges

Two types of strain gauges were employed to measure strains in the CFRP reinforcement during the test. The type FLA-5-11 strain gauges provided by Tokyo Sokki Company. The gauge factor and length are 2.12% and 5 mm respectively. The strain gauges were denoted as "SG" attached on the surface of the CFRP reinforcement in a vertical direction to record the CFRP strains during the test, and type FRA-5-11 (45^0-degree Rosette type) which consisted of three 5 mm strain gauges, two of them were employed to measure the strain in vertical and horizontal direction and one strain gauge oriented in the diagonal direction to measure the shear strain at different positions along the length and depth of the strengthened samples. The gauge factor of these strain gauges is 2.21 %. The stain gauges were installed at six positions along the length of the strengthened sample, located at 200 mm, 350 mm and 500 mm, respectively from the beams left side and the same layout was applied from the beams right side. The strain gauges were

installed at 75 mm, 150 mm, and 225 mm from the base of the beam. These arrangements were employed for all LWAC and NWAC strengthened samples. The instrumented CFRP reinforcements were denoted as "SF" combined with a number starting from 2, 3, 4, 7, 8 to 9 to identify their position from the left beam end. Figures (4.8) and (4.9) showed the strain gauge distribution and the referencing name of each gauge attached in the left and right end of U-shaped samples.

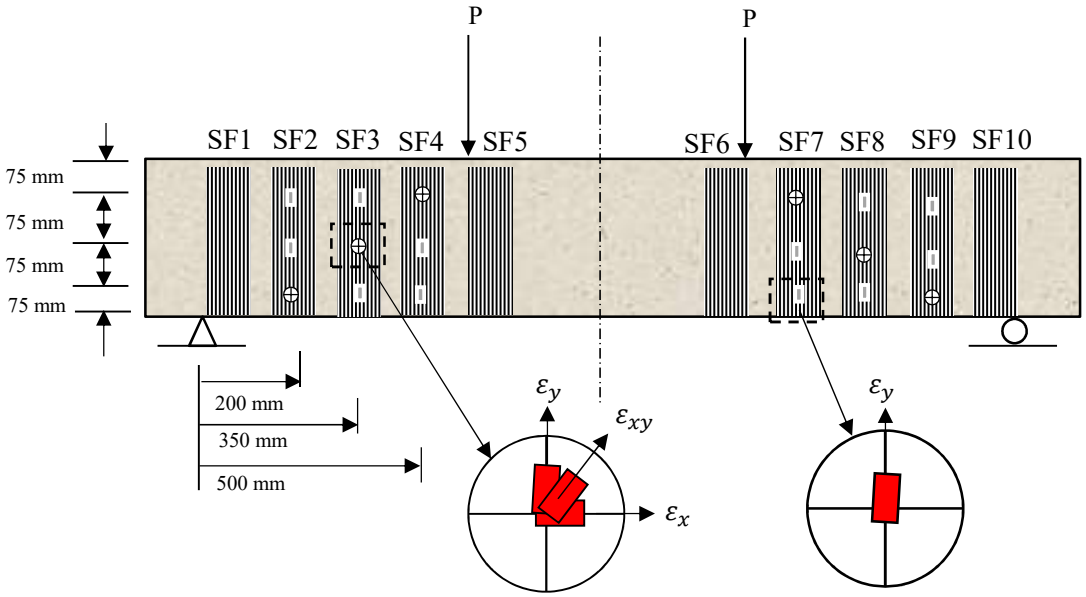

Figure (4.8): CFRP strain gauge arrangement.

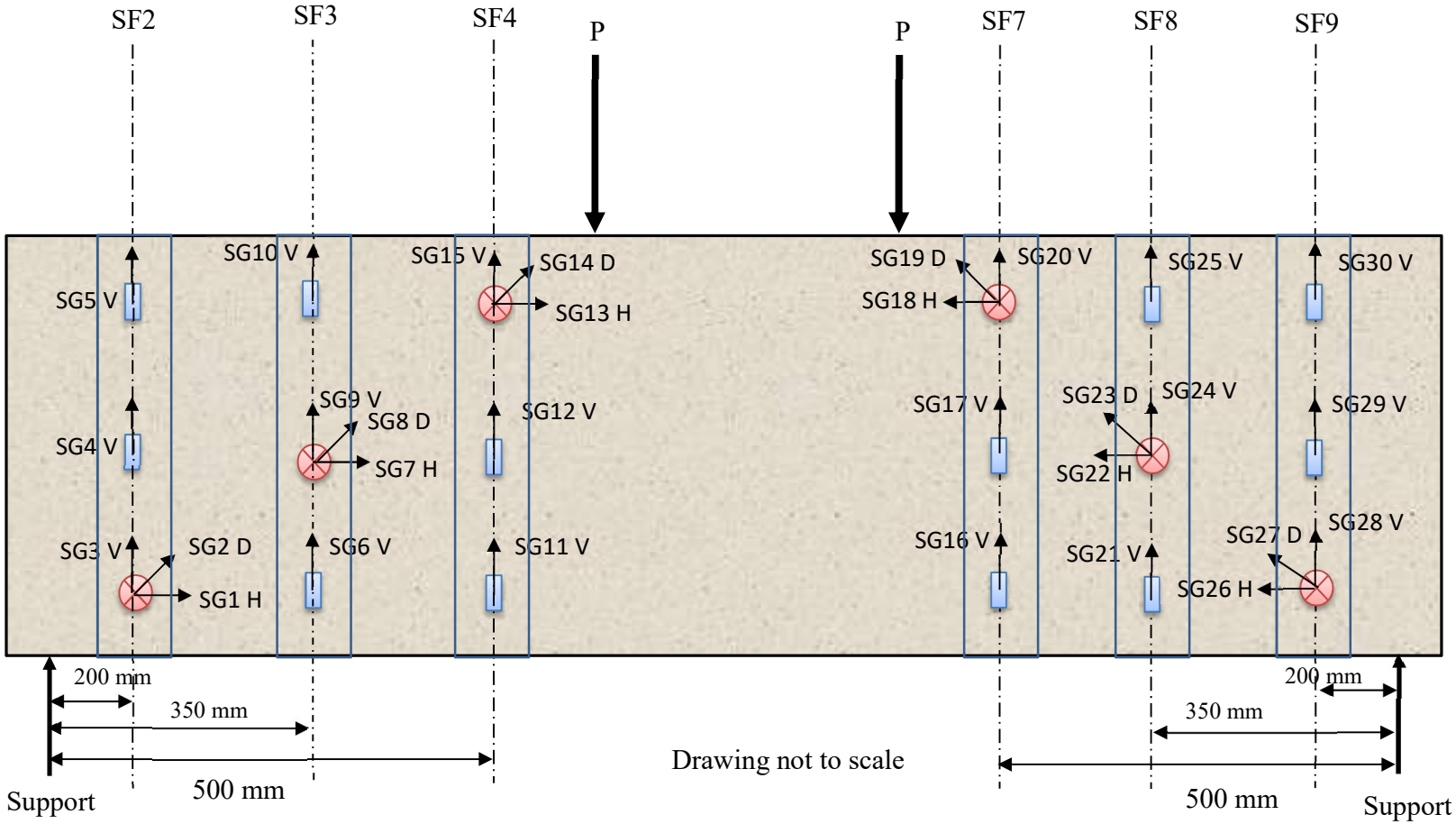

Figure (4.9): CFRP strain gauge arrangement.

4.7.2.3. Linear Variable Differential Transformers (LVDT)

Three Linear Voltage Displacement Transducers (LVDTs) were used in this test to record vertical deflections at various positions along the sample during the test. The LVDTs were positioned at mid-span and at each load point of the beam as seen in Figure (4.10). The LVDTs were mounted on a frame connected to the centre of concrete directly above the supports to measure the relative displacement along the beams, each LVDT was held by a steel hanger, and the LVDT plunger was rested directly versus the bottom soffit of the sample.

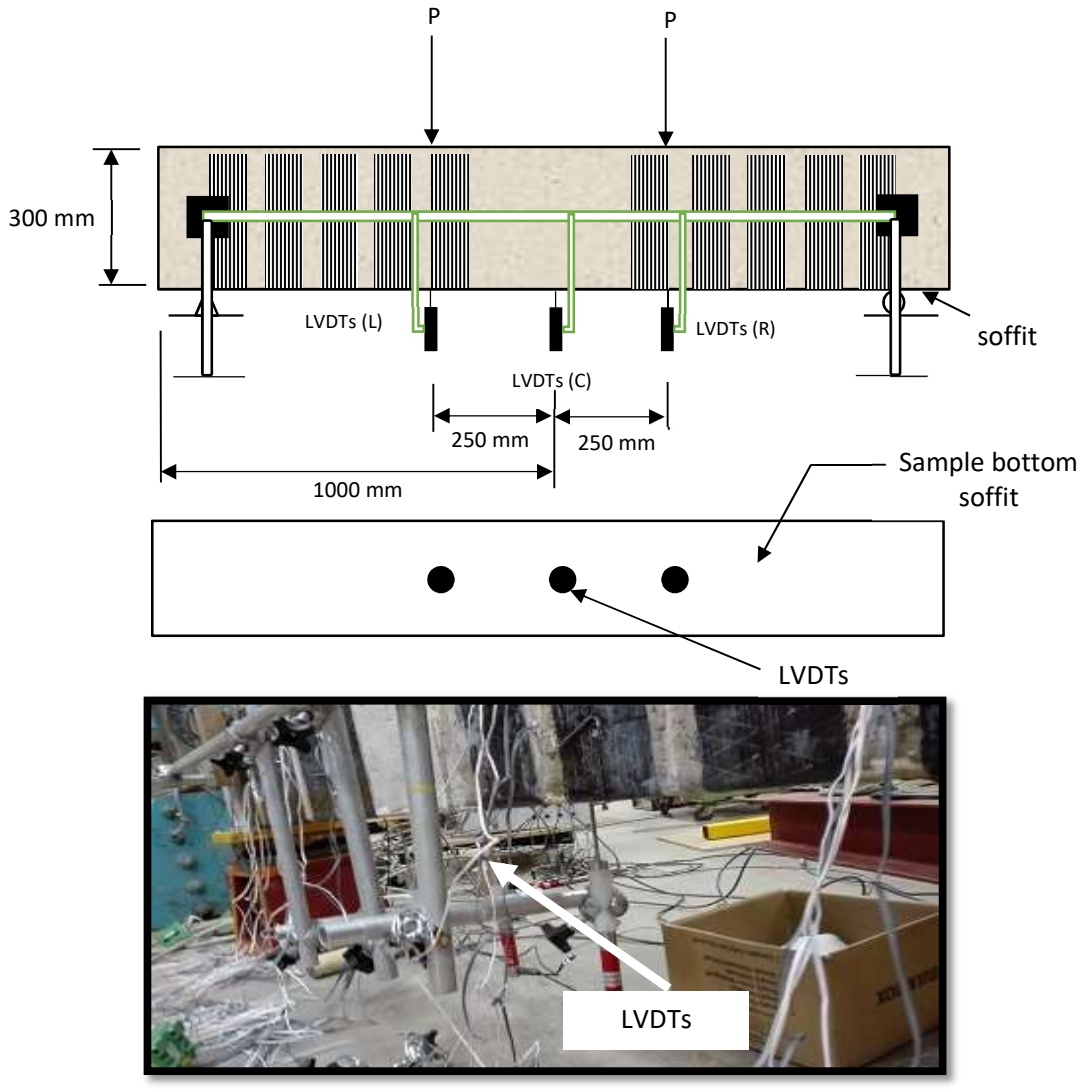

Figure (4.10): Location of the LVDTs underneath of the test samples.

4.7.3. Concrete Casting

All the LWAC and NWAC samples were cast at the same time in two concrete casting. The reinforced concrete beams were externally vibrated to achieve the required consolidation during the concrete casting. Then, the top surface of concrete was finished with trowels to the desired depth. Four hours after beams casting, the surface of the beam was covered with sheets to cure the samples in order to eliminate the small cracks produced by drying and shrinkage. Samples were de-molded and removed from the moulds five days after casting. All the concrete cubes and cylinders were taken at the casting day and tested at the 28 days.

4.7.4. CFRP Application

The unidirectional CFRP (C Sheet 240) sheets were used to retrofit the LWRC and NWRC beams. Epoxy plus primer (EN-Force primer) and epoxy plus adhesive (EN-Force bonding adhesive) were used to bond CFRP sheet to the concrete surface, respectively. The mechanical properties of the CFRP material and the adhesive material were described in sections (3.5.2) and (3.5.3). A concrete grinder machine was used to remove the weak concrete layer and lightly smooth the surface of the samples to secure the required bond between the CFRP and the surface of the concrete. Then, the surface was cleaned to remove the dust produced during the grinding process. Samples corners were rounded to prevent unwanted CFRP rupture which is developed as a result of the high-stress concentration in the CFRP reinforcement wrapped close the corner of the beam. For the U-shaped systems, the CFRP reinforcement was attached directly below the top surface of the beams by approximately 20 mm. A rounded corner is shown in Figure (4.11).

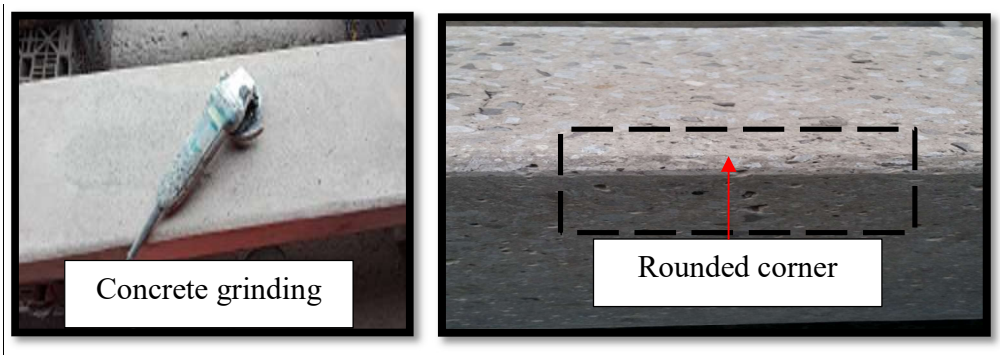

Figure (4.11): Concrete grinding and rounded edge to relieve stress concentrations on the CFRP reinforcement.

For this experimental test, the wet lay-up method was used for all test samples. The base and hardener of the epoxy primer material were mixed with each other for 3 min. Then, the surface of concrete was painted with a thin layer of epoxy primer. The CFRP reinforcement was covered on both sides with the mix of the bases and the hardener of the epoxy adhesive material. Then, the CFRP sheets were attached to the surface of the sample by hand. Firstly, the tension face was wrapped, then the CFRP reinforcements were applied around the beam side faces and finally the compression face for samples with Closed-shaped systems. To achieve the required bond between the CFRP reinforcement and the surface of concrete, the CFRP reinforcement was regularised manually to minimise an excessive amount of epoxy adhesive. Figure (4.12) shows the application of CFRP reinforcement around the test sample.

Figure (4.12): Application of CFRP reinforcement on a concrete surface.

4.8. Material Properties

The mechanical properties of the LWAC and NWAC samples are summarised in Table (4.2). The NWAC was provided by the local ready-mix concrete supplier. The concrete mixes were ordered to have a slump of 75 mm, and a 28-day cube compressive strength of 40 N/mm^2. For LWAC, the concrete was mixed in the laboratory due to the difficulty of providing a small batch of LWAC, the lightweight concrete was mixed according to the mix proportion for concrete used in the bond-slip tests (Section 3.5.4.). All the LWRC and NWRC beams were cast in a single batch each. Furthermore, a total of 18 concrete cubes (100 x 100 x 100 mm), six concrete cylinders (150 dia. x 300 mm) and six prisms (100 x 100 x 400 mm) were cast from each batch to determine the uniaxial compressive strength, the Young's modulus of elasticity and the modulus of rupture of lightweight and normal weight concrete (see Table (4.2)).

Table (4.2): Mechanical properties of concrete

Concrete Type	Average cube concrete strength f_{cu} (MPa)	Average concrete flexural tensile strength f_{ct} (MPa)	Average modulus of elasticity E_c (MPa)	Average concrete density ρ_c (kg/m^3)
NWAC	42.10	3.49	29860	2356
LWAC	43.34	3.026	23510	1823

The longitudinal steel reinforcing bars were provided by Travis Perkins Plc Company. 16 mm diameter steel bars were used for all the tested samples. In addition to two shear links of 8 mm diameter were used adjacent to supports either side of the beam, these links were used to assemble the steel reinforcing bars. Three samples of each type of the longitudinal steel reinforcing bars were tested to determine the steel properties as specified in ASTM A370, 2005 (direct tensile test) using the Instron testing machine. The material properties determined from these coupon tests are summarised in Table (4.3).

Table (4.3): Mechanical properties of steel reinforcement.

Bar No.	Yield stress (MPa)	Yield strain (μm/m)	Ultimate stress (MPa)	Ultimate strain (μm/m)	Modulus of elasticity, E_s (GPa)
16 mm	510	2600	650	130000	196.154
8 mm	501	2500	611	124000	200.400

4.9. Results Analysis

The overall results of the experimental test are provided in this section. The load-mid-span displacement trends and the strain reading collected from the strain gauges attached in the longitudinal steel and CFRP reinforcement are also included in this section. A summary of the samples shear strength based on the maximum shear carrying capacity and the recorded mid-span deflection are summarised in Table (4.4). The shear strength provided by CFRP reinforcement also included in this table. In this study, the shear strength of the strengthened

samples was subtracted from the shear strength of the control unstrengthened sample in each series to obtain the shear contribution provided by CFRP reinforcement.

Table (4.4): Summary of shear capacity, failure deflection, and mode of failure.

Sample	Max shear capacity (kN)	CFRP shear strength (kN)	Percentage increase in shear gain due to CFRP (%)	Mid-span deflection at failure (mm)	Failure mode, CFRP failure
BL	151.78	0		4.82	Shear
BL-UST	218.38	66.60	44	7.10	Shear, CFRP debonding
BL-CST*	267.14	115.36	76	11.30	Shear, CFRP rupture
BN	164.10	-		5.35	Shear
BN-UST	248.61	84.51	51	7.69	Shear, CFRP debonding
BN-CST*	320.80	156.70	95.4	10.31	Shear, CFRP rupture

* Shear failure was observed after flexural yielding.

Comparison of the maximum shear capacity between CFRP strengthened samples and the shear capacity of the control sample shows that the CFRP strengthening techniques were effective in enhancing the shear capacity of the LWRC and NWRC beams. As shown in Table (4.4), the shear capacity of the control samples in the LWRC and NWRC series samples are significantly lower than the shear capacity of all strengthened samples, the higher percentage increase in shear strength were assigned to the concrete type and the strengthening configurations.

The maximum achieved shear strength was used for the calculation of shear strength gained due to CFRP reinforcement, based on the assumption that the shear contributions provided by the concrete material keep the same with using the CFRP reinforcement (Khalifa and Nanni, 2002 and Mofidi & Chaallal, 2011). The change in shear capacity of the RC beam due to CFRP reinforcements was not accounted by using this approach of analysis (Subtracting method). However, this was used by the majority of the research to quantify the enhancement in shear strength due to CFRP reinforcement (Colalillo, 2012).

Figure (4.13) shows the shear strength gained due to CFRP reinforcement in the strengthened samples compared with the corresponding unstrengthened control samples of LWAC and NWAC. For the LWRC series, the shear strength provided by CFRP reinforcement for U-shaped and Closed-shaped samples were 44% and 76% respectively, when compared with the control sample, while for the NWAC series, the shear strength provided by CFRP reinforcement for U-shaped and Closed-shaped samples were 51% and 95% respectively, when compared with the control sample.

In this study, the shear strength of the control, U-wrapped and Closed-wrapped samples of LWAC are 92%, 87% and 83% of the control, U-wrapped and Closed-wrapped samples of the corresponding normal weight concrete samples respectively. The shear strength gained due to CFRP reinforcement for BL-UST is about 21% less than the normal weight concrete results (BN-UST). On the other hand, the BL-CST had results that were 26% less than the normal weight concrete results (BN-CST). This observation can be attributed to lower concrete surface tensile strength and aggregates interlock at the diagonal crack faces in LWAC which increases the stresses in CFRP reinforcements and at the concrete-CFRP interface. Increasing in interfacial and normal stresses with increasing plastic deformation leads to CFRP debonding and unexpected CFRP rupture failures, thus the effectiveness of FRP for shear strengthening LWRC beams will be affected by this issue. CFRP bond deterioration in LWAC requires consideration to ensure the safety of CFRP applications for shear strengthening of LWRC beams.

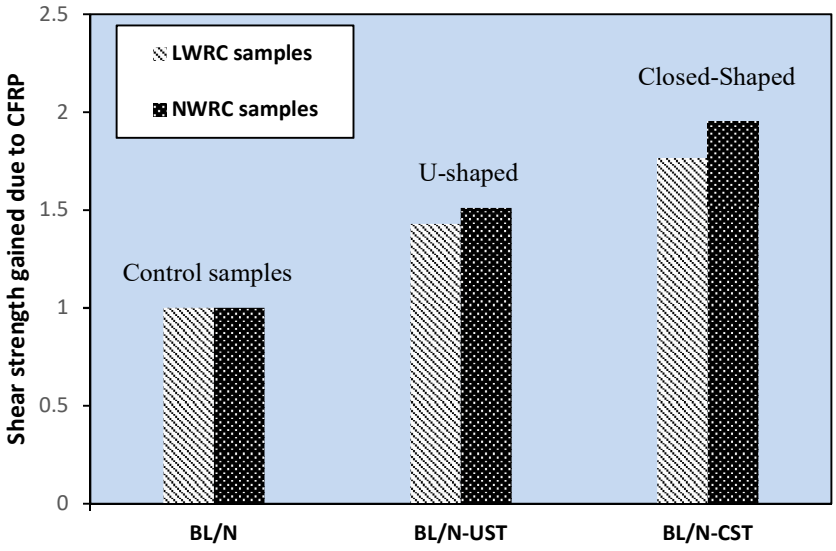

Figure (4.13): Comparison of the shear strength gained due to CFRP reinforcement.

Figure (4.14) compares the maximum deflection at failure for the LWAC and NWAC samples. All the strengthened samples revealed increases in the maximum deflection over the corresponding non-strengthened control sample at failure. LWAC and NWAC samples strengthened with U-wraps had 47% and 43% greater maximum deflection at failure over the control LWAC and NWAC samples.

Comparison with samples strengthened with Closed-wrapped had an increase in maximum deflection at the failure of 134% and 93% respectively. This observation resulted from the evidence that anchorage provided by Closed-shaped configurations could increase the shear strength of the BL-CST and BN-CST beams and yielded a better ductility over the control samples. Ductile behaviour was observed in lightweight samples strengthened with fully wrapped CFRP reinforcement thereby providing the desired mode of failure at ultimate limit state.

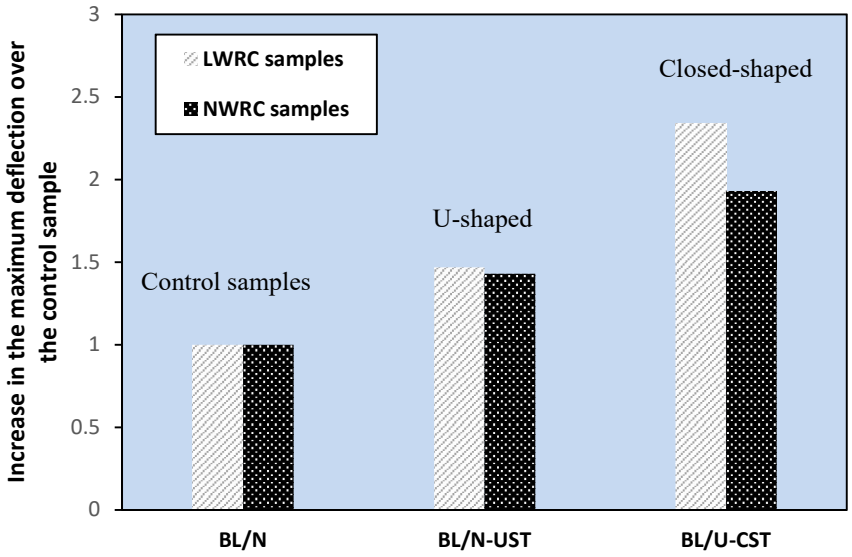

Figure (4.14): Increase in the maximum deflection at failure compared with the control sample.

4.9.1 Load-Deflection Behaviour

The load-deflection relationships measured curves obtained from the test results are presented in this section. The behaviour trends for the LWRC series specimens are shown in Figure (4.15) and Figure (4.16) for the NWRC series. In each Figure, the response of the strengthened samples is compared with non-strengthened control sample.

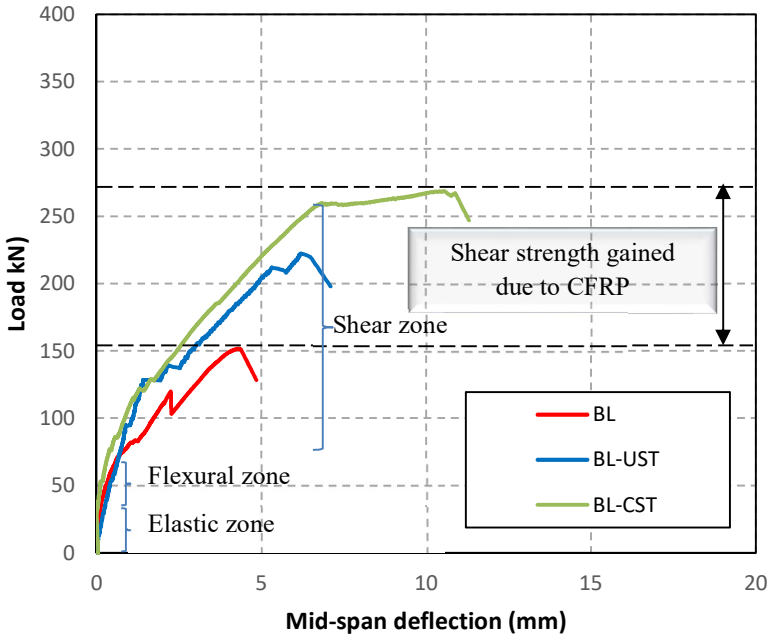

Figure (4.15): Load versus deflection response of the lightweight samples series.

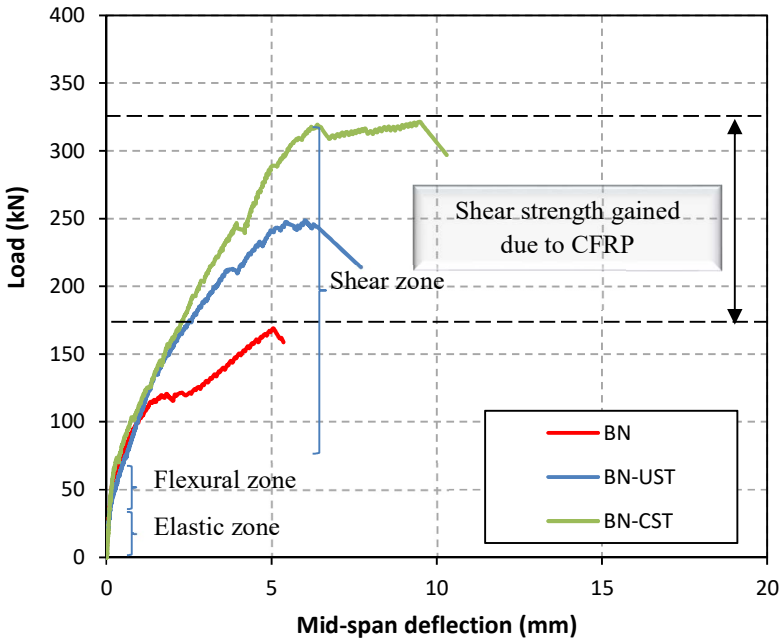

Figure (4.16): Load versus deflection response of the normal weight samples series.

The behaviour trends for NWAC and LWAC samples (see Figures (4.15) and (4.16) were described by three zones of stiffnesses: (i) elastic stiffness zone (uncracking zone), (ii) before first shear cracks or flexural stiffness zone, and (iii) shear stiffness zone. In general, all LWRC and NWRC beams showed the same elastic stiffness zone before first flexural cracks (approximately 50 kN). The flexural stiffness zone showed the same linear trend until a diagonal crack appears at the surface of concrete at the applied load between 100-130 kN load range for NWRC beams and 90-120 kN load range for LWRC beams, the same behaviour was observed by (Colalillo, 2012). It can be seen that the first diagonal crack in the LWRC beams appears approximately at the same load level as the NWRC beams. The load-displacement curves for these samples show that the CFRP strengthened sample had higher strength and greater flexural and shear stiffnesses compared with corresponding control samples, which is to be expected since CFRP strengthening is an efficient system that is only activated after flexural and shear cracks have developed.

For more details, the lightweight control sample was loaded till a maximum load of 151.78 kN as illustrated in Figure (4.15). The maximum central deflection at the corresponding maximum recorded load was 4.30 mm. Abrupt leap in applied load was developed at this stage which is attributed to the loss of friction at the interface of the diagonal shear crack. Examining the load-deflection trends of the LWAC samples with Closed-shaped and U-shaped shows identical stiffness's trend at a low level of loading. However, at the maximum load for Closed-shaped sample, the shear cracks zone was considerably higher than those observed in samples with U-shaped system. This is assigned to the premature failure for sample strengthened with U-shaped system. For the control NWAC samples (see Figure (4.16)) these experience a maximum load of 164.10 kN at the maximum central deflection of 5.30 mm. Similar response curves of the normal weight concrete samples can be observed for samples with U-shaped and Closed-shaped.

Figure (4.17) shows that the overall shear stiffness of LWAC samples is lower than those of NWAC samples with identical CFRP strengthening configurations after initial cracking. This behaviour is a result of the difference in rigidities of LWAC tested samples. LWAC samples had lower stiffness compared with NWRC samples. The lower stiffness of lightweight aggregate particles (LWA) and higher cement ratio results in large plastic deformation leading to changes in the load-deflection response after the initiation of the shear cracks.

Generally, the LWRC beams showed a similar response to the NWRC beams until the development of diagonal shear cracks. Subsequently, the NWRC beams were able to resist shear cracking and reach higher shear capacity, while LWAC samples were unable to develop sufficient shear resistance. Diagonal shear cracks occurred at an earlier stage in the LWAC samples compared with normal weight samples and this leads to premature CFRP reinforcement debonding or rupture. The tensile strength of LWAC is used for obtaining the diagonal crack strength of LWAC. The tests results obtained by Hanson, (1961) showed that the diagonal crack strengths of RC beams were closely related with a tensile strength of the concrete. It can be concluded that the lower tensile strength of lightweight concrete plays an important role in reducing the diagonal cracking resistance in LWAC samples which affects the behaviour of these samples.

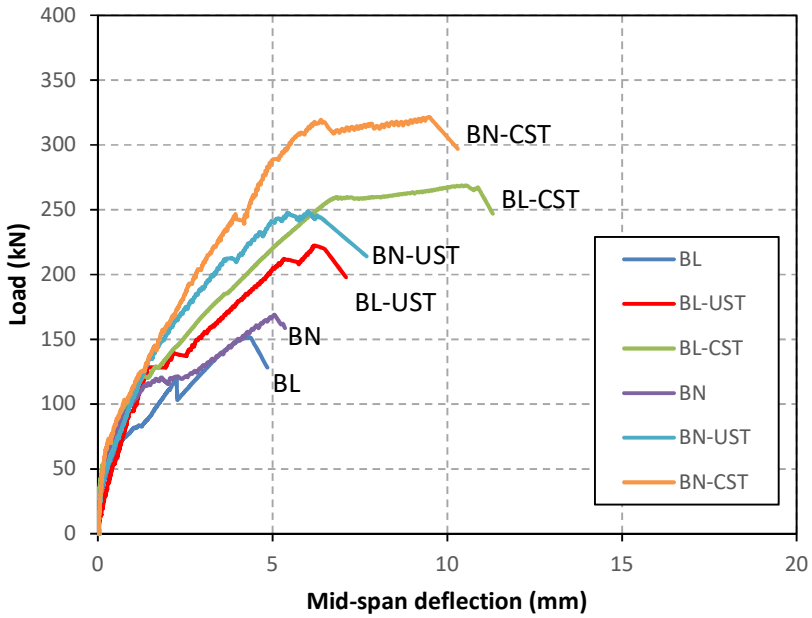

Figure (4.17): Comparison of load versus deflection of LWAC and NWAC samples.

4.9.2. Shear Component Analysis

The total shear strength on both side of the beam provided by concrete (V_c) and CFRP reinforcement (V_f) were calculated from the experimental results using the subtraction analysis method as described in section (4.9). An alternative method to calculate the shear strength provided by concrete and CFRP reinforcement using the CFRP strain measurements. In the latter

method, the applied load reordered by the load cell, and strains in the CFRP strips were used to calculate the shear components during the test. This method allowed to calculate the shear contribution provided by the concrete and CFRP reinforcements at any level of loading using simple numerical formulas which is useful an understanding the efficenicy of using CFRP reinforcment to strength lightweigh concrete beams.

To satisfy equilibrium conditions, the shear contribution provided by concrete and CFRP reinforcement should be equal to the externally applied loads. A simple free-body diagram of half of the cracked beam was used to calculate the shear strength provided by the CFRP reinforcement. Only CFRP reinforcement that bridging the diagonal shear crack were assumed to contribute to the total shear strength of the RC beams (Alotaibi, 2014) (see Figure (4.18)).

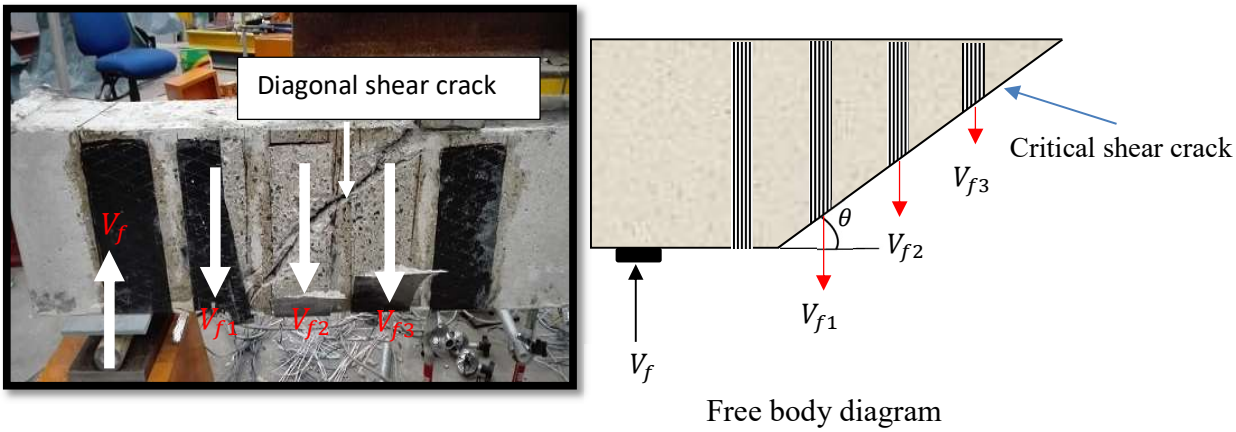

Figure (4.18): Internal forces in a cracked strengthened beam.

The elongation recorded from strain gauges applied vertically to the surface of the CFRP reinforcement was only used to calculate the shear strength gained due to CFRP reinforcement. The shear contribution of the CFRP strips can be evaluated by summing the contribution provided by CFRP reinforcement bridge the diagonal shear crack in each side of the beam as shown in Equation (4.1) (Kim, 2011):

$$V_f = \sum_{i=1}^{n} A_{fi} E_f \varepsilon_{fi} \qquad (4.1)$$

Where, V_f is the estimated shear force provided by CFRP reinforcement, A_{fi} is the area of the CFRP strip, E_f is is the elastic modulus of CFRP material, ε_{fi} is the strain measured from strain gauges attached to the CFRP strip and n is the number of stirrups or CFRP strips crossing the

diagonal shear crack, respectively. The shear strength provided by concrete is not readily to predict from the experimental results since it is assumed to include the rest of the shear strength (i.e., tensile strength of concrete, aggregate interlock at the diagonal crack faces, compressive strength of concrete, interfacial shear stress, dowel action provided by the longitudinal steel reinforcement) (Kim, 2011). In this study, the concrete contribution was obtained by subtracting the estimated contributions of CFRP reinforcement (V_f) from the total shear capacity (V_t) at a particular load level as given by Equation (4.2):

$$V_c = V_t - V_f \tag{4.2}$$

Figures (4.19) to (4.22) show the results of the shear component analysis for the LWRC and NWRC beam specimens. In these figures, the horizontal axis represents the total applied load recorded by the load cell and the vertical axis represents the total shear contribution of concrete and CFRP reinforcement on both side of the beam. The shear strength provided by CFRP reinforcements is indicated by the red trend and the portion between the diagonal black line and the CFRP trend represents the shear strength provided by the concrete.

It can be noted that the shear strength provided by CFRP reinforcement was very small and can be ignored before the occurrence of a diagonal shear crack. In this stage, external loads applied to the samples are taken mainly by concrete. By the development of the diagonal shear crack, a part of the loads is taken by the CFRP reinforcement as demonstrated by a sudden leap in the CFRP shear contribution response curves. The CFRP reinforcement gradually carries the external shear force as shown by the progress increase in shear strength provided by CFRP reinforcement, till the CFRP reinforcement detached from the surface of the concrete. Abrupt falls in the CFRP shear contribution trend can be highlighted when the CFRP reinforcement debonds or ruptures before the sample failure (see Figure (4.21)). At the ultimate limit state, shear failure was developed due to CFRP global debonding for U-shaped systems or CFRP fibre rupture for Closed-Shaped samples. A similar response obtained by Murphy, (2010) and Bousselham and Chaallal, (2008). It can be concluded that there was virtually no difference between the lightweight samples and their normal weight companions regarding the general trend of the CFRP reinforcement contribution, a similar response was observed for all the tested samples. However, the slopes of CFRP shear contribution for lightweight samples graphs are steeper compared to the identical normal weight samples. This indicates an increased rate of

straining of the CFRP reinforcement at lower loads compared with normal weight samples due to rapid openings of the shear crack as a result of loss of friction and aggregate interlock at the crack interface, thereby causing premature debonding of the CFRP strips.

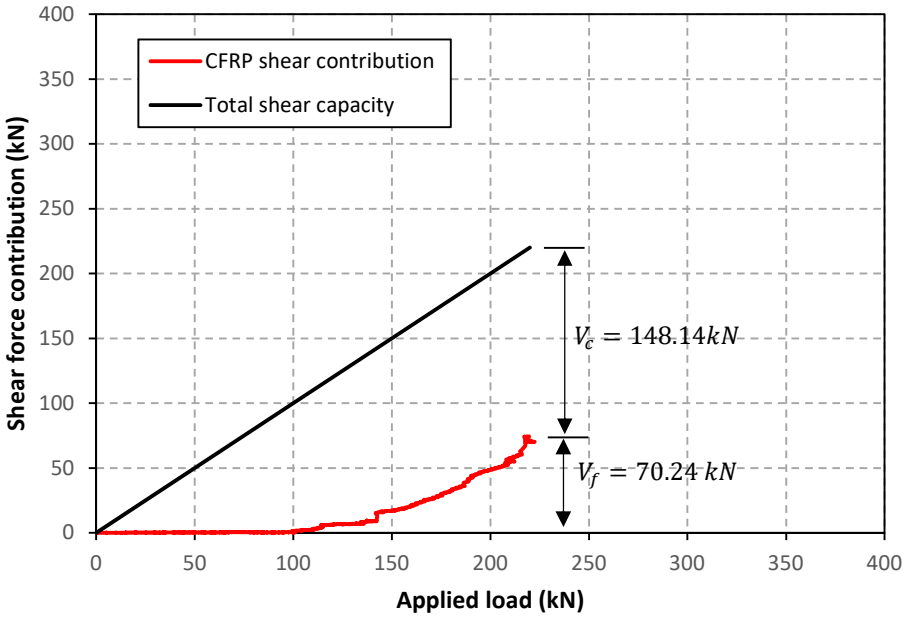

Figure (4.19): Estimated shear contributions for BL-UST specimen.

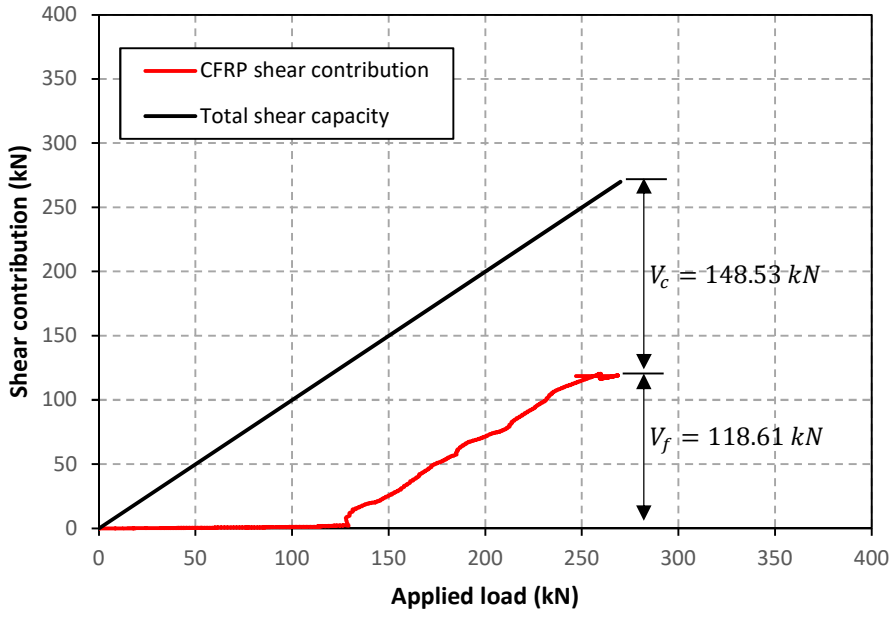

Figure (4.20): Estimated shear contributions for BL-CST specimen.

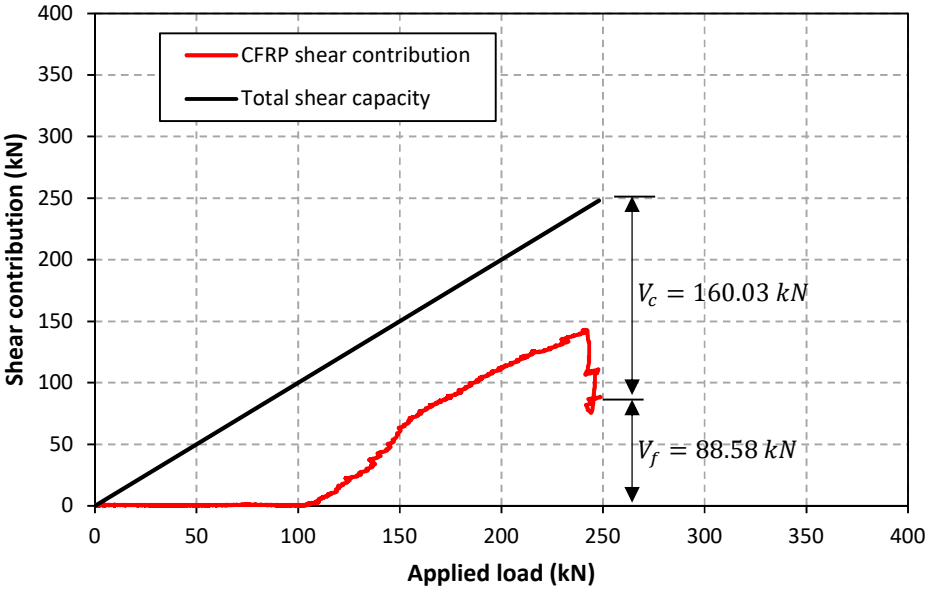

Figure (4.21): Estimated shear contributions for BN-UST specimen.

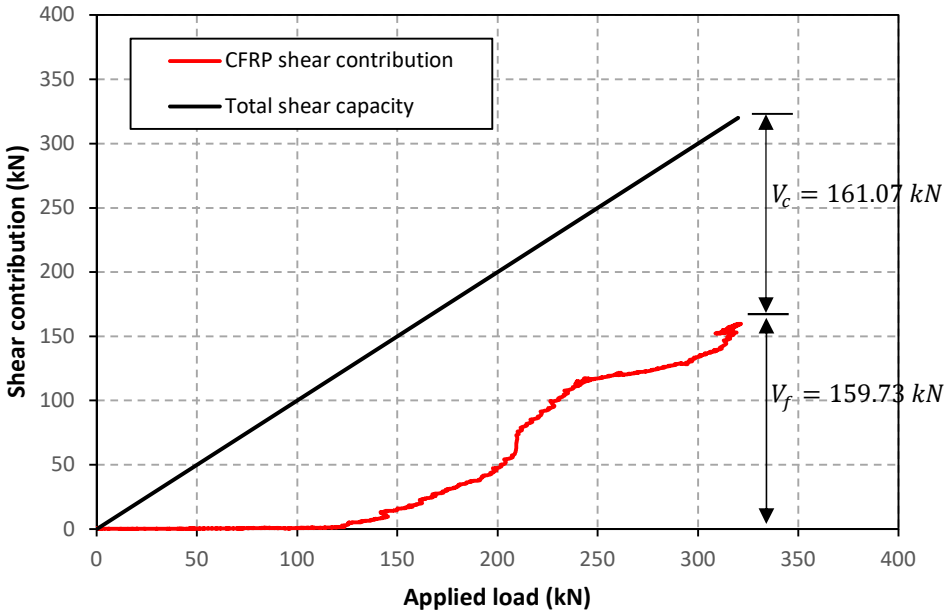

Figure (4.22): Estimated shear contributions for BN-CST specimen.

Table (4.5) summarised the maximum shear contribution provided by concrete (V_c) and CFRP (V_f). The total CFRP shear strength provided by CFRP reinforcement which was obtained by subtraction analysis in both side of the beam were 5% and 2.7% lower for the BL-UST and BL-CST samples as compared with those obtained from CFRP strain readings. In contrast, the CFRP contribution were 4.6% lower for the BN-UST sample and 1.9% lower for BN-CST sample as compared with those obtained from the CFRP strain readings. Thus, the CFRP contribution to shear using the subtraction analysis is very close to the values when the strain readings are used to evaluate the shear strength provided by CFRP reinforcement.

It can be noted that the shear contribution provided by concrete on both sides of the beam based on subtraction analysis was roughly the same as those obtained from CFRP strain readings for LWRC and NWRC beams strengthened with CFRP reinforcement. It can be concluded that the concrete shear strength increases constantly with the applied load, regardless the existence of the CFRP reinforcement.

Table (4.5): Summary of shear strength obtained from CFRP reinforcement strains.

Sample	Total shear strength (kN)	(V_f) (subtraction Method) (kN)	shear strength provided by concrete and CFRP reinforcement	
			V_c (kN)	V_f (kN)
BL	151.78	0	151.78	0
BL-UST	218.38	66.60	148.14	70.24
BL-CST	267.14	115.36	148.53	118.61
BN	164.10	0	164.10	0
BN-UST	248.61	84.51	160.03	88.58
BN-CST	320.80	156.70	161.07	159.73

4.9.3. Failure Modes

All the tested LWRC and NWRC beams failed in shear by the initiation of diagonal tension cracks in the shear span. In the case of samples strengthened with CFRP reinforcement, the CFRP strips crossing the diagonal shear cracks will either debond or rupture. The orientations of the major diagonal tension shear cracks are summarised in Table (4.6).

Table (4.6): Summary of the diagonal shear crack inclinations.

Sample	shear cracks angle			Average angle
	θ_1	θ_2	θ_3	
BL	42^0	40^0		41^0
BL-UST	34^0	30^0		32^0
BL-CST	33^0	37^0	35	35^0
BN	41^0	44^0		42^0
BN-UST	33^0			33^0
BN-CST	35^0	37^0	34^0	35^0

In general, the orientation of the diagonal tension crack for strengthened samples was lower than their corresponding control samples. It is well known that the presence of CFRP reinforcement influences the shear crack pattern. The diagonal tension crack inclinations of the strengthened lightweight and normal weight samples were slightly steeper compared with their control samples. The test results obviously reveal that there is no variance in response between lightweight and normal weight samples regarding the inclinations of diagonal shear cracks despite the clear difference in ultimate shear loads.

In this experiment, the control LWAC and NWAC samples failed in shear by diagonal tension cracks as shown in Figure (4.23) and (4.24). Loss of friction at the interface of the diagonal shear crack were the failure modes of the control samples. For strengthened samples, The CFRP reinforcements have significant effects on the beams crack distributions. The CFRP reinforcement delays the loss of friction at the diagonal crack faces by reducing diagonal crack opening and help to transfer further compression and interfacial shear stress through the crack faces. At the ultimate limit state for samples strengthened CFRP, the crack bridging effect is lost and the loss of friction was occurred suddenly without any warning. The failure patterns are extremely brittle when compared with non-strengthened samples. The same failure modes were observed by Bousselham & Chaallal, (2008) and by Colalillo, (2012).

The average major diagonal crack widths in the control LWAC sample was about 5 mm compared with the NWAC control sample which was approximately 3 mm. It can be noted that the lightweight samples had higher crack widths compared with normal weight samples due to lower friction and aggregate interlocks at the primary shear faces.

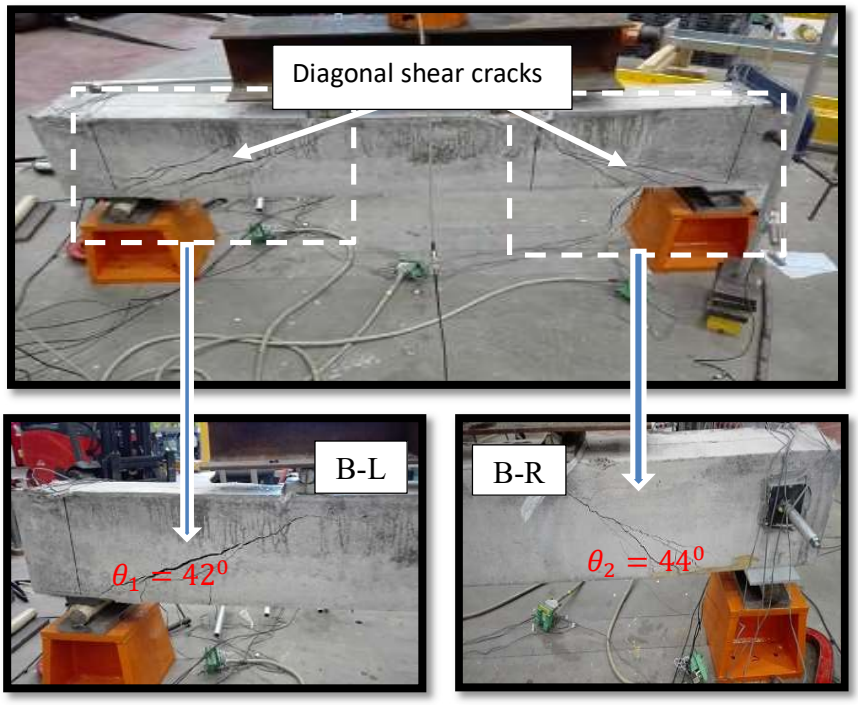

Figure (4.23): Typical failure mode of the control sample (BL).

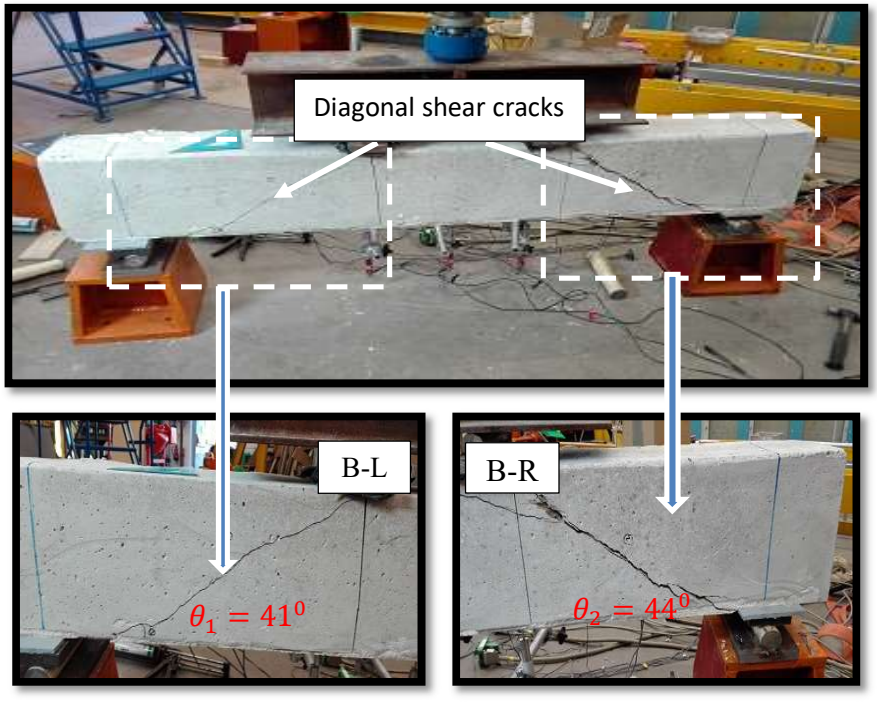

Figure (4.24): Typical failure mode of the control sample (BN).

Shear failure as a result of CFRP debonding was the failure mode of the LWAC sample strengthened with U-shaped techniques. The failure in bond between CFRP and concrete was initiated by debonding in a thick layer of concrete close the surface of the beam, (see Figure (4.25)). The CFRP reinforcement was detached locally from the surface of concrete at the diagonal shear cracks positions. With further loading, the debonding failure was gradually extended from the crack position and moved away towards the top and the bottom anchorage ends of the beam. A similar failure mode was observed for the NWAC sample strengthened with U-shaped, (see Figure (4.26)). However, the CFRP debonding initiated with a thin layer of concrete close the surface of concrete in case of NWAC samples. Generally, the lightweight samples showed higher crack intensity and widths compared with normal weight samples. The average major diagonal crack widths in the LWAC was about 7 mm. while for the NWAC samples, the crack widths were about 4 mm.

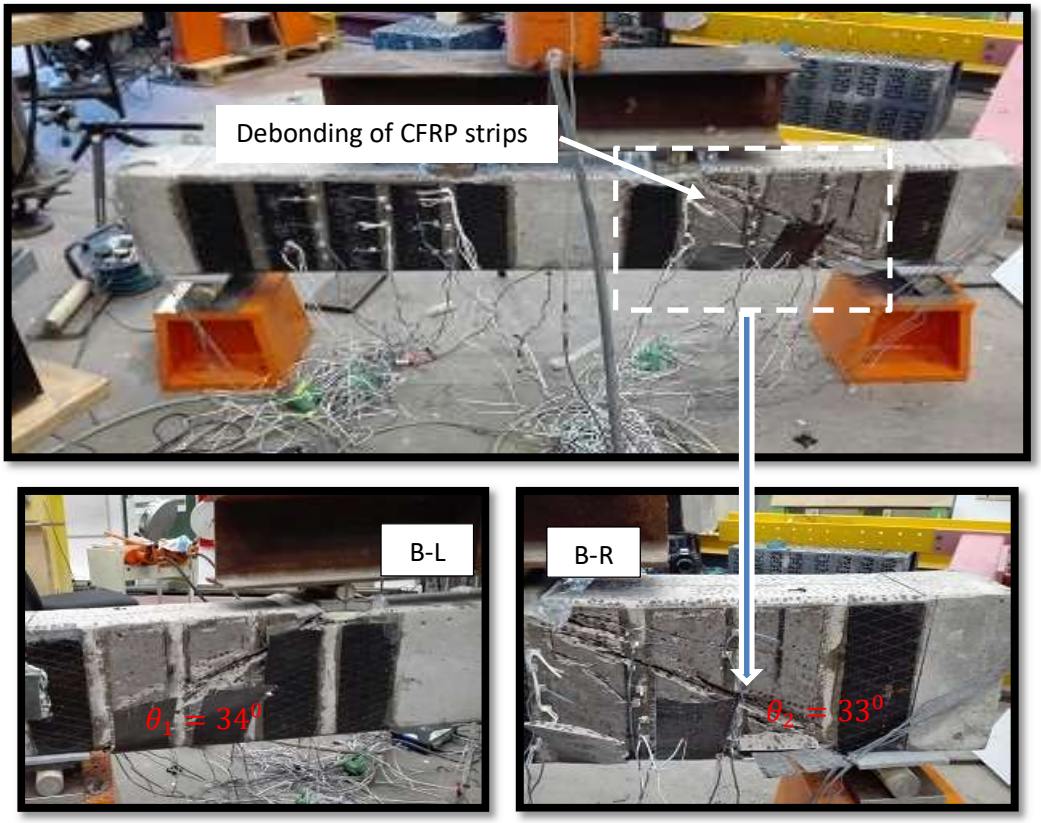

Figure (4.25): Typical failure mode of BL-UST sample.

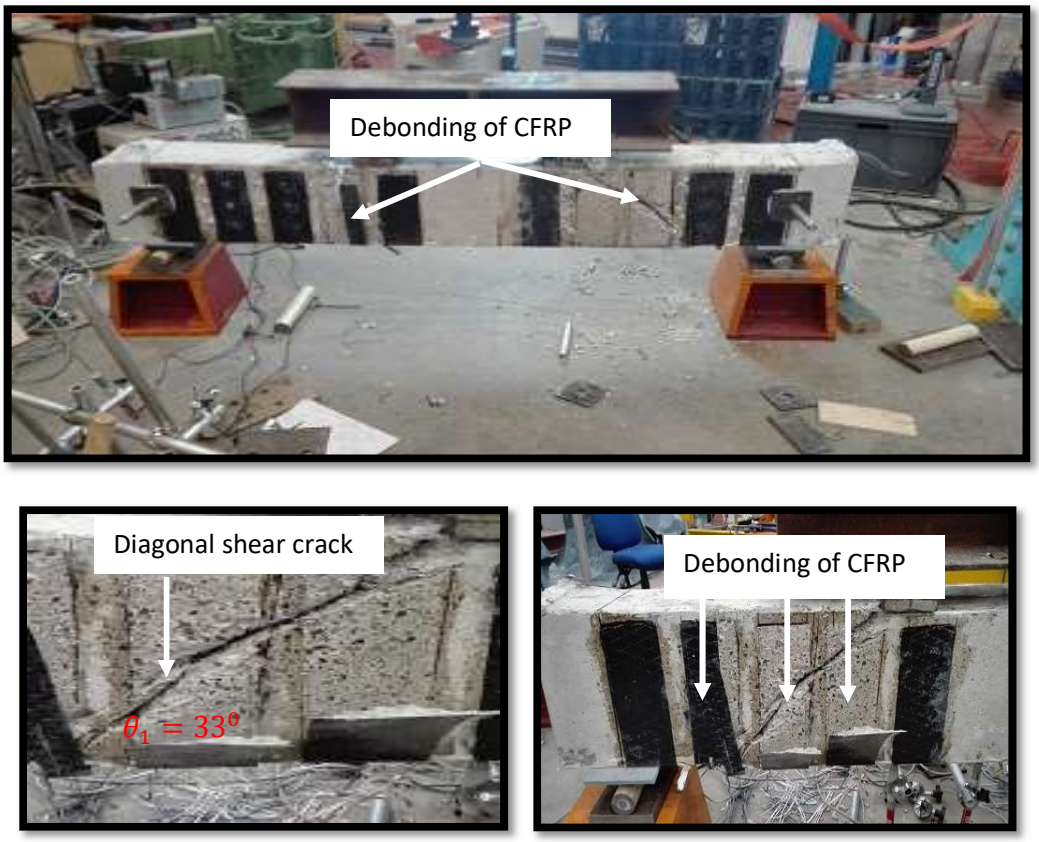

Figure (4.26): Typical failure mode of BN-UST sample.

Shear failure as a result of CFRP reinforcement rupture was the failure mode of the LWAC and NWAC samples strengthened with Closed-shaped system. CFRP rupture is observed by breaking of the CFRP fibres along the diagonal shear crack because of excessive straining, (see Figure (4.27) and (4.28)). CFRP rupture was developed after flexural steel yielding close the corners of the beam due to high-stress concentrations occurred in the CFRP reinforcement at this region.

In general, the lightweight and normal weight samples with Closed-wrapped were failed in extremely brittle failure modes compared with control samples. However, larger increases in shear strength are gained when the failure mode of the CFRP is occurred by CFRP rupture rather than debonding failure. No significant difference in the crack pattern was observed between lightweight and normal weight samples. However, a number of small cracks were noticed to have developed in the LWAC sample. The average major diagonal crack widths in the LWAC was about 4 mm. while for the NWAC samples, the crack widths were about 3 mm. In this test, LWAC and NWAC samples with Closed-shaped retrofitting system had many diagonal shear cracks compared with U-shaped samples which reveal one or two critical diagonal shear cracks.

It can be noted that the U-shaped strengthening system has less effect on beams crack pattern compared with Closed-shaped system.

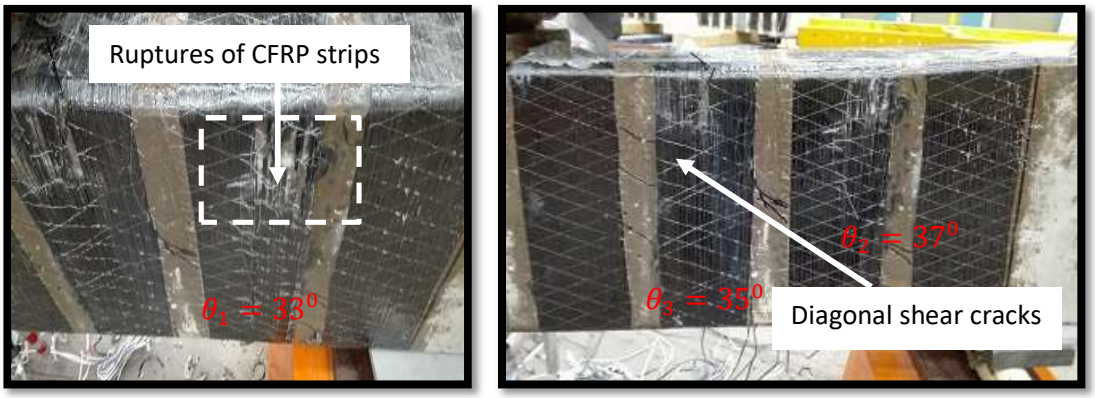

Figure (4.27): Typical failure mode of BL-CST sample.

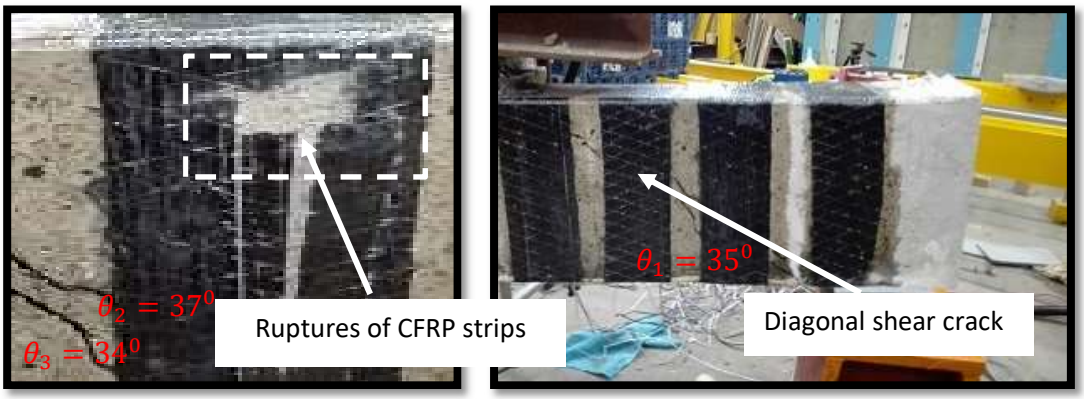

Figure (4.28): Typical failure mode of BN-CST sample.

4.9.4. Longitudinal Steel Strain

The data collected from ten longitudinal steel strain gauges installed at different section along the steel reinforcement are presented in this section to show the typical strain distribution profile and the variation of longitudinal steel strains along the length of the LWAC and NWAC samples at various load levels (20%, 40%, 60%, 80%, and 100% of the maximum load capacity). The longitudinal strain profiles for BL, BL-UST, and BL-CST are provided in Figures (4.29) to (4.31) and for BN, BN-UST, and BN-CST these are shown in Figures (4.32) to (4.34). All these figures are plotted on the same scale to show the comparison between the control and the strengthened samples of each series. The horizontal black line in these figures represents the yield strain of longitudinal steel reinforcement which is about (2600 μm/m). Unfortunately, the

data collected from strain gauges LS1, LS6, LS7, LS8, LS9, and LS10 in the BL-UST samples were missed during the test due to a technical fault whilst loading.

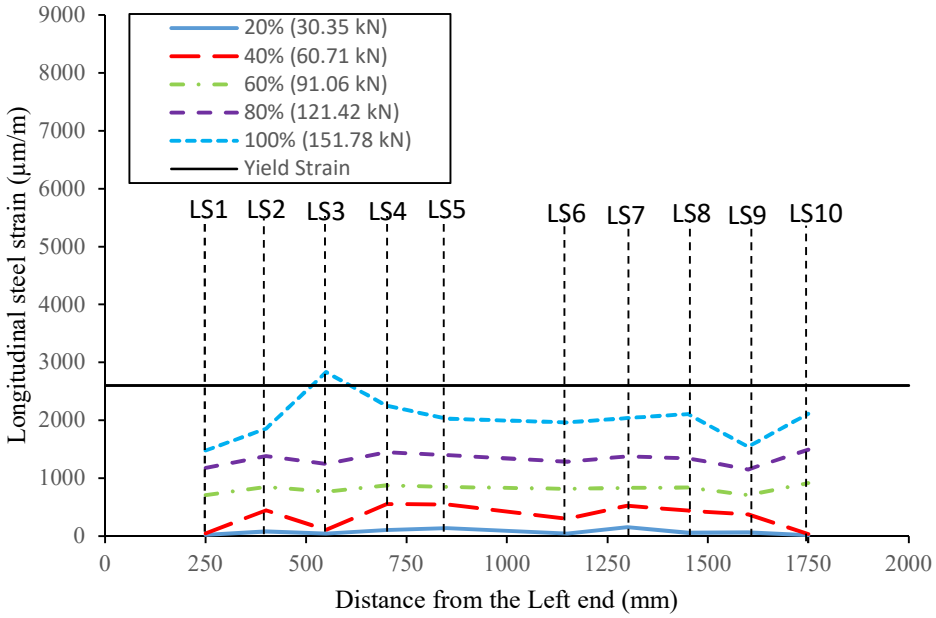

Figure (4.29): Longitudinal steel strains profile for BL specimen.

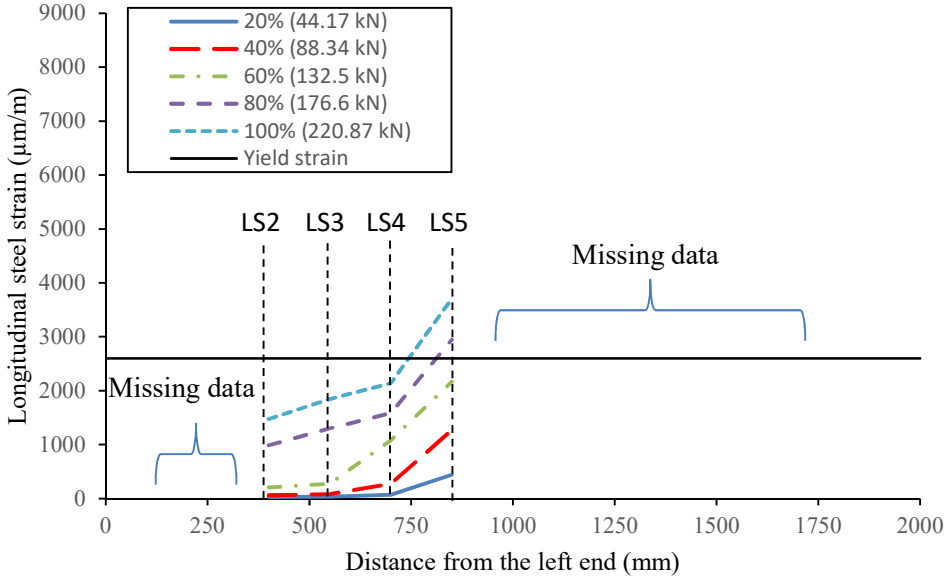

Figure (4.30): Longitudinal steel strains profile for BL-UST specimen.

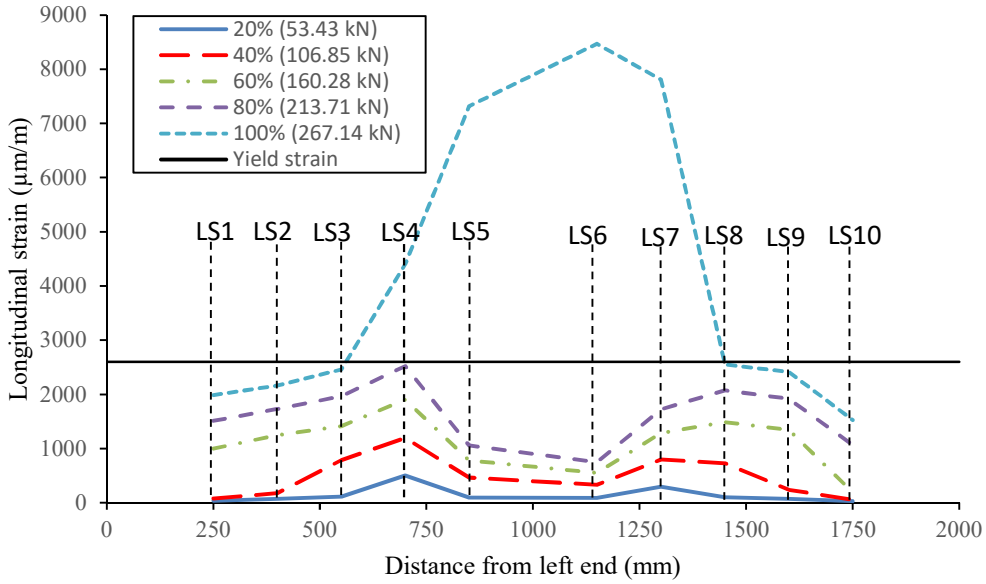

Figure (4.31): Longitudinal steel strains profile for BL-CST specimen.

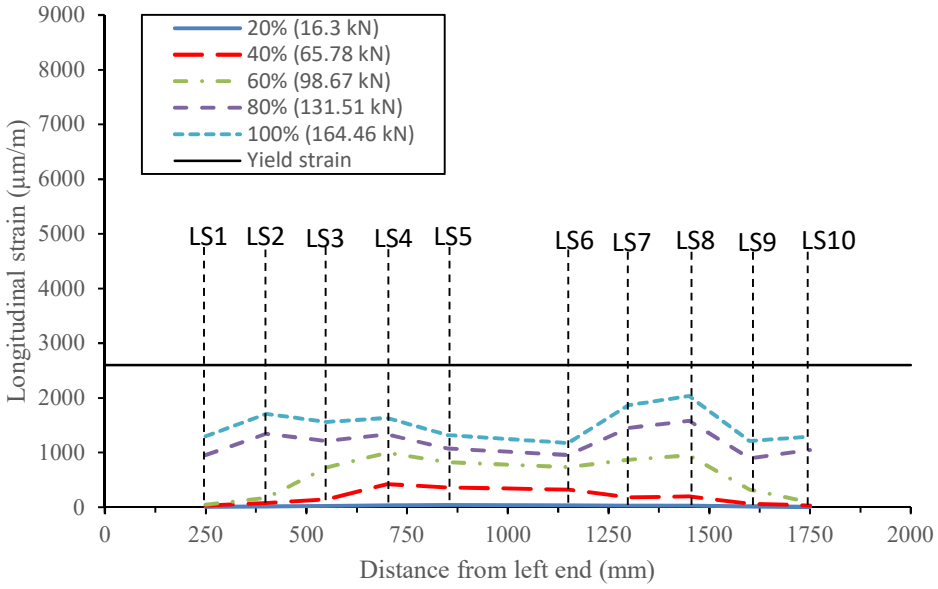

Figure (4.32): Longitudinal steel strains profile for BN specimen.

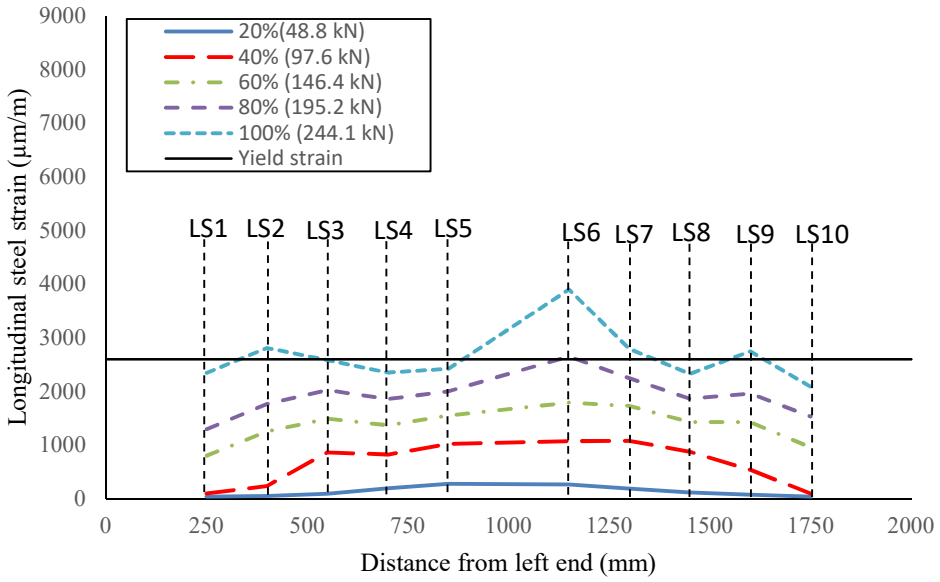

Figure (4.33): Longitudinal steel strains profile for BN-UST specimen.

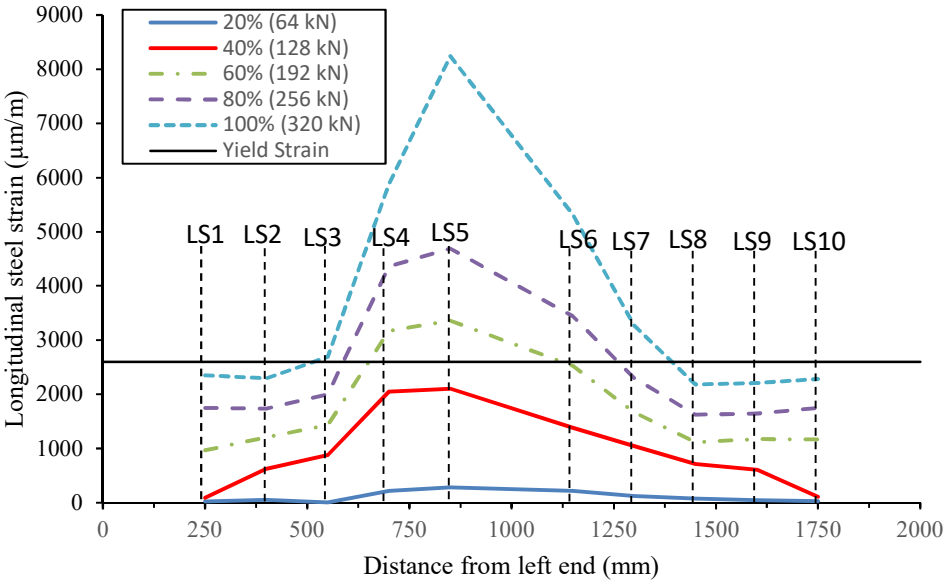

Figure (4.34): Longitudinal steel strains profile for BN-CST specimen.

In this test series, the steel bar strain gauges in both sides of the beam were located at mirrored positions with respect to the centerline of the sample in order to investigate the strain distribution along the length of the central steel bar in LWRC beams compared with identical NWRC beams. The majority of the strain gauges were placed in the shear span (see Figure (4.6)). It was noted that the tested samples showed approximately the same elongations at a low level of loading on both sides of the LWAC and NWAC samples. Variance in strain measurements was noticed at a higher level of loading in several samples, which can be imputed to the effect of diagonal shear cracks and shear distortions. The same behaviour was observed by Colalillo, (2012).

This study also revealed the concrete type had little effect on the strain profile along the longitudinal steel reinforcement. For lightweight concrete samples (BL-CST sample), the recorded strains at strain gauges close the centre of the beam are higher compared with normal weight samples. It can be concluded that the longitudinal steel reinforcement tends to increase the total load capacity of the LWAC samples due to the lower shear strength of the LWAC samples. Also, the dowel action of the longitudinal steel will increase the shear resistance in lightweight concrete samples.

It can also be noted that the control samples (BL/N) failed before achieving the yield strain of the steel, except the maximum steel tensile strain of 2830 μm/m which are recorded in LS3 (550 mm from the left end of the beam) for the BL sample. For samples strengthened with U-shaped of CFRP reinforcement, the maximum steel tensile strain of 3700 μm/m and 3900 μm/m were recorded in LS5 (850 mm from the left end of the beam) for BL-UST and LS6 (1150 mm from the left end of the beam) for BN-UST respectively.

Similarly, samples strengthened with Closed-shaped of CFRP reinforcement showed that the maximum steel tensile strain was adjacent to the mid-span. Maximum steel tensile strain of 8500 μm/m and 8200 μm/m were recorded in LS6 (1150 mm from the left end of the beam) for BL-CST and LS5 (850 mm from the left end of the beam) for BN-CST respectively. For Closed-shaped samples, the strain measurements collected from the central steel bar close the mid-span of the beam (850 mm and 1150 mm) were significantly higher than those recorded close the beam support (250 mm and 1750 mm) (see Figure (4.31) and (4.34)).

load versus strain in the central longitudinal steel reinforcement are illustrated in Figure (4.35) to (4.40). The longitudinal steel reinforcement was marginally strained at the onset of loading and start to elongate with the occurrence of flexural or shear cracks. Yielding of the longitudinal steel bar was not observed in the control normal and lightweight samples due to premature shear failure. As shown in Figures (4.35) to (4.40), the load-versus steel tensile strain trend for each tested sample consists of three zones: (i) linear zone, (ii) non-linear zone and (iii) post non-linear zone (second linear zone). During the loading stages, this strain was small and considerable straining was only observed after the flexural and shear cracks developed. Following the linear zone, diagonal shear cracks initiate, and the load-strain curve tends to form a plateau trend with marginal change in the applied load while the steel tensile strain increases. In the post non-linear zone, the longitudinal steel strain was observed to increase linearly with load before sample failure particularly for the control and U-shaped samples. In contrast, the samples with Closed-shaped showed similar response followed by another non-linear trend as a result of longitudinal steel yielding due to the samples flexural yielding. The similar load-strain response was observed for both LWAC and NWAC samples.

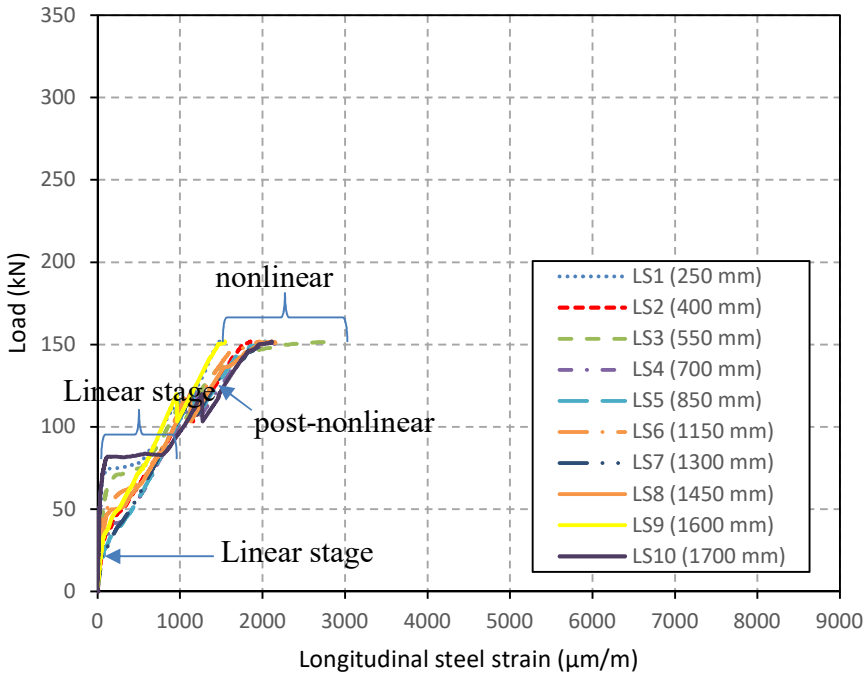

Figure (4.35): Load versus longitudinal steel strains for BL sample.

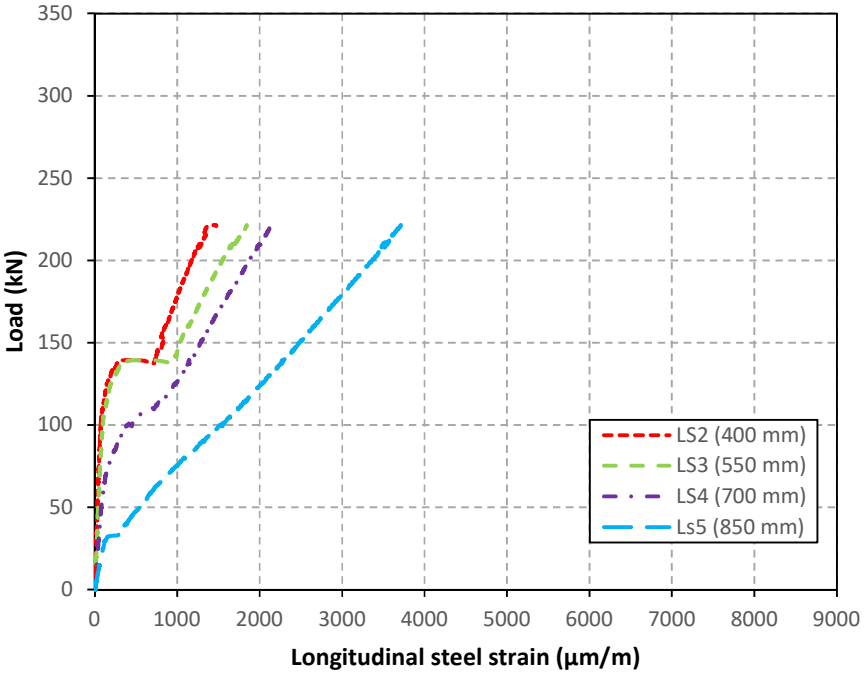

Figure (4.36): Load versus longitudinal steel strains for BL-UST sample.

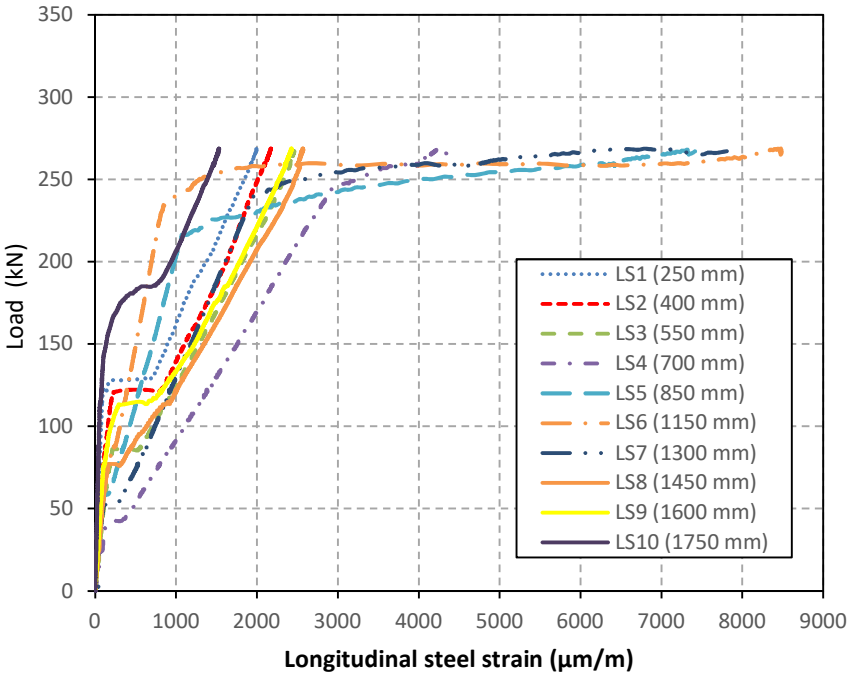

Figure (4.37): Load versus longitudinal steel strains for BL-CST sample.

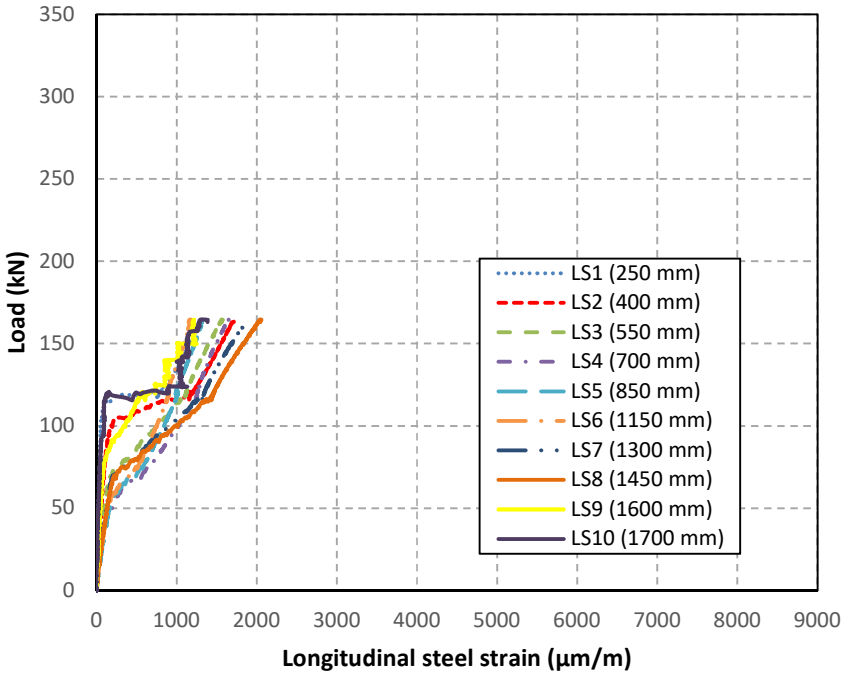

Figure (4.38): Load versus longitudinal steel strains for BN sample.

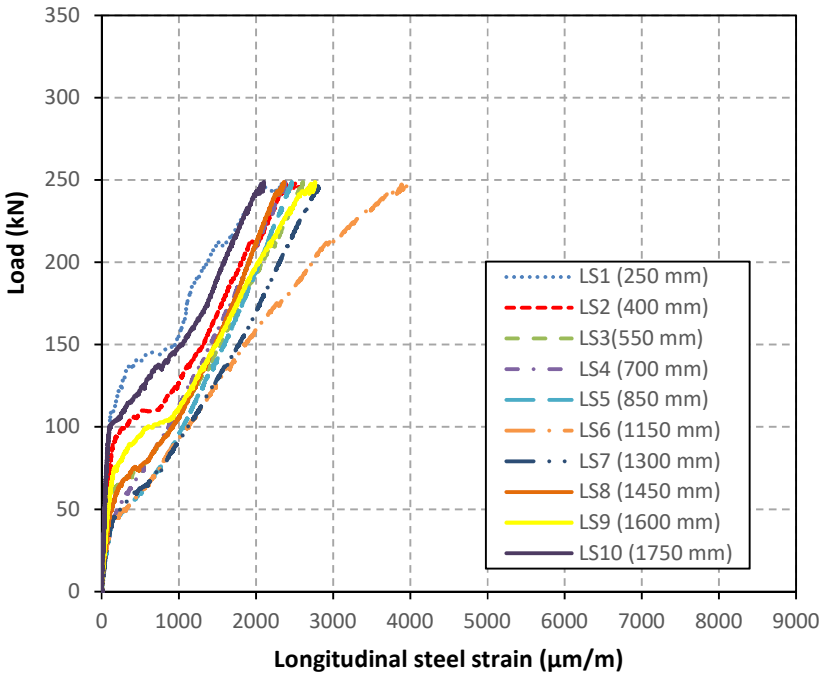

Figure (4.39): Load versus longitudinal steel strains for BN-UST sample.

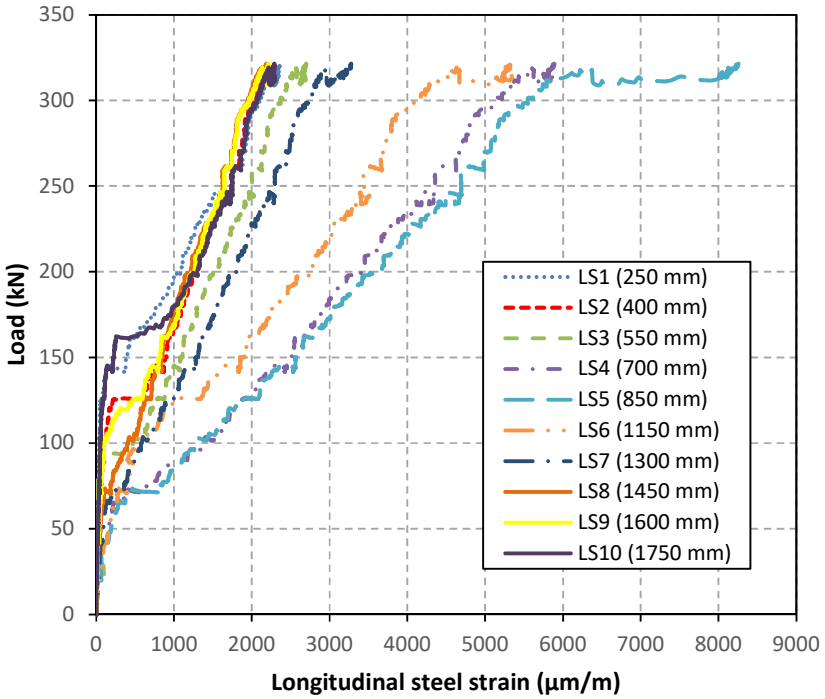

Figure (4.40): Load versus longitudinal steel strains for BN-CST sample.

4.9.5. CFRP Strain

This part of the chapter examined the variation of the average CFRP strains in the vertical direction of each of the instrumented strips for the LWRC and NWRC beams. The instrumented CFRP strips SF2, SF3, SF4, SF7, SF8 and SF9 are located at 200, 350, 500, 1200, 1350, 1500 mm respectively, from the left support of the beam (see Figure (4.9)). The average CFRP strains for the LWRC series are illustrated in Figure (4.41) and Figure (4.42), while the average strain variation for the NWRC series is shown in Figure (4.43) and Figure (4.44).

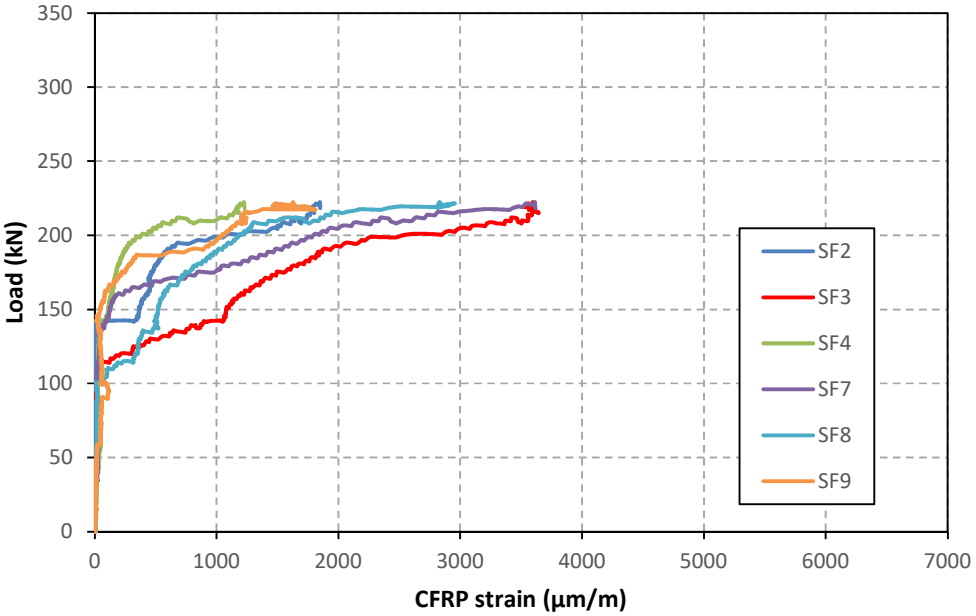

Figure (4.41): Average CFRP strains for specimen BL-UST.

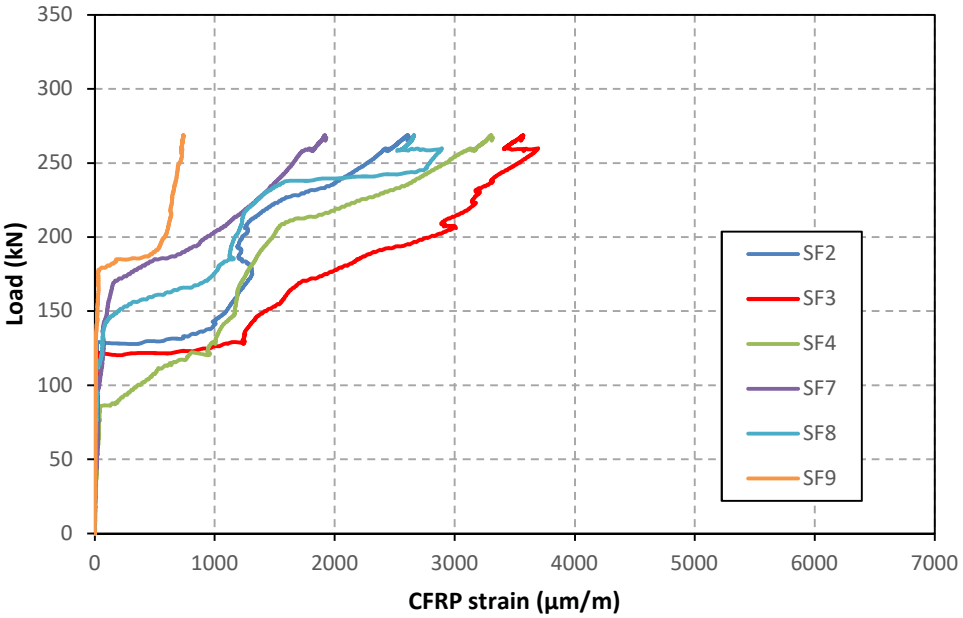

Figure (4.42): Average CFRP strains for specimen BL-CST.

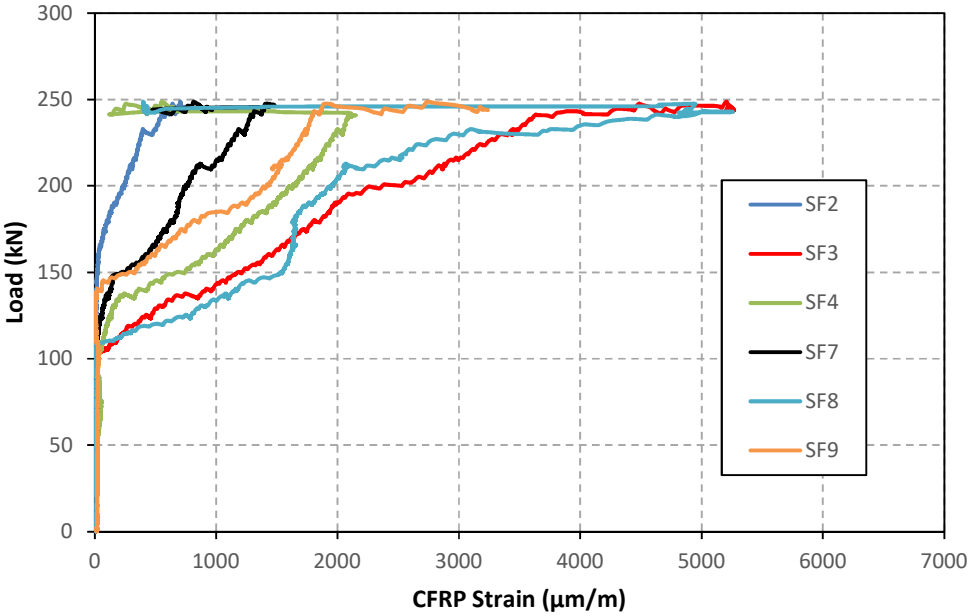

Figure (4.43): Average CFRP strains for specimen BN-UST.

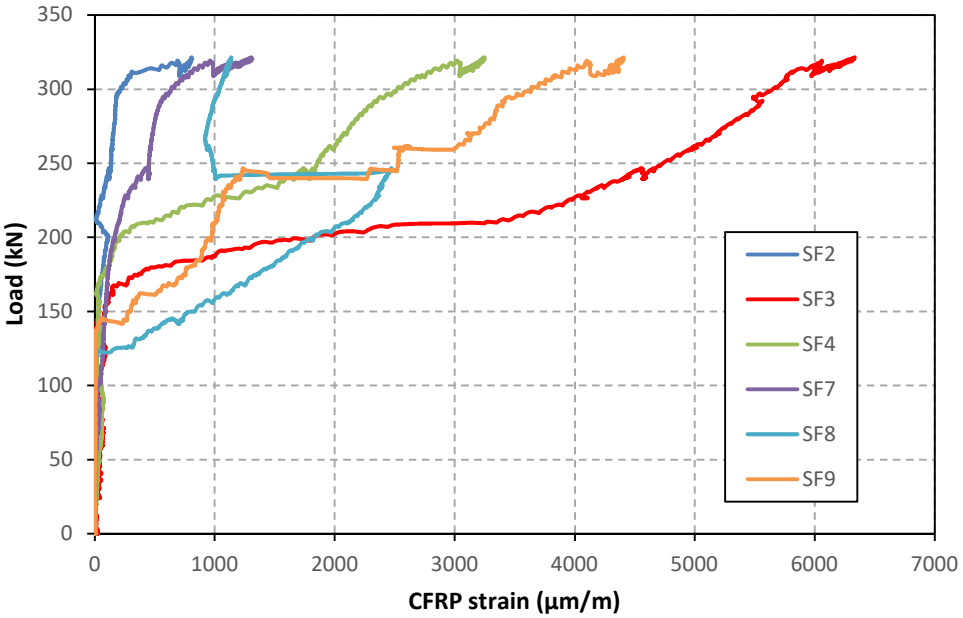

Figure (4.44): Average CFRP strains for specimen BN-CST.

Generally, the average strains response of CFRP reinforcement is characterised by two stages: the first stage is where the average CFRP strains are very small and the second stage where an abrupt increase of CFRP strains develops with further loading. The first considerable increase in CFRP strains developed at an applied load of 100 kN for BL-UST and 120 kN for BL-CST. For normal weight concrete samples, the first considerable increase in CFRP strain was observed at an applied load of 110 kN for BN-UST and 130 kN for BN-CST.

This was attributed to the CFRP strips bridging a shear crack that was noticed crossing it. This crack would subsequently initiate into the diagonal shear crack that could lead to failure of the sample. Up to this loading point (initial crack load), the contribution of the CFRP reinforcement to the total shear strength of the reinforced concrete beam is very small and can be ignored. With further loading, the crack opening increases and new shear cracks develop, leading to an increase in CFRP stress due to crack bridging forces of the CFRP strips.

Comparison through the LWRC test series shows that the samples strengthened with U-shaped reinforcement (BL-UST) had maximum average CFRP strains more than 3600 μm/m. Comparison of samples with Closed-shaped reinforcement shows that BL-CST had a maximum average CFRP strain more than 3300 μm/m. For the NWRC test series, the results show that the samples strengthened with U-shaped reinforcement (BN-UST) had a maximum average CFRP strains more than 5200 μm/m. Comparison of samples with Closed-shaped reinforcement shows that BN-CST had a maximum average CFRP strain more than 6300 μm/m.

It can be also noted that the average CFRP strain in strip no. 4 and strip no. 8 in sample BN-UST decreased as the load increased beyond the maximum load capacity. The decrease in average CFRP strain is developed by global debonding of the CFRP strips from the surface of the concrete. The load-CFRP strains collected from the strain gauges for each of the instrumented CFRP reinforcement for the LWRC and NWRC series are illustrated in Appendix A (see Figures (1) to (4)).

The maximum CFRP strains collected from strain gauges attached to the surface of the CFRP strips and the number of the strain gauge were summarised in Table (4.7). A significant variance in maximum measured CFRP strains between U-shaped samples and Closed-shaped samples. This is attributed to the premature failure of samples with U-wrapped strengthening technique.

The maximum achieved CFRP strain for the U-wrapped lightweight sample was about 4700 μm/m and for U-wrapped normal weight sample was about 5800 μm/m. In contrast, the maximum achieved strain for the Closed-shaped lightweight samples was about 5900 μm/m and 9400 μm/m. Samples with Closed-shaped CFRP reinforcement were able to sustain basically larger strains compared with U-shaped samples. This can be imputed to the end anchorages provided by the Closed-shaped system which helped the CFRP strip to achieve larger strains compared with U-shaped samples.

Comparison between lightweight and normal weight samples shows an obvious difference between the maximum measured strains as the normal weight concrete failed at higher load compared with lightweight concrete samples. The maximum recorded CFRP strains for the lightweight sample was significantly lower than the normal weight samples. This is attributed to premature debonding or rupture of the CFRP reinforcements from the lightweight concrete surface which accelerated the failure of the samples.

The results obtained in double lap shear test (see chapter three (section 3.7.3)) showed that the LWAC samples recorded higher strain reading compared with NWAC in most cases. The difference between CFRP reinforcement used to upgrade the strength of the RC beams and the CFRP bonded to the concrete surface in the bond shear test is the normal and shear stress developed in a thin layer of concrete adjacent the CFRP reinforcement. In the bond-slip test, the thin layer of concrete adjacent the FRP composite is carried a pure normal and shear stresses. While, for CFRP reinforcement used to strength the RC beam, the concrete layer underneath of the CFRP is subjected to compressive stresses parallel to the diagonal compressive strut inclination and tensile stresses perpendicular to the diagonal shear cracks inclination in addition to the interfacial shear stresses developed in FRP/concrete joint (Qu, 2005).

Generally, the stress destitution in the RC beam is much complex and may affect the CFRP-to-concrete interface, with an expectation to accelerate CFRP debonding and to minimise the maximum debonding strain. The stresses in lightweight samples are much higher and more complex. The increase in interfacial and normal stresses with increasing plastic deformation in lightweight concrete beams leads to unexpected CFRP reinforcement failures and thus leads to a reduction in the maximum debonding strains.

Table (4.7): Summary of maximum local CFRP strains at sample failure.

Sample	Maximum Shear capacity (kN)	Maximum strains at failure from strain gauges at each instrumented CFRP strips (µm/m)					
		SF2	SF3	SF4	SF7	SF8	SF9
BL-UST	218.38	4011.6 (SG 4)	4725.9 (SG 10)	2911 (SG 12)	**4728.6** (SG 17)	4216.7 (SG 25)	2217.5 (SG 28)
BL-CST	267.14	5819.4 (SG 3)	**5972.5** (SG6)	4800.3 (SG 15)	2788.3 (SG 17)	4466.5 (SG 21)	1846.85 (SG 28)
BN-UST	248.61	2120.8 (SG 3)	**5837.5** (SG 9)	1594.8 (SG 15)	1642.6 (SG 16)	846.1 (SG 25)	4919.4 (SG 28)
BN-CST	320.80	2392.98 (SG 3)	**9416** (SG 9)	7893.2 (SG 15)	2579.8 (SG20)	1948.12 (SG24)	4711.9 (SG 28)

The variation of CFRP strain cross the beam length and height can be investigated in this section. The CFRP strains collected from the strain gauges located at the mid-depth of the beam (150 mm) and the two quarter-depths of the beam (75 and 225 mm from the bottom of the beam). Figures (4.45) to (4.49) show the CFRP strains distributed over the cross section of LWRC and NWRC beams.

The trend of CFRP strains through the height of BL-UST samples (see Figure (4.45)) showed that the maximum measured strains were observed at 75 mm and at 225 from the bottom face of the beam in strip 3 (350 mm from the left support of the beam) and at mid-height of the beam in strip 7 (1200 mm from the left end of the beam). The highest measured strain was 4300 µm/m at 75 mm from the bottom face of the beam, 4700 µm/m at 225 mm from the bottom face of the beam in strip 3 and 4700 µm/m at 150 mm in strip 7. The rest of the strain gauges measured strain values between 700 µm/m - 4000 µm/m. The trend of the CFRP strain through the height of BL-CST sample (see Figure (4.46)) showed that the maximum measured CFRP strains were observed on strip 2(200 mm from the left end of the beam) at 75 mm from the bottom face of the beam and at 75 mm from the bottom face of the beam in strip 3. The highest measured CFRP strain was 5900 µm/m in strip 2 and 5800 µm/m in strip 2.

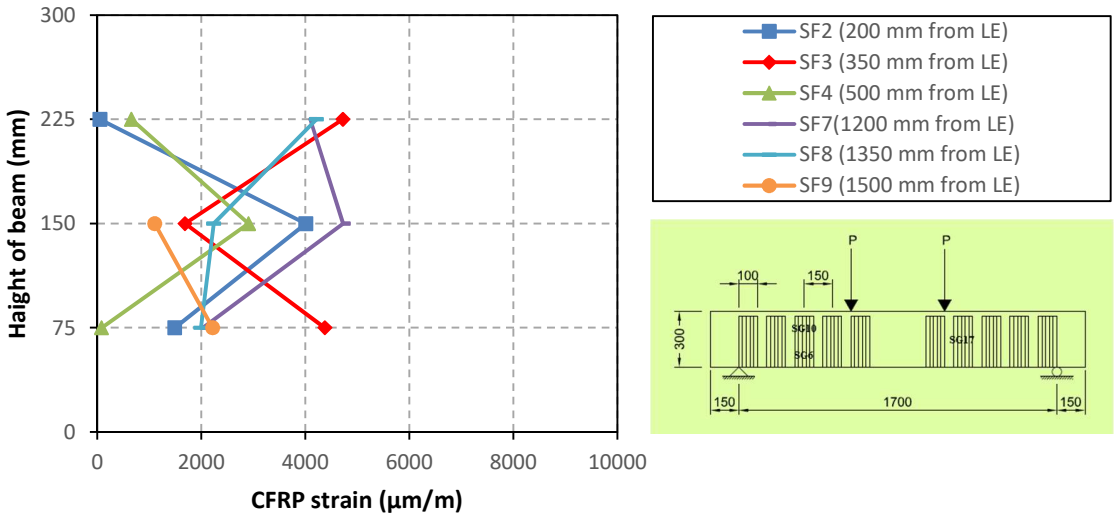

Figure (4.45): CFRP strain over the cross section of the BL-UST specimen.

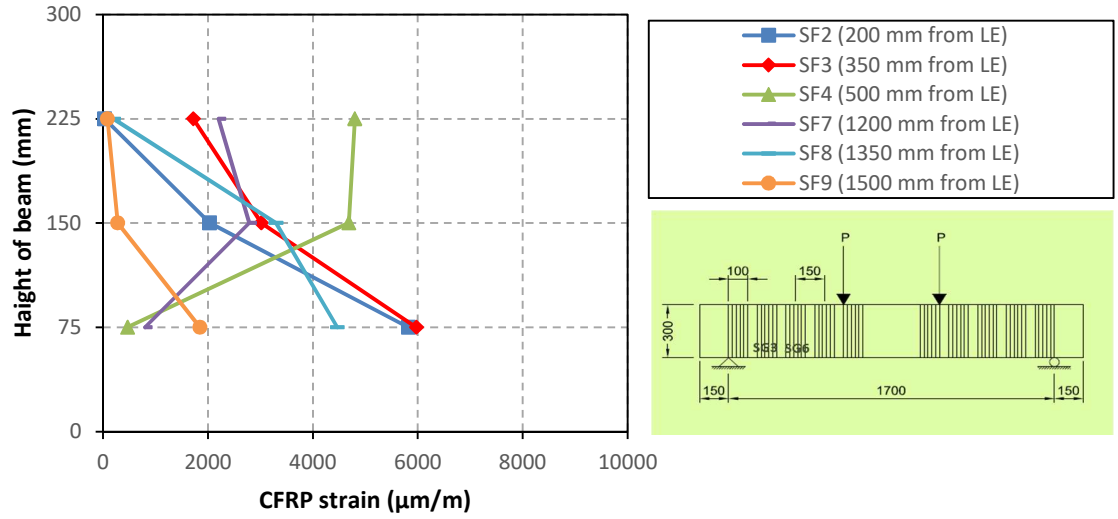

Figure (4.46): CFRP strain over the cross section of the BL-CST specimen.

The trend of the CFRP strains through the height of BN-UST sample (see Figure (4.47)) showed that the high measured CFRP strains were observed at 75 mm from the bottom face of the beam and at the mid-height of the beam (150 mm from the bottom of the beam) in strip 3 and at 75 mm of strip 9 (1500 mm from the left end of the beam). The highest measured CFRP strain was 4900 µm/m at 75 mm from the bottom face of the beam, 5800 µm/m at mid-height of the beam in strip 3 and 4900 µm/m at 75 mm in strip 9. The rest of the strain gauges measured strain values

between 660 µm/m - 3500 µm/m. The trend of the CFRP strains through the height of BN-CST sample (see Figure (4.48)) showed high measured strains were observed on strip 3 at mid-height of the beam and at 225 mm from the bottom face of the beam in strip 4. It can be noticed that the diagonal shear crack developed close the support (strip 3) of the beam and extended up to the point of load application (strip 4). The highest measured CFRP strain was 9400 µm/m at mid-height of the beam in strip 2 and 7800 µm/m at 225 mm from the bottom of the beam in strip 4.

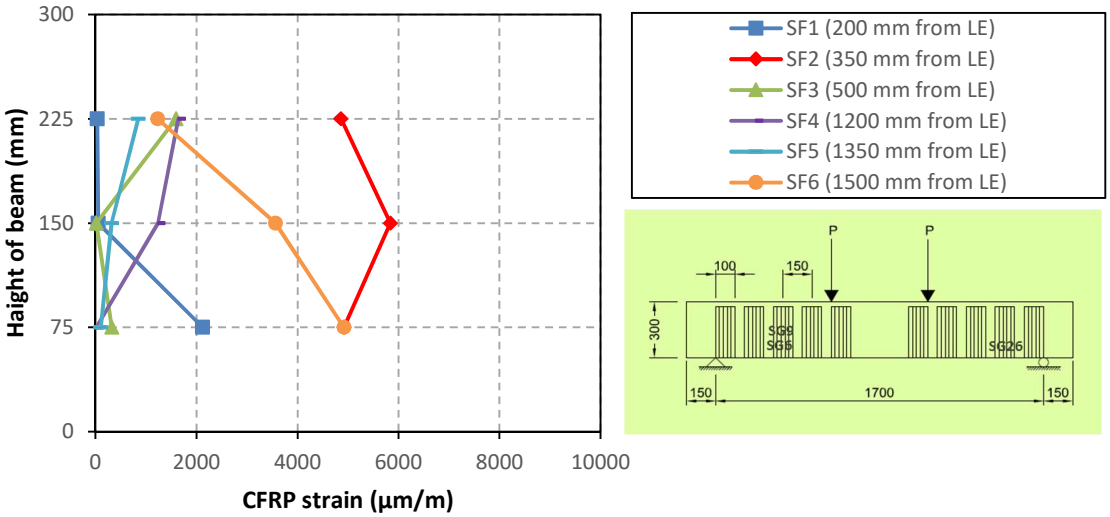

Figure (4.47): CFRP strain over the cross section of the BN-UST specimen.

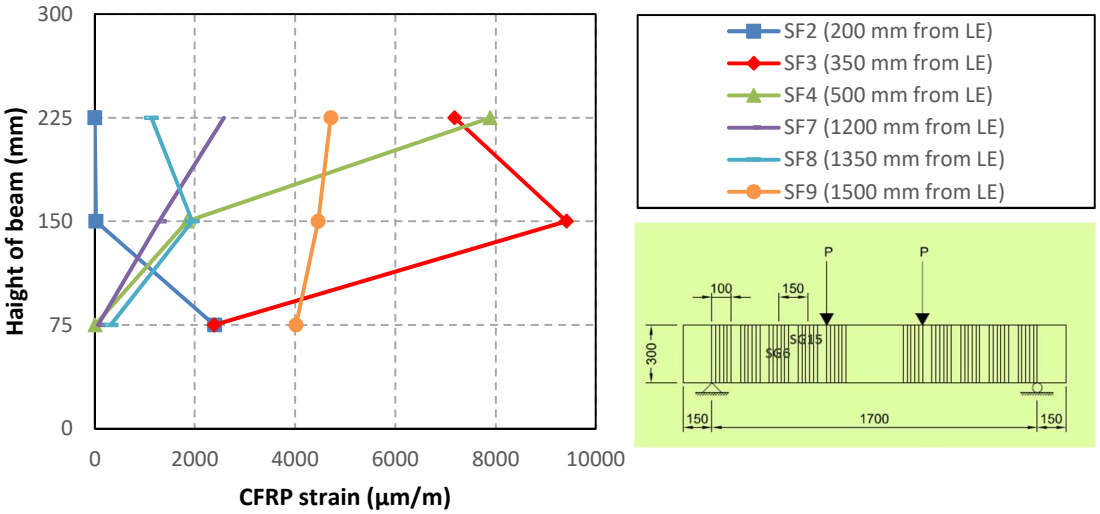

Figure (4.48): CFRP strain over the cross section of the BN-CST specimen.

The CFRP strains differ across the depth and length of the strengthened RC beams. It can be noted that the debonding between the FRP and concrete surface develops at the occurrence of the diagonal shear cracks. By bond action, stresses developed in a thin layer of concrete are travelled to the CFRP reinforcement, these stresses create tensile strains in the CFRP reinforcement across the diagonal shear cracks. As the applied load increased, the diagonal shear crack starts opening and multi-shear cracks occurred, more strains are induced in the CFRP reinforcement across these cracks. The bond stresses between the CFRP reinforcement and concrete substrate will keep increasing while the maximum bond strength is achieved and the CFRP strips detached from the concrete surface at the diagonal crack position. At this stage, the required bond length moves far away from the position of the crack plane and extended towards the top and bottom surface of the beam, more interfacial stresses occurred along the bond length away from the diagonal crack location (Monti and Liotta, 2007).

Once the complete debonding develops, no more normal and shear stresses transference cross the effective bond area. The interfacial shear stress shifts along the length of the CFRP reinforcement till achieving the far end of the beam, leading to the sudden bond failure. The CFRP reinforcement detached globally over the full depth of the beam. The CFRP strains will differ along the diagonal crack which depends on the bond length of the CFRP reinforcement above and below the diagonal crack plane (Colalillo, 2012).

Closed-shaped samples had similar mechanics of failure. However, the CFRP reinforcement achieved higher strains compared with U-shaped samples. The Closed-shaped system reduced the possibility of global debonding of the CFRP reinforcement from the surface of the concrete beam. In this study, it can be noted that there was no significant difference in behaviour in strain distribution or debonding failure mechanism between the LWAC and NWAC samples.

4.9.6. Scanning Electron Microscopy (SEM)

The scanning electron microscope (SEM) is one of the most versatile instruments available for the examination and analysis of microstructural characteristics of solid objects. The main reason for the SEM's usefulness is the high resolution that can be obtained when bulk samples are scanned. The microscope has been a useful approach in the study of cement and concrete since the early development of these materials. Le Chattelier (1882) used the microscope to the study

of cementitious materials. Le Chattelier (1882) assessed the chemical and physical aspects of hydration and setting, rather than to study cracks propagation. Tavasci (1941) successfully investigate the microscope to study the composition and structure of concrete. Tavasci's (1941) work noted a new information for the studies of cracks on the interior surfaces of cut specimens which were carried out in the 1960s. The electron microscope was apparently first used by Radczewski et al. (1939) and by Eitel (1941, 1942) to investigate the process of hydration of concrete. Although the majority of these studies were not directly related to cracks, they led the way to later studies of cracks in which electron microscopy was a powerful tool (Nemati, 1997).

In this study, microstructural examinations using a light microscope and scanning electron microscope (SEM) were conducted on samples of lightweight and normal weight concrete in order to detect the macro/micro and nano internal pore structures. Interestingly, light micrographs of lightweight concrete samples show that the path of diagonal tension cracks propagated through lightweight aggregates (see Figure (4.49a)) rather than in the concrete matrix around the aggregates as in normal weight samples (see Figure (4.50a)). This accounts for the lower tensile strength of lightweight aggregate. Hence, the aggregate interlock between the crack faces could be neglected in lightweight concrete beams and this eventually leads to the lower shear capacity of lightweight concrete beams. The diagonal failure crack path avoids the coarse aggregate in NWRC samples and the crack path always extended around the coarse aggregates due to the breakdown of the bond between the dense surface of the coarse aggregates and cement paste. The SEM micrographs of the lightweight concrete sample revealed the spherical shapes of Lytag particles with an extremely porous microstructure (see Figure (4.49b and e). It can be seen that the Lytag particles have many pore openings on their surface and the intra-particle bubbles are non-uniform, containing overgrown bubbles. In contrast, the normal weight aggregates are angular in shape with a non-porous surface (see Figure (4.50c)). Furthermore, the lightweight aggregate is surrounded by an orange coloured area (reacted zone) (see Figure (4.49a)). This is due to the chemical reaction between the lightweight particles and the cement matrix. Figure (4.49c) shows the reacted zone and the microstructure of lightweight particles, in which the voids are considerably higher than in the cement paste. Also, Figure (4.49d) illustrates the boundary between the reacted zone and the cement paste. It can also be observed that the cement paste and lightweight particles are well-bonded as illustrated in the typical microstructure of the interfacial zone for a composite of Lytag particle and cement paste (see Figure (4.49a)).

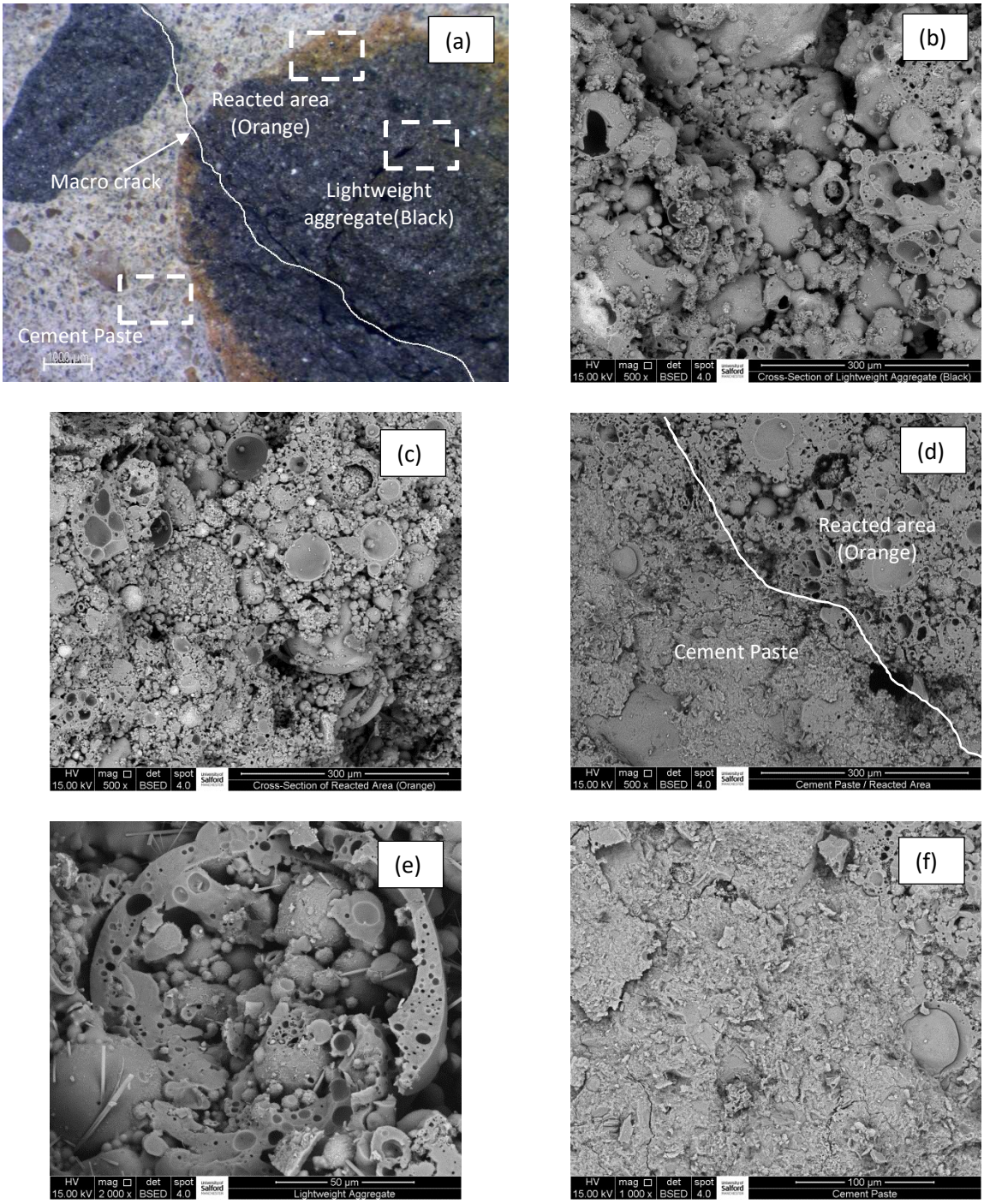

Figure (4.49): (a) Light micrograph of lightweight concrete sample, (b) SEM micrograph of lightweight aggregate, (c) SEM micrograph of reacted area of lightweight aggregate, (d) SEM micrograph of reacted area of lightweight aggregate and cement paste, (e) SEM micrograph of lightweight aggregate and (f) SEM micrograph of cement paste.

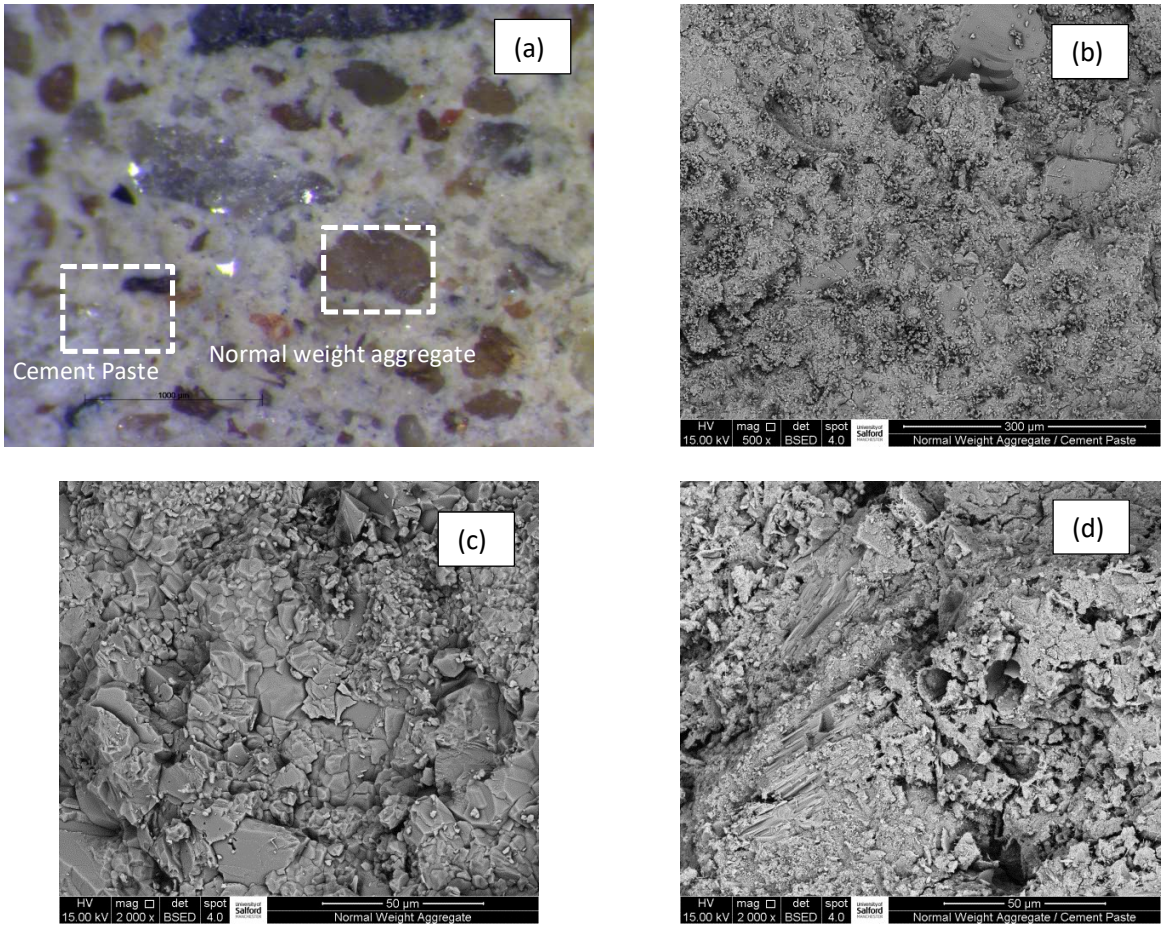

Figure (4.50): (a) Light micrograph of normal weight concrete sample, (b) SEM micrograph of normal weight aggregate and cement paste, (c) SEM micrograph of normal weight aggregate and (d) SEM micrograph of normal weight aggregate and cement paste.

Figures (4.50b and d) show that the normal aggregates are bonded with the cement paste rigidly and cracks develop around the aggregates. In this case, the aggregate interlock between the crack faces provides a significant contribution to ultimate shear carrying capacity. For the chemical analysis of the tested samples, X-ray line spectrum analysis using EDX (energy dispersive X-ray analysis system) linked with SEM and with an accelerating voltage of 9-14 kV was carried out to investigate the main chemical compounds in the lightweight concrete as shown in Figures (4.51) to (4.53). In the analysed samples, the cement paste and lightweight particles are well-connected and an almost no Ca-rich (calcium-rich) zone was observed near the aggregate particles (orange area) or inside lightweight particles (black area). It can also be noted line spectrum analysis using EDX that the aggregate particles are rich with Si (silica) while the cement paste is rich with Ca.

A slight difference in chemical composition was observed between the black and orange area. Aggregates containing silica will react with an alkali hydroxide in concrete to produce a gel that swells as it adsorbs water from the environment and the surrounding cement paste. These gels can cause sufficient expansive stress to damage concrete and develop cracking over a period of many years (Farny and Kosmatka, 1997).

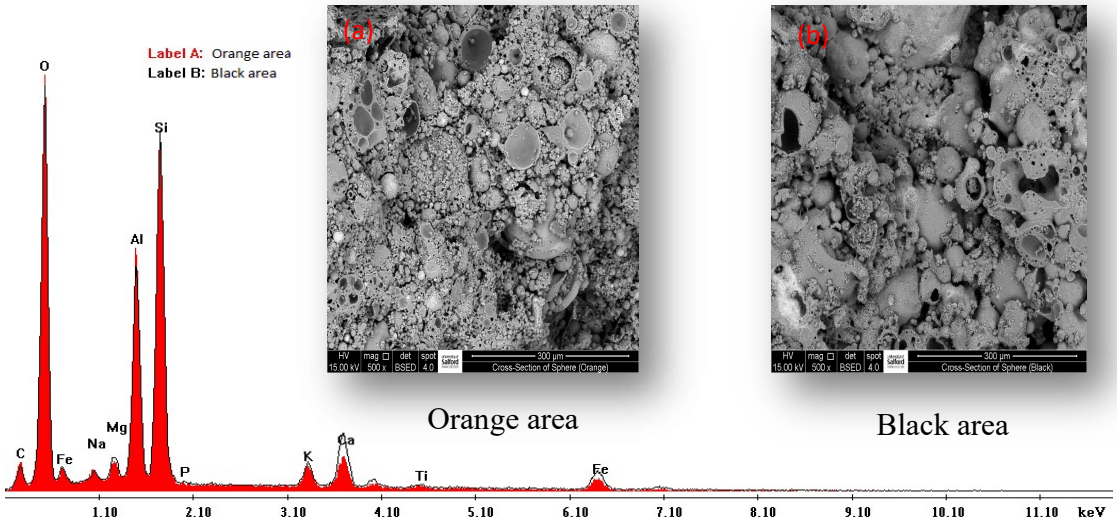

Figure (4.51): EDX spectra for: (a) orange area (b) Black area.

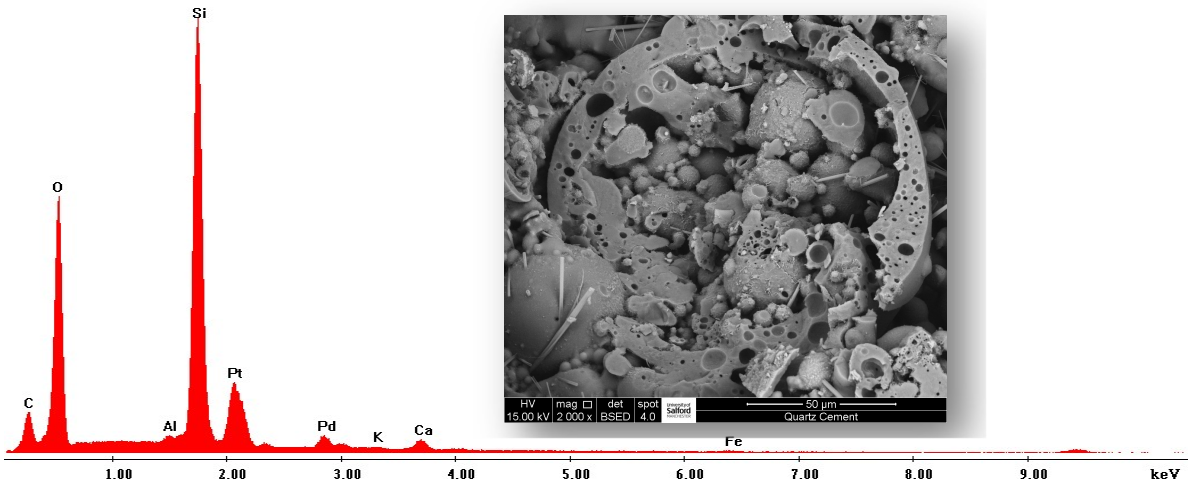

Figure (4.52): EDX spectra for Lytag particle.

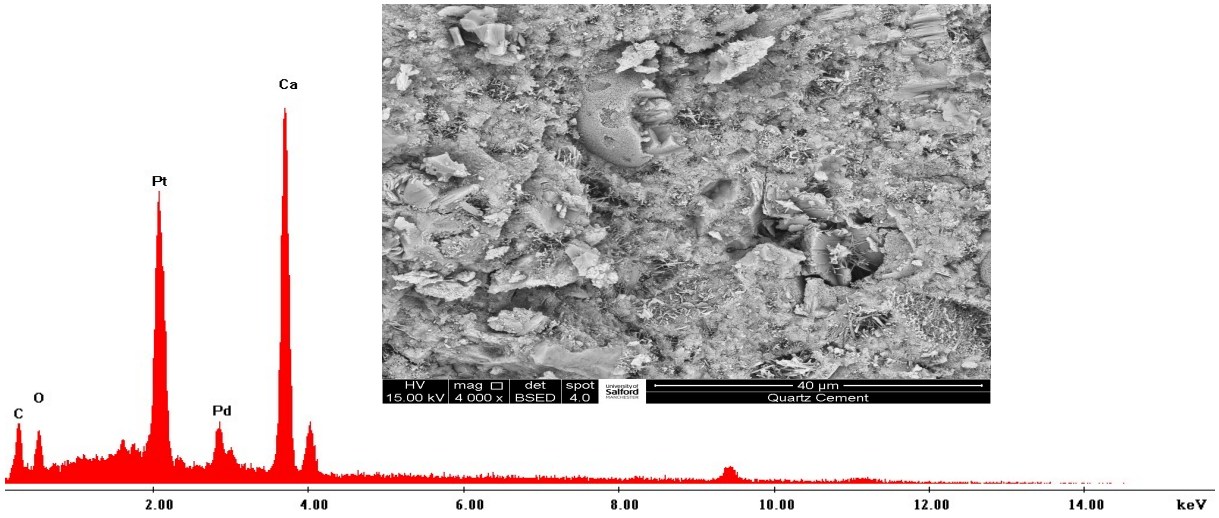

Figure (4.53): EDX spectra for cement paste.

4.9.7. Principal Strain State

To investigate the vertical, axial and shear strain as well as the principal strains in the web of LWRC and NWRC beams, a rosette strain was used in a diagonal direction across the shear cracks as shown in Figure (4.9).

Average strain measurements collected from rosette gauges attached on the left and right sides of the beam were employed to calculate the average vertical strain ε_y for each side of the beam. Strain measurements collected from the axial directions (horizontal directions) of each rosette in both sides of the beam were averaged to calculate the average horizontal strains ε_x. The average 45° diagonal strain measurements were employed to calculate the corresponding shear strains γ_{xy}. The principal strains, ε_1 and ε_2, can be calculate using the Mohr's circle of strain (see Figure (5.55)) as follows (Equation (4.3) and (4.4)):

$$\varepsilon_1 = \frac{1}{2}(\varepsilon_x + \varepsilon_y) + \frac{1}{2}\sqrt{(\varepsilon_x - \varepsilon_y)^2 + {\gamma_{xy}}^2} \quad (4.3)$$

$$\varepsilon_2 = \frac{1}{2}(\varepsilon_x + \varepsilon_y) - \frac{1}{2}\sqrt{(\varepsilon_x - \varepsilon_y)^2 + {\gamma_{xy}}^2} \quad (4.4)$$

The angle of principal strain is calculated by the following equation (Equation (4.5)):

$$\theta = \frac{1}{2}\tan^{-1}\left(\frac{\gamma_{xy}}{\varepsilon_y - \varepsilon_x}\right) \tag{4.5}$$

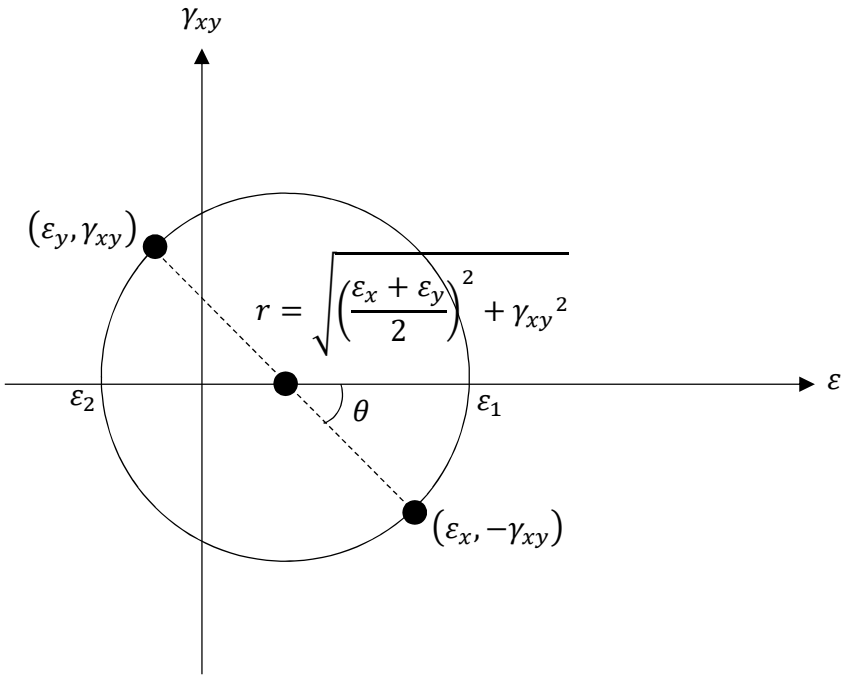

Figure (4.54): Moher's circle strain state.

Based on the previous equations (Megson, (2005)), the strains and principle strain inclinations measured before sample failure are summarised in Table (4.8). Generally, the average axial strains ε_x, the vertical strain ε_y and the diagonal shear strain γ_{xy} as well as the principal strain ε_1 and ε_2 are higher for normal weight samples compared with lightweight samples. It can also be noted that the mean horizontal CFRP strains ε_x, the vertical CFRP strains ε_y and the shear CFRP strains γ_{xy} are significantly higher at the maximum load for the samples with Closed-shaped compared with the samples strengthened with U-shaped reinforcement. This accounts for the higher shear capacity reached in Closed-wrapping samples.

For the Closed-shaped sample, it can also be noted that the principal strains are higher at failure for samples with Closed-shaped than U-shaped. The average angles of the principal strain θ are approximately the same for samples with different concrete type and strengthening techniques.

Table (4.8): Summary of strains in xy-axis and principal inclinations before samples failure.

Sample	Average strain in xy-axis (μm/m)						Principal strain (μm/m)					
	Left side of the beam			Right side of the beam			Left side of the beam		Right side of the beam		Principal inclinations θ	
	ε_x	ε_y	γ_{xy}	ε_x	ε_y	γ_{xy}	ε_1	ε_2	ε_1	ε_2	θ_1	θ_2
BL-UST	416	1291	2864	389	2849	2678	2350	-643	3437	-199	36^0	24^0
BL-CST	619	4544	5680	711	2484	3657	6033	-870	3629	-434	28^0	32^0
BN-UST	583	3184	3991	410	2293	3178	4265	-498	3198	-495	28^0	30^0
BN-CST	875	6564	8660	1338	2848	4550	8900	-1461	4490	-304	28^0	36^0

4.10. Summary

From the shear tests results and analysis, a number of conclusions can be derived from work presented in this chapter.

4.10.1. Shear Strength

- In this test, the shear strength gained due to CFRP reinforcement for lightweight samples was less than the normal weight concrete samples. This is due to lower concrete surface tensile strength and aggregate interlock which increase the stresses in CFRP reinforcement and at the concrete-CFRP interface. An increasing in interfacial and normal stresses leads to CFRP debonding and unexpected CFRP rupture failures.

4.10.2. Load-Displacement trend

- The load-displacement trends described by the following stiffnesses zone: elastic zones, flexural cracks zone, and shear cracks zone. The elastic and flexural stiffness zones were

uninfluenced by the concrete type and strengthening configurations, whilst the shear stiffness zone was stiffer for NWAC samples compared with LWAC samples. The load-displacement response for LWAC samples is flatter than those of NWAC samples with identical CFRP strengthening configurations.

- The shear stiffness zone was influenced by the strengthening techniques, the LWAC and NWAC samples strengthened with Closed-shaped showed a stiffer response compared with U-wrapped samples.

4.10.3. Failure Modes and Crack Pattern

- Shear failures were developed by the loss of aggregate interlock for the control samples and failure in CFRP reinforcement for strengthened samples. The test observations revealed that the controlled and U-shaped LWAC and NWAC samples were failed immediately after reaching maximum load carrying capacity. This was due to the fact that the crack bridging effect of diagonal crack was not available or fully reached its capacity in controlled and U-shaped retrofitted system respectively. However, both Closed-shaped LWAC and NWAC samples exhibited plastic behaviour before the rapture of the CFRP sheets.

- The test observations showed that there was virtually no difference between the lightweight beams and their normal weight companions regarding failure modes and shear cracks inclinations. However, it was noticed that the path of diagonal tension cracks on the tested LWAC samples extended through lightweight aggregates rather than in the concrete matrix around the aggregates as in NWAC samples. It can be also concluded that the LWAC samples had higher crack widths due to lower aggregate content at the primary shear crack interface.

4.10.4. Longitudinal Steel Strains

- The test results showed that the concrete type had little effect on the longitudinal steel straining. It can be noted that the strain gauges in the central steel bar of the lightweight concrete samples showed slightly higher strain readings compared with normal weight concrete samples. It can be concluded that the longitudinal steel reinforcement tends to increase the shear capacity of the lightweight concrete beams samples due to the lower shear strength of the lightweight concrete.

4.10.5. CFRP Reinforcement Strains

- Comparison between LWAC and NWAC samples shows a clear variance between the maximum recorded CFRP strain; the samples cast with lightweight concrete failed at lower load compared with normal weight samples. This is attributed to higher normal and interfacial shear stress developed in the CFRP-concrete interface at the crack interface leading to premature debonding or rupture of the CFRP reinforcement from the concrete surface, thereby accelerating the sample failure.
- Samples with Closed-shaped CFRP reinforcement experienced higher CFRP strains compared with U-shaped sample due to the premature debonding of the CFRP reinforcement from the surface of concrete at a lower load. The maximum recorded strain for the Closed-shaped LWAC and NWAC samples which failed by CFRP rupture was about 5900 μm/m and 9400 μm/m, respectively.

CHAPTER FIVE

FINITE ELEMENT ANALYSIS

5.1. Introduction

Finite element (FE) modelling techniques have significantly extended the ability to numerically simulate the behaviour of the actual physical models related to different structural difficulties, as The FE model superseded the actual member with an identical numerical model consisted of discretised node-linked elements. This chapter presents the finite element modelling of the experimental bond-slip and reinforced concrete normal and lightweight concrete beams using the ANSYS Ver.12 (ANSYS, 2009) software package.

Overall, the outcomes and methods of analysis are identical employing other finite element software. Each finite element software possesses his special elements and methods of analysis that require being utilised correctly. The user or the developer should be fully understood with the FEA stuffs needed to start modelling from simple to more advanced issues to achieve reliableness an employing of FEA techniques to understand the structural behaviour of the reinforced concrete structures with easy tools such as FE models (Damian et al., 2001).

Three-dimensional non-linear finite element models that use a smeared cracking approach are presented in this study. Solid, shell and link elements are used to model concrete, adhesive, CFRP composites and steel materials. The material properties of the experimental modelling were presented in Chapters 3 and 4 of this thesis. In the broadest sense, this model comprises all the nodes, elements, material properties, real constants, boundary conditions, and other characteristics that are required to simulate the physical model. The outcomes of the FE models are compared with those collected from the actual bond-slip and beam shear models. The failure modes and the smeared cracks distribution noticed in the FE models are also compared with those observed in the actual physical models.

5.2 Material Properties and Element Types

5.2.1 Concrete

Concrete is a quasi-brittle material and has different behavioural characteristics in compression and tension. Figure (5.1) shows a typical stress-strain curve for NWC. In the crushing zone, the stress-strain trend for concrete is linear/elastic till approximately 30% of the maximum crushing concrete strength. Beyond this stage, the compressive stress of concrete progressively rises up to the maximum crushing strength. Once it reaches the maximum compressive strength σ_{cu}, the trend steadily inclines into a softening region, and finally crushing failure develops at an ultimate concrete strain ε_{cu}. In the cracking zone, the stress-strain curve for concrete is linear-elastic up to the maximum cracking or tensile strength. Beyond this stage, the concrete cracks and the strength vanishes gradually to zero (Bangash, 1989). The cracking strength (tensile strength) of NWC is usually (8-15%) of the concrete crushing strength (compressive strength of concrete) (Shah, et al. 1995) and between (5-15%) of the concrete crushing strength in case of lightweight concrete (EuroLightCon, 1998).

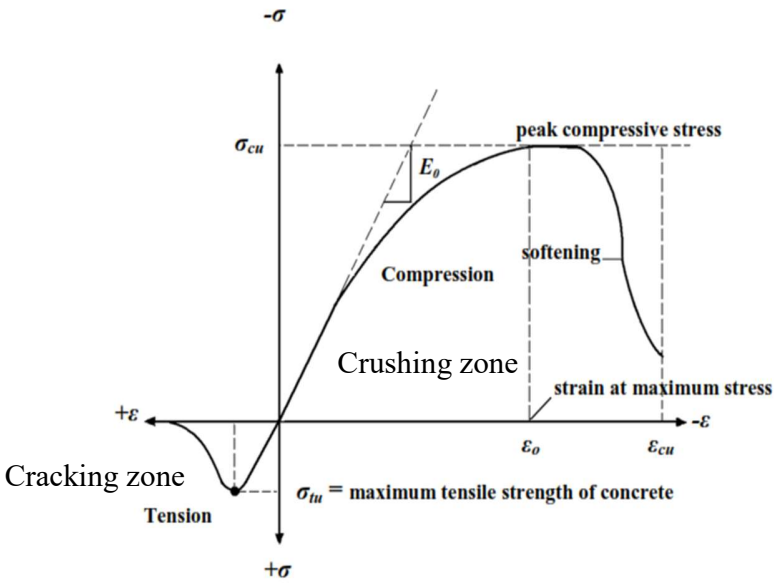

Figure (5.1): Typical uniaxial compressive and tensile stress-strain curve for concrete (Bangash, 1989).

Stress-strain curves for LWAC are generally characterised by a more linear ascending trend, more limited plastic strain and a steeper descending trend compared with NWAC as shown in Figure (5.2). The linear, brittle response is usually improved with increasing the strength of

concrete. The more linear and brittle behaviour for LWAC is possible assigned to a higher compatibility between the LWA and the surrounding concrete paste (CEB / FIP, 1983).

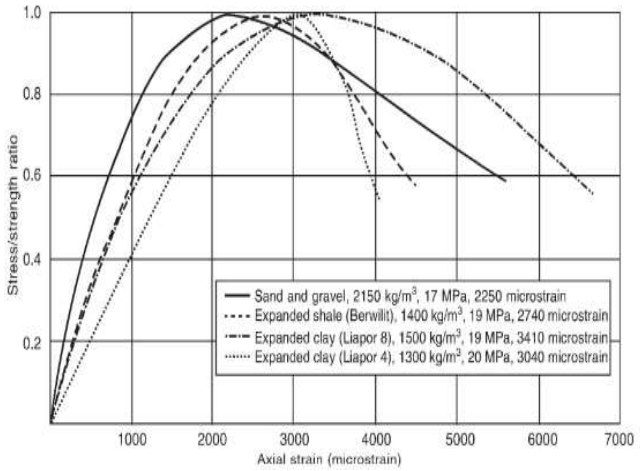

Figure (5.2): Stress–strain relationships for LWAC and NWAC (CEB / FIP, 1983).

5.2.1.1. Element type

The SOLID65 or 3-D reinforced concrete solid element type is used to model concrete in ANSYS (2009), the element can crack or crush at the 8 integration points. Also, cracking is based on exceedance of a principal tensile stress. This solid element has six faces and eight nodes with three translations in each node; three degrees of freedom in the nodal x, y, and z orientations at each node. The element is able to predicate the plastic strain, creep, cracking in concrete element with three orthogonal orientations, and concrete crushing (ANSYS 2009). The geometry and node definitions for this element are shown in Figure (5.3).

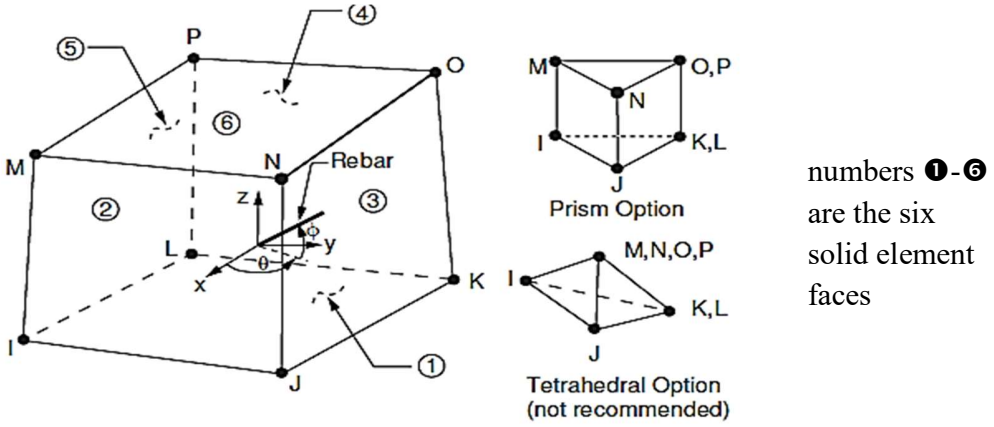

Figure (5.3): SOLID65 geometry (ANSYS 2009).

The SOLID65 element requires linear isotropic and multi-linear isotropic material properties to simulate the concrete behaviour (ANSYS, 2009). In this study, the multi-linear isotropic material uses the Von-Mises failure criteria combined with the William and Warnke (1975) model were employed to simulate the non-linear behaviour and failure criteria of normal and lightweight concrete. In addition, there are other variables needed to be set to define the William and Warnke model (William and Warnke, 1975). The following subsection will explain in detail the properties of the concrete material using ANSYS.

5.2.1.2. Linear Isotropic Properties

The experimental values of the modulus of elasticity (E_c) and the assumed values of the Poisson's ratio (υ) are used to specify the linear isotropic properties of the LWAC and NWAC used to simulate the double-lap shear test and beam shear tests.

5.2.1.3. Non-linear Material Properties

To model the non-linear properties of concrete using ANSYS, the following input data is required to be defined:

1. Coefficient of shear transfer (β_t).
2. Uniaxial concrete compressive strength (f_c').
3. Uniaxial concrete tensile strength (flexural tensile strength or modulus of rupture (f_r).
4. Concrete stress-strain in compression.

The coefficient of shear transfer varies between 0.0 to 1.0, the value of 0.0 representing a complete loss of shear transfer (smooth crack) and 1.0 representing no loss of shear transfer (rough crack) (ANSYS 2009). The coefficient of shear transfer for open crack ranged between 0.05 and 0.5 in several studies of RC members. The coefficient of shear transfer values varied between 0 and 1, but a value higher than 0 is vital to avoid numerical issues (Isenburg, 1993). In this study, the coefficients of the closed and open shear crack were assumed as 1.0 and 0.2, respectively (Chansawat et al. 2009). A summary of the lightweight and normal weight concrete properties used in the double-lap shear finite element models are shown Table (5.1) and in chapter three (see Table (3.9)). In this study, the main differences in modelling LWAC and NWAC specimens are in the modulus of elasticity and uniaxial tensile stress respectively, which

are approximately 77% and 85% of that of NWAC respectively. These two properties lead to significant differences in maximum bond strength between the LWAC and NWAC specimens.

Table (5.1): Summary of material properties for concrete used for DLS test.

Concrete type	f_c' (MPa)	β_t	υ
LWAC	32.08*	0.2	0.2**
NWAC	33.28*	0.2	0.2**

* The concrete cylinder compressive strength was calculated based on Equation (5.3).

** The Poisson's ratio (υ) of the NWAC and LWAC was assumed as 0.2 (ACI 213R, 2003).

ANSYS requires the uniaxial compression stress-strain relationship of concrete to model the non-linear response of concrete. The ideal stress-strain trend for LWAC and NWAC consists of two trends: an ascending trend and a descending or the softening trend. A convergence issue was obtained by many researchers when using the descending trend of the stress-strain curves of concrete in simulating the non-linear behaviour of concrete in ANSYS (Damian et al. 2001, Wolanski 2004). Therefore to avoid such issues, only the ascending trend of the compression stress-strain curve of concrete is considered in this research. The points on the ascending trend of the compressive multi-linear isotropic stress-strain curve are computed based on the following equations (Equation (5.1) and (5.2)) (Gere and Timoshenko, 1997).

$$f = \frac{E_c . \varepsilon}{1 + \left(\frac{\varepsilon}{\varepsilon_0}\right)^2} \tag{5.1}$$

$$\varepsilon_0 = \frac{2f_c'}{E_c} \tag{5.2}$$

Where,

f = Stress at any strain, ε in (MPa),

ε= Strain at any stress, f,

ε_0= strain at the maximum compressive stress, f_c'. The stress-strain curve for the LWAC and NWAC calculated according to the above equations and used in the bond-slip finite element models shown in Figure (5.4). In this study, the concrete cylinder compressive strength is calculated using Equation (5.3):

$$f_c' = 0.8 f_{cu} \tag{5.3}$$

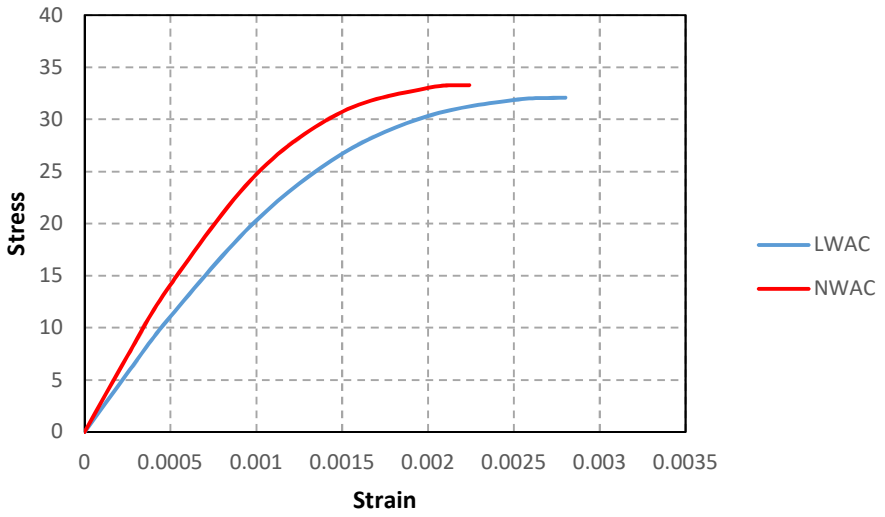

Figure (5.4): Concrete stress-strain curve for DLS test models**.**

5.2.2 Steel Reinforcement and Steel Plates

The properties of the threaded central steel bar used in the FE models of the bond slip tests, such as the modulus of elasticity and yield stress of the steel bar were obtained based on the experimental test results carried out as a part of this study. A Poisson's ratio of 0.3 was used for the threaded steel bar. Material properties for the steel bars for all bond-slip models are summarised in Table (5.2).

Table (5.2): Summary of material properties of steel bar.

Modulus of Elasticity (E_s) MPa	Yield Stress (f_y) MPa	Poisson's ratio (v)
205,000	275	0.3

The LINK8 element is used for the central steel reinforcing bar in the bond-slip model and all reinforcement in the beam shear test. LINK8 is a 3-D spar which may be used in wide range of engineering applications such as truss models, links, sagging cables, springs, etc. The three-dimensional link element is a uniaxial tension-compression element with three degrees of freedom at each node: translations of the nodes in x, y, and z-directions. Bending is not included in this element as those in a pin-jointed structure. Plasticity, creep, swelling, stress stiffening, and large deflection abilities are included in this element (ANSYS 2009). This element is used, in

this study, to simulate the behaviour of central steel bar used in the bond-slip models and all the steel reinforcement in beam shear tests. The geometry, node locations, and the coordinate system for this element are shown in Figure (5.5).

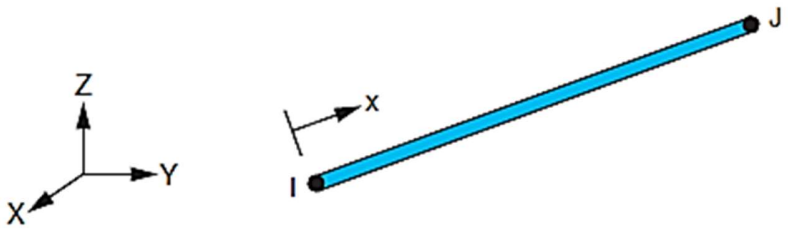

Figure (5.5): LINK8 geometry (ANSYS, 2009).

SOLID45 is used to model the steel plates which are used at beam support and load locations in the finite element models to simulate the actual steel load spreader and support plates adopted in the beam shear tests. The element has six faces and eight nodes and each node with three translational degrees of freedom in the nodal x, y and z directions as shown in Figure (5.6). It has hyperelasticity, plasticity, stress stiffening, large deflection, creep, and large strain abilities (ANSYS, 2009).

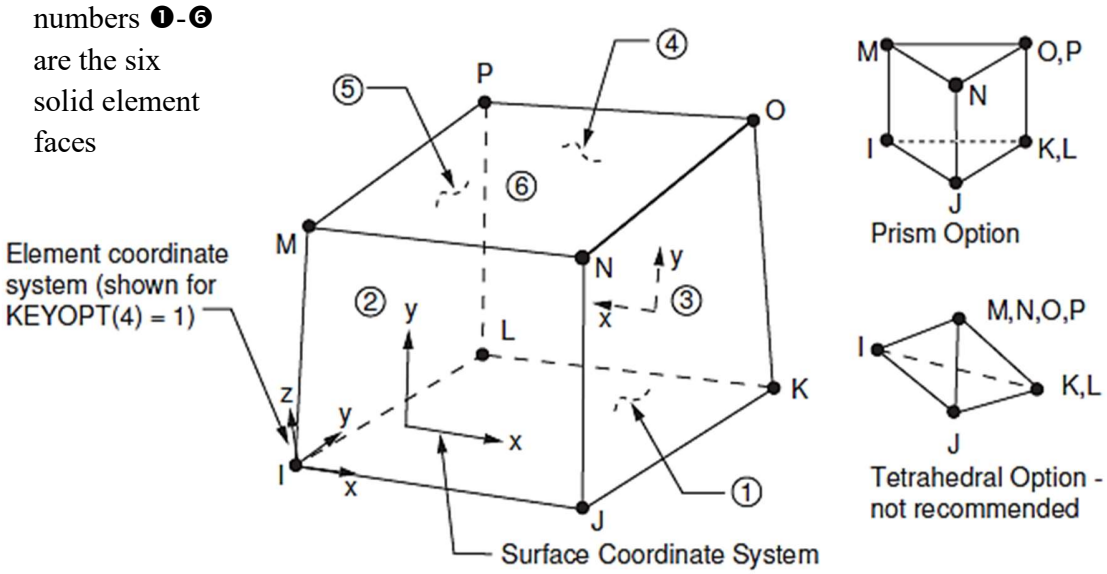

Figure (5.6): SOLID45 geometry (ANSYS, 2009).

5.2.3. CFRP Composites and Adhesive Material

In this study, linear elastic properties were assumed for both CFRP composites and adhesive material used to bond CFRP composite to the concrete surface. The CFRP composites are orthotropic materials, the properties of the CFRP composites are the same in any direction perpendicular to the principal fibres direction. It means the properties of CFRP in the *y*-direction are identical to the fibre's property in the *z*- direction, assuming the x-direction is parallel to the direction of the principal fibres in the CFRP reinforcement (Damian et al. 2001). To model CFRP composites using ANSYS the following input data for material properties required definition:

1. A number of CFRP layers.
2. The thickness of CFRP layer.
3. The direction of CFRP layer.
4. The FRP modulus of elasticity in each direction (E_x, E_y, *and* E_z).
5. The FRP modulus of shear in each plane (G_{xy}, G_{yz}, *and* G_{xz}).
6. Poisson's ratio in each plane (v_{xy}, v_{yz} *and* v_{xz}).

The adhesive material is isotropic and has the same properties in all directions, for example, the modulus of elasticity and Poisson's ratio, are similar in all directions of the adhesive material. Thus, no special symbols are needed to indicate to directional properties. A summary of material properties of CFRP and adhesive are shown in Table (5.3). The shear modulus, G of the CFRP composite sheet and the adhesive material are calculated based on the following Equation (Equation (5.4)):

$$G = \frac{E}{2(1+\upsilon)} \tag{5.4}$$

Table (5.3): Summary of material properties of CFRP and adhesive.

Material	Elastic modulus GPa	Poisson's ratio	Shear modulus GPa
CFRP composites	*Ex=240* *Ey=31* *Ez=31*	*vxy= 0.22* *vyz= 0.30* *vxz=0.22*	*Gxy=98.360* *Gyz=11.923* *Gxz=98.360*
Adhesive	*5*	*0.3*	*1.92*

A layered solid element, SOLID46, is used to model the CFRP sheet and the adhesive in the bond-slip and beam shear FE models. The geometry, node locations, and the coordinate system for this element are shown in Figure (5.7). The element includes up to 250 different material layers (ANSYS 2009). The element has three degrees of freedom at each node: translations in the nodal x, y, and z directions. As an alternative SHELL63 4-node 2D elements were used to model the thin layer of CFRP sheet in some models in bond-slip tests. The element has six faces and six degrees of freedom at each node: translations in the nodal x, y, and z directions and the rotations about the nodal x, y and z-axis. This element able to model the bending and membrane (ANSYS 2009). The geometry, node locations, and the coordinate system for this element are shown in Figure (5.8).

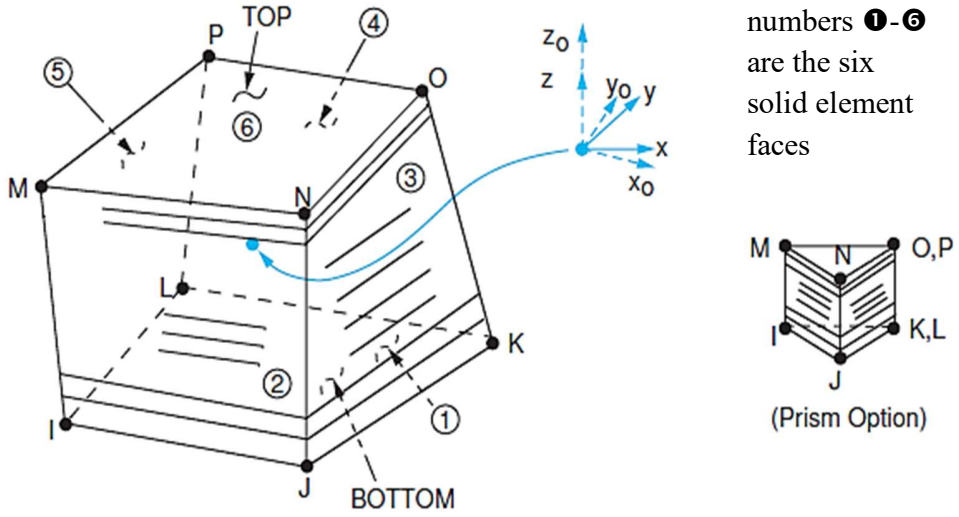

Figure (5.7): SOLID46 geometry (ANSYS, 2009).

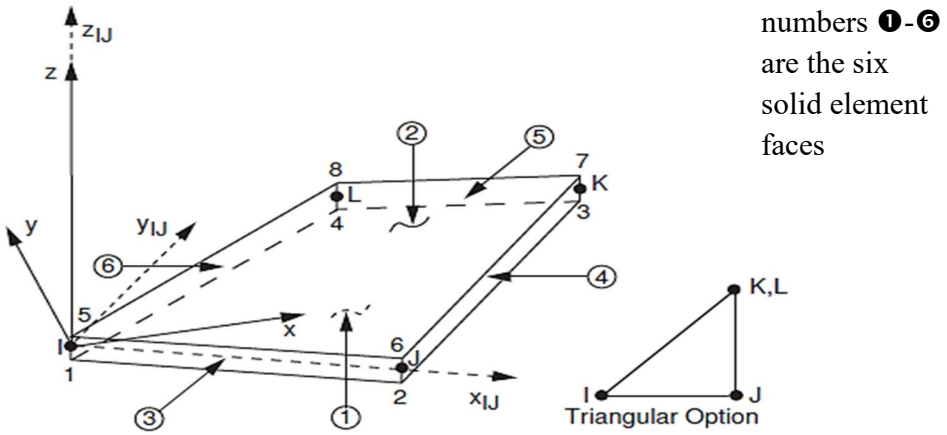

Figure (5.8): SHELL63 geometry (ANSYS, 2009).

5.3. Nonlinear Solution

In the nonlinear analysis, the total load applied to a finite element model is divided into a series of load increments called load steps. At the completion of each incremental solution, the stiffness matrix of the model is updated to show nonlinear changes in structural stiffness before going to the next load step. The ANSYS program uses the Newton-Raphson equilibrium iterations for updating the model stiffness. Newton-Raphson equilibrium iterations provide convergence at the end of each load increment within tolerance limits. Figure (5.9) shows the use of the Newton-Raphson method in a single degree of freedom nonlinear analysis (ANSYS, 2009).

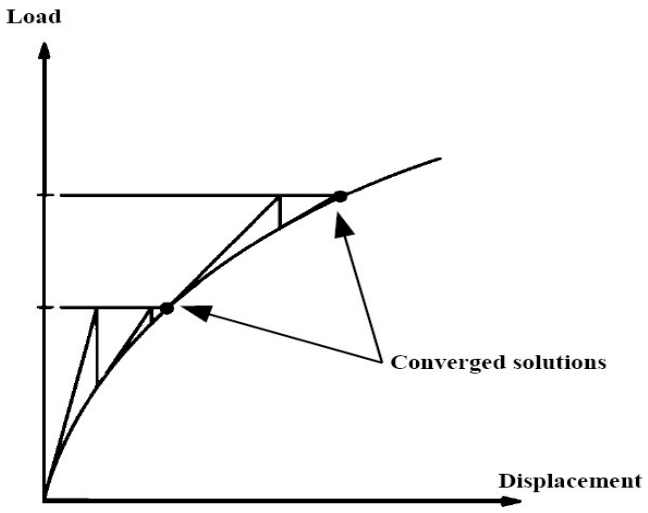

Figure (5.9): Newton-Raphson iterative solution (2 load increments) (ANSYS, 2009).

Before each solution, the Newton-Raphson approach evaluates the out-of-balance load vector, which is the variance between the loads corresponding to the element stresses and the applied loads. Subsequently, the program adopts a linear solution, using the out-of-balance loads, and examine for convergence. If convergence criteria are not successful, the out-of-balance load vector is re-assessed, the stiffness matrix is updated, and a new solution is attained. This process will be repeated until the converges problem is solved (ANSYS, 2009). In this research, the force and displacement convergence criteria were used and the default limitations of the convergence were firstly chosen by the ANSYS software.

5.4. Finite Element Models (Bond-Slip Model)

A full specimen was modelled to simulate the bond-slip specimens by creating two concrete blocks (200x 140x 90) mm disconnected at the middle contact surface by (1) mm gap as shown in Figure (5.10). The concrete blocks were re-joined by a thin layer of adhesive (1 mm thick) and CFRP composite (0.1178 mm thick /per one layer).

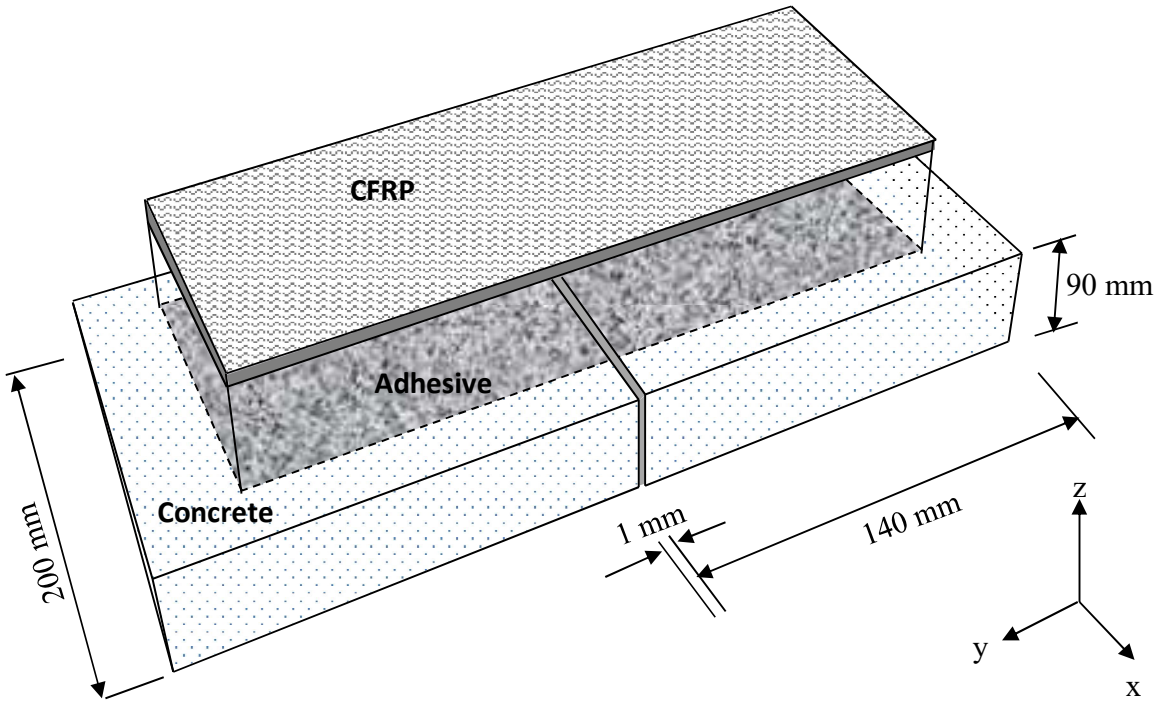

Figure (5.10): 3D Representation of the Bond-Slip FE Model.

Firstly, the FEA needs meshing of the proposed model, and after solving the problem, stresses and strains are obtained at integration points located within the model's elements. Chosen of an appropriate mesh density is critical in the FEA modelling. A convergence of results is achieved when a sufficient number of elements are employed in the simulated model (i.e. a mesh sensitivity study), this is can be obtained when the using finer mesh has marginal influence on the FE results (Damian et al., 2001). In this study, a convergence study was employed to choose the best mesh density. Figure (5.11) illustrates three different mesh densities for the BL/N1-1 case. The difference was in numbers of elements (2606, 1326, and 686). The comparisons between the experimental results and the FEA results of the three different numbers of element shows that the use of a 1326 element gives satisfactory convergence of the FE results (see Figure (5.11b)).

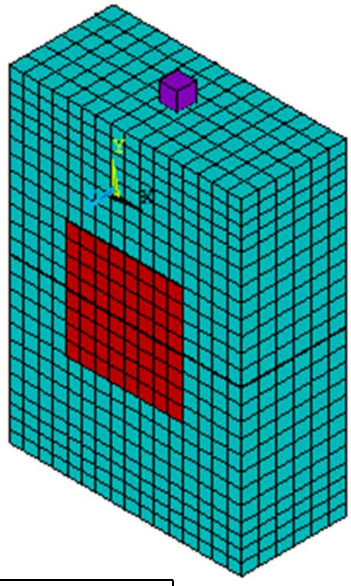

Element Type	Number of Elements
SOLID65	2304
LINK8	14
SOLID46	144
SOLID46	144

(a): FE model with 2606 elements.

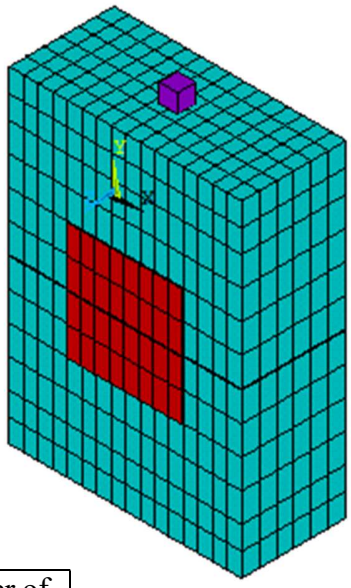

Element Type	Number of Elements
SOLID65	1152
LINK8	14
SOLID46	80
SOLID46	80

(b): FE model with 1326 elements.

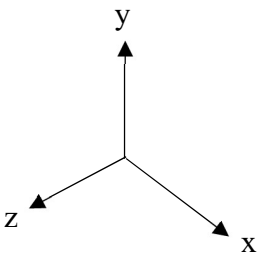

Element Type	Number of Elements
SOLID65	576
LINK8	14
SOLID46	48
SOLID46	48

(c): FE model with 686 elements.

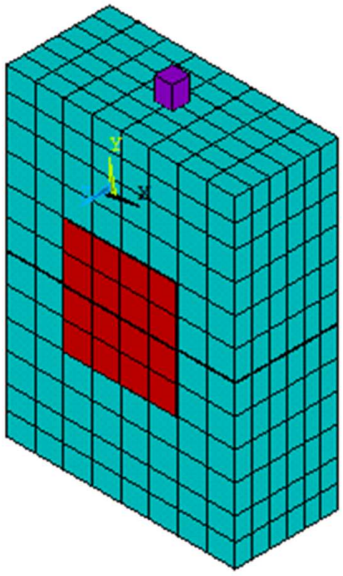

Figure (5.11): Mesh for full of the model in ANSYS (for example BL/N1-1).

Modelling the bond between CFRP reinforcement and concrete is still a complex problem, several studies provide an acceptable simulation to the FRP layer or the FRP-concrete interface. The majority of these studies assumed linear elastic response up to failure for the FRP reinforcement. In addition, these studies assumed a full connection between the FRP and concrete elements, the effect of adhesive material was ignored in most of these models. (Damian et al., 2001; Chansawat et al., 2009; Ronagh and Baji, 2014 and Shaker and Kamonna, 2016). In addition, some of these studies assumed a linear elastic response for concrete material. The outcomes of these FE models show a generally acceptable information about the structural response of concrete members strengthened with FRP reinforcement. However, the ability of these models to predicate the actual behaviour are very limited, the cracking behaviour of concrete, the failure in the adhesive layer and RP debonding were not replicated in these models.

In this study, the ANSYS models for implicit analysis were carried out within the ANSYS pre-processor. They consisted of SOLID65 elements to represent the concrete; this element is able to predict the non-linear behaviour of concrete materials using a smeared crack approach and LINK8 elements representing the central steel bar.

Various techniques were used to model the CFRP composite sheet and CFRP-concrete interface. SOLID46 and SHELL63 with orthotropic material properties have been widely used to simulate FRP reinforcement (Parvin and Granata, 2000 and Damian et al. 2001). SHELL41 and elastic SHELL99 have also been used to model the CFRP reinforcement (Mirmiran et al. 2000, Hawileh et al. 2012 and Ronagh and Baji, 2014).

In this study, the use of SOLID46 and SHELL63 elements shows the best solution for modelling the behaviour of the CFRP sheet. SOLID46 provides a simple method for modelling the direction of the single and double layers of the CFRP sheet. The CFRP sheet was assumed as a linear orthotropic material. To simulate the adhesive layer, two models were assumed in this study:

1. Model 1: The adhesive material was simulated by using SOLID46 elements which were used to connect the CFRP sheet nodes to the concrete nodes as explained in Figure (5.12).

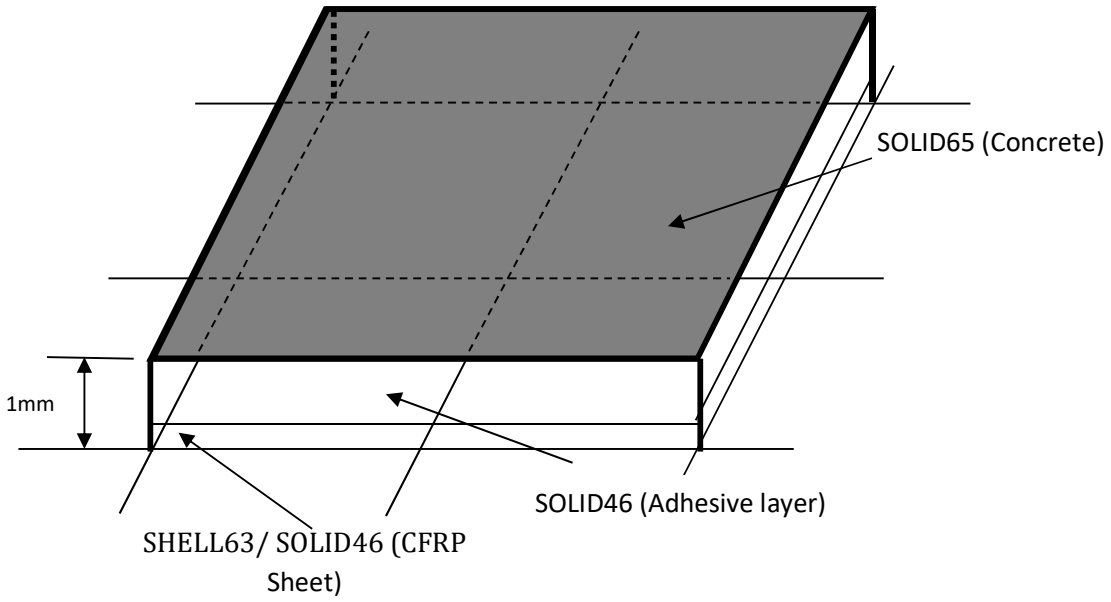

Figure (5.12): Simulated System of CFRP to Concrete interface (Model 1).

2. Model 2: CONTA174 elements are used to represent the surface between the concrete and adhesive layer. The adhesive layer is modelled using SOLID46 elements which are connected to the concrete through the zero thickness bonded contact elements (see Figure (5.13)). CONTA174 is used to represent contact and sliding between the 3-D "target" surfaces (TARGE170) and a deformable surface, defined by this element. This element has three degrees of freedom at each node: translations in the nodal x, y, and z directions (ANSYS 2009). This element is positioned on the surfaces of the 3-D solid or shell elements with mid-side nodes. It has the same geometric properties as the solid or shell element face with which it is connected as shown in Figure (5.14).

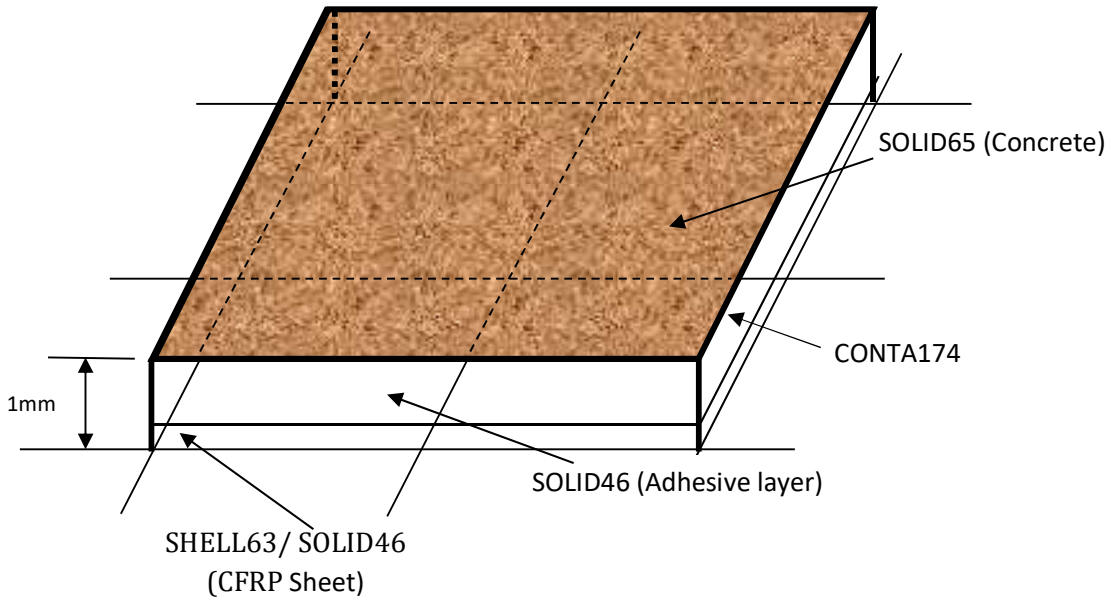

Figure (5.13): Simulated System of CFRP to Concrete interface (Model 2).

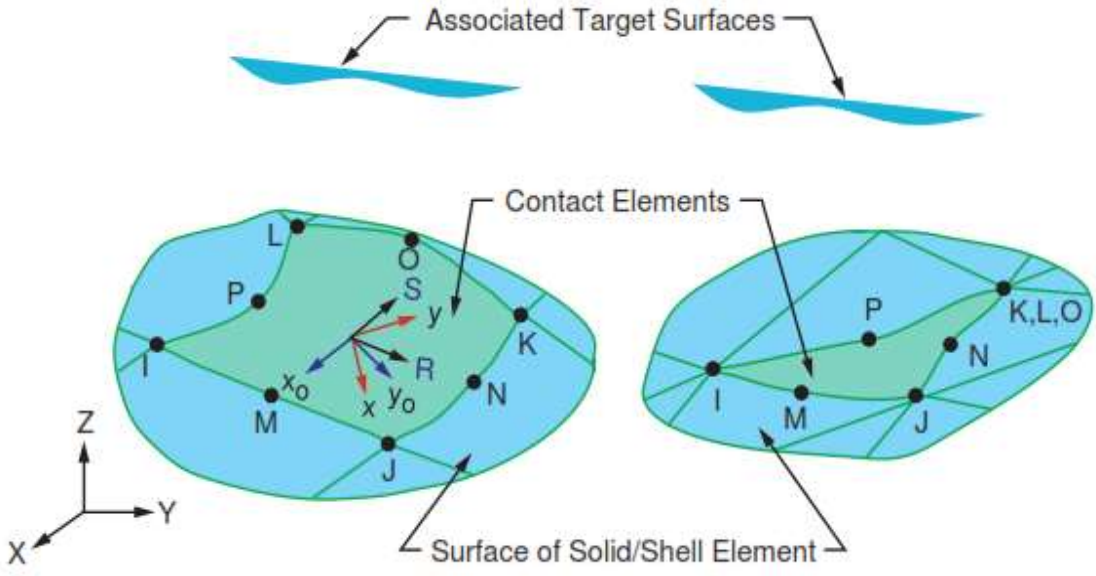

Figure (5.14): CONTA174 Element geometry (ANSYS 2009).

A comparative study was carried out for samples BL/N1-1, BL/N1-2 and BL/N1-3 to investigate the best technique to represent the adhesive layer and the CFRP-concrete interface. Figure (5.15) illustrates the load-slip curves of the BL1-1 samples. It can be noticed that the second model is stiffer than the first model. The load-slip trend of the first model is closer to reality than the second proposed model. In this study, the first technique was used to model the other cases due to the ability to predict the maximum debonding loads more closely and the failure modes, concrete cracks. However, the second model was able to predict the local debonding of CFRP sheet from the concrete surface as shown in Figure (5.16).

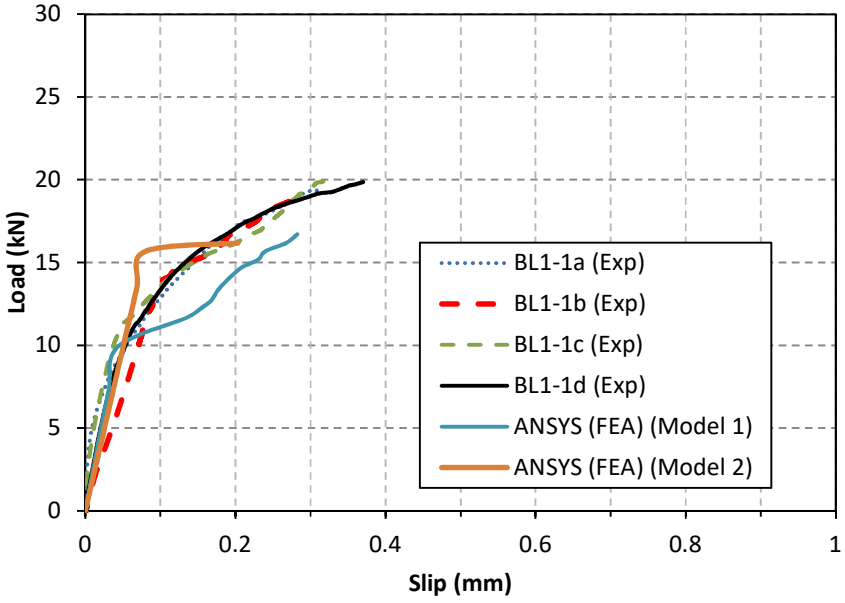

Figure (5.15): Load versus slip for BL1-1 samples.

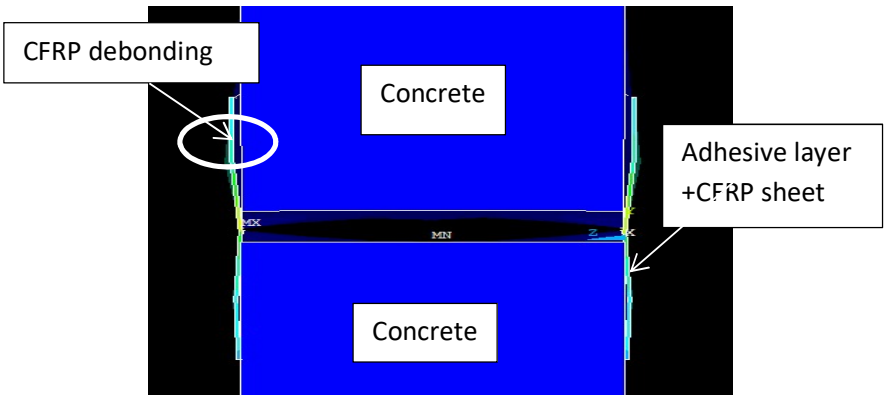

Figure (5.16): Typical debonding failure mode between concrete and adhesive layers.

The finite element models are loaded with the same conditions as the experimental bond-slip test models. A tensile load was applied to the top end of a steel bar, while the bottom bar was fixed as shown in Figure (5.17). The sample rotation was not permitted to keep sample alignment and to avoid the eccentricity between the top and bottom grip.

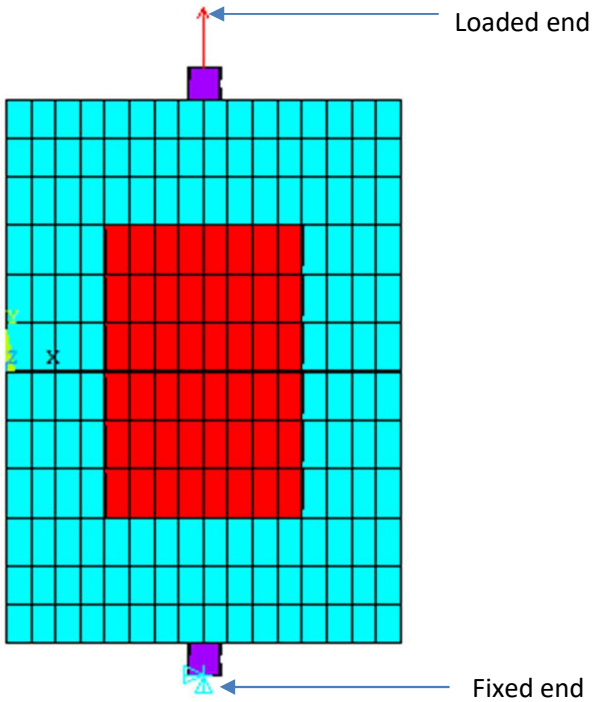

Figure (5.17): Loading and boundary conditions (for example BL/N1-2).

5.4.1. Load Stepping and Failure Definition for FE Models

In this study, a load step size of 0.5 kN was selected to allow the model to converge. Failure for each of the simulated models was defined when the solution for a 0.5 kN load increment diverged. ANSYS shows a message identifying that the models have a considerable large displacement, increased beyond the limits of the displacement defined in the ANSYS program.

5.4.2. Finite Element Results Discussion

This chapter presents a comparison between the outcomes of the FEA models and those data obtained from chapter three for the bond-slip test. The following comparisons are presented and discussed for the selected samples: (i) load-slip curve, (ii) load-strain curve (load versus the strain reading collected from the strain gauge located on the top surface of the centre line of the

bonded width of CFRP composite), (iii) the counter principal stresses developed in the CFRP reinforcement and (iv) smeared crack patterns at failure. The results of the FEA models were collected in identical positions as those recorded for the actual bond-slip tests.

5.4.3. Load-Slip Results

Figures (5.18) to (5.24) show the comparison between the finite element analyses and the experimental results for LWAC and NWAC specimens. It can be noticed that the FE predictions are in acceptable agreement compared with experimental tests results. The trends of the FEA models in the linear elastic zone were identical to those collected from the actual test samples. However, a divergence in behaviour between the analytical and experimental trends was observed in these figures within the cracking stage. This is attributed to the difficulties of the ANSYS software in simulating the real response when the stiffness of the simulated model is very small or close to zero. Another reason for this diverge in behaviour was due to the way of simulating the cracks in FEA models. Cracks are discrete in the actual physical model compared with smeared cracks in the FE model, this causes an underestimation of the relative slip between the CFRP reinforcement and concrete sample in ANSYS as well as a difference in behaviour between the numerical and the experimental load-slip trends. The same conclusion was obtained by Al-Juboori, (2011).

The average value of the ANSYS-to-experimental load ratio is 0.94 for LWAC specimens. The standard deviation (S.D) and the coefficient of variation C.V (%) are 0.11 and 12, respectively. Table (5.4) shows the comparison between experimental and ANSYS maximum bond strength. For NWAC the average value of the ANSYS-to-experimental load ratio is 0.94. The standard deviation (S.D) and the coefficient of variation C.V (%) are 0.05 and 6, respectively as shown in Table (5.5). Generally, a closer fit between experimental and theoretical load-slip trends are observed, indicating the simulations are reproducing the response of the stiffness of the CFRP sheets attached externally to concrete prism reasonably well.

Table (5.4): Comparisons between experimental and ANSYS maximum bond strength of LWAC samples.

Specimen ID	Maximum Experimental bond strength (kN)	Maximum ANSYS bond Strength (kN)	ANSYS to experimental load ratio
BL1-1a	19.34	16.20	0.84
BL1-1b	18.71	16.20	0.87
BL1-1c	19.99	16.20	0.81
BL1-1d	19.86	16.20	0.82
BL1-2a	27.31	23.40	0.86
BL1-2b	23.80	23.40	0.98
BL1-2c	27.80	23.40	0.84
BL1-2d	25.22	23.40	0.93
BL1-3a	26.15	23.74	0.91
BL1-3b	27.11	23.74	0.88
BL1-3c	18.50	23.74	1.28
BL1-3d	27.48	23.74	0.86
BL3-1a	24.16	22.34	0.92
BL3-1b	22.99	22.34	0.97
BL3-1c	18.19	22.34	1.23
BL3-2a	18.69	18.65	1.00
BL3-2b	19.54	18.65	0.95
BL3-2c	17.72	18.65	1.05
BL4-1a	13.20	12.09	0.92
BL4-1b	13.10	12.09	0.92
BL4-1c	13.60	12.09	0.89
BL4-1d	13.95	12.09	0.87
BL4-2a	21.04	20.70	0.98
BL4-2b	21.69	20.70	0.95
BL4-2c	21.51	20.70	0.96
		S.D.	0.11
		Mean	0.94
		C.V. (%)	12

Table (5.5): Comparisons between experimental and ANSYS maximum bond strength of NWAC samples.

Specimen ID	Maximum Experimental bond strength (kN)	Maximum ANSYS bond Strength (kN)	ANSYS to experimental load ratio
BN1-1a	18.13	19.56	1.08
BN1-1b	22.10	19.56	0.89
BN1-2a	29.60	27.40	0.93
BN1-2b	29.40	27.40	0.93
BN1-3a	28.40	27.80	0.98
BN1-3b	29.64	27.80	0.94
BN3-1a	28.01	26.04	0.93
BN3-1b	28.19	26.04	0.92
BN3-2a	22.44	21.96	0.98
BN3-2b	23.09	21.96	0.95
BN4-1a	14.80	14.45	0.98
BN4-1b	15.55	14.45	0.93
BN4-2a	28.10	24.40	0.87
BL4-2b	28.21	24.40	0.86
		S.D.	0.05
		Mean	0.94
		C.V. (%)	6

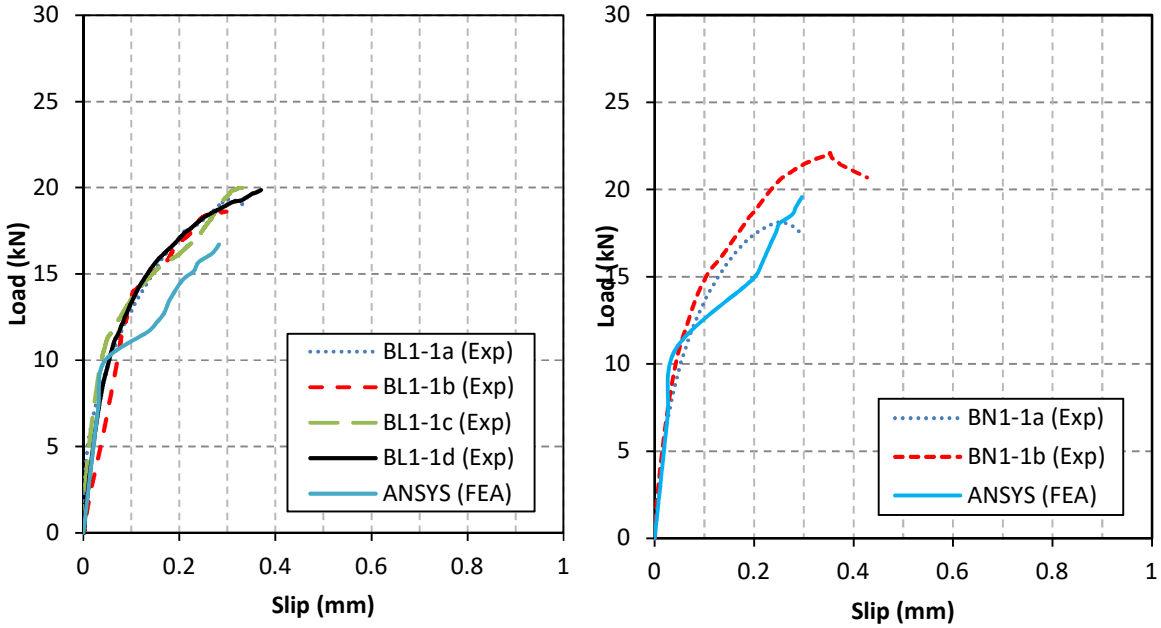

Figure (5.18): Load versus slip for BL/N1-1 samples.

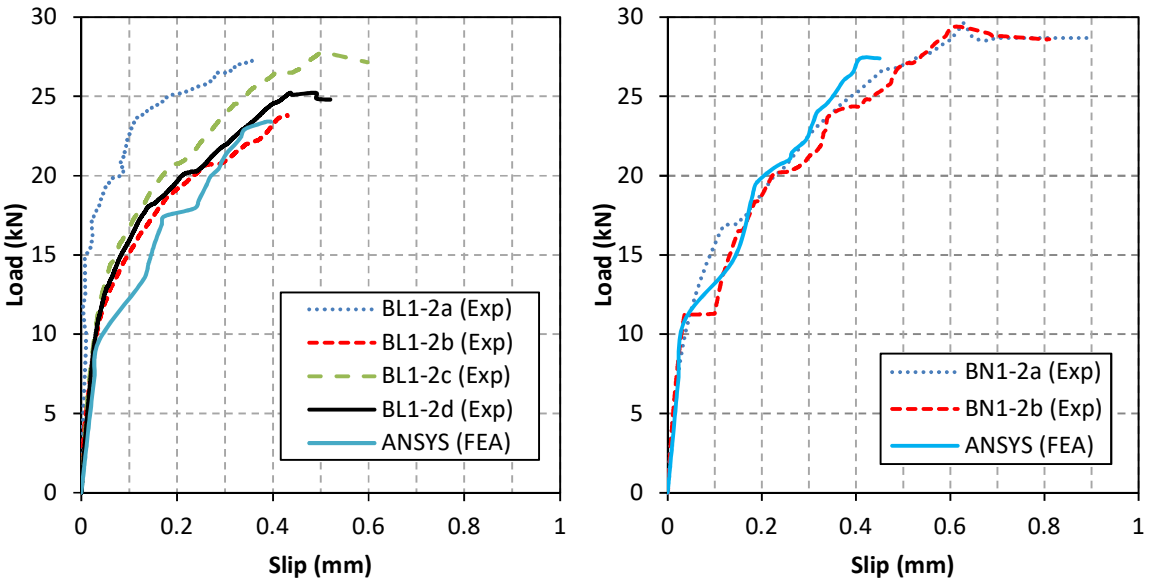

Figure (5.19): Load versus slip for BL/N1-2 samples.

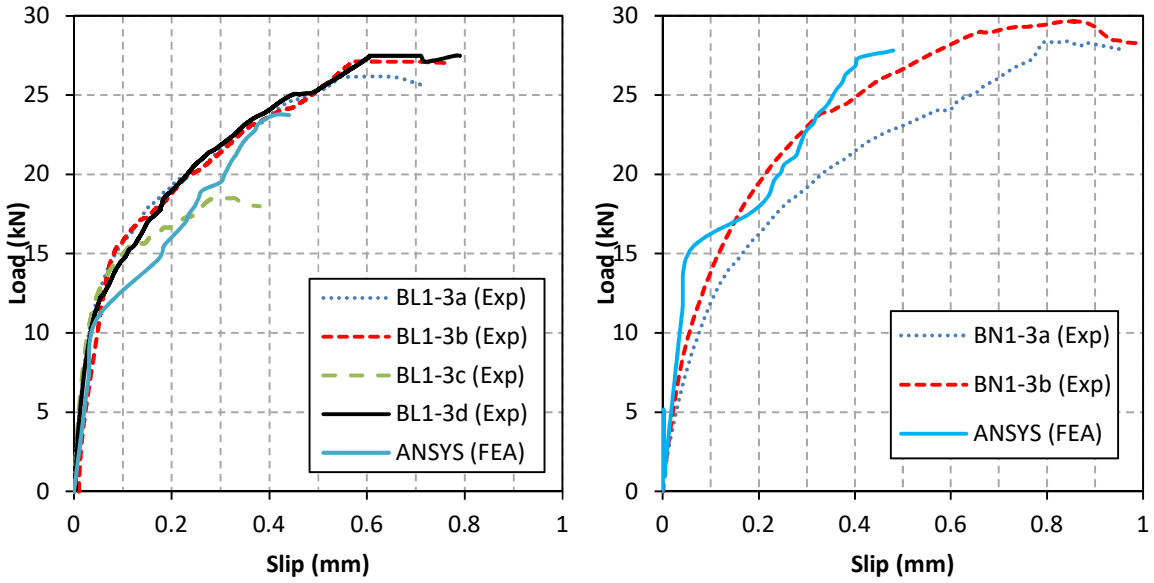

Figure (5.20): Load versus slip for BL/N1-3 samples.

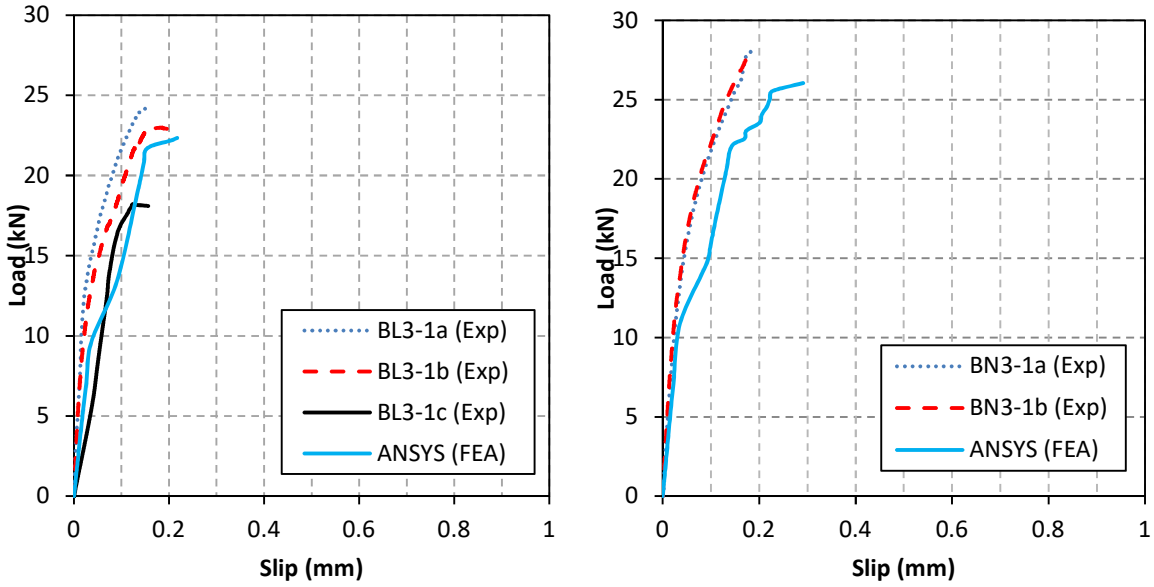

Figure (5.21): Load versus slip for BL/N3-1 samples.

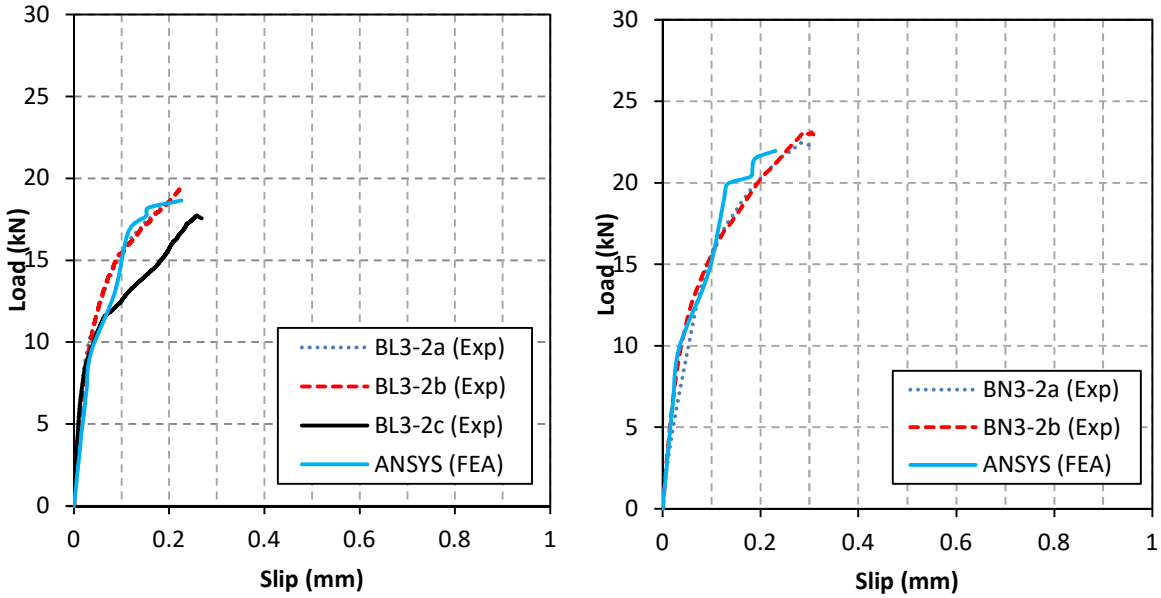

Figure (5.22): Load versus slip for BL/N3-2 samples.

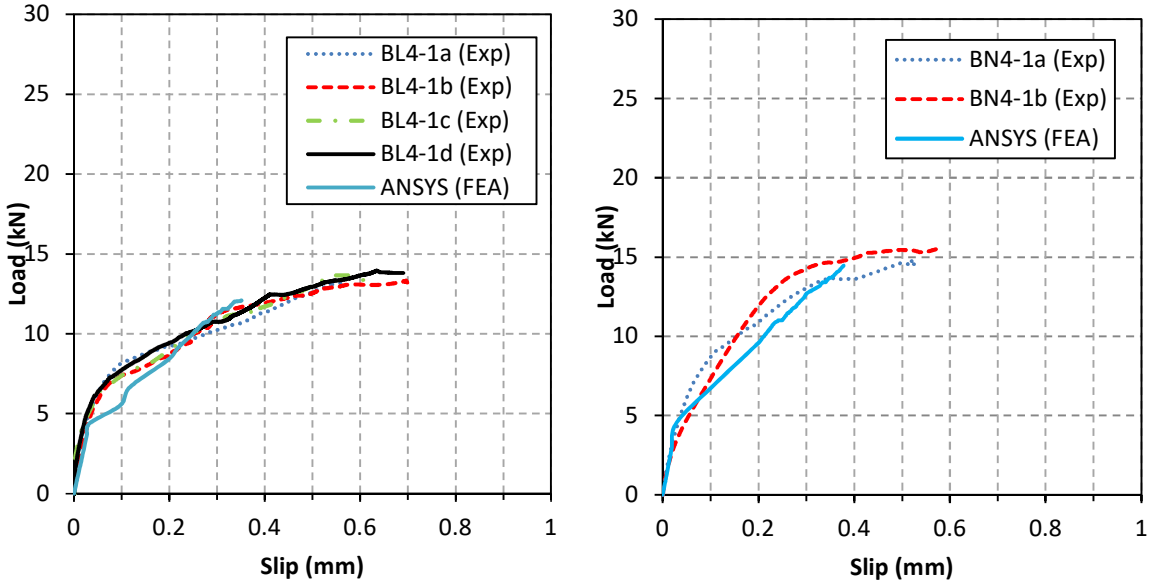

Figure (4.23): Load versus slip for BL/N4-1 samples.

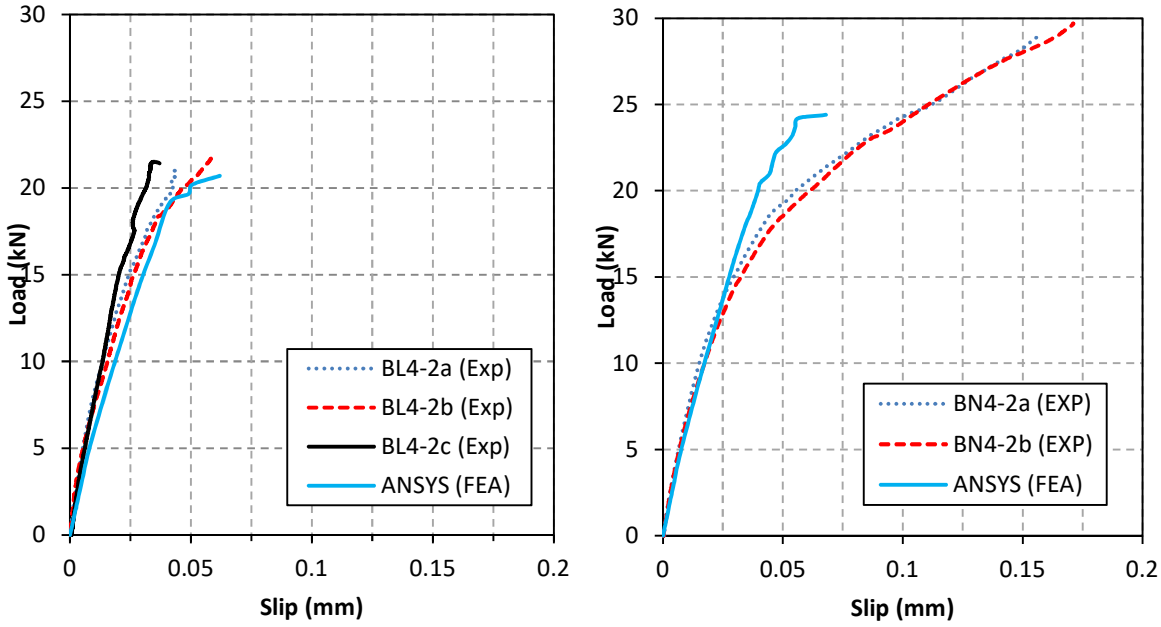

Figure (5.24): Load versus slip for BL/N4-2 samples.

5.4.4. Maximum Load-Strain

Comparisons of the maximum load versus CFRP strain trends of the finite element analyses with the experimental data collected from the strain gauges located in the same location as the FE models for specimens BL/N1-1, BL/N1-2 and BL/N1-3 are shown in Figures (5.26) to (5.28). At 25 mm from the centre of the specimens in the centre line of the bonded length, a node was used to record the strain on the CFRP sheet and to plot the load versus tensile strains in the CFRP reinforcement as shown in Figure (5.25). The maximum strain in the surface of CFRP composite was achieved near this point in most tested samples. Generally, identical responses were observed between the curves of load versus CFRP strains obtained from the FE models and those recorded from experimentally tested beams. The trends of the load versus CFRP strain observed in FEA models are characterised by two main stages, the uncracked stage where the CFRP strain is very small and can be ignored and the non-linear or cracked stage at which a significant strain measurement is obtained from these models. In elastic stage (uncracked stage), the CFRP strains obtained from the FE models were approximately similar to those recorded from the experimental strain gauges. However, a discrepancy in behaviour was observed between the FE models results and the experimental data after the inelastic stage (cracking stage). The CFRP strains obtained from the FE models are slightly lower than those collected from an experimental

sample in most cases, this is assigned to the local influence of the experimental strain caused by the large cracks occurring close to the strain gauge. The same conclusion was obtained by Damian et al., (2001). This response is not replicated in the FE model which uses a smeared cracking approach.

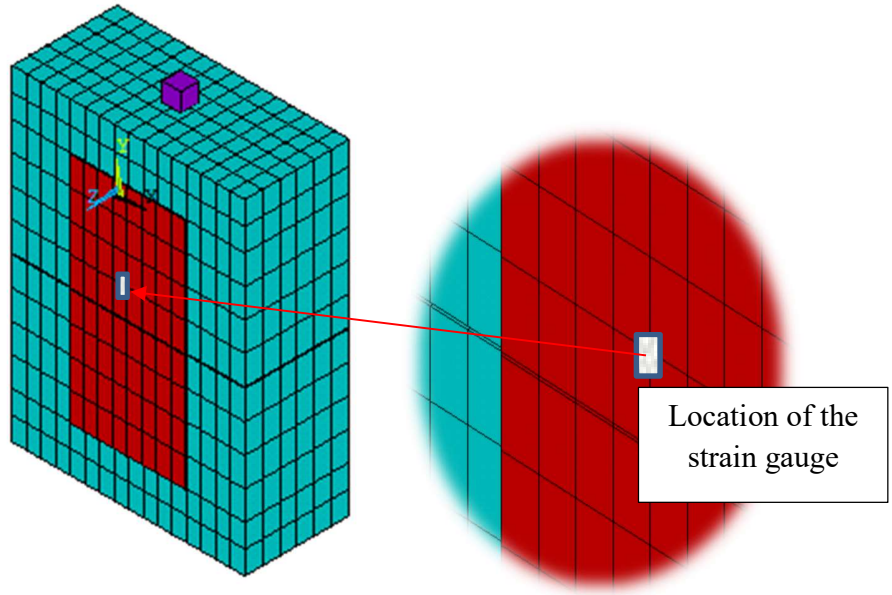

Figure (5.25): Selected strain gauge location in FE model.

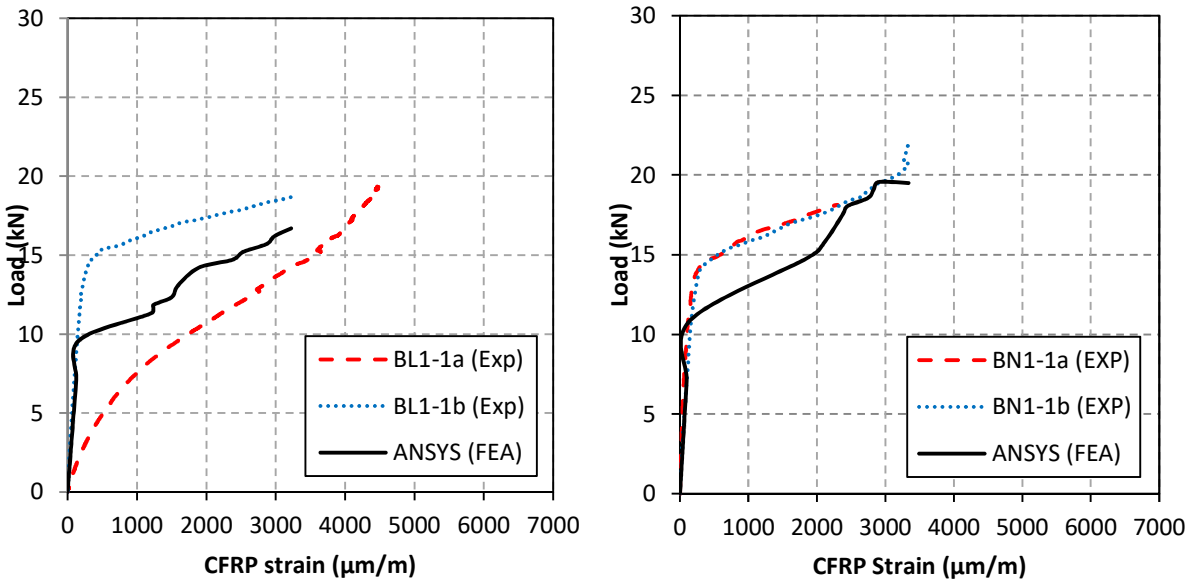

Figure (5.26): Maximum load versus tensile strain in the CFRP for the BL/N1-1 series.

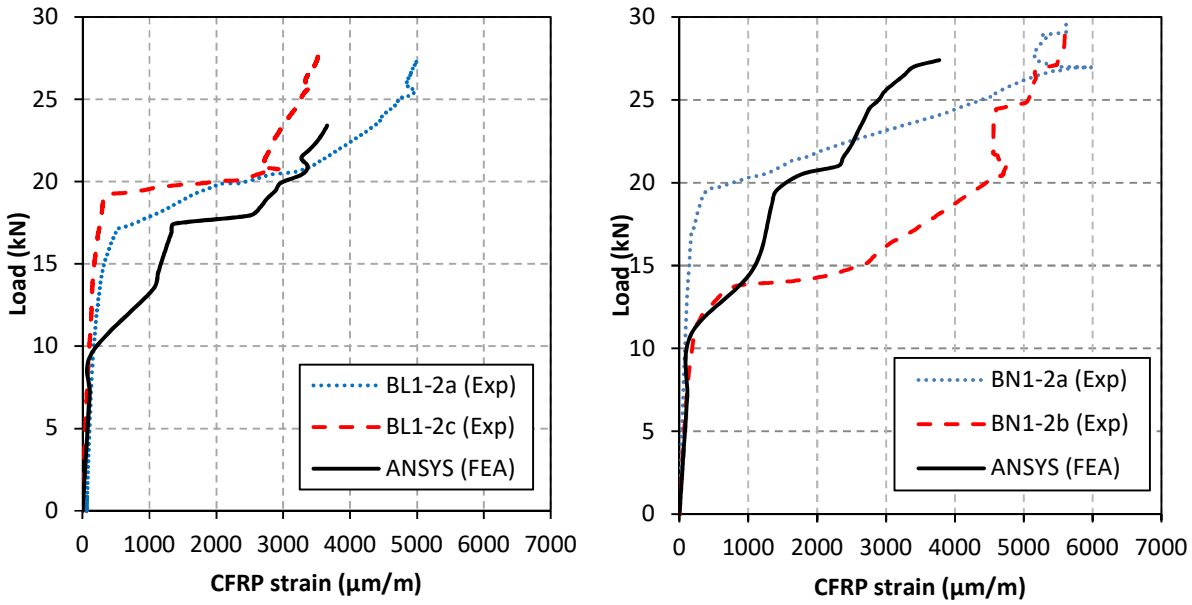

Figure (5.27): Maximum load versus tensile strain in the CFRP for the BL/N1-2 series.

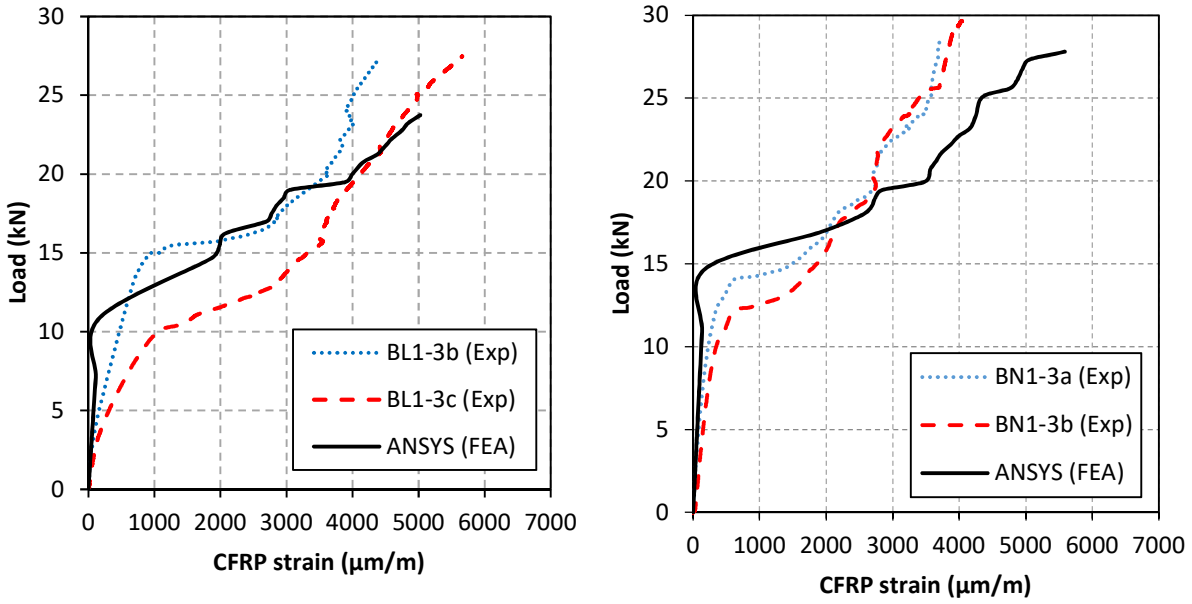

Figure (5.28): Maximum load versus tensile strain in the CFRP for the BL/N1-3 series.

5.4.5. Principal Stress Distribution

Figure (5.29) shows the contours of the principal stress of the FE model for BL4-1 and BN4-1 specimens which are used as an example in this study. Point A is located in the centre of the samples, point C is located at the end of the CFRP sheet and point B lies midway between points A and B.

Around the edge of the CFRP sheet (point C), the stress in the CFRP sheet is low in both of the LWAC and NWAC samples. Around the middle of the sheet (point B), the amount of stress around the CFRP sheet is moderate, showing a higher stress level than at point A, the stress in CFRP laminate around point A is higher than that at points B and C, due to higher stress concentration at the centre of the samples. It can be concluded that the load is increasing gradually along the CFRP sheet. According to the legend, the value of the stress ranges between (- 1.9 MPa to 10.3 MPa) at the failure load of 12.09 kN for the BL1-1 sample. While for BN1-1 ranges between (-0.29 MPa to 14.57 MPa) at the failure load of 14.45 kN.

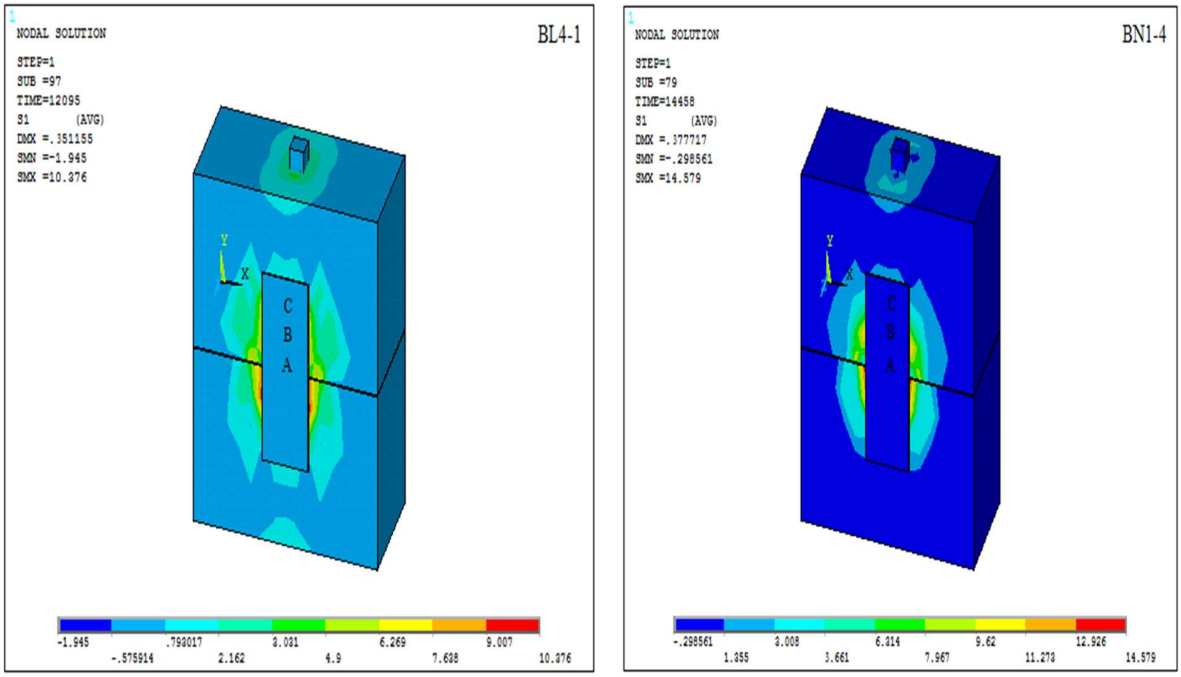

Figure (5.29): Contours of the principal stress of BL/N4-1 Specimen.

5.4.6. Evolution of Crack Patterns

In the non-linear analysis, the results of the FE models such as stresses and strains are obtained at integration points located within the concrete elements. Figure (5.30) illustrate the positions of the integration points in an SOLID65 elements. A cracking sign as a circle appeared in a perpendicular orientation to the direction of the principal stress when a principal tensile stress increases beyond the ultimate tensile strength of the concrete as shown in Figure (5.31) (ANSYS, 2009).

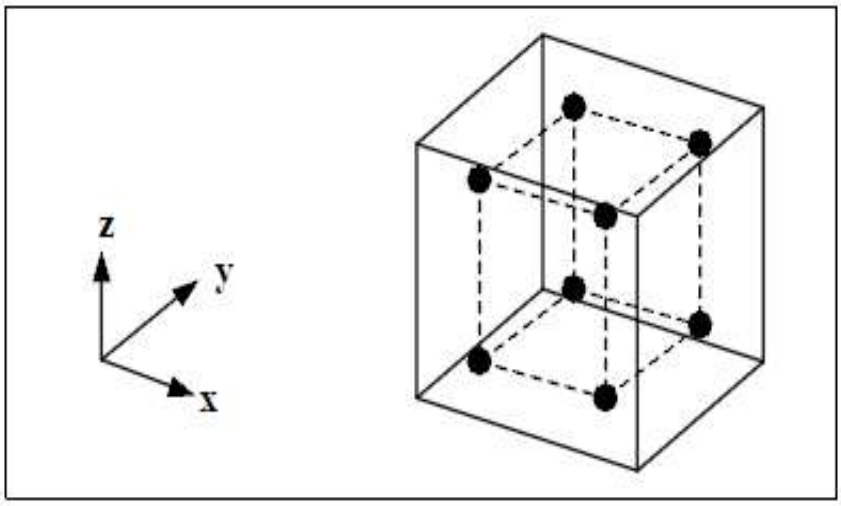

Figure (5.30): Integration points in concrete solid element (ANSYS, 2009).

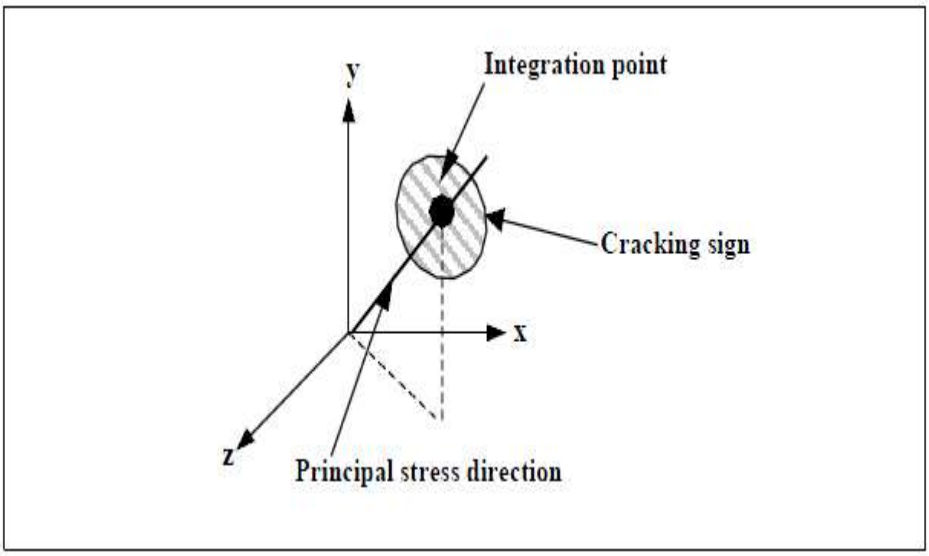

Figure (5.31): Crack representations (ANSYS, 2009).

Figure (5.32) shows typical cracking signs developing in the ANSYS model. A side face of a full FE model of sample BL4-2 is used to show the position of the cracks in the FE models. Cracking signs shown at the concrete element integration points are based on the status of all the element's integration points. Octahedron sign locates in the centre of the element If any integration point has crushed. The cracking sign develops at the element integration points if any integration point has cracked open or cracked and then closed. Eventually, the cracked and closed sign develops at the element centre if more than five integration points have cracked and then closed. Circle signs appeared at the centre of the element if more than one integration point has cracked, the circle outline at the element centre shows the average orientation of all cracked planes for that element (ANSYS, 2009).

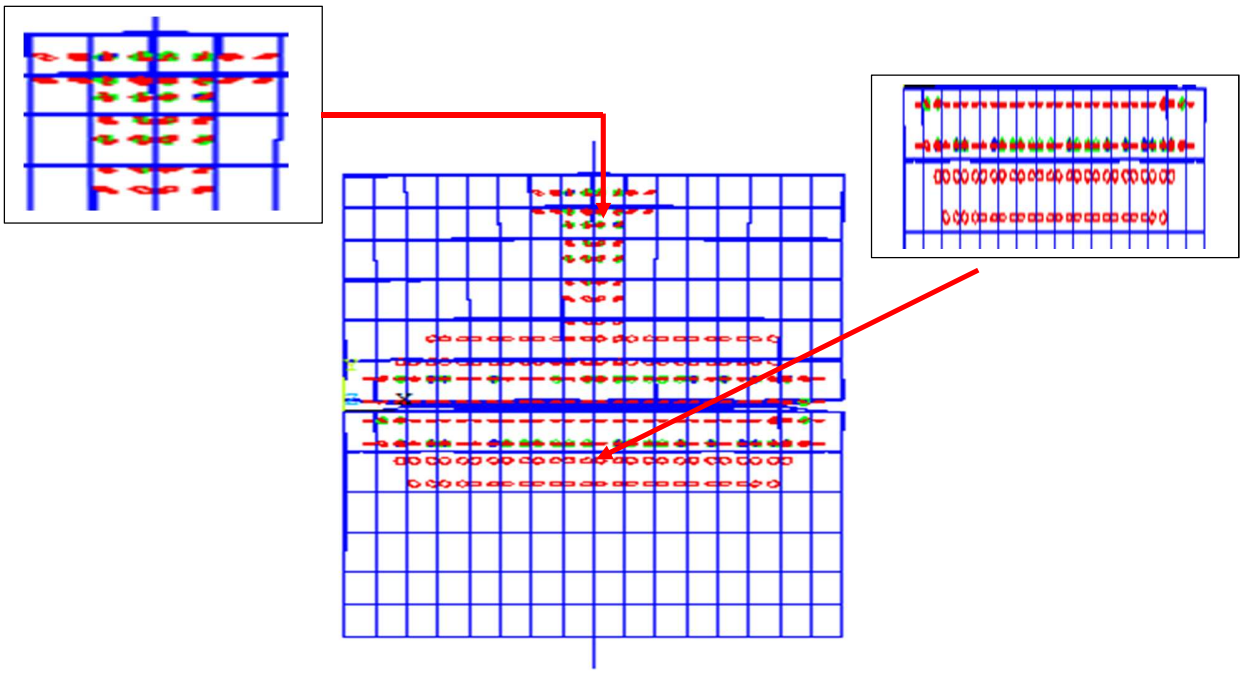

Figure (5.32): Typical cracking representation in an ANSYS model for the BL4-2 specimen.

Crack patterns observed from the FE models at the maximum failure load are compared to those obtained from experimental samples BL/N1-1, BL/N1-2 and BL/N4-1 as shown in Figures (5.33) and (5.38). A reasonable agreement in crack patterns between the actual specimens and those observed from FE models. The good agreement between the numerical and experimental results demonstrates the ability of the FEA models to predicate the failure patterns of the actual physical models with a reliable accuracy.

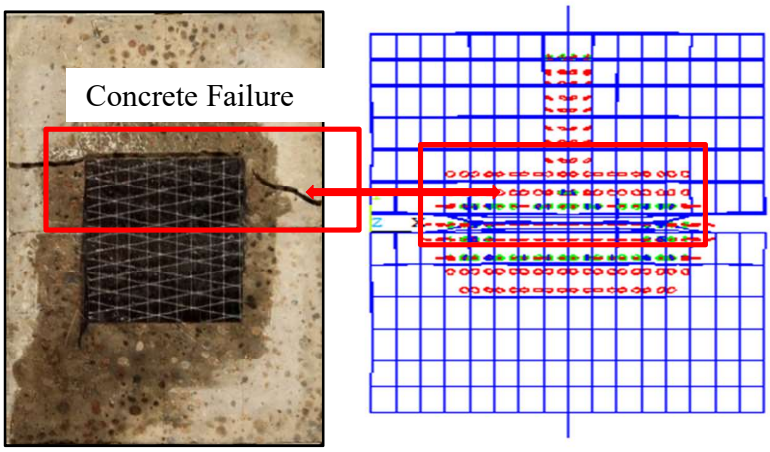

(a): Front view of actual specimen. (b): Side view of the FE models

Figure (5.33): Crack patterns at the failure of BL1-1 specimen.

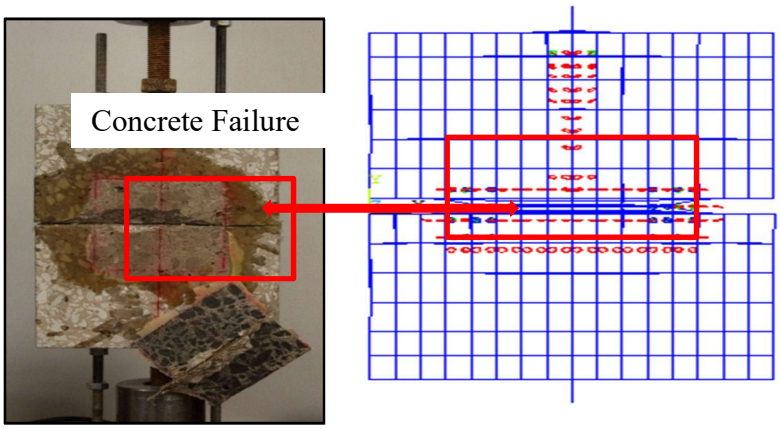

(a): Front view of actual specimen. (b): Front view of FE model.

Figure (5.34): Crack patterns at the failure of BN1-1 specimen.

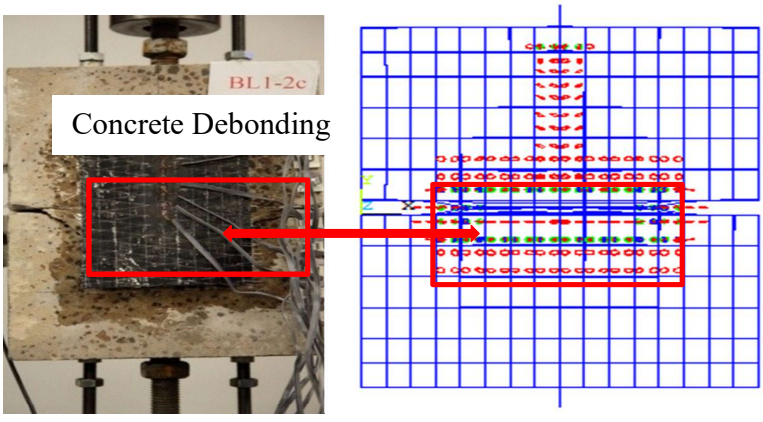

(a): Front view of actual specimen. (b): Front view of FE model.

Figure (5.35): Crack patterns at the failure of BL1-2 specimen.

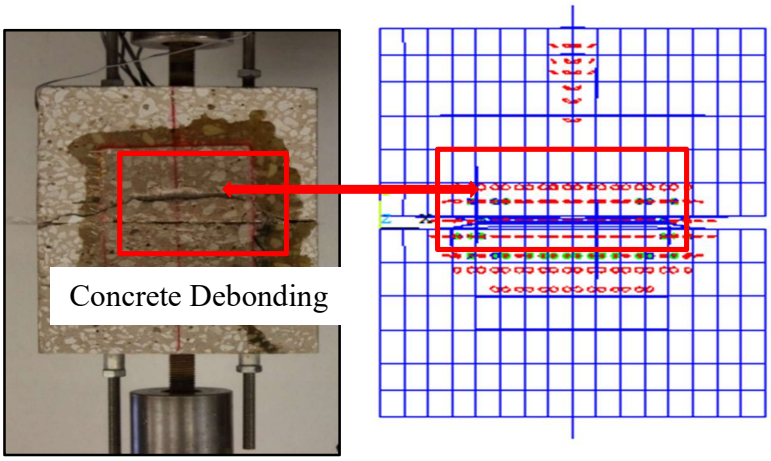

(a): Front view of actual specimen. (b): Front view of FE model.

Figure (5.36): Crack patterns at the failure of BN1-2 specimen.

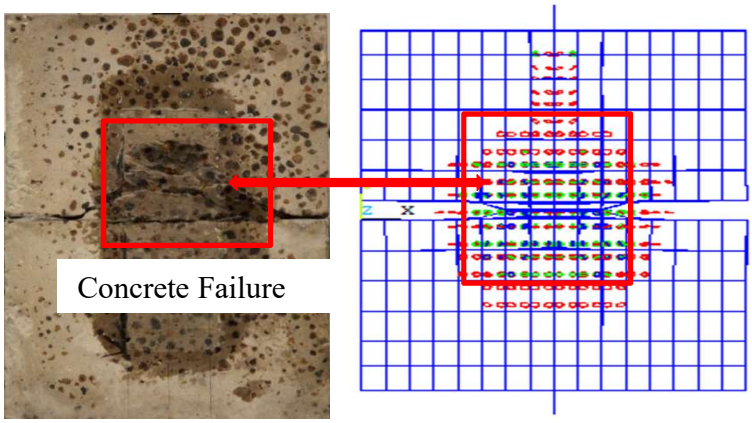

(a): Front view of actual specimen. (b): Front view of FE model.

Figure (5.37): Crack patterns at the failure of BL4-1 specimen.

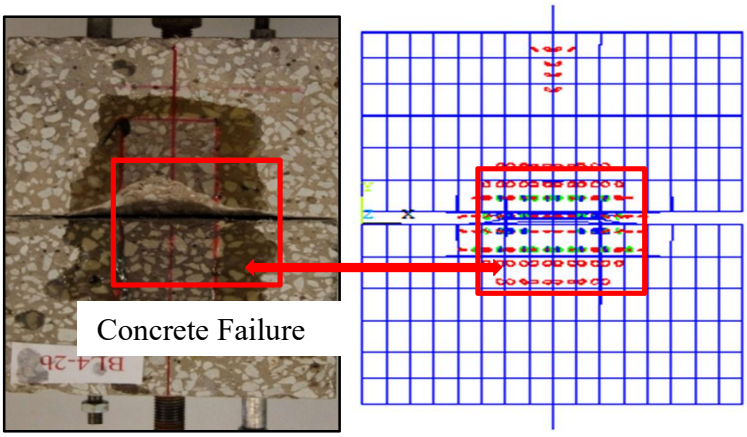

(a): Front view of actual specimen. (b): Front view of FE model.

Figure (5.38): Crack patterns at the failure of BN4-1 specimen.

5.4.7. Parametric Study

To understand numerically the interfacial behaviour between CFRP and LWAC or NWAC concrete substrate a parametric study was undertaken. In this study, the effect of different variables such as the concrete compressive strength, the stiffness of CFRP composite and CFRP sheet width were altered to investigate the effect of these parameters on the bond response of CFRP and concrete. The FE model presented in these sections was selected for this parametric study.

5.4.7.1. Effect of Concrete Compressive Strength

Figure (5.39) shows the effect of the concrete compressive strength on the maximum load carrying capacity for both LWAC and NWAC specimens. The concrete compressive and the concrete tensile strength were varied from 10 to 50 MPa in the FE model of specimen BL/N1-1 to examine the effect of concrete strength on the maximum load in FE models. The uniaxial stress-strain relationship for concrete in compression was computed based on Equation (5.1) and (5.2). The concrete modulus of rupture is estimated according to Equation (5.5) (ACI, 2008) for NWAC samples. The concrete modulus of rupture and uniaxial tensile stress for LWAC is assumed as 77% and 85% of that of NWAC which is obtained in chapter three (see section 3.5.4.3). The stress-strain trend of concrete in tension is assumed as linear/ elastic up to the maximum cracking strength.

$$f_r = 0.623\sqrt{f_c'} \text{ (MPa)} \tag{5.5}$$

The modulus of elasticity of normal weight concrete can be obtained using the following Equation (ACI, 2008) (Equation (5.6)):

$$E = 4733\sqrt{f_c'} \text{ (MPa)} \tag{5.6}$$

It can be concluded that higher concrete crushing strength leads to a higher load capacity for both lightweight and normal weight concrete samples. Similar behaviour was observed in the experimental study by LópezGonzález et al., (2012). They concluded that the maximum load carrying capacity of the FRP- concrete joint increases with higher concrete crushing strength.

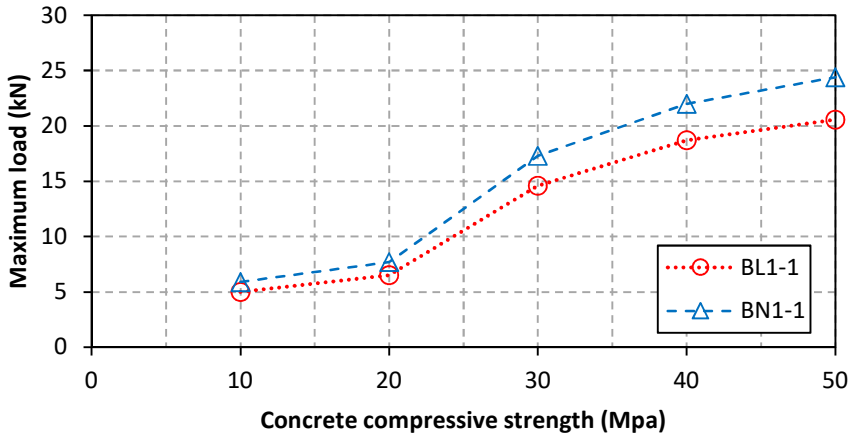

Figure (5.39): Maximum load versus concrete compressive strength for the BL/N1-1 specimen.

5.4.7.2. Effect of CFRP-Concrete Width Ratio Maximum Bond Strength

For further investigation, the FRP to concrete width ratio was varied for the sample with 75 mm CFRP sheet length using the FE models. In this study, the width of the CFRP composite was increased from 50 to 75, 100, 125 and 150 mm respectively. The plots of maximum load versus the CFRP to concrete width ratio are shown in Figure (5.40). It is observed that as the width ratio increases the maximum load increases up to a width ratio equal to (0.5) after that the load decreases for both LWAC and NWAC specimens. The same behaviour was observed in the experimental test, this is attributed to the limited width of concrete samples in the experimental and FE model.

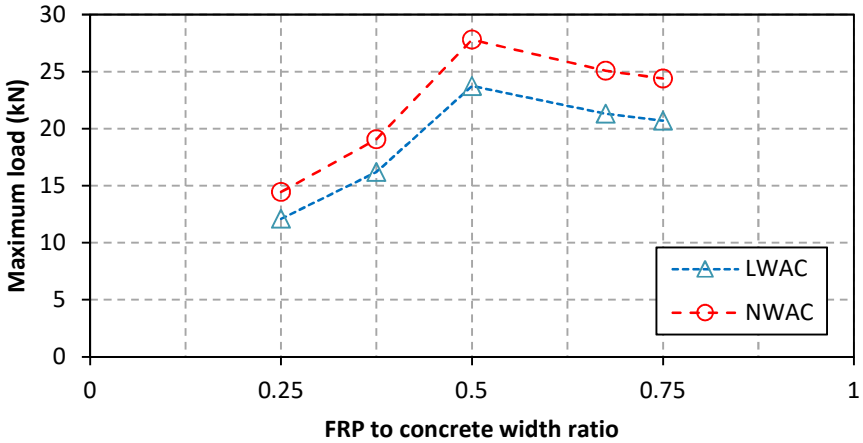

Figure (5.40): Maximum load versus FRP to concrete width ratio.

5.4.7.3. Effect of CFRP Stiffness on Maximum Bond Strength

Figure (5.41) shows the effect of CFRP stiffness on the maximum bond strength for LWAC and NWAC samples. The stiffness of CFRP composite is proportional to the sheet thickness multiplied by CFRP modulus of elasticity ($t_f . E_f$)(N/mm). In this study, the thickness of CFRP was varied by increasing the number of CFRP layers from one up to four layers in the FE models of the of specimen BL/N1-1. It can be observed that as the stiffness of the sheet increases, the maximum load increases. This may be assigned to the higher axial rigidity provided by the CFRP reinforcement with higher thicknesses and thus shows higher crack resistance. Similar conclusions were reached in the experimental tests results carried out by Barnes and Mays (2001). The outcomes of these FE models revealed that there is a specific thickness of CFRP sheets (changing from 3 to 4 layers of CFRP sheets) above that the bond strength of the joints does not increase significantly which confirmed the conclusion obtained by Hadigheh, (2014).

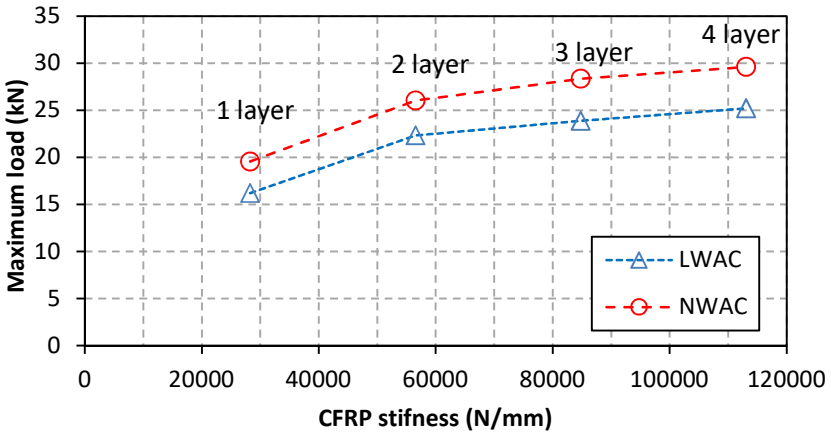

Figure (5.41): Maximum load versus FRP stiffnesses.

5.5. Shear Test for RC Beams

The main aim of this research was to investigate the response of RC lightweight and normal weight beams retrofitted with CFRP shear reinforcement. Thus, all the modelling methodology acquired from the bond-slip models is used in this models. Figures (5.42) to (5.44) show the proposed RC model in ANSYS. For a convergence study, one-half of the full beam was modelled by taking advantage of the symmetry of the beam in the x-direction (length direction). The FE models mesh density was chosen based on the convergence study carried out on the control samples without FRP reinforcement to determine an appropriate mesh. An element width

between 25 mm and 100 mm in the x-direction (length direction) was tried, respectively resulting in about 40 to 10 elements through the beam length. Select element widths of 50 mm or less resulted in less than 10% error when compared to the experimental maximum load, while the select element width of 100 mm resulted in a 30% error in the maximum load. The use of element widths less than 50 mm was not justified due to the increase in computational time with having more concrete elements, which did not show a considerable effect in precision. At the internal faces of the beam, A plane of symmetry is created because only one-half of the beam is simulated in this study. At the symmetry plane, the displacement in x-direction was assumed to zero as shown Figure (5.42). The half model of the constrained test beam (1000 mm length, 200 mm width, and 300 mm depth) was modelled using:

- SOLID65 elements for concrete material.
- LINK8 elements for longitudinal steel reinforcing bars.
- SOLID45 elements for the load and support bearing plates.
- SOLID46 elements for the adhesive layer or the CFRP strips.

Rollers were used to satisfy the boundary condition on the internal faces of the support. The material properties of the concrete used in the FE models are provided in Chapter Four (see section 4.8). The stress-strain curves of concrete are obtained using Equation (5.1) and (5.2). As before, the CFRP sheets were treated as an orthotropic material with linear elastic behaviour up to failure. The adhesive layer was assumed as an isotropic material with linear elastic behaviour. The steel reinforcement for the finite element models of the beam shear test was assumed to be an elastic-perfectly plastic material and has similar behaviour in tension and compression. The material properties of the steel reinforcement used to create reinforced concrete beams were summarised in Chapter Four (see section 4.8 (Table 4.3)). To simulate the load and support bearing plates used in beam shear tests, steel plates were modelled at support and load locations in the finite element models to provide further stress distribution and to eliminate local concrete crushing under the support and loaded regions. A linear elastic behaviour was assumed for these plates. The modulus of elasticity and Poisson's ratio of the steel plate was assumed as 200,000 MPa and 0.3 respectively, the theoretical values are assumed which is sufficient to solve the FEA models and get the required accuracy. The nonlinear time stepping procedure using the Newton-Raphson equilibrium iterations was used to solve the half of the full-scale beams. A gradually

non-zero incremental displacement was applied to the simulated models (displacement-control condition). The finite element models are loaded with the same conditions as the experimental beam shear models. The total reaction forces at the supports corresponding to the incremental displacement applied are used to obtain the maximum load.

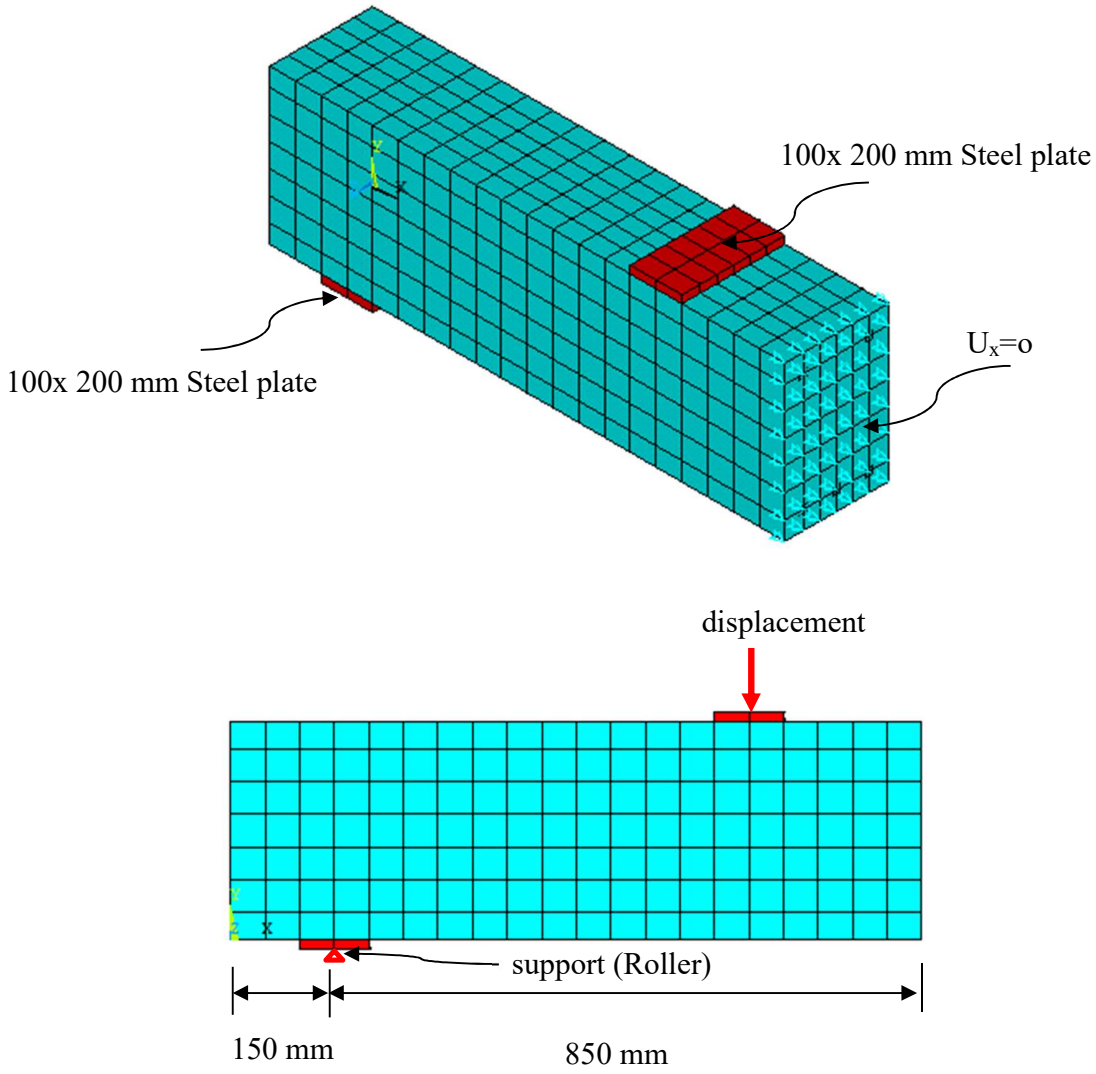

Element Type	Number of Elements
SOLID65	840
SOLID45	24
LINK8	136

Figure (5.42): 3D-Mesh for half beam model in ANSYS for BL/N samples.

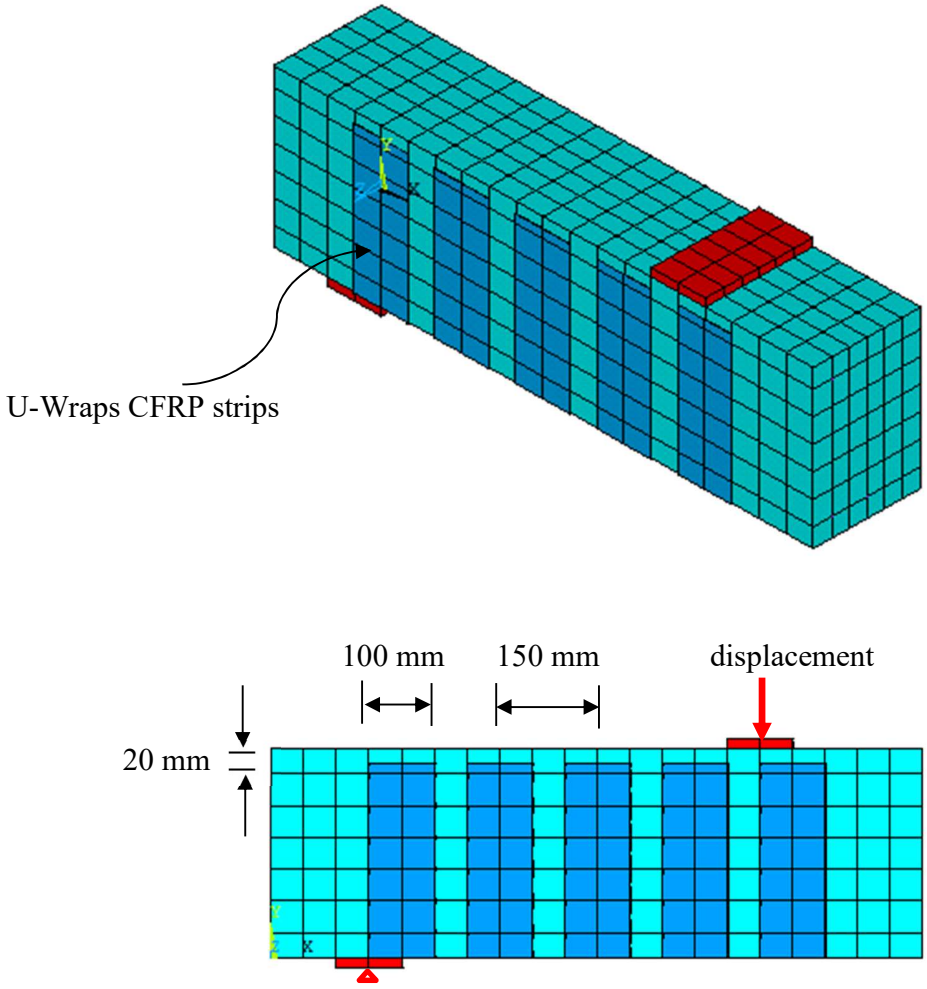

Element Type	Number of Elements
SOLID65	840
SOLID45	24
LINK8	136
SOLID46	200
SOLID46	200

Figure (5.43): 3D-Mesh for half beam model in ANSYS for BL/N-UST samples.

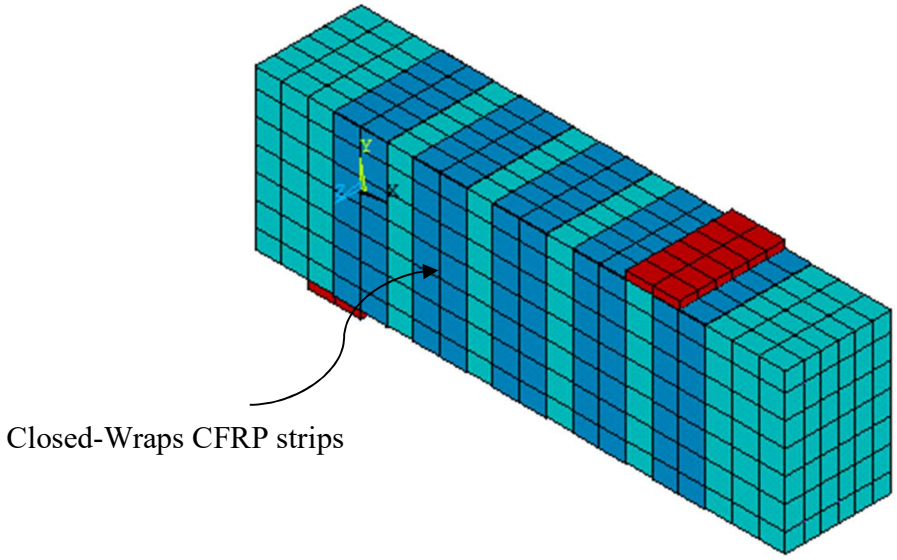

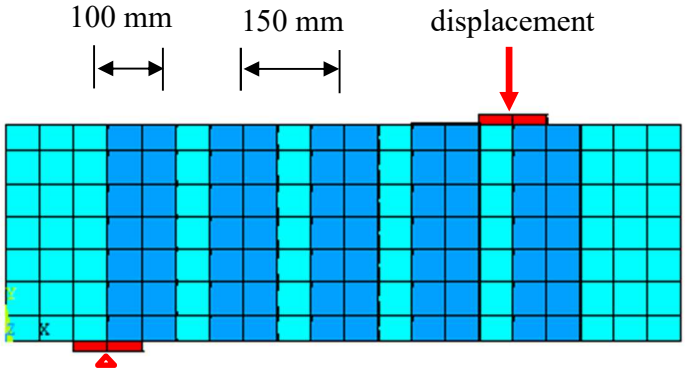

Element Type	Number of Elements
SOLID65	840
SOLID45	24
LINK8	136
SOLID46	260
SOLID46	260

Figure (5.44): 3D-Mesh for half beam model in ANSYS for BL/N-CST samples.

5.5.1. Load–Displacement Responses

The load-mid-span displacement curves obtained from the experimental results are compared with the data collected from FE models as shown in Figures (5.45) to (5.47). A comparable agreement in the linear-elastic region (uncracked stage) between the experimental curves and FE models. However, the stiffnesses of the FE models are significantly higher than those collected from the experimental tested samples curves in the inelastic region (cracking stage). The higher stiffnesses in FEA models were attributed to many variables regardless of the additional constraints on FE models response based on mesh density and the elements used to simulate these models. The following expected reasons are responsible for the higher stiffnesses in the FE models compared with the experimental model:

1. The small cracks developed in the actual physical samples before testing and may be occurred by the processing and the transportation of the samples or by drying shrinkage cracks produced in the concrete. ANSYS does not include these small cracks and can be decreased the stiffness of the actual physical models. A similar conclusion was obtained by Chansawat et al. (2009).
2. The bond between the steel reinforcing bars and concrete was considered as a full bond in the FE models, however, in the actual physical model, some interfacial slip occurs in the actual physical models. The interaction between concrete and steel reinforcing bars could reduce the stiffness of the actual experimental models. In addition, the assumption of the full connection between concrete, adhesive and the CFRP could also increase the stiffness of the FE model.
3. The complicated shear phenomenon at the diagonal shear crack faces which is the aggregate interlock or the friction at the crack faces may slightly reduce the stiffness of the experimental test sample. This phenomenon was not replicated in the FE models.
4. As was discussed in section 5.4.3, the difference in cracks simulation using SOLID65 element for concrete. The cracks are discrete in the actual experimental models compared with smeared in FE model, this causes an underestimation of the displacement in finite element models.

In more detail, the load-deflection curves of the FE models for lightweight concrete samples have an approximately similar response of those of normal weight samples. However, the

lightweight FE models have less stiffness compared with normal weight FE models. This can be attributed to the difference in material properties between LWAC and NWAC samples. The lower modulus of rupture and the modulus of elasticity of lightweight concrete reduces the stiffness of the FE models.

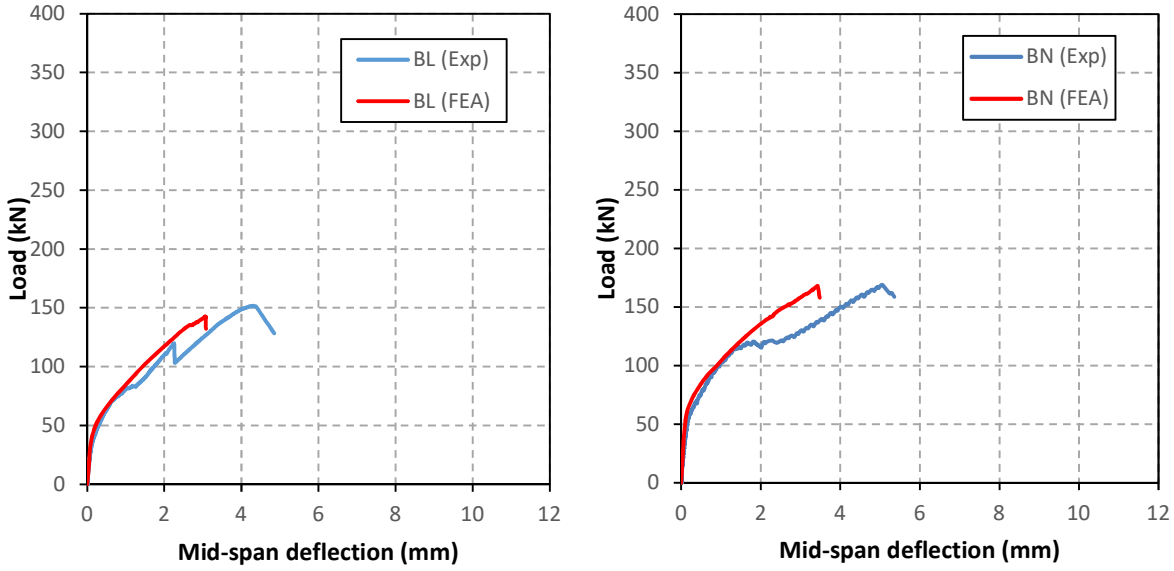

(a): BL sample. (b): BN sample.

Figure (5.45): Load versus deflection of the BN/L samples.

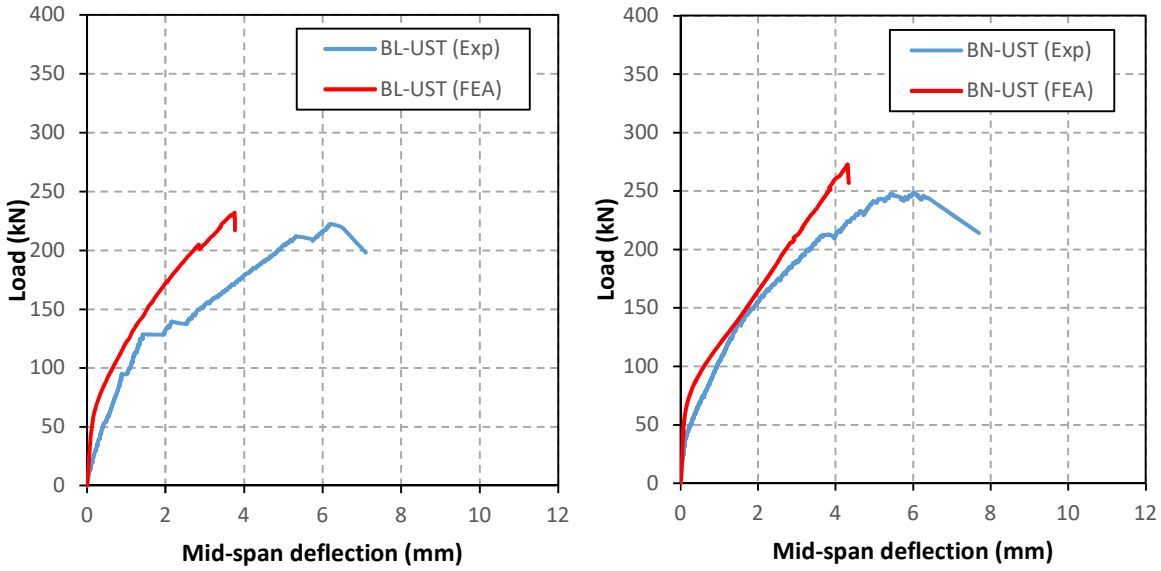

(a): BL-UST sample. (b): BN-UST sample.

Figure (5.46): Load versus deflection of the BN/L-UST samples.

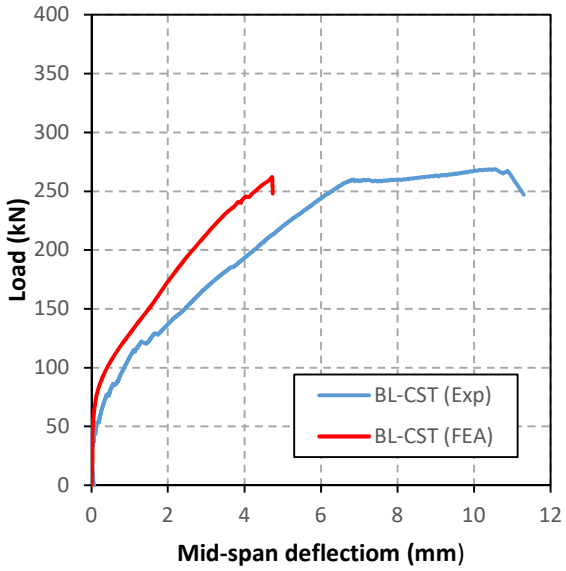

(a): BL-CST sample.

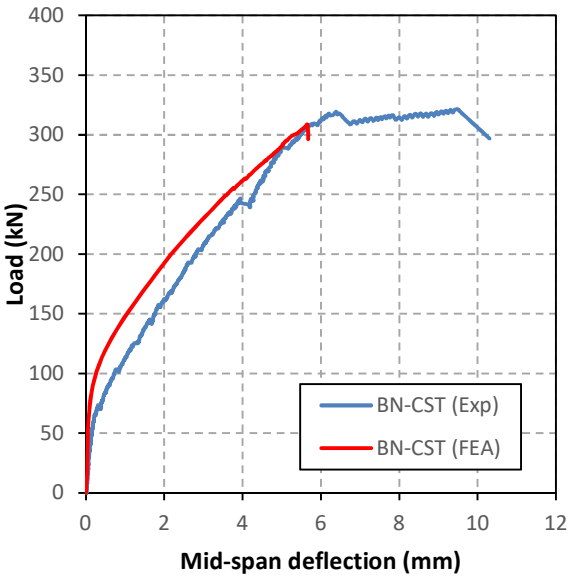

(b): BN-CST sample.

Figure (5.47): Load versus deflection of the BN/L-UST samples.

Table (5.6) reveals comparisons between the maximum load of the experimentally tested lightweight and the normal weight samples and those achieved at last load step in the FE models. It can be noted that the FE models successfully estimate the ultimate strength of the RC samples. The difference between the FE models and experimental maximum load range between 2 to 9%. It can be also noted that the maximum shear strength of FE models for lightweight concrete samples is about 85% of those of the normal weight samples and as previously discussed, this is attributed to the difference in material properties between LWAC and NWAC samples.

Table (5.6): Comparisons between the maximum Experimental and FE load.

Samples	Maximum experimental load (kN)	Maximum FE load (kN)	% difference
BL	151.78	142.25	6.5
BL-UST	218.38	231.88	6
BL-CST	267.14	261.82	2
BN	164.10	167.86	2
BN-UST	248.61	272.47	9
BN-CST	320.80	308.43	4

5.5.2. Cracks Patterns at the Failure

Crack patterns obtained from the FE models at failure are compared to failure photographs from the experimental tested lightweight samples. Figures (5.48) to (5.50) assess the crack patterns propagated in each of the lightweight samples from the FEA, including the direction of cracks which is appeared by red colours and multiple cracking signs shown by different colours. The appearance of cracks represents the failure modes for the sample models.

It can be noted that the crack distributions observed in the FE models at last load step and the failure patterns of the experimentally loaded samples are in reasonable agreement as shown in Figures (5.48) to (5.50). As shown in these figures, the diagonal smeared crack observed in the control samples (see Figure (5.48)) and the retrofitted samples (see Figures (5.49) and (5.50)) was extended over large shear stress area and develop gradually from support region and propagated toward the application of the load point.

Generally, the normal tensile stresses initiate in the horizontal direction of the beam parallel to the longitudinal direction of the beam and the shear stresses developed in the XZ plane. Hence, the tensile principal stresses direction inclined from the horizontal direction when the principal tensile stresses increased beyond the ultimate cracking strength of the concrete, evidently inclined circles develop as vertical lines oriented in a perpendicular direction to the principal stresses directions at the integration points located within the concrete elements. Subsequently, these will point out as critical shear cracks. While vertical straight lines occurring at the integration points of the concrete solid elements. These will point out as flexural cracks (Al-Juboori, 2011).

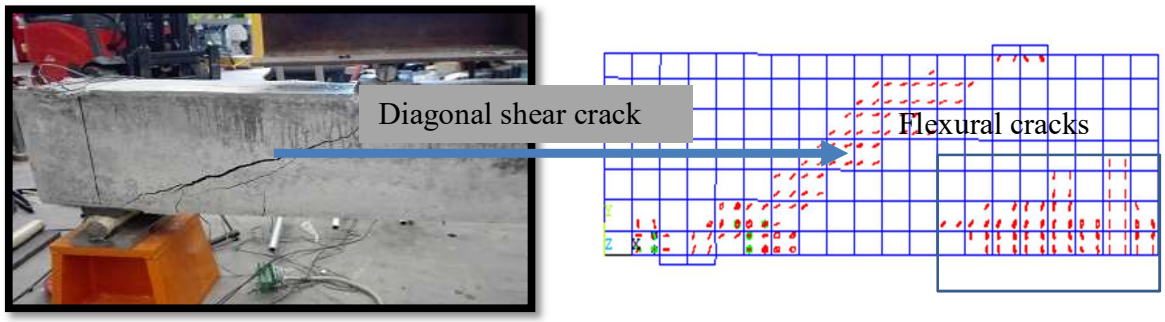

(a): Actual sample. (b): FE model.

Figure (5.48): Crack patterns at failure for BL sample.

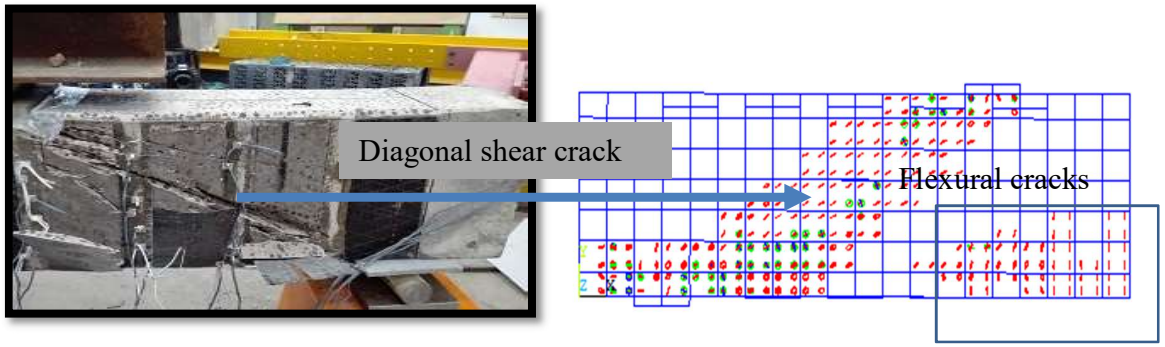

(a): Actual sample. (b): FE model.

Figure (5.49): Crack patterns at failure for BL-UST sample.

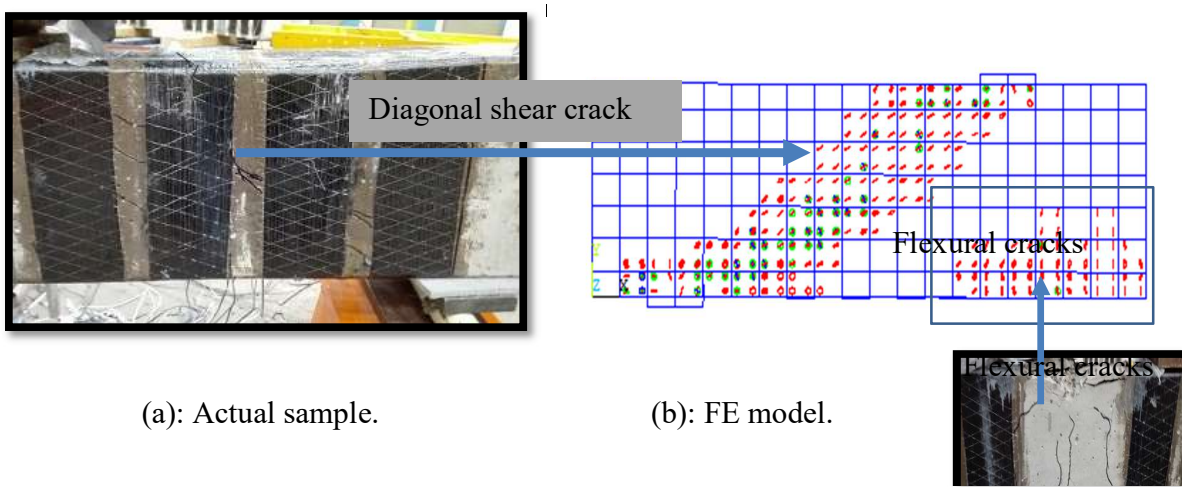

(a): Actual sample. (b): FE model.

Figure (5.50): Crack patterns at failure for BL-CST sample.

5.5.3. Load-CFRP Strain

The average strains collected from the three nodes located in strip SF3 at three different heights were used to obtain the average CFRP strain in the FE models as shown in Figure (5.51). Figure (5.52) and Figure (5.53) show the results of the load-average CFRP strain of the FE models compared with load-average CFRP strain recorded from strip SF4 in the experimental models. Comparisons of the load-CFRP strain trends for the retrofitted lightweight and normal weight samples reveal an acceptable agreement between the FE model results and those results collected from the actual physical models. The FE models successfully predicted that the resistance of the CFRP reinforcement to further shear cracks widening and then start to induce a strain with more loading (Chansawat et al. 2009). Specifically, the experimentally recorded and the numerically obtained CFRP strains corresponding to the maximum load of the BL-UST sample were 3597 µm/m and 3390 µm/m, respectively. While the experimentally recorded and the numerically obtained CFRP strains of the BL-CST sample were 3564 µm/m and 4836 µm/m, respectively. It can be noted that the CFRP strains obtained from FE models are higher than those collected from the experimental models in the case of BL-CST sample. This can be attributed to premature debonding of the CFRP strip SF3 from the surface of the lightweight concrete in the experimental tests. The CFRP strain recorded and predicted for BN-UST sample were 5205 µm/m and 4626 µm/m, respectively, and for BN-CST sample were 6327 µm/m and 5092 µm/m respectively. In general, the experimental CFRP strains in the tested samples are higher than those collected from the FE models. This is may be attributed to the local effect of the experimental strain caused by the concrete cracks and higher crack width. This response was not replicated in the numerical models using the smeared cracks approach.

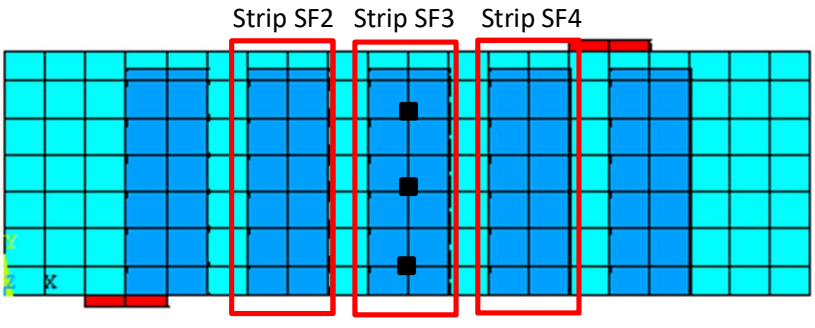

Figure (5.51): Location of CFRP strain gauges in FE model.

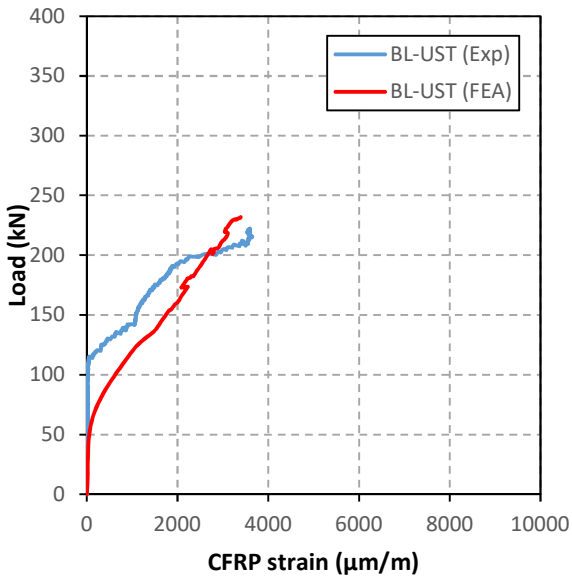

(a): BL-UST.

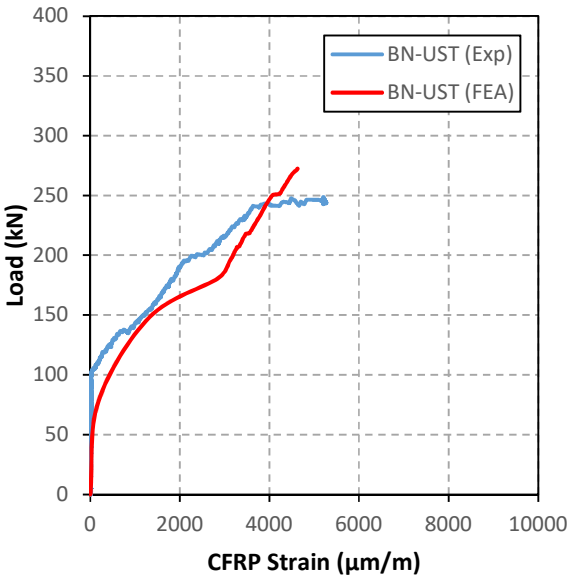

(b): BN-UST.

Figure (5.52): Load versus CFRP strain for BN/L-UST samples.

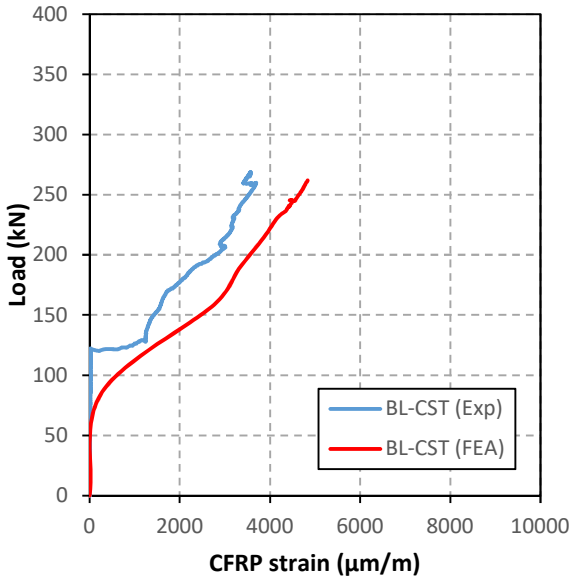

(a): BL-CST.

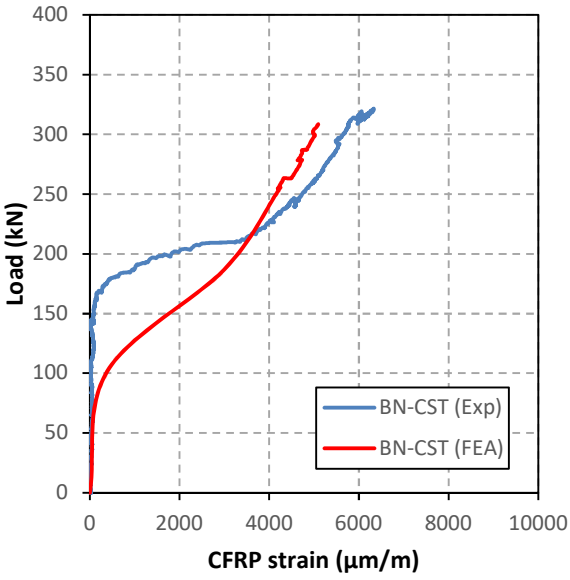

(b): BN-CST.

Figure (5.53): Load versus CFRP strain for BN/L-CST samples.

5.5.4. Parametric Study

The following subsections detail the effect of different parameters on the shear behaviour of the lightweight concrete samples. It should be noted that the predicted results reflect the response of the FE models rather than that of the actual physical samples. The shear strength gains due to CFRP reinforcement were obtained by subtracting the predicted control sample maximum shear strength capacity from the corresponding predicted retrofitted shear strength capacity.

5.5.4.1. Effect of Concrete Strength

Figure (5.54) show the influence of the concrete compressive strength of the maximum load capacity of lightweight reinforced concrete beam. Three different values of concrete compressive strength were used (30, 40 and 50 MPa) in the FE models of the control sample (BL) as well as the retrofitted sample BL-UST. The finite element models employed to examine the influence of the compressive strength of concrete on the behaviour of the FE models simulated in Section (5.5.1).

The outcomes of the FE models showed that the load capacity of the lightweight samples correlates linearly with concrete compressive strength. Increasing the concrete compressive strength from 30 MPa to 40 MPa results in an increasing in the load carrying capacity of the control sample (BL) by 63%. Varying the concrete uniaxial strength from 40 MPa to 50 MPa results in an increasing in the load carrying capacity of the control sample (BL) by 66%. The considerable increases in the maximum load were foreseeable because the LWAC samples were without shear reinforcement links. Therefore, the increasing in concrete uniaxial strength will increase the shear strength provided by concrete as results of that the load capacity of the reinforced concrete beams will improve. It can be noted that the increase in compressive strength of concrete showed a significant increasing in the shear strength provided by the CFRP reinforcement. The total shear strength provided by CFRP reinforcement in both sides of sample BL-UST were 68.9 kN, 66.6 kN and 70.2 kN, respectively when the compressive strength of concrete increased from 30 MPa to 50 MPa. In this study, the percentage increase in shear strength provided by CFRP reinforcement did not considerably influence by increasing the concrete compressive strength, as the shear strength provided by CFRP is increased constantly by roughly equal percentages increase respectively.

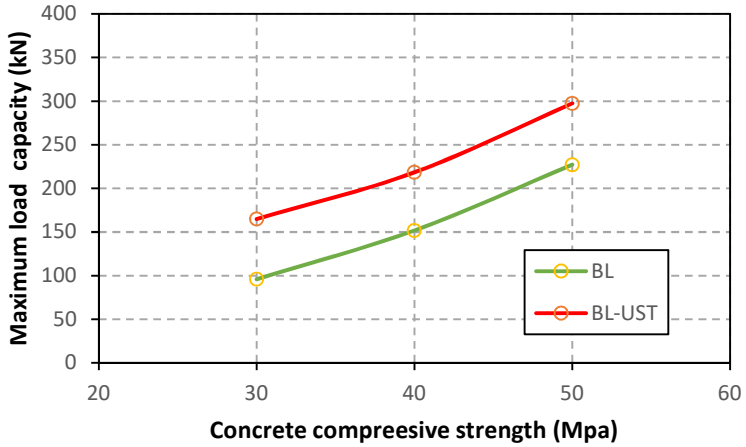

Figure (5.54): Effect of concrete compressive strength on the predicted load capacity.

5.5.4.2. Effect of CFRP Thickness

The influence of CFRP thickness was investigated by implementing sample BL-UST which is geometrically similar to the retrofitted samples simulated in this chapter. The thickness of CFRP strips was varied in the FE models by increasing the number of CFRP layers from one up to 3 layers. Figure (5.55) shows the relation between the maximum predicted load and the thickness of the CFRP reinforcement. It can be concluded that the effect of the CFRP thickness did not significantly improve the maximum load capacity of the simulated models. Increasing the CFRP thickness from 0.117 mm (one layer) to 0.234 mm (two layers) and 0.351mm (three layers) results in an increasing in the maximum load of BL-UST sample from 231.7 kN to 242.8 kN and 245.91 kN, respectively.

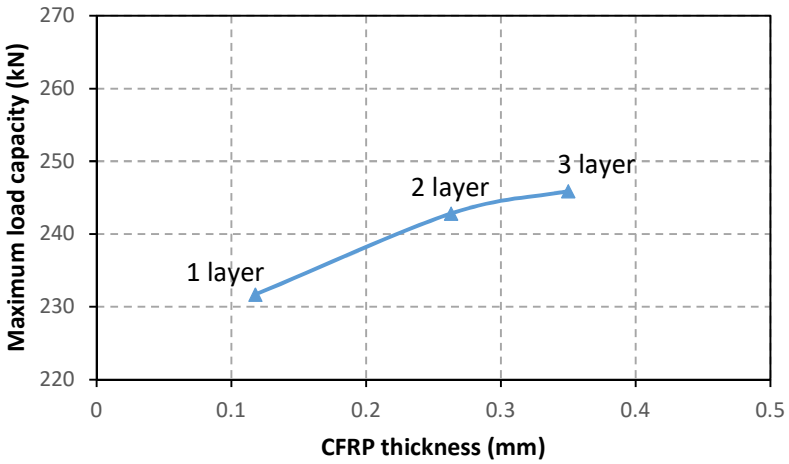

Figure (5.55): Effect of CFRP thickness on the predicted load capacity.

5.6. Summary

Three-dimensional FEA models with smeared crack approach were created to implement the bond-slip response and the behaviour of reinforced lightweight and normal weight concrete beams retrofitted with CFRP shear reinforcement. The response of the finite element models reveals reasonable curves in the predictions compared with results collected from the experimental models.

The response of load-mid span deflection curves of the beam shear test collected from FE models shows identical responses compared with actual physical models in the linear elastic stage. In this study, the FE models are stiffer in cracking stage compared with experimental models. This is attributed to the effect of the bond between concrete and steel reinforcement or between the CFRP reinforcement and concrete which are assumed as a full bond which cause the higher stiffness as well as a difference in behaviour between the FEA models and the actually tested samples. Cracks distribution at failure in numerical models correlates well with those observed in actual beam shear models.

The load-slip curves for bond-slip models as well the load-CFRP strain curves in beams shear tests and show good agreement with the experimental results. It can be concluded that the FE models simulated in this chapter show the ability of FE models to predicate the structural behaviour of the bond-slip and beam shear test and provide an additional tool to examine the effect of different variables in the behaviour of lightweight concrete beam retrofitted with CFRP reinforcement.

CHAPTER SIX

NEW DESIGN PROPOSAL

6.1. Introduction

Different numerical approaches had been used to model the relationships of the FPP/concrete joint which observed from the experimental models. Past numerical models were driven by the need to examine the effects of parameters which were either not addressed in the current literature or had been derived from the experimental test results. They have not been developed to various types of concrete such as lightweight concrete strengthened with CFRP composite. To address this, in this study new models are developed to estimate the characteristics of the FRP-to-concrete bond including the effects of lightweight concrete properties on the maximum bond strength between concrete and CFRP composite and the shear strength of these reinforced concrete beams with reasonable accuracy.

6.2. Theoretical Derivation of the First Proposed Model (Simplified Model)

The strain distribution along the length of FRP reinforcement may be correlated with various numerical formulas, for example, quadratic or exponential formulas (Bizindavyi and Neale 1999; Dai et al. 2005; Foster and Khomwan, 2005 Hadigheh, 2014 and Hadigheh and Gravina, 2016**)**. This study presents a new expression for the maximum bond strength and strain distribution along the length of the Carbon Fibre Reinforced Polymer (CFRP) composite. This is developed based on a polynomial strain formula which has been solved using the typical boundary conditions of the double-lap shear test to describe the characteristics of the FRP-to-lightweight concrete interface and the maximum bond strength between the FRP reinforcement and the lightweight concrete.

In this study, the strain distribution along the length of the CFRP reinforcement can be correlated with a fourth-degree polynomial formula for both specimens (lightweight and normal weight concrete (see Figure (3.25) to (3.36)). Figure (6.1) reveals an example of the correlated fourth-degree polynomial formula of the Proposed trend and the experimental test results which are obtained for CFRP strain gauges' measurements attached along the bonded length at the corresponding maximum load for samples cast with LWAC and NWAC. An acceptable fitting

available between the polynomial and the experimental curves at the maximum load. The strain profile as a function of the experimental applied load based on 4th and 3rd-degree polynomial formulas was proposed by **(**Foster and Khomwan, 2005; Hadigheh and Gravina, 2016**).** In the model presented here a new equation for the strain profile and the interface behaviour of the FRP-lightweight /normal weight concrete joints based on the maximum design debonding force developed in this study, (including the effects of concrete type, width and length of FRP reinforcement) are established.

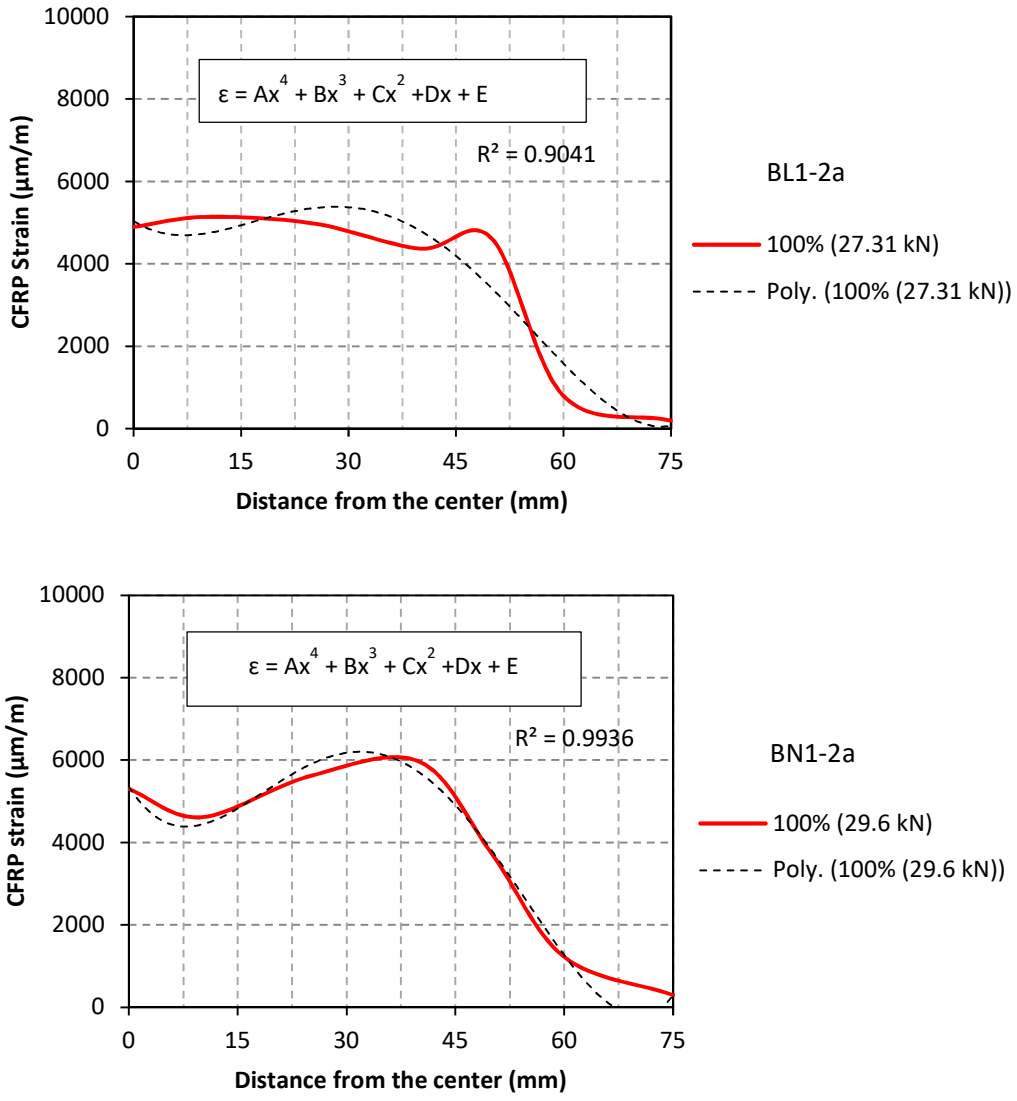

Figure (6.1): Strain distribution along CFRP Length and interpolation curves of the BL1-2a and BN1-2a samples.

Figure (6.2) shows the typical loading conditions of the double-lap test sample. Each of the FRP reinforcements can carry half of the total load applied at the bar ends of the sample or the maximum debonding load carried by one FRP reinforcement. The interfacial shear stress between the FRP reinforcement and the concrete given by τ_b. By bond action, stresses are transferred from the concrete substrate to the FRP reinforcement through the adhesive layer, the process of stress transference is illustrated in Figure (6.3). The interfacial shear stress increases linearly until point A in the shear stress-slip curve, the strain profile has a quadratic shape within this stage. As the loads increased, interfacial shear stress-slip curve achieved point B and the interfacial small cracks start to develop in FRP/concrete joints till the occurrence of the large interfacial crack. Beyond this stage, the maximum bond strength of the FRP/concrete joint achieve its maximum value and the cracks reach the required bond length (L_e) as shown at points C and D on the interfacial shear stress-slip curve. Along the bonded zone, the FRP strain measurements close the centre of the samples remains constant. At point E on the interfacial shear stress-slip curve, any trial to add more loads further this stage causes a sudden movement of the unbounded zone to the far end of the FRP reinforcement, causing abrupt brittle failure as the FRP detached from the concrete surface **(**Foster and Khomwan, 2005).

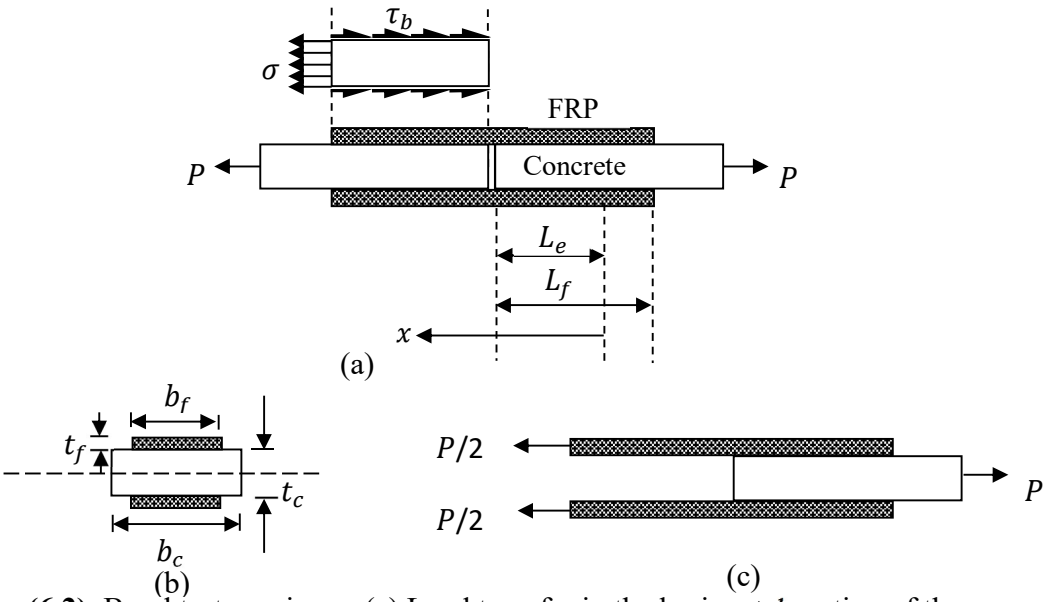

Figure (6.2): Bond test specimen: (a) Load transfer in the horizontal section of the concrete and CFRP sheet (b) Transverse section of concrete and CFRP sheet and (c) Free body diagram of half specimen.

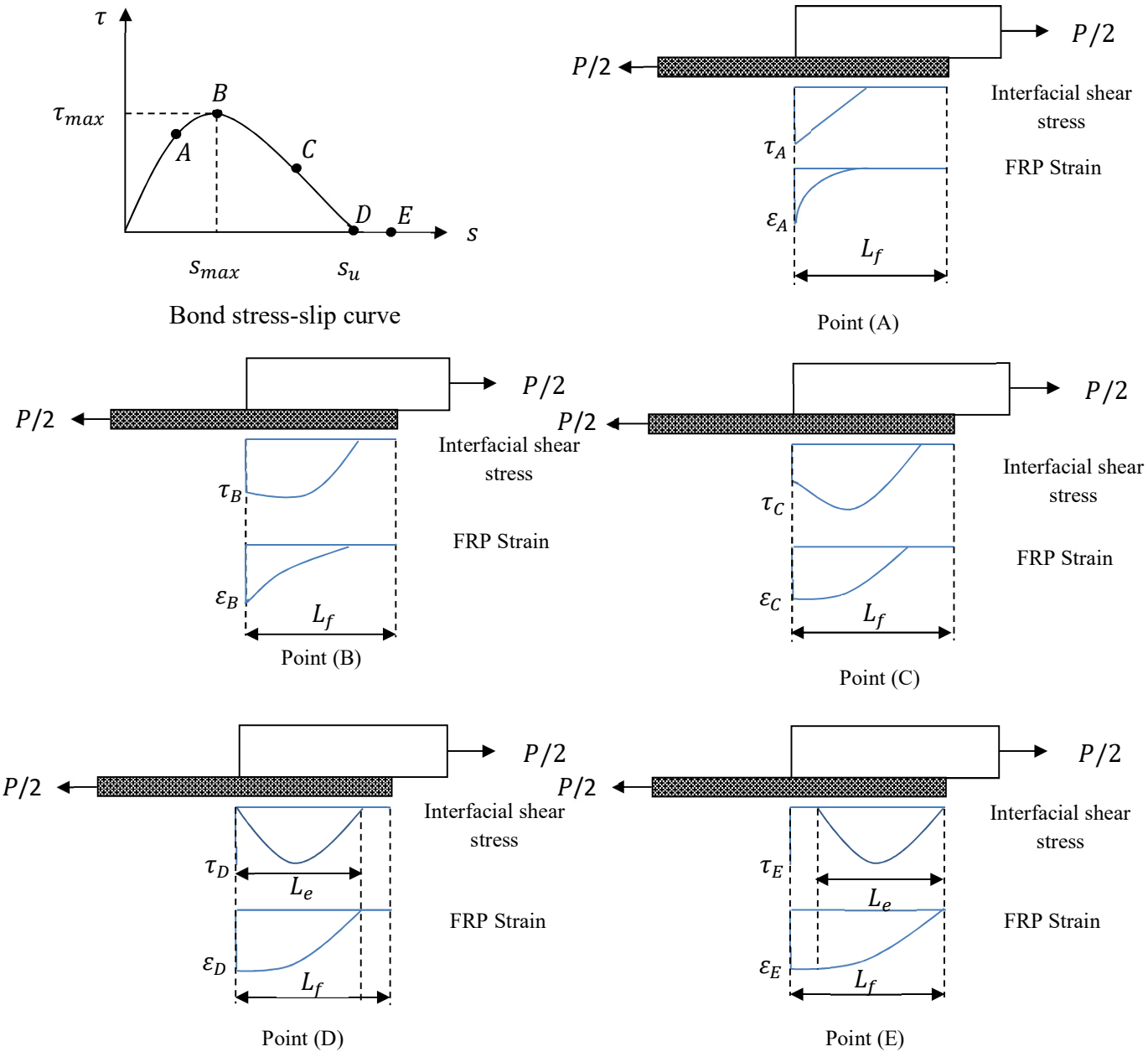

Figure (6.3): Stages of development of bond stress in the double-shear bond test.

6.2.1. Strain Profile

The location of the strain gauge along the length of the FRP reinforcement can considerably influence the strain measurements, for instance, strain gauges sited directly over the interfacial large crack will record higher elongation compared with gauges locate over aggregate particle (Lua et.al, 2005). To control the differences in strains reading which led to a noticeable flaw during the process of evaluation of the FRP-lightweight /normal weight concrete bond relationships, the strains distribution can be correlated with a fourth-degree polynomial formula for samples cast with LWAC and NWAC as shown in Figure (6.1). When the effective length (L_e) is known, the boundary conditions requirements of the double-lap shear tests can be expressed as a function of the effective bonded length of FRP reinforcement (L_e) as follows (Foster and Khomwan, 2005):

$at\ x = 0$

$$\varepsilon_{frp,x} = 0 \tag{6.1}$$

and,

$$\frac{d\varepsilon_{frp,x}}{dx} = 0 \tag{6.2}$$

$at\ x = L_e$

$$\varepsilon_{frp,x} = \varepsilon_{max} \tag{6.3}$$

$$\frac{d\varepsilon_{frp,x}}{dx} = 0, \frac{d^2\varepsilon_{frp,x}}{dx^2} = 0, \tag{6.4}$$

Where ε_{max}, is the maximum FRP strain at the centre of the sample. The strain along the length of the FRP reinforcement can be given by the 4th order polynomial function (Foster and Khomwan, 2005):

$$\varepsilon_{frp,x} = Ax^4 + Bx^3 + Cx^2 + Dx + E \tag{6.5}$$

$$\frac{d\varepsilon_{frp,x}}{dx} = 4Ax^3 + 3Bx^2 + 2Cx + D \tag{6.6}$$

$$\frac{d^2\varepsilon_{frp,x}}{dx^2} = 12Ax^2 + 6Bx + 2C \quad (6.7)$$

Where, A, B, C, D and E are constant values which are obtained by substituting the boundary conditions defined by Equations (6.1) to (6.4) and solving Equation (6.5) to (6.7) simultaneously this gives (Foster and Khomwan, 2005):

$$A = \frac{3\varepsilon_{max}}{L_e^4}, B\frac{-8\ \varepsilon_{max}}{L_e^3}, C = \frac{6\varepsilon_{max}}{L_e^2}, D = 0, E = 0 \quad (6.8)$$

Thus, the FRP strain profile along the bond length of FRP reinforcement can be expressed by the following equation (Foster and Khomwan, 2005):

$$\varepsilon_{frp,x} = \varepsilon_{max}(3\xi^4 - 8\xi^3 + 6\,\xi^2) \quad (6.9)$$

Where,

$$\xi = \frac{x}{L_e} \quad (6.10)$$

The maximum strain in the FRP reinforcement can be obtained from the following equation:

$$\varepsilon_{max} = \frac{P_d}{b_f t_f E_f} \quad (6.11)$$

Figure (6.4) shows the strain profile along the bonded length as a function of ξ which ranges between 0 and 1. It can be seen that just two parameters are required to describe the strain profile distribution along the length bonded FRP reinforcement, maximum debonding force and the effective length of FRP reinforcement. In this study, the strain distribution along the bond length of FRP reinforcement can be written as a function of the maximum debonding force as follows (Equation (6.12)):

$$\varepsilon_{frp,x} = \frac{P_d}{b_f t_f E_f}(3\xi^4 - 8\xi^3 + 6\,\xi^2) \quad (6.12)$$

Where b_f, t_f and E_f are the width, thickness and modulus of elasticity of FRP sheet, respectively and P_d is the maximum debonding force carried by one FRP reinforcement.

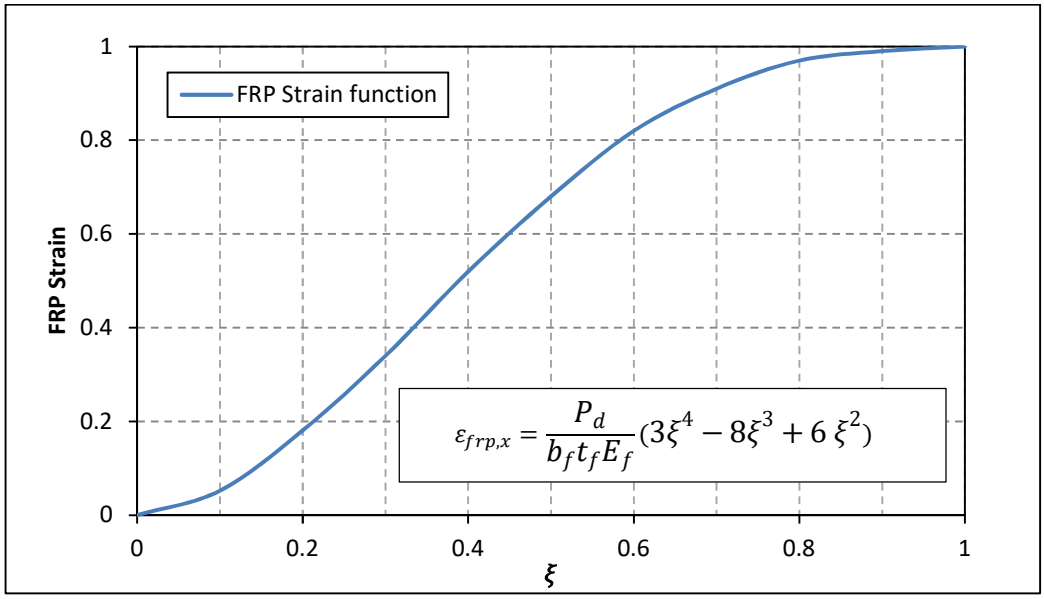

Figure (6.4): FRP strain function curve.

6.2.2. Interfacial Local Bond Stress

The bond shear stress along the length of FRP sheet $\tau_{b,x}$ can be calculated from the following equation (Equation (6.13)):

$$\tau_{b,x} = \frac{d\varepsilon}{dx} . t_f . E_f \tag{6.13}$$

By substituting Equation (6.10) and Equation (6.12) into (6.13) and differentiating this Equation gives (Equation (6.14)) (Foster and Khomwan, 2005):

$$\tau_{b,x} = \frac{12\ P_d}{b_f L_e}(\xi^3 - 2\xi^2 + \xi\ ) \tag{6.14}$$

6.2.3. Bond Strength of Pure Tensile Force

The bond between concrete surface and FRP reinforcement is vital for a concrete member attached externally by FRP reinforcement. It should be ensured that the required bond between FRP and concrete surface is attained which will help the FRP reinforcement to achieve good bond strength along the bond agent. The experimental test results of this study and other studies such theses carried out by Zhao, (2004) showed that the failure developed by the shear failure of the concrete block.

This means that the bond between FRP and concrete is affected by initiation of the cracks within the concrete layer adjacent to FRP reinforcement. It can be concluded that the main contributor to the resistance to the applied debonding force is the shear strength of concrete (see Figure (6.5)). For design purposes, the maximum debonding force that can be achieved at the initiation of the debonding is obtained by the following equation (Equation (6.15)):

$$P_d = b_f . L_e . \tau_{av} = b_f \int_0^{L_e} \tau(x)\, dx \quad (6.15)$$

Where τ_{av}, is the average bond shear stress that can be determined using Equation (6.16) ((Biscaia et al., 2012; Serbescu et.al., 2013):

$$\tau_{av} = \beta_r . \tau_{max} \quad (6.16)$$

Where, τ_{max} is maximum bond shear stress which is equivalent to the concrete shear strength assumed to be equal to the square root of the cylinder compressive strength of concrete, f_c' based on ACI-2008 (ACI, 2008).

In this study, the concrete cylinder compressive strength is assumed as 0.8 times the cube compressive strength. The difference between the cylinder and cube strengths for LWAC is less than for a NWAC concrete as stated in EN, (1992). However, the CEB-FIB codes and standards for LWAC assume a similar difference between the cylinder and cube strengths for design calculations as for NWAC (CEB-FIB, 1992 and CEB-FIB, 1999). Hence, a difference of 0.8 was assumed for both lightweight and normal weight concrete mixtures for comparison purposes.

The trem β_r in Equation (6.16) represents the ratio between the mean local shear stress and the maximum local shear stress which is suggested by Chen and Teng, (2001) as 0.315, this factor represents the most accurate value required to obtain the maximum design debonding force. For double lap shear tests, it was assumed as 0.63. By substituting Equation (6.16) into Equation (6.15) gives the maximum design force (Equation (6.17)):

$$P_d = \beta_r . b_f . L_e . \sqrt{f_c'} \quad (6.17)$$

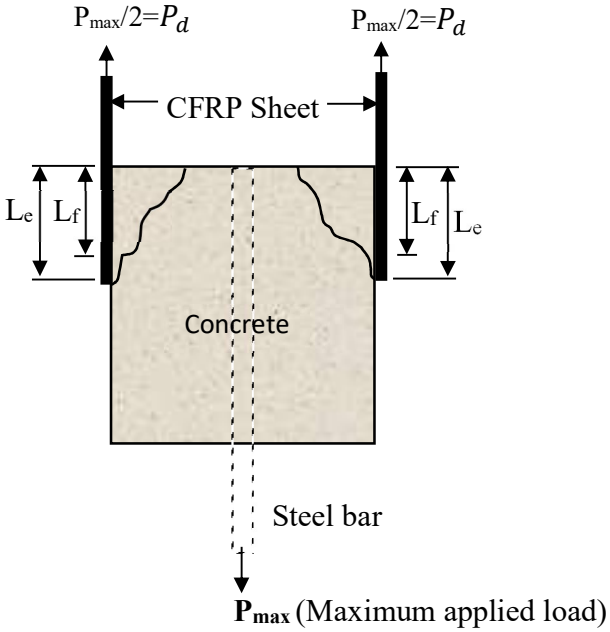

Figure (6.5): Failure of concrete block.

6.2.3.1. Effect of Concrete Type

To represent the effect of concrete types on the maximum bond between concrete and FRP composite, a new bond reduction factor was assumed in this model for LWAC, depending on the experimental results of this study (section 3.1.6.8.). This is shown in the following equation (Equation (6.18)):

$$R = \begin{cases} 1 & for\ NWAC\ concrete \\ 0.85 & for\ LWAC\ concrete \end{cases} \quad (6.18)$$

The ACI code for shear strengthening recommended using a reduction factor of 0.85 for bond-critical shear reinforcement structures which can be used for LWAC elements (ACI 440.2R, 2008).

6.2.3.2. Effect of FRP Width

The FRP width is one of the most influential parameters affecting the maximum bond between the FRP reinforcement and concrete. Thus, an FRP width factor β_w was adopted from Serbescu et.al., (2013) as (Equation (6.19)):

$$\beta_w = \frac{455}{b_f + 350} \quad (6.19)$$

6.2.3.3. Effect of FRP Length (L_e)

The outcomes of the previous studies and guidelines showed that the effective bond length of the FRP reinforcement increases as the FRP axial rigidity $(E_f.t_f)$ increases and decreases as the concrete compressive strength (f'_c) increases (Chen and Teng, 2001 and Parth Athawale, 2012). In this study, a new equation was developed to predict the effective length of the CFRP sheet based on linear calibration carried out on the current experimental results and the data of 65 experimental study (Ouezdou, 2008). (see Appendix B) as shown in Equation (6.20) and Figure (6.6). In this model, it is suggested to use the actual length of FRP reinforcement, when the length is less than the effective length predicted by Equation (6.20):

$$L_e = \begin{cases} 0.95\left(\sqrt{\frac{E_f.t_f}{\sqrt{f'_c}}}\right) + 3.4 & if \quad L_f > L_e \\ L_f & if \quad L_f < L_e \end{cases} \tag{6.20}$$

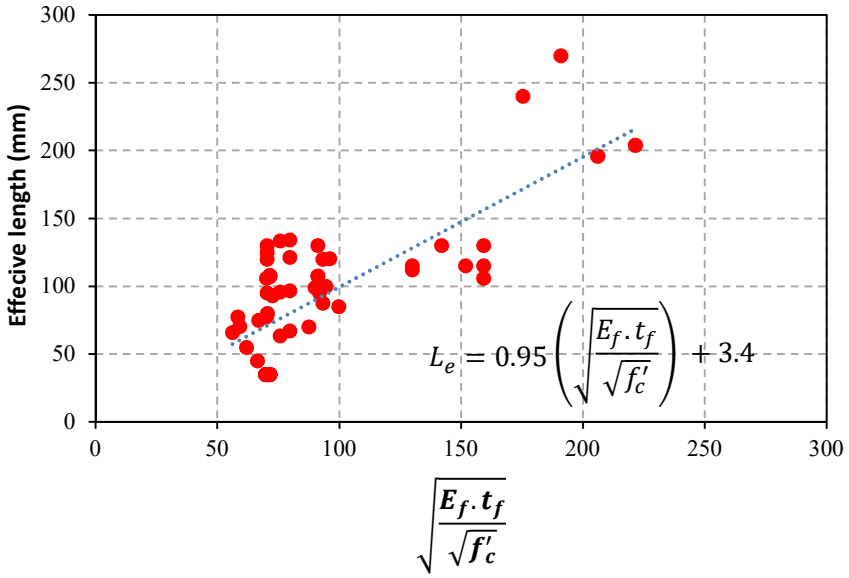

Figure (6.6): Relationship between the effective bond length of the FRP reinforcement and the affecting variables.

By introducing all the proposed parameters, the design debonding force can be expressed in Equation (6.21):

$$P_d = \beta_r . \beta_w . R . b_f . L_e . \sqrt{f_c'} \quad (6.21)$$

The proposed strain and the bond stress along the length of FRP composite can be expressed as a function of the maximum design debonding force carried by one FRP reinforcement by substituting Equation (6.21) into Equation (6.13) and (6.14) as follows (Equation (6.22) and (6.23)):

$$\varepsilon_{frp,x} = \frac{\beta_r . \beta_w . R . L_e . \sqrt{f_c'}}{t_f E_f} (3\xi^4 - 8\xi^3 + 6\,\xi^2) \quad (6.22)$$

$$\tau_{b,x} = 12\,\beta_r . \beta_w . R . \sqrt{f_c'} (\xi^3 - 2\xi^2 + \xi\,) \quad (6.23)$$

The maximum proposed design debonding FRP strain at the end of the effective length ($x=L_e$) can be obtained by the following equation (Equation (6.24)):

$$\varepsilon_{max,d} = \frac{\beta_r . \beta_w . R . L_e . \sqrt{f_c'}}{t_f E_f} \quad (6.24)$$

6.2.4. Slip Profile

The slip between FRP reinforcement and the concrete substrate at any point *x* along the bonded length of FRP reinforcement is defined as the difference between the displacement of the FRP and concrete sample. Figure (6.7) shows the compatibility of the axial and shear strains, as well as the equilibrium of the normal and shear stresses developed in a finite element of the FRP/concrete joint (Hadigheh, 2014). In this study, a new expression for the interface slip and the ultimate slip based on the maximum debonding force were developed in this study to obtain a more practical and general equation for double-lap and single-lap shear test. The interfacial relative slip can be obtained by the following equation (Equation (6.25)):

$$s_x = u_{frp,x} - u_{c,x} \quad (6.25)$$

Or,

$$s_x = \int_0^x \varepsilon_{frp,x} \,.\, d_x - \int_0^x \varepsilon_{c,x} \,.\, d_x \tag{6.26}$$

The displacement of the FRP reinforcement can be obtained by integrating the strain distribution along the length of the FRP reinforcement ($0 \leq x \leq L_e$) as follows (Equation (6.27)):

$$u_{frp,x} = \int_0^x \varepsilon_{frp,x} \,.\, d_x \tag{6.27}$$

By substituting Equation (6.12) into Equation (6.26) and solving this equation gives (Equation (6.28)) which:

$$u_{frp,x} = \frac{P_d}{b_f t_f E_f} L_e \, \xi^3 (0.6 \, \xi^2 - 2\xi + 2) \tag{6.28}$$

The past experimental and theoretical research of the bond shear tests addressed in Liu and Wu, (2012) and Hadigheh et al., (2016) show that the displacement of the concrete prism is very small compared with FRP strains and can be ignored in this model. The slip along the length of the FRP reinforcement can be obtained by the following (Equation (6.29)):

$$s_x = \frac{P_d}{b_f t_f E_f} L_e \, \xi^3 (0.6 \, \xi^2 - 2\xi + 2) \tag{6.29}$$

The slip as a function of the maximum debonding load can be obtained by substituting Equation (6.21) into Equation (6.29) as follows (Equation (6.30)):

$$s_x = \frac{\xi^3 \beta_r . \beta_w . R . {L_e}^2 . \sqrt{f_c'}}{t_f E_f} (0.6 \, \xi^2 - 2\xi + 2) \tag{6.30}$$

The ultimate slip corresponding to the maximum debonding force can be obtained by substituting ($x = L_e$) into Equation (6.31):

$$s_u = \frac{0.6 \, \beta_r . \beta_w \,.\, R . L_e^2 . \sqrt{f_c'}}{t_f E_f} \tag{6.31}$$

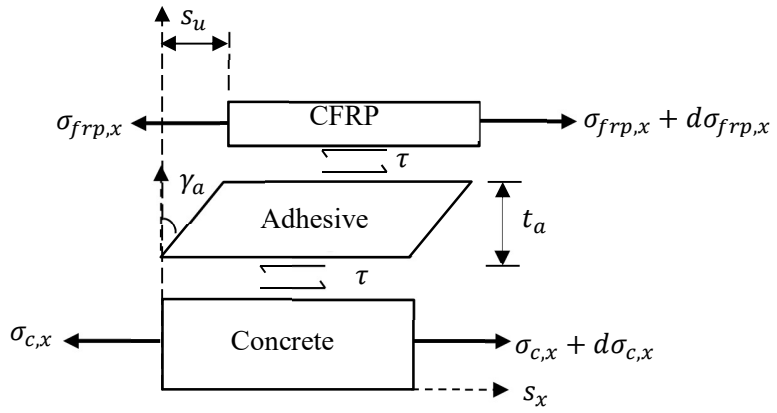

Figure (6.7): Axial and shear strains of the FRP-concrete interface.

6.2.5. Validation and Calibration of the Proposed Model

In this section of the chapter, the trustworthiness of the proposed models to evaluate the response of the FRP/concrete joints for LWAC and NWAC samples was examined in details. A comparison between the outcome of the analytical model developed in section (6.2) and the experimental test results collected from the double-lap shear tests. Various bond relationships were examined in this section, for example, the maximum bond strength for the double-lap shear tests, the strain distribution along the length of the FRP reinforcement and the ultimate slip corresponding the maximum debonding force.

6.2.5.1. Validation and Calibration of the Maximum Bond Strength and The Effective Length

In order to assess the use of the proposed and the existing models in LWAC, the prediction of the maximum load carrying capacity using Equation (6.21) for the double-lap shear test condition and the models or guidelines proposed by (FIB 14, 2001), (TR-55, 2013), (Yang et al., 2001) and (Iso, 2003) are considered in this study. The maximum bond between concrete and FRP composite, P_{max} and the effective bond length, L_e according to FIB 14 (FIB 14 ,2001) is as follows (Equation (6.32) and (6.34)):

$$P_{max} = \alpha . c_1 . k_c . k_b . b_f . \sqrt{E_f . t_f . f_{ctm}} \quad (6.32)$$

$$k_b = 1.06 \cdot \sqrt{\frac{2 - b_f/b_c}{1 + b_f/400}} \geq 1.0 \quad (6.33)$$

$$L_e = 0.7 \sqrt{\frac{E_f . t_f}{c_2 . f_{ctm}}} \quad (6.34)$$

$$P_{\max} = \left(P_{max} . \frac{L_f}{L_e}\right)\left(2 - \frac{L_f}{L_e}\right) \quad when, \qquad L_f < L_e \quad (6.35)$$

Where P_{max} , L_f and L_e are the maximum debonding force, the bonded length of the FRP reinforcement, and effective bond length respectively; t_f, b_f, and E_f are thickness, width, and the modulus of elasticity of the FRP reinforcement respectively; b_c is the width of the concrete sample; f_{ctm} is the mean tensile strength of concrete, α is a coefficient of reduction which is taken as 0.9, to account for the effect of inclined shear cracks close the loaded end on the bond strength capacity; k_c is a factor accounting for the state of compaction of concrete (it can be taken as 1.0); k_b is a geometric factor computed by Equation (6.33). The c_1 and c_2 in Equations (6.32) and (6.34) can be calculated by calibrating the theoretical value with test results. However, for CFRP sheet, c_1 and c_2 are assumed as 0.64 and 2.0 respectively. Moreover, for FRP bond lengths, $L_f < L_e$ the maximum debonding force can be computed by Equation (6.35).

The maximum debonding force of FRP reinforcement, P_{max} and the effective bond length, L_e in TR-55 (2013), are assessed based on the following expressions (Equation (6.36) and (6.38)):

$$P_{max} = 0.5 \cdot k_b \; b_f \cdot \sqrt{E_f . t_f . f_{ctk}} \quad (6.36)$$

$$k_b = 1.06 \cdot \sqrt{\frac{2 - b_f/b_c}{1 + b_f/400}} \geq 1.0 \quad (6.37)$$

$$L_e = 0.7 \sqrt{\frac{E_f . t_f}{f_{ctk}}} \quad (6.38)$$

$$P_{\max}\ (L_f < L_e) = \left(P_{max} . \frac{L_f}{L_e}\right)\left(2 - \frac{L_f}{L_e}\right) \quad when, \qquad L_f < L_e \quad (6.39)$$

Where P_{max}, L_f and L_e are debonding load, FRP bond length, and effective bond length respectively;t_f, b_f, and E_f are the thickness, width and the modulus of elasticity of the FRP

reinforcement respectively; b_c is the width of the concrete sample; f_{ctk} is the characteristic tensile strength of concrete.

The experimental values of the flexural tensile strength were used in this study to represent the characteristic or the mean tensile strength of concrete to achieve the required accuracy in the comparison between the proposed model and the other models. Similar to FIB 14, k_b can be calculated using Equation (6.37). The details of the (Yang et al., 2001) and (Iso, 2003) models are discussed in chapter two section (2.12).

The coefficient of variation of the predicted bond strength for the LWAC and NWAC are summarised in Figure (6.8) and (6.9). A certain disparity is apparent between the NWAC and LWAC results. The results of the average predicted to the experimental ratio of the LWAC and NWAC samples are summarised in Table (6.1) and (6.2).

Generally, The NWAC results show better agreement than those of the LWAC results. It can be seen that the model suggested by Iso (2003) and Yang et al. (2001) showed the highest coefficients of variation between the predicted-to-experimental load ratio in the case of specimens cast with LWAC and NWAC. The higher values of the coefficient of variation (C.V) for the (Iso's 2003) and (Yang's 2001) models were attributed to the effect of the width of the FRP sheet which is not considered in these models. In addition, the model proposed by (Iso's 2003) is derived based on the concrete cylinder strength, since the effect of concrete tensile strength not included in this model.

On the other hand, the model proposed by TR-55 (2013), simplified model (this study) and FIB 14 (2001), show the lowest values of the coefficient of variation (C.V) on account of the fact that they consider the effect of the width of the FRP sheet and the concrete tensile strength or concrete type (this study) in calculating the maximum debonding forces. The average prediction for test bond strength of the LWAC and NWAC specimens are summarised in Table (6.3).

For more detail, the overall average value of the predicated-to-experimental load ratio of the proposed model in this study is 0.91 for LWAC specimens. The standard deviation (S.D) and the coefficient of variation C.V (%) are 0.21 and 23, respectively. It can be noted that the theoretically calculated load for samples with width ratio of 0.75 is significantly higher than the experimental load by approximately 35%, It can be concluded that the outcomes of the proposed model

overestimated the bond strength for samples with higher FRP to width ratio, whilst the influence of the FRP-to-concrete width ratio using the factor developed by Serbescu et.al., (2013) was included in this model.

The results obtained from the proposed model and other bond strength models are in close agreement with the experimental test results of NWAC samples. The average value of the predicated-to-experimental load ratio of this study is 0.92. The standard deviation (S.D) and the coefficient of variation C.V (%) are 0.18 and 19.5, respectively.

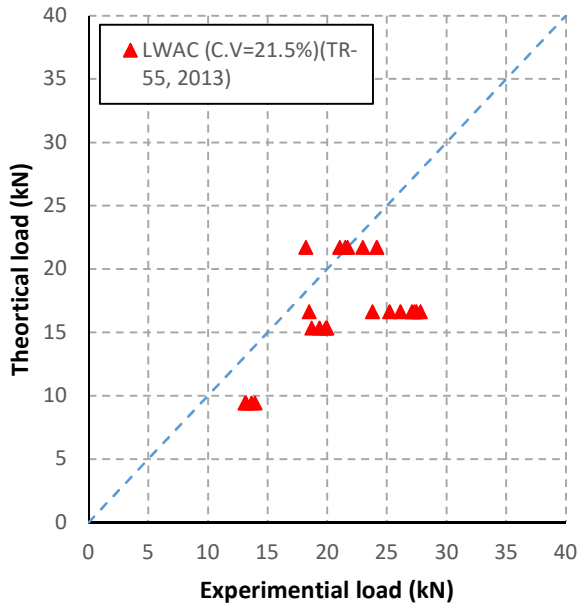

(a): TR-55.

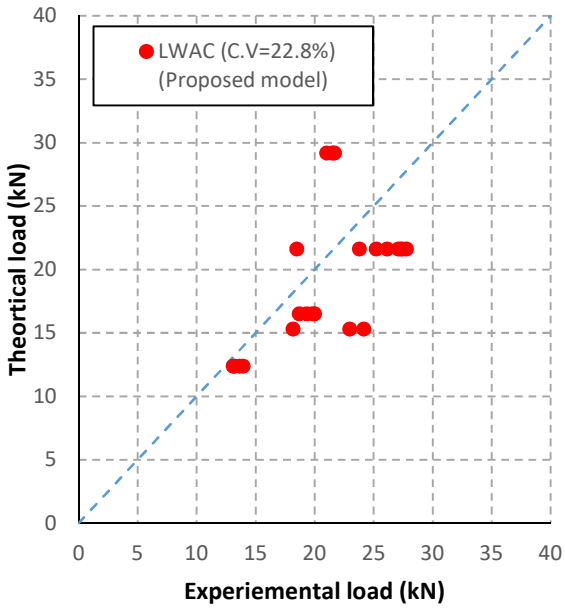

(b): Proposed model.

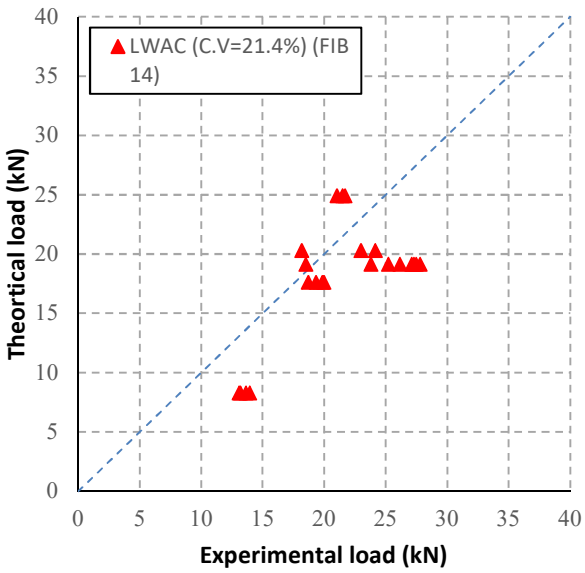

(c): FIB 14.

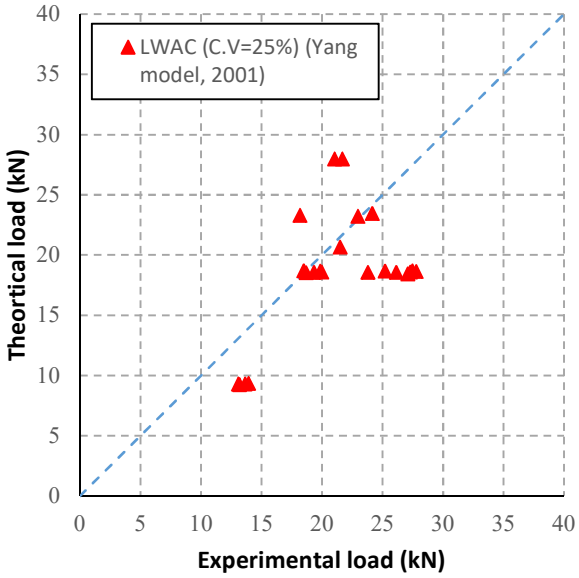

(d): Yang et al., 2001.

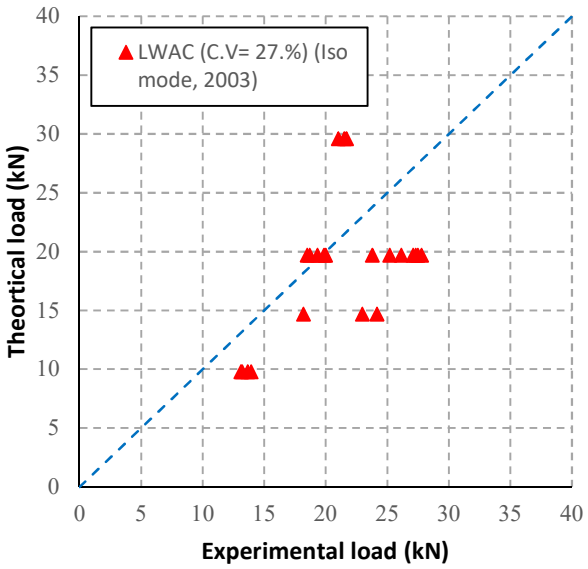

(e): Iso, 2003.

Figure (6.8): Theoretically predicted load versus experimental observation of LWAC samples.

Table (6.1): Average prediction to the experimental bond strength of LWAC samples.

Specimen ID	Exp load (kN)	Predicted to Experimental ratio				
		This study	TR-55	FIB 14	Yang's 2001	Iso's 2003
BL1-1a	19.34	0.85	0.79	0.91	0.96	1.02
BL1-1b	18.71	0.88	0.82	0.94	0.99	1.05
BL1-1c	19.99	0.83	0.77	0.88	0.93	0.99
BL1-1d	19.86	0.83	0.77	0.88	0.94	0.99
BL1-2a	27.31	0.79	0.61	0.70	0.68	0.72
BL1-2b	23.80	0.91	0.70	0.80	0.78	0.83
BL1-2c	27.80	0.78	0.60	0.68	0.67	0.71
BL1-2d	25.22	0.86	0.66	0.75	0.74	0.78
BL1-3a	26.15	0.83	0.64	0.73	0.71	0.75
BL1-3b	27.11	0.80	0.61	0.70	0.68	0.73
BL1-3c	18.50	0.90	0.90	1.03	1.01	1.06
BL1-3d	27.48	0.60	0.79	0.69	0.68	0.72
BL3-1a	24.16	1.17	0.63	0.84	0.97	0.61
BL3-1b	22.99	0.67	0.94	0.88	1.01	0.64
BL3-1c	18.19	0.84	1.19	1.11	1.28	0.81
BL4-1a	13.20	0.94	0.71	0.62	0.70	0.74
BL4-1b	13.10	0.95	0.72	0.63	0.71	0.75
BL4-1c	13.66	0.91	0.69	0.60	0.68	0.72
BL4-1d	13.95	0.89	0.67	0.59	0.67	0.70
BL4-2a	21.04	1.39	1.03	1.18	1.33	1.41
BL4-2b	21.69	1.35	1.00	1.14	1.29	1.36
BL4-2c	21.51	1.36	1.01	1.15	0.96	1.38
Mean		0.92	0.79	0.79	0.88	0.88
S.D.		0.21	0.17	0.18	0.22	0.24
C.V (%)		22.8	21.5	21.4	25	27.2

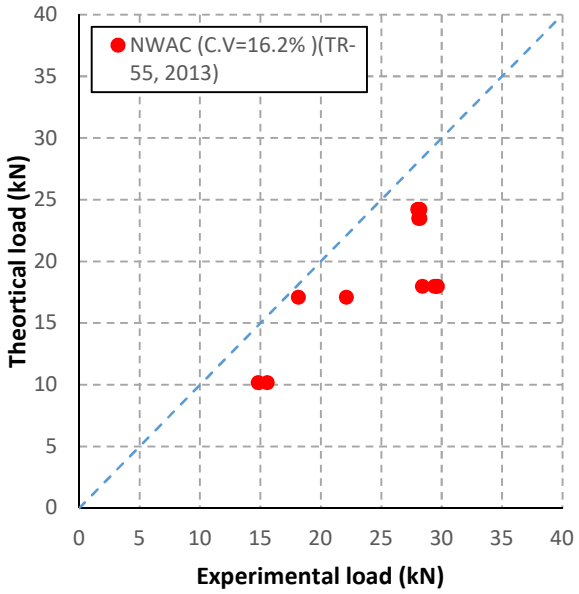

(a): TR-55.

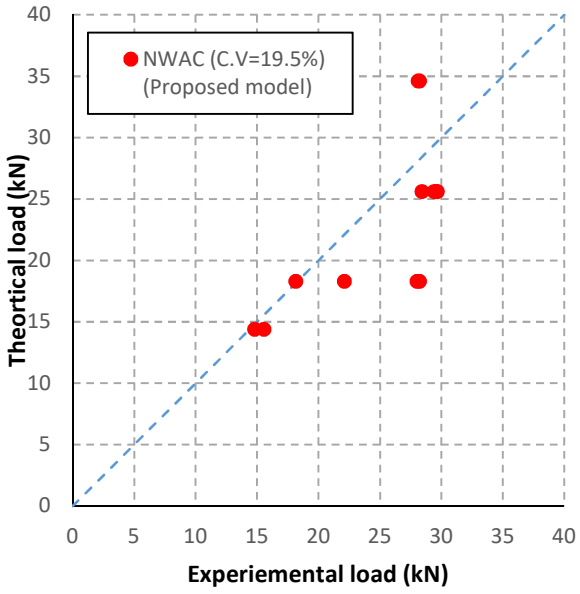

(b): Proposed model.

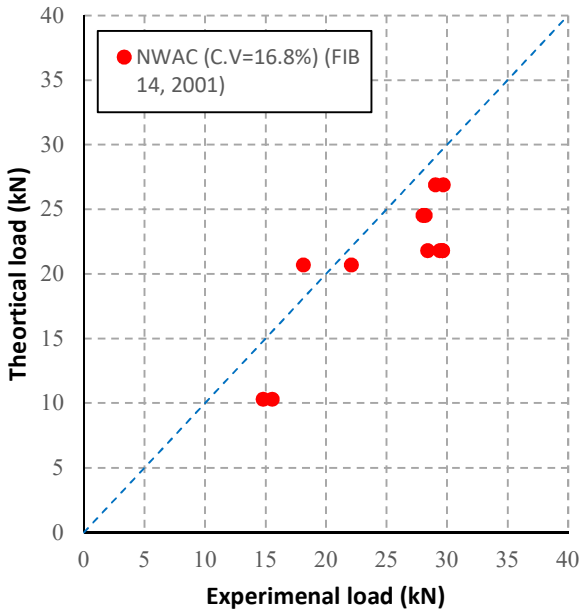

(c): FIB 14.

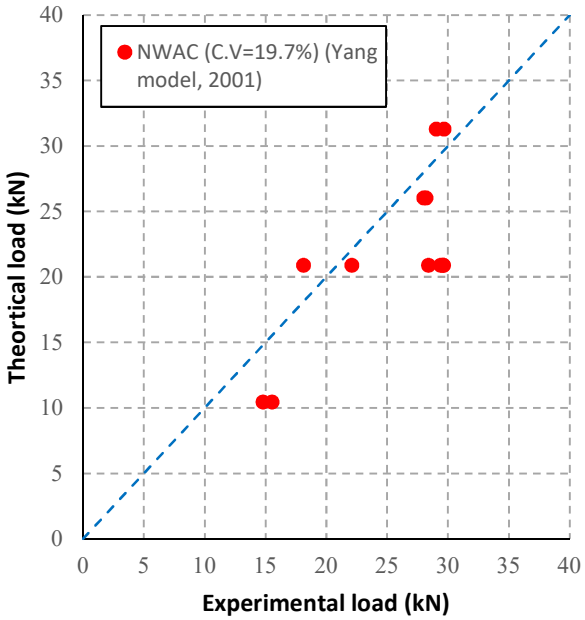

(d): Yang et al., 2001.

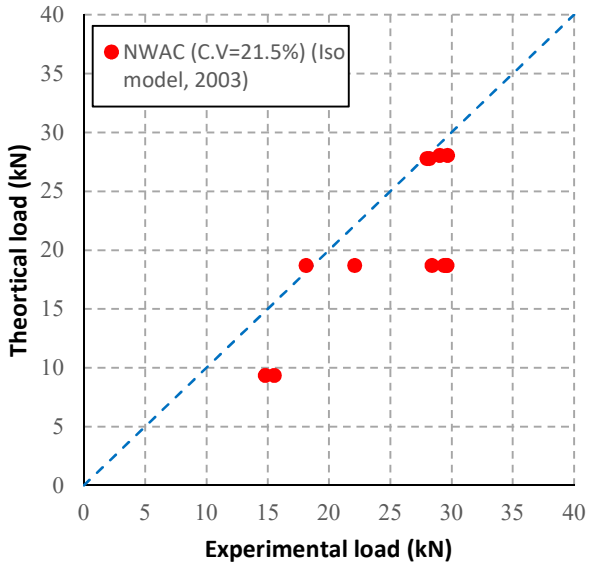

(e): Iso, 2003.

Figure (6.9): Theoretical prediction load versus experimental observation of NWAC samples.

Table (6.2): Average prediction to the experimental bond strength of NWAC samples.

Specimen ID	Exp load (kN)	Predicted to Experimental ratio				
		This study	TR-55	FIB 14	Yang's 2001	Iso's 2003
BN1-1a	18.13	1.01	0.94	1.14	1.15	1.03
BN1-1b	22.10	0.83	0.77	0.93	0.95	0.85
BN1-2a	29.60	0.86	0.61	0.74	0.71	0.63
BN1-2b	29.40	0.87	0.61	0.76	0.71	0.64
BN1-3a	28.40	0.90	0.63	0.87	0.74	0.66
BN1-3b	29.64	0.86	0.61	0.87	0.71	0.63
BN3-1a	28.01	0.65	0.86	0.66	0.93	0.99
BN3-1b	28.19	0.65	0.86	0.92	0.92	0.99
BN4-1a	14.80	0.97	0.69	0.90	0.71	0.63
BN4-1b	15.55	0.93	0.65	1.14	0.67	0.60
BN4-2a	28.10	1.23	0.84	0.93	1.08	0.97
BN4-2b	28.21	1.23	0.83	0.73	1.05	0.94
Mean		0.92	0.74	0.89	0.86	0.80
S.D.		0.18	0.12	0.15	0.17	0.18
C.V (%)		19.5	16.2	16.8	19.7	22.5

A database of 226 single and double- shear tests listed in Appendix C cited from Serbescu et.al., (2013) and Figure (6.10) to (6.12) was check the validity of Equation (6.21) and compared the accuracy of this equation with TR-55 and FIB models. It can be seen that the new proposed method gives results in acceptable agreement with the test results and is in reasonable agreement with TR-55 and FIB 14. The average value of the predicted-to-experimental load ratio of this study is 0.68. The standard deviation (S.D) and the coefficient of variation C.V (%) are 0.11 and 19.3, respectively.

The theoretical effective bond lengths of the CFRP sheet for both LWAC and NWAC tested samples predicted by the proposed model (simplified model), (FIB 14, 2001), (TR-55, 2013), (Yang et al., 2001) and (Iso, 2003) guidelines and models expressions are used in this study to evaluate the experimental effective length. The calculated effective length of the FRP reinforcement based on proposed model, FIB 14 and TR-55 guidelines are about 70.5 mm, 69.8 mm and 69.1 mm respectively in case of LWAC samples, while the predicted effective lengths for NWAC samples are about 69.9 mm, 64.4 mm and 63.8 mm respectively. A marginal variance in the calculated effective length between LWAC and NWAC samples. This is attributed to the difference in concrete cracking strengths of various concrete types. The predicted effective length based on Yang's model 2001 and Iso's 2003 model is about 100 mm and 43 mm respectively for both LWAC and NWAC. The experimental results show that increasing the bond length of the FRP reinforcement (L_f) further than 75 mm has marginal influence on maximum load capacity, and maximum loads are roughly the same for samples with L_f =100 mm. Thus, as mentioned in Chapter three the effective length observed in experimental tests in this study was about 75 mm. Contrasting between the experimental observed effective length and that obtained theoretically reveal that Yang's model 2001 model overestimate the effective length of the FRP reinforcement, whereas Iso's 2003 model significantly underestimates the effective length. The theoretically calculated values of the FRP effective length using the other models and guidelines show more accurate values for the effective length in most cases.

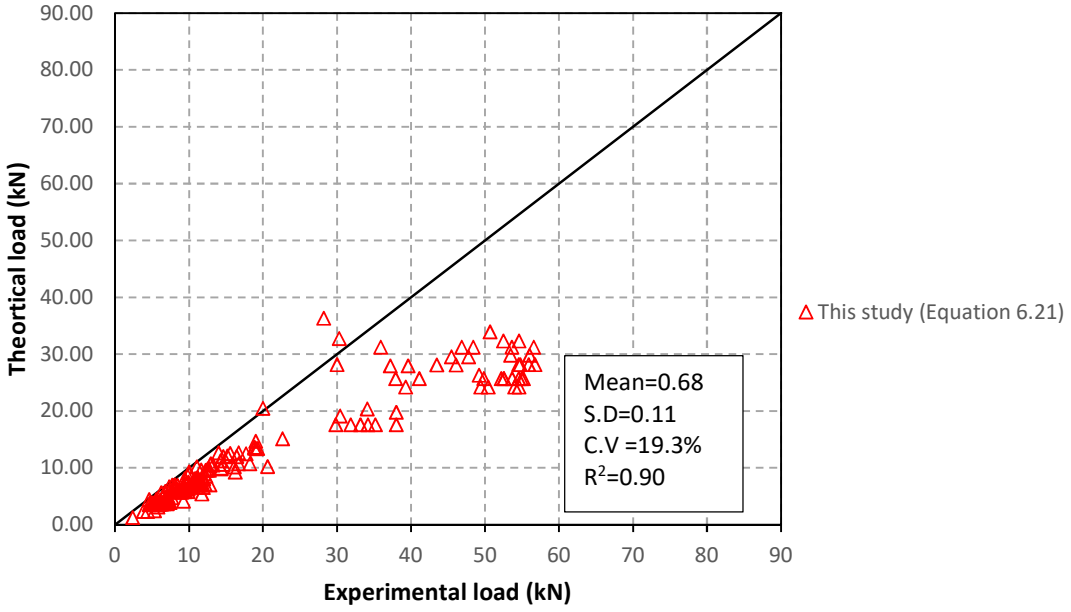

Figure (6.10): Theoretical predictions load versus experimental observation (Equation 6.21).

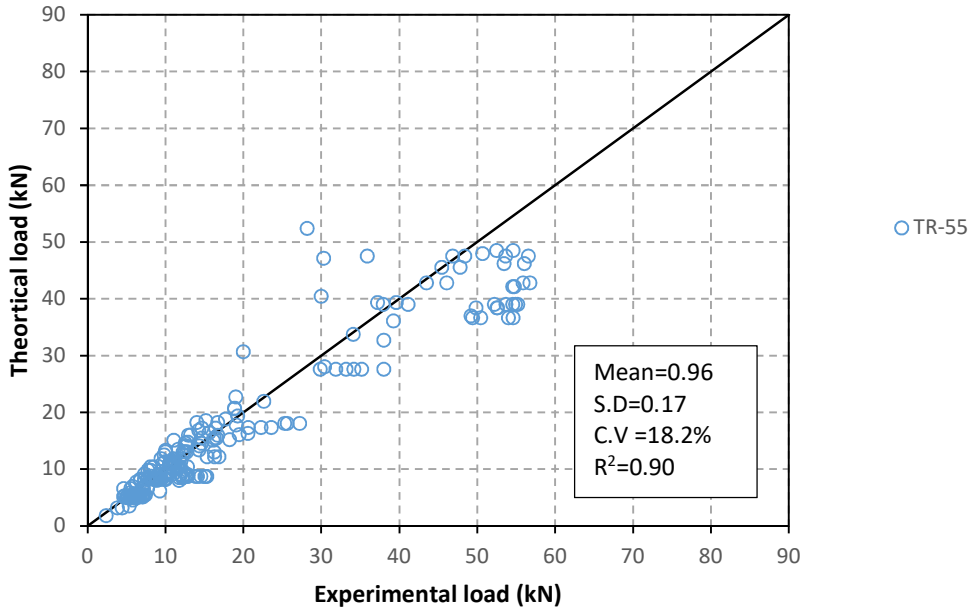

Figure (6.11): Theoretical predictions load versus experimental observation (TR-55).

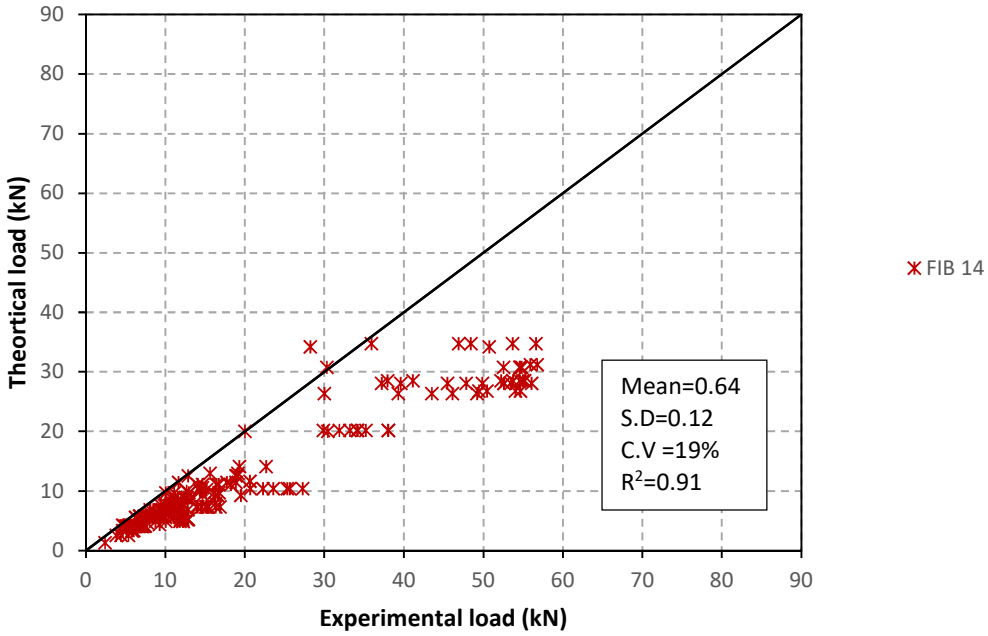

Figure (6.12): Theoretical predictions load versus experimental observation (FIB 14).

6.2.5.2. Validation of the Strain Profile

A comparison between the maximum debonding strains obtained using Equation (6.24) and those CFRP strains measurements collected from experimental test results at the centre of the LWAC and NWAC samples were presented in Figure (6.13). An acceptable agreement between the theoretically obtained debonding strains and the experimental test data as noticed in this figure. Generally, the mean value of the predicted-to-experimental debonding strain is 0.79 with a coefficient of variation (C.V) of 30.3% and a standard deviation (S.D) of 0.24 for LWAC samples. While for NWAC samples, the mean debonding strain is 0.93 with a coefficient of variation (C.V) of 9.6% and standard deviation (S.D) of 0.09. It can be noted that the maximum predicted strain in the case of NWAC samples is significantly better than those of the LWAC samples. This is attributed to the higher difference in the maximum recorded strain in the LWAC samples near the centre due to local concrete crushing close this region.

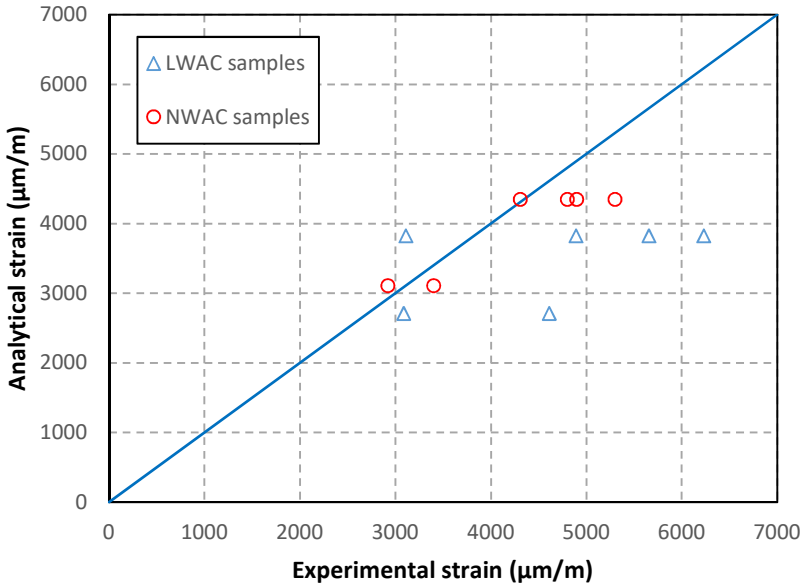

Figure (6.13): Comparison between experimental and predicted maximum strain value at the sample centre.

Figures (6.14) to (6.16) compare the CFRP strains distribution recorded from strain gauges mounted on the top surface of the CFRP sheet in double-lap shear test versus the theoretically predicted strain values obtained from the developed fourth-degree polynomial formula (Equation (6.22)) at the maximum level of loading (local debonding failure). Generally, the theoretically assumed model able to predict the FRP strains distribution along the length of the FRP reinforcement persistently and softly. The trends of the analytical model obtained from Equation (6.22) are in acceptable agreement with those collected from the experimental models. However, a difference in behaviour available between the experimental and the proposed curves. The differences in trend could be attributed to the high-stress concentrations developed in CFRP reinforcement at the centre of the concrete prism in the actual physical model or due to the influence of local concrete failure close the far end of the CFRP reinforcement, particularly in the LWAC samples.

It can be concluded that the proposed model can clearly describe the debonding process and the crack propagation along the FRP length at the proposed maximum debonding for both NWAC and LWAC samples. The analytical model shows a steadier trend when compared with the experimental FRP strain measurements. This is because the influence of variables is addressed in this model such as FRP width and length, debonding design force, and the concrete type.

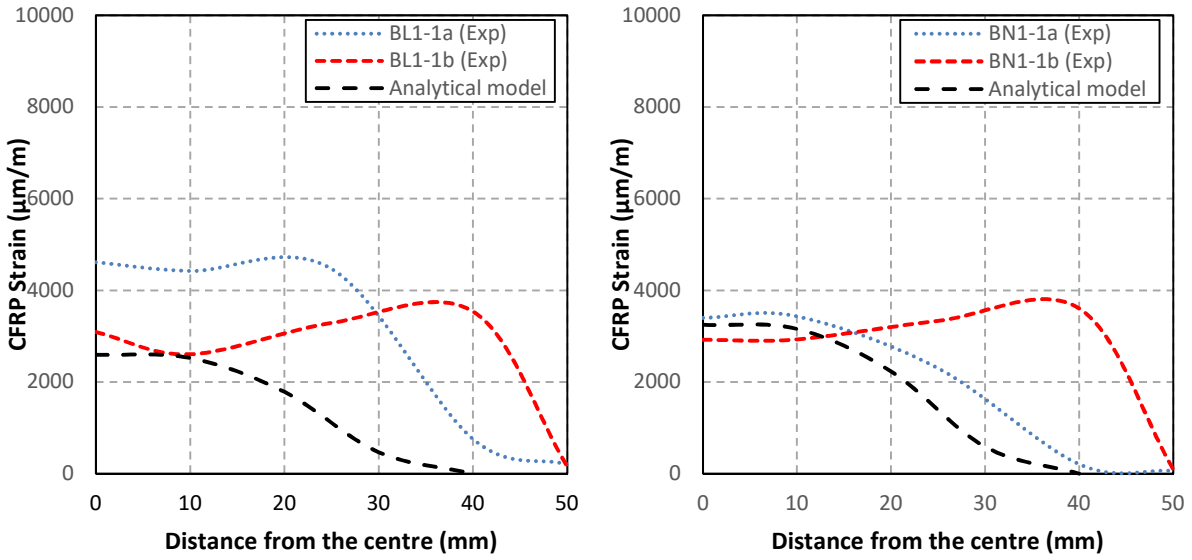

Figure (6.14): Analytical prediction of the strain distribution along the length of CFRP composite of BL/N1-1samples.

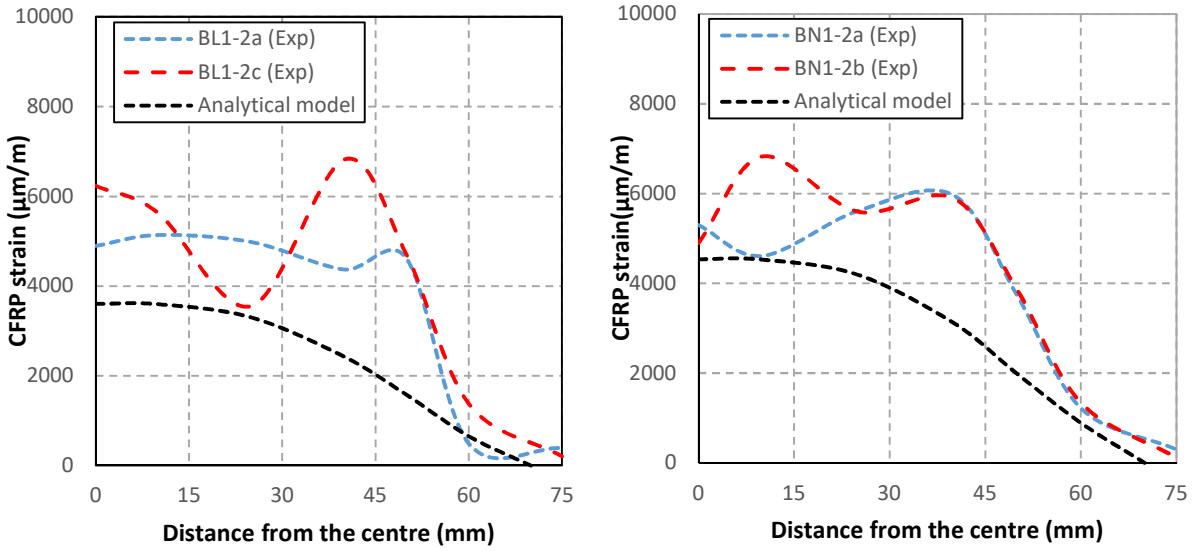

Figure (6.15): Analytical prediction of the strain distribution along the length of CFRP composite of BL/N1-2 samples.

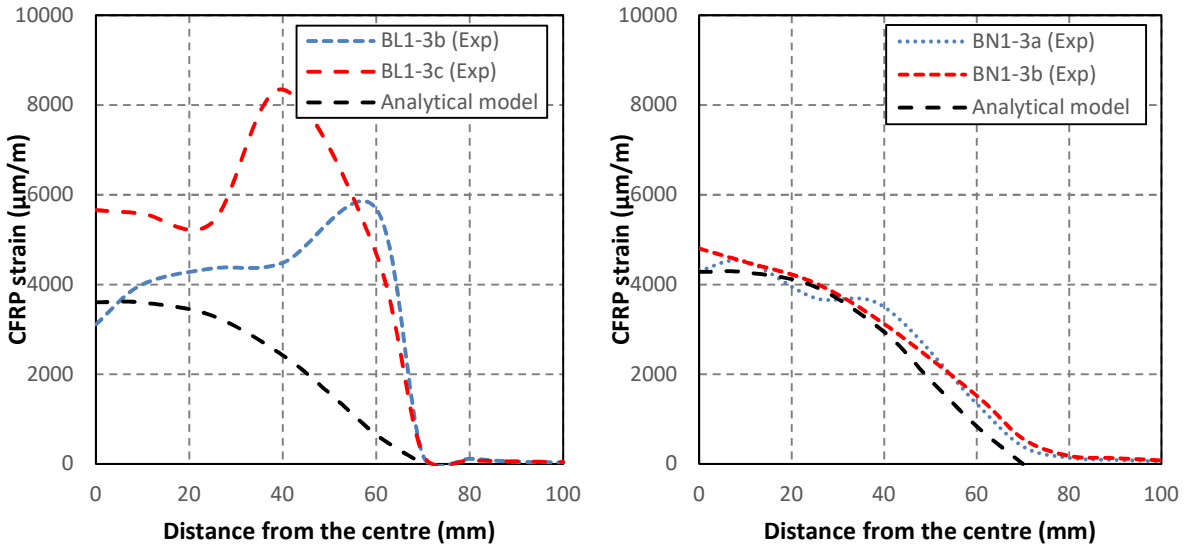

Figure (6.16): Analytical prediction of the strain distribution along the length of CFRP composite of BL/N1-3 samples.

6.2.5.3. Validation of the Ultimate Slip

The experimentally obtained ultimate global slip corresponding to the maximum applied load is compared with the analytical predictions based on Equation (6.31). Generally, the mean value of the predicted-to-experimental ultimate slip ratio is 0.50 for the LWAC specimens, while for NWAC the average value of the predicted-to-experimental ultimate slip ratio is 0.54. Differences in the interfacial ultimate slip can be observed at the maximum load stage, this may be assigned to the fracture behaviour of the concrete. The higher energy released after concrete fracture leads to a higher interfacial slip between the concrete sample and CFRP reinforcement in the experimental physical test as well as a significant variance in results between the predicted ultimate slip and experimental recorded global slip. Generally, this model able to predict the maximum debonding design force, maximum debonding strain and strain profile along the length of the CFRP reinforcement for FRP/lightweight concrete joint with satisfactory precision.

6.3. Second Proposed Model (Modified CEB-FIP 1990 Bond-Slip Models)

The modelling of the bond of FRP-to-concrete includes many influencing variables on the overall interface response. The only method to minimise the complexity resulting from this increasing number of variables is through experimental research results that provide the basis for enhanced

understanding of the influences on the bond behaviour of critical parameters. Simplified models and design equations for designers can only be obtained by ignoring some variables, which needs a reasonable understanding of the role of each variable. The FRP-to-concrete bond modelling must fit into the total design philosophy of the RC elements. From the full load-slip response of a bond-slip test, the design approach focuses only on the maximum load, while the full response behaviour of the model, for example, the bond-slip model between concrete steel and concrete based on CEB-FIP model code 1990, needs simulating the full response of the bond-slip response (Eltayeb, 2006).

6.3.1. Theoretical Derivation of the Second Proposed Model (Modified CEB-FIP 1990 Bond-Slip Model)

Modelling of the FRP-concrete interface has received much attention many years ago. Many theoretical models were developed to predict the characteristics of the FRP-concrete interface response. The available numerical method can be categorised into the following models: (i) empirical verified formulas, (ii) models derived based on theory of elasticity and (iii). a fracture approach models. Empirical verified formulas are employed based on specific experimental results of the single and double-lap shear tests by using simple statistical analysis or by fitting with these results to obtain general relationships able to predicate the interface characteristics with reliable accuracy. For mathematical methods, which are formulated based on the theory of elasticity, the main formulas are developed based on the boundary conditions of the examined models. In other studies, the fracture mechanics principle is used to model the FRP-concrete interface response (Hadigheh and Gravina, 2016). However, most of the design codes suggest the use of a combination of elastic-plastic models based on a fracture approach. The behaviour of adhesively bonded joints is described by the maximum bond strength capacity or by the interfacial shear stress-slip profiles. There are limited studies in the literature which derived the full loading response of the FRP-concrete interface.

The interfacial shear stress-slip relationships proposed available in the literate are summarised in Figure (6.17). Based on these relations, the shear stress-slip can be obtained at any point along the FRP-concrete joint at the different level of loading and various stages of debonding process. The shear stress-slip trends can be expressed by various form and the principal variables, for example,

the peak or the maximum bond stress, τ_{max}, the peak or the maximum interfacial slip, s_{max}, and ultimate interfacial slip, s_{ult}, (Hadigheh and Gravina, 2016).

Most of the existing models to predict the bond strength and the effective bond length were developed using normal weight concrete. However, the experiments in this study (chapter three) indicate that the mode of failure between lightweight concrete (LWC) and normal weight concrete (NWC) are different. while the LWCs' failure loads were slightly less than the NWC. Therefore, the effects of LWC should be considered in the theoretical models, such as the lower surface tensile strength which accelerates substrate failure as compared with NWC samples which show higher debonding forces. This study aims to develop an efficient and sound analytical model based on the shear stress-slip relation defined in the CEB model to describe the full range of behaviour of FRP-concrete joints cast with different types of concrete.

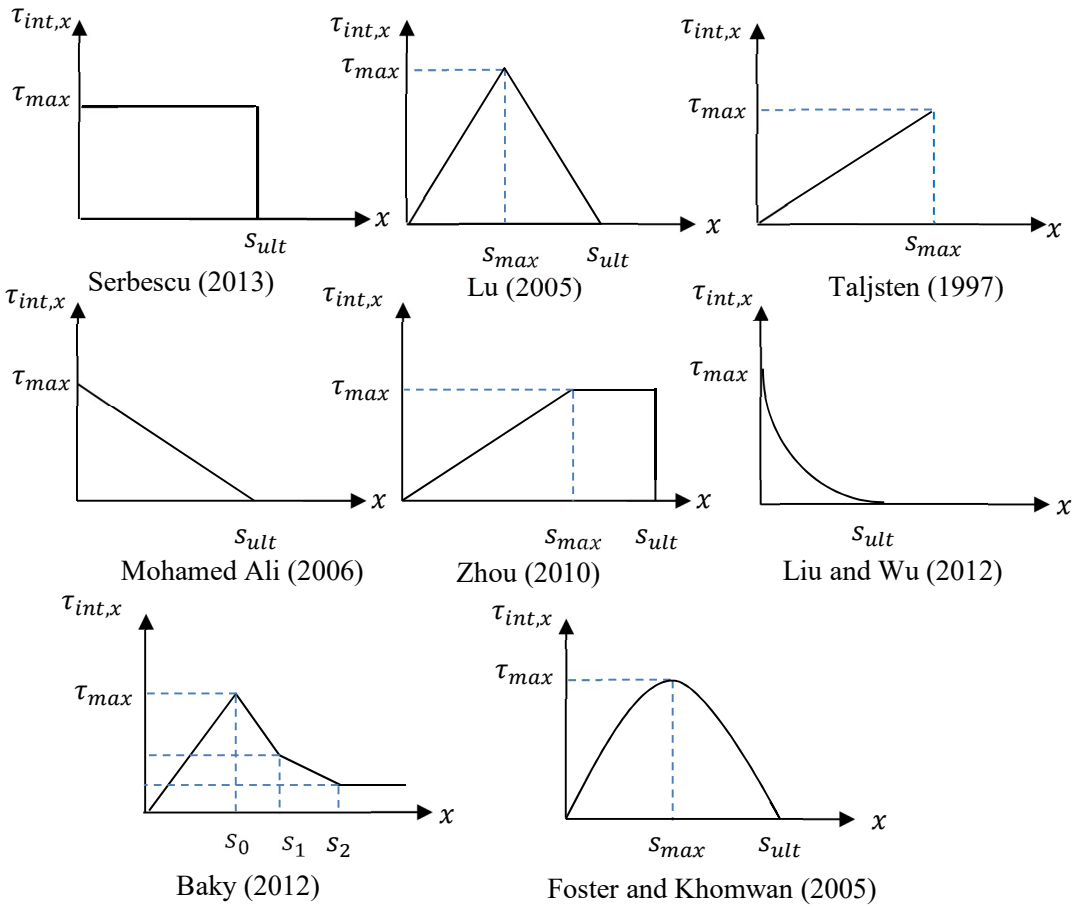

Figure (6.17): The existing bond stress-slip models.

As mentioned in the first proposed models, the slip between FRP sheet and the concrete substrate at any point x along the bonded length of FRP sheet is expressed as the difference between the displacement of the FRP reinforcement and the displacement of a concrete sample. The interfacial slip between the FRP reinforcement and concrete substrate can be obtained by the following equation:

$$s = u_f - u_c \tag{6.40}$$

Where, u_f and u_c are the FRP and concrete displacement respectively. In elastic models the strain-stress relationship for interface materials can be expressed in the following linear formulation:

The axial stress in concrete can be written as (Equation (6.41)):

$$\sigma_c = E_c . \varepsilon_c \tag{6.41}$$

And the axial stress in FRP reinforcement as (Equation (6.42)):

$$\sigma_f = E_f . \varepsilon_f \tag{6.42}$$

Where, E_c and E_f are the modulus of elasticity for concrete and FRP reinforcement. ε_c, is the concrete strain which is defined by the following equation (Equation (6.43)):

$$\varepsilon_c = \frac{du_c}{dx} \tag{6.43}$$

And, ε_f is the FRP strain is given by (Equation (6.44)):

$$\varepsilon_f = \frac{du_f}{dx} \tag{6.44}$$

The total strain can be obtained by deriving the Equation (6.40) as (Equation (6.45)):

$$\frac{ds}{dx} = \frac{du_f}{dx} - \frac{du_c}{dx} = \varepsilon_f - \varepsilon_c \tag{6.45}$$

The stress-strain relation can be expressed by substituting Equation (6.41) and Equation (6.42) into Equation (6.45) as (Equation (6.46)):

$$\frac{ds}{dx} = \frac{\sigma_f}{E_f} - \frac{\sigma_c}{E_C} \tag{6.46}$$

Differentiating Equation (6.46) yields (Equation (6.47)):

$$\frac{d^2s}{d^2x} = \frac{1}{E_f}.\frac{d\sigma_f}{dx} - \frac{1}{E_C}.\frac{d\sigma_c}{dx} = \frac{d\varepsilon_f}{dx} - \frac{d\varepsilon_c}{dx} \tag{6.47}$$

A differential section dx can be cut from the FRP-to-concrete bonded sample as shown in Figure (6.18c). This is consisted of three materials: concrete, adhesive and FRP composite. In the this study, linear elastic response is assumed for all the three materials; the interfacial shear stresses developed in surface concrete will transfer through the adhesive to the FRP composite. The direct stress will act orthogonally to the plane of the adhesive layer and it does not alter through the thickness of the FRP-concrete joint. The interfacial shear and the axial stresses in the FRP reinforcement are denoted by τ_f, and σ_f, respectively.

The equilibrium force in the FRP reinforcement in the x-direction gives (Equation (6.48)):

$$\tau_f.d_x.b_f = d\sigma_f.A_f \tag{6.48}$$

Or,

$$\tau_f = t_f.\frac{d\sigma_f}{dx} \tag{6.49}$$

Where,

$$A_f = b_f.t_f \tag{6.50}$$

The equilibrium in the FRP-concrete joint in the x-direction gives (Equation (6.51)):

$$d\sigma_f.t_f.b_f = d\sigma_c.t_c.b_c \tag{6.51}$$

Or,

$$d\sigma_c = \frac{d\sigma_f.t_f.b_f}{t_c.b_c} \tag{6.52}$$

By substituting Equation (6.52) into Equation (6.47) gives (Equation (6.53)):

$$\frac{d^2s}{dx^2} = \frac{1}{E_f}.\frac{d\sigma_f}{dx} - \frac{1}{E_C}.\frac{d\sigma_f}{dx}.\left(\frac{t_f.b_f}{t_c.b_c}\right) \quad (6.53)$$

Or,

$$\frac{d^2s}{dx^2} = \frac{d\sigma_f}{d_x}.\left(\frac{E_c.t_c.b_c - E_f.t_f.b_f}{E_f.E_c.t_c.b_c}\right) \quad (6.54)$$

Substituting $\frac{d\sigma_f}{dx}$, from Equation (6.49) in Equation (6.54) gives (Equation (6.55)):

$$\frac{d^2s}{dx^2} = \tau_f.\left(\frac{E_c.t_c.b_c - E_f.t_f.b_f}{E_f.t_f.E_c.t_c.b_c}\right) \quad (6.55)$$

Or,

$$\frac{d^2s}{dx^2} = K.\tau_f \quad (6.56)$$

Where,

$$K = \frac{E_c.t_c.b_c - E_f.t_f.b_f}{E_f.t_f.E_c.t_c.b_c} \quad (6.57)$$

Where, σ_c , E_c, t_c and ε_c are the axial stress, elastic Young's modulus of elasticity, thickness of the half concrete prism and strain of concrete respectively. Moreover, $\sigma_f, E_f,$ t_f and ε_f are the axial stress, Young's modulus of elasticity, thickness and strain of FRP reinforcement respectively. The differential equation of bond (Equation (6.56)) is general and can be solved for any local bond stress-slip law. This equation should be performed for each segment representing a particular τ-s relation.

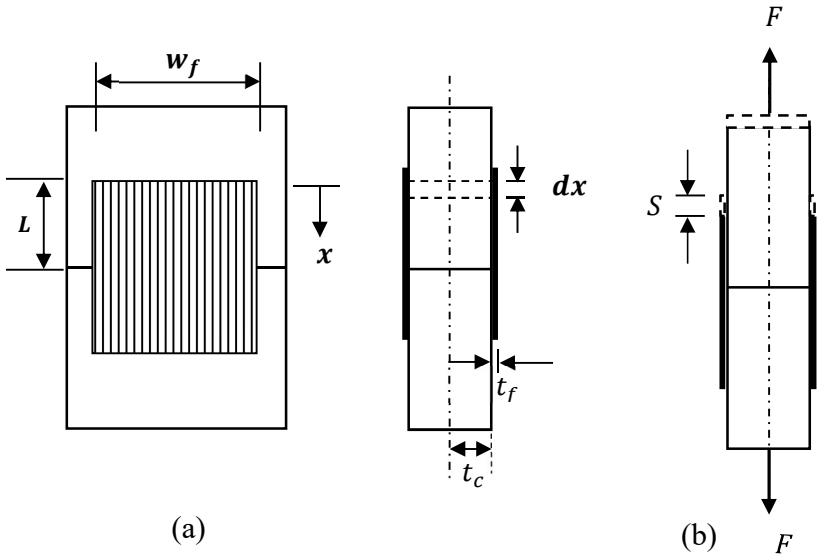

a) Two separate concrete blocks bonded together with FRP sheet; (b) Relative displacement between concrete and FRP reinforcement.

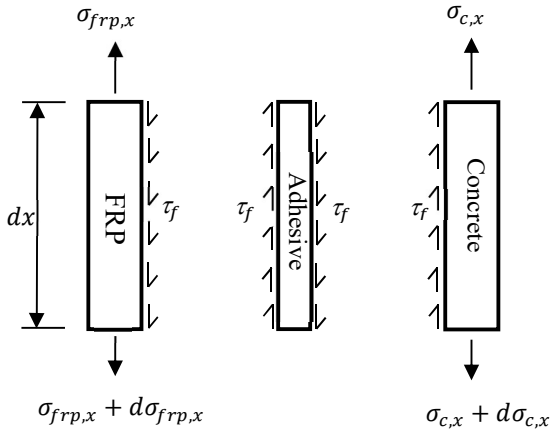

(c) A differential segment of the adhesively bonded joint.

Figure (6.18): Detail of FRP-concrete joint.

6.3.2. CEB Model

A more sophisticated bond stress-slip model was proposed by (CEB-FIB, 1992). The comprehensive bond-slip model for concrete and steel reinforcement, with four zones of behaviour, is described in the context of the different bond mechanisms in a CEB-FIB report**.** The equations of the CEB-FIB Bond–Slip model are successfully used to predict the full range of loading behaviour between steel reinforcement and concrete. The complete bond stress-slip

envelopes are divided into four main zones (primary zone, initial debonding zone, degradation zone and debonding zone) as shown in Figure (6.19).

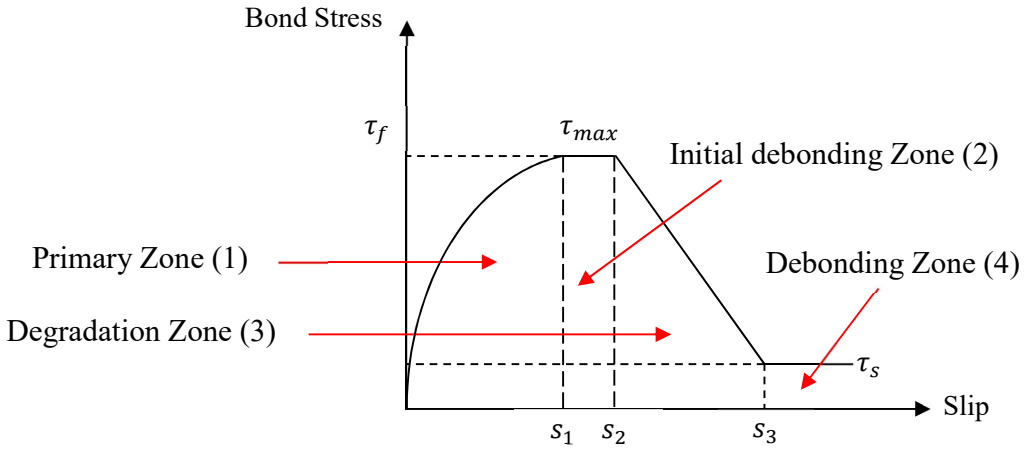

Figure (6.19): Analytical bond stress-slip relationship (monotonic loading) according to CEB-FIP model code 1990.

The full range of the bond stress-slip relationship is defined as (Equation (6.58)):

$$\tau_f = \begin{cases} \tau_{max}.\left(\frac{s}{s_1}\right)^{\alpha} & for\ 0 \le s \le s_1 \\ \tau_{max} & for\ s_1 < s \le s_2 \\ \tau_{max} - (\tau_{max} - \tau_s).\left(\frac{s - s_2}{s_3 - s_2}\right) & for\ s_2 < s \le s_3 \\ \eta\ .\tau_{max} & for\ \ s_3 < s \end{cases} \quad (6.58)$$

Where s_1, s_2 and s_3 are the values of slip which demonstrate each region of behaviour, τ_{max} is the maximum bond stress and τ_s is the constant bond stress when the slip is greater than s_3. The first section of this model is non-linear, which is a result of micro-cracking and local crushing of in the steel reinforcement-concrete interface. A peak plateau shear stress is included in the CEB models to reflect the initial debonding of the steel reinforcement from the concrete sample. The descending in the shear stress beyond the peak shear stress is attained shows the interfacial softening due to large-cracking developing at the steel-concrete interface. When the relative slip archives s_3, a residual bond resistance keeps along the bond length, where η is a constant assumed as 0.25. The CEB-FIB model allows to model the bond properties between the steel rebar and concrete under

confined and unconfined conditions. This is achieved by modifying the maximum bond strength (CEB-FIB, 1992).

6.3.3. Proposed Model

The CEB-FIB model must be modified to exhibit the characteristics of FRP in retrofitted lightweight concrete beams. This is because the epoxy bonded FRP increases the confinement effect of concrete and the interlock between the crack face in lightweight concrete is not significant as the normal weight concrete. In this study, therefore, a new bond stress-slip model is developed based on the CEB-FIB bond-stress slip relation to describe the full zone of debonding between FRP reinforcement and both NWAC and LWAC.

The debonding mechanism of the externally bonded FRP reinforcement from the concrete substrate can be summarised in the following three zones: (i) the linear/ elastic increase in bond stress till the maximum shear stress and the corresponding maximum relative slip at the loaded end of the FRP reinforcement (Primary zone), (ii) the incline or softening of the bond stress after achieving the maximum bond stress (degradation zone), and (iii) local debonding stage after achieving the ultimate relative slip at the loaded end (debonding zone). The bond stress differs along the length of the FRP reinforcement at various levels of loading. When the length of the FRP reinforcement is longer than the anchorage length required to achieve the maximum bond strength, the bond shear stress reaches the maximum value at the far end of the FRP reinforcement before the global debonding. Before achieving the maximum bond stress, which is related to the concrete tensile strength, the bond-slip section located within the primary zone or the elastic uncracked zone. After that, shear stress inclines into a softening region due to small cracks develops in the FRP-concrete joint within the degradation zone as specified by the bonded length l_d. When the length of the FRP reinforcement is equal to the required anchorage length, l_e, the maximum bond strength is attained and the relative slip between FRP and concrete substrate achieves the ultimate value at the loaded end and the debonding failure began within the debonding zone. When the bond length of FRP reinforcement is longer than the anchorage length, the maximum achievable shear stress attains the far end of the FRP reinforcement. The slip between FRP and concrete slip significantly increases and higher section of the FRP reinforcement was detached from the

concrete surface. The ultimate relative slip will be attained at a length of l_e from the far end and thus global debonding failure occurs suddenly as brittle failure develops (Colalillo, 2012).

In this study, the unconfined CEB bond stress-slip model was assumed based on the described debonding mechanism, the maximum slip is assumed as s_1. The initial debonding zone was neglected ($s_1 = s_2$) and the degradation zone starts to develop after point (A) (see Figure (6.20)) up to ultimate slip s_3. At point (B) the debonding occurs and the bond stress reduced to zero. The full range of behaviour of the bond stress-slip relationship was reformulated according to the full FRP debonding process as per the following equation (Equation (6.59)):

$$\tau_f = \begin{cases} \tau_{max}.\left(\frac{s}{s_1}\right)^{\alpha} & for\ 0 \le s \le s_1 \\ \tau_{max} - \tau_{max}.\left(\frac{s-s_2}{s_3-s_2}\right) & for\ s_2 < s \le s_3 \\ 0 & for\ s > s_3 \end{cases} \quad (6.59)$$

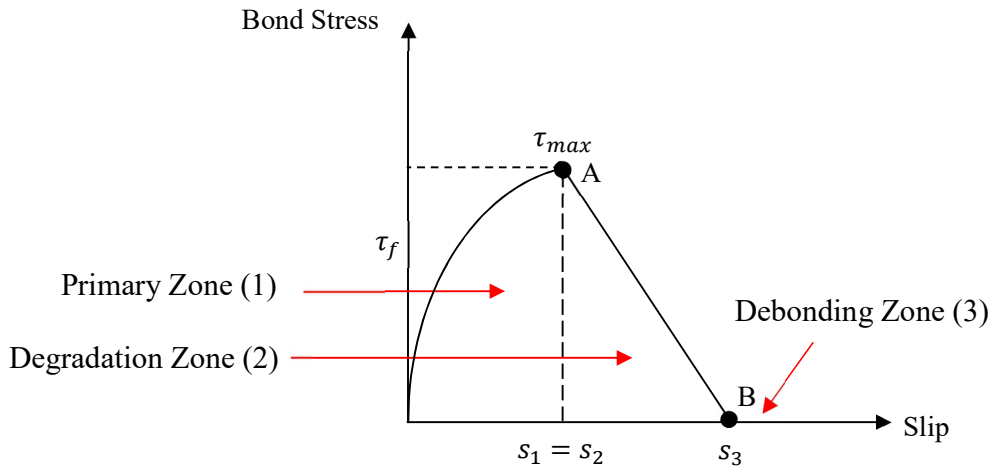

Figure (6.20): Proposed bond stress-slip relationship based on CEB-FIP model code 1990.

6.3.3.1. Case I (Primary Zone)

When the slip between FRP and concrete occurs $(s_{lp} < s_1)$ the primary zone is activated. The bond stress in the primary zone is defined by the following equation (Equation (6.60)):

$$\tau_f = \tau_{max}.\left(\frac{s}{s_1}\right)^{\alpha} \quad (6.60)$$

This equation can be simplified to:

$$\tau_f = \rho_1.s^{\alpha} \quad (6.61)$$

Where,

$$\rho_1 = \frac{\tau_{max}}{s_1^{\alpha}} \tag{6.62}$$

By substituting Equation (6.61) into Equation (6.56) gives (Equation (6.63)):

$$\frac{d^2s}{dx^2} = K.\rho_1.s^{\alpha} \tag{6.63}$$

Then Equation (6.63) can be solved as (Equation (6.64) and (6.65)) (see the derivation in Appendix D):

$$\frac{ds}{dx} = \sqrt{\frac{2\rho_1 K}{(1+\alpha)}}.s^{\frac{1+\alpha}{2}} \tag{6.64}$$

$$s = \left(\frac{K\rho_1(1-\alpha)^2}{2(1+\alpha)}\right)^{\frac{1}{1-\alpha}}.x^{\frac{2}{1-\alpha}} \tag{6.65}$$

The primary slip (s_{lp}) can be written as a function of the bonded length in the primary zone by substituting ($x = l_p$) into Equation (6.65) as follows (Equation (6.66)):

$$s_{lp} = \left(\frac{K\rho_1(1-\alpha)^2}{2(1+\alpha)}\right)^{\frac{1}{1-\alpha}}.l_p^{\frac{2}{1-\alpha}} \tag{6.66}$$

So, the length of the FRP composite (Primary length) in the primary zone can be written as (Equation (6.67)):

$$l_p = s_{lp}^{\frac{1-\alpha}{2}}.\left(\frac{2(1+\alpha)}{K\rho_1(1-\alpha)^2}\right)^{\frac{1}{2}} \tag{6.67}$$

The maximum primary length of the FRP composite can be obtained from Equation (6.68):

$$l_1 = s_1^{\frac{1-\alpha}{2}}.\left(\frac{2(1+\alpha)}{K\rho_1(1-\alpha)^2}\right)^{\frac{1}{2}} \tag{6.68}$$

Where, s_1 is the maximum slip. To obtain the strain and the bonded length of FRP reinforcement in the primary zone the following boundary conditions are assumed (Equation (6.69) and (6.70)) (see Figure (6.21)):

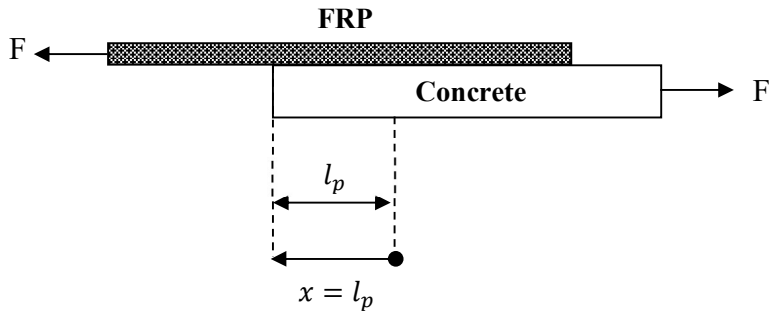

Figure (6.21): Primary slip zone.

$at\ x = 0$

$$\frac{ds}{dx} = 0 \quad \text{and} \quad s = 0 \tag{6.69}$$

$at\ x = l_p$

$$\frac{ds}{dx} = \left(\frac{ds}{dx}\right)_{lp} \text{ and } \quad s = s_{lp} \tag{6.70}$$

By substituting the second boundary condition into Equation (6.64) gives (Equation (6.71)):

$$\left(\frac{ds}{dx}\right)_{lp} = \sqrt{\frac{2\rho_1 K}{(1+\alpha)}} . s_{lp}^{\frac{1+\alpha}{2}} \tag{6.71}$$

The bond shear stress in the CFRP reinforcement as a function of the bonded length can be obtained by substituting Equation (6.65) into Equation (6.61) as (Equation (6.72)):

$$\tau_f = \rho_1 . \left(\frac{K\rho_1(1-\alpha)^2}{2(1+\alpha)}\right)^{\frac{\alpha}{1-\alpha}} . x^{\frac{2\alpha}{1-\alpha}} \tag{6.72}$$

The primary debonding force zone can be obtained from Equation 6.73):

$$F_P = b_f \int_0^{I_p} \tau_f \ . d_x \tag{6.73}$$

The debonding primary force as a function of the FRP bonded length in the primary zone can be obtained by solving Equation (6.73) as (Equation (6.74)):

$$F_P = b_f . \rho_1 \left[\frac{K\rho_1(1-\alpha)^2}{2(1+\alpha)}\right]^{\frac{\alpha}{1-\alpha}} . \frac{I_p^{\left(\frac{1+\alpha}{1-\alpha}\right)}}{\left(\frac{1+\alpha}{1-\alpha}\right)} \quad (6.74)$$

The maximum debonding primary force can be obtained using the following equation (Equation (6.75)):

$$F_{P,max} = b_f . \rho_1 \left[\frac{K\rho_1(1-\alpha)^2}{2(1+\alpha)}\right]^{\frac{\alpha}{1-\alpha}} . \frac{I_1^{\left(\frac{1+\alpha}{1-\alpha}\right)}}{\left(\frac{1+\alpha}{1-\alpha}\right)} \quad (6.75)$$

The FRP strain distribution as a function of the bonded length in the primary zone can be expressed by the following Equation (Equation (6.76)):

$$\varepsilon_f = \frac{1}{E_f . t_f} \int_0^x \tau_f = \frac{F_P}{b_f t_f E_f} \quad (6.76)$$

Solving Equation (6.76) gives (Equation (6.77)):

$$\varepsilon_{fp,x} = \frac{1}{E_f . t_f} \rho_1 \left[\frac{K\rho_1(1-\alpha)^2}{2(1+\alpha)}\right]^{\frac{\alpha}{1-\alpha}} . \frac{x^{\left(\frac{1+\alpha}{1-\alpha}\right)}}{\left(\frac{1+\alpha}{1-\alpha}\right)} \quad (6.77)$$

The maximum achieved strain in the primary zone can be expressed by the following Equation (Equation (6.78)):

$$\varepsilon_{fp,max} = \frac{1}{E_f . t_f} \rho_1 \left[\frac{K\rho_1(1-\alpha)^2}{2(1+\alpha)}\right]^{\frac{\alpha}{1-\alpha}} . \frac{I_1^{\left(\frac{1+\alpha}{1-\alpha}\right)}}{\left(\frac{1+\alpha}{1-\alpha}\right)} = \frac{F_{P,max}}{b_f t_f E_f} \quad (6.78)$$

An alternative method can be used to obtain the FRP strain distribution in the primary zone if the value of s is known by subsisting Equation (6.64) into Equation (6.45) as follows (Equation (6.79)):

$$\varepsilon_{fp,x} = \left[\sqrt{\frac{2\rho_1 K}{(1+\alpha)}} . s_{Ip}^{\frac{1+\alpha}{2}} + \frac{F_p}{t_c . b_c . E_c}\right] \quad (6.79)$$

Where the concrete strain in the primary zone is obtained from Equation (6.80):

$$\varepsilon_c = \frac{F}{t_c . b_c . E_c} \quad (6.80)$$

6.3.3.2. Case II (Primary Zone and Degradation Zone)

When the available bond length is greater than the primary length, the degradation zone is activated and the stress softening start to develop. The primary zone moves along the FRP length. The slip between FRP and concrete exceeds s_1. The primary length can be given as (Equation (6.81)):

$$l_1 = \sqrt{\frac{2(1+\alpha)}{K\rho_1(1-\alpha)^2}} . s_1^{\frac{1-\alpha}{2}} \tag{6.81}$$

At the boundary between the primary zone and degradation zone:

$$\left(\frac{ds}{dx}\right)_{l_1} = \sqrt{\frac{2\rho_1 K}{(1+\alpha)}} . s_1^{\frac{1+\alpha}{2}} \tag{6.82}$$

The equation for the degradation zone required to comply with the equilibrium and compatibility conditions is:

$$\frac{d^2 s}{dx^2} = K\ (\rho_2 - \rho_3 . s) \tag{6.83}$$

Where,

$$\rho_2 = \frac{\tau_{max} . s_3}{s_3 - s_2} \tag{6.84}$$

And,

$$\rho_3 = \frac{\tau_{max}}{s_3 - s_2} \tag{6.85}$$

Where, $s_2 = s_1$. The bond shear stress in the degradation zone can be obtained from the following equation (Equation (6.86)):

$$\tau_f = (\rho_2 - \rho_3 . s) \tag{6.86}$$

The Equation (6.83) can be solved using second-order nonlinear nonhomogeneous differential equation solution as (Equation (6.87) and (6.88)) (see the derivation in Appendix D):

$$s = B_1 \sin\left(x\sqrt{K\rho_3}\right) + B_2 \cos\left(x\sqrt{K\rho_3}\right) + \frac{\rho_2}{\rho_3} \tag{6.87}$$

And,

$$\frac{ds}{dx} = \sqrt{K\rho_3}\left[B_1 \cos\left(x\sqrt{K\rho_3}\right) - B_2 \sin\left(x\sqrt{K\rho_3}\right)\right] \quad (6.88)$$

Where, B_1 and B_2 are constant are for the continuity of s and $\frac{ds}{dx}$ at the boundary with primary zone $(x = l_1)$ leading to (Equation (6.89) and (6.90)):

$$B_1 = \sqrt{\frac{2\rho_1}{\rho_3\,(1+\alpha)}}.s_1^{\frac{1+\alpha}{2}}\left(\frac{1-\sin^2\left(l_1\sqrt{K\rho_3}\right)}{\cos\left(l_1\sqrt{K\rho_3}\right)}\right) + \left(s_1 - \frac{\rho_2}{\rho_3}\right)\sin\left(l_1\sqrt{K\rho_3}\right) \quad (6.89)$$

And,

$$B_2 = \left(s_1 - \sqrt{\frac{2\rho_1}{\rho_3\,(1+\alpha)}}.s_1^{\frac{1+\alpha}{2}}\tan\left(l_1\sqrt{K\rho_3}\right) - \frac{\rho_2}{\rho_3}\right)\cos\left(l_1\sqrt{K\rho_3}\right) \quad (6.90)$$

The ultimate slip between FRP and concrete can be obtained using the boundary condition at $(x = l_e)$ gives (Equation (6.91)) (see Figure (6.22)):

$$s = B_1 \sin\left(l_e\sqrt{K\rho_3}\right) + B_2 \cos\left(l_e\sqrt{K\rho_3}\right) + \frac{\rho_2}{\rho_3} \quad (6.91)$$

Where, I_e, is the effective bond length required to attain the maximum debonding force at the end of the degradation zone.

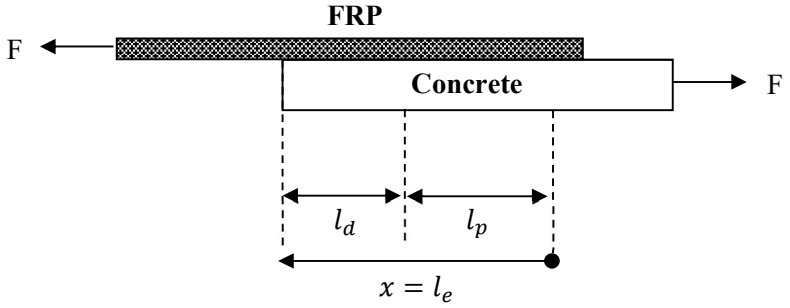

Figure (6.22): Degradation slip zone.

The degradation force as a function of the bonded length can be obtained using the following equation (Equation (6.92)):

$$F_d = b_f \int_{I_1}^{x} \tau_f \, .d_x = b_f \int_{I_1}^{x} (\rho_2 - \rho_3.s) \, .d_x \quad (6.92)$$

By substituting equation (6.86) into equation (6.92) and solving gives (Equation (6.93)) (see the derivation in Appendix D):

$$F_d = \frac{b_f \rho_3}{\sqrt{K\rho_3}}\left(B_1\left[\cos\left(x\sqrt{K\rho_3}\right) - \cos\left(I_1\sqrt{K\rho_3}\right)\right] - B_2\left[\sin\left(x\sqrt{K\rho_3}\right) - \sin\left(I_1\sqrt{K\rho_3}\right)\right]\right) \quad (6.93)$$

The force in the degradation zone can be obtained as a function of degradation length I_d by the following equation (Equation (6.94)):

$$F_d = \frac{b_f \rho_3}{\sqrt{K\rho_3}}\left(B_1\left[\cos\left(I_d\sqrt{K\rho_3}\right) - \cos\left(I_1\sqrt{K\rho_3}\right)\right] - B_2\left[\sin\left(I_d\sqrt{K\rho_3}\right) - \sin\left(I_1\sqrt{K\rho_3}\right)\right]\right) \quad (6.94)$$

The bond length in the degradation zone I_d can be obtained by the following equation (Equation (6.95)):

$$l_d = l_f - l_1 \quad (6.95)$$

Where, l_f is available bonded length of the FRP reinforcement which is equal or less than the effective bond length. The maximum degradation force at the end of the degradation zone corresponding to the maximum available bonded length of the FRP reinforcement can be obtained by the following equation (Equation (6.96)):

$$F_{d,max} = \frac{b_f \rho_3}{\sqrt{K\rho_3}}\left(B_1\left[\cos\left(l_f\sqrt{K\rho_3}\right) - \cos\left(I_1\sqrt{K\rho_3}\right)\right] - B_2\left[\sin\left(l_f\sqrt{K\rho_3}\right) - \sin\left(I_1\sqrt{K\rho_3}\right)\right]\right) \quad (6.96)$$

The maximum debonding force of the FRP-concrete joint can be calculated using the following equation (Equation (6.97)):

$$F_{max} = F_{p,max} + F_{d,\max} \quad (6.97)$$

The FRP strain in the degradation zone can be obtained from the following Equation (Equation 6.98)):

$$\varepsilon_{fd,x} = \frac{\rho_3}{E_f t_f \sqrt{K\rho_3}} \left(B_1\left[\cos\left(I_d\sqrt{K\rho_3}\right) - \cos\left(I_1\sqrt{K\rho_3}\right)\right] - B_2\left[\sin\left(I_d\sqrt{K\rho_3}\right) - \sin\left(I_1\sqrt{K\rho_3}\right)\right]\right) \quad (6.98)$$

The maximum strain at the end of the degradation as a function of the available bonded length can be calculated as (Equation (6.99)):

$$\varepsilon_{fd,max} = \frac{\rho_3}{E_f t_f \sqrt{K\rho_3}} \left(B_1\left[\cos\left(l_f\sqrt{K\rho_3}\right) - \cos\left(I_1\sqrt{K\rho_3}\right)\right] - B_2\left[\sin\left(l_f\sqrt{K\rho_3}\right) - \sin\left(I_1\sqrt{K\rho_3}\right)\right]\right) \quad (6.99)$$

The maximum FRP strain can be obtained by the following equation (Equation (6.100)):

$$\varepsilon_{f,max} = \frac{F_{max}}{b_f t_f E_f} \quad (6.100)$$

Where, F_{max} is the maximum achieved force at the end of degradation zone.

6.3.4. Validation and Discussion

In this study, parameters for the proposed theoretical models are calculated using the indirect numerical approach for the shear stress-slip relationship of the adhesively bonded joints. When a bond-slip relationship including some unknown variables is given and bond shear test results are available, an unknown variable can be obtained with numerical identification methods. Therefore, the proposed theoretical bond-slip model for the FRP-lightweight /normal weight concrete interface with several unknown variables is chosen at first. These unknown variables such as the value of α is then determined by minimizing the error between experimental and theoretical results. The test results reported in Chapter 3 are used in this identification procedure. To verify this model, a new MATLAB code was written to provide the load-slip curves and the maximum debonding strain.

The purpose of this code was to determine the unknown parameters for the load-slip relationship given in this model and to solve Equation (6.74) and Equation (6.94) at each small increment of slip to find the corresponding force and draw the full load-slip curve. Table (6.3) summarises the values of the main parameters assumed in this model. The following steps show the concept of this model:

Step (1):

This step is to determine the unknown parameter (α). The maximum slip value was taken as 0.065 mm based on the theoretical model developed by Nakaba (Nakaba et al., 2001). The α term is determined for the bond-slip relationship by minimizing the error between the experimental applied load-global slip curve (from zero load up to the load corresponding to 0.065 mm slip) and the total debonding force for double lap shear tests versus slip curve (see Equation (6.74)) using the following equation (Equation (6.101)) (Liu, 2011):

$$Min.Err(\alpha) = \sum_{i=1}^{n} \left[F_{Exp} - F_{p,CEB}\right]^2 \quad (6.101)$$

Where, F_{Exp} is the experimental force corresponding to 0.065 mm slip, and $F_{p,CEB}$ is the primary force calculated using Equation (6.80). Figure (6.23) summarises the steps of error minimizing in the primary zone. In this step, the initial value of α was assumed as 0.35 for LWAC samples (CEB, 1999) and 0.4 for NWAC samples (CEB-FIB, 1992). The initial assumed value of α was substituted in Equation (6.73) to obtain l_p as a function of the primary slip and the corresponding values were substituted in Equation (6.74) to plot the bond force F in the primary zone as a function of the primary slip s_{lp}. The total applied load versus slip obtained from Equation (6.80) is compared with experimental results and the step was repeated many times with various values of α to find the optimum value of α and to minimize the error between the proposed models and experimental trend.

Step (2):

This step will be created when the value of s exceed s_1. In this study, the ultimate slip between the FRP and concrete at the loaded end (centre of the sample) (s_3) was calculated based on the Equation (2.27) (see chapter two (section 2.11)) which is developed by Pellegrino and Modena, (2008). This value was found to produce the most accurate results of the proposed model compared with other proposed models. Finally, the full envelope of load-slip was obtained and compared with experimental results to describe the full range of behaviour of FRP- lightweight and normal weight concrete interface based on shear stress- slip relation reported in the CEB model. The MATLAB code can also be summarised using the following flowchart (see Figure (6.24)):

Table (6.3): Parameters identification.

Concrete Type	τ_{max} (MPa)	α
Normal weight concrete	$\sqrt{f_c'}$	0.5
Lightweight concrete	$0.85\sqrt{f_c'}$	0.45

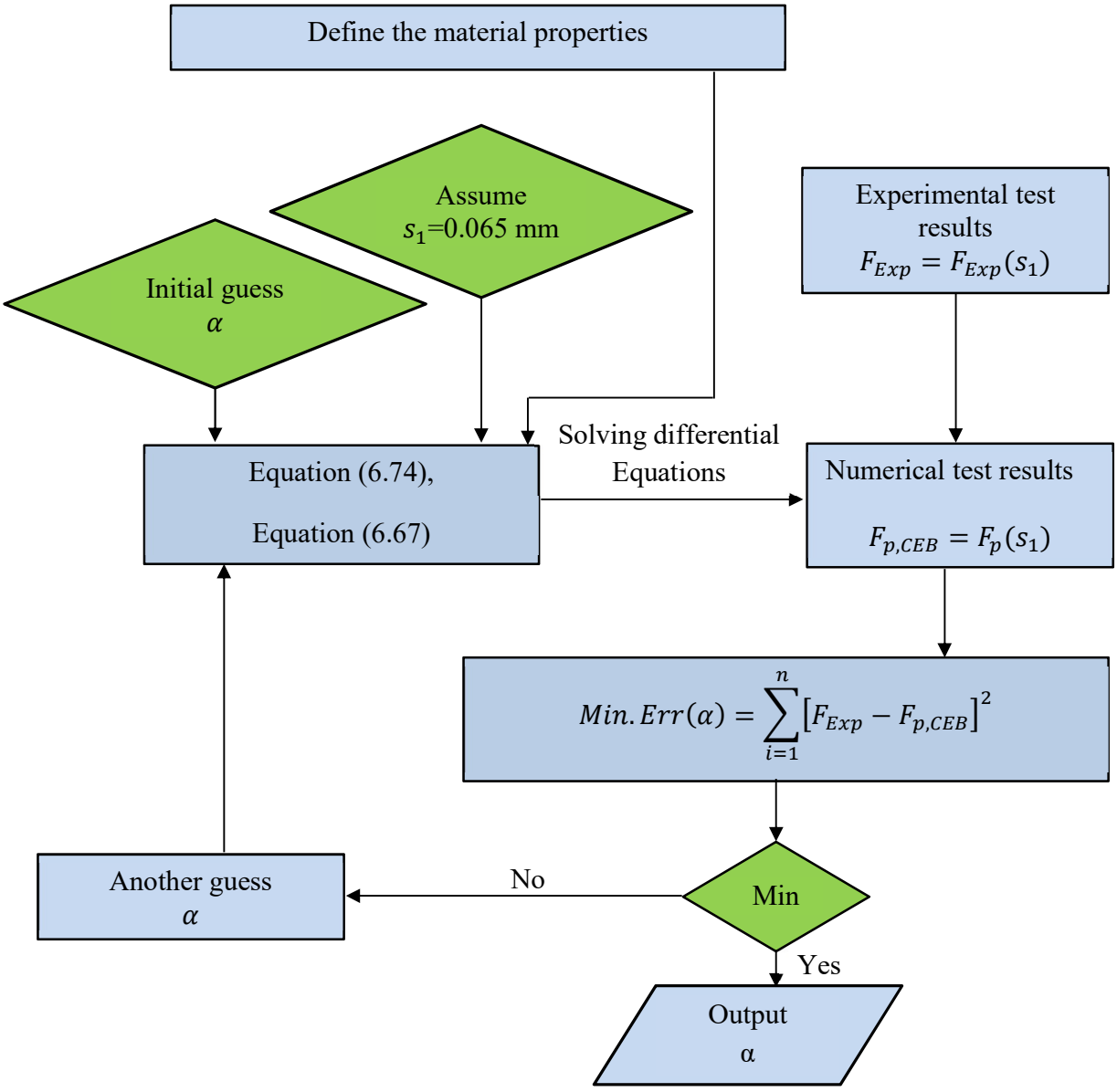

Figure (6.23): Unknown parameter identification.

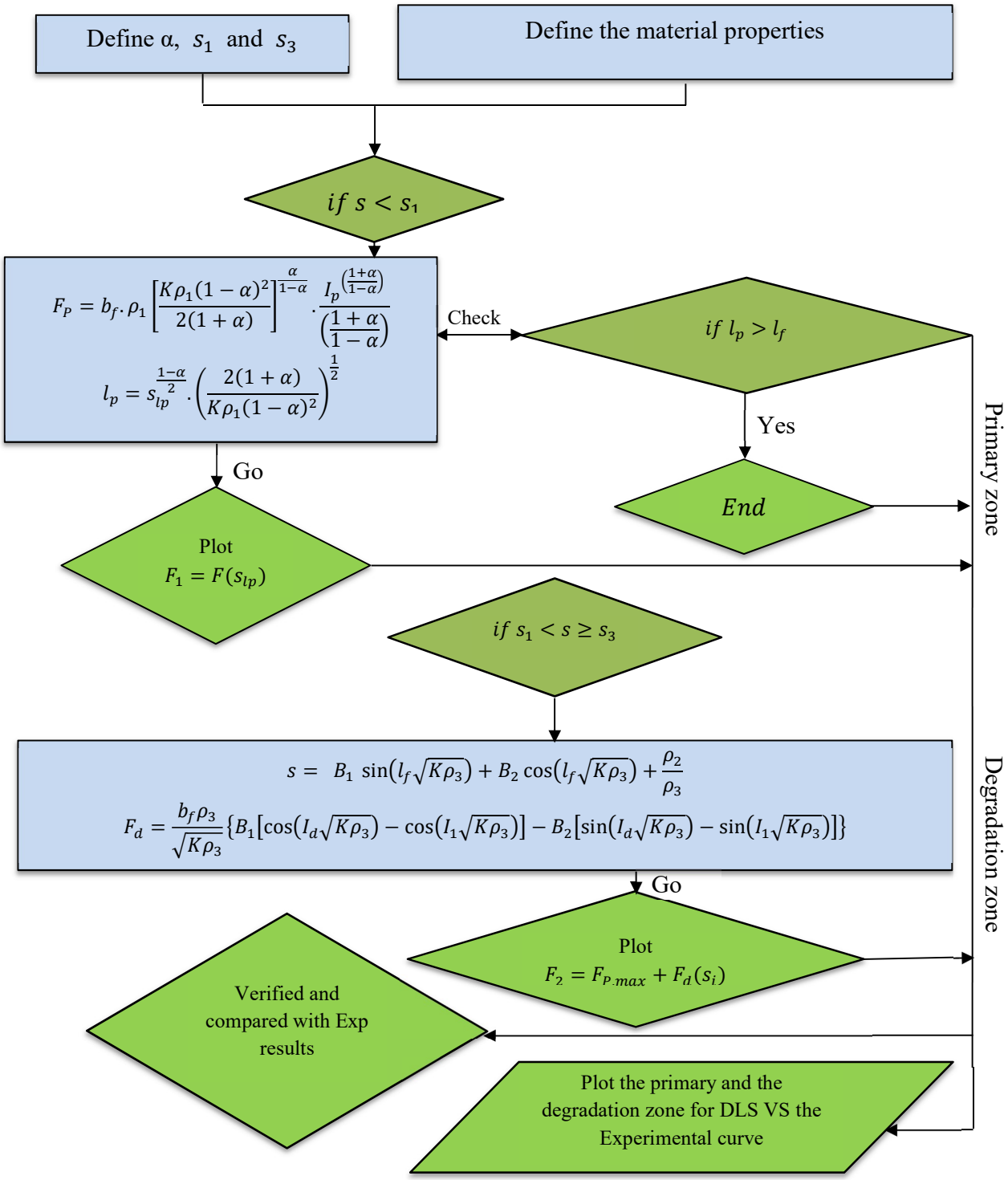

Figure (6.24): M.CEB solution steps.

6.3.5. Characteristics of the Load–Slip Curve

The complete load–slip curve and the bond stress-slip of the FRP-concrete interface (Figure 6.25) consists of a number of points corresponding to the loading stages. The cracking stage starts at Point A and the initiation of debonding (ultimate load achieved at the corresponding ultimate slip) occurs at point B. As a result, this model provides a useful tool for the calculation of the complete load-slip behaviour of the FRP-concrete interface.

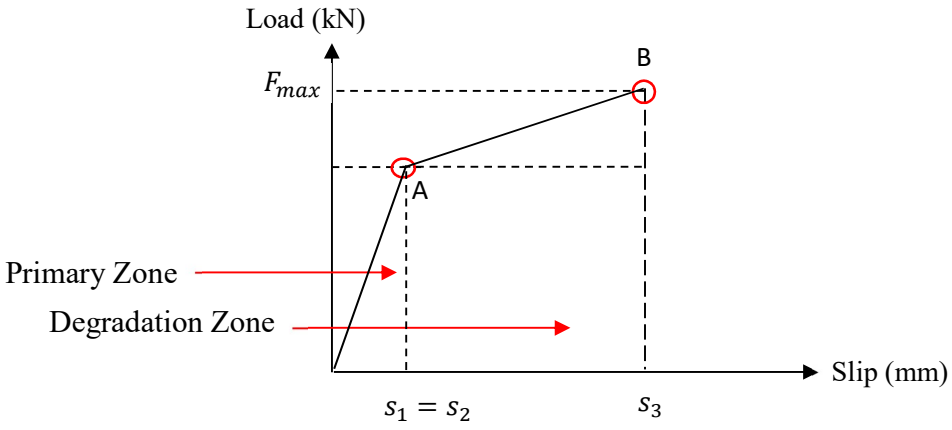

(a): Load versus slip relationship.

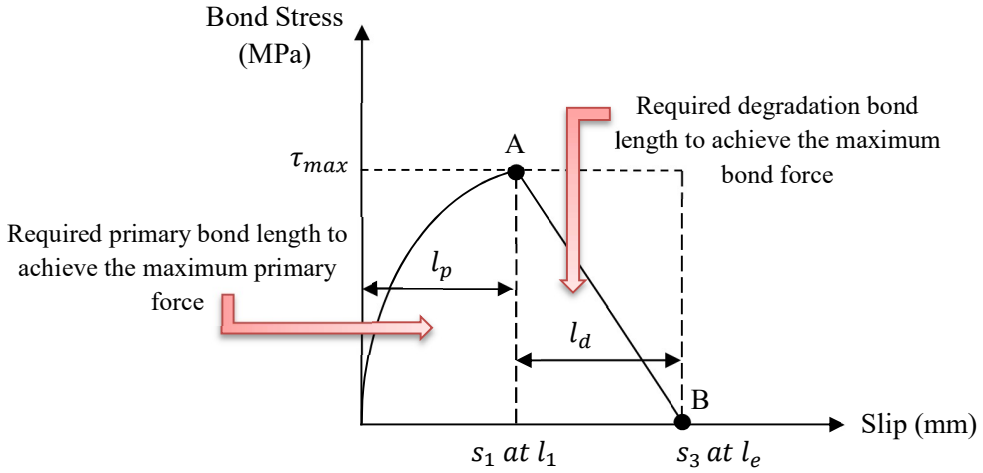

(b): Bond stress versus relationship.

Figure (6.25): Proposed model relationships.

The total applied load versus slip curves for double lap specimens BL/N1-2 and BL/N1-3 are calculated using the proposed model corresponding to available bonded length of the FRP reinforcement and compared with the experimental load versus global slip results as shown in

Figure (6.26). The test results and the analytical results can be seen to be in good agreement. The match with experimental results further demonstrates the excellent performance of the analytical models developed in this work.

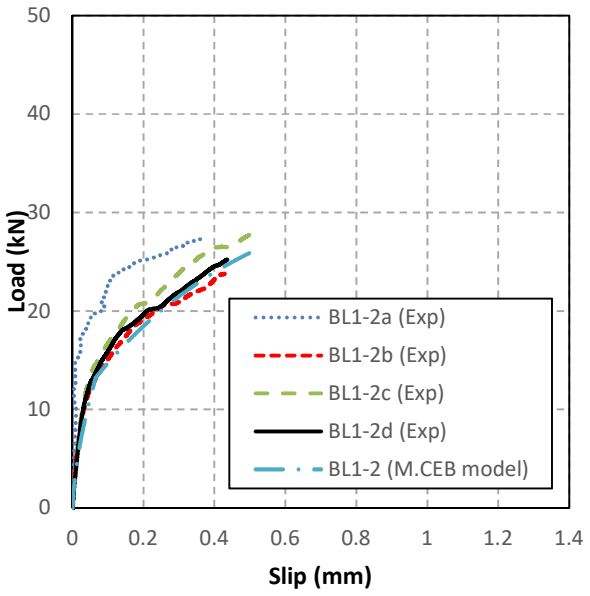

(a) BL1-2 samples.

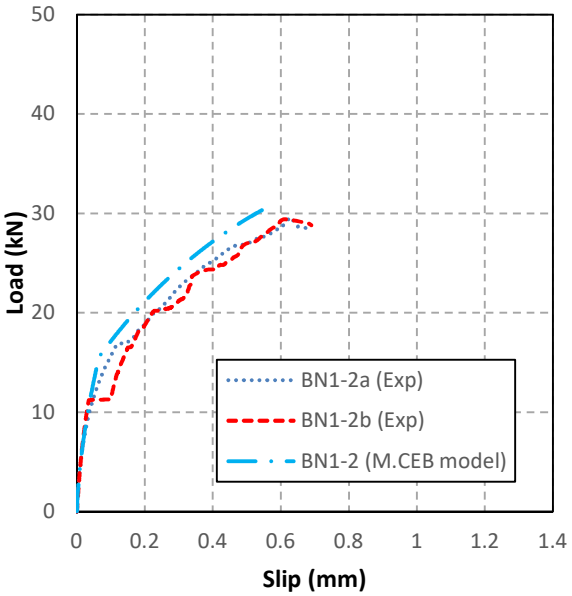

(b):BN1-1 samples.

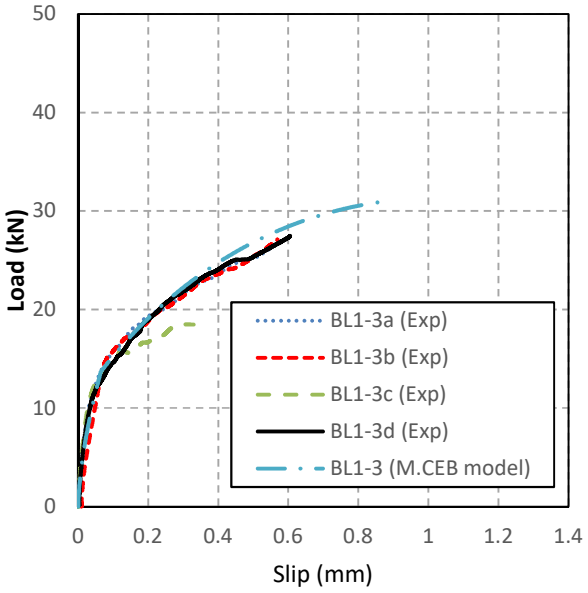

(c): BL1-2 samples.

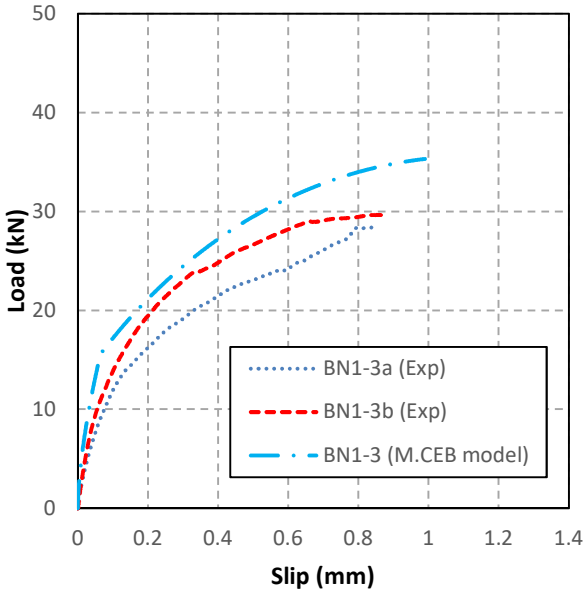

(d): BN1-2 samples.

Figure (6.26): Comparison of load-slip curves.

6.3.6. Validation of the Maximum Debonding Force

Figure (6.27) compares the maximum debonding force values which are obtained based on Equation (6.97) for double-lap shear tests conditions for the LWAC and NWAC specimens. It can be noted that Equation (6.97) shows a very good agreement with the experimental test data. The overall mean value of the predicted-to-experimental maximum load ratio for LWAC samples is 1.05 with a coefficient of variation (C.V) of 20.9% and a standard deviation (S.D) of 0.22 and While for NWAC samples, the average of the predicted-to-experimental maximum load ratio is 1.01 with a coefficient of variation (C.V) of 16.8% and a standard deviation (S.D) of 0.17 and. The maximum load values obtained in this model are compared with the average prediction of the experimental bond strength of LWAC and NWAC samples calculated from other models and guidelines equations as shown in Figure (6.27) (see Table (6.1) and (6.2)). The results of this model (Modified CEB model) are in good agreement compared with the results of other models and guidelines which demonstrates the capability of the model to predict the interface behaviour of lightweight concrete/FRP joints.

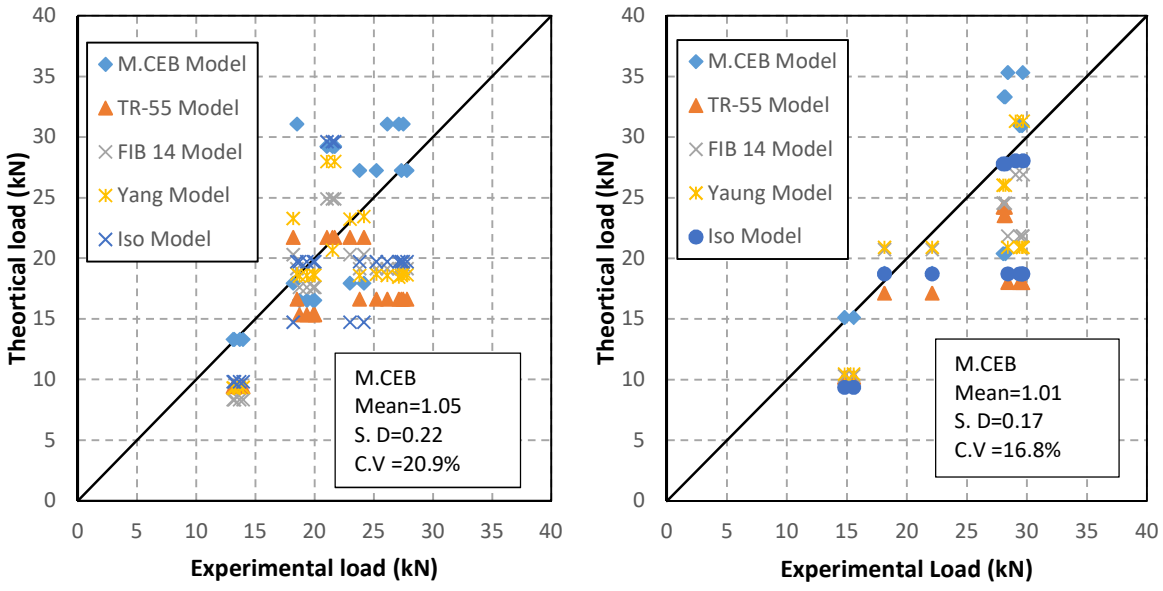

(a): LWAC (b): NWAC

Figure (6.27): Theoretical prediction load versus experimental observation of the tested samples.

6.3.7. Validation of the Maximum Debonding Strain

A comparison between the maximum debonding strains obtained using Equation (6.100) and those CFRP strains measurements collected from experimental test results at the centre of the LWAC and NWAC samples were presented in Table (6.4). A good agreement was obtained between the experimental test data and the theoretical value in the case of samples made with normal weight concrete. Generally, the average value of the predicted-to-average experimental maximum debonding strain ratio for NWAC samples is 1.15 while for LWAC samples, the average of the predicted-to- experimental maximum debonding strain ratio is 0.95. It can be also noted that there is a slight difference between the normal and lightweight concrete samples in maximum strain prediction. As previously discussed in section 6.2.5.2, this can be attributed to the clear variation of the strain reading in case of lightweight samples due to a lower stiffness and higher crack intensity at the centre of these samples.

Table (6.4): Average prediction to test bond strength of NWAC samples.

Specimen ID	$\left(\varepsilon_{max,p}/\varepsilon_{max,e}\right)_{NWAC}$	$\left(\varepsilon_{max,p}/\varepsilon_{max,e}\right)_{LWAC}$
BL/N1-1	0.74	1.05
BL/N1-2	0.86	1.04
BL/N1-3	1.25	1.37
Mean	0.95	1.15

6.3.8. Validation of the Ultimate Slip

Tables (6.5) and (6.6) compare the experimentally obtained ultimate global slip with the analytical values based on the modified CEB model. Close agreement is observed with the experimental data. The overall average value of the observed-to-predicted ultimate slip ratio is 1.03 for LWAC specimens while for NWAC the average value of the observed-to- predicted ultimate slip ratio is 0.79.

Table (6.5): Average prediction of test slip values of LWAC samples.

Specimen ID	Average Exp ultimate global slip (mm)	Predicted to Experimental slip ratio
BL1-1	0.31	0.39
BL1-2	0.43	1.21
BL1-3	0.49	1.82
BL3-1	0.15	0.85
BL4-1	0.57	0.83
BL4-2	0.046	1.09
	Mean	1.03

Table (6.6): Average prediction of test slip values of NWAC samples.

Specimen ID	Average Exp ultimate global slip (mm)	Predicted to Experimental slip ratio
BN1-1	0.30	0.43
BN1-2	0.65	0.88
BN1-3	0.82	1.21
BN3-1	0.18	0.83
BN4-1	0.55	0.97
BN4-2	0.14	0.42
	Mean	0.79

6.3.9. Parametric Study

The influence of the FRP bond length and concrete strength on the maximum load capacity is shown in Figure (6.28). Figure (6.28a) shows a plot of maximum load capacity versus the bond length of the FRP reinforcement. It can be noted that the maximum load capacity of the FRP/concrete joint increases as the length of the FRP reinforcement increases till the maximum anchorage length or effective length of the FRP reinforcement l_e is achieved which is approximately 107 mm based on the proposed model. Increasing the length of the FRP reinforcement further than the effective length dose not lead to increase in the maximum load capacity of the FRP/concrete joint.

It can be noted that the bond length of the FRP reinforcement is slightly less than the required length to achieve the full degradation zone based on the proposed degradation force (Equation 6.94) which is calculated based on of the ultimate slip limit proposed by Pellegrino and Modena, (2008). The proposed model slightly overestimates the effective length of FRP. However, this model provides a useful and accurate approach to describe the debonding process and the load-slip behaviour, maximum debonding force, maximum strain, slip during the debonding process.

Figure (6.28b) shows the influence of the concrete strength on the maximum bond strength for both BL/N1-2 samples. The concrete compressive strength was changed from 10 to 50 MPa in the proposed analytical model. It can be observed that as the concrete compressive strength increases, the maximum bond strength increases. The same behaviour was observed in FE models simulated in chapter five (see section 5.4.7.1) and the experimental test results obtained by LópezGonzález et al., (2012).

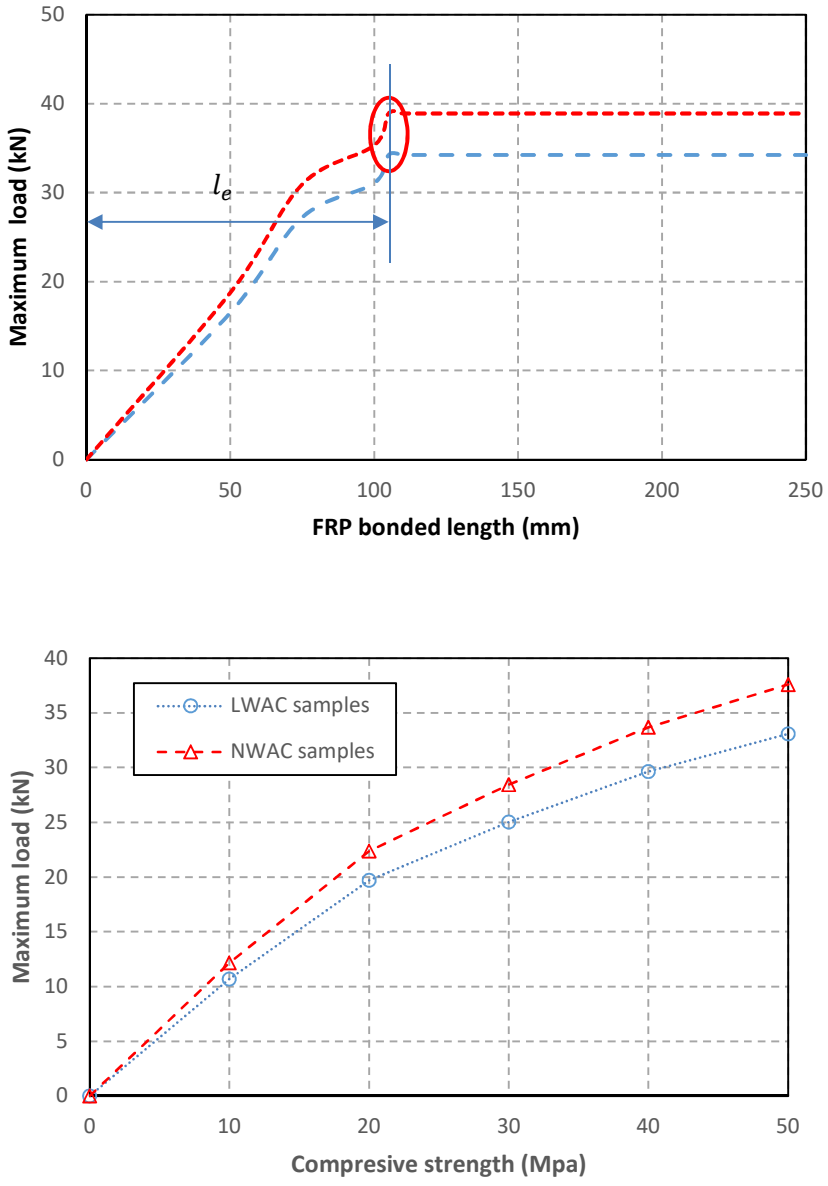

Figure (6.28): Maximum bond strength versus (a) FRP bond length and (b) concrete compressive strength for the sample BL/N1-2.

6.4. A New Design Proposal for FRP Shear Strength

An analytical model is developed in this section to predict the shear contribution of the FRP reinforcement used to retrofit reinforced normal/lightweight concrete beams. A new expression of the effective FRP debonding and rupture strain is suggested in this study. The proposed model and the design formulations are typically calibrated with the experimental results of LWRC and NWRC beams to assess the adequacy of the proposed and various shear prediction methods to estimate the shear strength gained due to FRP reinforcement.

6.4.1. FRP Strain Distribution Factor

The FRP measured strains differ along the length of the diagonal shear crack plane, this is may be attributed to the difference in the width of the shear crack and the bond length of FRP reinforcement at different locations along the length of the diagonal shear crack. For example, at the middle of the shear crack length, the width of crack and the bond length FRP reinforcement are higher compared with other locations such as the top and bottom ends of the shear crack, the width of the crack and the bond length of FRP reinforcement is small close this region (Colalillo, 2012).

For shear steel reinforcement, when the shear diagonal shear cracks are developed, the shear stirrup intersected by these cracks start yielding, with further loading the neighbouring shear stirrup begins to yield, etc. At the ultimate limit state, all shear links will be yielded and the shear strength provided by steel reinforcement can be defined as V_s, the design shear capacity V_{Ed}, is fulfilled (Al-Juboori, 2011). FRP is not ductile and it has linear elastic response. The strain distribution differs along the length of the crack plane, the strains of all FRP reinforcement crossing the diagonal shear crack should be included to obtain the shear contribution provided by FRP reinforcement. For design purposes, the effective FRP strain will consider to obtain the design shear strength provided by the FRP reinforcement which is defined as the average FRP strain along the length of the diagonal shear crack and should be less than the maximum debonding or rupture strain. The effective strain can be obtained by the following equation (Colalillo, 2012):

$$\varepsilon_{frp,e} = \varphi_{frp} \cdot \varepsilon_{frp,max} \tag{6.102}$$

Where $\varepsilon_{frp,max}$, is the maximum debonding or rupture strain, and φ_{frp}, is the strain distribution factor. The factor of the strain distribution of the FRP reinforcement can be assessed by summing all FRP strains along the length of the diagonal shear crack as shown in the following equation (Equation (6.103)) which is assumed by Cao et al., (2005):

$$\varphi_{frp} = \frac{\sum_{i=1}^{n} \varepsilon_{frp,i}}{n\ \varepsilon_{frp,max}} \cong \frac{\int_0^l \varepsilon_{frp,x} \,.\, dx}{l\ \varepsilon_{frp,max}} \tag{6.103}$$

Where l is the length of the diagonal shear crack and $\varepsilon_{frp,x}$ is the strain along the length of the shear crack. The FRP strain distribution factor along the length of the diagonal shear crack can be assessed at the maximum limit state of debonding failure.

Colalillo and Sheikh, (2014b) derived a new expression for the FRP strain distribution factor based on the closed-form solution developed by Mohamed Ali et al. (2006). Colalillo and Sheikh, (2014b) assumed that the maximum debonding FRP strain achieved at any point along the length of the crack when the length of the FRP reinforcement is larger than the anchorage length for samples strengthened with U-shaped or side-bonds strengthening system. This assumption is not reflecting the actual behaviour of the experimental tested samples as the concrete is non-homogenous material and the crack widths differ along the length of the crack as well as the strain values will differ, but its represent an acceptable and simple assumption for design purposes in order to obtain a reliable expression for the shear strength provided by FRP reinforcement.

According to the above assumption, a similar analysis was carried out based on the maximum debonding strain developed in this study to derive a simplified expression for the FRP strain distribution factor for samples retrofitted with U-wrapped or side-bond strengthening techniques. The triangular critical area from the crack plane to the top free end of the beam in case of samples with U-shaped reinforcement and from the crack plane to the top and bottom free ends of the beam in case of sample with side-bonds can be divided into two zones, the effective and ineffective shear zone as shown in Figure (6.29).

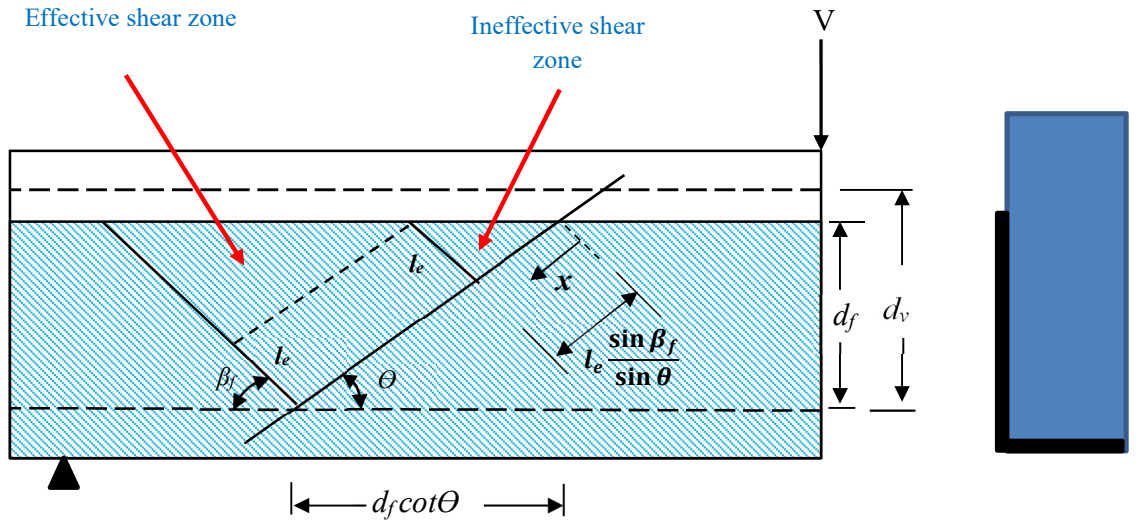

(a): U-wrap strengthening.

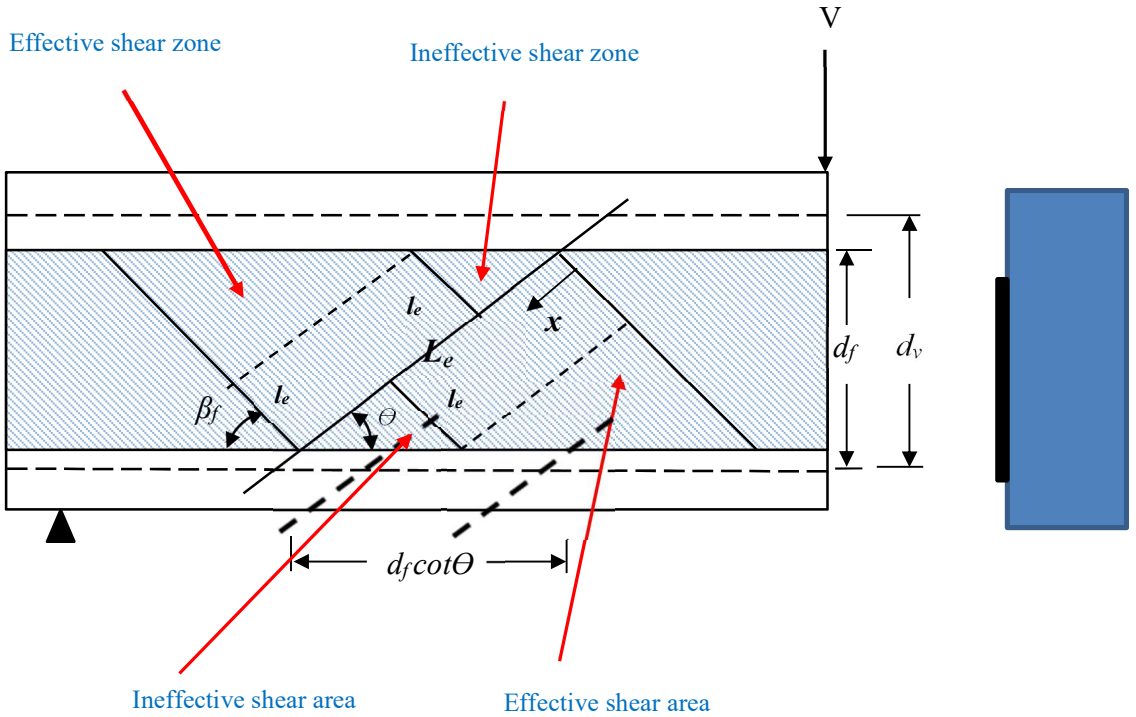

(b): Side bond wraps

Figure (6.29): Typical bonded area for RC beams retrofitted with FRP reinforcement (adopted by Colalillo and Sheikh, (2014b)).

The shear contribution of the FRP reinforcement to the total shear capacity of the beam in the ineffective shear zone is small compared with the effective shear zone, so its effect was ignored in the following equation:

$$\varphi_{frp} = \frac{\sin\theta}{d_f \varepsilon_{frp,max}} \int_{l_e \frac{\sin \beta_f}{\sin\theta}}^{\frac{d_f}{\sin\theta}} \varepsilon_{frp,max}\, d_x \tag{6.104}$$

$$\varphi_{frp} = \frac{\sin\theta}{d_f} \; |x| \; {}_{l_e \frac{\sin\beta_f}{\sin\theta}}^{\frac{d_f}{\sin\theta}} \tag{6.105}$$

Where, $\varepsilon_{frp,max}$ is the maximum debonding FRP strain (Equation (6.109)). The FRP strain distribution factor for U-shaped can be calculated by Equation (6.106):

$$\varphi_{frp} = \left(\frac{d_f - l_e \sin\beta_f}{d_f} \right) \tag{6.106}$$

This expression (Equation (6.106)) is similar to the simplified terms that obtained by Colalillo and Sheikh, (2014b). For a side-shaped sample, the FRP strain distribution factor can be calculated by the following equation (Equation (6.107) (Colalillo and Sheikh, 2014b):

$$\varphi_{frp} = \left(\frac{d_f - 2l_e \sin\beta_f}{d_f} \right) \tag{6.107}$$

6.5.2. Suggested Effective FRP Debonding and Rupture Strain

This model assumes that debonding develops within a thin layer of concrete underneath of the FRP reinforcement. This failure pattern is typical for most the experimental test results carried out so far. The effective FRP debonding strain was developed in this study based on simplified bond-slip model bond proposed in section 6.2.3. The loading arrangement of reinforced concrete beams retrofitted by FRP U-shaped or side-bonds can be implemented by an FRP reinforcement attached on both sides of concrete prisms as the same condition in the double-lap shear test (Dirar, 2009) as shown in Figure (6.30). The summation of the forces carried by the FRP reinforcement is equal to V_f.

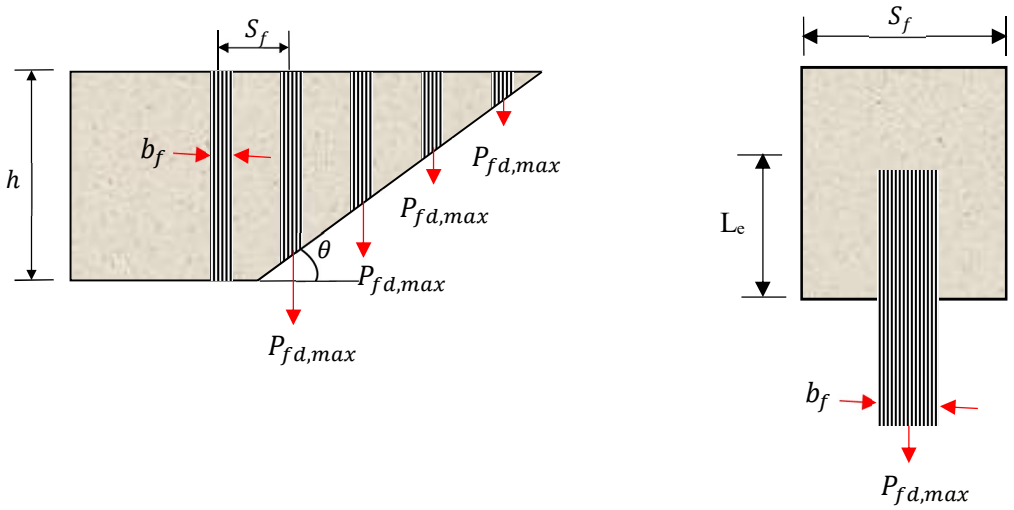

Figure (6.30): Loading condition of the reinforced concrete beam strengthened with externally bonded FRP reinforcement.

The maximum design force that can be carried by the one FRP reinforcement at the occurance of debonding is given by Equation (6.108):

$$P_{fd,max} = \varepsilon_{f,d,max}.t_f.b_f.E_f \tag{6.108}$$

In this study, the FRP debonding strain is developed based on the maximum debonding load $P_{d,max}$ given by Equation (6.21). The maximum design debonding strain can be obtained by substituting Equation (6.21) into Equation (6.108):

$$\varepsilon_{f,d,max} = \frac{\beta_r.\beta_w.R.L_e.\sqrt{f_c'}}{t_f E_f} \tag{6.109}$$

$$\varepsilon_{frp,e} = \varphi_{frp}.\frac{\beta_r.\beta_w.R.L_e.\sqrt{f_c'}}{t_f E_f} \tag{6.110}$$

The strain distribution factor for the effective debonding strain φ_{frp}, can be obtained using equations (6.106) and (6.106). The equation (6.110) accounts only for the debonding mode of failure. For other modes of failure such as rupture of the RC beam strengthened externally with closed wrapped FRP composite, the following effective rupture strain is proposed in this study:

$$\varepsilon_{frp,e} = \varphi_{frp}.\varepsilon_u \tag{6.111}$$

Where φ_{frp} is taken as 0.5 for design according to (Chen and Teng, 2003a) (which assumed a linear strain distribution along the length of the crack in the case of RC beams strengthened with closed-shaped system) and ε_u is ultimate FRP strain. the unfactored shear contribution of the FRP reinforcement can be obtained by the following equation (Equation (6.112)):

$$V_f = \varepsilon_{frp,e} E_f \, b_w d_f \left(\cot\theta + \cot\beta_f\right) \sin\beta_f \qquad (6.112)$$

Where ρ_f is the ratio of the FRP reinforcement, b_w is the width of beam, $f_{frp,e}$ is the effective stress developed in the FRP reinforcement, and θ is the compressive strut inclinations. For practical design, it can be assumed that $\theta=45^0$. β_f is the angle of the FRP reinforcement. d_f is the effective depth of the FRP reinforcement. The ratio of the FRP reinforcement can be calculated from the following equations (Equation (6.113)):

$$\rho_f = \left(\frac{A_f}{S_f b_w}\right) = \left(\frac{2t_f b_f}{S_f b_w}\right) \qquad (6.113)$$

Where A_f is area of the FRP reinforcement. The shear contribution of the FRP reinforcement can be expressed as a function of the effective FRP strain by substituting Equation (6.113) into Equation (6.112)) as (Equation (6.114)):

$$V_f = \varepsilon_{frp,e} E_f \left(\frac{2t_f b_f}{S_f}\right) d_f \left(\cot\theta + \cot\beta_f\right) \sin\beta_f \qquad (6.114)$$

the nominal shear capacity of the reinforced concrete beam strengthened with FRP reinforcement in shear can be obtained by the following equation (Equation (6.115)):

$$V_n = V_c + V_s + V_f \qquad (6.115)$$

Where,V_c and V_s are the shear strength provided by concrete and steel reinforcement respectively.

6.4.3. Further Design Considerations

The proposed model accounts the unfactored shear contribution of the FRP reinforcement applied externally to retrofit lightweight and normal weight concrete members. However, there are further design limitations that should be included in this model. This section addresses these considerations.

6.4.3.1. FRP Effective Depth

The effective depth of the FRP reinforcement can be obtained from the following equations:

For U-wrap and side bond:

$$d_f = d - t_a \tag{6.116}$$

For closed wrap:

$$d_f = d \tag{6.117}$$

Where, t_a is the distance from the top free ends of the FRP reinforcement to the top of the beam.

6.4.3.2. Spacing of the FRP Reinforcement

The FRP strips should be spaced adequately to achive the maximum shear strength provided by the strengthening system. For this purposes, the following equation proposed by the UK concrete society (TR 55, 2013) may be used (Equation (6.118)):

$$s_f = min\begin{cases} b_f + \dfrac{d}{4} \\ 0.8\,d \end{cases} \tag{6.118}$$

6.4.4. Model Validation Compared with Design Codes and Guidelines

The trustworthiness of the proposed model to predict the shear contribution of CFRP reinforcement in the case of beams cast with lightweight concrete and beams cast with normal weight concrete was evaluated and compared with current design codes and guidelines such as (ACI 440.2R, 2008), (TR 55, 2013) and (CAN/CSA S6, 2006), as summarised in Table (6.7). In this study, the nominal

predicted contribution of FRP reinforcement for the purpose of comparison was used in this study as summarised in Table (6.7).

From Table (6.7), the shear strength model suggested by the proposed model to predict the contribution of FRP reinforcement resulted incomparably higher mean predicted-to-experimental ratio in the case of samples with closed-shaped, particularly for LWAC samples. In contrast, TR55 (2013), ACI 440.2R (2008) and CSA S6 (2006) showed the lower mean predicted-to-experimental ratio. This may be attributed to the limit of the maximum FRP effective strain to 0.004 in some of these models, which results in overly conservative failure predictions for closed-shaped samples and the highest coefficients of variation. The experimental test results carried out by Colalillo and Sheikh, (2014a) showed that the rupture strains at failure were more than the design effective strain limit of 0.004 as suggested by TR55 (2013), ACI 440.2R (2008) and CSA S6 (2006) (Colalillo and Sheikh, 2014a). The higher value of the mean predicted-to-experimental load ratio in the proposed model in the case of lightweight and normal weight samples retrofitted with closed wrapped CFRP reinforcement is attributed to the value of the strain distribution factor which is assumed in this study as 0.5, based on Chen and Teng (2003b).

Generally, the predictions of the ACI 440.2R (2008), TR 55 (2013) and CAN/CSA S6 (2006) overestimate the contributions of FRP reinforcement for LWAC retrofitted with U-shaped CFRP reinforcement. It can be noted that the prediction of lightweight samples are statistically better than normal weight samples, this is probably due to the premature failures of LWAC due to the lower bond between CFRP reinforcement and beam concrete surface which is accelerating CFRP debonding or rupture.

A database of NWRC beams retrofitted with a different configuration of FRP reinforcement listed in Appendix E (Table 1) was used to assess the accuracy of the proposed FRP shear models compared with ACI 440.2R (2008) model. The diagonal shear crack angle was assumed as $\theta=45^0$ in this analysis. The predictions of the proposed model is shown in Figure (6.31). The average predicted- to- the experimental ratio of 0.60 and a standard deviation of 0.17 resulted in 28.3% coefficients of variation. Comparison with test results of the LWAC deep beams strengthened by FRP reinforcement carried by Asghari et al., (2014) also summarised in Appendix E (Table 2). The average predicted to the experimental ratio of 0.97 and a standard deviation of 0.21 resulted in 22% coefficients of variation.

In contrast, the ACI 440.2R (2008) design model has an average predicted-to- experimental load ratio of 0.58 and a standard deviation of 0.38 resulting in 65.5% coefficients of variation as illustrated in Figure (6.30). The higher coefficient of variation is probably because the bond model proposed in the ACI 440.2R (2008) design model is derived based on a specific experimental data (Belarbi et al, 2007).

Table (6.7): Predicted-to-experimental CFRP shear contribution for strengthened samples.

Sample	FRP shear Strength (kN)	Predicted-to experimental strength ratio (V_{pre}/V_{exp})			
		Proposed model	ACI 440.2R (2008)	TR-55 (2013)	CAN/CSA S6 (2006)
BL-UST	66.60	0.75	1.1	1.2	1.08
BL-CST	115.36	0.98	0.68	0.7	0.62
Mean		0.86	0.89	0.95	0.85
BN-UST	84.51	0.75	0.86	0.94	0.84
BN-CST	156.70	1	0.5	0.46	0.46
Mean		0.87	0.68	0.7	0.65

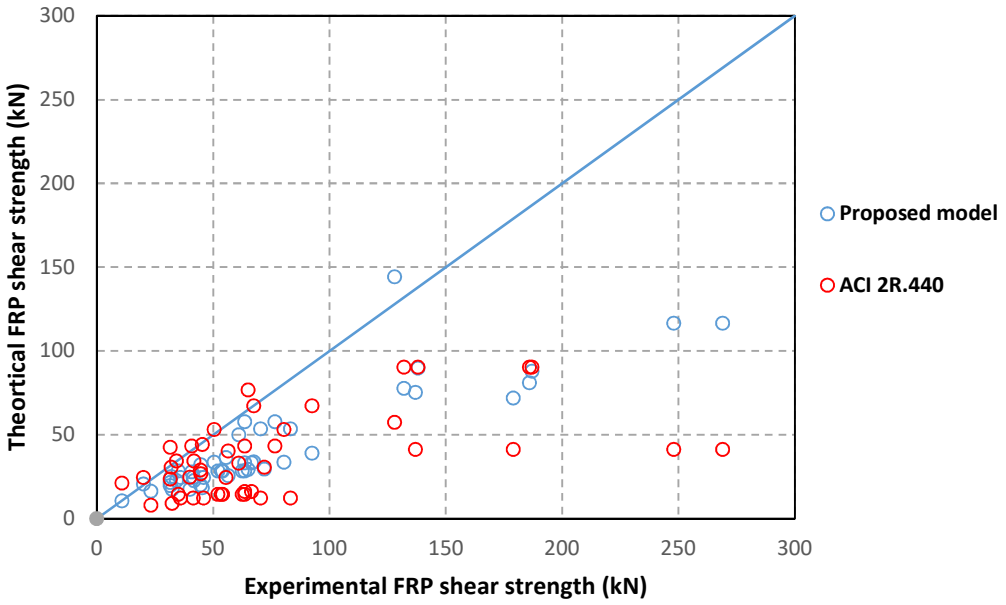

Figure (6.31): Predictions of the proposed model.

6.5. Summary

Appropriate shear stress transference in the FRP/concrete joint is needed to achieve the required bond strength between FRP reinforcement and the surface of concrete. A significant amount of research has been carried out to model the response of the FRP-normal weight concrete joints. However, the bond-slip relationships of FRP-to-lightweight concrete joints and the maximum shear strength provided by FRP reinforcement in RC beam are not investigated yet. In this chapter, new methods were derived for the determination of the interface characteristics of the FRP-concrete joints. Based on these models, new equations are proposed to estimate the load-slip relationships, the maximum debonding load, ultimate slip, FRP strain and shear stress of the FRP-lightweight /normal weight joints.

In the first proposed model (simplified model), the FRP strain distribution along the bonded length was defined by a fourth-degree polynomial formula. In this model, new expressions were proposed and verified for the interface characteristics such as bond strength, strain distribution and ultimate slip. The influence of different variables was considered in these relationships. The analytical results of this model showed closer agreement with the experimental results.

Based on this maximum bond strength equation developed in the simplified model, a new model to predict the shear contribution provided by FRP reinforcement were derived and verified in this chapter. The effect of the bond between FRP reinforcement and the lightweight substrate was considered in this model which is one of the most important goals of this study. The predictions of this model reveal a reasonable agreement with the experimental contribution of the FRP reinforcement and when compared with some available design codes and guidelines.

The second proposed model (modified CEB-FIP 1990 Bond-Slip models) is a more sophisticated load-slip model which has been proposed in this study. The complete model for lightweight and normal concrete, with the full range of loading behaviour between FRP reinforcement and concrete, is developed based on the shear stress-slip relation reported in the CEB model to describe the full range of behaviour of the FRP- concrete interface. To verify this model, a new MATLAB code was written to provide the bond force-slip curves, and the maximum FRP reinforcement strain predictions. The results of this model showed reasonable agreement with experimental results.

CHAPTER SEVEN

CONCLUSION AND RECOMMENDATIONS

7.1. Summary

Epoxy bonded fibre reinforced polymer (FRP) composites are widely used for the retrofit of ailing reinforced concrete structures, for both shear and flexure. The behaviour of retrofitted concrete structures is governed by the bond strength and the material characteristics of the epoxy bonded FRP and the concrete. Previous studies show that lightweight aggregate concrete (LWAC), which uses Pulverised Fuel Ash (Lytag) instead of coarse normal weight aggregates, has significantly lower tensile strength and aggregate interlock compared to normal weight concrete. The performance of shear retrofitted concrete elements is primarily governed by the aggregate interlock and tensile strength. Thus, the study of FRP enhancement techniques in LWAC is paramount for limit state design.

Many studies have been conducted to understand the bond-slip behaviour between normal weight aggregate concrete (NWAC) and FRP composites and the shear behaviour of the normal weight concrete beams strengthened with FRP system, where the increasing interfacial (shear) and normal stresses with increasing plastic deformation leads to FRP debonding and/or FRP rupture failures. However, the bond between the lightweight concrete and FRP and the shear behaviour of reinforced concrete beams strengthened with FRP composite have not received much attention. Hence, this research has investigated the bond behaviour between the CFRP and concrete substrates cast with LWAC and NWAC and the shear behaviour of LWRC and NWRC beams retrofitted with CFRP reinforcement.

An extensive literature review was carried out in this study and a new test arrangement of the double-lap shear test was developed to investigate the behaviour of the CFRP/lightweight concrete joint. In addition, the beam shear tests were also carried out to investigate the shear behaviour and failure patterns of LWRC beams retrofitted with CFRP reinforcement.

7.2 Conclusions

From the experimental model tests, the finite element analyses and analytical models, a number of conclusions are summarised in the following section.

7.2.1. Bond-Slip Tests

The interfacial behaviour of LWAC was studied in this research. For this purpose, 55 concrete blocks (34 LWAC prisms and 21 NWAC prisms) were cast and tested using the modified double-lap shear test set-up. The effect of different variables, such as the bonded length, thickness, width and direction of unidirectional bonded CFRP sheets were studied in order to understand the fracture of concrete and the effectiveness of CFRP. Overall, the experimental results show that the crack propagation occurred within the LWAC specimens while peeling of CFRP was the main cause of failure in NWAC specimens. The effectiveness of using FRP to retrofit RC structures is mainly affected by the concrete properties. Since the existing design codes and numerical models were developed based on test data of normal weight concrete, the performance of FRP with LWAC was investigated.

A new FEA and analytical models were developed in this thesis to investigate the response of the FRP/lightweight concrete joints. The outcomes of the FEA and the analytical proposed models demonstrate the ability of these models to predict the characteristics of the FRP/concrete joint with reasonable accuracy. From the experimental model tests, the finite element analyses and analytical models, a number of conclusions can be derived

7.2.1.1. Conclusions from experimental works

1. The effect of concrete type on bond strength and slip at failure was examined in this study. In general, LWAC bond test samples revealed considerably lower bond strength and slightly lower slip at failure than those of NWAC of similar strength grade and identical CFRP retrofitting configurations. The results of the double-lap shear tests presented in chapter three of this thesis showed that the average bond strength between CFRP reinforcement and the lightweight concrete substrate is 85% of those samples cast with normal weight concrete and having the same strengthening configurations of CFRP reinforcement. This is attributed to lower tensile strength of concrete and aggregate interlocks for LWAC which significantly influence the performance of FRP used to strengthen lightweight concrete members.

2. The results of this study showed that the increase of CFRP sheet length further than 75 mm does not lead to higher load capacity in both samples cast with LWAC and NWAC. However, a larger bond length leads to a longer deformation process as debonding propagates along the interface, the effective bond length was assumed about 75 mm for LWAC and NWAC samples which showed similar behaviour. Hence it can be concluded that the effective bond length is not influenced by concrete type.
3. The orientation of the CFRP sheet is one of the parameters that most influences the behaviour of the CFRP-to-concrete interface which is critical in the shear retrofitting system. Therefore, if there is an angle between the load and the fibre direction, this tends toward a lesser contribution of the CFRP sheet to the strength. No significant difference in response was noticed between LWAC and NWAC specimens. However, the LWAC samples with 45^0 fibre orientation were failed by concrete failure close to the centre of the samples. While the NWAC samples were failed by adhesive debonding close to the centre of the samples.
4. The effects of increasing the CFRP thickness from one layer to two parallel or perpendicular layers were investigated in this study. It can be concluded that the maximum debonding load for samples with double-parallel layers of CFRP sheets is higher than the load capacity for samples with double-perpendicular layers of CFRP sheets. This may be attributed to the higher axial rigidity of samples with two parallel layers of CFRP sheets. A similar response was noticed for both LWAC and NWAC samples. However, LWAC samples showed lower debonding load and extremely brittle failure of the interfacial joints compared with NWAC samples.
5. If there is an increase in the CFRP-to-concrete width ratio from width ratio 0.25 to 0.5, the maximum bond strength of the FRP/concrete joint is increased. While, the bond strength was significantly reduced for samples with width ratio of 0.75, especially for LWAC specimens which failed at lower load. This is attributed to the small width of the concrete prism compared with the width of the CFRP reinforcement thereby accelerating joint failure.

7.2.1.2. Conclusions from the Finite Element Analysis works

The interface behaviour of the CFRP-lightweight/ normal weight concrete joints was modelled using three-dimensional nonlinear FE models and smeared crack approaches were undertaken to simulate the behaviour of the tested specimens. On the basis of the FE results, the following conclusions are drawn:

1. Several approaches were used in this study to simulate the behaviour of the CFRP/lightweight concrete joint. The use of SOLID46 layered elements showed the best method to simulate the adhesive and the CFRP reinforcement.
2. The qualitative results, which explicate the response of the FEA models, are much critical than the quantitative results. For instance, the failure pattern, the load-slip curve and the load-strain trend which shows that the non-linear response is much important than the maximum load and slip.

7.2.1.3. Conclusions from Analytical works

A new analytical approach was developed to define the interfacial behaviour of the adhesively bonded joints:

1. In the simplified model, the strain distribution along the bonded length of the CFRP reinforcement was defined by a polynomial formula. In general, new the simplified equations were proposed to obtain the interface relationships (bond strength, strain distribution and slip) of FRP-lightweight/normal weight joints. The analytical results showed close agreement with the experimental results.
2. The CEB-FIB model was modified to include the characteristic of FRP in retrofitted lightweight concrete beams. The complete model for concrete, with full zones of behaviour, was developed based on shear stress slip relations reported in the CEB model to describe the full range behaviour of FRP- lightweight/ normal weight concrete interface. The prediction of the load-slip response and the maximum strain, stress and slip showed good agreement which indicates the successfully proposed models of the modified CEB models based on the full debonding process of the FRP debonding from the concrete substrate of LWAC and NWAC samples.

7.2.2. Beam Shear Tests

The experimental test program consisted of loading of six reinforced lightweight and normal weight concrete beams without shear reinforcement under monotonic loads to evaluate the performance and shear strengthening gained from using the CFRP to retrofit LWRC beams compared with companion NWRC beams. Samples were divided into two series based on the concrete type, and the strengthening configurations. Lightweight and normal weight samples strengthened with U-shaped CFRP reinforcement failed in shear by CFRP debonding while the samples strengthened with closed-shaped failed in shear due to CFRP reinforcement rupture.

Finite element analysis using ANSYS software was employed to predict the experimental behaviour of the test samples and a new analytical model was presented in the study to calculate the effective FRP debonding and rupture strain taking into consideration the effect of the lightweight concrete properties on the shear contribution of CFRP reinforcements. From the experimental model tests, the finite element analyses and analytical models, a number of conclusions can be drawn.

7.2.2.1. Conclusions from experimental works:

1. The load-deflection trends for LWRC beams are flatter than those of NWAC beams with identical CFRP retrofitting techniques after the initiation of diagonal shear cracks. The retrofitting techniques had a noticeable influence in the shear stiffness zone, the LWAC and NWAC samples retrofitted with closed-shaped revealed stiffer response compared with U-shaped samples.
2. In this test, the shear strength provided by CFRP reinforcement for LWAC samples is less than the NWAC. This is probably due to lower concrete surface tensile strength and aggregate interlock at the crack faces in LWAC.
3. The test results show that there was virtually no difference between the LWAC samples and their NWAC companions regarding failure patterns and the inclination of diagonal shear cracks. The failure pattern of LWAC samples was the same as the NWAC samples. It can be also concluded that the LWAC samples had higher cracks width compared with NWAC specimens. This is attributed to lower friction and aggregate interlock at the interface of the primary shear crack.

4. The influence of concrete type on the longitudinal steel straining was considered in this test. It can be concluded that the reading of strain gauges in LWAC samples is slightly higher compared with NWAC samples. The longitudinal steel reinforcements tend to increase the shear strength of the LWAC specimens due to the lower modulus of rupture for lightweight concrete.
5. Comparison between LWAC and NWAC samples reveals a significant variance in maximum recorded CFRP strains. The maximum recorded CFRP strains for the LWAC sample was significantly lower than the NWAC samples. This is attributed to higher normal and interfacial shear stress developed in CFRP-concrete interface at the cracks interface leading to premature debonding or rupture of the CFRP reinforcements from the concrete surface which accelerated sample failure.
6. For the closed-shaped test samples, the average recorded CFRP strains are higher than those of samples with U-shaped reinforcement due to CFRP strips debonding at lower applied load.

7.2.2.2. Conclusions from Finite Element Analysis work:

3D finite element models were implemented to predict the shear response and failure patterns of the LWRC and NWRC beams strengthened in shear with CFRP strips. The general response of the FE models shows acceptable agreement in the predictions with the experimental test results.

In general, the finite element models have a stiffer response compared with experimentally loaded samples. This attributed to the loss of the bond between the longitudinal steel reinforcement and the concrete in the real case which is not replicated in the finite element models simulated in this study. Furthermore, the difficulty to simulate concrete discrete cracks mathematically which increases the stiffness of the FEA models compared with actual physical models.

The shear failure mechanisms of the RC beams are very complex especially for samples retrofitted with FRP reinforcement. There are many factors that affect the shear behaviour of the RC beams such as aggregate interlock, aggregates size, aggregate distribution along the crack faces, etc., these factors are not included in the FE models and this leads to significant increase in the FE models stiffness compared with the actual physical model.

It can be concluded that the 3D cracking FE models created in this study provide an additional tool to investigate the shear mechanism and the influence of various variables on the shear behaviour

of LWRC beams retrofitted with CFRP reinforcement. It can be concluded that the FE modelling philosophy will be useful for CFRP reinforcing in general.

7.2.2.3. Conclusions from Analytical work:

A new expression for the effective debonding strain and FRP rupture strain as well the shear contribution of the FRP reinforcement based on the maximum bond strength equation was developed in this study (Simplified Model). The effect of lightweight concrete was considered in this model by introducing a new reduction factor based on the MDLS test results. The outcomes of this model show a good agreement with the experimental shear strength of CFRP reinforcement compared with available design codes.

7.3. Recommendations for Future Work

Valuable conclusions concerning the response of the lightweight concrete retrofitted in shear with CFRP reinforcement were presented in this thesis. However, there are still areas where more studies are required. Research on the performance of FRP-strengthened reinforced concrete structural elements under repeated cyclic load has received little attention. Many existing reinforced concrete members are insufficiently designed for shear and they are exposed to millions of cycles of loading during their service life, particularly for those elements constructed from lightweight concrete. The expected life of FRP used for shear retrofitting of concrete members such as bridges under repeated cyclic loading is uncertain. A vital concern regarding FRP shear strengthening systems is the potential debonding caused by cyclic loads and extending cracks with time. In addition to this, the design code equations are based on static tests, their validity and the performance of FRP strengthened lightweight concrete beams and the bond performance under repeated cyclic loading is still an area which needs an investigation to assess the FRP performance under repeated cyclic load.

Testing large-size samples have not studied compressively to investigate the influence of this variable on the shear response. Further study is necessary to assess the behaviour of CFRP used to strengthen practical sizes of beams. The effect of different parameters such as the effect of the internal steel reinforcement and the concrete compressive on the behaviour of reinforced lightweight concrete beams should be considered to provide more information about their effect

on the maximum shear capacity, failure modes and crack pattern of the lightweight concrete structures.

The current design code and guidelines for FRP shear retrofitting system are emerging. However, the available models such as (ACI 440.2R, 2008), (TR 55, 2013) and (CAN/CSA S6, 2006) have not given an accurate perdition for the available database. Additional analytical studies are required in this research area to develop new design proposals that can estimate the shear strength provided by the FRP reinforcements with reliable precision.

The effect of lightweight concrete should receive more attention in the current design codes and guidelines. Since most of the design codes and guidelines formulae which are used to evaluate the FRP performance are derived and verified with data from testing normal weight concrete. Further research was recommended by ACI 440.2R to investigate the effect of lightweight concrete on the performance of FRP strengthened members which is addressed in Appendix C of this code (ACI 440.2R, 2008). Further analytical and experimental studies are required to include the characteristics of the FRP/ lightweight joints in current codes and guidelines to evaluate the bond between the lightweight concrete substrate and the FRP reinforcement. This will also assess the validity of the proposed reduction factor derived in this study with large data set. It is also recommended to explore the use of other FE codes to compare with ANSYS or create simple purpose written programmes to address CFRP behaviour, specifically to better finite element predictions and facilitate the non-linear analysis of the reinforced concrete members retrofitted with FRP reinforcement subject to various types of loading conditions.

REFERENCES

Alotaibi, N. K. (2014). Shear strengthening of reinforced concrete beams with bi-directional carbon fiber reinforced polymer (CFRP) strips and CFRP anchors (Master's dissertation, The University of Texas at Austin), 247.

ABAQUS (2007). Theory Manual, User Manual and Example Manual. Version 6.10, Providence, RI.

Abbas, A. L. (2010). Non-linear analysis of reinforced concrete beams strengthened with steel and CFRP plates. *Diyala Journal of Engineering Sciences*, 249-256.

Abdalla, H. (2002). Evaluation of deflection in concrete members reinforced with fibre reinforced polymer (FRP) bars. *Composite Structures*, 56(1), 63-71.

ACI 213 Committee 213R-03 (2003). Guide for Structural Lightweight Aggregate Concrete. American Concrete Institute, Farmington Hills.

ACI 318-08 (2008). Building code requirements for structural concrete and commentary. ACI Committee 213, American Concrete Institute. Farmington Hills, Michigan.

ACI 440.2R-08 (2008). Guide for the design and construction of externally bonded FRP systems for strengthening concrete structures. ACI Commit tee 440, American Concrete Institute.Farmington Hills, Michigan.

Adhikary, B. B., & Mutsuyoshi, H. (2004). Behavior of concrete beams strengthened in shear with carbon-fiber sheets. *Journal of Composites for Construction*, 8(3), 258-264.

Adhikary, B. B., Mutsuyoshi, H., & Ashraf, M. (2004). Shear strengthening of reinforced concrete beams using fiber-reinforced polymer sheets with bonded anchorage. *ACI Structural Journal*, 101(5), 660-668.

Ahamad, S. H., Xie, Y., & Yu, T. (1994). Shear strength of reinforced lightweight concrete beams of normal and high strength concrete. *Magazine of Concrete Research*, 46(166), 57-66.

Ali, M. M., Oehlers, D. J., & Seracino, R. (2006). Vertical shear interaction model between external FRP transverse plates and internal steel stirrups. *Engineering Structures*, 28(3), 381-389.

Aljaafreh, T (2016). Strengthening of lightweight reinforced concrete beams using carbon fiber reinforced polymers (CFRP). Master dissertation, The university of Texas at Arlington,74.

Al-Juboori, W. S. (2011). The shear behaviour of concrete beams strengthened with CFRP. PhD. Thesis, University of Salford, 208.

Al-Mahaidi, R., Lee, K., & Taplin, G. (2001). Behavior and analysis of RC T-beams partially damaged in shear and repaired with CFRP laminates. *In Proc., 2001 Structural Congress and Exposition*. ASCE, Washington, DC.

Al-Rousan, R., & Issa, M. (2011). Fatigue performance of reinforced concrete beams strengthened with CFRP sheets. *Construction and Building Materials*, 25(8), 3520-3529.

Alrousan, R., Issa, M., Ovitigala, T., & Issa, M. A. (2011). Shear strength of lightweight reinforced concrete beams strengthened with CFRP strips. *Proceedings In 10th International Symposium on Fiber-Reinforced Polymer Reinforcement for Concrete Structures (FRPRCS-10)*, in conjunction with the ACI Spring 2011 Convention.

Alsayed, S. H., & Siddiqui, N. A. (2013). Reliability of shear-deficient RC beams strengthened with CFRP-strips. *Construction and Building Materials*, 42, 238-247.

Al-Shamaa, M. F. K. (2010). Behaviour of lightweight concrete beams reinforced with fibre reinforced polymer bars. PhD. Thesis, University of Technology, 210.

Al-Sulaimani, G. J., Sharif, A., Basunbul, I. A., Baluch, M. H., & Ghaleb, B. N. (1994). Shear repair for reinforced concrete by fiberglass plate bonding. *ACI Structural Journal*, 91(4), 458.

Anil, Ö. (2006). Improving shear capacity of RC T-beams using CFRP composites subjected to cyclic load. *Cement and Concrete Composites*, 28(7), 638-649.

Anil, Ö. (2008). Strengthening of RC T-section beams with low strength concrete using CFRP composites subjected to cyclic load. *Construction and Building Materials*, 22(12), 2355-2368.

ANSYS (2009). ANSYS User's Manual, ANSYS, Inc., Canonsburg, Pennsylvania.

Arduini, M., Tommaso, A. D. and Nanni, A. (1997). Brittle failure in FRP plate and sheet bonded beams. *ACI Structural Journal*, 94(4), 363-70.

Asghari A.A., Tabrizian Z., Beygi M.H., Ghodrati Amiri G. and Navayineya B. (2014). An experimental study on shear strengthening of RC lightweight deep beams using CFRP. *Journal of Rehabilitation in Civil Engineering*. 2-2, 9-19.

Bangash, M. Y. H. (1989). *Concrete and Concrete Structures: Numerical Modeling and Applications*. Elsevier Science Publishers Ltd., London, England.

Barbieri, G., Biolzi, L., Bocciarelli, M., & Cattaneo, S. (2016). Size and shape effect in the pull-out of FRP reinforcement from concrete. *Composite Structures*, 143, 395-417.

Barbosa, A. F., & Ribeiro, G. O. (2004). Analysis of reinforced concrete structures using ANSYS nonlinear concrete model. *Comput. Mech*. 1, 1-7.

Barnes, R. A. and Mays, G. C. (2001). The transfer of stress through a steel to concrete adhesive bond. *International Journal of Adhesion and Adhesives*, 21(6), 495-502.

Barros, J. A., Dias, S. J., & Lima, J. L. (2007). Efficacy of CFRP-based techniques for the flexural and shear strengthening of concrete beams. *Cement and Concrete Composites*, 29(3), 203-217.

Beber, A. J., & Campos Filho, A. (2005). CFRP composites on the shear strengthening of reinforced concrete beams. *Revista IBRACON de Estruturas*, 1(2).

Belarbi, A., Bae, S.-W., & Brancaccio, A. (2012). Behavior of full-scale RC T-beams strengthened in shear with externally bonded FRP sheets. *Construction and Building Materials*, 32, 27-40.

Belarbi, A., Bae, W., & Tumialan, R. (2007). Toward design guidelines for shear strengthening of concrete structures using externally bonded FRP systems. *Proceedings of the Advanced Composites in Construction*, University of Bath, Bath, United Kingdom.

Bellamkonda, S. A. (2013). Modeling of Shear Strengthening of Reinforced Concrete Beams Retrofitted with Externally Bonded Fiber Reinforced Polymers (Master disertation, Louisiana State University).

Bilotta, A., DI Ludovico, M. and Nigro, E. (2009). Influence of effective bond length on FRP-concrete debonding under monotonic and cyclic actions. FRPRCS-9, Sydney, Australia.

Bilotta, A., Faella, C., Martinelli, E., & Nigro, E. (2011). Indirect identification method of bilinear interface laws for FRP bonded on a concrete substrate. *Journal of Composites for Construction*, 16(2), 171-184.

Biscaia, H. C., Chastre, C., & Silva, M. A. (2012). Double shear tests to evaluate the bond strength between GFRP/concrete elements. *Composite Structures*, 94(2), 681-694.

Bizindavyi, L. and Neale, K. W. (1999). Transfer lengths and bond strengths for composites bonded to concrete. *Journal of Composites for Construction*, 3(4), 153-60.

Bonacci, J., & Maalej, M. (2000). Externally bonded FRP for service-life extension of RC infrastructure. *Journal of infrastructure systems*, 6(1), 41-51.

Boschetto, G., Pellegrino, C., Tinazzi, D., & Modena, C. (2006). Bond behaviour between FRP sheets and concrete: an experimental study. *In Proceedings of the 2nd fib Congress*.

Bousselham, A. and Chaallal, O. (2008). Mechanisms of shear resistance of concrete beams strengthened in shear with externally bonded FRP. *Journal of Composites for Construction*, 12(5), 499-512.

Bousselham, A., & Chaallal, O. (2006a). Behavior of Reinforced Concrete T-Beams Strengthened in Shear with Carbon Fiber-Reinforced Polymer. An Experimental Study. *ACI Structural Journal*, 103(3), 339-347.

Bousselham, A., & Chaallal, O. (2006b). Effect of transverse steel and shear span on the performance of RC beams strengthened in shear with CFRP. *Composites Part B: Engineering*, 37(1), 37-46.

Bousselham, A., & Chaallal, O. (2013). Experimental investigations on the influence of size on the performance of RC T-beams retrofitted in shear with CFRP fabrics. *Engineering structures*, 56, 1070-1079.

Brosens, K. and Van Gemert, D. (1998). Plate end shear design for external CFRP laminates. *Journal of Fracture Mechanics of Concrete Structures (FRAMCOS-3)*, Germany, 1793-804.

BS 1881, Part 114 (1983). Methods for Determination of Density Of Hardened Concrete. British Standards Institution, London.

BS 3797 (1990). Specification for Lightweight Aggregates for Masonry Units and Structural Concrete. British Standards Institution, London.

BS 8110 (1985). Structural use of concrete: Part 2: Code of practice for special circumstances. British Standards Institution, London.

BS 882 (1992). Specification for Aggregate from Natural Sources for Concrete", British Standards Institution. British Standards Institution, London.

BS EN 13055 (2016). Lightweight aggregates. British Standards Institution, London.

BS EN 197, Part 1 (2000). Composition, specifications and conformity criteria for common cements. British Standards Institution, London.

BS1881, Part 116 (1983). Testing concrete: method for determination of compressive strength of concrete cubes. British Standards Institution, London.

BS1881, Part 118 (1983). Testing concrete: Method for determination of flexural strength. British Standards Institution, London.

BS1881, Part 121 (1983). Testing concrete: method for determination of static modulus of elasticity in compression. British Standards Institution, London.

BS1881, Part 125 (2013). Testing concrete: Methods for mixing and sampling fresh concrete in the laboratory. British Standards Institution, London.

Camli, U. S. and Binici, B. (2007). Strength of carbon fiber reinforced polymers bonded to concrete and masonry. *Construction and Building Materials*, 21(7), 1431-46.

CAN, C. S. (2002). CSA-S806-02, Design and construction of building components with fibre-reinforced polymers. Canadian Standards Association, Mississauga, Ontario, Canada.

CAN/CSA-A23.3-04 (2004). Design of concrete structures. Canadian Standards Associat ion.Mississauga, Ontario.

CAN/CSA-S6-06 (2006). Canadian highway bridge design code. Canadian Standards Associat ion. Mississauga, Ontario.

Cao, S. Y., Chen, J. F., Teng, J. G., Hao, Z., and Chen, J. (2005). Debonding in RC beams shear strengthened with complete FRP wraps. *Journal of Composites for Construction*, 9(5), 417-428.

Cao, S., Chen, J., Pan, J. and Sun, N. (2007). ESPI Measurement of Bond-Slip Relationships of FRP-Concrete Interface. *Journal of Composites for Construction*, 11(2), 149-60.

Carolin, A., & Täljsten, B. (2005). Experimental study of strengthening for increased shear bearing capacity. *Journal of Composites for Construction*, 9(6), 488-496.

CEB. (1992). CEB-FIP Model Code 90. Fédérat ion Internat ionale du Béton. Lausanne, Switzerland.

CEB. (1999). Lightweight aggregate concrete - Codes and standards. Task Group 8.1, Fédérat ion Internat ionale du Béton. Lausane, Switzerland.

Chaallal, O., Nollet, M.-J., & Perraton, D. (1998). Shear strengthening of RC beams by externally bonded side CFRP strips. *Journal of Composites for Construction*, 2(2), 111-113.

Chaallal, O., Shahawy, M., & Hassan, M. (2002). Performance of reinforced concrete T-girders strengthened in shear with carbon fiber-reinforced polymer fabric. *ACI Structural Journal*, 99(3), 335-343.

Chajes, M. J., Finch Jr, W. W., Januszka, T. F. and Thomson Jr, T. A. (1996). Bond and force transfer of composite material plates bonded to concrete. *ACI Structural Journal*, 93(2), 208-17.

Chajes, M. J., Januszka, T. F., Mertz, D. R., Thomson Jr, T. A., & Finch Jr, W. W. (1995). Shear strengthening of reinforced concrete beams using externally applied composite fabrics. *ACI Structural Journal*, 92(3), 295-303.

Chandra, S., & Berntsson, L. (2002). *Lightweight aggregate concrete. Elsevier*, 430 (book).

Chansawat, K., Potisuk, T., Miller, T. H., Yim, S. C., & Kachlakev, D. I. (2009). FE models of GFRP and CFRP strengthening of reinforced concrete beams. *Advances in Civil Engineering*.

Chen, G. M., Chen, J. F. and Teng, J. G. (2007). Behaviour of FRP-to-concrete interfaces between two adjacent cracks in FRP-plated concrete memebrs: A numerical investigation. Asia-Pacific *Conference on FRP in Structures (APFIS 2007)*, Hong Kong, China, 683-8.

Chen, G., Teng, J. and Chen, J. (2011). Finite-Element Modeling of Intermediate Crack Debonding in FRP-Plated RC Beams. *Journal of Composites for Construction*, 15(3), 33953.

Chen, J. and Teng, J. (2001). Anchorage Strength Models for FRP and Steel Plates Bonded to Concrete. *Journal of Structural Engineering*, 127(7), 784-91.

Chen, J. F., Teng, J. G., Lam, L., and Smith, S. T. (2003). Behaviour and strength of FRP-strengthened RC structures: A state-of-the-art review. *Proceedings of the ICE - Structures and Buildings*, 156(1), 51-62.

Chen, J., & Teng, J. (2003a). Shear capacity of fiber-reinforced polymer-strengthened reinforced concrete beams: Fiber reinforced polymer rupture. *Journal of Structural Engineering*, 129(5), 615-625.

Chen, J., & Teng, J. (2003b). Shear capacity of FRP-strengthened RC beams: FRP debonding. *Construction and Building Materials*, 17(1), 27-41.

Clarke, J. L. (Ed.). (2002). *Structural lightweight aggregate concrete*. CRC Press, 161 (book).

CNR-DT 200/2004 (2004). Guide for the design and construction of externally bonded FRP systems for strengthening exist ing structures. Consiglio Nazionale delle Ricerche (National Research Council). Rome, Italy.

Colalillo, A. and Sheikh, A (2014a). Behavior of Shear-Critical Reinforced Concrete Beams Strengthened with Fiber-Reinforced Polymer—Experimentation. *ACI Structural Journal*, 11(46), 1373-1384.

Colalillo, M. A. (2012). Behaviour of Shear-Critical Reinforced Concrete Beams Retrofitted with Externally Applied Fibre-Reinforced Polymers. (PhD. Thesis, University of Toronto), 432.

Colalillo, M. A., & Sheikh, S. A. (2014b). Behavior of Shear-Critical Reinforced Concrete Beams Strengthened with Fiber-Reinforced Polymer—Analytical Method. *Journal of ACI Structural Journal*, 111(6), 1385-1396.

Concrete Society (1978). Structural lightweight aggregate concrete for marine and offshore applications. Report of a Concrete Society working party.

Cornetti, P., & Carpinteri, A. (2011). Modelling the FRP-concrete delamination by means of an exponential softening law. *Engineering Structures*, *33*(6), 1988-2001.

Coronado, C. A., & Lopez, M. M. (2006). Sensitivity analysis of reinforced concrete beams strengthened with FRP laminates. *Cement and Concrete Composites*, 28(1), 102-114.

Crocombe, A. D., Hua, Y. X., Loh, W. K., Wahab, M. A., & Ashcroft, I. A. (2006). Predicting the residual strength for environmentally degraded adhesive lap joints. *International Journal of Adhesion and Adhesives*, 26(5), 325-336.

Czaderski, C., & Olia, S. (2012). En-core round robin testing program–contribution of Empa. *In of the sixth international conference on FRP composites in civil engineering*. CICE.

Dai, J., Ueda, T. and Sato, Y. (2005). Development of the Nonlinear Bond Stress-Slip Model of Fiber Reinforced Plastics Sheet-Concrete Interfaces with a Simple Method. *Journal of Composites for Construction*, 9(1), 52-62.

Dai, J., Ueda, T. and Sato, Y. (2006). Unified Analytical Approaches for Determining Shear Bond Characteristics of FRP-Concrete Interfaces through Pull-out Tests. *Journal of Advanced Concrete Technology*, 4(1), 133-45.

Damian, K., Thomas, M., Solomon, Y., Kasidit, C., & Tanarat, P. (2001). Finite element modeling of reinforced concrete structures strengthened with FRP laminates. Report for Oregon Department Of Transportation‟, Salem.

Daud, R. A., Cunningham, L. S., & Wang, Y. C. (2015). Static and fatigue behaviour of the bond interface between concrete and externally bonded CFRP in single shear. *Journal of Engineering Structures*, 97, 54-67.

De Lorenzis, L., Miller, B. and Nanni, A. (2001). Bond of FRP laminates to concrete. *ACI Materials Journal*, 98(3), 256-64.

de Normalisation, C. E. (2004). Design of concrete structures—Part 1-1: General rules and rules for buildings. Eurocode 2, EN 1992-1-1: 2004: E.

Deniaud, C., & Cheng, J. R. (2001). Shear behavior of reinforced concrete T-beams with externally bonded fiber-reinforced polymer sheets. *ACI Structural Journal*, 98(3), 386-394.Professional, 240.

Deniaud, C., & Cheng, J. R. (2004). Simplified shear design method for concrete beams strengthened with fiber reinforced polymer sheets. *Journal of Composites for Construction*, *8*(5), 425-433.

Dirar, H., & Osman, S. M. (2009). Shear strengthening of pre-cracked reinforced concrete T-beams using carbon fibre systems (PhD thesis, University of Cambridge), 196.

Diagana, C., Li, A., Gedalia, B., & Delmas, Y. (2003). Shear strengthening effectiveness with CFF strips. Engineering structures, 25(4), 507-516.

Eltayeb, M. F. E., (2006). Non-linear Bond Modelling For Reinforced Concrete (Master's dissertation, University of Cambridge), 86.

Eurocode 2 (2014). BS EN 1992-1-1:2004+A1:2014. Eurocode 2: Design of concrete structures-Part 1-1: General rules and rules for buildings. European Committee for Standardizat ion (CEN). Brussels, Belgium.

EuroLightCon (1988). Definitions and International Consensus Report. report No. R1, The European Union – Brite EuRam.

EuroLightCon (1998) . LWAC Properties, State-of-the-Art. report No R2.

Evans, R., & Dongre, A. (1963). The suitability of a lightweight aggregate (Aglite) for structural concrete. *Magazine of Concrete Research*, 15(44), 93-100.

Farny, J. A., & Kosmatka, S. H. (1997). Diagnosis and control of alkali-aggregate reactions in concrete. Portland Cement Association, 26 (book).

Fathelbab, F., Ramadan, M., & Al-Tantawy, A. (2011). Finite element modelling of strengthed simple beams using FRP techniques. *Concrete Research Letters*, 2(2), 228-240.

Ferracuti, B., Savoia, M. and Mazzotti, C. (2007). Interface law for FRP–concrete delamination. *Journal of Composite Structures*, 80(4), 523-31.

Fib Bulletin 14 (2001). Externally bonded FRP reinforcement for RC structures. Task Group 9.3, Fédérat ion Internat ionale du Béton. Lausanne, Switzerland.

Fib Manual of lighweight aggrgate concrete (1983). 2nd ed., Surry University press, 259. (book)

Foster, R. M., Brindley, M., Lees, J. M., Ibell, T. J., Morley, C. T., Darby, A. P., & Evernden, M. C. (2016). Experimental Investigation of Reinforced Concrete T-Beams Strengthened in Shear with Externally Bonded CFRP Sheets. *Journal of Composites for Construction*, 04016086.

Foster, S. J. and Khomwan, N. (2005). Determination of bond stress versus slip fo externally bonded FRP from standardised bond strength tests. *Proceedings of the International Symposium on Bond Behaviour of FRP in Structures (BBFS 2005)*, Hong Kong, China, 85-90.

Gao, B., Kim, J. K., & Leung, C. K. (2004). Experimental study on RC beams with FRP strips bonded with rubber modified resins. *Composites science and technology*, 64(16), 2557-2564.

Gere, J. M. and Timoshenko, S. P. (1997). Mechanics of Materials. PWS Publishing Company, Boston, Massachusetts (book).

Grace, N. F., Sayed, G., Soliman, A., & Saleh, K. (1999). Strengthening reinforced concrete beams using fiber reinforced polymer (FRP) laminates. *ACI Structural Journal*, 96(5), 865-874.

Grande, E., Imbimbo, M. and Sacco, E. (2011). Bond behaviour of CFRP laminates glued on clay bricks: Experimental and numerical study. *Journal of Composites Part B: Engineering*, 42(2), 330-40.

Grande, E., Imbimbo, M., & Rasulo, A. (2008). Experimental study on the capacity of RC beams strengthened in shear by CFRP-sheets. *In Fourth International Conference on FRP Composites in Civil Engineering (CICE2008)*.

Grande, E., Imbimbo, M., & Rasulo, A. (2009). Effect of transverse steel on the response of RC beams strengthened in shear by FRP: Experimental study. *Journal of Composites for Construction*, 13(5), 405-414.

Guadagnini, M., Serbescu, A., Palmieri, A., Matthys, S., Bilotta, A., Nigro, E., & Balazs, G. (2012). Round robin test on the bond behaviour of externally bonded FRP systems to concrete. *In Proceedings of CICE 2012, 6th International Conference on FRP Composites in Civil Engineering*, Rome, Italy, CD ROM (13-15).

Gunes, O., Lau, D., Tuakta, C. and Büyüköztürk, O. (2013). Ductility of FRP–concrete systems: Investigations at different length scales. *Construction and Building Materials*, 49, 915-25.

Guo, Z. G., Cao, S. Y., Sun, W. M. and Lin, X. Y. (2005). Experimental study on bond stress-slip behaviour between FRP sheets and concrete. *Proceedings of the International Symposium on Bond Behaviour of FRP in Structures (BBFS 2005)*, 77-83.

Hadigheh, S. A. (2014). Bond behaviour of fibre reinforced polymer strengthened concrete structures using advanced composite processing techniques (PhD Thesis, RMIT University), 299.

Hadigheh, S. A., & Gravina, R. J. (2016). Generalization of the interface law for different FRP processing techniques in FRP-to-concrete bonded interfaces. *Composites Part B: Engineering*, 91, 399-407.

Hadigheh, S. A., Gravina, R. J., & Setunge, S. (2015). Influence of the Processing Techniques on the Bond Characteristics in Externally Bonded Joints: Experimental and Analytical Investigations. *Journal of Composites for Construction*, 20(3), 04015081.

Hanson, J. (1958). Shear Strength of Lightweight Reinforced Concrete Beams. Paper presented at the ACI Journal Proceedings, 30(3), 387-403.

Hanson, J. (1961). Tensile strength and diagonal tension resistance of structural lightweight concrete. Paper presented at the ACI Journal Proceedings in the U.K.. *Proceedings of the First International Congress on Lightweight*,58(1), 1-40.

Hawileh, R. A. (2012). Nonlinear finite element modeling of RC beams strengthened with NSM FRP rods. *Construction and Building Materials*, 27(1), 461-471.

Hosseini, A., & Mostofinejad, D. (2014). Effective bond length of FRP-to-concrete adhesively-bonded joints: Experimental evaluation of existing models. *International Journal of Adhesion and Adhesives*, 48, 150-158.

Hutchinson, R. L., & Rizkalla, S. H. (1999). Shear strengthening of AASHTO bridge girders using carbon fiber reinforced polymer sheets. Special Publication, 188, 945-958.

Isenberg, J. (1993). Finite element analysis of reinforced concrete structures II. ASCE.

ISIS Design Manual 4 (2008). FRP rehabilitation of reinforced concrete structures. Version 2. The Canadian Network of Centres of Excellence on Intelligent Sensing for Innovat ive Structures (ISIS). Winnipeg.

Iwashita, K., Wu, Z., Ishikawa, T., Hamaguchi, Y. and Suzuki, T. (2007). Bonding and debonding behavior of FRP sheets under fatigue loading. *Advanced Composite Materials*, 16(1), 31-44.

Izumo, K., Saeki, N., Fukao, M., and Horiguchi, T. (1999). Bond behavior and strength between fiber sheets and concrete. Transactions of the Japan Concrete Institute, 21, 423-430.

Jayajothi, P., Kumutha, R., & Vijai, K. (2013). Finite element analysis of FRP strengthened rc beams using ansys. *Asian Journal of Civil Engineering (BHRC)*, 14(4), 631-642.

JCI (Japanese Society of Civil Engineers Code recommends) (2007). Standard specifications for concrete structures-2007 design).

JCI (Japanese Concrete Institute) (2003). Technical Report of Technical Committee on Retrofit Technology. Proceedings of the International Symposium on Latest Achievement of Technology and Research on Retrofitting Concrete Structures. Kyoto, Japan, 4-42.

Juan, K. Y. (2011). Cracking mode and shear strength of lightweight concrete beams. (PhD. Thesis, National University of Singapore), 182.

Karbhari, V. M., Niu, H., & Sikorsky, C. (2006). Review and comparison of fracture mechanics-based bond strength models for FRP-strengthened structures. Journal of reinforced plastics and composites, 25(17), 1757-1794.

Khalifa, A., & Nanni, A. (2000). Improving shear capacity of existing RC T-section beams using CFRP composites. *Cement and Concrete Composites*, 22(3), 165-174.

Khalifa, A., & Nanni, A. (2002). Rehabilitation of rectangular simply supported RC beams with shear deficiencies using CFRP composites. *Construction and Building Materials*, 16(3), 135-146.

Khalifa, A., Gold, W. J., Nanni, A., & MI, A. A. (1998). Contribution of externally bonded FRP to shear capacity of RC flexural members. *Journal of Composites for Construction*, 2(4), 195-202.

Khalifa, A., Tumialan, G., Nanni, A., & Belarbi, A. (1999). Shear strengthening of continuous reinforced concrete beams using externally bonded carbon fiber reinforced polymer sheets. ACI Special Publication, 188.

Kim, G., Sim, J., & Oh, H. (2008). Shear strength of strengthened RC beams wit h FRPs in shear. *Construction and Building Materials*, 22(6), 1261-1270.

Kim, S.-W., & Vecchio, F. J. (2008). Modeling of shear-critical reinforced concrete structures repaired with fiber-reinforced polymer composites. *Journal of Structural Engineering*, 134(8), 1288-1299.

Kim, Y. J. and Harries, K. A. (2011). Fatigue behavior of damaged steel beams repaired with CFRP strips. *Engineering Structures*, 33(5), 1491-502.

Kim, Yun Gon (2011). Shear behavior of reinforced concrete T-beams strengthened with carbon fiber reinforced polymer (CFRP) sheets and CFRP anchors. (PhD. Thesis, The University of Texas at Austin), 431.

Lau, K. T., Dutta, P. K., Zhou, L. M., & Hui, D. (2001). Mechanics of bonds in an FRP bonded concrete beam. *Composites Part B: Engineering*, 32(6), 491-502.

Lawrence, K. L. (2003). ANSYS® Tutorial. Release 7.0 and 6.1, SDC Publications, Canonsburg, 174.

Lee, H., Cheong, S., Ha, S., & Lee, C. (2011). Behavior and performance of RC T-section deep beams externally strengthened in shear with CFRP sheets. *Composite Structures*, 93(2), 911-922.

Lee, J.-Y., Hwang, H.-B., & Doh, J.-H. (2012). Effective strain of RC beams strengthened in shear with FRP. *Composites Part B: Engineering*, 43(2), 754-765.

Leung, C. K., Chen, Z., Lee, S., Ng, M., Xu, M., & Tang, J. (2007). Effect of size on the failure of geometrically similar concrete beams strengthened in shear with FRP strips. *Journal of Composites for Construction*, 11(5), 487-496.

Liu, K. (2011). Computational modeling, experimental and theoretical study on bond behaviors of hybrid-bonded FRP strengthened concrete structures. (PhD. Thesis, University of Hong Kong), 265.

López-González, J., Fernández-Gómez, J. and González-Valle, E. (2012). Effect of Adhesive Thickness and Concrete Strength on FRP-Concrete Bonds. *Journal of Composites for Construction*, 16(6), 705-11.

Lu XY, Ye LP, Teng JG, Huang YL, Tan Z, Zhang ZX (2004). Recent research on interfacial behaviour of FRP sheets externally bonded to RC structures. *In Proceedings of CICE-2. Adelaide*, 389–98.

Lu, X. Z., Ye, L. P., Teng, J. G. and Jiang, J. J. (2005). Meso-scale finite element model for FRP sheets/plates bonded to concrete. *Engineering Structures*, 27(564-75.

Lu, X., Chen, J., Ye, L., Teng, J., & Rotter, J. (2009). RC beams shear-strengthened with FRP: Stress distributions in the FRP reinforcement. *Construction and Building Materials*, 23(4), 1544-1554.

Lu, X., Jiang, J., Teng, J., & Ye, L. (2006). Finite element simulation of debonding in FRP-to-concrete bonded joints. *Construction and Building Materials*, 20(6), 412-424.

Lu, X., Teng, J., Ye, L., & Jiang, J. (2005). Bond–slip models for FRP sheets/plates bonded to concrete. *Engineering structures*, 27(6), 920-937.

Lytag UK (2006), Mix Designs for Lytag concrete. Technical Manual - Section 3 (www.lytag.net).

Lytag UK (2009), Design Guidance for Lytag® LWAC (Concrete). Technical Manual - Section 4 (www.lytag.net).

Lytag UK (2011), Introduction to Lytag® lightweight aggregate. Technical Manual - Section (www.lytag.net).

Megson, T. H. G. (2005). *Structural and stress analysis*. Great Britain, Butterworth-Heinemann.

MacGregor JG, Wight JK (2005). Reinforced concrete mechanics and design. 4th edition, Pearson Prentice Hall, 1177 (book).

Madandoust, R. (1990). Strength Assessment of Lightweight Concrete. (PhD. Thesis, University of Liverpool), 365.

Mahmoud, A. M. (2012). Strengthening of concrete beams having shear zone openings using orthotropic CFRP modeling. *Ain Shams Engineering Journal*, 3(3), 177-190.

Martian, B., and Pantazopoulou, S.J. (2001). Effect of bond, aggregate interlock and dowel action on the shear strength degradation of reinforced concrete. *Engineering Structures* 23, 214–227.

Matta, F., Nanni, A., Abdelrazaq, A., Gremel, D., & Koch, R. (2009). Externally post-tensioned carbon FRP bar system for deflection control. *Construction and Building Materials*, 23(4), 1628-1639.

Mazzotti, C., Ferracuti, B., & Savoia, M. (2004). An experimental study on FRP–concrete delamination. Proc. FraMCoS, Vail USA, 2, 795-802.

Mazzotti, C., Ferracuti, B., Bilotta, A., Ceroni, F., Nigro, E., & Pecce, M. (2012). Sensitivity of FRP-concrete bond behaviour to modification of the experimental set-up. *In Proceedings of the sixth international conference on FRP composites in civil engineering*. CICE.

Mazzotti, C., Savoia, M. and Ferracuti, B. (2008). An experimental study on delamination of FRP plates bonded to concrete. *Construction and Building Materials*, 22(7), 1409-21.

McSweeney, B.M., &Lopez. M.M. (2005). FRP-Concrete Bond Behaviour. A parametric Study through Pull-Off Testing. In C.K Shield & J.P. Busel (Eds). *Proceeding of the 7th International Symposium FRP Reinforcement for Concrete Structures*, Kansas City, Missouri (PP.441-460).

Mertoğlu, Ç., Anil, Ö., & Durucan, C. (2016). Bond slip behavior of anchored CFRP strips on concrete surfaces. *Construction and Building Materials,* 123, 553-564.

Mirmiran, A., Zagers, K., & Yuan, W. (2000). Nonlinear finite element modeling of concrete confined by fiber composites. *Finite Elements in Analysis and Design*, 35(1), 79-96.

Mofidi, A., & Chaallal, O. (2011). Shear strengthening of RC beams with externally bonded FRP composites: Effect of strip-width-to-strip-spacing ratio. *Journal of Composites for Construction*, 15(5), 732-742.

Mofidi, A., & Chaallal, O. (2014). Effect of steel stirrups on shear resistance gain due to externally bonded fiber-reinforced polymer strips and sheets. *ACI Structural Journal*, 111(2), 353.

Monti, G., & Liotta, M. A. (2007). Tests and design equations for FRP-strengthening in shear. *Construction and Building Materials*, 21(4), 799-809.

Mosallam, A. S., & Banerjee, S. (2007). Shear enhancement of reinforced concrete beams strengthened with FRP composite laminates. *Composites Part B: Engineering*, 38(5), 781-793.

Mostofinejad, D., Hosseini, S.A. and Razavi, S.B. (2016). Influence of different bonding and wrapping techniques on performance of beams strengthened in shear using CFRP reinforcement. *Journal of Construction and Building Materials*, 116, 310-320.

Murphy, M. S. (2010). Behavior of externally bonded fiber reinforced polymer systems for strengthening concrete girders in shear.(PhD thesis, Missouri University of Science and Technology), 371.

Nakaba, K., Kanakubo, T., Furuta, T., & Yoshizawa, H. (2001). Bond behaviour between fiber-reinforced polymer laminates and concrete. *ACI Structural Journal*, 98(3), 359-367.

Nehdi, M., El Damatty, A. and Rahimi, R. (2003). Investigation on lap-joint behaviour of GFRP plates bonded to silica fume and rice husk ash concrete. *International Journal of Adhesion and Adhesives*, 23(4), 323-33.

Nemati, K. (1997). Fracture analysis of concrete using scanning electron microscopy. Scanning-New York And Baden Baden Then Mahwah-, 19, 426-430.

Obaidat, Y. T., Dahlblom, O., & Heyden, S. (2010). Nonlinear FE modelling of shear behaviour in RC beam retrofitted with CFRP. Structural Retrofitting Of Reinforced Concrete Beams Using Carbon Fibre Reinforced Polymer. (PhD Thesis, Lund University), 78.

Oehlers, D. J. (2006). FRP Plates Adhesively Bonded to Reinforced Concrete Beams: Generic Debonding Mechanisms. *Advances in Structural Engineering Journal*, 9(6), 737 -50.

Oehlers, D. J., Park, S. M. and Mohamed Ali, M. S. (2003). A structural engineering approach to adhesive bonding longitudinal plates to RC beams and slabs. *Journal of Composites Part A: Applied Science and Manufacturing*, 34(9), 887-97.

O'Mahoney, D. C., Katnam, K. B., O'Dowd, N. P., McCarthy, C. T. and Young, T. M. (2013). Taguchi analysis of bonded composite single-lap joints using a combined interface– adhesive damage model. *International Journal of Adhesion and Adhesives*, 40(0), 168-78.

Ouezdou, M. B., Belarbi, A., & Bae, S. W. (2009). Effective bond length of FRP sheets externally bonded to concrete. *International Journal of Concrete Structures and Materials*, 3(2), 127-131.

Ozden, S., Atalay, H. M., Akpinar, E., Erdogan, H., & Vulaş, Y. Z. (2014). Shear strengthening of reinforced concrete T-beams with fully or partially bonded fibre-reinforced polymer composites. *Journal of Structural Concrete*, 15(2), 229-239.

Pan, J. and Leung, C. K. Y. (2007). Effect of Concrete Composition on FRP/Concrete Bond Capacity. *Journal of Composites for Construction*, 11(6), 611-8.

Panda, K., Bhattacharyya, S., & Barai, S. (2013). Effect of transverse steel on the performance of RC T-beams strengthened in shear zone with GFRP sheet. *Construction and Building Materials*, 41, 79-90.

Parth Athawale, B.E. (2012). Analysis of factors affecting effective bond length for fiber reinforced polymer composite laminate externally bonded to concrete substrate (Master Dissertation, Texas tech university), 116.

Parvin, A., & Granata, P. (2000). Investigation on the effects of fiber composites at concrete joints. *Composites Part B: Engineering*, 31(6), 499-509.

Pellegrino C., Tinazzi D., and Modena C. (2008), Experimental Study on Bond Behaviour between Concrete and FRP Reinforcement. *Journal of Composites for Construction*, 12 (2), 180-189.

Pellegrino, C., & Modena, C. (2002). Fiber reinforced polymer shear strengthening of reinforced concrete beams with transverse steel reinforcement. *Journal of Composites for Construction*, 6(2), 104-111.

Pellegrino, C., & Modena, C. (2006). Fiber-reinforced polymer shear strengthening of reinforced concrete beams: experimental study and analytical modeling. *ACI Structural Journal*, 103(5), 720.

Pellegrino, C., & Modena, C. (2008). An experimentally based analytical model for the shear capacity of FRP-strengthened reinforced concrete beams. *Mechanics of Composite Materials*, 44(3), 231-244.

Pellegrino, C., & Sena-Cruz, J. (Eds.). (2015). Design Procedures for the Use of Composites in Strengthening of Reinforced Concrete Structures: State-of-the-Art Report of the RILEM Technical Committee 234-DUC (Vol. 19). Springer, 392 (book).

Perera, R., Recuero, A., Diego, A. D. and López, C. (2004). Adherence analysis of fiber reinforce polymer strengthened RC beams. *Journal of Computers & Structures*, 82(23–26), 1865-73.

Qu, Z., Lu, X. Z., & Ye, L. P. (2005). Size effect of shear contribution of externally bonded FRP U-Jackets for RC beams. In Chen JF, Teng J G. *Proceedings of the International Symposium on Bond Behavior of FRP in Structures*. Hong Kong: Intertnational Institute for FRP in Construction (pp. 371-379).

Ronagh, H. R., & Baji, H. (2014). On the FE Modeling of FRP-Retrofitted Beam–Column Subassemblies. *International Journal of Concrete Structures and Materials*, 8(2), 141-155.

Santhakumar, R., Chandrasekaran, E., & Dhanaraj, R. (2004). Analysis of retrofitted reinforced concrete shear beams using carbon fiber composites. *Electronic journal of structural engineering*, 4, 66-74.

Sas, G. (2011). FRP Shear Strengthening of Reinforced Concrete Beams. (PhD. Thesis, Luleå University of Technology), 248.

Sato, Y. and Vecchio, F. J. (2003). Tension stiffening and crack formation in reinforced concrete members wit h fiber-reinforced polymer sheets. *Journal of Structural Engineering*, 129 (6), 717-724.

Sato, Y., Asano, Y., and Ueda, T. (2001). Fundamental study on bond mechanism of carbon fiber sheet. Concrete Library International, JSCE, 37,97-115.

Sato, Y., Kimura, K., and Kobatake, Y. (1997). Bond behaviors between CFRP sheet and concrete, *Journal of Structural and Construction Engineering*, 500, 75-82.

SCGSM Laboratory Sheet (1983). Chemical Properties of Lytage aggragtes, the State Company of Geological Survey and Mining, Baghdad, Iraq.

Seracino, R. (2001). Axial intermediate crack debonding of plates glued to concrete surfaces. FRP Composites in Civil Engineering (CICE 2001), Hong Kong, 365-72.

Serbescu, A, Guadagnini, M., & Pilakoutas (2013). Standardised double-shear test for determining bond of FRP to concrete and corresponding model development. *Composites Part B Engineering*, 55, 277-279.

Shah, S. P., Swartz, S. E., and Ouyang, C. (1995). Fracture Mechanics of Concrete. John Wiley & Sons, Inc., New York, New York.

Shaker, Q. M., & Kamonna, H. H. (2016). Nonlinear Analysis of Reinforced Concrete Beams Strengthened by Prestressed CFRP Sheets under Static Loads. Jordan Journal of Civil Engineering, 10(1).

Sheikh, S. A., DeRose, D., & Mardukhi, J. (2002). Retrofitting of concrete structures for shear and flexure with fiber-reinforced polymers. *ACI Structural Journal*, 99(4), 451.

Smith, S. T. and Teng, J. G. (2002a). FRP-strengthened RC beams. I: review of debonding strength models. *Engineering Structures Journal*, 24(4), 385-95.

Smith, S. T. and Teng, J. G. (2002b). FRP-strengthened RC beams. II: assessment of debonding strength models. *Engineering Structures Journal*, 24(4), 397-417.

Standard, A. S. T. M. (2005). A370, Standard test methods and definitions for mechanical testing of steel products.

Subramaniam, K. V., Carloni, C. and Nobile, L. (2007). Width effect in the interface fracture during shear debonding of FRP sheets from concrete. *Engineering Fracture Mechanics*, 74(4), 578-94.

Sundarraja, M., & Rajamohan, S. (2009). Strengthening of RC beams in shear using GFRP inclined strips–An experimental study. *Construction and Building Materials*, 23(2), 856-864.

Sundarraja, M., Rajamohan, S., & Bhaskar, D. (2008). Shear strengthening of RC beams using GFRP vertical strips—An experimental study. Journal of reinforced plastics and composites, 27(14), 1477-1495.

Swamy, R., & Bandyopadhyay, A. (1979). Shear behaviour of structural lightweight concrete T-beams without web reinforcment. Paper presented at the ICE Proceedings, 67(2), 341-354.

Täljsten, B. (1991). Strengthening of existing concrete structures with glued steel plates. Chapman and Hall, 5(1), 208-219.

Taljsten, B. (1997). Defining anchor lengths of steel and CFRP plates bonded to concrete. *International Journal of Adhesion and Adhesives*, 17(4), 319-27.

Täljsten, B. (2003). Strengthening concrete beams for shear with CFRP sheets. *Construction and Building Materials*, 17(1), 15-26.

Tang, C.-W., Yen, T., & Chen, H.-J. (2009). Shear Behavior of Reinforced Concrete Beams Made with Sedimentary Lightweight Aggregate without Shear Reinforcement. *Journal of Materials in Civil Engineering*, 21(12), 730-739.

Teng, J. G., Smith, S. T., Yao, J., & Chen, J. F. (2003). Intermediate crack-induced debonding in RC beams and slabs. *Construction and building materials*, 17(6), 447-462.

Teychenné, D. C., Franklin, R. E., Erntroy, H. C., Nicholls, J. C., Hobbs, D. W., & MARSH, D. (1997). *Design of normal concrete mixes*, 45 (book).

The Concrete Society (2013). Design Guidance for Strengthening Concrete Structures Using Fibre Composites Materials. Concrete Society, CS-TR-55-UK, Technical Report No. 55, third edition., Report of a Concrete Society Committee, Eynsham.

Toutanji, H. Ortiz, G. (2001). The effect of surface preparation on the bond interface between FRP sheets and concrete members. *Journal of Composite Structures*, (53), 457-6

Toutanji, H., Saxena, P., Zhao, L., & Ooi, T. (2007). Prediction of interfacial bond failure of FRP–concrete surface. *Journal of composites for construction*, 11(4), 427-436.

Triantafillou, T. C. (1998). Shear strengthening of reinforced concrete beams using epoxy-bonded FRP composites. *ACI Structural Journal*, 95(2), 107-115.

Triantafillou, T. C., & Antonopoulos, C. P. (2000). Design of concrete flexural members strengthened in shear with FRP. *Journal of Composites for Construction*, 4(4), 198-205.

Ueda, T. and Dai, J. (2005). Interface bond between FRP sheets and concrete substrates: properties, numerical modeling and roles in member behaviour. Progress in Structural Engineering and Materials, 7(1), 27-43.

Ueda, T., Sato, Y. and Asano, Y. (1999). Experimental study on bond strength of continuous carbon fiber sheet. Proc. *4th international symposium on fiber reinforced polymer reinforcement for reinforced concrete structures*, 407–16.

Vecchio, F. J., & Collins, M. P. (1986). The modified compression-field theory for reinforced concrete elements subjected to shear. ACI J., 83(2), 219-231.

Weber UK, High-performance carbon fibre sheet reinforcement for structural strengthening. Technical Report, July (2008).

Weber UK, Moisture-tolerant epoxy bonding adhesive for weber.tec force composite sheets. Technical Report, Auguest (2013).

Willam, K. J., & Warnke, E. P. (1975). Constitutive model for the triaxial behavior of concrete. *In Proceedings, international association for bridge and structural engineering* (Vol. 19, No. 1, pp. 1-30). ISMES, Bergamo, Italy.

Wolanski, A. J. (2004). Flexural behavior of reinforced and prestressed concrete beams using finite element analysis. (PhD thesis, Marquette University),87.

Wong, R. S. Y. and Vecchio, F. J. (2003). Towards modeling of reinforced concrete members with externally bonded fiber-reinforced polymer composites. *ACI Structural Journal*, 100(1), 47-55.

Woo, S. and Lee, Y. (2010). “Experimental Study on Interfacial Behavior of CFRP-Bonded Concrete. *KSCE Journal of Civil Engineering*, 4(3):385-393.

Wu, Z., Li, W. and Sakuma, N. (2006). Innovative externally bonded FRP/concrete hybrid flexural members. *Journal of Composite Structures*, 72(3), 289-300.

Wu, Z., Yuan, H., & Niu, H. (2002). Stress transfer and fracture propagation in different kinds of adhesive joints. *Journal of Engineering Mechanics*, 128(5), 562-573.

Xia, S. H. and Teng, J. G. (2005). Behaviour of FRP-to-concrete bonded joints. *Proceedings of the International Symposium on Bond Behaviour of FRP in Structures (BBFS 2005)*, Hong Kong, 411-8.

Xiao, J., Li, J. and Zha, Q. (2004). Experimental study on bond behavior between FRP and concrete. *Construction and Building Materials*, 18(10), 745-52.

Xu, W. and Wei, Y. (2013). Influence of adhesive thickness on local interface fracture and overall strength of metallic adhesive bonding structures. *International Journal of Adhesion and Adhesives*, 40(0), 158-67.

Yang, D.-S., Hong, S.-N. and Park, S. K. (2007). Experimental observation on bond-slip behavior between concrete and CFRP plate. *International Journal of Concrete Structures and Materials*, 1(1), 37-43.

Yang, Y., Yue, Q. and Hu, Y. (2001). Experimental study on bond performance between carbon fiber sheets and concrete. *Journal of Building Structures*, 22(3), 36–42.

Yao, J., Teng, J. G. and Chen, J. F. (2005). Experimental study on FRP-to-concrete bonded Joints. *Composites Part B: Engineering*, 36(2), 99-113.

Yoshizawa, H. Myojo, T. Okoshi, M. Mitzukoshi, M. Kliger HS (1996). Effect of Sheet Bonding Condition on Concrete Members Having Externally Bonded Carbon Fiber Sheet. *Proceedings of the 4th Materials Engineering Conference, Materials for the New Millennium*, (2), 1608-16.

Yuan, H., Teng, J. G., Seracino, R., Wu, Z. S., and Yao, J. (2004). Full-range behavior of FRP-to-concrete bonded joints. *Engineering Structures*, 26(5), 553-565.

Zarnic, R., Gostic, S., Bosiljkov, V., & Bokan-Bosiljkov, V. (1999). Improvement of bending load-bearing capacity by externally bonded plates. Proc., Creating with Concrete, Thomas Telford, London, 433-442.

Zareef, M. E. (2010). Conceptual and structural design of buildings made of lightweight and infra-lightweight concrete (Ph.D thesis, Berlin, Techn. Univ), 119.

Zhang, C., & Wang, J. (2012). Interface stress redistribution in FRP-strengthened reinforced concrete beams using a three-parameter viscoelastic foundation model. *Composites Part B: Engineering*, 43(8), 3009-3019.

Zhang, Z., & Hsu, C.-T. T. (2005). Shear strengthening of reinforced concrete beams using carbon-fiber-reinforced polymer laminates. *Journal of Composites for Construction*, 9(2), 158-169.

Zhao, M., Dong, Y., Zhao, Y., Tennant, A. and Ansari, F. (2007). Monitoring of Bond in FRP Retrofitted Concrete Structures. *Journal of Intelligent Material Systems and Structures*, (18), 853-60.

Zhao, M., & Ansari, F. (2004, August). Bond properties of FRP fabrics and concrete joints. In 13th world conference on earthquake engineering, Vancouver, BC, Canada, Paper (No. 35).

Zunz, G. J. (1968). Some Notes of the Use of Lightweight Concrete In Structures. *Proceedings of the First International Congress on Lightweight Concrete*, 1, 187-202.

APPENDIX A

The load -CFRP strains collected from individual gauges for each of the instrumented CFRP strips in the LWRC and NWRC series

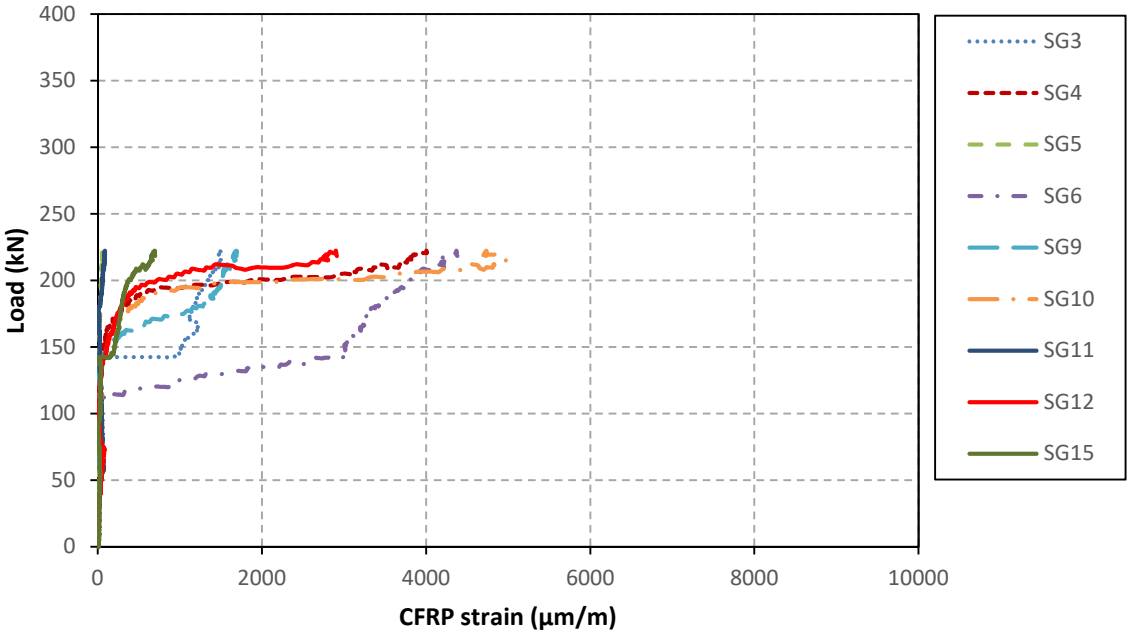

(a): Beam left end.

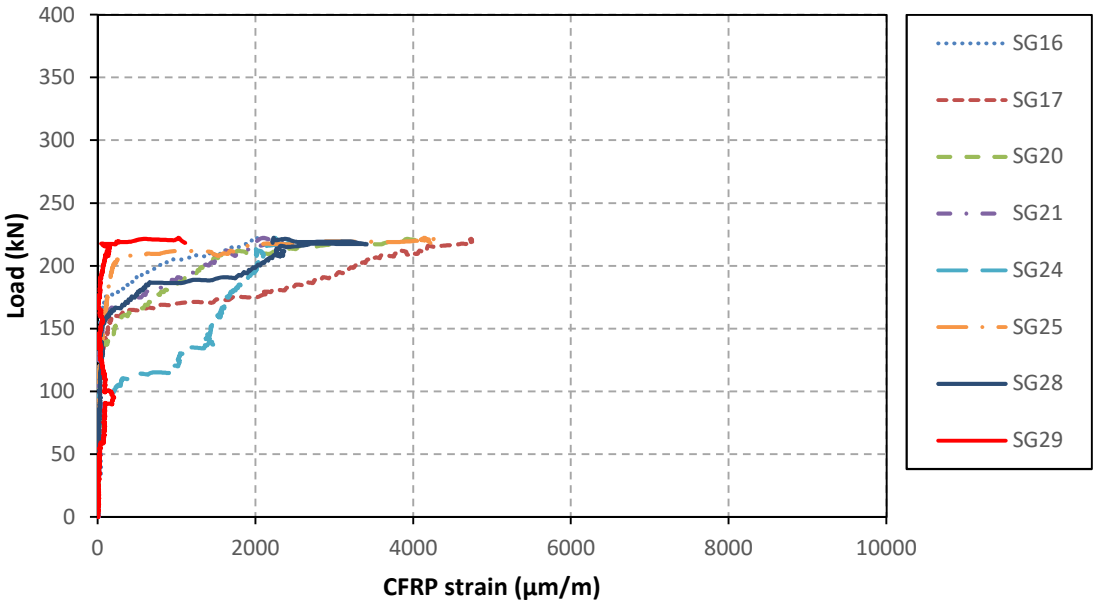

(b): Beam right end.

Figure (1): Load- CFRP strains for specimen BL-UST.

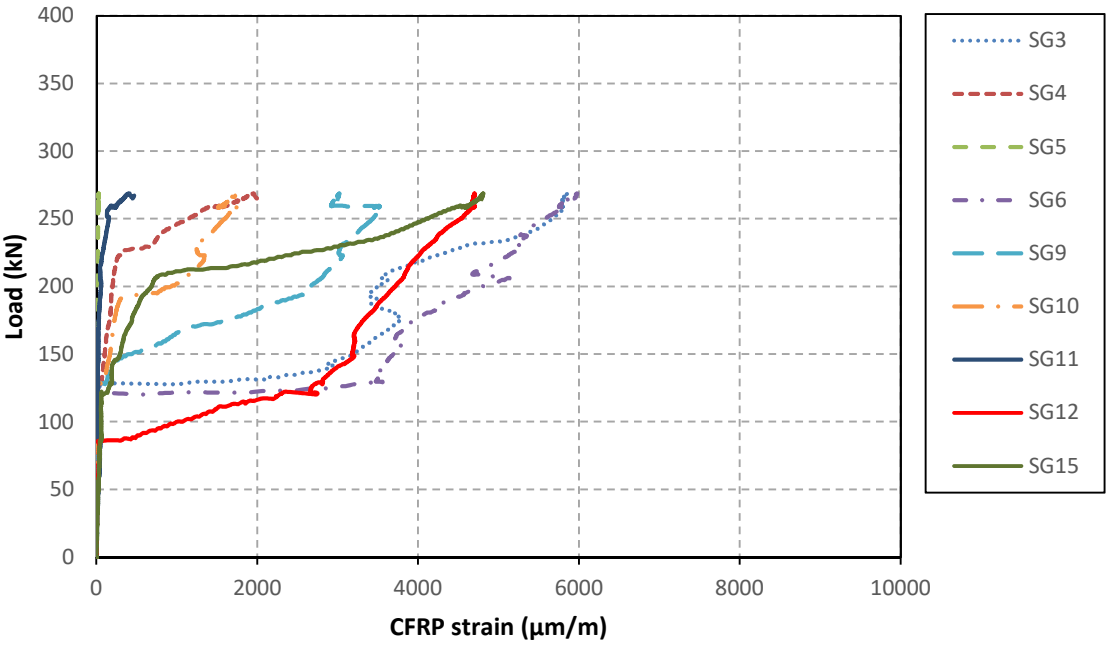

(a): Beam left end.

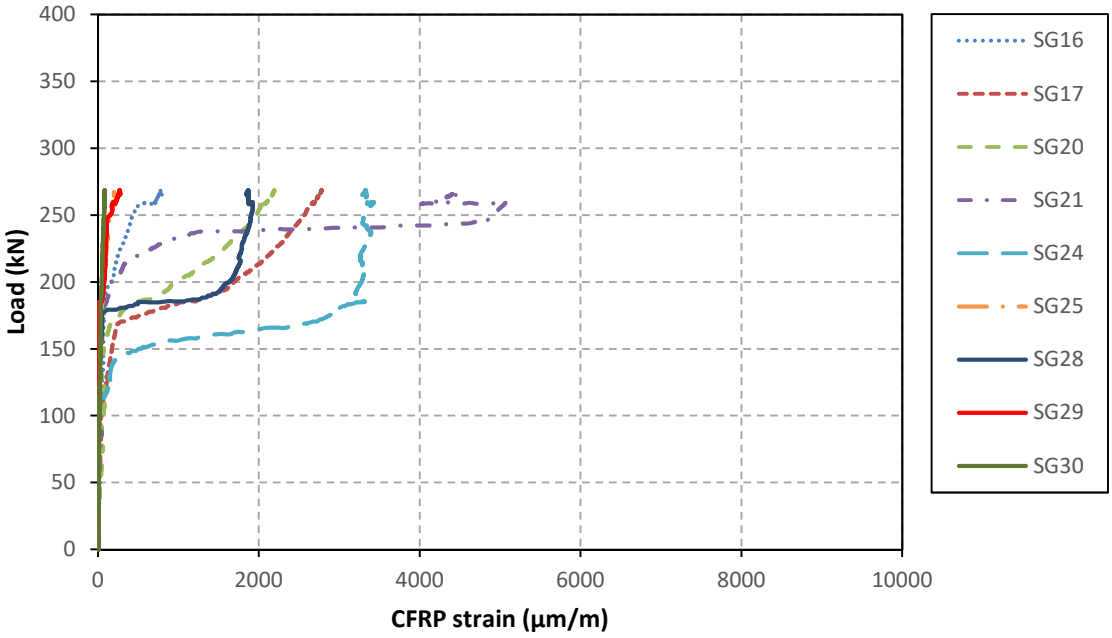

(b): Beam right end.

Figure (2): Load- CFRP strains for specimen BL-CST.

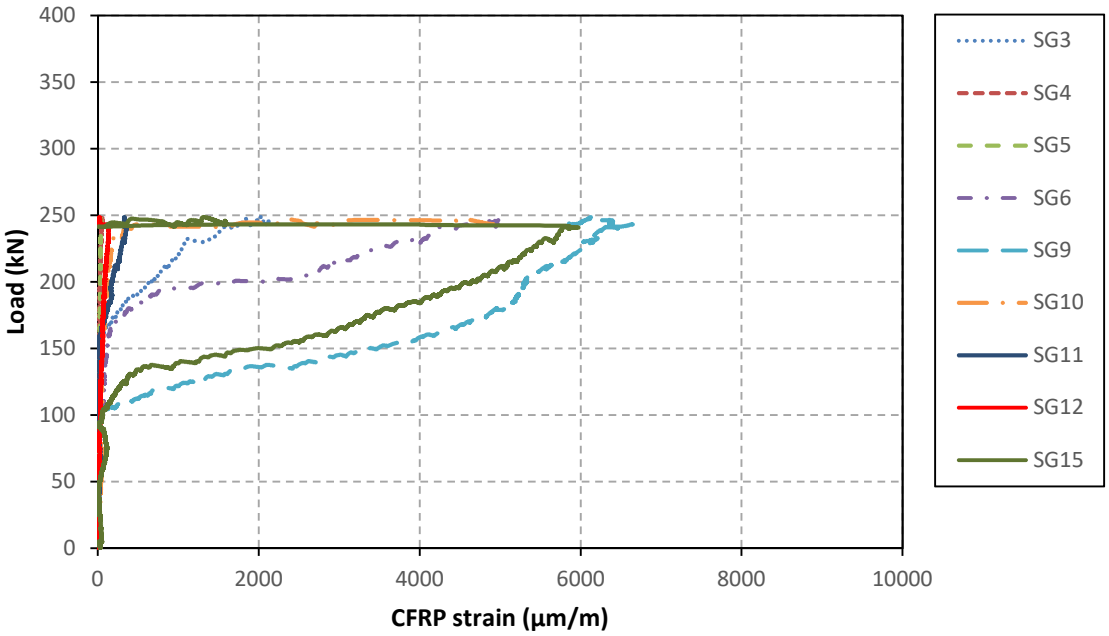

(a): Beam left end.

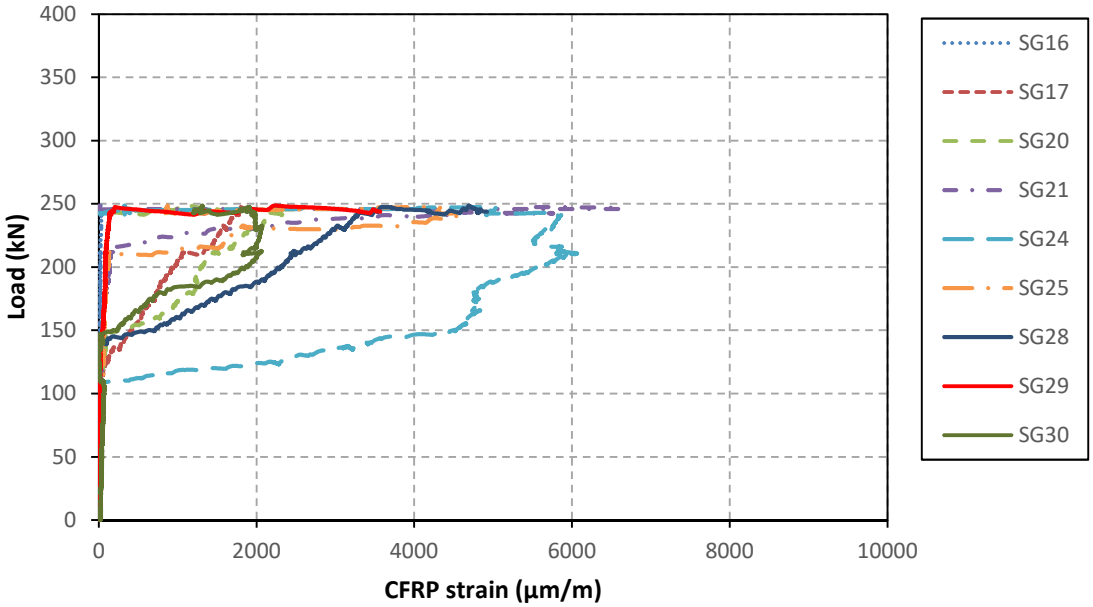

(b): Beam right end.

Figure (3): Load- CFRP strains for specimen BN-UST.

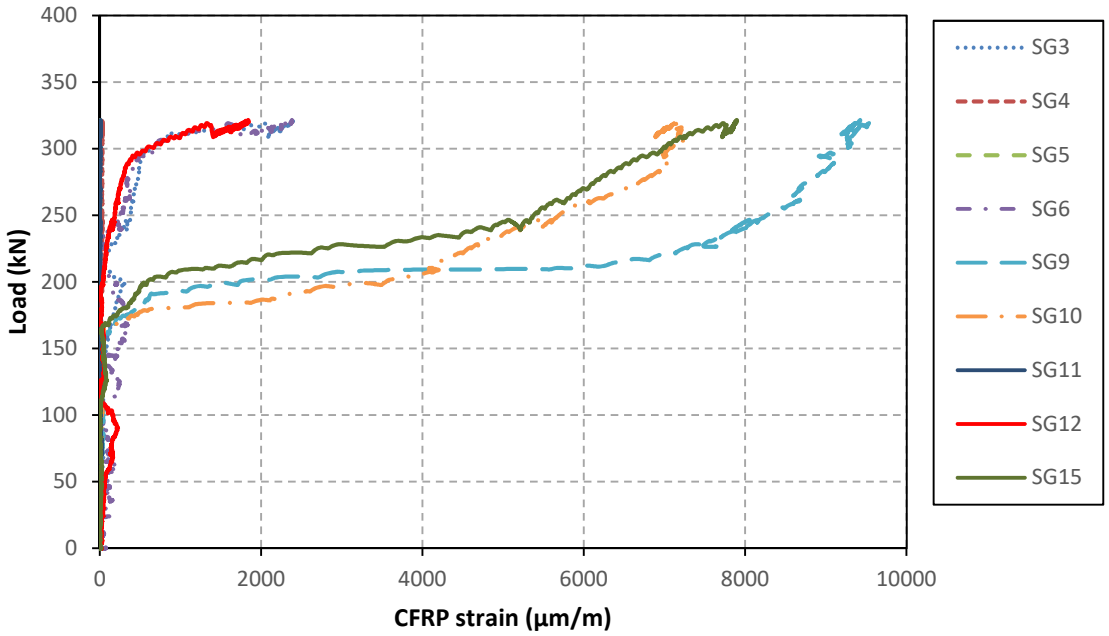

(a): Beam left end.

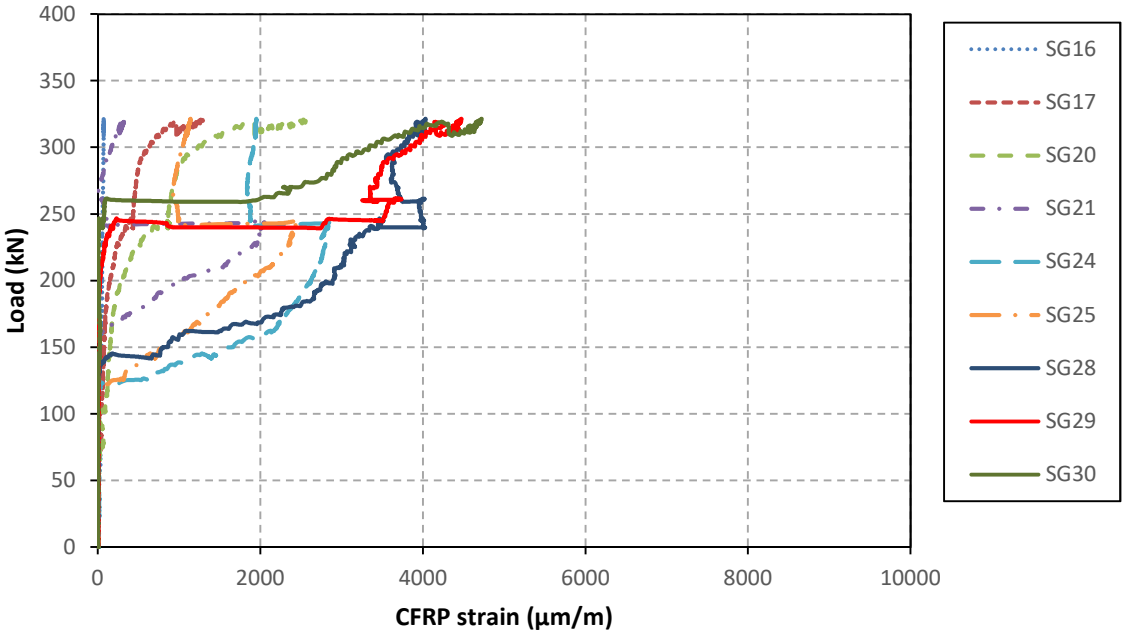

(b): Beam right end.

Figure (4): Load- CFRP strains for specimen BN-CST.

APPENDIX B

Database of the Experimental Results of the Effective Bond Length Available in the Literature (Most of these data are cited by Ouezdou, (2008).

Reference	Sample ID	f_c' (MPa)	E_f (GPa)	t_f (mm)	L_e (mm)
Sato et al, 1997	-	37.6	236	0.115	45.2
Bizindavyi and Neale, 1999	-	42.5	29.2	1.00	75
	-	42.5	29.2	2.00	100
	-	42.5	75.7	0.33	55
	-	42.5	75.7	0.66	70
De Lorenzis et al. 2001	-	47.3	227	0.16	93
Nakaba et al. 2001	C5-ARF	57.6	124.5	0.193	65.9
	C5-SCF	57.6	261.1	0.167	95.7
	C5-SCFL	57.6	261.1	0.167	63.5
	C5-SCFH	57.6	261.1	0.167	133.5
	C5-HCF	57.6	425.1	0.165	120.3
	M5-ARF	47.1	124.5	0.193	70.3
	M5-SCF	47.1	261.1	0.167	96.6
	M5-SCFL	47.1	261.1	0.167	67.0
	M5-SCFH	47.1	261.1	0.167	134.1
	M5-HCF	47.1	261.1	0.167	121.2
	C2-SCF	23.8	261.1	0.167	99.1
Foster and Khomwan, 2005	BS37	37	160	1.4	270
	BS53	53	160	1.4	240
Boshetto et al. 2006	2 C2 a	58	390	0.33	112
	2 C1 a	58	230	0.33	85
	2 C2 c	58	390	0.33	115
	3 C2 a	58	390	0.495	115
	1 C1 b	58	230	0.165	80
	2 C2 d	40	390	0.33	130
	1 C2 c	58	390	0.165	95
	3 C2 b	58	390	0.495	130
	3 C1 a	58	230	0.495	115
	3 C1 b	58	230	0.495	106
Iwashita et al.2007	CS- 1	36.8	235	0.128	130
	CS- 2	36.8	235	0.128	125
	CS- 3	36.8	235	0.128	95
	CF-20-1	36.8	235	0.128	120
Yang et al. 2007	D21-20	21	173	1.3	204
	D21-25	21	173	1.3	204
	D28-20	28	173	1.3	196
	D28-25	28	173	1.3	196
Hosseini and Mostofinejad, 2014	EBR-20-1	36.8	238	0.13	35
	EBR-20-2	36.8	238	0.13	35
	EBR-35-1	36.8	238	0.13	35

	EBR-35-2	36.8	238	0.13	35
	EBR-50-1	36.8	238	0.13	35
	EBR-50-2	36.8	238	0.13	35
	EBR-75-1	36.5	238	0.13	35
	EBR-75-2	36.5	238	0.13	35
	EBR-100-1	36.5	238	0.13	35
	EBR-100-2	36.5	238	0.13	35
	EBR-125-1	36.5	238	0.13	35
	EBR-125-2	39.1	238	0.13	35
	EBR-150-1	39.1	238	0.13	35
	EBR-150-2	39.1	238	0.13	35
	EBR-175-1	39.1	238	0.13	35
	EBR-175-2	41.1	238	0.13	35
	EBR-200-1	41.1	238	0.13	35
Pellegrino et. al, 2008	S1C5c	58	230	0.165	87.5
	S2C1a	64	230	0.165	77.5
	S2C1c	58	230	0.165	77.5
	S3C1c	58	230	0.165	107.5
	S2C5b	58	230	0.165	100
	S3C1a	63	230	0.165	106
	S3C1b	58	230	0.165	108
	S1C1a	58	230	0.165	72.5
	S3C1c	58	230	0.165	107.5
	S3C5a	63	230	0.165	107.5
	S3C5b	58	230	0.165	130
	S3C5c	63	230	0.165	120

APPENDIX C

Database of Shear Bond Tests (Serbescu et.al., 2013)

Author, test type	Sample ID	P_{Exp} (kN)	This Study		TR-55		FIB 14	
			L_e (mm)	P_{the} (kN)	L_e (mm)	P_{the} (kN)	L_e (mm)	P_{the} (kN)
Tan (2002), DLS	PG1-12	7.13	55.34	4.95	52.63	6.67	37.21	4.51
	PG1-12	7.13	55.34	4.95	52.63	6.67	37.21	4.51
	PG1-1W1	10.07	55.34	6.98	52.63	8.89	37.21	6.02
	PG1-1W2	10.07	55.34	6.98	52.63	8.89	37.21	6.02
	PG1-1L11	7.13	55.34	4.95	52.63	6.67	37.21	4.51
	PG1-1L12	7.13	55.34	4.95	52.63	6.67	37.21	4.51
	PG1-1L21	7.13	55.34	4.95	52.63	6.67	37.21	4.51
	PG1-1L22	7.13	55.34	4.95	52.63	6.67	37.21	4.51
	PG1-21	10.09	76.85	6.86	74.43	9.44	52.63	6.38
	PG1-22	10.09	76.85	6.86	74.43	9.44	52.63	6.38
	PC1-1C1	9	68.92	6.15	66.39	8.42	46.94	5.69
	PC1-1C2	9	68.92	6.15	66.39	8.42	46.94	5.69
Bilotta et.al, 2011, SLS	C1A-1	41.13	207.22	25.70	197.39	39.03	139.58	28.49
	C1A-2	37.94	207.22	25.70	197.39	39.03	139.58	28.49
	C1B-1	48.4	251.76	31.21	240.53	47.56	170.08	34.72
	C1B-2	35.9	251.76	31.21	240.53	47.56	170.08	34.72
	C1B-3	53.64	251.76	31.21	240.53	47.56	170.08	34.72
	C1C-1	33.18	215.54	17.60	205.45	27.63	145.28	20.17

	C1C-2	29.86	215.54	17.60	205.45	27.63	145.28	20.17
	C1C-3	31.88	215.54	17.60	205.45	27.63	145.28	20.17
	C2-1	49.41	195.01	24.19	185.57	36.69	131.22	26.79
	C2-2	39.26	195.01	24.19	185.57	36.13	131.22	26.38
	C3-1	49.85	207.22	25.70	197.39	38.43	139.58	28.06
	C3-2	52.6	207.22	25.70	197.39	38.43	139.58	28.06
	C3-3	52.55	207.22	25.70	197.39	38.43	139.58	28.06
	C4-1	54.79	226.86	28.13	216.41	42.14	153.03	30.76
	C4-3	54.57	226.86	28.13	216.41	42.14	153.03	30.76
Guadagnini et. al, 2012, DLS	C1A	39.6	191.33	27.91	192.80	39.35	136.33	28.06
	C1B	50.7	232.40	33.89	234.94	47.95	166.13	34.19
	C1C	30.42	199.00	19.12	200.67	28.07	141.90	20.01
	C2	49.2	180.08	26.27	181.26	36.99	128.17	26.38
	C3	37.2	191.33	27.91	192.80	39.35	136.33	28.06
	C1B	28.2	217.35	36.32	214.88	52.43	151.94	34.19
	C1C	19.98	186.15	20.49	183.54	30.69	129.78	20.01
	C2	30	168.47	28.16	165.78	40.45	117.23	26.38
	C4	30.3	195.90	32.74	193.33	47.17	136.71	30.76
Mazzotti et.al, 2012, SLS	C1A-1	54.56	207.22	25.70	197.39	39.03	139.58	28.49
	C1A-3	52.22	207.22	25.70	197.39	39.03	139.58	28.49
	C1B-2	56.58	251.76	31.21	240.53	47.56	170.08	34.72
	C1B-3	46.87	251.76	31.21	240.53	47.56	170.08	34.72
	C1C-1	35.19	215.54	17.60	205.45	27.63	145.28	20.17
	C1C-2	38	215.54	17.60	205.45	27.63	145.28	20.17

	C1C-3	34.17	215.54	17.60	205.45	27.63	145.28	20.17
	C2-1	50.44	195.01	24.19	185.57	36.69	131.22	26.79
	C2-2	54.62	195.01	24.19	185.57	36.69	131.22	26.79
	C2-3	54.02	195.01	24.19	185.57	36.69	131.22	26.79
	C3-1	53.69	207.22	25.70	197.39	39.03	139.58	28.49
	C3-2	55.2	207.22	25.70	197.39	39.03	139.58	28.49
	C3-3	54.94	207.22	25.70	197.39	39.03	139.58	28.49
	C4-2	56.76	226.86	28.13	216.41	42.79	153.03	31.24
	C4-3	55.89	226.86	28.13	216.41	42.79	153.03	31.24
Czaderski et.al, 2012, DLS	C1A-1	56.05	179.50	29.83	164.16	46.21	116.08	28.06
	C1A-2	53.45	179.50	29.83	164.16	46.21	116.08	28.06
	C2-1	43.5	168.96	28.08	156.52	42.84	110.68	26.38
	C2-2	46.1	168.96	28.08	156.52	42.84	110.68	26.38
	C3-1	45.45	181.13	29.55	166.49	45.57	117.73	28.06
	C3-2	47.8	181.13	29.55	166.49	45.57	117.73	28.06
	C4-1	54.6	198.26	32.34	187.99	48.51	132.93	30.76
	C4-2	52.5	198.26	32.34	187.99	48.51	132.93	30.76
Zhao et al. (2000), SLS	NJ2	11	70.03	8.20	68.50	11.14	48.44	8.90
	NJ3	11.25	70.03	8.20	68.50	11.14	48.44	8.90
	NJ4	12.5	61.00	9.57	58.32	13.09	41.24	8.90
	NJ5	12.25	61.00	9.57	58.32	13.09	41.24	8.90
	NJ6	12.75	61.00	9.57	58.32	13.09	41.24	8.90
Takeo et al.	1-11	8.75	83.46	6.02	81.12	8.47	57.36	5.77

(1997), SLS	1-12	8.85	85.08	5.90	82.88	8.29	58.60	5.77
	1-00	9.3	83.46	6.02	81.12	8.47	57.36	5.77
	1-22	8.5	85.08	5.90	82.88	8.29	58.60	5.77
	1-31	9.3	83.46	6.02	81.12	8.47	57.36	5.77
	1-32	8.3	85.08	5.90	82.88	8.29	58.60	5.77
	1-41	8.05	83.46	6.02	81.12	8.47	57.36	5.77
	1-42	8.05	83.46	6.02	81.12	8.47	57.36	5.77
	1-51	8.45	85.23	5.89	83.03	8.28	58.71	5.77
	1-52	7.3	85.23	5.89	83.03	8.28	58.71	5.77
	2-11	8.75	86.41	5.80	84.43	8.14	59.70	5.77
	2-12	8.85	86.41	5.80	84.43	8.14	59.70	5.77
	2-13	7.75	85.46	5.87	83.34	8.25	58.93	5.77
	2-14	7.65	85.46	5.87	83.34	8.25	58.93	5.77
	2-15	9	86.91	5.76	84.92	8.10	60.05	5.77
	2-21	12	120.80	8.10	119.41	11.51	84.43	8.16
	2-22	10.8	120.80	8.10	119.41	11.51	84.43	8.16
	2-31	12.65	147.18	9.86	146.24	14.10	103.41	10.00
	2-32	14.35	147.18	9.86	146.24	14.10	103.41	10.00
	2-41	11.55	109.11	7.23	107.49	10.25	76.01	7.31
	2-42	11	109.11	7.23	107.49	10.25	76.01	7.31
	2-51	9.85	85.46	5.87	83.34	8.25	58.93	5.77
	2-52	9.5	85.46	5.87	83.34	8.25	58.93	5.77
	2-61	8.8	85.46	5.87	83.34	8.25	58.93	5.77
	2-62	9.25	85.46	5.87	83.34	8.25	58.93	5.77

	2-71	7.65	85.46	5.87	83.34	8.25	58.93	5.77
	2-72	6.8	85.46	5.87	83.34	8.25	58.93	5.77
	2-81	7.75	73.21	6.95	69.74	9.86	49.31	5.77
	2-82	8.05	73.21	6.95	69.74	9.86	49.31	5.77
	2-91	6.75	86.91	5.76	84.92	8.10	60.05	5.77
	2-92	6.8	86.91	5.76	84.92	8.10	60.05	5.77
	2-101	7.7	71.08	4.77	68.84	6.64	48.68	4.71
	2-102	6.95	70.30	4.83	67.94	6.73	48.04	4.71
Ren (2003), SLS	DLUT15-2G	5.81	92.44	3.11	90.83	4.58	64.23	3.34
	DLUT15-5G	10.6	92.44	7.20	90.83	10.46	64.23	7.62
	DLUT15-7G	18.23	92.44	10.71	90.83	15.21	64.23	11.08
	DLUT30-1G	4.63	82.84	3.51	80.04	5.20	56.59	3.34
	DLUT30-2G	5.77	82.84	3.51	80.04	5.20	56.59	3.34
	DLUT30-3G	9.42	82.84	8.11	80.04	11.88	56.59	7.62
	DLUT30-4G	11.03	83.29	8.06	80.04	11.88	56.59	7.62
	DLUT30-6G	11.8	83.29	8.06	80.04	11.88	56.59	7.62
	DLUT30-7G	14.65	83.29	12.00	80.04	17.26	56.59	11.08
	DLUT30-8G	16.44	83.29	12.00	80.04	17.26	56.59	11.08
	DLUT50-1G	5.99	79.25	3.68	75.70	5.50	53.52	3.34
	DLUT50-2G	5.9	79.25	3.68	75.70	5.50	53.52	3.34
	DLUT50-4G	9.84	79.25	8.51	75.70	12.56	53.52	7.62
	DLUT50-5G	12.28	79.25	8.51	75.70	12.56	53.52	7.62
	DLUT50-6G	14.02	79.25	12.67	75.70	18.25	53.52	11.08
	DLUT50-7G	16.71	79.25	12.67	75.70	18.25	53.52	11.08

	DLUT15-2C	5.48	117.84	3.90	115.71	5.84	81.82	4.26
	DLUT15-5C	10.02	117.84	9.01	115.71	13.33	81.82	9.71
	DLUT15-7C	19.27	117.84	13.41	115.71	19.37	81.82	14.11
	DLUT30-1C	5.54	105.16	4.40	101.96	6.63	72.09	4.26
	DLUT30-2C	4.61	105.16	4.40	101.96	6.63	72.09	4.26
	DLUT30-4C	11.08	105.16	10.17	101.96	15.13	72.09	9.71
	DLUT30-5C	16.1	105.16	10.17	101.96	15.13	72.09	9.71
	DLUT30-7C	22.64	105.16	15.14	101.96	21.98	72.09	14.11
	DLUT50-1C	5.78	100.03	4.64	96.42	7.01	68.18	4.26
	DLUT50-4C	12.95	100.03	10.73	96.42	16.00	68.18	9.71
	DLUT50-5C	16.72	100.03	10.73	96.42	16.00	68.18	9.71
Chajes et al.,1996, SLS	C1	8.462	132.08	6.97	133.30	10.39	94.26	6.86
	C2	9.931	123.80	7.47	121.99	11.35	86.26	6.86
	C3	10.638	123.80	7.47	121.99	11.35	86.26	6.86
	C4	10.638	123.80	7.47	121.99	11.35	86.26	6.86
	C5	10.531	126.15	7.32	125.13	11.06	88.48	6.86
	C7	9.61	126.15	7.32	125.13	11.06	88.48	6.86
	C8	10.518	126.15	7.32	125.13	11.06	88.48	6.86
	C9	11.199	126.15	7.32	125.13	11.06	88.48	6.86
	C10	9.869	145.91	6.28	152.59	9.07	107.89	6.86
	C11	9.343	139.44	6.59	143.59	9.64	101.53	6.86
	C12	11.204	126.08	7.32	124.95	11.08	88.35	6.86
	C13	8.094	131.81	6.99	132.86	10.42	93.95	6.86
	C14	12.811	131.81	6.99	132.86	10.42	93.95	6.86

	C15	11.917	131.81	6.99	132.86	10.42	93.95	6.86
	C16	11.57	131.81	6.99	132.86	10.42	93.95	6.86
Yao (2005), SLS	I-1	4.75	92.56	3.85	96.12	5.35	67.97	4.12
	I-2	5.69	92.56	3.85	95.91	5.37	67.82	4.12
	I-3	5.76	92.56	3.85	95.91	5.37	67.82	4.12
	I-4	5.76	92.56	3.85	95.91	5.37	67.82	4.12
	I-5	6.17	92.56	3.85	95.91	5.37	67.82	4.12
	I-6	5.96	92.56	3.85	95.91	5.37	67.82	4.12
	I-7	5.95	92.56	3.85	95.91	5.37	67.82	4.12
	I-8	6.68	92.56	3.85	95.91	5.37	67.82	4.12
	I-9	6.35	92.56	3.85	95.91	5.37	67.82	4.12
	I-10	6.17	92.56	3.85	95.91	5.37	67.82	4.12
	I-11	5.72	92.56	3.85	95.91	5.37	67.82	4.12
	I-12	6	92.56	3.85	95.91	5.37	67.82	4.12
	I-13	6.14	92.56	3.85	95.91	5.37	67.82	4.12
	I-14	6.1	92.56	3.85	95.91	5.37	67.82	4.12
	I-15	6.27	92.56	3.85	95.91	5.37	67.82	4.12
	I-16	7.03	92.56	3.85	95.91	5.37	67.82	4.12
	II-1	5.2	92.65	3.84	95.91	5.37	67.82	4.12
	II-2	6.75	92.65	3.84	95.91	5.37	67.82	4.12
	II-3	5.51	92.65	3.84	95.91	5.37	67.82	4.12
	II-4	7.02	92.65	3.84	95.91	5.37	67.82	4.12
	II-5	7.07	92.65	3.84	95.91	5.37	67.82	4.12
	II-6	6.98	92.65	3.84	95.91	5.37	67.82	4.12

	III-1	5.94	88.97	4.02	90.81	5.67	64.21	4.12
	III-2	11.66	88.97	7.53	90.81	10.50	64.21	7.64
	III-3	14.63	88.97	10.63	90.81	14.55	64.21	10.58
	III-4	19.07	88.97	13.38	90.81	17.82	64.21	12.96
	III-8	8.02	73.78	6.36	74.69	8.78	52.81	6.39
	IV-1	5.86	97.04	3.66	102.24	5.03	72.30	4.12
	IV-2	5.9	97.04	3.66	102.24	5.03	72.30	4.12
	IV-3	5.43	95.96	3.70	100.73	5.11	71.22	4.12
	IV-4	5.76	95.96	3.70	100.73	5.11	71.22	4.12
	IV-5	5	97.04	3.66	102.24	5.03	72.30	4.12
	IV-6	7.08	95.96	3.70	100.73	5.11	71.22	4.12
	IV-7	5.5	97.04	3.66	102.24	5.03	72.30	4.12
	IV-8	5.93	95.96	3.70	100.73	5.11	71.22	4.12
	IV-9	5.38	97.04	3.66	102.24	5.03	72.30	4.12
	IV-10	6.6	95.96	3.70	100.73	5.11	71.22	4.12
	IV-11	5.51	97.04	3.66	102.24	5.03	72.30	4.12
	IV-12	5.67	95.96	3.70	100.73	5.11	71.22	4.12
	IV-13	6.31	97.04	3.66	102.24	5.03	72.30	4.12
	IV-14	6.19	95.96	3.70	100.73	5.11	71.22	4.12
	V-1	3.81	94.50	2.32	98.58	3.23	69.70	2.55
	V-2	4.41	94.50	2.32	98.58	3.23	69.70	2.55
	V-3	6.26	94.50	3.76	98.58	5.22	69.70	4.12
	V-4	12.22	94.50	7.05	98.58	9.67	69.70	7.64
	V-5	14.29	94.50	9.96	98.58	13.40	69.70	10.58

	V-6	15.58	94.50	12.54	98.58	16.42	69.70	12.96
	VI-1	6.01	93.66	3.80	97.44	5.28	68.90	4.12
	VI-2	5.85	93.66	3.80	97.44	5.28	68.90	4.12
	VI-3	5.76	93.66	3.80	97.44	5.28	68.90	4.12
	VI-4	5.73	93.66	3.80	97.44	5.28	68.90	4.12
	VI-5	5.56	93.66	3.80	97.44	5.28	68.90	4.12
	VI-6	5.58	93.66	3.80	97.44	5.28	68.90	4.12
	VI-7	5.91	93.66	3.80	97.44	5.28	68.90	4.12
	VI-8	5.05	93.66	3.80	97.44	5.28	68.90	4.12
	VII-1	6.8	90.80	3.93	93.45	5.51	66.08	4.12
	VII-2	6.62	90.80	3.93	93.45	5.51	66.08	4.12
	VII-3	7.33	90.80	3.93	93.45	5.51	66.08	4.12
	VII-4	6.49	90.80	3.93	93.45	5.51	66.08	4.12
	VII-5	7.07	90.80	3.93	93.45	5.51	66.08	4.12
	VII-6	7.44	90.80	3.93	93.45	5.51	66.08	4.12
	VII-7	7.16	90.80	3.93	93.45	5.51	66.08	4.12
	VII-8	6.24	90.80	3.93	93.45	5.51	66.08	4.12
Toutanji et al, 2007, SLS	I-3	11.64	144.34	9.66	155.46	13.51	109.93	11.47
	I-4	12.86	157.79	10.56	170.30	14.79	120.42	12.56
	II-1	12.55	88.43	9.77	86.21	14.61	60.96	8.88
	II-2	14.25	101.58	11.22	99.54	16.87	70.39	10.26
	II-3	17.72	113.17	12.49	111.29	18.87	78.70	11.47
	II-4	18.86	123.65	13.65	121.92	20.67	86.21	12.56
	III-1	13.24	82.56	10.53	78.41	16.07	55.44	8.88

	III-2	15.17	94.81	12.08	90.54	18.55	64.02	10.26
	III-3	18.86	105.59	13.45	101.22	20.74	71.58	11.47
	III-4	19.03	115.35	14.69	110.88	22.72	78.41	12.56
Ueda et al. (1999), DLS	A1	6.25	72.41	5.65	69.72	7.77	49.30	5.61
	A2	9.2	63.10	6.58	59.69	9.08	42.20	5.61
	A3	11.95	63.10	6.58	59.69	9.08	42.20	5.61
	A4	10	86.56	9.29	82.99	13.06	58.68	7.93
	A5	7.3	62.52	6.65	59.01	9.18	41.73	5.61
	A7	16.25	86.85	9.26	83.34	13.01	58.93	7.93
	A8	11	62.41	6.66	58.93	9.20	41.67	5.61
	A9	10	63.48	6.54	60.12	9.01	42.51	5.61
	A10	2.4	71.95	1.26	69.18	1.85	48.92	1.32
	A11	5.35	71.95	2.46	69.18	3.55	48.92	2.54
	A12	9.25	122.14	4.17	119.83	6.15	84.73	4.40
	A13	11.75	155.22	5.39	153.23	8.02	108.35	5.69
Ueda et al. (1999), SLS	B1	20.6	71.29	10.22	69.05	16.31	48.83	11.65
	B2	38	106.73	19.77	103.23	32.73	72.99	20.19
	B3	34.1	103.75	20.38	100.12	33.75	70.80	20.19

APPENDIX D

Derivation of the Modified CEB Model

1. DERIVATION OF EQUATION (6.69)

The general First-order nonlinear ordinary differential equation solution of the Equation (6.69) is:

$$\frac{ds}{dx} = \sqrt{\frac{2\rho_1 K}{(1+\alpha)}} . s^{\frac{1+\alpha}{2}}$$

Prove:

$$\frac{d^2 s}{dx^2} = a . s^b \tag{1}$$

Where,

$$a = \rho_1 K, b = \alpha \tag{2}$$

The First-order nonlinear ordinary differential equation solution of the Equation (1) is (Equation (3)):

$$\frac{ds}{dx} = \sqrt{\frac{2a}{1+b}} . s^{\frac{1+b}{2}} \tag{3}$$

Using the general solution of the First-order nonlinear ordinary differential equation solution as addressed in Equation (1) to solve Equation (6.69) gives:

$$\frac{ds}{dx} = \sqrt{\frac{2\rho_1 K}{(1+\alpha)}} . s^{\frac{1+\alpha}{2}} \tag{4}$$

$$\frac{d^2 s}{dx^2} = \sqrt{\frac{2\rho_1 K}{(1+\alpha)}} . \left(\frac{1+\alpha}{2}\right) . s^{\frac{\alpha-1}{2}} . \frac{ds}{dx} \tag{5}$$

$$\frac{d^2 s}{dx^2} = \sqrt{\frac{2\rho_1 K}{(1+\alpha)}} . \left(\frac{1+\alpha}{2}\right) . s^{\frac{\alpha-1}{2}} . \sqrt{\frac{2\rho_1 K}{(1+\alpha)}} . s^{\frac{1+\alpha}{2}} \tag{6}$$

$$\frac{d^2 s}{dx^2} = \frac{2\rho_1 K}{(1+\alpha)} . \left(\frac{1+\alpha}{2}\right) . s^{\left(\frac{\alpha-1+\alpha+1}{2}\right)} \tag{7}$$

The form of Equation (6.69) is:

$$\frac{d^2s}{dx^2} = K.\rho_1.s^{\alpha}$$

2. SOLUTION OF EQUATION (6.70)

$$\frac{ds}{dx} = \sqrt{\frac{2\rho_1 K}{(1+\alpha)}}\,.s^{\frac{1+\alpha}{2}}$$

Or,

$$\frac{ds}{dx} = a.s^{b} \tag{1}$$

Where,

$$a = \sqrt{\frac{2\rho_1 K}{(1+\alpha)}}, \qquad b = \frac{1+\alpha}{2} \tag{2}$$

Divided both sides by s^b gives (Equation (3)):

$$\frac{\frac{ds}{dx}}{s^b} = a \tag{3}$$

By integrating both sides of Equation (3) with respect x and solving it gives (Equation (4) and (5)):

$$\int \frac{\frac{ds}{dx}}{s^b} d_x = \int a\ d_x \tag{4}$$

$$\frac{s^{-b+1}}{-b+1} = ax + c_1 \tag{5}$$

Solving for s gives (Equation (6)):

$$s = [(b-1)(c_1 - ax)]^{\left[\frac{1}{1-b}\right]} \tag{6}$$

3. **DERIVATION OF EQUATION (6.71):**

The general solution of the first-order nonlinear ordinary differential equation solution is (Equation (1)):

$$s = [(b-1)(c_1 - ax)]^{\left[\frac{1}{1-b}\right]} \tag{1}$$

Boundary condition

$$x = 0,\ s = 0 \rightarrow \begin{cases} x = 0 \\ s(x) = 0 \end{cases} \tag{2}$$

Subsisting the boundary condition into the Equation (2) gives:

$$0 = [(b-1)(c_1 - 0)]^{\left[\frac{1}{1-b}\right]} \tag{3}$$

$$0 = [(b-1)(c_1)]^{\left[\frac{1}{1-b}\right]} \tag{4}$$

$$0 = \left[\left(\frac{1+\alpha}{2} - 1\right)(c_1)\right]^{\left[\frac{1}{1-b}\right]} \tag{5}$$

$$0 = \left[\left(\frac{\alpha - 1}{2}\right)(c_1)\right]^{\left[\frac{1}{1-b}\right]} \tag{6}$$

$$\therefore\ c_1 = 0 \tag{7}$$

$$s = [(b-1)(-ax)]^{\left[\frac{1}{1-b}\right]} \tag{8}$$

$$s = [(1-b)(ax)]^{\left[\frac{1}{1-b}\right]} \tag{9}$$

$$s = \left[\left(1 - \frac{1+\alpha}{2}\right)\left(\sqrt{\frac{2\rho_1 K}{(1+\alpha)}}x\right)\right]^{\left[\frac{1}{1-b}\right]} \tag{10}$$

Or,

$$s = \left[\left(\frac{1-\alpha}{2}\right)\left(\sqrt{\frac{2\rho_1 K}{(1+\alpha)}}x\right)\right]^{\left[\frac{1}{1-b}\right]} \tag{11}$$

$$s = \left[\left(\sqrt{\frac{(1-\alpha)^2\rho_1 K}{2\,(1+\alpha)}}\,x\right)\right]^{\left[\frac{2}{1-\alpha}\right]} \tag{12}$$

The final form of Equation (6.71) is:

$$s = \left(\frac{K\rho_1(1-\alpha)^2}{2(1+\alpha)}\right)^{\frac{1}{1-\alpha}} . x^{\frac{2}{1-\alpha}}$$

4. DERIVATION OF EQUATION (6.93)

The full derivation of this equation (Equation (6.93)) was obtained using wolfram alpha software as shown:

$$\frac{d^2s}{dx^2} = K\,(\rho_2 - \rho_3 . s) \tag{1}$$

Or,

$$\frac{d^2s}{dx^2} = K\rho_2 - K\rho_3 . s \tag{2}$$

The Equation (2) can be written as:

$$\frac{d^2s}{dx^2} = a - b . s \tag{3}$$

Where,

$$a = K\rho_2, b = K\rho_3 \tag{4}$$

The general solution of the second-order nonlinear nonhomogeneous differential equation solution of (4)

$$s = B_1 \sin\left(x\sqrt{b}\right) + B_2 \cos\left(x\sqrt{b}\right) + \frac{a}{b}$$

Prove:

$$\frac{d^2s}{dx^2} = a - b . s \tag{1}$$

The general solution will be the sum of the complementary solution and particular solution:

complementary solution:

$$\frac{d^2s}{dx^2} + b.s = 0 \quad (2)$$

Assume a solution will be proportional to $e^{\lambda x}$ for some constant:

Substitute $s = e^{\lambda x}$ into the differential equation (Equation (2)) gives (Equation (3)):

$$\frac{d^2}{dx^2}\left(e^{\lambda x}\right) + b.e^{\lambda x} = 0 \quad (3)$$

Where,

$$\frac{d^2}{dx^2}\left(e^{\lambda x}\right) = \lambda^2 e^{\lambda x} \quad (4)$$

Substitute Equation (4) into Equation (3) gives (Equation (5)):

$$\lambda^2 e^{\lambda x} + b.e^{\lambda x} = 0 \quad (5)$$

Or,

$$(\lambda^2 + b)e^{\lambda x} = 0 \quad (6)$$

Since $e^{\lambda x} \neq 0$ for any finite λ, the zero must come from the polynomial:

$$\lambda^2 + b = 0 \quad (7)$$

Solving for λ:

$$\lambda = i\sqrt{b} \text{ or } \lambda = -i\sqrt{b} \quad (8)$$

The root $\lambda = -i\sqrt{b}$ gives (Equation (9)):

$$s_1 = c_1 e^{-i\sqrt{b}x} \quad (9)$$

Where, c_1 is constant.

The root $\lambda = i\sqrt{b}$ gives (Equation (10)):

$$s_2 = c_2 e^{i\sqrt{b}x} \quad (10)$$

Where, c_2 is constant.

The general solution is the sum of the Equation (9) and Equation (10) as (Equation (11)):

$$s = s_1 + s_2 = \frac{c_1}{e^{i\sqrt{b}x}} + c_2 e^{i\sqrt{b}x} \quad (11)$$

Applying Euler's identity (Equation (12)):

$$e^{\alpha+i\beta} = e^{\alpha}\cos\ (\beta) + i\sin(\beta) \quad (12)$$

$$s = c_1\ (\cos(\sqrt{b}\,x) - i\ \sin(\sqrt{b}\,x)\ ) + c_2\ (\cos(\sqrt{b}\,x) + i\ \sin(\sqrt{b}\,x)) \quad (13)$$

Regroup terms as (Equation 14)):

$$s = (c_1 + c_2)\ \cos(\sqrt{b}\,x) + i\ (-c_1 + c_2)\ \sin(\sqrt{b}\,x) \quad (14)$$

Redefine $(c_1 + c_2)$ as B_1 and $i\ (-c_1 + c_2)$ as B_2, Sine these are the constant. By Substituting these constant in Equation (14) gives (Equation (15)):

$$s_c = B_1\cos(\sqrt{b}\,x) + B_2\sin(\sqrt{b}\,x) \quad (15)$$

Particular solution:

Determinate the particular solution to (Equation (16))

$$\frac{d^2s}{dx^2} + b.s = a \quad (16)$$

By using the method of undetermined coefficient as (Equation (17)):

$$s_P = P_1 \quad (17)$$

Where,

$$\frac{d^2s_p}{dx^2} = \frac{d^2}{dx^2}\ (P_1) = 0 \quad (18)$$

Substitute Equation (17) into Equation (16) gives (Equation (19)):

$$b.P_1 = a \quad (19)$$

Or,

$$P_1 = \frac{a}{b} \quad (20)$$

Substitute Equation (20) into Equation (17) gives (Equation (21)):

$$s_P = \frac{a}{b} \quad (21)$$

The general solution of Equation (6.93) is (Equation (22)):

$$s = s_c + s_p = B_1 \cos(\sqrt{b}\, x) + B_2 \sin(\sqrt{b}\, x) + \frac{a}{b} \tag{22}$$

So,

The final form of Equation (6.93) is:

$$s = B_1 \sin\left(x\sqrt{K\rho_3}\right) + B_2 \cos\left(x\sqrt{K\rho_3}\right) + \frac{\rho_2}{\rho_3}$$

5. **DERIVATION OF EQUATION (6.99)**

$$F_d = \int_{l1}^{x} \tau_f \,.\, d_x \tag{1}$$

$$F_d = b_f \int_{l1}^{x} (\rho_2 - \rho_3 s).\, d_x \tag{2}$$

$$F_d = b_f \left\{ \rho_2 x|_{l1}^{x} - \rho_3 \int_{l1}^{x} s \,.\, d_x \right\} \tag{3}$$

By subsisting Equation (6.93) into Equation (3) gives:

$$F_d = b_f \left\{ \rho_2 (x - l_1) - \rho_3 \int_{l1}^{x} B_1 \sin\left(x\sqrt{k}\rho_3\right) + B_2 \cos\left(x\sqrt{k}\rho_3\right) + \frac{\rho_2}{\rho_3}.\, d_x \right\} \tag{5}$$

$$F_d = b_f \left\{ \rho_2 (x - l_1) - \rho_3 \left(\frac{-B_1 \cos\left(x\sqrt{k}\rho_3\right)}{\sqrt{k}\rho_3} + \frac{B_2 \sin\left(x\sqrt{k}\rho_3\right)}{\sqrt{k}\rho_3} \Bigg|_{l2}^{x} + \frac{\rho_2}{\rho_3} x|_{l1}^{x} \right) \right\} \tag{6}$$

$$F_d = b_f \rho_2 (x - l_1) + \frac{b_f \rho_3}{\sqrt{k}\rho_3} \cos\left(x\sqrt{k}\rho_3\right) \Bigg|_{l2}^{x} - \frac{b_f \rho_3}{\sqrt{k}\rho_3} \sin\left(x\sqrt{k}\rho_3\right) \Bigg|_{l2}^{x} - b_f \rho_2 (x - l_1) \tag{7}$$

The final from of Equation (6.99) is:

$$F_d = \frac{b_f \rho_3}{\sqrt{K\rho_3}} \left(B_1 \left[\cos\left(x\sqrt{K\rho_3}\right) - \cos\left(I_1\sqrt{K\rho_3}\right) \right] - B_2 \left[\sin\left(x\sqrt{K\rho_3}\right) - \sin\left(I_1\sqrt{K\rho_3}\right) \right] \right)$$

APPENDIX E

Data of Externally Bond of FRP Shear Strengthening for RC Beams

Table (1)

Reference	No.	Name	FRP	FRP shear strength		
				Exp	This study	ACI 2008
Khalifa et al, 2000	1	BT2	CS-U	65	29.42	76.8
	2	BT4	S50 mm@125-U	72	29.50	30.7
	3	BT5	S50 mm@125-S	31.5	21.52	23.6
Khalifa et al, 2002	4	SW3-2	CS- U/S	50.5	33.67	53.1
	5	SW4-2	CS-U/S	80.5	33.67	53.1
	6	SO3-3	S75 mm @125-U	56.5	25.69	40.4
	7	SO3-4	CS-U	67.5	33.76	67.3
	8	SO3-5	CS- U/S	92.5	39.05	67.3
Barros et al, 2006	9	A10_M	S25 mm@190-U	10.8	10.67	21.2
	10	A12_M	S25 mm@95-U	31.5	19.79	42.5
Diagana et al, 2003	11	PU1	S40mm@200-U	32	25.17	30.7
	12	PU2	S40mm@250-U	20	20.65	24.6
	13	PU3	S40mm@300-U	44.5	20.13	29
	14	PU4	S40mm@350-U	40	17.52	24.8
Pellegrino et al, 2002	15	TR30C2	CS-S	45.3	18.39	44.2
	16	RS90-1	S50@100-U	34.25	22.72	34.4
	17	RS90-2	S50@100-U	41.75	22.72	34.4
	18	RS45-1	S50@100-U	40.75	27.94	43.3
Carolin and Täljsten, 2005	19	A145	CS-S	128	144.37	57.56
	20	A245a	CS-S	138	89.73	90.44
	21	A245b	CS-S	186	81.09	90.44
	22	A245Ra	CS-S	187	87.96	90.44
	23	A245Rb	CS-S	132	77.74	90.44
	24	A290a	CS-S	137	75.25	41.32
	25	A290b	CS-S	179	72.01	41.32
	26	A290W	CS-W	248	116.66	41.32
	27	A290WR	CS-W	269	116.66	41.32
	28	B290	CS-S	61	49.94	33.06
Bousselham and	29	SBS01L	CS-U	23.2	16.43	8.08

Chaallal, 2006a	30	SBS02L	CS-U	32.4	17.51	9.16
Feng et a, 2004 Cited in Sas (2011)	31	SB1_3	CS-U	63.5	57.83	43.39
	32	SB1_4	CS-U	76.5	57.83	43.39
	33	SB1_6	CS-U	53.5	28.45	14.46
	34	SB1_7	CS-U	63.5	28.45	14.46
	35	SB1_8	S40@100-U	62.5	28.45	14.46
	36	SB1_9	S40@100-U	63.5	33.33	16.20
	37	SB1_10	S40@100-U	66.5	33.33	16.20
	38	SB2_3	S40@100-U	52	28.45	14.46
	39	SB3_2	S40@100-U	35	28.45	14.46
	40	SB3_3	S40@100-U	54	28.45	14.46
Beber, 2005	41	V17_A	S50@100-U	45.87	24.49	12.30
	42	V11_A	S50@100-U	41.51	24.49	12.30
	43	V17_B	S50@100-U	36.01	24.49	12.30
	44	V18_A	S50@100-W	70.37	53.50	12.30
	45	V20_A	S50@100-W	83.2	53.50	12.30
	46	V12_B	S50@141.4-S	44.73	32.19	26.84
	47	V16_B	CS-U	55.51	36.51	24.59

Note: CS= continuous FRP sheet, S= FRP strips, U= U strengthening shape, S=side bonds, W=closed strengthening shape

Data of Externally Bond of FRP Shear Strengthening for lightweight RC Beams

Table (2)

Asghari, 2014	N0.	Name	FRP	Ex FRP Shear strength	This study
	1	CONa-VW(C)	CS50-S	155	109.46
	2	CONa-DW(C)	CS50-5	194	176.66
	3	CONa-VS2	CS50-S	104	111.78
	4	CONa-DS	CS50-S	130	156.46

APPENDIX E

Data of Externally Bond of FRP Shear Strengthening for RC Beams

Table (1)

Reference	No.	Name	FRP	FRP shear strength		
				Exp	This study	ACI 2008
Khalifa et al, 2000	1	BT2	CS-U	65	29.42	76.8
	2	BT4	S50 mm@125-U	72	29.50	30.7
	3	BT5	S50 mm@125-S	31.5	21.52	23.6
Khalifa et al, 2002	4	SW3-2	CS- U/S	50.5	33.67	53.1
	5	SW4-2	CS-U/S	80.5	33.67	53.1
	6	SO3-3	S75 mm @125-U	56.5	25.69	40.4
	7	SO3-4	CS-U	67.5	33.76	67.3
	8	SO3-5	CS- U/S	92.5	39.05	67.3
Barros et al, 2006	9	A10_M	S25 mm@190-U	10.8	10.67	21.2
	10	A12_M	S25 mm@95-U	31.5	19.79	42.5
Diagana et al, 2003	11	PU1	S40mm@200-U	32	25.17	30.7
	12	PU2	S40mm@250-U	20	20.65	24.6
	13	PU3	S40mm@300-U	44.5	20.13	29
	14	PU4	S40mm@350-U	40	17.52	24.8
Pellegrino et al, 2002	15	TR30C2	CS-S	45.3	18.39	44.2
	16	RS90-1	S50@100-U	34.25	22.72	34.4
	17	RS90-2	S50@100-U	41.75	22.72	34.4
	18	RS45-1	S50@100-U	40.75	27.94	43.3
Carolin and Täljsten, 2005	19	A145	CS-S	128	144.37	57.56
	20	A245a	CS-S	138	89.73	90.44
	21	A245b	CS-S	186	81.09	90.44
	22	A245Ra	CS-S	187	87.96	90.44
	23	A245Rb	CS-S	132	77.74	90.44
	24	A290a	CS-S	137	75.25	41.32
	25	A290b	CS-S	179	72.01	41.32
	26	A290W	CS-W	248	116.66	41.32
	27	A290WR	CS-W	269	116.66	41.32
	28	B290	CS-S	61	49.94	33.06
Bousselham and	29	SBS01L	CS-U	23.2	16.43	8.08

Chaallal, 2006a	30	SBS02L	CS-U	32.4	17.51	9.16
Feng et a, 2004 Cited in Sas (2011)	31	SB1_3	CS-U	63.5	57.83	43.39
	32	SB1_4	CS-U	76.5	57.83	43.39
	33	SB1_6	CS-U	53.5	28.45	14.46
	34	SB1_7	CS-U	63.5	28.45	14.46
	35	SB1_8	S40@100-U	62.5	28.45	14.46
	36	SB1_9	S40@100-U	63.5	33.33	16.20
	37	SB1_10	S40@100-U	66.5	33.33	16.20
	38	SB2_3	S40@100-U	52	28.45	14.46
	39	SB3_2	S40@100-U	35	28.45	14.46
	40	SB3_3	S40@100-U	54	28.45	14.46
Beber, 2005	41	V17_A	S50@100-U	45.87	24.49	12.30
	42	V11_A	S50@100-U	41.51	24.49	12.30
	43	V17_B	S50@100-U	36.01	24.49	12.30
	44	V18_A	S50@100-W	70.37	53.50	12.30
	45	V20_A	S50@100-W	83.2	53.50	12.30
	46	V12_B	S50@141.4-S	44.73	32.19	26.84
	47	V16_B	CS-U	55.51	36.51	24.59

Note: CS= continuous FRP sheet, S= FRP strips, U= U strengthening shape, S=side bonds, W=closed strengthening shape

Data of Externally Bond of FRP Shear Strengthening for lightweight RC Beams

Table (2)

Asghari, 2014	N0.	Name	FRP	Ex FRP Shear strength	This study
	1	CONa-VW(C)	CS50-S	155	109.46
	2	CONa-DW(C)	CS50-5	194	176.66
	3	CONa-VS2	CS50-S	104	111.78
	4	CONa-DS	CS50-S	130	156.46